# “Energy and mass balance modelling for glaciers on the Tibetan Plateau
-
# Extension, validation and application of a coupled snow and energy balance model“

Von der Fakultät für Georessourcen und Materialtechnik

der Rheinisch-Westfälischen Technischen Hochschule Aachen

zur Erlangung des akademischen Grades eines

**Doktors der Naturwissenschaften**

genehmigte Dissertation

vorgelegt von **M.A.**

**Eva Huintjes**

aus Aachen

**Berichter:** Univ.-Prof. Dr. rer. nat. Christoph Schneider
Univ.-Prof. Dr. phil. Dieter Scherer

Tag der mündlichen Prüfung: 16. Oktober 2014

Tashi Dor Monastery at Nam Co, April 2009.

„Die Berge,
die es zu versetzen gilt,
sind in unserem Bewusstsein.“
(R. Messner)

# Abstract

The Tibetan Plateau is the source region of five of the largest Asian rivers. The large amount of ice, snow and permafrost on the plateau and its surrounding mountain ranges and the stored water therein is important in sustaining seasonal water availability. According to the overall trend of increasing air temperatures on the Tibetan Plateau and its adjacent areas since several decades, most glaciers are retreating. The regional patterns of glacier change are contrasting, influenced by local factors and the spatial and temporal heterogeneity of climate and climate variability. The individual feedback mechanisms between atmosphere and glacier, and the role of the various components of the glacier surface energy and mass balance in the melt process for different climate regions on the Tibetan Plateau have not yet been analysed in detail.

This thesis deals with the modelling of glacier surface energy and mass balances on the Tibetan Plateau. Four glaciers and one ice cap on the plateau and its surrounding mountain ranges form the regional study sites: Zhadang glacier (south eastern Tibetan Plateau), Purogangri ice cap (central plateau), Naimona'nyi glacier (western Himalayas), Halji glacier (western Himalayas) and Muztag Ata glacier (eastern Pamirs). The study sites have a maximum distance of ≈1700 km from each other and are located in different climate regions. As it is the case for most remote regions of the world, data availability from in-situ observations is insufficient for more complex, physically-based glacier energy and mass balance models. Hence, we use the in-situ measurement data from the intensive observation period at Zhadang glacier to evaluate the surface energy and mass balance model performance in detail. For decadal model simulations high resolution atmospheric model data from the *High Asia Reanalysis* is applied. The model scheme couples the atmospheric energy balance to a subsurface multi-layer snow module in order to analyse the atmosphere-cryosphere interactions.

For Zhadang glacier the different model components are thoroughly validated using different methods and data sources. The installed complex monitoring system including a time-lapse camera system at Zhadang glacier is the first of its kind on the Tibetan Plateau. It provides an excellent data base for model evaluation and provides new opportunities for further analysis. The developed surface energy and mass balance model is applied to the five study sites. From every regional study we obtain a 10-year time series of glacier-wide surface energy and mass balance components. At each study site model results are compared to either in-situ meteorological or glaciological data or remote sensing analyses which provide evidence for further constraints regarding the tuning parameters of the modelling chain. This is the largest and most detailed homogeneous glaciological data set from the Tibetan Plateau so far regarding the modelling of surface energy and mass balance. The thesis contributes to a further and detailed understanding of the role of the various energy and mass balance components for glacier change in the different climate regions of the Tibetan Plateau. It serves to increase knowledge on the various driving mechanisms for the energy and mass balance components. The findings are crucial for estimating future glacier evolution. It forms the basis for further analysis and research on glacier related water availability on the Tibetan Plateau.

## Zusammenfassung

Das Tibetische Plateau ist Quellgebiet von fünf der größten Flüsse Asiens. Das in den großen Eis-, Schnee- und Permafrostgebieten auf dem Plateau und den angrenzenden Gebirgszügen gespeicherte Wasser ist wichtig, um die saisonale Wasserverfügbarkeit zu gewährleisten. Aufgrund der in den letzten Jahrzehnten steigenden Temperaturen verlieren viele der Gletscher an Masse. Die regionalen Muster der Gletscherveränderungen sind gegensätzlich, beeinflusst von lokalen Faktoren, sowie der räumlichen und zeitlichen Heterogenität des Klimas und seiner Variabilität. Die verschiedenen Rückkopplungen zwischen Atmosphäre und Gletschern, sowie die Rolle der einzelnen Komponenten der Energie- und Massenbilanz der Gletscher im Schmelzprozess innerhalb der verschiedenen Klimaregionen auf dem Tibetischen Plateau wurden bislang noch nicht detailliert betrachtet.

Die vorliegende Arbeit beschäftigt sich mit der Modellierung von Oberflächenenergie- und -massenbilanzen von Gletschern auf dem Tibetplateau. Vier Gletscher und eine Eiskappe in verschiedenen Regionen des Plateaus und der umliegenden Gebirgszüge dienen als regionale Beispiele: Zhadang Gletscher (südöstliches Tibetplateau), Purogangri Eiskappe (zentrales Tibetplateau), Naimona'nyi Gletscher (westlicher Himalaya), Halji Gletscher (westlicher Himalaya) und Muztagh Ata Gletscher (östlicher Pamir). Die Untersuchungsgebiete liegen in einer maximalen Entfernung von ≈1700 km zueinander und befinden sich in unterschiedlichen Klimaregionen. Wie in den meisten abgelegenen Regionen der Erde ist die Datenverfügbarkeit aus lokalen Messungen für die Verwendung in komplexen, physikalisch basierten Gletscherenergie- und –massenbilanzmodellen unzureichend. Wir verwenden Daten aus lokalen Messungen einer Intensivmesskampagne am Zhadang Gletscher um das Ergebnis des entwickelten Energie- und Massenbilanzmodells im Detail zu validieren. Für 10-jährige Modellläufe werden hoch aufgelöste atmosphärische Modelldaten der *High Asia Reanalysis* verwendet. Das Modellschema koppelt die atmosphärische Energiebilanz mit einem mehrschichtigen Schneemodul, um die Wechselbeziehungen zwischen Atmosphäre und Kryosphäre zu analysieren.

Am Beispiel des Zhadang Gletschers werden die verschiedenen Modellkomponenten anhand unterschiedlichster Methoden und Datengrundlagen validiert. Die am Zhadang Gletscher installierte komplexe Messapparatur beinhaltet ein Zeitraffer-Kamerasystem, welches das erste dieser Art auf dem Tibetischen Plateau ist. Es bietet eine exzellente Datengrundlage für die Modellevaluierung und eröffnet neue Möglichkeiten für weitergehende Analysen. Das entwickelte Gletscherenergie- und -massenbilanzmodell wird auf alle fünf Untersuchungsgebiete angewendet, um eine 10-jährige Zeitreihe aller Energie- und Massenbilanzkomponenten zu erzeugen. Für jedes Untersuchungsgebiet werden die Modellergebnisse mit meteorologischen oder glaziologischen Messungen oder Ergebnissen aus Fernerkundungsstudien verglichen und so das mögliche Parameterset zur Modellabstimmung eingeschränkt. Dies ist der bislang größte und detaillierteste homogene glaziologische Datensatz auf dem Tibetischen Plateau bezüglich der Komponenten der Energie- und Massenbilanz von Gletschern. Somit trägt diese Arbeit zu einem besseren Verständnis der Rolle der einzelnen Energie- und Massenbilanzkomponenten für die Gletscherveränderung in verschiedenen Klimaregionen auf dem Tibetplateau bei. Sie dient weiterhin dazu, das Wissen über die verschiedenen Antriebsmechanismen der Gletscherenergie- und -massenbilanzkomponenten zu erweitern. Dieser Aspekt ist entscheidend, um Angaben über die zukünftige Gletscherentwicklung zu treffen. Sie bildet die Basis für weitergehende Analysen, die die Einflüsse von Gletschern auf die Wasserverfügbarkeit in Tibet untersuchen.

## Acknowledgements

During the last years lots of people supported me in their very own way.

First of all I thank Christoph Schneider for being a great supervisor. Thank you for your trust, your good ideas, the endless support and last but not least for the opportunity to work at such an overwhelming place like Tibet.

I am especially thankful to Tobias Sauter from whom I learned so much over the past years. He is largely responsible for the development and the programming of the MB model applied in this thesis.

Many thanks to Thomas Mölg and to Peter Kuipers Munneke for supporting me in the model development and for being available for my questions.

Thanks to Thomas Foken, Wolfgang Babel and Tobias Biermann from Bayreuth for their support with the EC data and for having a great time not only in Bayreuth.

I thank my present and former colleagues in Aachen for the pleasant atmosphere, the enriching discussions and the great support throughout the years: Gunnar, Elke, Tobias, Marco, Lars, Stephanie, Marinka, Georg, Oliver, Katja, Isabell, Timo, Mareike, Bastian, Achim, Hendrik, Miriam. A special thank you goes to you, Gunnar, for being always around for any kind of questions, good advice, motivation or just a nice chat. Thank you Gernot for the perfect IT support!

Thanks to my colleagues in the WET and DynRG-TiP projects and my fellow travellers during various field campaigns to Tibet for the great support: Fabien, Dieter, Niklas, Nicolai, Sophie, Benny, Tobias, Christoph, Manfred B., Tino, Jan K., Marinka, Julia, Frank, Manfred F., Volker, Holm, Jochen.

Many thanks to my Chinese colleagues for the scientific collaboration and for the successful organization of various field campaigns: Yang Wei, Liu Xiaobo, Zhang Guoshuai.

Unschätzbarer Dank gilt meiner Familie und meinen Freunden, die mich in den letzten Jahren immer begleitet und unterstützt haben.

Thanks to IT for arranging everything so perfectly.

# Content

**Content** i

**List of figures** iv

**List of tables** xi

**List of acronyms, symbols and abbreviations** xiii

**1 Introduction** 1

1.1 Motivation and intention 1

1.2 Thesis outline and published research papers 2

1.3 Current state of research 5

1.3.1 Present atmospheric circulation patterns over the Tibetan Plateau and its surroundings 5

1.3.2 Climate and glacier change on the Tibetan Plateau and adjacent areas since the Little Ice Age 7

1.3.3 Comprehensive physical geography of the Tibetan Plateau 10

1.3.4 Methodological background 15

1.3.4.1 Glacier surface energy balance 15

1.3.4.2 Glacier mass balance 17

1.3.5 Characteristics of glaciers on the Tibetan Plateau 21

1.4 Study sites 22

1.4.1 Regional climate setting and glacier characteristics of the study sites 22

1.4.2 In-situ measurements 30

1.4.2.1 Zhadang glacier 30

1.4.2.2 Naimona'nyi glacier 35

**2 Evaluation of a coupled snow and energy balance model for Zhadang glacier, southern central Tibetan Plateau, using glaciological measurements and time-lapse photography** 41

2.1 Introduction and regional climate conditions 41

2.2 Data basis 44

2.2.1 In-situ measurements relevant for the SEB/MB model 44

2.2.2 Time-lapse photography 45

2.2.3 High Asia Reanalysis 45

2.3 Methods 47

2.3.1 SEB/MB modelling 48

2.3.2 Image processing 53

2.4 Results and Discussion 54

2.4.1 MB model calibration and uncertainty assessment 55

2.4.2 MB model performance 55

2.4.2.1 AWS driven point MB model 55

2.4.2.2 HAR driven point MB model 56

2.4.2.3 Density profiles from the point MB model 58
2.4.2.4 Evaluation of the distributed MB model with ablation stakes 59
2.4.2.5 Evaluation of the distributed MB model using time-lapse photography 61
2.4.3 SEB/MB from the AWS driven distributed model 2009-2012 63
2.4.4 Snow line characteristics from the AWS driven distributed model 2010-2012 67
2.4.5 Strong ablation event in winter 83
2.4.6 SEB/MB characteristics for the WRF driven model 2001-2011 92
2.5 Discussion of uncertainties 98
2.6 Conclusion regarding model results for Zhadang glacier 99

**3 Energy and mass balance for Purogangri ice cap, central Tibetan Plateau, 2000-2011 103**
3.1 Introduction and regional climate conditions 103
3.2 Data basis 104
3.3 Initialisation of the SEB/MB model for application at Purogangri ice cap 106
3.4 Results and discussion 106
3.4.1 SEB/MB characteristics 2000-2011 107
3.4.2 Snow line and ELA characteristics 2000-2011 114
3.5 Conclusion regarding model results for Purogangri ice cap 118

**4 Energy and mass balance for Naimona'nyi glacier, south western Tibetan Plateau, 2000–2012 121**
4.1 Introduction and regional climate conditions 121
4.2 Data basis 122
4.3 Initialisation of the SEB/MB model for application at Naimona'nyi glacier 124
4.4 Results and discussion 124
4.4.1 SEB/MB characteristics 2000-2012 125
4.4.2 Snow line and ELA characteristics 2000-2012 132
4.5 Discussion of uncertainties 134
4.6 Conclusion regarding model results for Naimona'nyi glacier 138

**5 Energy and mass balance for Halji glacier, north western Nepal, 2000-2011, as derived from a coupled snow and energy balance model 141**
5.1 Introduction and regional climate conditions 141
5.2 Data basis 142
5.3 Initialisation of the SEB/MB model for application at Halji glacier 144
5.4 Results and discussion 144
5.4.1 SEB/MB characteristics 2000-2011 145
5.4.2 Snow line and ELA characteristics 2000-2011 151
5.5 Discussion of uncertainties and comparison to measured elevation changes 154
5.6 Conclusion regarding model results at Halji glacier 159

**6 Energy and mass balance for a glacier in the Muztagh Ata region, north western Tibetan Plateau, 2000-2012** **161**

6.1 Introduction and regional climate conditions 161

6.2 Data basis 162

6.3 Initialisation of the SEB/MB model for the application at Muztagh Ata glacier 163

6.4 Results and discussion 164
6.4.1 SEB/MB characteristics 2000-2012 164
6.4.2 Snow line and ELA characteristics 2000-2012 171

6.5 Discussion of uncertainties 173

6.6 Conclusion regarding model results for Muztagh Ata region 174

**7 Comparison and interpretation of the glacier characteristics at the five study sites on the Tibetan Plateau, 2001-2012** **175**

7.1 Comparison and interpretation of the SEB and MB components at the five study sites, 2001-2012 175

7.2 Air temperature, precipitation and MB at the five study sites and their link to atmospheric teleconnection patterns, 2001-2012 184
7.2.1 Description of the chosen teleconnection patterns 184
7.2.2 Seasonal influences of the teleconnection patterns at the study sites 186
7.2.3 Summary regarding the influences of teleconnection patterns on glacier mass balance at the study sites 192

**8 Overall conclusion** **193**

**References** **199**

**Appendix** **215**

A Monthly glacier-wide SEB/MB components for the model runs with precipitation scaling factors 0.31 and 0.81 for the four glaciers and ice caps, 2000-2012 216

B Comparison of monthly glacier-wide SEB and MB components for the five glaciers and ice caps, 2000-2012 220

C Monthly indices for selected teleconnection patterns, 2000-2012 222

# List of figures

**Chapter 1**

Fig. 1.1: Map of the Tibetan Plateau with main mountain ridges, natural regions, climate zones, important ice core sites and location of the study areas of this thesis 5

Fig. 1.2: Examples of the schematic representation of the wind systems influencing the climate of the TP 6

Fig. 1.3: Schematic representation of main wind directions in Central Asia and adjacent areas 7

Fig. 1.4: Elevation history of the Tibetan Plateau. Solid lines show the development of the 4000 m contour as derived from oxygen-isotope data from sedimentary basins 11

Fig. 1.5: Schematic picture of the major energy fluxes at the glacier surface 17

Fig. 1.6: Components of the mass balance of a glacier 18

Fig. 1.7: Glacial mass balance components considered in the MB model applied in this thesis 18

Fig. 1.8: Stake measurements of seasonal MB in a year of positive and a year of negative surface MB, with no superimposed ice 20

Fig. 1.9: Classification of glacier accumulation regimes according to precipitation seasonality 23

Fig. 1.10: Glacier hypsometry and climate chart for Zhadang glacier 24

Fig. 1.11: Wind direction and intensity from hourly HAR data at Zhadang glacier for summer and winter season between October 2001 and September 2011 24

Fig. 1.12: Glacier hypsometry and climate chart for Halji glacier 26

Fig. 1.13: Wind direction and intensity from hourly HAR data at Halji glacier for summer and winter season between October 2000 and September 2011 26

Fig. 1.14: Glacier hypsometry and climate chart for Naimona'nyi glacier 27

Fig. 1.15: Wind direction and intensity from hourly HAR data at Naimona'nyi glacier for summer and winter season between October 2000 and September 2012 27

Fig. 1.16: Glacier hypsometry and climate chart for Purogangri ice cap 29

Fig. 1.17: Wind direction and intensity from hourly HAR data at PIC for summer and winter season between October 2000 and September 2011 29

Fig. 1.18: Glacier hypsometry and climate chart for Muztagh Ata glacier 30

Fig. 1.19: Wind direction and intensity from hourly HAR data at Muztagh Ata glacier for summer and winter season between October 2000 and September 2012 30

Fig. 1.20: Daily mean air and ice temperatures at AWS1 on Zhadang glacier, 2009-2011 32

Fig. 1.21: Wind direction and intensity from hourly observations at AWS1 (Zhadang glacier) for summer and winter season between 27 April 2009 and 10 June 2012 33

Fig. 1.22: Comparison of different published glacier outlines for Zhadang glacier 33

Fig. 1.23: Ranges of electrical conductivity for aqueous solutions at 25°C 34

Fig. 1.24: Measurements of electrical conductivity in melt water channels in the forefield of Zhadang glacier, May / October 2010 and May 2011 35

Fig. 1.25: Daily mean values of air temperature, relative humidity, shortwave incoming radiation, wind speed and longwave incoming radiation at the AWS at Naimona'nyi glacier 37

Fig. 1.26: Differences in hourly mean air temperature between the AWS at Naimona'nyi glacier and the respective HAR grid cell 38

Fig. 1.27: Wind direction and intensity from daily AWS data (2.2 m, Naimona'nyi glacier) for summer and winter season between September 2011 and August 2012 38

Fig. 1.28: Qualitative comparison of the retreat of the dead ice body at Naimona'nyi glacier between September 2011 and August 2012 39

Fig. 1.29: Qualitative comparison of the glacier surface elevation change at the tongue of Naimona'nyi glacier between September 2011 and August 2012 39

Fig. 1.30: Daily mean ice temperatures in three depths and AWS air temperature at an ice cored moraine west of Naimona'nyi glacier, 10 September 2011 – 20 August 2012 39

**Chapter 2**

Fig. 2.1: Zhadang glacier with glacier outline from 2009 and locations of available measurements and fields of view of the cameras 42

Fig. 2.2: Daily means of incoming shortwave radiation, air temperature, relative humidity, cloud cover fraction, wind speed, air pressure, and daily sums of solid precipitation at AWS1 between 27 April 2009 and 10 June 2012 43

Fig. 2.3: Monthly means or sums (precipitation) of meteorological variables from the HAR dataset at the atmospheric grid cell containing Zhadang glacier (5611 m a.s.l.), October 2001-September 2011 46

Fig. 2.4: Effect of altitude difference between AWS1 and HAR grid cell and its correction for daily mean values 48

Fig. 2.5: Altitude dependency of the HAR variables that serve as input for the MB model at Zhadang glacier 49

Fig. 2.6: Left: Illustration of an SEB model including a multi-layer snow model. Right: Flow chart of the MB model 50

Fig. 2.7: Measured and modelled daily means of incoming longwave radiation and surface albedo at AWS1 between 24 April 2009 and 10 June 2012. 56

Fig. 2.8: Measurements and AWS forced MB model results at AWS1. (a) accumulated surface height change; (b) glacier surface temperature and temperature deviations; (c) subsurface temperature and temperature deviations 57

Fig. 2.9: Measurements and HAR forced MB model results at the location of AWS1. (a) accumulated surface height change; (b) glacier surface temperature and temperature deviations; (c) subsurface temperature and temperature deviations 58

Fig. 2.10: Observed and modelled snow density profiles for 17 May 2010 and 22 May 2011 at Zhadang glacier 59

Fig. 2.11: Observed and modelled surface height change and MB over the available ablation stakes at Zhadang glacier. The MB model is forced with AWS data 60

Fig. 2.12: Observed and modelled surface height change and MB over the available ablation stakes at Zhadang glacier. The MB model is forced with HAR data 60

Fig. 2.13: Mapped and modelled temporal evolution of the mean transient snow line altitude at 16:00 BT for the three ablation seasons at Zhadang glacier 61

Fig. 2.14: Mapped and modelled mean transient snow line altitude in the ablation season in 2010, 2011 and 2012 at 16:00 BT at Zhadang glacier 62

Fig. 2.15: Examples of the direct spatial evaluation of the transient snow line for two days in 2010 and 2011 at Zhadang glacier 63

Fig. 2.16: Modelled vertical profiles of the annual specific mass balance and its components and mean SEB components on Zhadang glacier for the MB years 2009/10 and 2010/11 65

Fig. 2.17: Glacier-wide monthly (a) SEB components and (b) MB components from May 2009 to May 2012 at Zhadang glacier 67

Fig. 2.18: Transient snow line on 4 June 2012 68

Fig. 2.19: Spatial and temporal evolution of the transient snow line at Zhadang glacier 2010 83

Fig. 2.20: Time series of ortho-images of the ablation event in winter 2012 at Zhadang glacier 90

Fig. 2.21: Period of strong ablation in winter 2012 at Zhadang glacier; (a) hourly and daily means of $T_{air}$ and $T_s$, hourly means of $u$ at AWS2; (b) selected MB components at the lowermost pixel of the glacier tongue 91

Fig. 2.22: Two-hourly means for (a) $T_s$, $T_{air}$, $u$ and $RH$, (b) SEB components and (c) MB components during 5-15 March 2012 at the lowermost pixel of the glacier tongue 92

Fig. 2.23: Modelled vertical profiles of the specific mass balance and its components and mean SEB components on Zhadang glacier averaged over the simulation period October 2001 – September 2011 94

Fig. 2.24: Relation between annual MB and AAR at Zhadang glacier, 2001-2011 95

Fig. 2.25: Glacier-wide monthly (a) SEB components and (b) MB components from October 2001 to September 2011 at Zhadang glacier. 95

Fig. 2.26: Glacier-wide annual MB for MB years 2001-2011 estimated by the HAR forced MB model and compared to values from other studies 98

Fig. 2.27: Glacier-wide annual mean differences in SEB components between the results of Mölg et al. (2014) and this study 99

Fig. 2.28: Glacier-wide annual differences in MB components between the results of Mölg et al. (2014) and this study 99

**Chapter 3**

Fig. 3.1: Purogangri Ice Cap with glacier outlines from 2000 104

Fig. 3.2: Monthly means or sums (precipitation) of meteorological variables at the highest and lowest atmospheric grid cell containing Purogangri ice cap, October 2000-September 2011 105

Fig. 3.3: Altitude dependency of the HAR variables that serve as input for the MB model at PIC 106

Fig. 3.4: Modelled vertical profiles of the specific mass balance and its components and mean SEB components at PIC averaged over the simulation period October 2000 – September 2011 108

Fig. 3.5: Glacier-wide monthly (a) SEB components and (b) MB components from October 2000 to September 2011 at PIC (reference run) 110

Fig. 3.6: Glacier-wide annual MB for MB years 2000-2011 estimated by the HAR forced MB model for PIC 113

Fig. 3.7: Mean total surface height change and mean annual MB for the single glaciers of PIC, 2001-2011 113

Fig. 3.8: Spatial comparison of modelled surface height change of PIC for the reference run, 2001-2011, with the results of Neckel et al. (2013) 114

Fig. 3.9: Comparison of modelled mean intra-annual snow line pattern at PIC, 2001-2011, with the results of Spieß et al. (2014) 116

Fig. 3.10: Comparison of modelled annual ELA at PIC, 2000-2011, with the results of Spieß et al. (2014) 117

Fig. 3.11: Relation between annual MB and AAR at PIC, 2001-2011, for the MB model run with a precipitation scaling factor of 0.56 118

**Chapter 4**

Fig. 4.1: Naimona'nyi glacier with glacier outlines from 2005 122

Fig. 4.2: Monthly means or sums (precipitation) of meteorological variables at the atmospheric grid cell containing Naimona'nyi glacier, October 2000-September 2012 123

Fig. 4.3: Altitude dependency of the HAR variables that serve as input for the MB model at Naimona'nyi glacier 124

Fig. 4.4: Modelled vertical profiles of the specific mass balance and its components and mean SEB components at Naimona'nyi glacier averaged over the simulation period October 2000 – September 2012 126

Fig. 4.5 Glacier-wide monthly (a) SEB components and (b) MB components from October 2000 to September 2012 at Naimona'nyi glacier (reference run) 128

Fig. 4.6: Glacier-wide annual MB for MB years 2000-2012 estimated by the HAR forced MB model for Naimona'nyi glacier and compared to the results published in Yao et al. (2012) 130

Fig. 4.7: Spatial comparison of modelled surface height change of Naimona'nyi glacier for the 0.31-model run, 2001-2012, with the results of Holzer et al. (2014) 131

Fig. 4.8: Modelled mean intra-annual snow line altitude at Naimona'nyi glacier, 2001-2012 133

Fig. 4.9: Glacier-wide annual ELA at Naimona'nyi glacier, 2000-2012, calculated by the HAR forced MB model and compared to the results published in Yao et al. (2012) 133

Fig. 4.10: Relation between annual MB and AAR at Naimona'nyi glacier, 2001-2012, for the MB model run with a precipitation scaling factor of 0.31 134

Fig. 4.11: MB and surface height change for 2001-2012 along a north-south profile at Naimona'nyi glacier for HAR precipitation and temperature offsets 136

Fig. 4.12: Glacier-wide monthly (a) SEB components and (b) MB components from October 2000 to September 2012 at Naimona'nyi glacier (precipitation scaling factor 0.31 / $T_{air}$ +3 K) 137

Fig. 4.13: Glacier-wide annual MB for MB years 2000-2012 estimated by the HAR forced MB model for Naimona'nyi glacier glacier (precipitation scaling factor 0.31 / $T_{air}$ +3 K) and compared to the results published in Yao et al. (2012) 137

**Chapter 5**

Fig. 5.1: Halji glacier with glacier outlines from 2001 142

Fig. 5.2: Monthly means or sums (precipitation) of meteorological variables at the atmospheric grid cell containing Halji glacier, October 2000-September 2011 143

Fig. 5.3: Altitude dependency of the HAR variables that serve as input for the MB model at Halji glacier 144

Fig. 5.4: Modelled vertical profiles of the specific mass balance and its components and mean SEB components on Halji glacier averaged over the simulation period October 2000 – September 2011 147

Fig. 5.5: Glacier-wide monthly (a) SEB components and (b) MB components from October 2000 to September 2011 at Halji glacier (reference run) 148

Fig. 5.6: Glacier-wide annual MB and runoff for MB years 2000-2011 estimated by the HAR forced MB model for Halji glacier 151

Fig. 5.7: Modelled mean intra-annual snow line pattern at Halji glacier, 2001-2011 153

Fig. 5.8: Glacier-wide annual ELA at Halji glacier, 2000-2011 153

Fig. 5.9: Relation between annual MB and AAR at Halji glacier, 2001-2011, for the MB model run with a precipitation scaling factor of 0.56 153

Fig. 5.10: Surface elevation differences at Halji glacier and its surroundings from ICESat, 2004-2009 154

Fig. 5.11: Spatial comparison of modelled surface height change of Halji glacier (precipitation scaling factor 0.56 / $T_{air}$ +1 K), 2001-2011, with the results provided by N. Holzer 156

Fig. 5.12: MB and surface height change for 2001-2011 along a northeast-south profile at Halji glacier for HAR precipitation and temperature offsets 157

Fig. 5.13: Glacier-wide monthly (a) SEB components and (b) MB components from October 2000 to September 2011 at Halji glacier (precipitation scaling factor 0.56 / $T_{air}$ +1 K) 158

Fig. 5.14: Glacier-wide annual MB and runoff for MB years 2000-2011 estimated by the HAR forced MB model for Halji glacier (precipitation scaling factor 0.56 / $T_{air}$ +1 K) 158

**Chapter 6**

Fig. 6.1: Selected glacier at Muztagh Ata with glacier outlines from 2001 162

Fig. 6.2: Monthly means or sums (precipitation) of meteorological variables at the atmospheric grid cell containing the analyzed glacier at Muztagh Ata, October 2000-September 2012 163

Fig. 6.3: Altitude dependency of the HAR variables that serve as input for the MB model at Muztagh Ata 164

Fig. 6.4: Modelled vertical profiles of the specific mass balance and its components and mean SEB components at Muztagh Ata glacier averaged over the simulation period October 2000 – September 2012 166

Fig. 6.5: Glacier-wide monthly (a) SEB components and (b) MB components at Muztag Ata glacier from October 2001 to September 2011 (reference run) 167

Fig. 6.6: Glacier-wide annual MB for MB years 2000-2012 estimated by the HAR forced MB model for Muztagh Ata glacier and compared to the results published in Yao et al. (2012) 170

Fig. 6.7: Spatial comparison of modelled surface height change of Muztagh Ata glacier for the 0.31-model run, 2001-2012, with the results provided by N. Holzer 171

Fig. 6.8: Modelled mean intra-annual cycle of the snow line at Muztagh Ata glacier, 2001-2012 172

Fig. 6.9: Glacier-wide annual ELA at Muztagh Ata glacier, 2000-2012, calculated by the HAR forced MB model and compared to the results published in Yao et al. (2012) 172

Fig. 6.10: Relation between annual MB and AAR at Muztagh Ata glacier, 2001-2012, for the MB model run with a precipitation scaling factor of 0.31 173

**Chapter 7**

Fig. 7.1: Glacier-wide mean annual cycles of the SEB components for the studied glaciers on the TP as derived from the HAR driven MB model, 2001-2011/12 179

Fig. 7.2: Glacier-wide mean annual cycles of the MB components including liquid precipitation, runoff and $T_{air}$ for the studied glaciers on the TP as derived from the HAR driven MB model, 2001-2011/12 180

Fig. 7.3: Glacier-wide inter-annual variation of the SEB components for the five studied glaciers and ice caps, 2001-2012 181

Fig. 7.4: Glacier-wide inter-annual variation of the MB components and $T_{air}$ for the five studied glaciers and ice caps, 2001-2012 182

Fig. 7.5: Monthly glacier-wide anomalies of $T_{air}$, precipitation, snowfall and MB at Zhadang glacier, PIC, Halji glacier, Naimona'nyi glacier and Muztagh Ata glacier, 2000-2012, as derived from the HAR driven MB model 183

Fig. 7.6: Location of the air pressure anomaly centres of the chosen teleconnection patterns 187

**Appendix**

Fig. A.1: Glacier-wide monthly (a) SEB components and (b) MB components from October 2000 to September 2011 at PIC (precipitation scaling factor 0.31) 216

Fig. A.2: Glacier-wide monthly (a) SEB components and (b) MB components from October 2000 to September 2011 at PIC (precipitation scaling factor 0.81) 216

Fig. A.3: Glacier-wide monthly (a) SEB components and (b) MB components from October 2000 to September 2011 at Naimona'nyi glacier (precipitation scaling factor 0.31) 217

Fig. A.4: Glacier-wide monthly (a) SEB components and (b) MB components from October 2000 to September 2011 at Naimona'nyi glacier (precipitation scaling factor 0.81) 217

Fig. A.5: Glacier-wide monthly (a) SEB components and (b) MB components from October 2000 to September 2012 at Halji glacier (precipitation scaling factor 0.31) 218

Fig. A.6: Glacier-wide monthly (a) SEB components and (b) MB components from October 2000 to September 2012 at Halji glacier (precipitation scaling factor 0.81) 218

Fig. A.7: Glacier-wide monthly (a) SEB components and (b) MB components from October 2000 to September 2012 at Muztagh Ata glacier (precipitation scaling factor 0.31) 219

Fig. A.8: Glacier-wide monthly (a) SEB components and (b) MB components from October 2000 to September 2012 at Muztagh Ata glacier (precipitation scaling factor 0.81) 219

Fig. B.1: Glacier-wide monthly SEB components for the five study sites, 2000-2012, derived from the HAR driven MB model 220

Fig. B.2: Glacier-wide monthly MB components and $T_{air}$ for the five study sites, 2000-2012, derived from the HAR driven MB model 221

Fig. C.1: Monthly indices for selected teleconnection patterns that influence the TP, 2000-2012 222

# List of tables

**Chapter 1**

Table 1.1: Sensor specifications at Zhadang glacier AWS1 31

Table 1.2: Sensor specifications at Zhadang glacier AWS2 32

Table 1.3: Sensor specifications at Naimona'nyi glacier AWS 38

**Chapter 2**

Table 2.1: Measurement specifications for AWS1 located at 5665 m a.s.l. 45

Table 2.2: Energy fluxes at the glacier surface and their physical links as treated in the MB model 50

Table 2.3: Free parameters in the MB model 54

Table 2.4: Mean absolute values of energy flux components as modelled for 27 April 2009 – 10 June 2012 and for the two MB years at Zhadang glacier with proportional contribution to total energy flux 66

Table 2.5: Calculated glacier-wide mass balance components for the total period 27 April 2009 – 10 June 2012 and for the two MB years at Zhadang glacier 66

Table 2.6: Mean absolute values of energy flux components as modelled for October 2001 – September 2011 and for the respective MB years at Zhadang glacier with proportional contribution to total energy flux 97

Table 2.7: Calculated glacier-wide mass balance components for the total period October 2001 – September 2011 and for the respective MB years at Zhadang glacier 97

Table 2.8: Comparison of the main parameterizations within the coupled snow and SEB model developed and applied in this study and applied in Mölg et al. (2014) 101

**Chapter 3**

Table 3.1: Mean absolute values of energy flux components as modelled for October 2000 – September 2011 and for the respective MB years with proportional contribution to total energy flux at PIC 112

Table 3.2: Calculated glacier-wide mass balance components for the total period October 2000 – September 2011 and for the respective MB years at PIC 112

**Chapter 4**

Table 4.1: Mean absolute values of energy flux components as modelled for October 2000 – September 2012 and for the respective MB years with proportional contribution to total energy flux at Naimona'nyi glacier 129

Table 4.2: Calculated glacier-wide mass balance components for the total period October 2001 – September 2012 and for the respective MB years at Naimona'nyi glacier 130

**Chapter 5**

Table 5.1: Mean absolute values of energy flux components as modelled for October 2000 – September 2011 and for the respective MB years with proportional contribution to total energy flux at Halji glacier 149

Table 5.2: Calculated glacier-wide mass balance components for the total period October 2000 – September 2011 and for the respective MB years at Halji glacier 149

Table 5.3: Surface height change for the period 1 October 2003 – 30 September 2007 for the ICESat profile at Halji glacier for several precipitation scaling factors and $T_{air}$ offsets 155

**Chapter 6**

Table 6.1: Mean absolute values of energy flux components as modelled for October 2000 – September 2012 and for the respective MB years with proportional contribution to total energy flux at Muztag Ata glacier 169

Table 6.2: Calculated glacier-wide mass balance components for the total period October 2000 – September 2012 and for the respective MB years at Muztagh Ata glacier 169

**Chapter 7**

Table 7.1: SEB and MB components at the five studied glaciers for the total simulation periods 2001-2011/12 178

Table 7.2: Pearson's R and $R^2$ for monthly anomalies of $T_{air}$, precipitation and MB at the five study sites within the simulation period 2001-2011/12 183

Table 7.3: Seasonal Pearson's R for selected northern Hemisphere teleconnection patterns and SO for glacier-wide $T_{air}$, total precipitation and MB at Zhadang glacier, 2001-2011 189

Table 7.4: Seasonal Pearson's R for selected northern Hemisphere teleconnection patterns and SO for glacier-wide $T_{air}$, total precipitation and MB at PIC, 2001-2011 190

Table 7.5: Seasonal Pearson's R for selected northern Hemisphere teleconnection patterns and SO for glacier-wide $T_{air}$, total precipitation and MB at Naimona'nyi glacier, 2001-2012 190

Table 7.6: Seasonal Pearson's R for selected northern Hemisphere teleconnection patterns and SO for glacier-wide $T_{air}$, total precipitation and MB at Halji glacier, 2001-2011 191

Table 7.7: Seasonal Pearson's R for selected northern Hemisphere teleconnection patterns and SO for glacier-wide $T_{air}$, total precipitation and MB at Muztagh Ata glacier, 2001-2012 191

# List of acronyms, symbols and abbreviations

| | |
|---|---|
| A | glacier area |
| $A_C$ | accumulation area of a glacier |
| AAR | accumulation area ratio |
| $AAR_0$ | accumulation area ratio at glacier equilibrium |
| AO | Arctic Oscillation |
| AWS | automatic weather station |
| BMBF | Bundesministerium für Bildung und Forschung (Federal Ministry of Education and Research) |
| CAME | Central Asia – Monsoon dynamics and Geo-ecosystems (BMBF programme) |
| CAS | Chinese Academy of Sciences |
| $C_{lat}$ | bulk-transfer coefficient for latent heat |
| $C_{se}$ | bulk-transfer coefficient for sensible heat |
| CRN | cosmogenic radionuclides |
| DEM | digital elevation model |
| DFG | Deutsche Forschungsgemeinschaft (German Research Foundation) |
| DInSAR | differential synthetic aperture radar interferometry |
| DynRG-TiP | Dynamic Response of Glaciers on the Tibetan Plateau to Climate Change (DFG project) |
| E | activation energy for snow pack densification |
| EAWR | East Atlantic/Western Russia teleconnection pattern |
| ELA | equilibrium line altitude |
| ENSO | El Nino Southern Oscillation |
| F | refreezing rate |
| GCP | ground control point |
| GIS | geographic information system |
| GLOF | glacier lake outburst flood |
| GPS | global positioning system |
| GRACE | gravity recovery and climate experiment |
| HAR | High Asia reanalysis |
| ICESat | ice, cloud and land elevation satellite |
| ITP | Institute for Tibetan Plateau Research (CAS) |
| K | rate factor for snow pack densification |
| $L_E$ | latent heat for evaporation |
| LGM | Last Glacial Maximum |
| LIA | Little Ice Age |
| $L_M$ | latent heat for melt |
| $LW_{in}$ | longwave incoming radiation (atmospheric radiation) |
| $LW_{net}$ | net longwave radiation |
| $LW_{out}$ | longwave outgoing (emitted) radiation) |
| $L_S$ | latent heat for sublimation |
| M | melt rate |
| MB | mass balance |
| MODIS | moderate resolution imaging spectroradiometer |
| N | cloud cover factor |

| | |
|---|---|
| NAO | North Atlantic Oscillation |
| NOAA | National Oceanic and Atmospheric Administration |
| PDH | positive degree hours |
| PIC | Purogangri Ice Cap |
| PNA | Pacific/North America teleconnection pattern |
| POL | Polar/Eurasia teleconnection pattern |
| PT | Pacific transition teleconnection pattern |
| $Q_C$ | conductive heat flux |
| $Q_G$ | ground heat flux |
| $Q_{lat}$ | latent heat flux |
| $Q_{melt}$ | melt energy |
| $Q_{PS}$ | energy flux from penetrating shortwave radiation |
| $Q_{sens}$ | sensible heat flux |
| R | correlation coefficient |
| RH | relative humidity |
| Ri | bulk Richardson number |
| RMSE | root mean squared error |
| $RMSE_h$ | root mean squared error explicitly for snow depth |
| $R_{net}$ | net radiation |
| RSG | remote sensing software Graz |
| S | electrical conductance |
| SEB | surface energy balance |
| SO | Southern Oscillation teleconnection pattern |
| SRTM | shuttle radar topography mission |
| $SW_{in}$ | shortwave incoming radiation (global radiation) |
| $SW_{in,pot}$ | potential shortwave incoming radiation (without the influence of clouds) |
| $SW_{net}$ | net shortwave radiation |
| $SW_{out}$ | shortwave outgoing (reflected) radiation |
| $SW_{TOA}$ | top of atmosphere solar irradiance |
| T | subsurface temperature |
| $T_{air}$ | air temperature |
| $T_{air(C)}$ | air temperature explicitly in °C |
| $T_b$ | base temperature |
| $T_s$ | surface temperature |
| TerraSAR-X | radar earth observation satellite |
| TP | Tibetan Plateau and surrounding mountain ranges |
| U | uncertainty |
| UTM | universal transverse Mercator (coordinate system) |
| WET | Variability and Trends in Water Balance Components of Benchmark Drainage Basins on the Tibetan Plateau (BMBF project) |
| WGS | world geodetic system |
| WP | West Pacific teleconnection pattern |
| WRF | weather research and forecasting |
| a | constant for the calculation of atmospheric emissivity |
| b | constant for the calculation of atmospheric emissivity |
| $c_p$ | specific heat capacity of air |
| $c_{pi}$ | specific heat capacity of ice |

| | |
|---|---|
| $c_{ref}$ | accumulation by refreezing of percolating water |
| $c_{solid}$ | accumulation by solid precipitation |
| d* | constant for the effect of snow depth an albedo |
| e | water vapour pressure |
| f | constant for snow pack densification |
| g | acceleration of gravity |
| h | snow depth |
| mm w.e. | millimetre water equivalent |
| np | number of SRTM pixels along the glacier flow line |
| p | air pressure |
| $q_{air}$ | specific humidity in 2 m |
| $q_s$ | specific humidity at the surface |
| r | gas constant |
| ri | ratio of $SW_{in,pot}$ at any location of the glacier to $SW_{in,pot}$ at a specific point |
| $t_{snow}$ | time since the last snowfall |
| t* | constant for the effect of ageing on snow albedo |
| u | wind speed |
| w | liquid water content |
| $w_i$ | irreducible water content |
| z | distance to the ice surface / instrument height |
| $z_0$ | surface roughness length |
| ΔH | altitude difference |
| ΔHp | altitude difference per SRTM pixel |
| Δh | snow depth difference |
| Δhp | snow depth difference per SRTM pixel |
| Ω | electrical resistance |
| α | surface albedo |
| $\alpha_d$ | index to define the difference of AAR and $AAR_0$ |
| β | extinction coefficient |
| γ | cold content |
| ε | atmospheric emissivity |
| $\varepsilon_{cl}$ | cloud emissivity |
| $\varepsilon_{cs}$ | clear-sky emissivity |
| ζ | absorbed fraction of $SW_{net}$ |
| κ | thermal diffusivity |
| λ | thermal conductivity |
| ρ | subsurface density (snow/firn and ice) |
| $\rho_{air}$ | air density |
| $\rho_{ice}$ | density of ice |
| $\rho_{snow}$ | density of snow/firn |

# 1 Introduction

## 1.1 Motivation and intention

Due to the unique topography, climate characteristics, geological history, natural environment and cultural heritage, the Tibetan Plateau and its surrounding mountain ranges (TP) are of considerable interest for scientists of various fields. More than 1.4 billion people depend on the water from five of the largest Asian rivers originating on the TP (Immerzeel et al. 2010). The large amount of ice, snow and permafrost and the stored water therein is important in sustaining seasonal water availability. Therefore, the TP is also called the "*Asian Water Tower*" (Immerzeel et al. 2010) or the "*Third Pole*" (Qiu 2008). According to the overall trend of increasing air temperatures on the TP and its adjacent areas since several decades, most glaciers on the TP (Kang et al. 2010, Yao et al. 2012) and in the Himalayas (Bolch et al. 2012, Kargel et al. 2011) are retreating. Generally, the rates of area loss have been increasing in recent years (e.g. Bolch et al. 2012, Yao et al. 2012). The regional patterns are contrasting (Kääb et al. 2012), influenced by local factors (e.g. topography, debris cover, glacier type) and the spatial and temporal heterogeneity of climate and climate variability (Kang et al. 2010). Remote sensing technologies incredibly increased the knowledge on spatially heterogeneous glacier responses especially in regions where in-situ measurements are lacking (e.g. Bolch et al. 2012, Gardelle et al. 2012, 2013a, Kääb et al. 2012, Neckel et al. 2014). However, the individual feedback mechanisms between atmosphere and glacier, and the role of the various components of the glacier surface energy (SEB) and mass balance (MB) in the melt process for different climate regions on the TP have not yet been analyzed.

In 2008, the German Research Foundation (DFG) initiated a Sino-German Priority Programme (*Tibetan Plateau: Formation – Climate – Ecosystem*) to focus on the interactions of the major forcing mechanisms on the TP: plateau formation, climate evolution, human impact, and their effects on ecosystems. The DynRG-TiP project (*Dynamic Response of Glaciers on the Tibetan Plateau to Climate Change*) is part of this priority programme and focuses on the atmosphere-cryosphere interactions on the TP. The project is a cooperation between RWTH Aachen University, TU Berlin and TU Dresden. It is funded for 2008-2014. Since 2011, the DFG project is complemented by a R&D collaborative project of the Federal Ministry of Education and Research (BMBF) (*Central Asia – Monsoon dynamics and Geo-ecosystems (CAME)*). Within this framework, the WET project (*Variability and Trends in Water Balance Components of Benchmark Drainage Basins on the Tibetan Plateau*) deals with the relation of the relevant atmospheric, hydrological and glaciological variables within drainage basins on

the TP. The project is a cooperation between RWTH Aachen University, TU Berlin, TU Dresden, Uni Marburg, Uni Tübingen and Uni Jena and is funded for 2011-2014. The subproject of RWTH Aachen University focuses on the glacier SEB and MB in the different benchmark drainage basins on the TP. This includes the development of a model scheme that couples the atmospheric energy balance to a subsurface module in order to analyze the atmosphere-cryosphere interactions. Within the two projects, seven Sino-German field campaigns on the TP have been carried out since 2009. All of these were supported by the Institute of Tibetan Plateau Research (ITP) of the Chinese Academy of Sciences (CAS). The work presented in this thesis is the result of these projects and cooperation.

The following key questions are in the focus of this thesis:

1. How precise can glacier surface elevation change and MB be modelled for individual glaciers and validated through in-situ measurements and remote sensing methods?
2. How much of the generated melt water at the glacier surface effectively runs off and how does this proportion vary regionally and seasonally?
3. How do climate variables modify the glacier SEB and MB? How do these influences vary regionally and seasonally?
4. Which components dominate the glacier SEB and MB and how does their influence vary regionally and seasonally?

## 1.2 Thesis outline and published research papers

This thesis is organized into four main parts. It starts with an overview on the regional description of the broader study area, the TP, with a focus on atmospheric circulation patterns (section 1.3.1), climate and glacier change since the Little Ice Age (section 1.3.2) and a comprehensive view on the physical geography (section 1.3.3). A second overview is given on the theoretical background of the scientific methods related to the modelling of glacier SEB and MB (section 1.3.4). An introduction into the basic principles of both, surface energy and mass balance, various feedback mechanisms and observation methods provide the framework for this thesis. A section on the glacier characteristics on the TP attempts to integrate both natural boundary conditions and related glaciological couplings to identify the distinct regional patterns (section 1.3.5). After presenting a plateau-wide overview in terms of different aspects of the physical geography, the following section focuses on the five study sites selected for this thesis (section 1.4). Each study area (glacier or ice cap) is presented based on the previous summaries. Additionally, the in-situ measurements carried out on two of the selected glaciers (Zhadang glacier and Naimona'nyi glacier, Fig. 1.1) are described.

Following the introductory overviews the five studies forming the main part of this thesis are presented. These five studies can be grouped into two main parts (chapter 2 and chapters 3-6).

Chapter 2 presents a detailed description of the developed and applied coupled SEB/MB model. The different steps of model calibration and validation for the reference glacier (Zhadang glacier) using different methods and data sources are explained. The installed complex monitoring system including a time-lapse camera system at Zhadang glacier is the first of its kind on the TP so far. It provides an excellent data base for the model evaluation and opens up new opportunities for further analysis. Finally, the study derives a 10-year SEB and MB time series for Zhadang glacier that is integrated in previously published findings of other authors.

Chapters 3-6 present regional studies on the characteristics of four glaciers and ice caps on the TP. The developed and verified SEB/MB model is directly transferred and applied to the Purogangri ice

cap (central TP, chapter 3), Naimona'nyi glacier (western Himalayas, chapter 4), Halji glacier (south western TP, chapter 5) and Muztag Ata glacier (north western TP, chapter 6) (Fig. 1.1). The model structure, the applied parameterizations, constants, and assumptions made for Zhadang glacier (chapter 2) remain unchanged to ensure the required transferability of the model to other regions without in-situ measurements. Every regional study derives a 10-year time series of the different SEB and MB components. This is the largest and most detailed homogeneous glaciological data set on the TP so far regarding modelling of SEB/MB.

Chapter 7 integrates the derived model results to an overall picture and understanding of the glaciers on the TP. Knowledge on the various driving mechanisms for the SEB and MB components is crucial for estimations of future glacier evolution and forms the basis for further analysis and research.

The author was responsible for or contributed to the following publications and conference contributions which are of relevance for this thesis:

Publications:

- Bolch, T., Yao, T., Kang, S., Buchroithner, M., Scherer, D., Maussion, F., **Huintjes, E.** and Schneider, C. (2010): A glacier inventory for the western Nyainqentanglha Range and Nam Co Basin, Tibet, and glacier changes 1976-2009. The Cryosphere, 4, 419-43.
  (Contribution to the literature review, minor contribution to the analysis and writing) Referred to in section 1.4

- Maussion, F., Yang, W., **Huintjes, E.**, Pieczonka, T., Scherer, D., Yao, T., Kang, S., Bolch, T., Buchroithner, M. and Schneider, C. (2011a): Glaciological field studies at Zhadang Glacier (5500 - 6095 m), Tibetan Plateau. Workshop on the use of automatic measuring systems on glaciers, IASC Workshop, Pontresina (Switzerland).
  (Contribution to the field work, data acquisition, structure, figures, data analysis and writing) Referred to in section 1.4

- Zhang, G., Kang, S., Fujita, K., Wei, Y., **Huintjes, E.**, Xu, J., Yamazaki, T., Haginoya, S., Scherer, D., Schneider, C. and Yao, T. (2013): Energy and mass balance of the Zhadang Glacier surface, central Tibetan Plateau. Journal of Glaciology, 59, 213, 137-148.
  (Contribution to the field work, data acquisition, minor contribution to analysis and writing) Referred to in chapter 2

Conference contributions:

- **Huintjes, E.**, Neckel, N., Maussion, F., Spieß, M., Scherer, D., Hochschild, V., Sauter, T. and Schneider, C. (2013a): Evolution of Purogangri Ice Cap, central Tibetan Plateau, 2000-2012 - a comparison of two glaciological methods. Himalayan Karakorum Tibet Workshop & International Symposium on Tibetan Plateau 2013, Tübingen.
  (Responsible for the study design, numerical simulations, model data preparation and analysis, contribution to figures and writing) Referred to in chapter 3

- **Huintjes, E.**, Sauter, T., Schröter, B., Maussion, F., Kropacek, J., Yang, W., Kang, K., Zhang, G., Scherer, D., Buchroithner, M. and Schneider, C. (2013b): Evaluation of a distributed energy balance model for a high-altitude glacier on the Tibetan Plateau using glaciological measurements and a time-lapse camera system. Himalayan Karakorum Tibet Workshop & International Symposium on Tibetan Plateau 2013, Tübingen.
  (Responsible for the study design, numerical simulations, data preparation and analysis, figures and writing; contribution to the field work and data acquisition) Referred to in chapter 2

- **Huintjes, E.**, Sauter, T., Krenscher, T., Maussion, F., Kropacek J., Yang, W., Zhang, G., Kang, S., Scherer, D., Buchroithner, M. and Schneider, C. (2013c): Evaluation of a distributed energy balance model for a high-altitude glacier on the Tibetan Plateau using a time lapse camera system. EGU General Assembly 2013, Vienna.
  (Responsible for the study design, numerical simulations, data preparation and analysis, figures and writing; contribution to the field work and data acquisition) Referred to in chapter 2

- Kropacek, J., Neckel, N., Tyrna, B., **Huintjes, E.**, Schneider, C., Maussion, F. and Scherer, D. (2013): Exploration of a periodic GLOF in Halji, West Nepal using modeling and remote sensing. Himalayan Karakorum Tibet Workshop & International Symposium on Tibetan Plateau 2013, Tübingen.
  (Responsible for the numerical simulations, model data preparation and analysis; contribution to figures and writing) Referred to in chapter 5

- Schneider, C., Yao, T., Scherer, D., Kang, S., Buchroithner, M., Fink, M., Hochschild, V., Bendix, J., Kropacek, J., Maussion, F., Yang, W., **Huintjes, E.**, Biskop, S., Curio, J., Zhang, G., Ruethrich, F., Thies, B., Spiess, M., Neckel, N, Holzer, N. and Schroeter, B. (2013): Advances in the process-related understanding of atmosphere-cryosphere-hydrosphere couplings on the Tibetan Plateau. Himalayan Karakorum Tibet Workshop & International Symposium on Tibetan Plateau 2013, Tübingen.
  (Responsible for the glaciological data preparation; contribution to the field work, data acquisition and figures) Referred to in chapters 2, 3, 4

- **Huintjes, E.**, Spieß, M., Sauter, T., Scherer, D. and Schneider, C. (2012): Gletscher als „Messinstrumente" großräumiger Klimavariabilität auf dem Tibetischen Plateau – Ansätze basierend auf Massenbilanzmodellierung und Schneefernerkundung. Arbeitskreis Klima, Berlin.
  (Responsible for the study design and numerical simulations; contribution to the field work, data acquisition and data preparation, analysis, figures and writing) Referred to in chapter 3

- **Huintjes, E.**, Yang, W., Kang, S. and Schneider, C. (2011a): Mass balance modelling of Zhadang Glacier, Tibetan Plateau. 7th Sino-German Workshop on Tibetan Plateau Research, Hamburg.
  (Responsible for the study design, numerical simulations, data preparation and analysis, figures and writing; contribution to the field work and data acquisition) Referred to in chapter 1

- **Huintjes, E.**, Yang, W., Pieczonka, T., Maussion, F., Sauter, T., Kang, S., Yao, T., Bolch, T., Buchroithner, M., Scherer, D. and Schneider, C. (2011b): Glaciological field studies at Zhadang Glacier, Tibetan Plateau. 7th Sino-German Workshop on Tibetan Plateau Research, Hamburg.
  (Responsible for the study design; contribution to the field work, data acquisition, data preparation, analysis, figures and writing) Referred to in section 1.4

- Maussion, F., **Huintjes, E.**, Yang, W., Scherer, D. and Schneider, C. (2011b): Atmospheric data retrieval at Zhadang Glacier, Tibetan Plateau. 7th Sino-German Workshop on Tibetan Plateau Research, Hamburg.
  (Responsible for the analysis of the turbulence data; contribution to the field work, data acquisition, figures and writing) Referred to in section 1.4

- Schneider, C., **Huintjes, E.**, Bhattacharya, A., Sauter, T., Yang, W., Bolch, T., Pieczonka, T., Maussion, F., Kang, S., Buchroithner, M., Scherer, D. and Yao, T. (2011): Calibration of a distributed ablation model for Zhadang Glacier, Tibetan Plateau, using a time lapse camera system. AGU Fall Meeting 2011, San Francisco.
  (Contribution to the field work, data acquisition, numerical simulations, data preparation, analysis and figures) Referred to in chapter 2

- Maussion, F., **Huintjes, E.**, Schneider, C. and Scherer, D. (2010): Exceptional ablation season 2009 on the Zhadang Glacier, Central Tibet - An approach combining field measurements and numerical modelling. EGU General Assembly 2010, Vienna.
  (Contribution to the study design, field work, data acquisition and analysis) Referred to in section 1.4

## 1.3 Current state of research

In the following section a short overview on the physical geography of the TP with a focus on atmospheric circulation patterns, climate change and glacier change is given. The methodological background (section 1.3.4) and derived glacier characteristics (section 1.3.5) provide the framework and basis for the SEB and MB studies within this thesis. The locations and geographical features referred to in this thesis are summarized in Fig. 1.1.

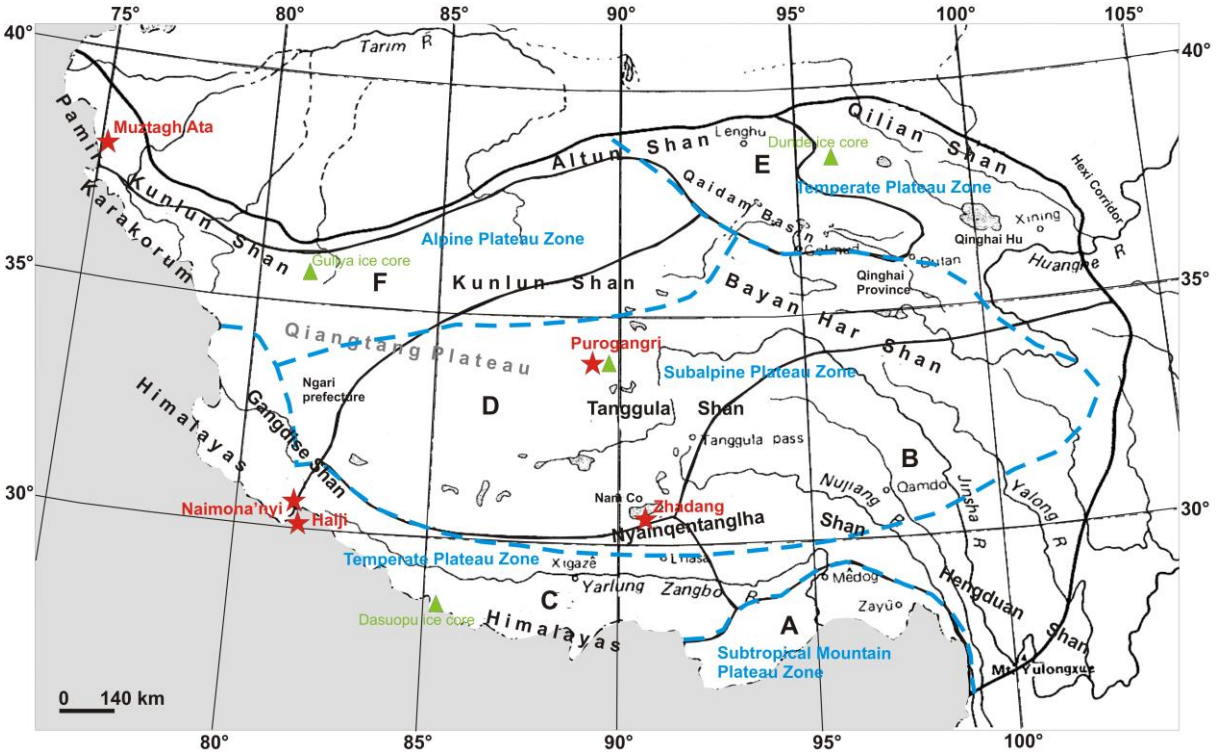


**Fig. 1.1: Map of the Tibetan Plateau with main mountain ridges, natural regions (black lines and capital letters A-F, after Zhao 1986), climate zones (blue dashed lines and blue text, after Domrös & Peng 1988), important ice core sites (green triangles) and location of the study areas of this thesis (red stars) (modified after Zhao 1986). For the explanation of different natural regions, see section 1.3.3.**

### 1.3.1 Present atmospheric circulation patterns over the Tibetan Plateau and its surroundings

The climate of the TP and its surroundings is mainly controlled by the interaction and varying dominance of the mid-latitude westerlies and the Indian and southeast Asian monsoon systems (Fig. 1.2). The influences of monsoons and westerlies vary regionally as well as seasonally (e.g. Benn & Owen 1998, see section 1.4.1) and result in distinct mean circulation patterns in summer and winter (Fig. 1.3, section 1.4.1, Böhner 2006, Lehmkuhl & Haselein 2000). The various concurrent interactions and feedback mechanisms of both circulation patterns are still an active field of research (e.g. Bothe et al. 2011, 2012, Chen et al. 2012, Gao et al. 2013, Mölg et al. 2012).

The thermally induced pressure gradient between the inner and outer tropics generates the mid-latitude westerly jet in the mid to upper troposphere (Lauer & Bendix 2004). In winter, the latitudinal pressure gradient is larger, resulting in a more intense westerly jet shifted further south (30°N). When the cold and dry air masses reach the western border of the TP, the main zonal stream is divided into an upper and lower branch (Domrös & Peng 1988, Fig. 1.3). The maximum averaged zonal

wind speed is located south of the TP. In the northern, western and southern borders of the TP, westerly winds penetrate on the plateau and form an important moisture source (Maussion et al. 2014). In all five study areas winds from westerly directions dominate in winter (see section 1.4.1). In the lower troposphere, an anticyclonic system is formed over India, closely related to the winter monsoonal flow. The period April to June marks the transition from winter to summer circulation conditions. The westerly jet migrates northward while its intensity weakens and its latitudinal position varies largely (Schiemann et al. 2009). In summer, the mid-latitude westerlies are located north of the TP. The mid tropospheric low pressure systems over India (monsoonal depression) and over the TP (thermal low) cause the development of the Indian summer monsoon system (Fig. 1.3) with deep convection and heavy rainfalls along the southern flank of the Himalayas (Molnar et al. 2010). The strong convective heating over the high elevated TP contributes to a high pressure system (Tibetan High) in the upper troposphere, centred south of the TP (Boos & Kuang 2010, Domrös & Peng 1988). Winds from southern directions are prominent over the southern TP and in the Himalayas (see section 1.4.1). Moisture is transported to the plateau through the deep Himalayan gorges. In autumn, the westerly jet gradually migrates to the south and is typically more intense than in spring (Schiemann et al. 2009). The East Asian monsoon is fundamentally different from the Indian monsoon. It is an extratropical phenomenon, associated with frontal systems that migrate northward during spring. Precipitation from this frontal system influences the eastern TP and reaches a maximum in mid June (Molnar et al. 2010).

The TP has a mean elevation of more than 4500 m a.s.l. and reaches up into the mid-troposphere. The influence of the TP on the atmospheric circulation of the adjacent regions as well as on both hemispheres was already stated since the 1950s (Flohn 1957, Manabe & Terpstra 1974, Hahn & Manabe 1975, Ye 1981, Tao & Ding 1981, Ding 1992). The high and extensive terrain of the TP between 30 and 40°N acts as a mechanical barrier to meridional and zonal air flow. It separates the warm and moist air masses over India from the cold and dry extratropics to a large extent and affects the position and strength of the northern hemisphere westerly jet (e.g. Boos & Kuang 2010, Ding 1992, Schiemann et al. 2009). The TP and its adjacent high mountain systems play also a significant role in the Indian monsoon system (e.g. Hahn & Manabe 1975, Manabe & Terpstra 1974). Weather these influences are more thermal or mechanical induced is still under debate (e.g. Yang et al. 2010a, Boos & Kuang 2010, 2013, Wu et al. 2012, Chen & Bordoni 2014, Ma et al. 2014) and is particularly relevant with respect to paleoclimate evolution (Molnar et al. 2010).

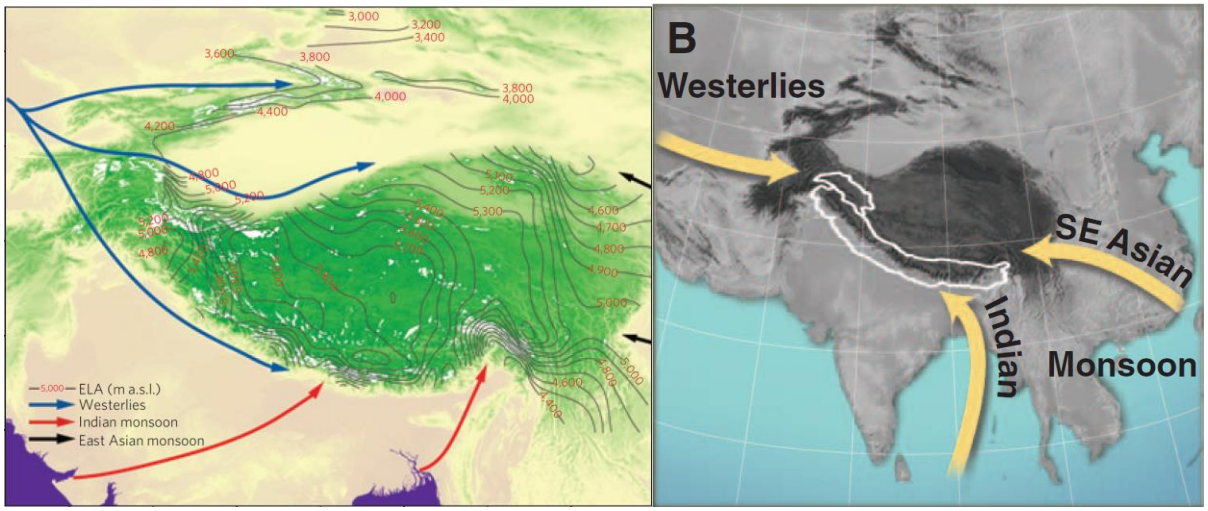


**Fig. 1.2: Examples of the schematic representation of the wind systems influencing the climate of the TP (Yao et al. 2012, Bolch et al. 2012)**

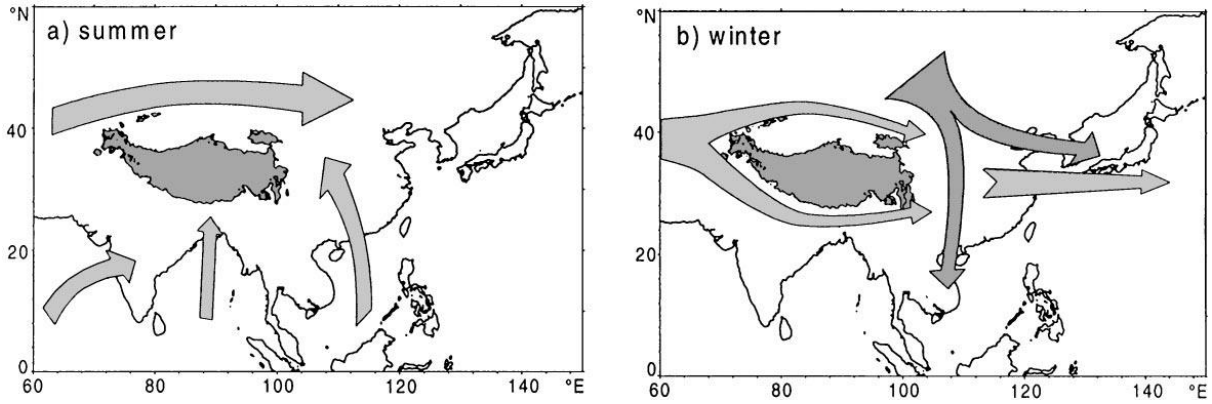


**Fig. 1.3: Schematic representation of main wind directions in Central Asia and adjacent areas: (a) summer situation, (b) winter situation (Lehmkuhl & Haselein 2000)**

### 1.3.2 Climate and glacier change on the Tibetan Plateau and adjacent areas since the Little Ice Age

The present atmospheric circulation patterns explained in section 1.3.1 do not differ significantly from those that controlled the TP over the past millions of years. The uplift of the TP and of the surrounding mountain ranges is closely connected with modifications in the feedback mechanisms of mid-latitude westerlies and Asian monsoon systems (see sections 1.3.1 and 1.3.3). An et al. (2001) use records from aeolian and marine sediments to reconstruct the Asian climate since 9 Myr ago. Results on varying temperature and moisture patterns over the TP as the result of changing intensities of the governing circulation systems are in agreement with other authors (Li et al. 2014a, Sun 2004). However, the derived signals are not uniformly in the different regions of the TP.

Climate reconstructions since the Pleistocene on the TP are mostly derived from lacustrine (e.g. Herzschuh et al. 2009, 2010, Lehmkuhl & Haselein 2000, Mischke & Zhang 2010, Wang et al. 2002, Zhang & Mischke 2009) and glacial (eg. Heyman et al. 2011, Lehmkuhl 1997, Owen et al. 2002, 2003, 2008, 2010) records. Although a general climatic trend for the whole TP can not be established (Wischnewski et al. 2011) certain phases of glacier advances and lake level rise in large parts of the TP could be revealed (Lehmkuhl & Haselein 2000). Generally, when interpreting glacier variations, it has to be considered that both different climate conditions and different glacier response times may lead to asynchronous glacier fluctuations (Haeberli 1995, Oerlemans 2007, Raper & Braithwaite 2009). The theory of a Pleistocene inland glaciation on the TP after Kuhle (1994) was refuted by various authors (e.g. Zheng & Rutter 1998, Lehmkuhl 1997, Shi et al. 1992, Yi et al. 2002) who showed for different regions on the TP that glaciations were limited to isolated mountain ranges and ice caps. In the drier regions on the western TP (e.g. Muztagh Ata, Fig. 1.1) glacial moraines can be reconstructed back to ≈300.000 years ago with the youngest from the Little Ice Age (LIA) advances. Evidence from old glaciations in wet regions on the TP was mostly destroyed by weathering, fluvial erosion and mass movements (Owen 2009, Seong et al. 2009a, Xu & Yi 2014). Over large parts of the TP and adjacent mountain ranges the extent of glaciation decreased progressively over the last glacial cycles (Owen et al. 2006, 2010). This possibly reflects a reduction in the moisture flux that could be the result of an increasing barrier effect through the uplift of the surrounding mountain ranges (Seong et al. 2009a). The same picture is evident in other mountain regions of the world (Denton et al. 1999, Barrows et al. 2002, Smith et al. 2002, Singer et al. 2004). From the Last Glacial Maximum (LGM) at ≈21000 years ago to the LIA paleolimnological records from the eastern TP reveal a sequence of cooling and warming phases associated with glacier advance and retreat (Mischke & Zhang 2010, Zhang & Mischke 2009). Whereas some of the identified cold events could be related to a catchment-specific response

to climate variations, the majority corresponds to cold events also identified at sites on the central and western TP within the same periods or slightly shifted in time (Mischke & Zhang 2010).
The LIA is considered to be a global cooling period although its timing and nature are highly variable for different regions (Bradley & Jones 1993, Jones et al. 1998, 1999, Mann et al. 1999). In Europe, the LIA began in the 16th century and lasted until the end of the 19th century (Grove & Switsur 1994) associated with significant glacier advances (Holzhauser et al. 2005, Ivy-Ochs et al. 2009, Nussbaumer et al. 2007). For the reconstruction of LIA climate fluctuations on the TP the majority of authors draw their conclusions based on the extents and chronologies of glacial moraines (e.g. Owen 2009, Xu & Yi 2014). During the LIA three well pronounced terminal moraine systems have been formed in many regions that are associated with three colder periods. The second period can be related to the Maunder Minimum (1645-1715) (Shi & Liu 2000). Dating methods are mainly based on radiocarbon $^{14}C$, lichenometry and cosmogenic radionuclides (CRN, $^{10}Be$). The latter is a comparatively new method and could provide new insights into the timing of the LIA in recent years (Xu & Yi 2014). The maritime (temperate) glaciers on the wetter eastern and south eastern TP are highly sensitive to climate variations (see section 1.3.5). Therefore, research on late Holocene changes of the monsoonal climate and glacier fluctuations especially focuses on this area (e.g. Loibl et al. 2014, Su & Shi 2002, Yang et al. 2008, Zhou et al. 2010). The climate and the lower altitude favour the growth of trees on the glacial moraines. Bräuning (2006) reconstructed multiple glacier advances between 1580 and 1987 in eastern and south eastern TP from dendrochronological moraine dating. In general, subsequent moraine formations beyond the contemporary glaciers indicate multiple periods of glacier advance and retreat during the LIA on the TP. However, the uncertainties within the different applied dating methods recommend the comparison of the timing of the LIA maximum glacier extents only, especially the retreating time (Xu & Yi 2014). The majority of glaciers on the southern TP (Himalayas, Nyainqentanglha Shan, Hengduan Shan, Fig. 1.1) reached their LIA maximum extent in the late 14th century and retreated from that extent during the 16th to the early 18th century. At some glaciers a re-advance in the late 18th to the early 19th century can be identified (e.g. Barnard 2004a,b, Owen et al. 2005, 2010, Xu & Yi 2014). On the north western TP (Karakorum, Pamir, Fig. 1.1) glaciers advanced to their LIA maximum extents in the early 14th century and retreated between the late 14th and the early 15th century. Some glacial moraines again show re-advances between late 18th and early 19th century (e.g. Seong et al. 2007, 2009a,b, Xu & Yi 2014). For the glaciers on the north eastern TP (Qilian Shan, Fig. 1.1) the periods of glacier advance can not be inferred. They retreated quite synchronously from the LIA maximum extents in the early 16th, the late 18th and the late 19th century, respectively (e.g. Chen 1989, Xu & Yi 2014). On the central TP LIA moraine datings are scarce. Few lichenometry samples on LIA moraines in the Tanggula Shan (Fig. 1.1) are dated to the 19th century (Xu & Yi 2014). From these results it can be concluded that the glaciers on the TP reacted quite synchronously between the late 18th to the late 19th century. However, the glacier retreat from the LIA maximum extents (outermost LIA moraines) was not synchronous in the different regions of the TP. To compare the moraine dated LIA glacier fluctuations to climate variations, ice core records from Dasuopu, Purogangri, Dunde and Guliya ice cores from the Himalayas, the Tanggula Shan, the Qilian Shan and the Kunlun Shan (Fig. 1.1), respectively, need to be evaluated (Yang et al. 2009, Yao et al. 2007, 2008). The dating of the Dasuopu ice core indicates a long period of generally low temperatures before the 17th century and between the late 18th and the early 19th century. These periods agree with phases of glacier advances on the southern TP. During the late 19th century precipitation increased. However, no signals for glacier advances during this time could be revealed on the southern TP. The ice core from the Purogangri ice cap revealed several cold periods from the 15th century to the early 19th century that correspond to LIA glacier advance of glaciers on the eastern and southern TP (Yang et al. 2009). An abrupt warming occurred between 1910 and 1920 suggesting a transi-

tion to a warmer, wetter climate (Thompson et al. 2006). The Guliya ice core record shows cold periods around 1230-1360, 1480-1520 and 1670-1880 (Xu & Yi 2014). During the latter period precipitation decreased and therefore can not have contributed to the glacier advances between late 18th and early 19th century on the north western TP. Generally, the periods of lower temperatures correspond well with the phases of glacier advances in this region. The temperature record of the Dunde ice core is closely related to glacier fluctuations on the north eastern TP with phases of higher temperatures during inferred glacier retreat. The relationship between TP ice core records and LIA moraines implies that temperature variations on the TP during the LIA had a stronger influence on glacier fluctuations than precipitation changes.

The climate and glacier change on the TP since the 20th century can be revealed from meteorological and glaciological field observations as well as from satellite data. Numerous studies agree, that air temperatures on the TP and its adjacent areas increased since the late 19th century with an accelerating trend in the 1950s and since the 1980s and 1990s (e.g. Yang et al. 2009, Liu & Chen 2000, Sheng & Yao 2009, Takeuchi et al. 2009, Xue et al. 2009, You et al. 2010). Highest significant temperature increases could be observed in winter and autumn, whereas warming in spring and summer is less pronounced (Liu & Chen 2000, Wei & Fang 2013, Xie et al. 2010, You et al. 2010). Spatially, the regions of highest elevations (and lowest temperatures) and the warmer temperature zones in low altitudes on the TP experienced less temperature increase. These areas only account for a small proportion of the total area of the TP (≈20%). Therefore, the largest warming trends can be identified in the central, north western and north eastern plateau regions (Wei & Fang 2013). You et al. (2010) also found the north eastern TP to experience the most significant warming trends especially in winter and autumn. Furthermore, the authors find large scale atmospheric circulation patterns (e.g. sea level pressure anomalies, El Nino) to be contributing factors to the observed decadal and seasonal TP temperature trends. Further air temperature evaluations show that the warming rates both in summer and winter increase with altitude from 3000 to 4000 m a.s.l. Above 4000 m a.s.l. they are stable with altitude or show a slight decline (Liu & Chen 2000, Qin et al. 2009). Wei & Fang (2013) showed that this pattern was predominating on the TP during 1961-2010. However, this trend has been weakened due to more rapid warming at lower altitudes. This is an important finding because most glaciers on the TP are located at higher altitudes above 4500 m a.s.l. Precipitation variations on the TP are less pronounced and regionally contrasting. For the south western TP Li et al. (2010, 2011) show a weak overall decreasing trend 1961-2008, with increasing precipitation only in winter and spring. This is in agreement with Yao et al. (2012) who give decreasing precipitation in the Himalayas and increasing amounts in the eastern Pamir mountains. Palazzi et al. (2013) indicate a statistically significant decreasing trend in summer in the Hindukush-Karakorum-Himalaya region. Reasons for this spatial variability might be the weakening of the Indian monsoon and the strengthening of the westerlies as found in recent studies (Wu 2005, Zhao et al. 2012).

According to the overall trend of increasing air temperatures on the TP and its adjacent areas since several decades, most glaciers on the TP (Kang et al. 2010, Yao et al. 2012) and in the Himalayas (Bolch et al. 2012, Kargel et al. 2011) are retreating. Generally, the rates of area loss have been increasing in recent years. The regional patterns are contrasting (Kääb et al. 2012), influenced by local factors (e.g. topography, debris cover, glacier type) and the spatial and temporal heterogeneity of climate and climate variability mentioned above in this section and in section 1.3.1. Yao et al. (2012) summarize the systematic differences in glacier behaviour in the different regions of the TP over the past 30 years based on satellite imagery and in-situ observations. The Himalayan glaciers and the glaciers of the Hengduan Shan experienced the greatest reduction in mass, length and area, whereas the observed shrinkage decreases to the central and northern TP (Neckel et al. 2014, Wei et al. 2014). The region of the eastern Pamir and Karakorum mountains showed even positive MB and

smallest retreat rates. Bolch et al. (2012) and Scherler et al. (2011) draw a similar picture for the Himalaya-Karakorum region but stress the high variability both in time between the decades and in space between individual glaciers. Between 1920 and 1940 half of the recorded Himalayan glaciers were stable or advanced. During 1976 to 2007 some glaciers in the Hindukush and the Kunlun Shan (1970-1990) showed a similar pattern (Bolch et al. 2012, Shangguan et al. 2007). The heterogeneous and oscillatory response of individual glaciers in the Himalayas to climate variability is also shown by Fujita & Nuimura (2011) based on in-situ measurements. The so called '*Karakorum anomaly*' or '*Pamir-Karakorum anomaly*' was subject to a number of publications with the attempt to explain the observed glacier expansions through surging, winter temperature decrease and increased solid precipitation (Hewitt 2005, Gardelle et al. 2012, 2013a, Mukhopadhyay & Khan 2014). Bhambri et al. (2013) found that the observed glaciers in the northeast Karakorum show an irregular behaviour since 1973 with phases of retreat and advance. Evaluations of glacier changes based on GRACE reveal an overall negative trend in this area since 2002 with a strong five-year cycle (Yi & Sun 2014). The authors conclude from their analyses that this five-year signal of glacier change in the Pamir-Karakorum region is controlled by both the ENSO and AO. The former plays a greater role because its correlation with precipitation is much stronger (-0.62, AO: -0.20).

Yao et al. (2012) give an overview on the distribution of the ELA on the TP and its adjacent mountain ranges. Generally, the ELA is lower where accumulation is greater (Bolch et al. 2012). Thus, a low ELA concentrates on the south eastern and the north western TP, influenced by high precipitation amounts from Indian monsoon and mid-latitude westerlies, respectively (see section 1.4.1). These regions coincide with the two centres of recent glaciation on the TP (see section 1.3.3). The smaller number of glaciers and the higher ELA on the interior plateau are the result of decreased moisture supply through the barrier-effect of the surrounding mountain ridges (see section 1.3.1). However, the local ELA for single glaciers can be highly variable both in time and space (see section 1.4.1).

### 1.3.3 Comprehensive physical geography of the Tibetan Plateau

Due to its unique topography, climate and geological history, the Tibetan Plateau (TP, also Qinghai-Xizang Plateau) forms a single natural unit within China (Zhao 1986). Its mean elevation is around 4700 m a.s.l. With an area of around 2.5 million km$^2$ it contains 25% of the total land area of China (Meyerhoff et al. 1991, Zhao 1986). It is surrounded by a series of high mountain ranges. The Kunlun Shan, the Altun Shan and the Qilian Shan in the north, the Hengduan Shan in the southeast, the Himalayas in the south and the Karakoram and the Pamir moutains in the west (Fig. 1.1).

The present physical environment both of the TP and of the whole country is the product of its geological history. The Indo-China tectonic movement during the early and the Yanshan tectonic movement during the late Mesozoic era determined the broad geological structures of China. Since the Eocene the Himalayan tectonic movement, caused by the collision of the Indo-Australian Plate and the Eurasian Plate, shaped the Chinese physical environment. Crustal thickening by subduction during the early Cretaceous perhaps caused the raising of the southern TP to an elevation of 3000-4000 m a.s.l. prior to the actual collision (Murphy et al. 1997). After collision, intracontinental deformation and uplift continued and stepwise migrated northward to involve the whole TP (Fig. 1.4, Li et al. 2014a, Mulch & Chamberlain 2006). The uplift of the eastern plateau occurred much later through crustal shortening in the western and central TP and an eastward flow within the deep crust (Royden et al. 2008). The phase of the Himalayan tectonic movement can be subdivided into several stages (Li 1987, Wang & Li 1985). The first occurred in the middle Eocene when the Himalayas were folded and the Tethys Sea was closed through the emergence of the TP. From the end of the Oligocene to the middle Miocene intensive folding, metamorphism and magmatic activities characterized the Hima-

laya region. As a result a depression area formed north and south of the Himalayas. The northern depression area is called "*Gandise-Yarlung Zangbo Basin*" (Wang & Li 1985) and forms the recent valley of the Yarlung Zangbo (Brahmaputra, Fig. 1.1). The major episode of the Himalayan tectonic movement started in late Miocene (Hsü & Chen 1999, Meyerhoff et al. 1991). The Gandise-Yarlung Zangbo depression basin and the whole TP including the eastern parts were uplifted and new mountains formed. The uplift of the Himalayas and of the TP is closely correlated with the formation of the modern monsoon climate and the increasing desiccation in north western China (see section 1.3.1, An et al. 2001, Han et al. 2014, Molnar 2005). Recent publications state that the function of the high-elevated TP as a heat source is less important for the development of the circulation system than the barrier-function of the surrounding high mountain ridges (see section 1.3.1, Molnar et al. 2010, Seong et al. 2009a).

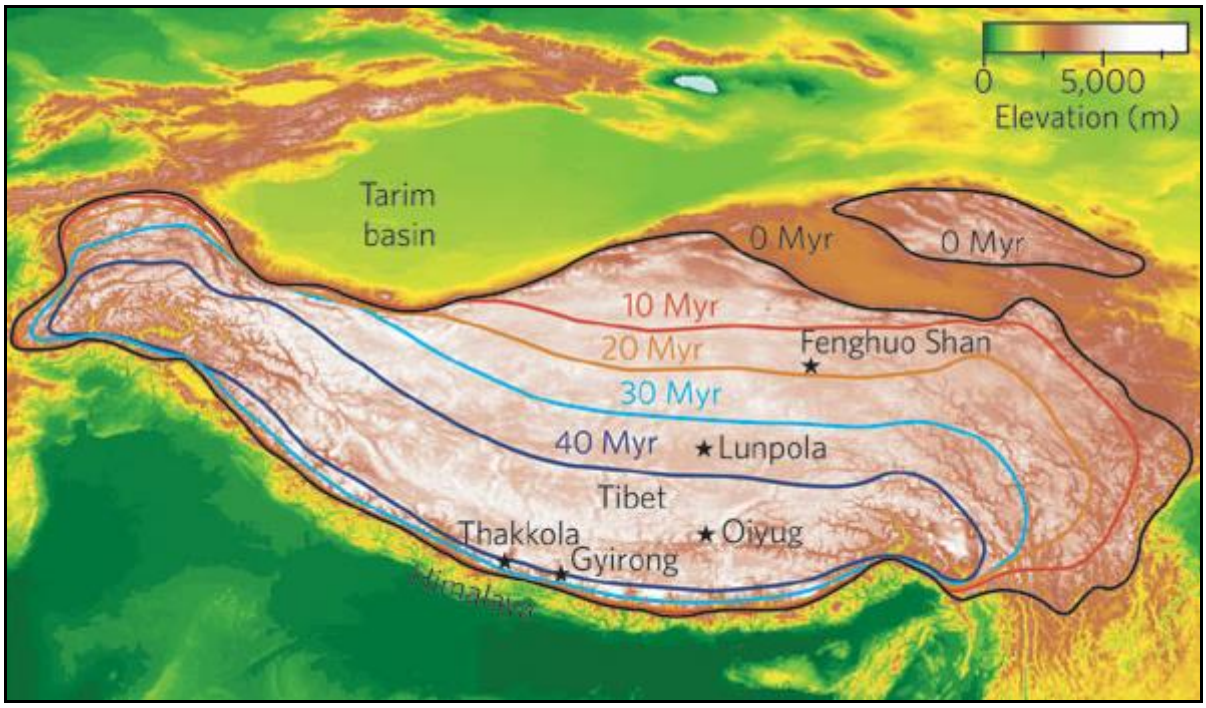


**Fig. 1.4: Elevation history of the Tibetan Plateau. Solid lines show the development of the 4000 m contour as derived from oxygen-isotope data from sedimentary basins (stars) (Mulch & Chamberlain 2006).**

The intensity of the tectonic uplift in geological recent past, the closely linked climatic shifts, the large spatial dimension and the low latitudinal location of the TP (28°-40°N) lead to a complicated and spatially highly variable physical environment. The high mean elevation of the TP with 2500-3000 m a.s.l. in the south- and northeast and above 4500-5000 m a.s.l. in the north western plateau results in generally low temperatures. In spite of rather low latitudes and high amounts of solar radiation there is no frost-free season in most regions of the TP (Zhao 1986). These conditions together with relics of Quaternary glaciation (see section 1.3.2) have led to numerous glaciers and ice caps and to widely distributed permafrost. Aside from the numerous valley glaciers in the Himalayas and other mountain ridges the glaciers on the TP concentrate in two regions. The maritime (temperate) glacier type is located in the south eastern regions, favoured by large amounts of accumulation from the summer monsoon. The extreme continental (polar) type is distributed in the northwest. Despite very low accumulation rates through the westerlies, the glaciers are preserved due to the low temperatures. In the transition zone exist a large number of subcontinental (subpolar) glaciers (Shi & Liu 2000, see section 1.3.5). In the central and north western TP permafrost is well developed and reaches a total thickness of 80 to 90 m. In total, on 1.5 million km$^2$ of the TP permafrost ground

occurs, corresponding to 60% of the plateau area (Cui & Graf 2009). It is the highest and most extensive high-altitude permafrost area on Earth (Liu & Chen 2000) and influences the alpine ecosystem (Wang et al. 2006). From the 1970s to the 1990s, permafrost temperatures rose by up to 0.5°C over most of the TP along with an increasing thickness of the active layer (Wu & Zhang 2010). The reduction of the permafrost area over the same period is estimated to be 100 000 $km^2$ (Kang et al. 2010). The mean lower elevation of permafrost occurrence rose by 25 m on the northern TP and up to 80 m in the southern regions of the TP during the past decades (Cheng & Wu 2007). The widespread degradation of permafrost and seasonally frozen ground caused desertification processes in the eastern and western TP through surface drying and decrease in vegetation cover (Xue et al. 2009, Yang et al. 2010b).

The tectonic uplift of the ancient erosional surface forced the rejuvenation of geomorphic processes and landforms. In the humid south eastern parts of the TP the valley-within-a-valley structure is commonly seen in the middle and lower reaches of large rivers. The domination of fluvial erosion leads to a deeply dissected landscape. The relatively warm and humid climate favours strong biochemical weathering. In the more arid central and north western parts desiccation and nivation processes dominate. Physical weathering through freeze-thaw cycles plays a major role for denudation. In these areas an undulating and almost undissected high plateau surface with periglacial landforms prevails. Due to the recent geological development, the strong glaciation and weak chemical weathering, soils are generally young and slightly developed in most regions of the TP. The hydrological drainage system changes from exorheic in the southeast to endorheic in the interior regions (Neckel et al. 2014, Zhao 1986). In recent years, lake level changes of the endorheic basin lakes on the TP have been subject to extensive research because they are considered to be sensitive indicators of climate variability (Song et al. 2014). Water level fluctuations may reflect regional-scale variations in evaporation, precipitation amounts and glacier melt water supply (Wu et al. 2014). The regional patterns of lake area changes on the TP are diverse (Song et al. 2014a). In general, inland lakes were stable or shrinking before 2000 and expanded in the 2000s. These results were confirmed in various studies using different methods (e.g. Huang et al. 2011, Kropacek et al. 2012, Liu et al. 2009, Wu & Zu 2008, Ye et al. 2007, Zhu et al. 2010). Phan et al. (2011), Song et al. (2014b), Zhang et al. (2011a) and Zhang et al. (2013) report a rapid increase in water levels between 2003 and 2009/10 for the majority of closed basin lakes on the TP. Although some authors emphasize the contribution of glacier melt water to lake level rise (Chen et al. 2007, Wu & Zhu 2008), recent studies agree that lake expansions on the TP in the 2000s were driven primarily by changes in precipitation and evaporation (Song et al. 2014b, Wu et al. 2014, Ye et al. 2007, Zhu et al. 2010).

Both flora and fauna on the TP follow the temperature and moisture induced southeast-northwest gradient. The continental central and north-western regions belong to the paleoarctic realm with dwarf shrubs and montane desert steppe. The warmer and more humid south eastern parts pertain to the oriental realm. Vegetation becomes more diverse with large areas of needle-leaved forests. The east-west oriented high elevated Himalayas south of the TP serve as an effective barrier for tropical and subtropical fauna and flora from the Indian subcontinent. The Kunlun-Altun-Qilian mountain system in the north has a lower relative altitude and numerous mountain passes. The less effective barrier leads to many species of flora and fauna appearing both on the TP and in the Northwest of China. The favourable orientation of the Hengduan Shan in the southeast and the Karakoram in the west enable the migrating and mixing of different species. Furthermore, the noticeable vertical zonation on the TP due to the large relief energy favoured the survival of many pre-Tertiary species (Zhao 1986).

The horizontal zonation on the TP is mainly characterized by the moisture gradient, caused by the atmospheric circulation and the barrier-effect of the surrounding mountain ranges. A latitudinal temperature change exists as well but is usually disguised by the much stronger vertical zonation. The integration of horizontal and vertical zonation leads to the definition of six natural regions on the TP (Fig. 1.1). The regions basically correspond to the climate zones on the TP described by Domrös & Peng (1988). The transition zones between the different regions are continuous. The region of the *southern Himalayan slopes* (A in Fig. 1.1) comprises the East Himalayas at the southern border of the TP. The crest line is remarkably lower than in the Central and West Himalayas and there are a number of maritime (temperate) type glaciers. The glaciers exist even at low altitudes and characteristically run through the montane needle-leaved forest belt and end in the evergreen broad-leaved forest belt. The region experiences no dry period. It is the most humid section of the Himalayas. The Indian summer monsoon lasts from May to October. The humid air masses are directed to the southern slopes of the Himalayas and through the river gorges onto the TP. The elevation of maximum precipitation depends on the location, exposition and topography of the mountain ranges. In the East Himalayas it is generally located around 2500 m a.s.l. (Zhao 1986). At the lowest altitudes tropical rainforests appear, followed by the lower montane belt of evergreen broad-leaved forest. The latter covers the largest area within the vertical zonation and corresponds with the altitude of maximum precipitation. Above this vegetation belt the montane needle and broad-leaved mixed forest belt and the montane coniferous forest belt occur. The upper forest limit is located in an altitude between 3700 and 4100 m a.s.l. Miehe et al. (2007) found the highest tree stands of *Juniperus indica* at an elevation of 4750 m a.s.l. in northern Bhutan. Above the forest belt, there are alpine scrubs and meadows followed by the subnival and nival belts.

The *south-eastern part of the TP* comprises mainly the middle-northern parts of the Hengduan Shan and the eastern parts of the Nyainqentanglha Shan (B in Fig. 1.1). Between June and September the region is under the influence of monsoons, both from the southeast and the southwest. Precipitation amounts decrease to the northwest. Generally, the region inclines from north to south. The upper reaches of the rivers in the north are located in a slightly dissected plateau with broad valleys and gentle slopes. The landscape is shaped by periglacial structures and freezing-thawing processes. A large number of maritime (temperate) type glaciers are located in the eastern Nyainqentanglha Shan. The predominant vegetation consists of alpine scrubs and meadow. The south of the defined region (Zhao 1986) is characterized by a series of north-south directed high mountain ridges and deep river gorges. The foehn and rainshadow effects result in a number of warm, dry valleys in the gorge area. Vegetation consists of thorny and succulent shrubs. With the exception of the dry valleys, a number of montane evergreen broadleaf forests exist. Most areas are covered by mixed leaf and needle-leaved forests (Zhao 1986). Forest areas decrease to the northwest. The upper forest limit is around 4500 m a.s.l. Miehe et al. (2007) even located the highest forest stand of *Juniperus tibetica* at 4900 m a.s.l. This is the highest treeline in the northern hemisphere (Miehe et al. 2007). Above the tree line occur alpine shrubs and meadows.

The *southern TP* is defined as the region between the Gangdise-Nyainqentanglha ranges in the north and the highest section of the Himalayas in the south (C in Fig. 1.1). A large number of maritime (temperate) and subcontinental (subpolar) type glaciers are located in the mountain ranges. The southern side of the Himalayan range is steep-sloped whereas the northern slopes descend gradually to the TP. The latter are characterized by large glaciofluvial fans, morainic platforms and fault basins (Zhao 1986). The Yarlung Zangbo (Brahmaputra) flows from west to east in the graben structure at the southern foot of the Gangdise-Nyainqentanglha ranges. Broad valleys with alluvial plains, barchan sand dunes and braided channels alternate with narrow gorges. As a result of the barrier function of the Himalayas, precipitation amounts generally decrease from east to west. Total precipita-

tion reaches its minimum in the areas of rainshadow to the north of the Himalayas. The predominant vegetation is montane shrubby-steppe and alpine steppe. The broad valleys and lower lower slopes are mainly covered by montane steppe. Above altitudes of around 4500 m a.s.l. the alpine steppe occurs, followed by alpine meadow from around 5000 m a.s.l. upwards. In the valley of the Yarlung Zangbo and adjacent areas, the alpine meadow consists mainly of *Kobresia pygmaea*. The *Kobresia pygmaea* pastures of the southern, south-eastern and central TP are the world's largest ecosystem (Miehe et al. 2008). The extremely firm turf protects large surfaces against erosion. Recent dynamics show a degradation of the pastures under the grazing impact of increasing livestock numbers (Miehe et al. 2008). In recent years, the forest areas of southern and south-eastern TP decreased signifycantly and were replaced by cropland (Cui & Graf 2009).

The *central TP* stretches from southwest to northeast in the central part of the plateau and includes the eastern Qiangtang Plateau, southern Qinghai Province and the eastern Qinghai-Qilian Shan (D in Fig. 1.1). The lofty Qiangtang Plateau is an intramontane basin at around 4700 m a.s.l. between the Kunlun Shan in the north and the Gangdise-Nyainqentanglha Shan in the south (Fig. 1.1). The area belongs to the interior/endorheic drainage system and contains a large number of lakes (e.g. Nam Co). The numerous glaciers in the mountain ranges belong to the subcontinental (subpolar) and the extreme continental (polar) type. The Qiangtang Plateau is characterized by strong cryo-weathering and significant alternation of freezing and thawing. The Qilian Shan in the northeast is separated from the TP by the Hexi Corridor and Lake Qinghai (Qinghai Hu, Fig. 1.1). The latter is the largest lake in China (Zhao 1986). The eastern region of Qinghai is covered by loess. Intense fluvial activity leads to the occurrence of erosional terraces. The climate is subhumid to semi-arid because the lofty, near parallel mountain ranges in the south are an effective precipitation barrier. Generally, precipitation amounts decrease from east to west. The main type of vegetation on Qiangtang Plateau is the alpine steppe, followed by the alpine meadow that consists of *Kobresia pygmaea*. Valleys and basins are covered by marshy meadows. Vegetation in the valleys of the Qilian Shan is dominated by montane forest steppe with needle-leaved forest. Above, alpine scrubs and meadows occur.

The region which includes the Qaidam Basin, the western Qilian Shan, the Altun Shan and the northern slopes of the Kunlun Shan, almost extends in east-west direction on the northern TP (E in Fig. 1.1). It is the transition from the TP to the desert regions of northwest China. The region, especially the Qaidam Basin, is characterized by a temperate desert. On the basis of its thermal conditions and its geological formation it is still considered to be part of the TP. The Qaidam basin is a graben structure between 2600 and 3000 m a.s.l. with a series of concentric belts from the outer mountain barriers to the piedmont plain with lakes in the centre. Land types are composed from sandy deserts with dunes and yardangs, and gravel desert. The central part is covered by clay, silt and salty marshlands (Zhao 1986). The western Qilian Shan consists of a series of mountain ranges with a crest line altitude of about 4000 to 5000 m a.s.l., trending nearly northwest-southeast. The Altun Shan with an altitude of 3600 to 4000 m a.s.l. runs from northeast to southwest. The Kunlun Shan is nearly west-east directed and high ridges reach over 6000 m a.s.l. in the middle section. In the high mountain ranges a number of extreme continental (polar) type glaciers occur (Shi & Liu 2000). The region is influenced by mid-latitude westerlies year round. The numerous mountain ranges in the south cut off the moisture transport from the monsoonal air masses. The Qaidam basin is the driest area on the TP. The desert vegetation mainly consists of xerophilous shrubs. The montane desert occurs at altitudes up to 3800 m a.s.l. followed by the montane steppe.

The *Ngari-Kunlun Shan region* is located in the north-western part of the TP (F in Fig. 1.1). It includes the western Ngari prefecture and the southern side of the middle and western Kunlun Shan. The Ngari prefecture is surrounded by the western Himalayas, the Gangdise Shan and the Karakorum with crest lines of more than 6000 m a.s.l. Due to the dry climate, only few glaciers appear. The Kun-

lun Shan trends towards the northern rim of the TP. Because of its higher elevation and continental location, the climate in the Kunlun Shan is arid and cold. Permafrost occurs everywhere and the western part of the Kunlun Shan is one centre of glaciation with glaciers of the extreme continental (polar) type. The Ngari area is rather temperate. The montane desert steppe and the alpine shrubby-steppe are limited to the Ngari area. In the region of the Kunlun Shan, alpine desert vegetation, characterized by sparse cover and dwarf plants, dominates. The vegetation mainly consists of the shrub *Ajania tibetica* which is a species endemic to the TP (Zhao 1986).

During the Holocene the natural environment of the TP changed due to varying forcing of the mid-latitude westerlies and the monsoonal circulation. Analyses of pollen records show strong regional differrences in vegetation changes over the TP (Herzschuh et al. 2010). In the central, northern and eastern regions of the TP, vegetation types were relatively stable. Environmental changes were primarily characterized by the evolution from steppe to desert steppe in the north (Li et al. 1985) and by a gradual variation from temperate steppe to alpine meadows in the central and eastern regions. In the Qaidam Basin, temperate desert was the dominating land cover throughout the Holocene (Herzschuh et al. 2010). The greatest environmental changes are found in the north- and south-eastern regions of the TP. Pollen records from Lake Qinghai indicate that forest areas were replaced by forest steppe since the mid Holocene. In the south and southeast TP, forest and savanne vegetation gradually changed to shrubby steppe and steppe (Herzschuh et al. 2010, Li et al. 1985).

### 1.3.4 Methodological background

The methods used in this thesis are centred in the field of numerical glacier mass balance modelling. A conceptual, physically based model has been developed that directly couples the glacier SEB to a subsurface multi-layer snow model in order to derive glacier MB and runoff (see section 2.3.1). The major physical processes are represented by mathematical relationships. A first outline of such a model was given by Anderson (1976). These formulations are in contrast to index models that use one or more variables in an empirical expression to estimate glacier melt (Singh & Singh 2001). Air temperature is the most commonly used index because it strongly influences the most important energy sources for melt on most glaciers (longwave incoming radiation and sensible heat flux) (Ohmura 2001). This section gives an overview of the basic assumptions and concepts in glacier SEB (section 1.3.4.1) and MB modelling (section 1.3.4.2).

#### 1.3.4.1 Glacier surface energy balance

The glacier SEB describes the balance in the amount of energy of the glacier near-surface layer due to flows of energy to or away from this layer (Cogley et al. 2011). The near-surface layer links atmospheric processes and the glacier body and is assumed to be an interface, the thickness of which approaches zero and therefore cannot store energy. The energy fluxes that govern the energy exchange between glacier surface and atmosphere or subsurface are presented in Fig. 1.5. If the sum of these fluxes, the energy balance, is positive and surface temperature is at the melting point, melt occurs. Phase changes, such as melting and sublimation, couple the surface energy balance to the mass balance. Hence, it is crucial to determine the energy balance to model glacier ablation and, in general, to understand the influence of meteorological conditions to the energy budget of a glacier surface.

On most glaciers, shortwave and longwave radiation and the turbulent fluxes play a major role in the surface energy balance (Fig. 1.5). Incoming shortwave radiation ($SW_{in}$) shows both a daily and seasonal cycle and is additionally modified through the structure of the atmosphere, cloud cover and local

topography. Thus, the total shortwave radiation (or global radiation) reaching the glacier surface consists of direct and diffuse radiation (Singh & Singh 2001). Direct radiation is oriented parallel to the sun rays while diffuse radiation reaches the glacier from all directions. Depending on surface albedo ($\alpha$) a certain proportion of $SW_{in}$ is directly reflected ($SW_{out}$) by the surface and the rest is absorbed. The amount of absorbed $SW_{in}$ penetrates to different depths within the snow or ice and functions as an internal heat source. The exponentially decreasing trend of the radiation flux with depth causes the major proportion of radiation being absorbed in the upper 10 cm beneath the surface (Singh & Singh 2001). Longwave incoming radiation ($LW_{in}$) as emitted by the atmosphere increases with increasing air temperature, air humidity and cloud cover. Surrounding slopes also become a source of longwave radiation both for the glacier surface and the atmosphere depending on the surface temperature. The glacier surface has an emissivity of approx. one and almost all $LW_{in}$ is absorbed. Longwave outgoing radiation ($LW_{out}$) emitted by the glacier surface is generally larger than $LW_{in}$. As the range of $LW_{out}$ is restricted by a maximum glacier surface temperature at the melting point, net longwave radiation can be close to zero or even positive on warm and cloudy summer days (Oerlemans 2010). The effect of clouds on net shortwave ($SW_{net}$) and longwave radiation ($LW_{net}$) is of opposite sign and additionally depends on $\alpha$. Generally, increasing cloud cover leads to less $SW_{in}$ and more $LW_{in}$. If $\alpha$ is high, the change in $LW_{net}$ is larger than the change in $SW_{net}$ and the net radiation balance increases (Oerlemans 2010). If the atmospheric boundary layer above the glacier is not dominated by stable conditions, heat is transferred between atmosphere and glacier through turbulent exchange processes. The turbulent fluxes are distinguished between sensible and latent heat flux. Depending on the temperature difference between glacier surface and air, the sensible heat flux ($Q_{sens}$) transfers heat to or from the surface. When the overlying air is warmer than the glacier surface sensible heat is directly transferred from the lower part of the boundary layer to the snow or ice. The direction of the latent heat flux ($Q_{lat}$) is controlled by the vapour pressure gradient. When the vapour pressure in the air is larger than that at the glacier surface, moisture is transferred from the boundary layer to the glacier. This results in the release of latent heat. On most glaciers a significant proportion of the energy available for melt is transferred from the atmosphere through the turbulent fluxes. The importance of turbulent exchange processes for the glacier surface was already discussed by Morris (1989). The subsurface or ground heat flux ($Q_G$) is small compared to the other fluxes and approximates zero averaged over longer periods. As it depends on the temperature difference between glacier surface and subsurface, it is generally directed to the surface in winter and from the surface in summer. When rain falls on the glacier surface, it is cooled to the surface temperature. The heat transferred from the rain to the snow or ice is the difference between the energy content of the water before and after cooling. The amount of heat transfer from rain depends on the quantity of rain and its temperature difference to the surface. Depending on the temperature of the snow or ice surface, the heat release through rain can result in melt or in a temperature rise (Singh & Singh 2001). On some glaciers this process is important for SEB and MB calculations. For glaciers on the TP it is negligible and therefore not considered within this thesis.

When the sum of these energy fluxes, the energy balance, is positive, the glacier surface layer is heated to the melting point. After this, the energy surplus is defined as melt energy ($Q_{melt}$) and used for melting the snow or ice surface. The parameterizations of the various energy fluxes as applied in the presented SEB/MB model in this thesis are presented in detail in section 2.3.1. The proportion of the various energy balance components to the glacier SEB varies with the surrounding climate. The large area of the TP is under the influence of concurrent interactions and feedback mechanisms of different circulation systems (see section 1.3.1). It is obvious that glaciers in different climate regions on the TP and adjacent mountain ranges show contrasting behaviour in recent years (section 1.3.2).

Possible reasons from the SEB components are revealed in chapters 2 to 6 and are jointly analyzed in chapter 7.

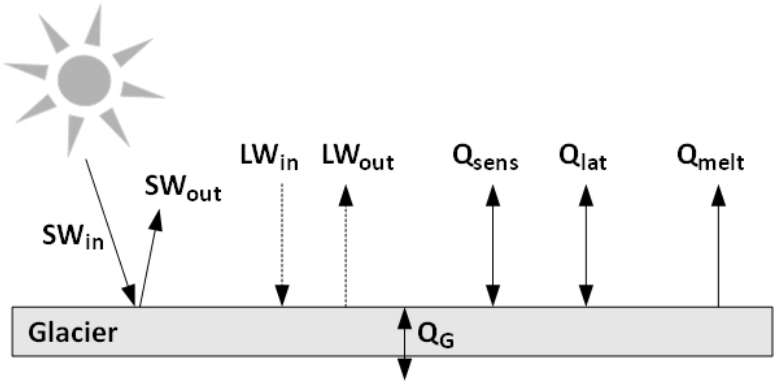


**Fig. 1.5: Schematic picture of the major energy fluxes at the glacier surface. Symbols are explained in section 1.3.4.1.**

### 1.3.4.2 Glacier mass balance

The glacier MB describes the change of mass of a glacier as a whole or a particular part of the glacier over a certain period (Cogley et al. 2011). Generally, this period spans from minimum total mass in one year to minimum total mass in the next year (end of ablation season to end of ablation season) (Hubbard & Glasser 2005). For glaciers on the TP we apply MB years from 1 October to 30 September. Elsberg et al. (2001) further divide the glacier-wide MB into a conventional balance that includes topographic feedbacks of the glacier, and into a reference-surface balance that refers to an unchanged glacier surface and area over the entire period. In this thesis the reference-surface balance is calculated for the various glaciers, respectively. As the reference-surface balance does not incorporate any feedback effects of glacier response to climate, it is more closely related to climate variations than the conventional balance (Cogley et al. 2011). The total MB of a glacier incorporates different components of accumulation and ablation for surface, interior and the base of a glacier (Fig. 1.6). The surface MB includes all mass changes within the layer above the summer surface of the previous year and is largely determined by climate conditions. The internal MB is the change in mass in the interior of the glacier beneath the summer surface, e.g. internal ablation through heat release from percolating melt water and internal accumulation through refreezing within the firn or ice. Thus, the internal MB is also influenced by climate conditions. The sum of surface MB and internal MB is therefore called climatic mass balance (Cogley et al. 2011). The basal MB accounts for mass changes at the base of a glacier (Fig. 1.6).

The MB model applied in this thesis calculates the surface MB and to a certain degree also the internal MB (Fig. 1.7). The amount of $SW_{in}$ that penetrates into the snow or glacier ice is explicitly calculated and may lead to subsurface melt (see section 2.3.1). If the subsurface melt happens in layers beneath the last summer surface, this mass change is part of the internal ablation. The MB model structure allows surface and subsurface melt water to percolate down to the ice surface (see section 2.3.1). In glacier regions where a cold firn layer is present beneath the snow, the refreezing would be part of the internal accumulation. This effect has to be considered especially in the accumulation zones of glaciers with slightly negative or positive MBs and only little precipitation. This is the case for glaciers on the central TP (see chapter 3). Within the applied MB model it is not possible to distinguish properly between surface MB and internal MB.

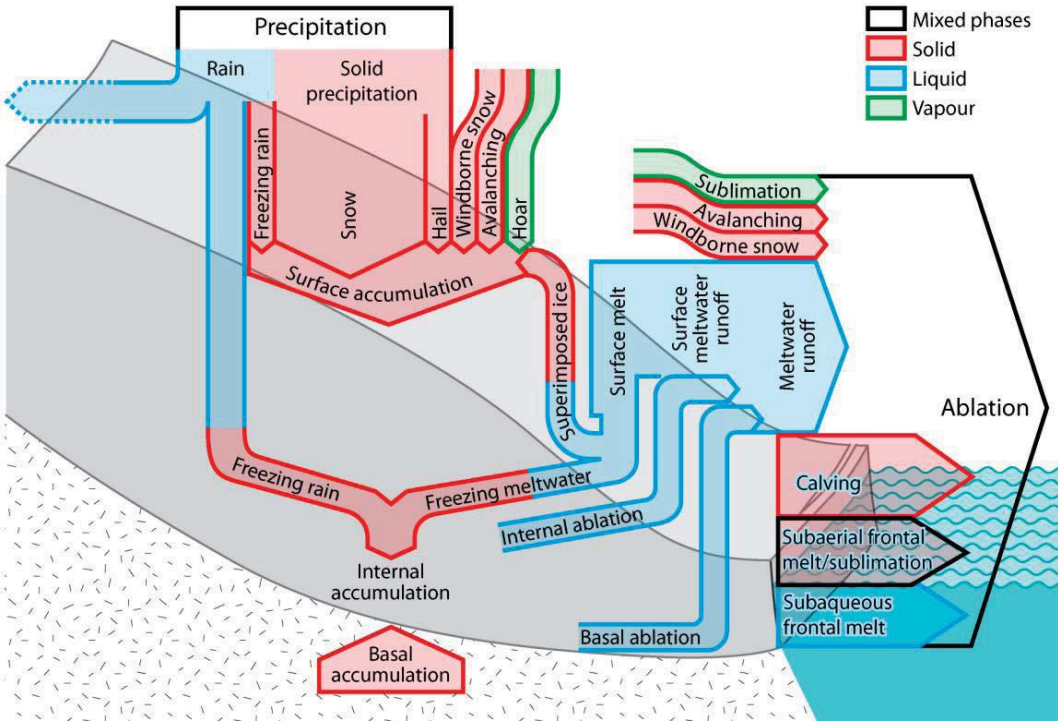


**Fig. 1.6: Components of the mass balance of a glacier. The arrows have arbitrary widths and do not indicate physical pathways of mass transfer. (Cogley et al. 2011)**

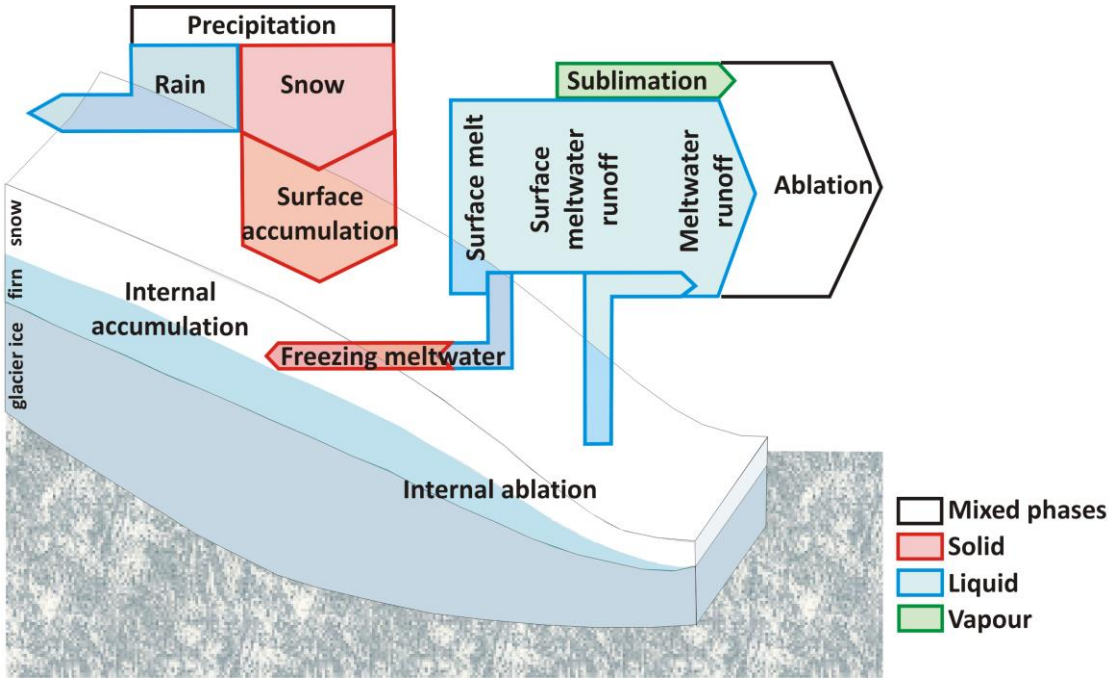


**Fig. 1.7: Glacial mass balance components considered in the MB model applied in this thesis. The arrows have arbitrary widths and do not indicate physical pathways of mass transfer. (modified after Cogley et al. 2011)**

In this thesis glacier MB is assessed solely by SEB model calculations and results are evaluated both with observations on point scale and with the results of remote sensing approaches for the total glacier area. The calculation of the MB through SEB models or through statistical approaches (e.g. temperature-index models) is called *indirect method* (Kaser et al. 2003, Schöner 2003). Common methods to measure the MB of a glacier are the glaciological method, the geodetic method and the hydrological method. Less common because the requirements are less practicable are the flux meth-

od and the flux-divergence method (Kaser et al. 2003). The SEB model applied in this thesis to calculate the MB of various glaciers on the TP is explained in detail in section 2.3.1. The integrated MB components are visualized in Fig. 1.7. The evaluation and discussion of the model results is mainly based on MB data obtained by the glaciological and the geodetic method. Therefore, these methods are explained in more detail below.

The glaciological method (or direct method) determines the surface MB in-situ on the glacier surface by repeated point measurements of accumulation and ablation through ablation stakes and snow pits. Therefore, the length of the stake above the surface, the snow depth and the corresponding density is measured at every stake. Through repeat measurements the surface MB is calculated from the relative change in height of both snow and ice surfaces, multiplied by the vertically-averaged density of the snow, firn or ice that has been added or removed. Also the amount of refrozen melt water within the snow and the amount of superimposed ice can be derived. These rates may contribute to the internal MB. Nevertheless, per definition the glaciological method only refers to the surface MB (Cogley et al. 2011). The result of this method is a point surface MB. A simplified scheme of the measurement and calculation procedure is presented in Fig. 1.8. The change of mass (*Δmass*) at a point *i* within a period $t_1$ to $t_2$ can be determined after Dyurgerov (2002) from

$$\Delta mass_i = \rho_{snow1} \cdot h_1 + \rho_{ice} \cdot (z_1 - z_2) - \rho_{snow2} \cdot h_2 , \quad (1.1)$$

where $\rho$ is the density of ice or snow/firn, $h$ is the snow height (if any) and $z$ is the distance from the top of the stake to the ice surface. The dimension of MB is [kg] (mass). When the MB is given per unit area, it is termed specific MB and it is generally given in the dimension [kg $m^{-2}$] or in [mm w.e.] (millimetre water equivalent). The units kg $m^{-2}$ and mm w.e. are numerically identical because 1 kg of liquid water with a density of 1000 kg $m^{-3}$ has a vertical extent of 1 mm when distributed uniformly over 1 $m^2$ (Cogley et al. 2011). The glaciological method is the only method that is based on in-situ measurements and is considered to be the most accurate (Kaser et al. 2003). However, it requires repeated field measurements under sometimes challenging conditions. In this thesis we use measured surface height changes and density measurements of the ablation stake network at Zhadang glacier from 2009 to 2011 to calculate point surface MB that are compared to the MB model (see chapter 2). Staff from ITP maintains 25 ablation stakes in the ablation zone and accumulation zone of the glacier since 2005. The time span between two consecutive measurements ranges between four days and seven month.

Geodetic methods determine glacier MB by the volumetric change of the ice mass through time from repeated mapping of the surface elevation (Hubbard & Glasser 2005). Repeated high-resolution altimetry data can be obtained from satellite missions like ICESat, TerraSAR-X and SRTM (e.g. Bolch et al. 2012, Neckel et al. 2013, 2014, Holzer et al. 2014, see chapters 3, 5 and 6). The data is used to investigate spatial patterns of mass thickening or thinning on a glacier or ice cap. Due to the satellite image resolution the concerned ice mass has to exceed a certain minimum area. The volume change can be investigated only for the entire glacier and between the dates given by the available satellite images (Paterson 1994). The conversion from a volume or elevation change again requires information on the density of the mass that was lost or gained (Cogley et al. 2011). In regions where no in-situ measurements for snow and firn densities are available a mean density has to be assumed (Neckel et al. 2013, 2014). Thus, mass changes in the accumulation areas are difficult to determine accurately (Kaser et al. 2003). The geodetic method does not yield altitudinal gradients of MB but is very useful complementary to the glaciological method and for the evaluation of MB models over longer periods.

When comparing surface elevation changes and associated MB from the geodetic method and the applied SEB/MB model, the effect of mass transition and redistribution between accumulation and

ablation areas through ice flow has to be considered. The vectors of ice movement are not perfectly horizontal to the glacier surface. In the accumulation are there is a small downward component and an upward component in the ablation area. Thus, ice flow balances the elevation changes through accumulation (glacier thickening) and ablation (glacier thinning) (Paterson 1994). Large accumulation or ablation rates increase the flow speed (Bolch et al. 2012). Also the thermal structure of a glacier influences its motion because the viscosity of cold ice is higher than the viscosity of temperate ice (Aschwanden & Blatter 2006). Thus, the presence of cold ice leads to lower velocities. The SEB/MB model applied in this thesis does not account for glacier dynamics. Therefore, it will produce a steepening of the surface elevation gradient over time, with increased glacier thickening in the accumulation areas and increased glacier thinning in the ablation areas. Most of the processed glaciers and ice caps are of polythermal or cold thermal regime with relatively small precipitation amounts (see sections 1.3.5 and 1.4), characterized by generally low ice velocities (e.g. Hu et al. 2014). Thus, we assume that the derived discrepancies from the neglectance of glacier dynamics are within the calculated model uncertainties.

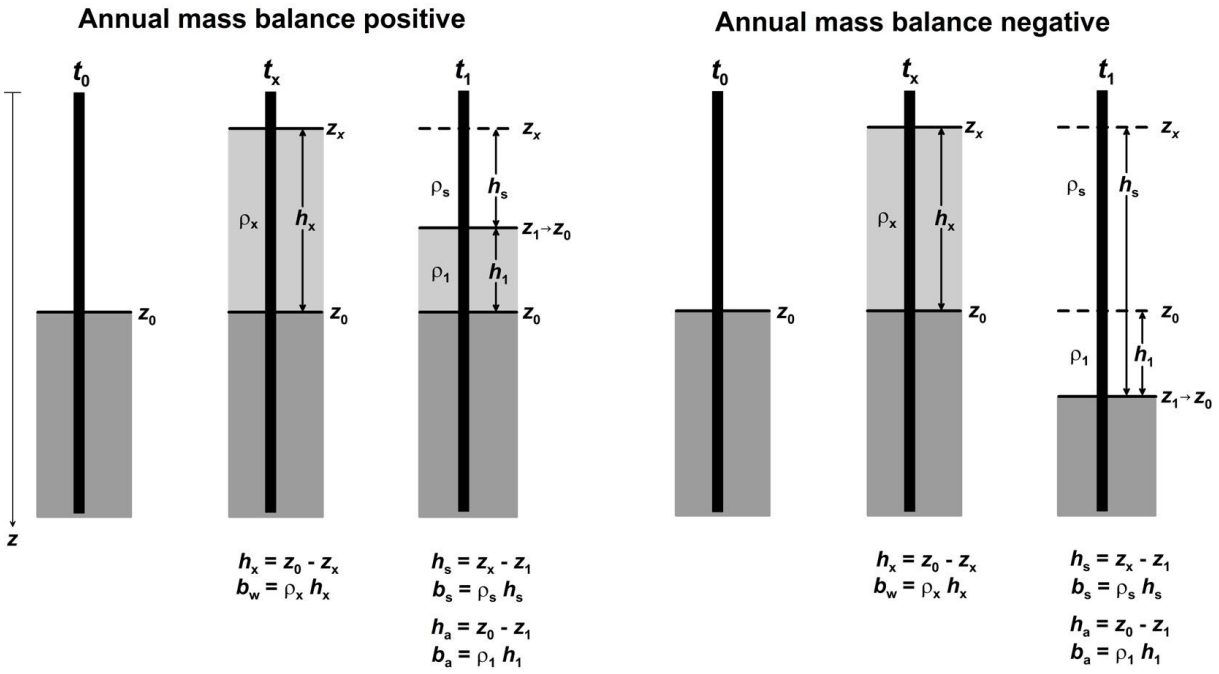


**Fig. 1.8: Stake measurements of seasonal MB in a year of positive (left) and a year of negative (right) surface MB, with no superimposed ice. The *z* coordinate is positive downwards, with origin *z* = 0 at the top of the stake. Light shading represents snow; dark shading represents firn or glacier ice. Measurements are made at $t_0$, the start of the accumulation season; at $t_x$, the start of the ablation season (strictly, the date when the mass of the column is at its maximum for the MB year); and at $t_1$, the end of the MB year. The quantities measured are: at $t_0$, when by definition there is no snow, the glacier surface height $z_0$ (the height of the summer surface); at $t_x$, the glacier surface height $z_x$ and (in a nearby snow pit) the mean snow density $\rho_x$; and at $t_1$, the surface height $z_1$ and the mean density $\rho_1$ of the snow (if any). The winter balance $b_w$ is the change of mass between $t_0$ and $t_x$. The summer balance $b_s$ is the change of mass between $t_x$ and $t_1$. It is impractical to measure $\rho_s$ or $\rho_1$ when the annual balance is negative. In these cases the density of the lost mass is supplied by making an appropriate assumption. At the instant following $t_1$, any residual snow is deemed to become firn and the glacier surface, at $z_1$, becomes the summer surface $z_0$ of the next MB year. Subscript *a* denotes the annual value for *h* and *b* (Möller 2011 after Cogley et al. 2011).**

### 1.3.5 Characteristics of glaciers on the Tibetan Plateau

When working on glaciers on the TP the different climate influences in the different regions have to be considered. It is obvious that the varying atmospheric circulation patterns in the past (section 1.3.1) led to spatially and temporal heterogeneous climate and glacier changes in the past (section 1.3.2) with an on-going influence on the present physical environment of the TP (section 1.3.3). Taking into account the numerous feedback mechanisms within the glacier SEB and MB (section 1.3.4) it is practical to classify the glaciers on the TP according to their thermal regime and their accumulation regime.

The timing and amount of snowfall is revealed to be a key process for the SEB and MB of glaciers on the TP (Fujita 2008a,b, Fujita & Ageta 2000, Kang et al. 2009, Mölg et al. 2012, Yang et al. 2011, 2013). According to the governing circulation patterns, the glaciers on the TP receive their major accumulation in different seasons. Most glaciers on the eastern, southern and southern central TP and in the eastern and central Himalayas belong to the so called "*summer-accumulation type*" that was defined by Ageta & Higuchi (1984). They are gaining mass mainly from the summer monsoon snowfall. Maximum annual ablation and accumulation occur simultaneously in summer. The annual variation in MB is generally small (Ageta & Fujita 1996, Cogley et al. 2011). "*Summer-accumulation type*" glaciers are very sensitive to changes in air temperature because they highly depend on summer snowfall associated with the positive albedo feedback that restrains the heat supply from $SW_{in}$ (see section 1.3.4.1). A temperature rise will not only increase melt directly, but also cause a decrease in the solid proportion of total precipitation and additionally decrease $\alpha$ (Fujita 2008a,b, Fujita et al. 2007). In a humid environment, more liquid precipitation also increases the glacier sensitivity. "*Winter-accumulation type*" glaciers as known in Europe and North America are concentrated on the western TP including the western Himalayas. They are characterized by distinct accumulation and ablation seasons and are less sensitive to changes in air temperature (Fujita 2008). Based on atmospheric model data Maussion et al. (2014) modified the classification of TP glaciers depending on their precipitation seasonality. Using an objective clustering approach with the percentage of precipitation falling in December-January-February (DJF), March-April-May (MAM) and June-July-August (JJA) as input variables, the authors define five distinct output classes (Fig. 1.9). The classes are named after their cluster centres' characteristics. The dominant classes are the winter- (DJF) and summer- (JJA) accumulation types with the largest occurrence at glaciers on the TP. The spring-accumulation type (MAM) has fewer elements (Fig. 1.9). Two intermediate classes are defined for glaciers that experience maximum precipitation in summer (MAM/JJA) or the winter (MAM/DJF) but with less defined centres (Maussion et al. 2014). The mean seasonal cycle of each class shows that the JJA, MAM and DJF classes each have a distinct precipitation peak (Fig. 1.9) whereas the two mixed classes have a less pronounced seasonal cycle. The MAM/DJF class experiences precipitation all year with two peaks in February and August. Except for the DJF class, all precipitation classes show their minimum in November/December. It is obvious from Fig. 1.9 that the glaciers on the western TP and the adjacent mountain ranges are dominated by the DJF and the southern central and north eastern regions are dominated by the JJA precipitation class. The MAM class is distributed on the northern and north western TP. On the southeast, northeast, northwest and western central TP as well as along the Himalayas, large regions of the mixed precipitation classes occur and classes change over short distances. The high variability in the precipitation regimes has been observed by many authors at least for the Himalayas (e.g. Fujita & Nuimura 2011, Kansakar 2004). Local factors such as the glacier exposition and the topographic surroundings with respect to the wind direction play a significant role. The data basis for the study of Maussion et al. (2014) is total precipitation. As mentioned in section 1.3.3 air temperatures on the TP are generally low and decrease with altitude. Therefore, large propor-

tions of the total precipitation fall as snow even in summer. The derived precipitation regimes can be directly related to the accumulation regimes of the glaciers.

Huang (1990) and Shi & Liu (2000) group the glaciers in China based on air temperature, annual precipitation and their mean ice temperatures. The maritime (or temperate) glaciers are mainly distributed on the south eastern TP (Hengduan Shan, eastern Nyainqentanglha Shan) and in the eastern Himalayas (Fig. 1.1). The glaciers consist of temperate ice that is at its pressure-melting point over their entire ice column (Cogley et al. 2011). Only the near-surface layer experiences seasonal cooling because the winter snow cover is generally thin. Temperate glaciers are very sensitive to air temperature changes because the whole ice body is already at the melting point. A small temperature rise results in a large uplift of the ELA. During the maximum of the LIA glaciers of this type were about 29% larger than in 2000 (Huang 1990, Shi & Liu 2000). Subcontinental (or subpolar, polythermal) glaciers are mainly distributed in the mid to eastern Qilian Shan, the eastern Kunlun and Tanggula Shan, the Bayan Har Shan, the western Nyainqentanglha Shan, at the northern slopes of the mid to western Himalayas and the Karakorum (Fig. 1.1). Glaciers of this type are characterized by a thermal layering of both cold and temperate ice. Different polythermal structures can be found depending on the climate and glacier geometry. In cold regions, the bulk of ice is cold except for a temperate layer near the bed which is due to the geothermal heat flux. When high melt rates occur on the glacier, the refreezing of the infiltrating water produces latent heat that warms up the cold firn or the glacier ice and allows for the formation of temperate ice within a cold glacier (Aschwanden 2008, Cogley et al. 2011, Gilbert et al. 2014, Huang 1990). The subcontinental glaciers on the TP were about 23% larger during the LIA maximum (Shi & Liu 2000). The extremely continental (or polar, cold) glaciers are developed mainly on the western TP, in the western Kunlun Shan, the Qiangtang Plateau, the eastern Pamirs and the western sections of the Tanggula and Qilian Shan (Fig. 1.1). Climate conditions are generally cold and dry and most of the available energy at the glacier surface is used for sublimation. Besides the near-surface layer and possibly the bottom layer, the glaciers consist of cold ice throughout (Cogley et al. 2011). Cold glaciers generally show low velocities (Aschwanden & Blatter 2006) and are less sensitive to changes in air temperature. During the LIA maximum they were only 10% larger than in 2000 (Huang 1990, Shi & Liu 2000). Shi & Liu (2000) estimate the glacier change on the TP until the end of the 21st century. From the knowledge of the different thermal glacier types it is not surprising that the area and volume decrease is largest for the temperate glaciers and smallest for the cold glaciers. This corresponds to the recent observations published by Yao et al. (2012) (see section 1.3.2).

## 1.4 Study sites

After giving a plateau-wide overview in terms of atmospheric circulation and different aspects of the physical geography, this section focuses on the five study sites selected for this thesis. The four glaciers and one ice cap are distributed over different regions and climate zones (Fig. 1.1). These are influenced by different precipitation regimes (Fig. 1.9) on the TP. In the following section (1.4.1) each study area is presented based on the previous summaries (section 1.3).

### 1.4.1 Regional climate setting and glacier characteristics of the study sites

Five glaciers and ice caps of various size, climate and thermal characteristics have been chosen for SEB and MB studies. These are Zhadang glacier on the southern central TP, Halji glacier in the western Himalayas, Naimona'nyi glacier on the south western TP, Purogangri Ice Cap on the central TP and a glacier in the Muztagh Ata Shan on the north western TP (Fig. 1.1, 1.9). The maximum distance

between the regions is 1700 km (Zhadang glacier to Muztagh Ata). For the climatological analyses, data from the *High Asia Reanalysis* (HAR, Maussion et al. 2014) is applied (see section 2.2.3).

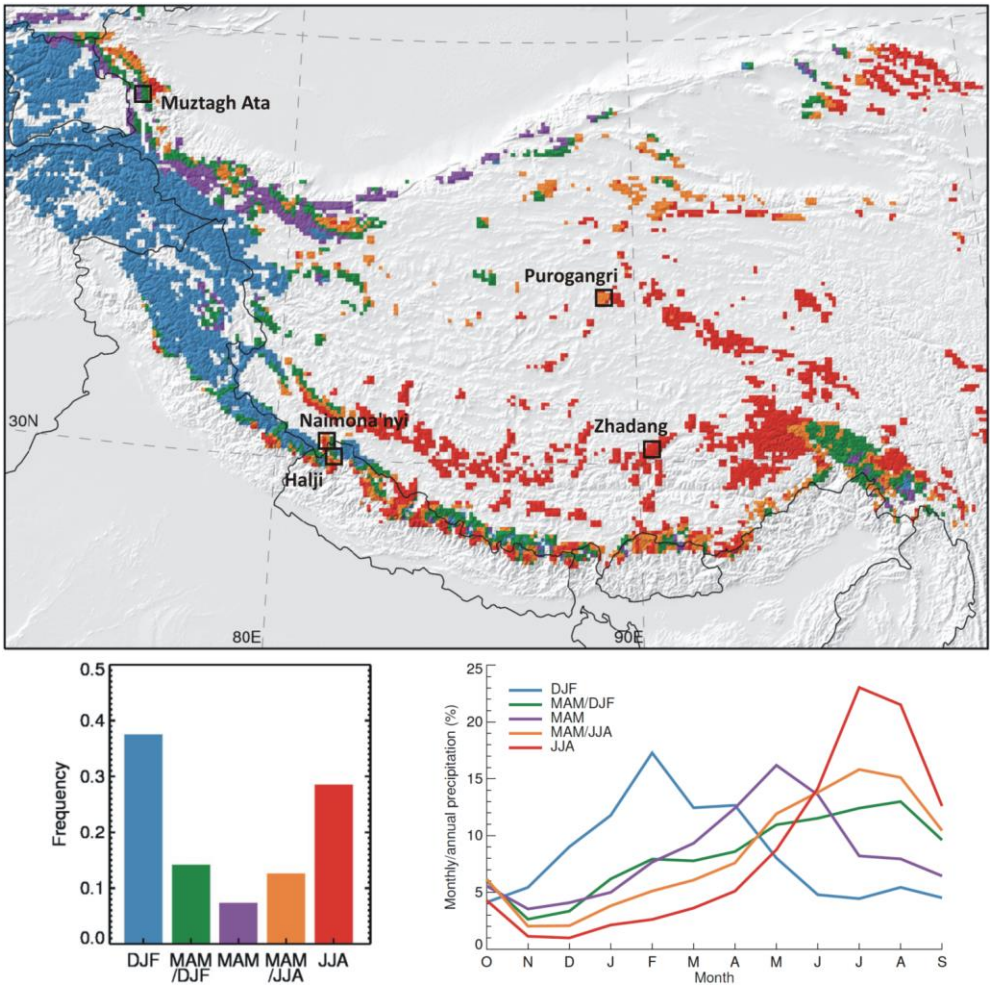


**Fig. 1.9: Classification of glacier accumulation regimes according to precipitation seasonality. Only glacierized grid points are shown. The black boxes show the location of the study areas of this thesis. The colour legend is described in the lower left histogram plot, showing the relative occurrence of each class in the map. The lower right plot shows the mean contribution of each month to annual precipitation for the five glacier clusters (modified after Maussion et al. 2014).**

***Zhadang glacier***

The Zhadang glacier is a northwest exposed valley glacier (≈2 km$^2$) at the northern slope of the western Nyainqentanglha Shan in the southern central TP (Fig. 1.1, 2.1). The region is dominated both by Indian monsoon and mid-latitude westerlies (Kang et al. 2009), leading to a pronounced seasonal contrast, mostly in terms of precipitation, temperature and wind directions (Fig. 1.10, 1.11, Domrös & Peng 1988). Winter months are cold, dry and characterized by strong westerly winds. In summer, winds from south western directions dominate at the glacier site indicating the summer monsoon circulation (Fig. 1.11, see section 1.3.1). It is obvious from Fig. 1.9 and 1.10 that the glacier is under the JJA precipitation regime. Observations at nearby Nam Co Station in 2005/06 show that more than 90% of the annual total precipitation was recorded between May and September (You et al. 2007; Zhang et al. 2013). Snowfall measurements on Zhadang glacier and atmospheric model precipitation also show this distinct seasonality (Fig. 1.10, 2.2, 2.3). The mean annual precipitation amount from HAR is 534 mm and around 81% of the annual total falls between May and September. Pronounced precipitation maxima in summer and minima in November and December are characteristic features

of the subhumid eastern parts of the so called "*Subalpine Plateau Zone*" and "*Temperate Plateau Zone*" (Domrös & Peng 1988) on the southern central TP (Maussion et al. 2014) (Fig. 1.1, 1.9). Therefore, glaciers in this region belong to the so called "*summer-accumulation type"* glaciers (Ageta & Higuchi 1984) that show a strong sensitivity to air temperature variations during the monsoon season. Thermally, Zhadang glacier belongs to the polythermal glacier type (see section 1.3.5).

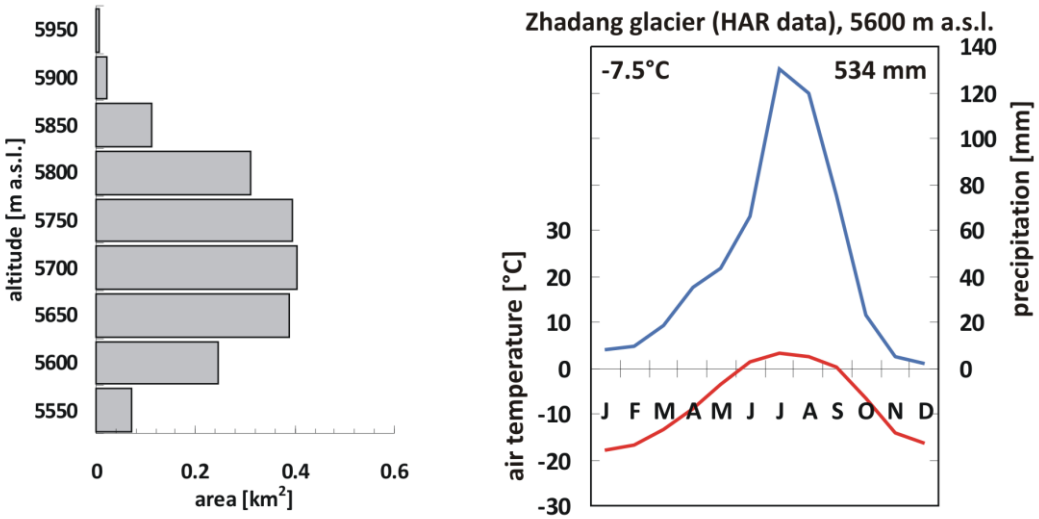


**Fig. 1.10: Glacier hypsometry and climate chart for Zhadang glacier. The plots are generated from the data used in chapter 2.**

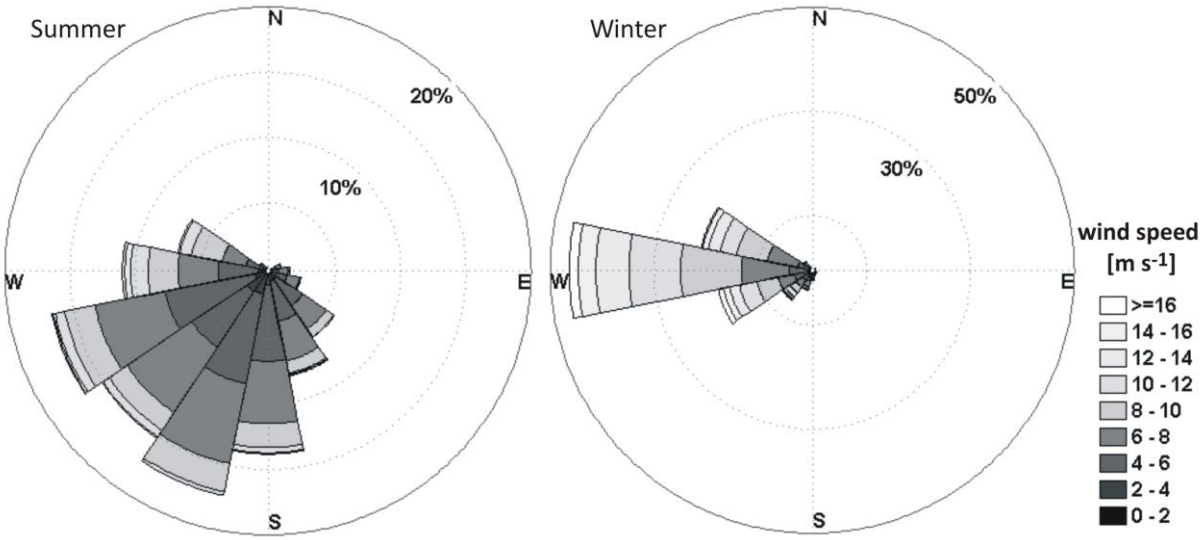


**Fig. 1.11: Wind direction and intensity from hourly HAR data at Zhadang glacier for summer and winter season between October 2001 and September 2011 (summer: 1 April – 30 September, winter: 1 October – 31 March).**

Bolch et al. (2010) derived glacier changes between 1976 and 2009 for the western Nyainqentanglha Shan. Generally, ice cover is higher in the south eastern regions, reflecting the luv-side to the summer monsoon circulation. The total glacier area decreased by ≈6% between 1976 and 2001 and length measurements of five glaciers indicate a retreat of ≈10 m $yr^{-1}$. Relative mass loss was greater for smaller glaciers and for glaciers with lower median elevation. Analyses of the glacier hypsometry in 1976 and 2001 revealed that highest absolute ice loss occurred between 5500 and 5700 m a.s.l. (Bolch et al. 2010). A detailed study of Zhadang glacier confirmed these results. The small glacier is in the altitude range of the highest observed mass loss (Fig. 1.10) and experienced the greatest relative

area loss (-14.2%). Measured retreat at the glacier tongue is ≈300 m in 1976-2009 (Bolch et al. 2010). Wu et al. (2014) determined glacier surface elevation changes for the total western Nyainqentanglha Shan from ICESat and SRTM data between 2003 and 2009. Glacier surface elevations decreased by 8.39±0.45 m over the period of seven years. The authors calculate a mean glacier MB of -490 kg $m^{-2}$ over the corresponding period. They conclude that the contribution of glacier melt water to the observed lake level rise of Nam Co between 2003 and 2009 is ≈21% (Wu et al. 2014).

***Halji glacier***

The glacier is located in Limi valley, north western Nepal, around 6 km from the village Halji. Therefore, within this thesis it is named Halji glacier. The northeast exposed debris free valley glacier (≈2.3 $km^2$) is situated on the southern slope of the Nalakankar Himal, a northern ridge of the western Himalayas near the border to Tibet (Fig. 1.1, 4.1). According to the climate classification of Domrös & Peng (1988) the region is located within the semi-arid part of the "*Temperate Plateau Zone*". The region is dominated by Indian monsoon in summer and mid-latitude westerlies in winter. This is evident in a pronounced seasonal contrast of precipitation, temperature and wind direction (Fig. 1.12, 1.13). The wind direction in summer shows a second maximum in the north western sector (Fig. 1.13). This might be the effect of the northern and southern shift of the westerly jet (see section 1.3.1). The winter months are cold, relatively dry and maximum wind speeds occur predominantly from the northwest (Fig. 1.13). In summer, winds from southern directions dominate due to the strong influence of the monsoon circulation. The mean annual precipitation amount from HAR is 605 mm. Miehe et al. (2001) give an annual total of 176 mm $yr^{-1}$ for the period 1973-84 for the station Burang (3880 m a.s.l.) ≈30 km northwest of the glacier. The two values can be hardly compared because precipitation amounts and seasonality vary largely over short distances in this region (Fig. 1.9). Around 64% of the annual total at Halji falls between May and September. A second precipitation maximum is evident around February (Fig. 1.12). This implies that the region is influenced by different precipitation regimes governed by the spatially heterogeneous relief of the Himalayan range. According to Maussion et al. (2014) (Fig. 1.9) the glacier is situated in a zone where spring, summer and winter accumulation regimes converge (MAM/ DJF, MAM/JJA), mostly depending on the location of the glaciers to the main wind direction. This region of mixed type glaciers expands along the Himalayan range to the east and corresponds to the transition zone between temperate and polythermal glaciers (see section 1.3.5). Despite its lower altitude Halji glacier receives more precipitation than Zhadang glacier but with a different seasonal pattern. Air temperatures show the same annual cycle and are slightly lower at Halji glacier (Fig. 1.10, 1.12). Analyses of ICESat data for the period 2003-2009 indicate a fast loss of volume of the glacier (Kropacek et al. 2013).

***Naimona'nyi glacier***

The Naimona'nyi glacier is a north to northwest exposed debris free valley glacier (≈7.8 $km^2$), located in the north western Naimona'nyi massif (Gurla Mandhata, south western TP). The massif rises from ≈3800 m a.s.l. to the highest peak of the Nalakankar Himal (Gurla Mandhata: ≈7700 m a.s.l.) (Fig. 1.1, 5.1, see section 1.4.2.2). The glacier is situated in the same mountain ridge as Halji glacier but ≈26 km to the north. This lee-effect is clearly evident in mean annual precipitation amounts (506 mm $yr^{-1}$) that are considerably smaller than at Halji glacier (605 mm $yr^{-1}$) despite the higher altitude of Naimona'nyi glacier. Around 68% of the annual total falls between May and September The seasonal pattern is comparable to that at Halji glacier with a second precipitation maximum in February (Fig. 1.12, 1.14). Precipitation in winter is likely transported to the area by westerly winds, whereas summer precipitation is caused by the Indian monsoon (Fig. 1.15, Owen et al. 2010). Climatologically, the gla-

cier lies within the semi-arid part of the "*Temperate Plateau Zone*" (Domrös & Peng 1988, Fig. 1.1). After Benn & Owen (2002) glaciers in the Gurla Mandhata massif are of cold-based continental type, whereas the classification of Shi and Liu (2000) indicates polythermal glacier types (see section 1.3.5). Naimona'nyi glacier has a larger area and a greater altitudinal extent than Zhadang and Halji (Fig. 1.10, 1.12. 1.14). The largest proportion of glaciated area is located between 6000 and 6100 m a.s.l. (Fig. 1.14) with a mean ELA around 6300 m a.s.l. between 2004 and 2010 (Yao et al. 2012). This suggests strong mass loss and significant negative MB despite of its high elevation and low temperatures.

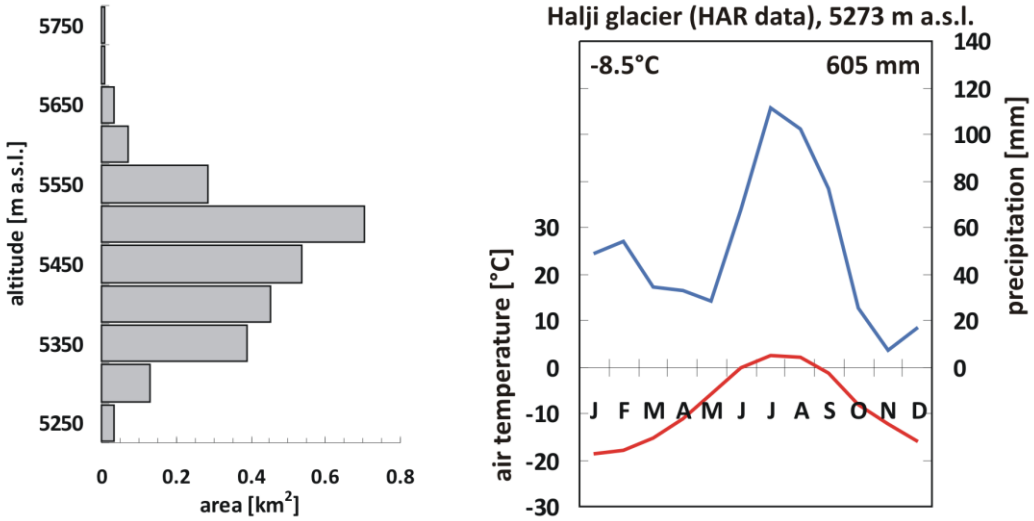


**Fig. 1.12: Glacier hypsometry and climate chart for Halji glacier. The plots are generated from the data used in chapter 5.**

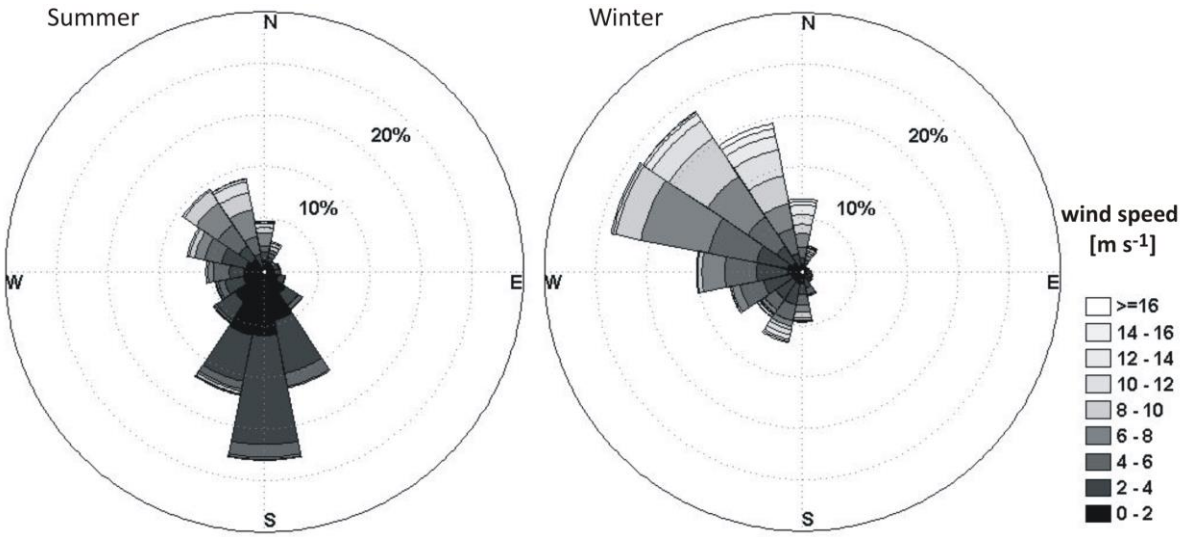


**Fig. 1.13: Wind direction and intensity from hourly HAR data at Halji glacier for summer and winter season between October 2000 and September 2011 (summer: 1 April – 30 September, winter: 1 October – 31 March).**

Ye et al. (2006) obtained glacier variations in the Naimona'nyi region from satellite imagery between 1976 and 2003. The authors reveal that glacier area decreased by 8.4% in total, with accelerated recession during 1999-2003. Glaciers in the southeast were found to retreat faster than those in the northwest. This is reasonable because glaciers in the southeast are stronger influenced by changing

summer temperatures during the monsoon (see section 1.3.5). Mass loss of Naimona'nyi glacier was comparably small and predominantly in the north eastern parts of the glacier tongue.

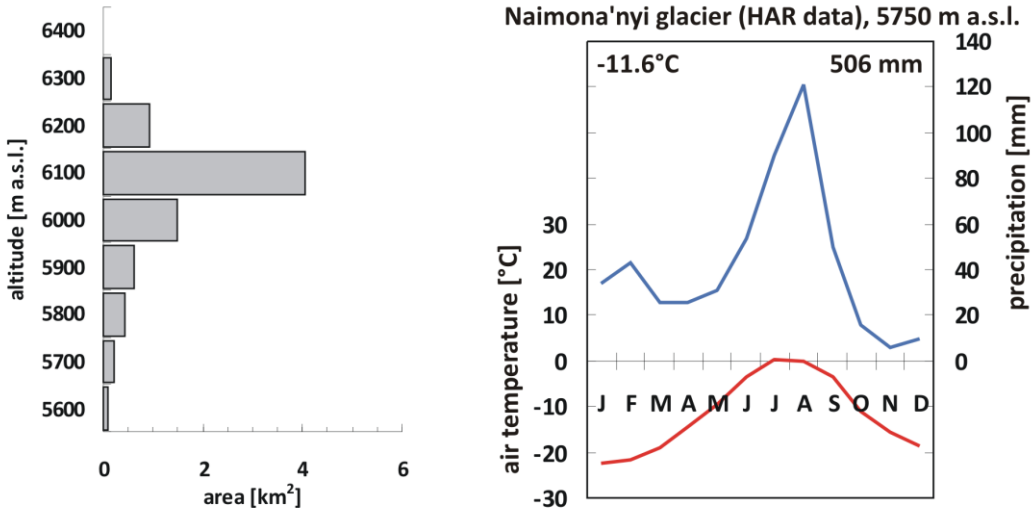


**Fig. 1.14: Glacier hypsometry and climate chart for Naimona'nyi glacier. The plots are generated from the data used in chapter 4.**

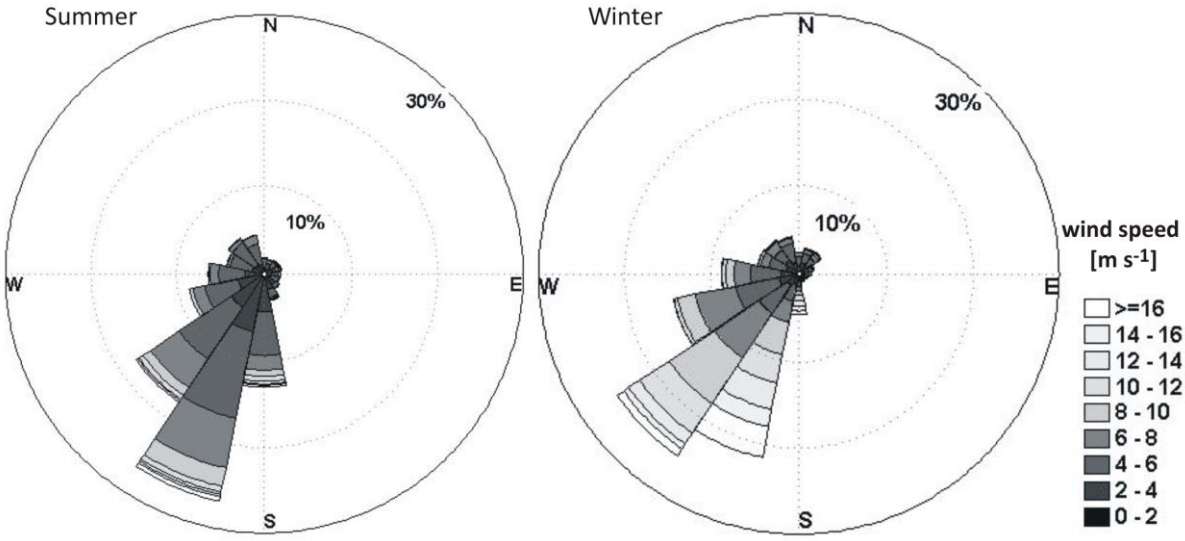


**Fig. 1.15: Wind direction and intensity from hourly HAR data at Naimona'nyi glacier for summer and winter season between October 2000 and September 2012 (summer: 1 April – 30 September, winter: 1 October – 31 March).**

***Purogangri ice cap (PIC)***

The Purogangri ice cap covers an area of ≈400 km$^2$ (Lei et al. 2012, Neckel et al. 2013, Shi et al. 2009) and is the largest ice cap on the Tibetan Plateau (Yi et al. 2002). It is located in the northern central part of the TP, in the western part of the Tanggula Shan (Fig. 1.1). Altitudes range between ≈5300 and ≈6400 m a.s.l. with flat platforms at elevations around 5800 m a.s.l. (Fig. 1.16, 3.1). The region is dominated by a cold and relatively dry continental climate. According to the climate classification of Domrös & Peng (1988) PIC is located in the "*Subalpine Plateau Zone*" in the transition between the subhumid eastern and the semi-arid western part. Mean annual precipitation amounts range between 300 mm in the lower and more than 380 mm in the upper parts of the ice cap and emphasize the semi-arid character of the region. This is reasonable compared to precipitation values deter-

mined by Lei et al. (2012) around Linggo Co according to a regional map (150-200 mm). Around 70% of the annual total falls between May and September. Including the months March and April this proportion rises to 86%. This implies that the region is still dominated by Indian monsoon circulation in summer and mid-latitude westerlies in winter. However, precipitation season already starts in March, when the westerly jet starts to shift northward (see section 1.3.1). HAR wind directions verify this explanation (Fig. 1.17). The winter months are clearly dominated by strong westerly winds whereas wind directions in summer do not show a clear influence of the monsoon. Moreover, the effect of the north- and southward shift of the westerly jet seems to be evident in the summer pattern. According to Maussion et al. (2014) PIC is therefore a mixed '*spring- and summer-accumulation type*' glacier (MAM/JJA) (Fig. 1.9). Due to the low air temperatures all spring precipitation falls as snow, positively affecting glacier MB both through increasing accumulation and albedo (see section 1.3.5). As the positive effect of an early monsoon onset on glacier MB could be already revealed at Zhadang glacier (see section 2.2) regular spring accumulation might be a reason for the observed below-average mass loss at PIC during 2000-2011 (Neckel et al. 2013, Lei et al. 2012) compared to other MB studies for glaciers in High Asia over similar time periods (see sections 1.3.2 and 2.4.6). Additionally, the ice cap contains cold glacier ice throughout and is less dominated by monsoon precipitation in high summer. Therefore it is less sensitive to temperature changes (see section 1.3.5). This conclusion is supported by the fact that large parts of PIC are located at higher altitudes between 5800 and 6000 m a.s.l., experiencing generally low temperatures (Fig. 1.16). The long term ELA is estimated to be approx. 5700 m a.s.l. (Yao et al. 2012).
Around 30% of PIC belongs to the catchment of Linggo Co, 40 km west of the ice cap. Glacier melt water is the primary water source for the closed basin and suggests a direct connection between lake level rise and slightly increased glacier mass loss in recent decades (Lei et al. 2012).

***Muztagh Ata glacier***

The Muztagh Ata massif is located in the eastern Pamirs at the western margin of the TP. It contains the third highest peak of the Pamirs (Muztag Ata: 7546 m a.s.l.) (Fig. 1.1). The region is highly glaciated with glaciers ranging between ≈3900 and ≈7500 m a.s.l. Most of the glaciers are debris covered (Shangguan et al. 2006). The selected glacier is a debris-free west exposed valley glacier in the western Muztagh Ata massif with an area of ≈8.0 $km^2$ (Fig. 6.1). Climatologically, the region is situated within the "*Alpine Plateau Zone*" (Domrös & Peng 1988, Fig. 1.1), characterized by cold and semi-arid conditions (Fig. 1.18). The westerlies are the most important moisture source whereas the impact of the Indian monsoon circulation is nearly absent (Seong et al. 2009b). HAR wind directions indicate a strong influence from the westerly jet both in winter and summer (Fig. 1.19). Wind speeds are significantly higher in winter (see section 1.3.1).
The mean annual precipitation amount from HAR is 392 mm. Miehe et al. (2001) give an annual total of 127 mm $yr^{-1}$ for the period 1956-68 for the station Bulunkul (3310 m a.s.l.) ≈50 km north of the glacier. Only 49% of the annual total falls between May and September whereas 59% falls between March and July (Fig. 1.18). Analyses of Maussion et al. (2014) reveal that the western Muztagh Ata region lies within a cluster of maximum precipitation between March and May (MAM), directly adjacent to mixed type '*spring- and winter-accumulation type*' glaciers(DJF/MAM) (Fig. 1.9). A clear annual minimum can not be defined as average monthly sums between 2000 and 2012 do not fall below 20 mm and are equally distributed all year round (Fig. 1.18). Low air temperatures and little precipitation amounts lead to a clear assignment of these glaciers to the cold type (see section 1.3.5, Shangguan et al. 2006). The glaciated area is rather equally distributed over the altitudinal bands between 4800 and 6800 m a.s.l. and shows the greatest altitudinal gradient of all selected glaciers and ice caps

(Fig. 1.18). The regional ELA between 2001 and 2010 is estimated between 5400 and 5500 m a.s.l. (Yao et al. 2012) implying an overall balanced to positive MB.

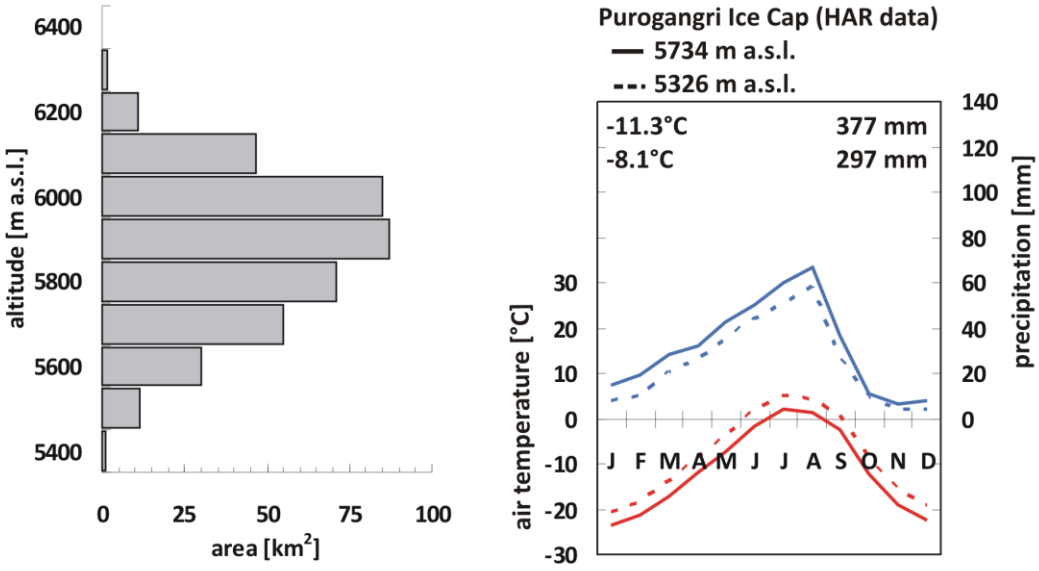


**Fig. 1.16: Glacier hypsometry and climate chart for Purogangri ice cap. The plots are generated from the data used in chapter 3.**

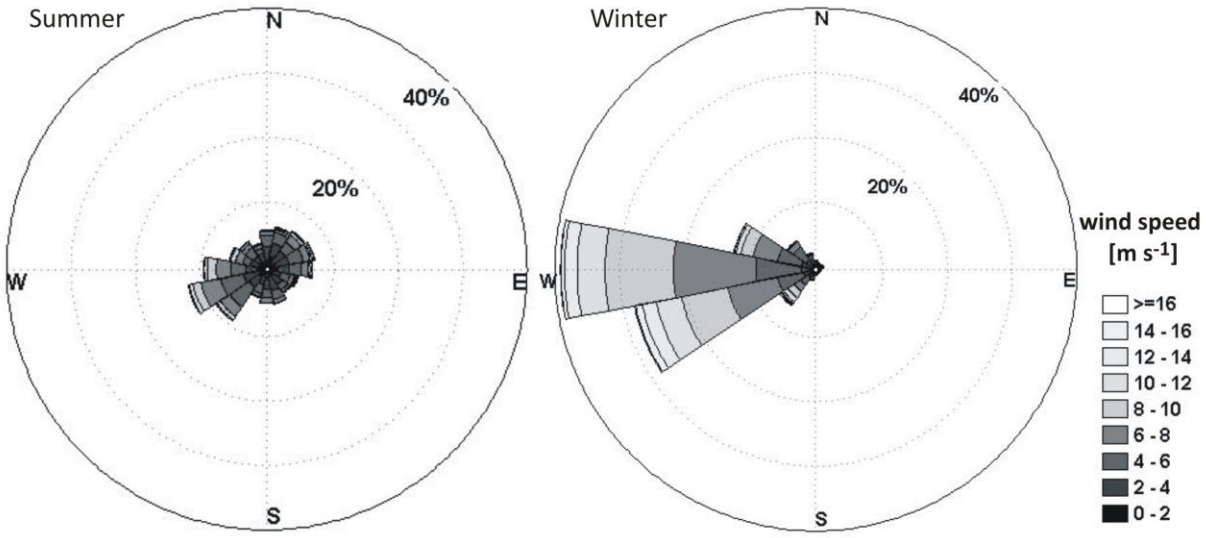


**Fig. 1.17: Wind direction and intensity from hourly HAR data at PIC for summer and winter season between October 2000 and September 2011 (summer: 1 April – 30 September, winter: 1 October – 31 March).**

Shangguan et al. (2006) obtained glacier variations in the Muztagh Ata and Konggur Shan from aerial photographs and satellite images between 1962 and 1999. Results show that glacier area at Muztagh Ata decreased by 7.9% during the total period, with increasing retreat since the 1990s. Mean frontal retreat increased from 6.0 m $a^{-1}$ in 1962-1990 to 11.2 m $a^{-1}$ in 1990-99. These values are rather low, compared to other studies on glaciers on the TP and adjacent mountain ranges (e.g. Ding et al. 2006, Fujita & Nuimura 2011, Ren et al. 2006). It is reasonable because the glaciers at Muztagh Ata prevail under very low temperatures and are hardly influenced by monsoon precipitation. Therefore, they are less sensitive to temperature changes. The year-round low air temperatures support the suggestion of numerous authors, that glaciers in this region are more sensitive to changes in precipitation than in temperatures (e.g. Derbyshire 1981, Shi 2002, Owen et al. 2005, see section 1.3.5).

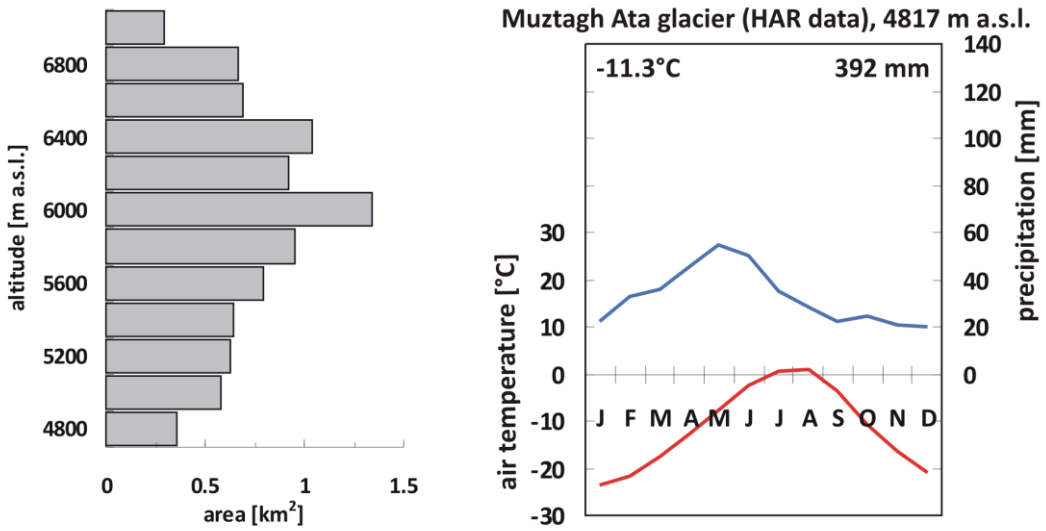


**Fig. 1.18: Glacier hypsometry and climate chart for Muztagh Ata glacier. The plots are generated from the data used in chapter 6.**

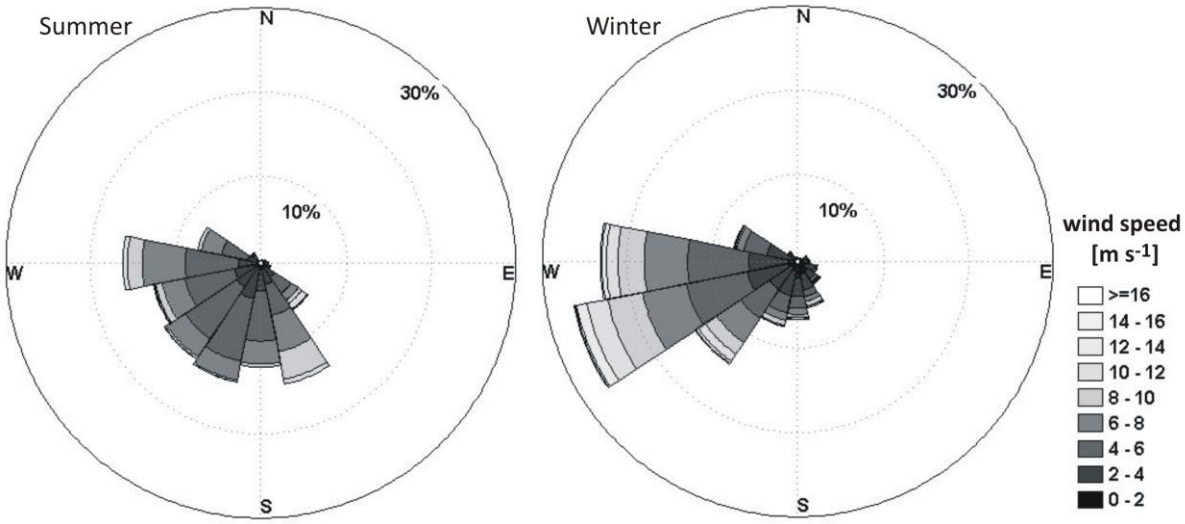


**Fig. 1.19: Wind direction and intensity from hourly HAR data at Muztagh Ata glacier for summer and winter season between October 2000 and September 2012 (summer: 1 April – 30 September, winter: 1 October – 31 March).**

## 1.4.2 In-situ measurements

Since 2009, seven field campaigns to Zhadang glacier on the southern central TP and two campaigns to Naimona'nyi glacier, south-western TP, have been realized within the framework of the DynRG-TiP and WET projects. In the following two sections (1.4.2.1 and 1.4.2.2) the in-situ measurements carried out on both glaciers under participation of the RWTH Aachen University are summarized.

### 1.4.2.1 Zhadang glacier

Zhadang glacier is a small valley glacier (≈2 km$^2$, altitude: 5500-6000 m a.s.l.) at the northern slope of the western Nyainqentanglha mountain range (Fig. 2.1). It is located approx. 200 km north of Lhasa and drains into Nam Co (4725 m a.s.l.), which is the largest salt water lake on the TP. Lake level fluctuations at Nam Co are intensively monitored and can be reconstructed at least to the LGM (Schütt et al. 2008). Between 1970 and 2006, the lake area increased by more than 50 km$^2$ (Liu et al. 2010). Zhadang glacier was chosen as a measurement site within the DynRG-TiP project because the ITP

operates two automatic weather stations (AWS) in its surroundings since 2005 (Maussion et al. 2011a). The Chinese measurements are completed by mass balance measurements applying the glaciological method (see sections 1.3.4.2 and 2.2). Since May 2009 these measurements are complemented by two AWS from TU Berlin and RWTH Aachen (AWS1 and AWS2, Fig. 2.1).

AWS1 is located in the ablation zone of Zhadang glacier in 5665 m a.s.l. since May 2009. AWS2 was first installed in the accumulation area of the neighbouring south facing glacier in 5740 m a.s.l. In September 2009, AWS2 was first relocated to the lower glacier tongue of Zhadang glacier (5560 m a.s.l.) and finally relocated in September 2010 to the terminal moraine close to the glacier tongue (5550 m a.s.l.). Additionally, two time-lapse camera systems were installed by TU Dresden in May 2010 (see section 2.2.2). The position of the glacier tongue was annually measured with GPS. The comparison with a Quickbird satellite image from 2005 reveals that the glacier retreated by ≈100 m since 2005 (Huintjes et al. 2011b). Hydrological measurements of electrical conductivity and water temperature of various melt water channels in the forefield of Zhadang glacier have been conducted in 2010 and 2011 by RWTH Aachen (Fig. 1.17).

The instrumentation of AWS1 and AWS2 is nearly identical (Tables 1.1 and 1.2). Initially, the sensors were mounted on a mast drilled into the glacier ice up to 2.5 m depth. The exceptionally large ablation of approx. 3.5 m at the site of AWS1 in 2009 (see section 2.4.2, Huintjes et al. 2011b, Maussion et al. 2010) caused the fall of both stations around mid July. Therefore, the station set-up was changed to a tripod with a separate mast for the sonic ranger (Campbell Sci. SR50) (Maussion et al. 2011b). In summer 2010, AWS1 fell over again probably due to debris within the ice that appeared at the surface after strong ablation of approx. 2.5 m (see section 2.4.2). Besides these two breaks both stations worked reliably. Only standard corrections of the measured data are necessary, such as the correction of *RH* for $T_{air}$ below 0°C (correction factors provided by Campbell Sci.), interpolation of $T_{air}$ and *RH* to 2 m height and the sonic range correction for temperature (correction formula given by Campbell Sci.). Data of AWS1 is used as input data, for the setting of several model parameters and for the validation process of the MB model presented in this thesis (see section 2.2.1). It is favourable that the stations' position remained unchanged since 2009. Snow and ice temperatures at AWS1 were initially measured in eight depths down to 8.5 m (Table 1.1, Fig. 1.15). The upper sensors melted out within the first summer due to the strong ablation. Some of them have been re-installed during the second field campaign in August 2009 (Fig. 1.15).

**Table 1.1: Sensor specifications at Zhadang glacier AWS1.**

| Variable | Instrument | Sample interval |
|---|---|---|
| Air temperature, relative humidity top[1] | CS215 (Campbell Sci.) | 10 min |
| Air temperature, relative humidity bottom[1] | CS215 (Campbell Sci.) | 10 min |
| Air pressure | DPI 740 (TH Friedrichs) | 10 min |
| Net radiation | NR-LITE (Campbell Sci.) | 10 min |
| Incoming shortwave radiation | CS300 (Campbell Sci.) | 10 min |
| Reflected shortwave radiation | CS300 (Campbell Sci.) | 10 min |
| Subsurface temperature (8 depths, down to 8.5 m) | TP107 (Campbell Sci.) | 10 min |
| Surface temperature | IRTS-P (Apogee) | 10 min |
| Surface height | SR50 (Campbell Sci.) | 10 min |
| Wind speed and direction | 05103-45 (Young) | 10 sec sample, 10 min storage |
| Wind (sonic anemometer) | Windmaster (Gill) | 10 Hz sample, 10 min storage |
| Mast inclination (2D) | SCA121T (VTI Tech) | 10 min |

[1] with ventilated radiation shield

**Table 1.2: Sensor specifications at Zhadang glacier AWS2.**

| Variable | Instrument | Sample interval |
|---|---|---|
| Control device | CR1000 (Campbell Sci.) | |
| Air temperature, relative humidity top[1] | CS215 (Campbell Sci.) | 10 min |
| Air temperature, relative humidity bottom[1] | CS215 (Campbell Sci.) | 10 min |
| Air pressure | DPI 740 (TH Friedrichs) | 10 min |
| Net radiation | NR-LITE (Campbell Sci.) | 10 min |
| Incoming shortwave radiation | CS300 (Campbell Sci.) | 10 min |
| Reflected shortwave radiation | CS300 (Campbell Sci.) | 10 min |
| Subsurface temperature (5 depths) | TP107 (Campbell Sci.) | 10 min |
| Surface temperature | IRTS-P (Apogee) | 10 min |
| Surface height | SR50 (Campbell Sci.) | 10 min |
| Wind speed and direction | 05103-45 (Young) | 10 sec sample, 10 min storage |
| Mast inclination (2D) | SCA121T (VTI Tech) | 10 min |

[1] with ventilated radiation shield

The evaluation of the measured subsurface temperatures is not trivial because the measurement depth changes continuously due to ablation and accumulation processes. A comparison of mean air temperature and the ice temperatures of the two lowermost sensors reveals that Zhadang glacier contains cold ice throughout the year at least at the surroundings of AWS1. This proves the stated polythermal character of the glacier (see section 1.4.1).

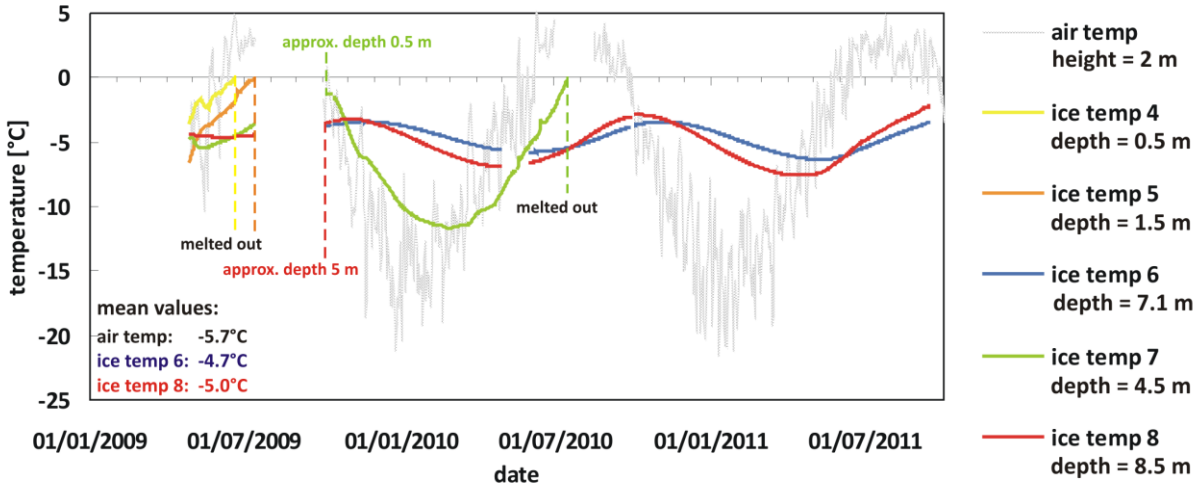


**Fig. 1.20: Daily mean air and ice temperatures at AWS1 on Zhadang glacier, 2009-2011.**

At AWS1 an ultrasonic anemometer (Gill Windmaster) was installed to measure sonic wind speeds and covariances to directly calculate the sensible heat flux ($Q_{sens}$). The overall data quality of the sensor is not satisfying because of inappropriate conditions for the installation and maintenance. The harsh environment at the glacier site would require the possibility of regular control and adjustment. Additionally, unstable conditions that allow turbulence are generally rare in the glacier boundary layer. Therefore, data from this sensor has only been analyzed exemplary for a short period in September 2009 (Huintjes et al. 2011a, Maussion et al. 2011b).

In-situ measurements that are relevant for the MB model are mentioned in detail in section 2.2.1. The comparison of atmospheric measurements at AWS1 and the respective HAR data reveals only minor discrepancies, except for a linear altitude dependency resulting from the different elevation of AWS1 and the respective HAR pixel (see section 2.2.3). Also the wind directions correspond very well although the reference height changes from 2 m (AWS1) to 10 m (HAR) above the ground (Fig. 1.11,

1.21). Obviously, wind directions measured at AWS1 show a pattern that is modified by terrain effects and follows the southeast-northwest direction of the valley (Fig. 2.1). HAR wind directions are averaged over 100 km$^2$ and indicate the meso-scale circulation pattern being modified at 10 m above the ground by the surface roughness according to average meso-scale terrain (Fig. 1.11).

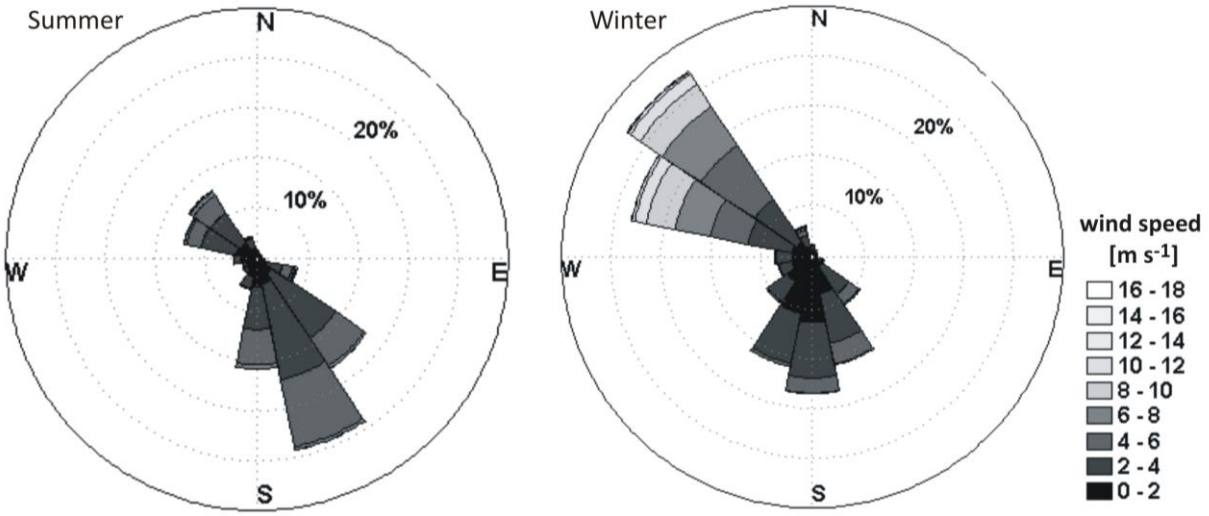


**Fig. 1.21: Wind direction and intensity from hourly observations at AWS1 (Zhadang glacier) for summer and winter season between 27 April 2009 and 10 June 2012 (summer: 1 April – 30 September, winter: 1 October – 31 March).**

Information on the glacier outline and area of Zhadang glacier are differing depending on different authors. Bolch et al. (2010) give a total area of 2.36 km$^2$ for 2009 calculated by a semi-automated GIS approach using a Landsat satellite image. An area of ≈2 km$^2$ is given by Yu et al. (2013), Zhang et al. (2013) and Zhou et al. (2010) for 2007 based on the manual mapping from a Landsat image. Despite minor changes in the lowermost areas of the glacier tongue by glacier retreat, the major area difference is obvious in the highest parts of the accumulation area in the southwest (Fig. 1.22). The glacier outline of Yu et al. (2013), Zhang et al. (2013) and Zhou et al. (2010) is based on in-situ measurements of the ITP. Therefore, this shape is used for the SEB and MB calculations of Zhadang glacier presented in this thesis (see chapter 2). Nevertheless, the results are compared to studies in which the glacier outline of Bolch et al. (2011) is applied (Mölg et al. 2012, 2014, see section 2.5).

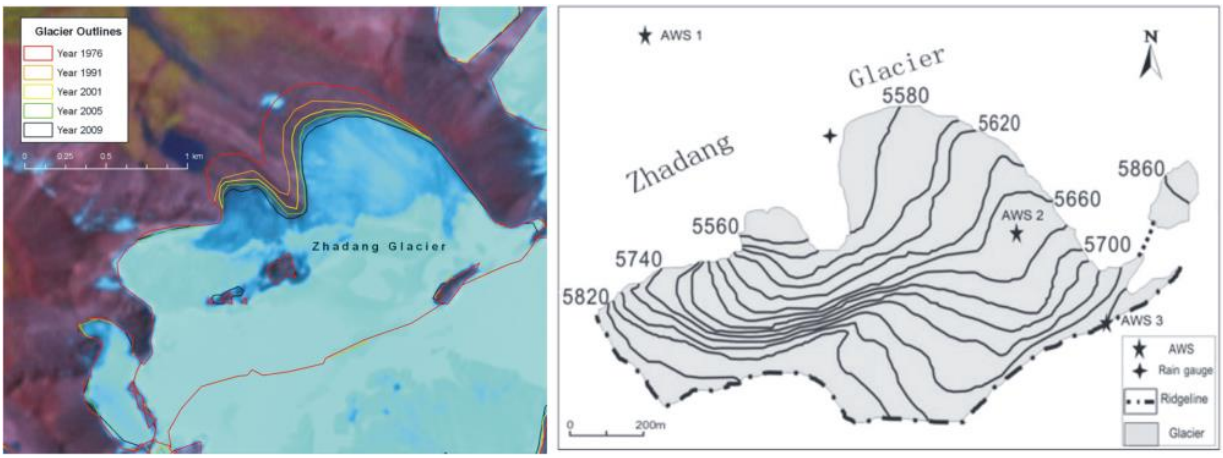


**Fig. 1.22: Comparison of different published glacier outlines for Zhadang glacier, left: Bolch et al. (2011), right: Yu et al. (2013), Zhang et al. (2013) and Zhou et al. (2010).**

During field campaigns in 2010 and 2011 electrical conductivity has been measured in various melt water channels in the forefield of Zhadang glacier. The idea of these measurements was to discriminate the total melt water flux from the glaciated area in glacier melt and permafrost melt. This would also allow the quantification of permafrost distribution and degradation which is important when considering its contribution to the water balance of a drainage basin. Studies on permafrost on the TP mostly analyse large-scale changes in permafrost distribution and thickness (Wu et al. 2010, Wu & Zhang 2010, Yang et al. 2010b). Qualitative research on the contribution of permafrost melt to runoff and how runoff characteristics respond to permafrost variations is limited (Wang et al. 2009, Zhang et al. 2003). The few existing studies are limited to watersheds where glacier and snow melt water can be ignored. The distinction of influences from glacier and snow melt from permafrost thawing is difficult. Therefore, the electrical conductivity of runoff in front of Zhadang glacier was measured. Electrical conductivity depends on the total ion concentration in a solution and is expressed through the electrical resistance Ω ($S = 1/\Omega$) referred to a cube of 1 $cm^3$ (1 S $cm^{-1}$ = 1000 mS $cm^{-1}$; 1 mS $cm^{-1}$ = 1000 µS $cm^{-1}$). More dissolved salts, acids and bases result in higher conductivity because in solution they decay into cations and anions (Chow 1964). In water, conductivity is mainly influenced by dissolved salts and can be measured through Ω. For measurements in the forefield of Zhadang glacier, a combined temperature and conductivity sensor, the latter containing two metal electrodes, was applied (PCE-PHD 1, ±4 µS $cm^{-1}$, UIT undated). From measured electricity, electrical conductivity is calculated for the actual temperature of the melt water flux. The direct temperature measurement allows the automatic correction of the conductivity for a consistent reference temperature (25°C). Standard ranges for electrical conductivity for different aqueous solutions are given in Fig. 1.23. Conductivities measured in the forefield of Zhadang glacier are within the range of drinking water. Lowest conductivities can be found in the melt water directly coming from the glacier (3.4-15 µS $cm^{-1}$). Highest values are found in the eastern regions (80-120 µS $cm^{-1}$) (Fig. 1.24). The measurements coincide with the numbers given by Penna et al. (2014) for a glacierized catchment in the Alps. Generally, conductivity increases with increasing distance from the glacier tongue.

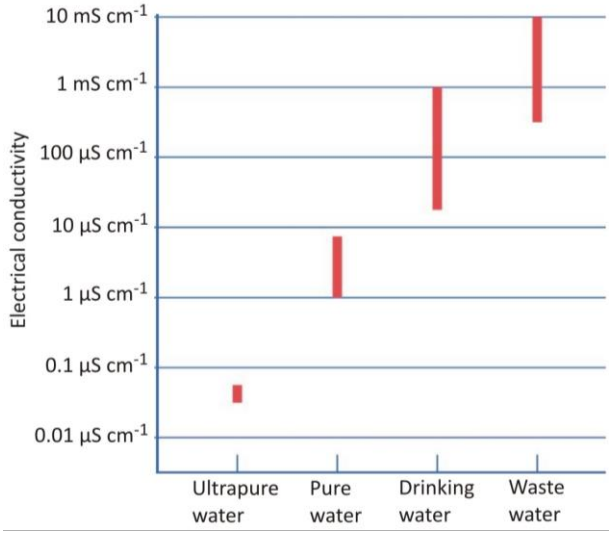


**Fig. 1.23: Ranges of electrical conductivity for aqueous solutions at 25°C (modified after Hamilton Messtechnik, undated).**

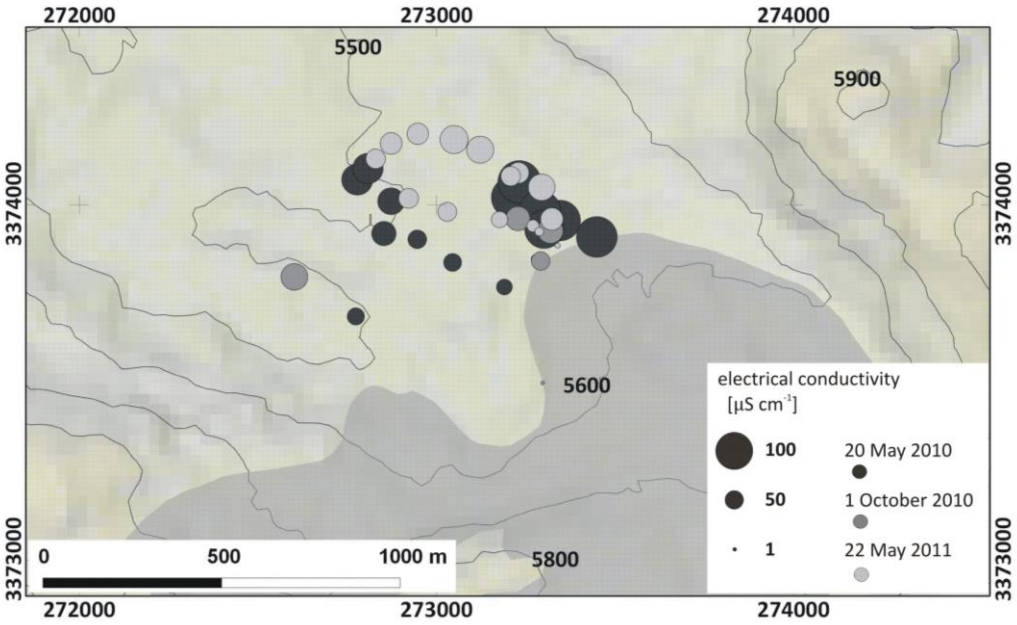


**Fig. 1.24: Measurements of electrical conductivity in melt water channels in the forefield of Zhadang glacier, May / October 2010 and May 2011. Values range between 3.4 and 120 µS cm$^{-1}$.**

This pattern can be explained by the amount of mineral salts that dissolve in the water while flowing through the moraine material in the forefield. In the eastern regions of the tongue, conductivity is highest despite the short distance to the glacier. The runoff in this place only partly originates from the glacier but also from the permafrost slopes in the east. Therefore, it already contains a large number of dissolved minerals. In spring 2010 measured conductivities are generally larger than in spring 2011. Observed and modelled earlier and increased surface melt at the glacier surface in 2010 (see section 2.4.2) might also be transferred to the permafrost surroundings. Generally lower albedo values of the moraine debris compared to the glacier surface suggest even an earlier start of permafrost thawing leading to higher mineral concentrations in the melt water in spring 2010. The results suggest a direct linkage between the inter-annual variability of glacier melt and permafrost thawing but also reveal the different temporal pattern. Timing and amount of permafrost thawing has an impact on the hydrological cycle and becomes more important in a warming climate. The long-term inter- and intra-annual monitoring of the contribution of permafrost thawing to runoff requires continuous measurements of electrical conductivity, water temperature and runoff itself. The installation and maintenance of a hydrological sensor in the glacier forefield is difficult because the runoff channels change significantly from year to year due to the harsh environment. It is for this reasons that there does not exist any more detailed data on conductivity from the glacier forefield. Therefore, the interpretation of these measurements must remain vague and rather speculative.

### 1.4.2.2 Naimona'nyi glacier

Naimona'nyi glacier is a north to northwest exposed valley glacier (≈7.8 km$^2$, 5500-6600 m a.s.l.), located northeast of Naimona'nyi (chin. Gurla Mandhata) the highest peak of the Nalakankar Himal (≈7700 m a.s.l.) (Fig. 4.1, section 1.4.1).The Nalakankar Himal is one of the northern Himalayan ranges in the western TP and inherits a number of cirque and valley glaciers and a small ice cap. Glaciers at the northern slopes drain into Lake Manasarovar (Mapam Yumco) whereas Naimona'nyi glacier at the western slope drains into the Karnali River. The Karnali River is directed to the south, crosses the town Burang (3880 m a.s.l.), cuts through the Himalayas to Nepal and joins the Ganges in India (Owen et al. 2010, Zomer & Oli 2011). The region of Lake Manasarovar, Lake Rakshastal (La'nga Co)

and Mt. Kailash is the source region of three of the largest rivers in Asia: Indus, Brahmaputra and Karnali (Ganges) and forms the major part of the *Kailash Sacred Landscape Conservation Initiative* (Zomer & Oli 2011). The project aims at the protection of both biodiversity and cultural diversity in the transboundary region.

Naimona'nyi glacier was chosen as a measurement site within the WET project because the ITP conducted climatological and glaciological measurements at the glacier over a shorter period a few years ago (Yao et al. 2012) and the glacier is one of the ice core drilling sites of the ITP (Liu et al. 2006). In September 2011 an AWS including an external data logger for ice temperature sensors from RWTH Aachen was installed on an ice cored moraine west of the glacier tongue in 5665 m a.s.l. The instrumentation is given in Table 1.3. A time-lapse camera has been set up to monitor glacier changes but the storage module did not resist the low winter temperatures. Thus, no camera pictures are available. The AWS worked reliably and only the standard correction of *RH* for $T_{air}$ below 0°C (correction factors provided by Campbell Sci.) is necessary. The wind sensor broke in winter 2012/13 due to the harsh environment. The two-year period of measurements is not directly used to force or to validate the MB model but to validate the atmospheric model data input (HAR). Both datasets overlap by about one year (1 September 2011 – 31 December 2012, Fig. 1.25). Calculated discrepancies for air temperature, relative humidity, shortwave incoming radiation and wind speed show strong seasonal variations. Wind directions in 2.2 m (AWS) and 10 m (HAR) are even opposite (Fig. 1.15 and 1.27). Within the considered period the altitude corrected $T_{air}$ from HAR data exhibits a cold bias of 3.8 K in winter and 2.0 K in summer compared to the AWS measurements (Fig. 1.26). The sum of positive degree hours (PDH) from HAR at the altitude of the AWS is nearly half of the PDH measured at the AWS (Fig. 2.26). This means that the HAR forced MB model will produce approximately only half of the amounts of surface melt at the lower tongue of Naimona'nyi glacier that can be assumed according to the AWS measurements. The period available for the validation of the HAR data is short. Nevertheless, a pronounced cold bias in HAR $T_{air}$ can be revealed that will influence the MB model results for Naimona'nyi glacier especially in summer. Halji glacier is located only 26 km south of Naimona'nyi (see section 1.4.1). Thus, the cold bias in HAR $T_{air}$ observed at Naimona'nyi glacier might also be evident in the Halji region. The large differences between measurements and HAR data can be explained by small scale terrain effects that influence the AWS site and can not be captured by the atmospheric model (10 km resolution, see section 2.2.3). The Naimona'nyi valley is much narrower than the Zhadang valley and slopes are steep (Fig. 4.1). Therefore, the discrepancies between atmospheric measurements and HAR data are more pronounced than at Zhadang glacier (see section 1.4.2.1). The wind directions measured at the AWS show a pattern that is controlled by terrain effects and sharply follows the southeast-northwest direction of the valley (Fig. 1.25, 4.1). In summer, monsoon related winds from southern directions are largely blocked by the Gurla Mandhata main ridge (Fig. 4.1). HAR wind directions show the meso-scale circulation pattern (Fig. 1.15). The performed SEB and MB calculations for Naimona'nyi glacier within this thesis are based solely on HAR data (see chapter 4).

An independent sensor for the combined measurement of runoff, water temperature and electrical conductivity was installed in the main melt water channel in front of Naimona'nyi glacier in 2011. During the campaign in 2012 the sensor could not be retrieved. The observed relocation of large boulders in the glacier forefield within one year suggests that at times large amounts of snow and glacier melt water and/or precipitation occur. This complicates the installation and maintenance of a hydrological sensor in the glacier forefield.

In addition to the AWS three ice temperature sensors and two ablation stakes have been installed in September 2011 at a debris covered dead ice body next to the AWS. Two pictures of the installation, taken in September 2011 and in August 2012, and the depth of the remaining ablation stake show

that the dead ice body remained stable concerning its thickness whereas considerable mass loss is evident at the debris free slope (Fig. 1.28). A small amount of surface lowering is visible at the glacier tongue next to the debris covered ice (Fig. 1.29).

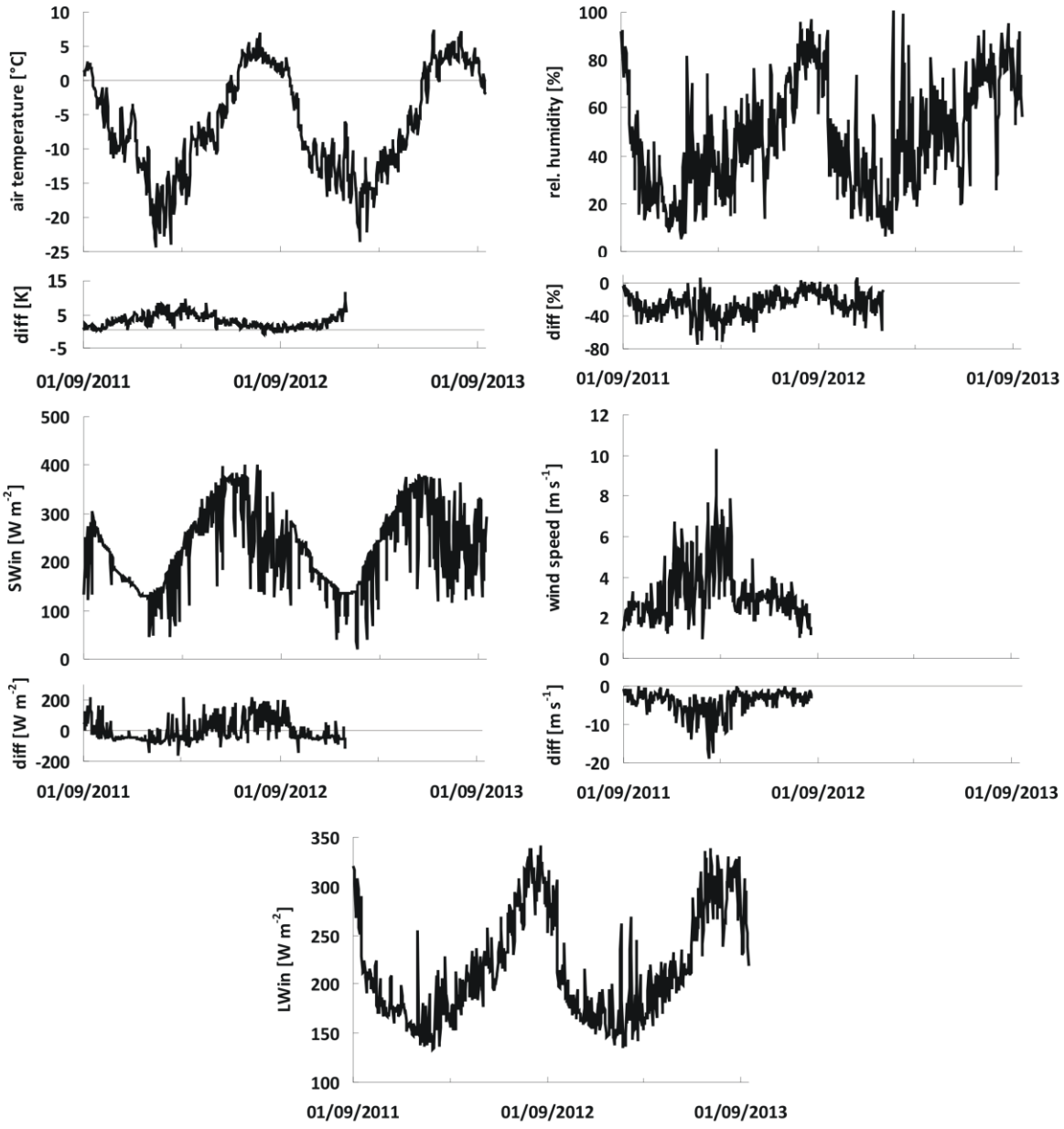


**Fig. 1.25: Daily mean values of air temperature, relative humidity, shortwave incoming radiation, wind speed and longwave incoming radiation at the AWS at Naimona'nyi glacier. Differences between AWS and HAR data are shown. Altitude differences between HAR grid cell and position of the AWS are corrected for air temperature and relative humidity applying lapse rates calculated from the HAR data (see section 4.2).**

The wall of the ice body retreated approx. 2.5 m during one year and one ablation stake (A1) fell down the slope. Fig. 1.30 illustrates daily mean ice temperatures in three depths compared to AWS air temperature. Although daily mean air temperatures rise up to 7°C with hourly maxima of +13°C ice temperatures in a depth of 0.85 m constantly stay below zero. Temperatures directly below the debris cover have not been measured. Therefore, the assumed isolating effects of the thick debris cover on the ice body that lead to decreased ablation underneath (Nicholson & Benn 2006, Zhang et

al. 2011b) cannot be validated quantitatively. Nevertheless, the constant ice thickness despite a two-month period of continuously positive daily mean air temperatures (Fig. 1.30) supports this assumption. Mean ice temperatures over the whole period are nearly identical for the three depths (-0.85 m: -6.3°C; -2.35 m: -6.2°C; -3.35 m: -6.3°C) and differences are within the sensor uncertainty (Table. 1.3). Mean air temperature is only slightly lower (-6.8°C). Standard deviations decrease with depth ($T_{air}$: 7.4°C; -0.85 m: 4.5°C; -2.35 m: 3.0°C; -3.35 m: 2.5°C) caused by the attenuation of the air temperature signal with depth.

**Table 1.3: Sensor specifications at Naimona'nyi glacier AWS with independent subsurface temperature measurements.**

| Variable | Instrument | Sample interval | Nominal accuracy |
|---|---|---|---|
| Controle device | CR1000 (Campbell Sci.) | | |
| Air temperature, relative humidity (2 m)[1] | CS215 (Campbell Sci.) | 1 hr sample | 0.9°C (-40°C to +70°C) and 4% (0-100%) |
| Wind speed and direction (2.2 m) | 05103-45 (Young) | 10 sec sample, 1 hr storage | 0.3 m $s^{-1}$ |
| Incoming shortwave radiation | CS300 (Campbell Sci.) | 1 hr sample | 5% (daily totals) |
| Incoming longwave radiation | CGR3 (Kipp & Zonen) | 1 hr sample | 5.6% |
| Subsurface temperatures (3 depths, down to 3.35 m) | Logger: U12 (HOBO); Sensors: 3x TMC20-HD | 3 hrs sample | Logger: 1% for logger-powered sensors; sensors: 0.3°C (-20°C to 0°C) |

[1] with ventilated radiation shield

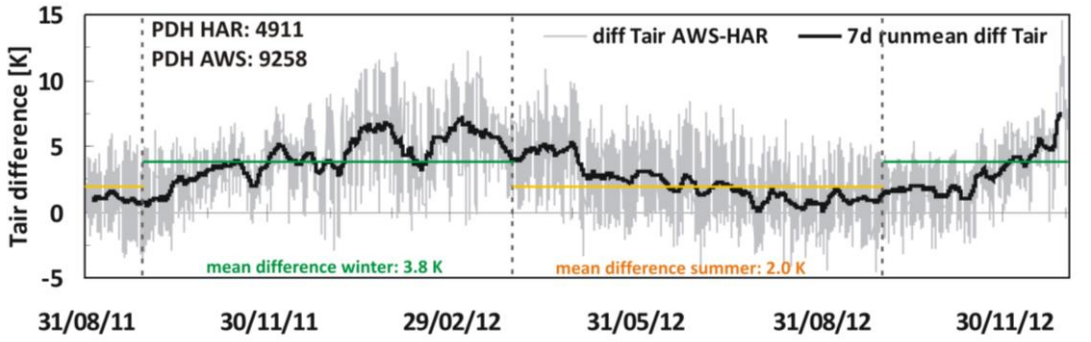


**Fig. 1.26: Differences in hourly mean air temperature between the AWS at Naimona'nyi glacier and the respective HAR grid cell. Altitude differences are corrected (see Fig. 1.17). Positive values indicate that AWS values are larger than HAR values. The positive degree hours (PDH) are the sum of hourly $T_{air}$ > 0°C at the AWS and from HAR, respectively.**

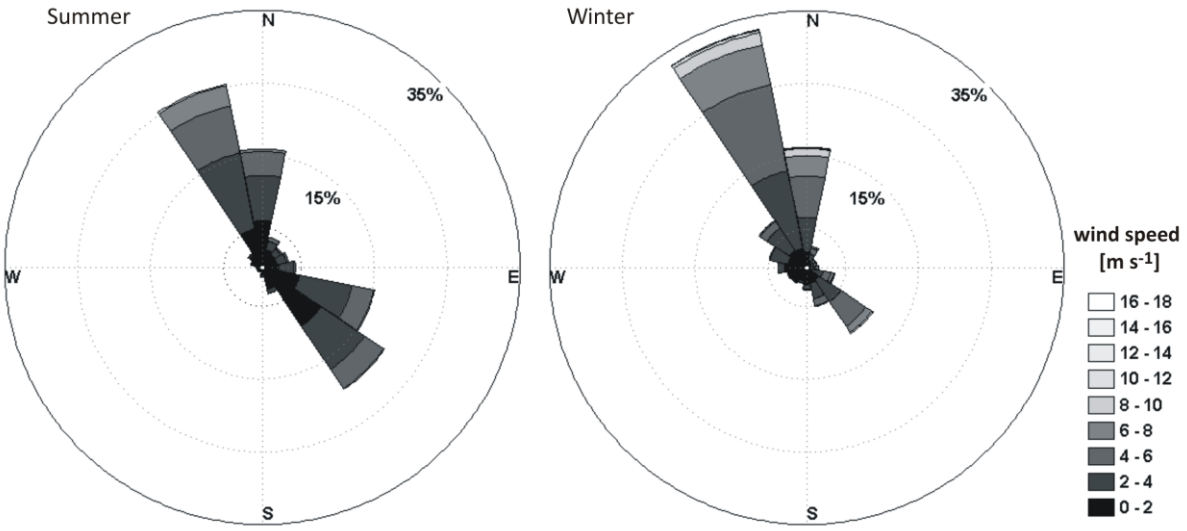


**Fig. 1.27: Wind direction and intensity from daily AWS data (2.2 m, Naimona'nyi glacier) for summer and winter season between September 2011 and August 2012 (summer: 1 April – 30 September, winter: 1 October – 31 March).**


**Fig. 1.28: Qualitative comparison of the retreat of the dead ice body between September 2011 (left) and August 2012 (right). The distance of ablation stake 1 (A1) to the edge (green arrow) was measured in 2011 (A2: ablation stake 2; It: ice temperature sensors).**

**Fig. 1.29: Qualitative comparison of the glacier surface elevation change at the tongue of Naimona'nyi glacier between September 2011 (left) and August 2012 (right).**

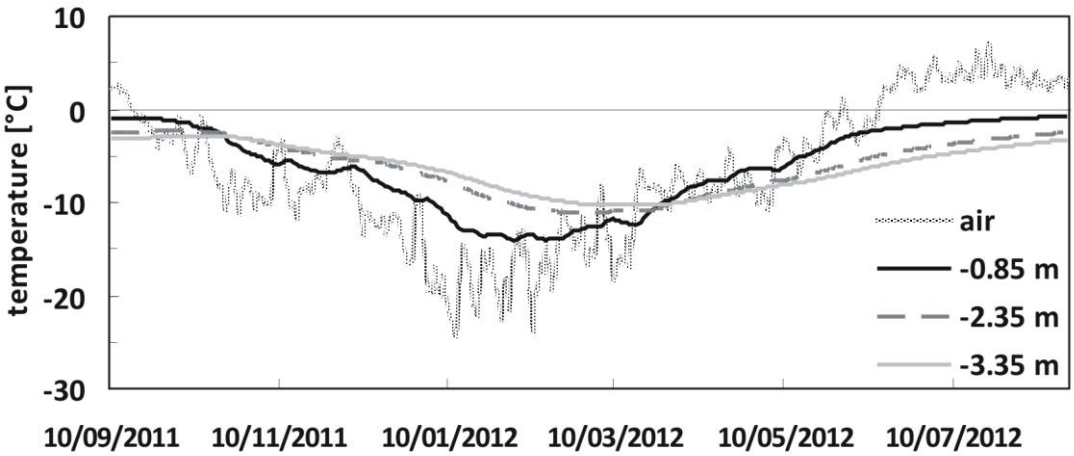


**Fig. 1.30: Daily mean ice temperatures in three depths and AWS air temperature at an ice cored moraine west of Naimona'nyi glacier, 10 September 2011 – 20 August 2012.**

# 2 Evaluation of a coupled snow and energy balance model for Zhadang glacier, southern central Tibetan Plateau, using glaciological measurements and time-lapse photography

## 2.1 Introduction and regional climate conditions

Zhadang glacier is a northwest exposed valley glacier (≈2 $km^2$) at the northern slope of the western Nyainqentanglha Shan on the southern central TP (Fig. 2.1, see sections 1.4.1 and 1.4.2.1). The glacier is subject of intensive in-situ measurements by the ITP, both climatologically and glaciologically, since 2005. In 2009, the glacier was further equipped with two AWS and a time-lapse camera system within the Sino-German cooperation (see section 1.4.2.1). The high data availability is unique on the TP. It led to two publications on short-term MB studies at Zhadang glacier (Mölg et al. 2012, Zhang et al. 2013). The generation of a 10-year time series of atmospheric model data by TU Berlin (HAR, Maussion et al. 2014) offers the opportunity of longer MB simulations (Mölg et al. 2014). This chapter presents the newly developed and applied SEB/MB model followed by the various steps of model calibration and validation for Zhadang glacier using different data sources. The installed time-lapse camera system is the first of its kind on the TP and provides an excellent data base for spatial and temporal model evaluation. Besides the analysis of single observed phenomena between 2009 and 2012 with the help of the generated SEB and MB model output, the study at Zhadang glacier derives and interprets a 10-year data series of all SEB and MB components.

Fig. 2.2 presents daily meteorological variables measured at AWS1 on Zhadang glacier between 2009 and 2012 (Fig. 2.1 and sections 1.4.2.1 and 2.2.1). The summer months are characterized by intense solar radiation (Fig. 2.2a) and the maximum of monthly precipitation amounts in the annual cycle (see section 1.4.1). Measured hourly means of incoming shortwave radiation on the glacier can even exceed the value of the solar constant (1368 W $m^{-2}$) due to multiple reflections from snow covered slopes. Monthly values of atmospheric model data (HAR) for the region of Zhadang glacier between 2001 and 2011 are shown in Fig. 2.3 (see section 2.2.3). It is obvious that incoming shortwave radiation reaches its maximum not in summer, when solar insolation is largest, but in spring. This is caused by monsoonal cloud cover that is larger in summer. Daily mean air temperatures generally rise above zero from late May to September and range between -25.1°C and +5.9 C during the observation period 2009-2012 (Fig. 2.2b).

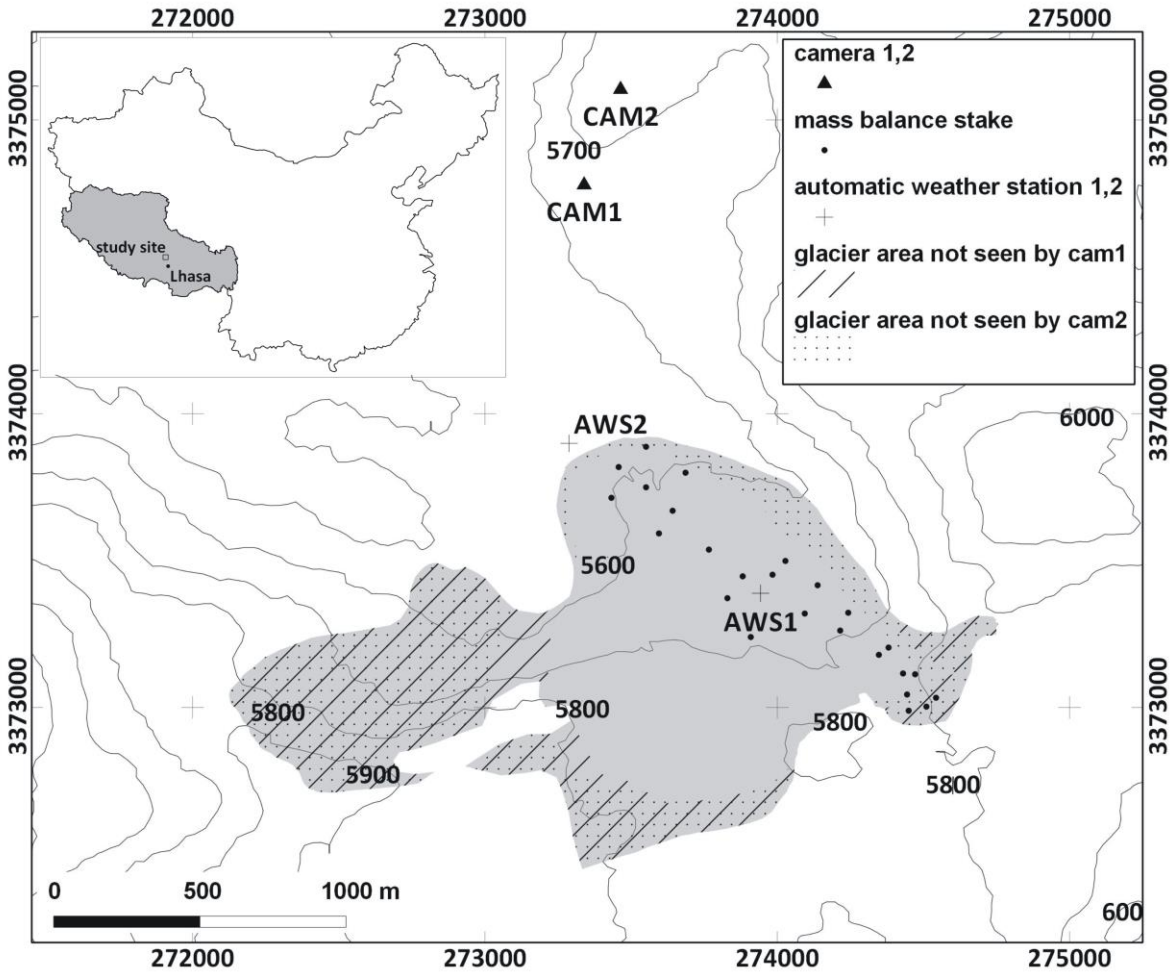


**Fig. 2.1: Zhadang glacier (grey area) with glacier outline from 2009 and locations of available measurements and fields of view of the cameras. Contours are in meters a.s.l. (100 m spacing). UTM 46N, WGS84. The inlay shows the location of the study site within China and Tibet Autonomous Region (grey).**

The influence of the precipitation seasonality on the glacier MB is explained in section 1.3.5. Zhadang glacier is a clear "*summer-accumulation type*" glacier that shows a strong sensitivity to air temperature variations during the monsoon season (see section 1.4.1). The key factor is the precipitation phase, which solely depends on air temperature and has an effect on glacier MB both through changes in accumulation and through changes in albedo and therefore absorption of solar radiation (see section 1.3.5, e.g. Ageta & Fujita 1996; Caidong & Sorteberg 2010; Fujita & Ageta 2000; Fujita et al. 2007; Kayastha et al. 1999). Runoff observations downstream of Zhadang glacier confirm this finding (Kang et al. 2009, Zhou et al. 2010). Besides air temperature, interannual precipitation variability plays an important role for glacier MB and is even more important than the total annual precipitation amount (Fujita 2008a,b). Kang et al. (2009) demonstrate that an early onset of the Indian Summer Monsoon in 2008 suppressed glacier melt at Zhadang glacier and therefore positively affected annual MB. We could confirm this effect from our MB model calculations (see section 2.4.6). More detailed analyses of Mölg et al. (2012) show, that monsoon onset strongly affects the ablation season of Zhadang glacier, whereas no direct impact could be revealed in the main monsoon season. There are indications that this result applies to all monsoonal influenced glaciers on the TP. Furthermore, regional atmospheric patterns prevail against the monsoon circulation in summer (Mölg et al. 2012).

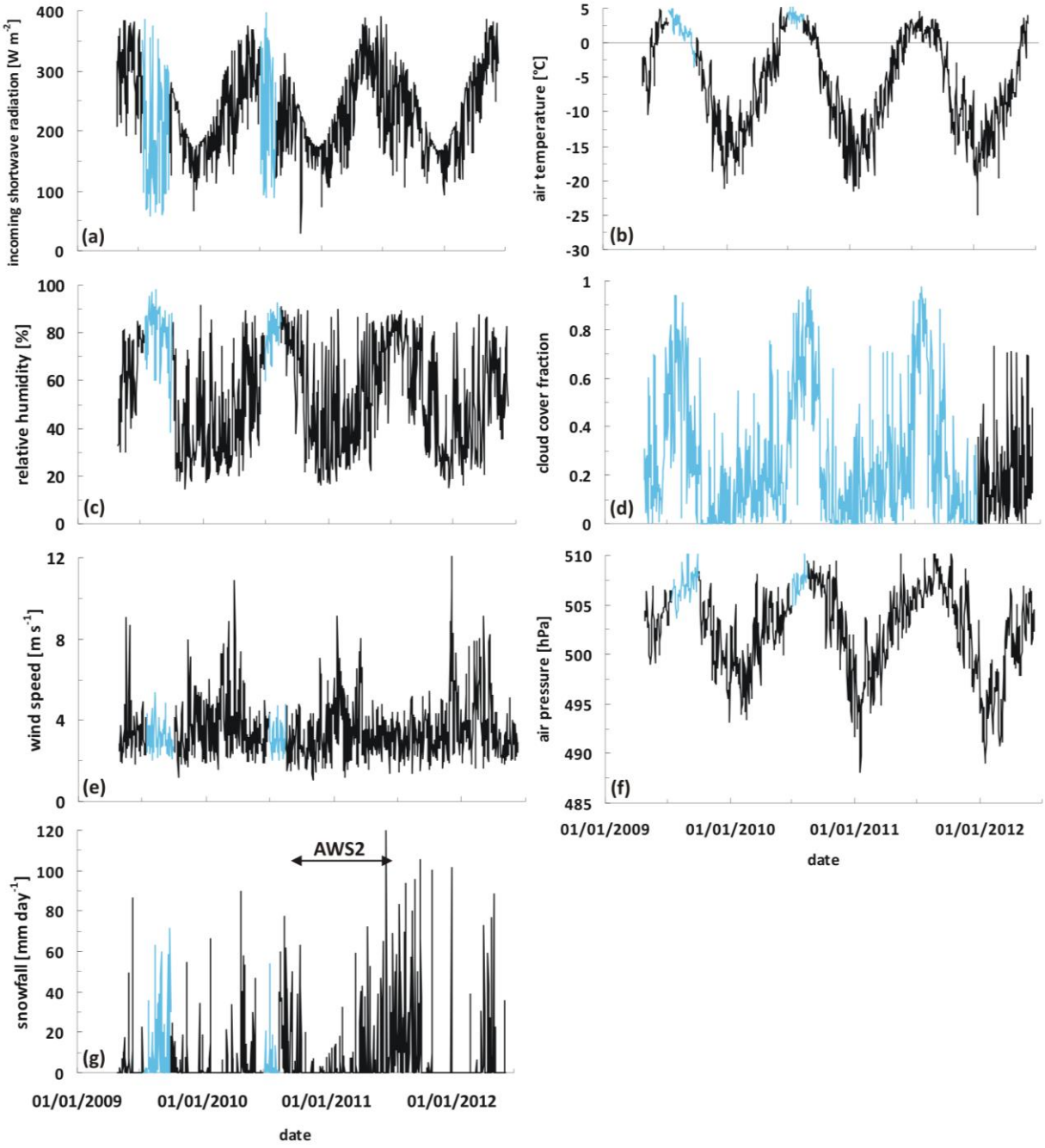


**Fig. 2.2: Daily means of (a) incoming shortwave radiation, (b) air temperature, (c) relative humidity, (d) cloud cover fraction, (e) wind speed, (f) air pressure, and (g) daily sums of solid precipitation at AWS1 between 27 April 2009 and 10 June 2012. Measurements are indicated by black colour, atmospheric model output is blue. In panel (g), the different location of measurements for surface accumulation between 4 October 2010 and 30 June 2011 is indicated. Atmospheric model all-phase precipitation is scaled by 0.56 in order to match measurements. The solid proportion of precipitation is converted to actual snow height applying a density of 250 kg $m^{-3}$ (see section 2.2.3).**

## 2.2 Data basis

In this study we use various data from in-situ measurements at the glacier site to force (see sections 2.2.1 and 2.3.1), calibrate (see section 2.4.1) and evaluate the SEB/MB model between 2009 and 2012 (see section 2.4.2). Measurements not used for forcing and calibration are applied to evaluate the model performance. Additionally, we calibrated (see section 2.4.1) and evaluated (see section 2.4.2) the model forced by atmospheric model output from the High Asia Reanalysis (HAR) and ran it for the period 2001 to 2011 (see section 2.4.6). The distributed model runs on a SRTM digital elevation model (DEM) (Rabus et al. 2003) resampled to 45 m resolution. The glacier size is kept constant throughout the modelling period and is based on the 2009 glacier extent (glacier outlines at the tongue based on Bolch et al. 2010, see section 1.4.2.1).

### 2.2.1 In-situ measurements relevant for the SEB/MB model

In a first step, we use observational data from an automatic weather station (AWS1) to force the SEB/MB model (Table 2.1). AWS1 is operated in the ablation zone of Zhadang Glacier at 5665 m a.s.l. since 2009 (Fig. 2.1, 2.2). Due to the extreme environment, two data gaps are evident in late summer 2009 and 2010 respectively (see section 1.4.2.1). Therefore, three periods are sufficiently covered by AWS data: (P1) 27 April 2009 – 14 July 2009, (P2) 1 October 2009 – 1 July 2010, (P3) 16 August 2010 – 10 June 2012. To obtain a continuous data series from 2009 to 2012 these gaps were filled with data from HAR (see section 2.2.3). Except for the period 4 October 2010 – 30 June 2011 within P3, snow accumulation recorded by the sonic ranger (SR50) is directly used as model input. The heat flux from liquid precipitation is neglected (see section 2.3.1). The missing period was characterized by weak ablation (Fig. 2.8a) and the sensor at AWS1 was buried by snow. We used SR50 data from nearby AWS2 (Fig. 2.1) that is operated since 2010 at 5550 m a.s.l. in front of the glacier instead. Subsurface temperatures have been measured at AWS1 until a maximum initial depth of ≈ 8.5 m (7.1 m), where ice temperature is almost constant (-4.7°C, see section 1.4.2.1). This value is used to define the lower boundary condition ($T_b$) of the MB model. Further, temperature measurements at the surface and in ≈ 1.5 m, ≈ 4.5 m and ≈ 5 m depth initially served for initialization of the temperature profile and the latter also for model evaluation. In the final model run, the temperature profile is initialized with air temperature ($T_{air}$) and $T_b$ only (see section 2.3.1). According to Mölg et al. 2012, the actual height of the $T_{air}$/ relative humidity ($RH$) sensor, as well as the depth of the subsurface sensors, has been estimated from the SR50 record. From sensors in two heights, $T_{air}$ and $RH$ have been linearly interpolated to the 2 m standard height (see section 1.4.2.1). $T_{air}$ at AWS1 and AWS2 was used to calculate a linear vertical gradient (-0.007 K $m^{-1}$) that is applied in the distributed model version (see section 2.4).

The AWS data was processed according to the instruments' manuals and screened in order to detect and correct measurement errors. No further corrections for radiative sensor heating and/or riming were conducted as Mölg et al. (2012) identified only 0.9% of wind data and between 0 and 0.7% of the other variables to be erroneous.

A total of 25 ablation stakes in the eastern part of the glacier serve for MB model calibration and evaluation (see section 1.3.4.2). Measurements are available for 16 intervals within the ablation seasons between May 2009 and October 2011. The intervals range between four days and seven months (see Fig. 2.8a and section 2.4.2.4). Snow pits were dug at AWS1 in 2009, 2010 and 2011 in order to measure vertical density profiles that serve for density assumptions within the model (see section 2.3.1) and for model evaluation (see section 2.4.2.3).

**Table 2.1: Measurement specifications for AWS1 located at 5665 m a.s.l. The last column indicates the usage for the MB modelling: forcing (F), parameter setting (P), or model evaluation (E). The two shortwave radiation components yield measured surface albedo. Net radiation is used to obtain measured incoming longwave radiation.**

| Variable | Instrument | Nominal accuracy | Usage |
|---|---|---|---|
| Air temperature, relative humidity (2 m)[1] | Campbell CS215 | 0.9°C (-40°C to +70°C) and 4% (0-100%) | F |
| Wind speed (2 m) | Young 05103-45 | 0.3 m $s^{-1}$ | F |
| Air pressure | TH Friedrichs DPI 740 | 0.15 hPa | F |
| Snow accumulation | Campbell SR50 | 1cm or 0.4% to target | F |
| Incoming shortwave radiation | Campbell CS300 | 5% (daily totals) | F |
| Reflected shortwave radiation | Campbell CS300 | 5% (daily totals) | P, E |
| Net radiation | Campbell NR-LITE | 20% (assumption) | E |
| Surface height change | Campbell SR50 | 1 cm or 0.4% to target | E |
| Glacier surface temperature | Campbell IRTS-P | 0.3°C | E |
| Subsurface temperature at 4.5 m / 5 m | Campbell TP107 | 0.3°C | E |
| Subsurface temperature at 8.5 m / 7.1 m | Campbell TP107 | 0.3°C | P |

[1] with ventilated radiation shield

### 2.2.2 Time-lapse photography

In addition to the ablation stakes, we use images of a terrestrial time-lapse camera system installed on a mountain ridge nearby the glacier for distributed MB model evaluation (Schneider et al. 2011, 2013). The two cameras (cam1 and cam2, Canon EOS 60D/50D) were located about 1 km north of the glacier tongue and the field of view covers between 57% (cam2) and 60% (cam1) of the glacier area, respectively (Fig. 2.1). Pictures were taken automatically with a 28 mm lens every four hours between 2010 and 2012 (00:00, 04:00, 08:00, 12:00, 16:00, 20:00 Beijing Time (BT)). Cam1 was operating from 23 May 2011 until 18 June 2012, cam2 with interruptions between 22 May 2010 and 2 September 2012. For this study, we focused on daily pictures at 16:00 BT during the melting seasons in order to detect the spatial pattern and the mean altitude of the transient snow line (see section 2.4.2.5). The accurate estimation of the transient snow line's temporal evolution is an important factor for melt modelling because the snow line separates two regions with totally different albedo and therefore SEB processes (Hock & Holmgren 2005, see section 1.3.4.1).The timing of the pictures was chosen based on cloud cover formation and the incidence angle of the sun (Farinotti et al. 2010). In order to orthorectify the sequence of pictures, several ground control points (GCPs) have been taken at the glacier side between 2009 and 2011.

Farinotti et al. (2010) and Huss et al. (2013) used time-lapse photography at remote glaciers in the Swiss Alps to infer the snow accumulation distribution. Farinotti et al. (2010) adjusted a simple snow accumulation and temperature index melt model to the observed melt patterns. Huss et al. (2013) directly combined the fraction of snow-covered glacier surface from the orthorectified camera pictures with a simple accumulation and melt model to derive glacier MB.

### 2.2.3 High Asia Reanalysis

We use data from the High Asia Reanalysis (HAR) generated at TU Berlin both to fill the gaps in the AWS data from April 2009 to June 2012 and to continuously run the MB model for the period October 2001 to September 2011. In the first case our aim is to use as many in-situ measurements as possible and to evaluate the distributed MB model performance in detail (see section 2.4.2). The latter enables MB studies over periods of up to ten years without the need of direct measurements (see section 2.4.6).

HAR is a dataset generated using the Weather Research and Forecast (WRF) atmospheric model (Skamarock & Klemp 2008) version 3.3.1 with a domain covering Central Asia with 30 km and the TP with 10 km resolution. HAR is initialized daily by the final analysis data from the Global Forecasting System and provides gridded fields for several atmospheric and surface variables. All details of the model configuration such as grid structure, model options and forcing strategy are published in Maussion et al. (2011, 2014).

To simulate SEB and MB of Zhadang glacier, we use hourly data from the 10 km-resolution grid. Generated incoming shortwave radiation, air temperature (2 m), relative humidity (2 m), air pressure, wind speed (10 m), all-phase precipitation and cloud cover fraction (*N*) are extracted from the grid cell that directly covers the glacier area and at the same time has the least altitude difference to AWS1 (-39 m) (Fig. 2.3). As *N* is not directly available from measurements this is the only parameter continuously taken from HAR. For the period 1 January to 10 June 2012 that is not covered by HAR data (Fig. 2.2d), we apply a formulation after Favier et al. (2004) to calculate N (see section 2.3.1).

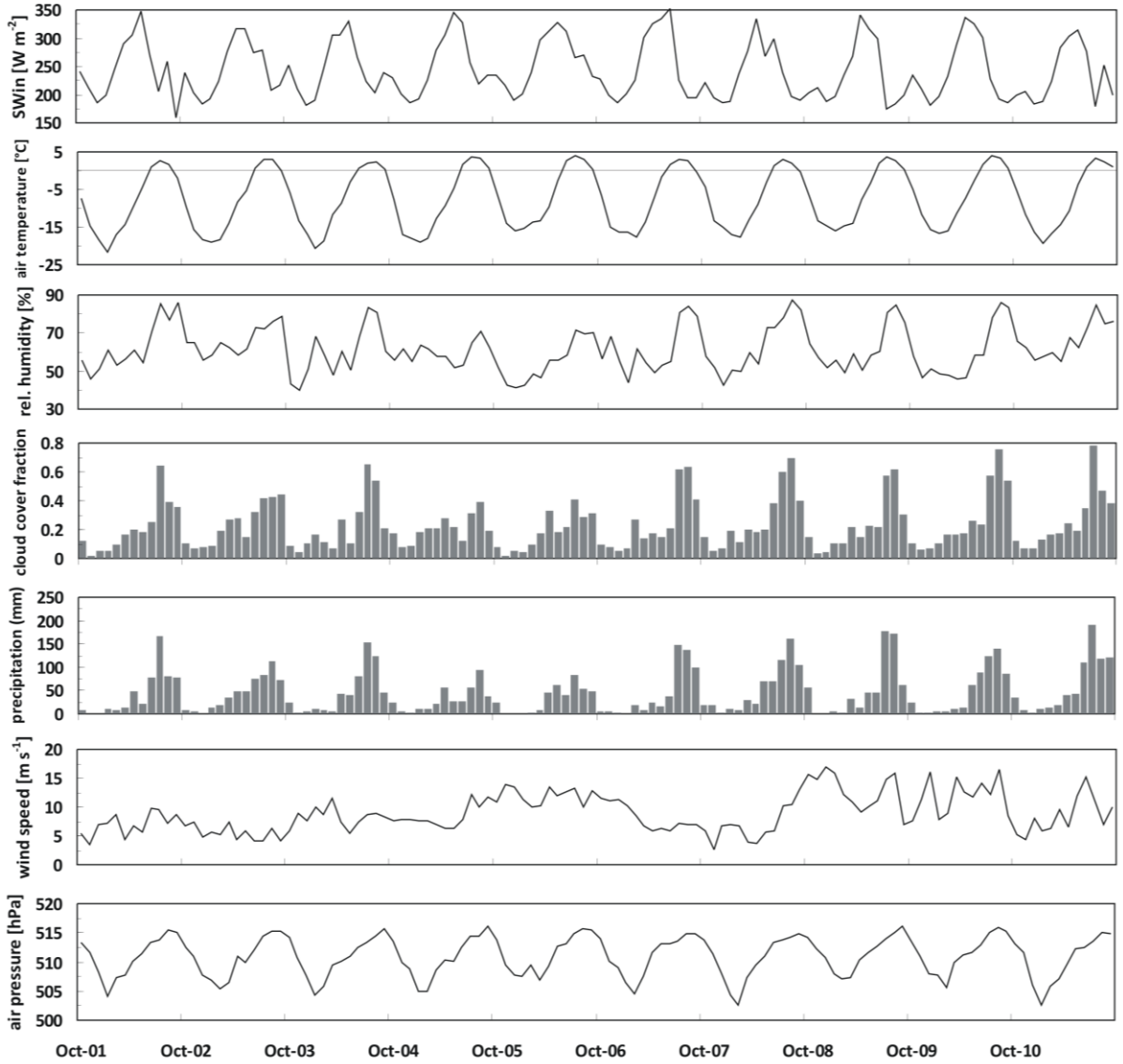


**Fig. 2.3: Monthly means or sums (precipitation) of meteorological variables from the HAR dataset at the atmospheric grid cell containing Zhadang glacier (5611 m a.s.l.), October 2001-September 2011. The MB model is forced with hourly values of these variables. The scaling factor of 0.56 (see section 2.2.3) is already applied on precipitation amounts.**

For air pressure and wind speed the altitude difference between AWS1 and the HAR grid cell is obvious in the data series (Fig. 2.4) and much larger than the standard deviation of hourly values. Therefore, it was corrected for the AWS gap filling by reducing hourly HAR values by their mean deviation from the corresponding AWS data (air pressure: -8.3 hPa; wind speed: -4.7 m $s^{-1}$). For wind speed only values larger than 5 m $s^{-1}$ were corrected. For air temperature and relative humidity discrepancies are generally smaller and negligible concerning mean standard deviations and are therefore not corrected for altitude. Daily mean differences in $SW_{in}$ can be large in summer (Fig. 2.4, max. 260 W $m^{-2}$). Hourly differences even reach ±1000 W $m^{-2}$ in cases when HAR cloud cover differs from actual cloud cover around noon when maximum radiation amounts occur. However, as variations in $SW_{in}$ are rather caused by cloud cover and terrain effects than by altitude, these differences are not corrected. Total sums of $SW_{in}$ show only small discrepancies. For the MB model runs solely forced by HAR data no correction of altitude was performed.
Mölg et al. (2012) compared HAR precipitation with measurements from a precipitation gauge in front of the Zhadang glacier over ≈ 16 months and found a good correlation with the measured seasonal cycle but obtained a scaling factor of 0.56 for the amount of HAR precipitation. This factor is seen to rather reflect the underestimation of the precipitation gauge and/or the loss of snow on the glacier by wind drift. The latter has been observed during field work and is also captured by the time-lapse photography but is not integrated in the MB model scheme (see section 2.4.5). Applying this scaling factor to HAR precipitation is suitable for AWS gap filling (Fig. 2.8a) and leads to a good result for the solely HAR forced point MB model run (Fig. 2.9a). Annual totals for total precipitation and snowfall are in the range of values given by Zhang et al. (2013) for Zhadang glacier supporting a reasonable scaling factor (Table 2.7). The annual precipitation pattern is similar to that observed at Nam Co Station, with 81% of the annual total occurring between May and September. Precipitation minima are found in November and December (Fig. 1.10, 2.3, see section 1.4.2.1). We apply a sinusoidal function (Möller et al. 2007) to describe the transition between solid and liquid precipitation in a temperature range between +1°C and +5°C (Fujita & Ageta 2000, Zhou et al. 2010, Mölg et al. 2012). To convert solid precipitation to actual snow height, a density of 250 kg $m^{-3}$ is chosen following Mölg & Scherer (2012).

For the distributed MB model runs, altitudinal gradients for relative humidity and air pressure are calculated from four HAR grid cells surrounding AWS1, with gradients of 0.022% $m^{-1}$ for relative humidity and -0.067 hPa $m^{-1}$ for air pressure (Fig. 2.5a,b). For wind speed and cloud cover we assume no distinct altitude dependency although the correlation of wind speed with altitude within the HAR dataset is large (Fig. 2.6e,f). Comparisons with other regions on the TP (e.g. Purogangri (chapter 3) and Naimona'nyi (chapter 4)) suggest that this result is a coincidence possibly due to the small number of grid cells considered. For air temperature we apply the altitudinal lapse rate calculated from AWS data (see section 2.2.1). The precipitation gradient is derived from the calibration process (see section 2.4.1).

## 2.3 Methods

The physically based SEB/MB model (see section 2.3.1) is the main tool within this study. It has been newly developed at RWTH Aachen University (Huintjes et al. 2013b,c), based on similar existing structures and parameterizations. To detect the transient snow line from the time-lapse camera pictures, an image processing had to be applied in order to calculate geo-referenced ortho-images (see section 2.3.2).

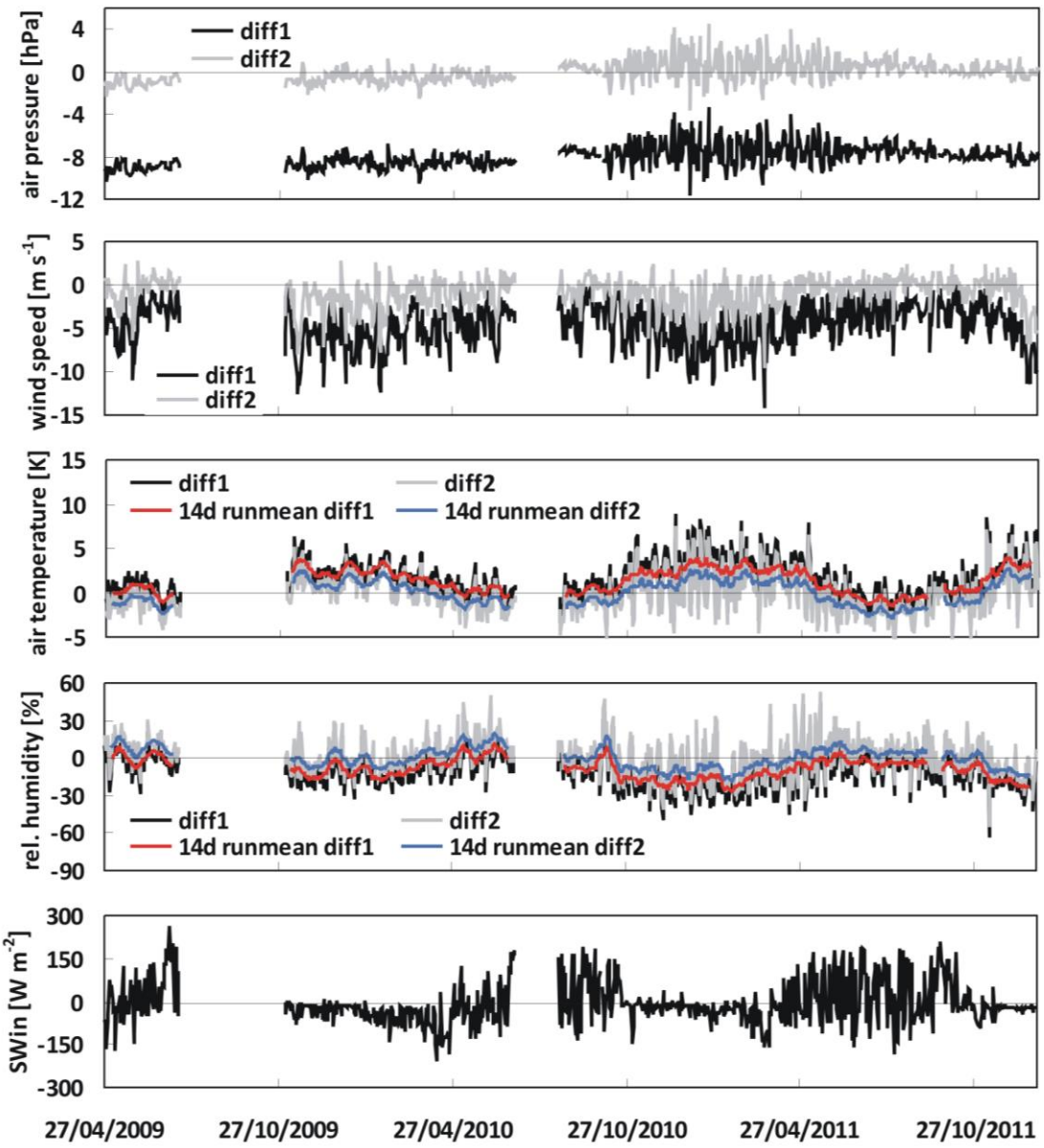


**Fig. 2.4: Effect of altitude difference between AWS1 and HAR grid cell and its correction for daily mean values (note that the discrepancies are calculated from hourly values). Negative values indicate that HAR values are larger than AWS values, diff1 is the difference between original values, diff2 is the difference after altitude correction of HAR data. For air temperature, rel. humidity and $SW_{in}$ no altitude correction is applied.**

### 2.3.1 SEB/MB modelling

The MB model couples a SEB to a multi-layer snow model. It computes the specific mass balance (*MB*) at an hourly time step from the sum of accumulation by solid precipitation ($c_{solid}$) and refreezing of percolating water in the snow pack ($c_{ref}$), and ablation by melt and sublimation as follows:

$$MB = \frac{Q_{melt}}{L_M} + \frac{Q_{lat}}{L_S} + c_{solid} + c_{ref}\,, \tag{2.1}$$

where $Q_{melt}$ is the energy available for surface melting, $Q_{lat}$ is the turbulent latent heat flux, $L_M$ and $L_S$ are the latent heats of melt ($3.34\times10^5$ J kg$^{-1}$) and sublimation ($2.849\times10^6$ J kg$^{-1}$), respectively. Mass fluxes that lead to a mass gain for the glacier are positive. $Q_{melt}$ and $Q_{lat}$ are calculated within the SEB (in W m$^{-2}$):

$$F = SW_{in} \cdot (1-\alpha) + LW_{in} + LW_{out} + Q_{sens} + Q_{lat} + Q_G\,, \tag{2.2}$$

where $SW_{in}$ is incoming shortwave radiation, α is the surface albedo, $LW_{in}$ and $LW_{out}$ are incoming and outgoing longwave radiation, $Q_{sens}$ is the turbulent sensible heat flux, $Q_{lat}$ is the turbulent latent heat flux and $Q_G$ is the ground heat flux which consists of fluxes of heat conduction and penetrating shortwave radiation.

Heat flux from liquid precipitation is neglected. Energy fluxes towards the surface have a positive sign. The resulting flux $F$ is equal to $Q_{melt}$ only if the surface temperature ($T_s$) is at the melting point (273.15 K). $T_s$ is a key variable in the model (Table 2.2). It is necessary to solve Eq. (2.2) as it is used to calculate $LW_{out}$, $Q_{sens}$, $Q_{lat}$ and $Q_G$. It links surface and subsurface modules. $T_s$ is calculated iteratively through Eq. (2.2) from the energy available at the surface. In case $T_s$ exceeds the melting point, it is reset to 273.15 K and the remaining energy flux F equals $Q_{melt}$. Fig. 2.6 illustrates the coupled SEB and multi-layer snow model and presents an overview of the procedure followed in the model.

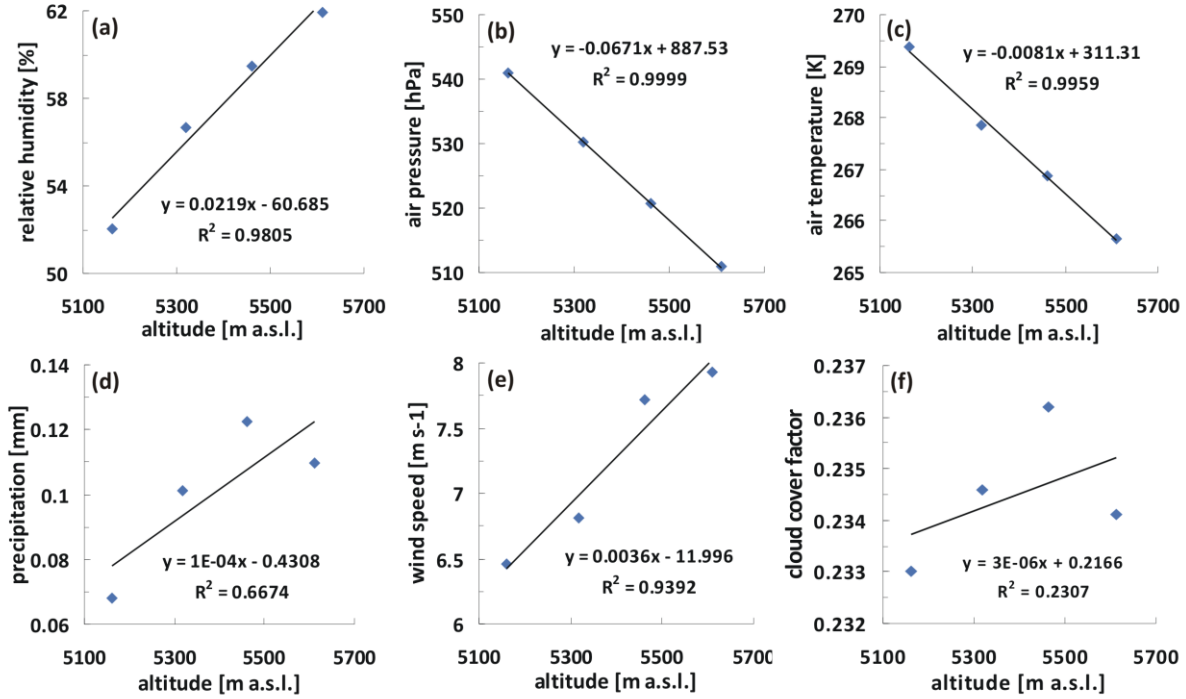


**Fig. 2.5: Altitude dependency of the HAR variables that serve as input for the MB model (without $SW_{in}$). The slope of the regression line defines the respective altitude gradient per meter. Values are means for each HAR grid cell, 2001-2011.**

For the application of the model at the point location at AWS1, $SW_{in}$ is the only SEB component which comes from direct measurements. In the distributed model run, $SW_{in}$ is derived from a radiation model after Kumar et al. (1997) that computes clear-sky direct and diffuse shortwave radiation in response to geographical position, altitude, elevation, shading by the surrounding terrain, slope and aspect of the grid cell and albedo of the surrounding terrain. The radiation model runs on the SRTM DEM (45 m). Potential $SW_{in}$ ($SW_{in,pot}$) is corrected for cloud cover through measured $SW_{in}$ (or HAR $SW_{in}$) as follows: For each time step $SW_{in,j}$ at the chosen location $j$ is set to $SW_{in,HAR}$. At Zhadang glacier, $j$ is the position of AWS1. At the other glaciers we choose a DEM pixel with minimum terrain shading (see chapters 3-6). Then, at each time step we calculate the ratio ($ri$) of $SW_{in,pot}$ at any location ($x,y$) in the domain to $SW_{in,j,pot}$:

$$ri_{x,y} = SW_{in,x,y,pot} / SW_{in,j,pot}. \tag{2.3}$$

$SW_{in,j,pot}$ is potential $SW_{in}$ according to Kumar et al. (1997) at the chosen location *j*. The spatial matrix of cloud-corrected shortwave irradiance $SW_{in}$ at any location (*x,y*) in the domain calculated by

$$SW_{in,x,y} = SW_{in,j} * ri_{x,y} \quad (2.4)$$

for each time step finally provides a spatial mask of $SW_{in}$ including effects from terrain shading and from cloud cover.

**Table 2.2: Energy fluxes at the glacier surface and their physical links as treated in the MB model.**

| SEB component | Determined from[a] |
|---|---|
| $SW_{in}$ (incoming shortwave radiation) | Direct measurement of solar radiation / radiation model |
| α (surface albedo) | Snowfall amount and frequency, snow depth |
| $LW_{in}$ (incoming longwave radiation) | Water vapour pressure, air temperature, cloud cover factor |
| $LW_{out}$ (outgoing longwave radiation) | Glacier surface temperature ($T_s$) |
| $Q_{sens}$ (turbulent sensible heat flux) | Air temperature, $T_s$, wind speed, air pressure |
| $Q_{lat}$ (turbulent latent heat flux) | Air humidity, $T_s$, wind speed, air pressure |
| $Q_G$ (ground heat flux) | Thermodynamic heat equation (forced by $T_s$) |

[a] for details see section 2.3.1

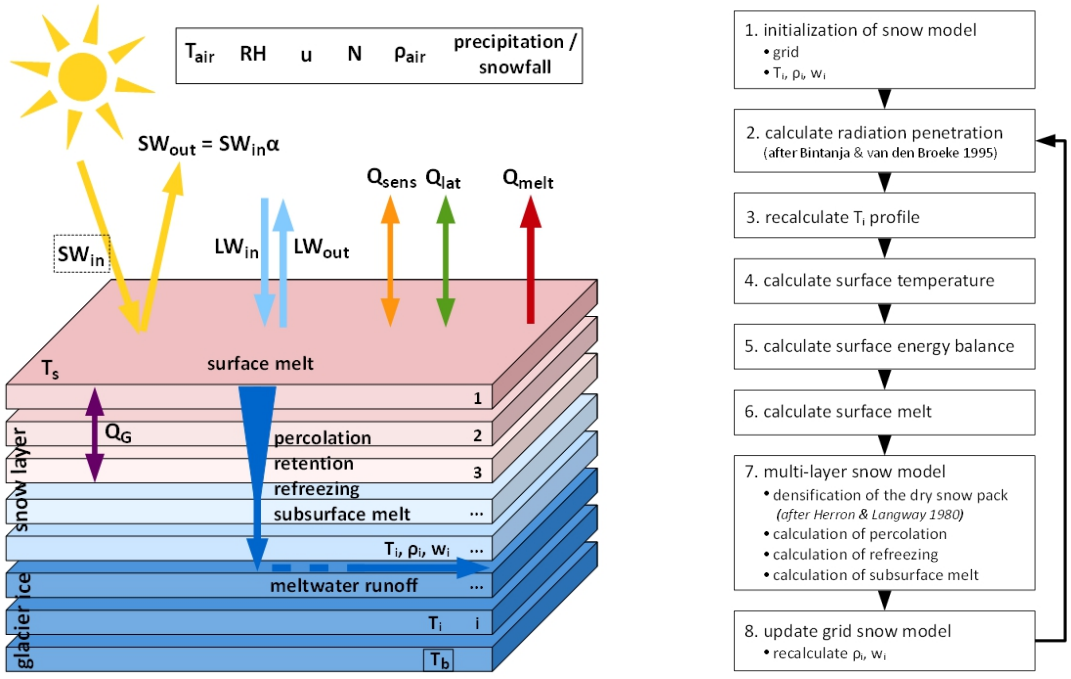


**Fig. 2.6: Left: Illustration of an SEB model including a multi-layer snow model. Symbols are as in the text, subscript *i* denotes the *i*th model level. Parameters obtained from measurements or atmospheric model output are outlined. Arrows indicate the direction of the energy flux. Fluxes directed towards the surface are defined positive. Right: Flow chart of the MB model.**

The parameterization of surface albedo follows the scheme of Oerlemans & Knap (1998) where α is determined as a function of snowfall frequency and snow depth:

$$\alpha_{snow} = \alpha_{firn} + (\alpha_{frsnow} - \alpha_{firn}) \exp(t_{snow} / t^*) \text{ and} \quad (2.5)$$

$$\alpha = \alpha_{snow} + \alpha_{ice} - \alpha_{snow} \exp(-h / d^*) . \quad (2.6)$$

$t_{snow}$ is the time since the last snowfall, $t^*$ is a constant for the effect of ageing on snow albedo, *h* is the snow depth and $d^*$ is a constant for the effect of snow depth on albedo. The free parameters in the albedo scheme are determined from measurements of $SW_{in}$ and $SW_{out}$ at AWS1 between 2009 and 2011 (see section 2.2.1) and according to Mölg et al. (2012). Final values are: albedo fresh snow

($\alpha_{frsnow}$) = 0.9, albedo firn ($\alpha_{firn}$) = 0.55, albedo ice ($\alpha_{ice}$) = 0.3, $t^*$ = 6 days and $d^*$ = 8 cm. A comparison of measured daily mean $\alpha$ with the respective modelled $\alpha$ is given in Fig. 2.7.

$LW_{in}$ and $LW_{out}$ are obtained by the Stefan-Boltzmann law. For $LW_{in}$, the atmospheric emissivity $\varepsilon$ is calculated after Klok & Oerlemans (2002):

$$\varepsilon = \varepsilon_{cs} \cdot (1 - N^a) + \varepsilon_{cl} \cdot N^a , \tag{2.7}$$

where $\varepsilon_{cs}$ is clear-sky emissivity and $\varepsilon_{cl}$ is cloud emissivity, $N$ is cloud cover factor. $\varepsilon_{cs}$ is calculated as follows:

$$\varepsilon_{cs} = 0.23 + b(e / T_{air})^{1/8} , \tag{2.8}$$

where $e$ is water vapour pressure and $T_{air}$ is air temperature. For $a$, $b$ and $\varepsilon_{cl}$ we take the values of 2, 0.433 and 0.984, respectively, as determined by Klok & Oerlemans (2002). $N$ is directly taken from HAR except during the period 1 January to 10 June 2012 that is not covered by HAR data (Fig. 2.2d). During the latter period we determine $N$ by comparing $SW_{in}$ to the theoretical values of the top of atmosphere solar irradiance ($SW_{TOA}$) using the expression after Favier et al. (2004):

$$N = 1.3 - 1.4 \cdot (SW_{in} / SW_{TOA}) . \tag{2.9}$$

$SW_{TOA}$ is calculated through the radiation model after Kumar et al. (1997) considering solar constant and geographical position.

Turbulent heat fluxes $Q_{sens}$ and $Q_{lat}$ are calculated through the bulk aerodynamic method after Oerlemans (2001) between the surface and 2 m, using $T_{air}$, $RH$ and wind speed ($u$) data from AWS1:

$$Q_{sens} = \rho_{air} \cdot c_p \cdot C_{se} \cdot u \cdot (T_{air} - T_s) \tag{2.10}$$

$$Q_{lat} = \rho_{air} \cdot L_{E/S} \cdot C_{lat} \cdot u \cdot (q_{air} - q_s) . \tag{2.11}$$

$\rho_{air}$ is air density, calculated from air pressure, $T_{air}$ and specific humidity in 2 m, $c_p$ is specific heat capacity of air (1004.67 J kg$^{-1}$ K$^{-1}$), $L_E$ is latent heat of evaporation (2.514×10$^6$ J kg$^{-1}$), $L_S$ for sublimation (2.849×10$^6$ J kg$^{-1}$), $q_{air}$ and $q_s$ are specific humidity at 2 m and at the surface, calculated from $RH$, $p$ (air pressure) and saturation water vapour pressure. $RH$ is assumed to be 100% at the surface. $C_{se}$ and $C_{lat}$ are bulk-transfer coefficients for sensible and latent heat. Oerlemans (2001) found $C_{se}$ and $C_{lat}$ to differ by less than 5%, therefore we assume $C_{se}$ = $C_{lat}$. $C_{se}$ is calculated after Braithwaite (1995):

$$C_{se} = k^2 / [\ln(z / z_0)]^2 , \tag{2.12}$$

with $k$ the von Karman constant (0.41), $z$ the instrument height (2 m) and $z_0$ the surface roughness length that changes time dependent ($z_{0m}$ = $z_{0h}$) (Mölg et al. 2009a). Similar to Mölg et al. 2012, $z_0$ increases linearly from 0.24 mm for fresh snow (Gromke et al. 2011) to 4 mm for aged snow (Brock et al. 2006). If the surface is snow free, we assume $z_0$ to be 1.7 mm (Cullen et al. 2007). A correction of turbulent fluxes for stable conditions is carried out after Braithwaite (1995):

$$\begin{aligned} Q_{sens/lat} &= Q_{sens/lat} \cdot (1 - 5 \cdot Ri)^2 \qquad 0.2 > Ri > 0.01 \\ Q_{sens/lat} &= 0 \qquad\qquad\qquad\qquad\quad Ri > 0.2 \end{aligned} , \tag{2.13}$$

were $Ri$ is the bulk Richardson number, calculated from $T_{air}$ and $u$:

$$Ri = (g \cdot T_{air(C)} \cdot z) / T_{air} \cdot u^2 . \tag{2.14}$$

In formula 2.12 after Braithwaite (1995) $g$ is the acceleration of gravity (9.81 m s$^{-1}$) and $T_{air(C)}$ is the air temperature in °C.

$Q_G$ is the sum of the conductive heat flux ($Q_C$) and the energy flux from penetrating shortwave radiation ($Q_{PS}$). $Q_{PS}$ is calculated following Bintanja & van den Broeke (1995). By

$$S_i(z) = SW_{net} \cdot (1-\zeta) \cdot e^{\beta \cdot z} \tag{2.15}$$

the extinction of $SW_{net}$ in the snow or ice layers is parameterized. In the top model layer, a fraction $\zeta$ is absorbed and an exponentially decreasing flux with constant extinction coefficient $\beta$ reaches the layers at depth $-z$ and increases subsurface temperatures. Thus, $Q_{PS}$ is equal to $SW_{net}(1-\zeta)$. For $\zeta$ and $\beta$ we take the values of 0.8 and 2.5 for ice, and 0.9 and 17.1 for snow, respectively, as determined by Bintanja & van den Broeke (1995).

$Q_C$ is determined from the temperature difference between the surface and the two uppermost subsurface layers and depends on the thermal conductivity ($\lambda$) of the medium (ice or snow). $\lambda$ is calculated from the subsurface density ($\rho$, in kg m$^{-3}$) after Anderson (1976):

$$\lambda = 0.021 + 2.5 \cdot (\rho / 1000)^2 . \tag{2.16}$$

Thus, in order to calculate $Q_G$ vertical profiles of subsurface temperature ($T$) and density ($\rho$) need to be known which are calculated within the subsurface snow model. The snow model uses a vertical grid that consists of layers with an equal thickness ($dz$) of 0.1 m in the point model version and 0.2 m in the distributed model runs. Each layer is characterized by a temperature, density, liquid water content ($w$) and depth ($z$). On this grid, $T$ is solved from the thermodynamic heat equation:

$$\frac{\delta T}{\delta t} = \kappa \cdot \frac{\delta^2 T}{\delta z^2} . \tag{2.17}$$

$\kappa$ is the thermal diffusivity and is calculated using the expression after Sturm et al. (1997) ($\rho$ in kg m$^{-3}$):

$$\kappa = \lambda / (\rho \cdot c_{pi}) , \tag{2.18}$$

where $c_{pi}$ is the specific heat of ice, that is a function of $T$: $c_{pi} = 152.2 + 7.122 \cdot T$ (Paterson, 1994).

The initial temperature profile is defined from the available subsurface measurements (see section 2.2.1) by linear interpolation. Tests showed that model results are the same for an initial temperature profile linearly interpolated between $T_{air}$ (= $T_s$) and $T_b$ as for an initial temperature profile linearly interpolated between the subsurface measurements. The density profile of the initial snow pack is calculated by a linear interpolation between 250 and 550 kg m$^{-3}$ as estimated from the snow pits (see section 2.2.1).

First, the temperature profile is calculated without considering the effects of refreezing or subsurface melt but considering temperature increase by $Q_{PS}$ only. In case a snow/firn pack is present, the model then calculates the densification of the dry snow pack through an empirical relation after Herron & Langway (1980):

$$\frac{d\rho}{dt} = K \exp(-E/(r \cdot T)) \cdot {c_{solid}}^f \cdot (\rho_{ice} - \rho) / \rho_{ice} , \tag{2.19}$$

where $K$ is a rate factor, $E$ is activation energy (J mol$^{-1}$), $r$ is the gas constant (8.3144 J K$^{-1}$ mol$^{-1}$), $c_{solid}$ is the accumulation rate (in mm w.e.) and $f$ is a factor that is approximately equal to 1 (Reijmer & Hock 2008). For $K$ and $E$ we take the values as determined by Herron & Langway (1980) for two stages of densification: for $\rho$<550 kg m$^{-3}$ we take $K$ = 11 and $E$ = 10160, for 550 kg m$^{-3}$<$\rho$<800 kg m$^{-3}$ we take $K$ = 575 and $E$ = 21400.

After the densification process, the available amount of surface and subsurface melt water percolates downwards and a small amount is held in each layer. We choose constant percolation velocities of 0.06 cm s$^{-1}$ for unsaturated layers and 0.042 cm s$^{-1}$ (70%) for saturated layers where the liquid water content ($w$) exceeds the irreducible water content ($w_i$). These values are within the boundaries

for water film flow and tubular flow through homogenous snow layers (Baumgartner et al. 1990). $w_i$ is assumed to be 5% of the total mass of the layer (Fujita & Ageta 2000). Then $w$ is calculated and depending on the cold content ($\gamma$) of the layer, the available water can refreeze. $\gamma$ is defined as the amount of energy that is required to raise the temperature of the respective layer to the melting point and is calculated as follows (Cogley et al. 2011):

$$\gamma = c_p \cdot \rho \cdot (273.15 - T) . \tag{2.20}$$

Therefore, the amount of refreezing is limited by $T$, which cannot be raised above the melting point, and by $w$. Refreezing is largest in early summer, when percolating melt water reaches cold winter snow layers, and in autumn, when capillary water freezes (van Pelt et al. 2012). When a wet snow layer is present in summer, internal water can refreeze at night. This leads to an increase in $T$ and $\rho$ in the respective layer. When $T$ exceeds the melting point in the model, $T$ is reset to 273.15 K and the remaining energy is used for subsurface melt. This melt water is added to the water content of the respective layer. If $w$ exceeds $w_i$, the remaining water percolates downwards into the next layer until it reaches the glacier ice and runs off.
Including the described processes, the subsurface temperature evolution can be expressed as:

$$\frac{\delta T}{\delta t} = \kappa \cdot \frac{\delta^2 T}{\delta z^2} + \frac{\delta Q_C}{\delta z} + \frac{\delta S_i(z)}{\delta z} + \frac{F \cdot L_M}{\delta z} + \frac{M \cdot L_M}{\delta z} , \tag{2.21}$$

where $F$ and $M$ are refreezing and melt rate, respectively.
Table 2.3 summarizes the free parameters within the MB model and the chosen values.

The application of the presented model to a number of glaciers on the TP shows that a spin-up time of about one year is needed for the subsurface module to adapt to the surrounding conditions (see sections 2.4.6, 3.4.1, 4.4.1, 5.4.1). In the first months of simulation, $w$ is zero and no refreezing can happen. This influences both the temperature and the density profiles and leads to a number of feedback processes that generally result in above average melt rates. Therefore, calculated values for the first year of simulation should be treated with caution.

### 2.3.2 Image processing

In order to obtain quantitative information, e.g. the transient snow line from the sequence of pictures taken by the two fixed time-lapse cameras, the landscape images had to be geo-referenced and orthorectified (Huss et al. 2013). This procedure including the manual snow line mapping was carried out at TU Dresden applying the software RSG (Remote Sensing Software Graz) for the image orthorectification. In a first step, one image per week and camera had to be manually orthorectified because of shifts in the camera position due to ground deformation. The orthorectification requires the definition of a transfer function relating the two-dimensional pixels of the picture to the three-dimensional orography as represented by the DEM (SRTM bicubically resampled to 1 m resolution). The correct scaling functions were defined by adjusting the position of five to six selected GCP (see section 2.2.2) to the corresponding locations in the pictures. The image coordinates of the GCP and therefore the scaling functions changed due to the movement of cameras over time. Applying a spline function the weekly detected GCP positions have been interpolated to all available camera pictures for automatic orthorectification. The transformation results in geo-referenced ortho-images that were further evaluated with regard to the spatial and temporal evolution of the transient snow line (see section 2.4.2.5). All pictures have been thoroughly checked and transient snow lines were manually digitized for daily images at 16:00 BT. The intersection of the digital snow lines with the re-

sampled SRTM DEM allows to calculate the mean elevation which is further compared to the MB model output (see section 2.4.2.5).

**Table 2.3: Free parameters in the MB model as explained in section 2.3.1. Vertical gradients for air temperature, precipitation, relative humidity and air pressure are only valid for Zhadang glacier.**

| Parameter(ization) | Value | References |
|---|---|---|
| SWin | n.a. | Kumar et al. (1997) |
| LWin | n.a. | Klok & Oerlemans (2002) |
| N (only for AWS data) | n.a. | Favier et al. (2004) |
| turbulent heat fluxes | n.a. | Oerlemans (2001) |
| bulk-transfer coefficients | n.a. | Braithwaite (1995) |
| stable condition effect on turbulence | n.a. | Braithwaite (1995) |
| upper threshold for precipitation phase (all liquid above) | 1°C | Fujita & Ageta (2000), Zhou et al. (2010), Mölg et al. (2012) |
| lower threshold for precipitation phase (all solid below) | 5°C | Fujita & Ageta (2000), Zhou et al. (2010), Mölg et al. (2012) |
| vertical precipitation gradient | AWS forced: 0.046±0.004% $m^{-1}$; HAR forced: 0.04±0.003% $m^{-1}$ | MB model calibration |
| density of solid precipitation | 250 kg $m^{-3}$ | Mölg & Scherer (2012) |
| vertical air temperature gradient | -0.007 K $m^{-1}$ | measurement |
| vertical humidity gradient | 0.022% $m^{-1}$ | HAR |
| vertical air pressure gradient | -0.067 hPa $m^{-1}$ | HAR |
| total domain depth | 10 m | by definition in the MB model |
| layer thickness for subsurface processes | 0.1 / 0.2 m | by definition in the MB model |
| roughness length ice | 1.7 mm | Cullen et al. (2007), Mölg et al. (2012) |
| roughness length fresh snow | 0.24 mm | Gromke et al. (2011), Mölg et al. (2012) |
| roughness length aged snow | 4 mm | Brock et al. (2006), Mölg et al. (2012) |
| initial snow depth gradient | 0.0015 m $m^{-1}$ | measurement |
| initial snow density profile for the total snow pack | linear increase with depth from 250 to 550 kg $m^{-3}$ | assumption |
| initial temperature profile for the total domain depth | linear from air to bottom temperature | assumption |
| fixed bottom temperature in 10 m | 268 K | measurement |
| thermal conductivity | n.a. | Anderson (1976) |
| densification of dry snow pack | n.a. | Herron & Langway (1980) |
| thermal diffusivity | n.a. | Sturm et al. (1997) |
| cold content | n.a. | Cogley et al. (2011) |
| fraction of Snet absorbed in surface layer (ice) | 0.8 | Bintanja & van den Broeke (1995), Mölg et al. (2012) |
| fraction of Snet absorbed in surface layer (snow) | 0.9 | Bintanja & van den Broeke (1995), Mölg et al. (2012) |
| extinction coefficient of penetrating SW radiation (ice) | 2.5 $m^{-1}$ | Bintanja & van den Broeke (1995), Mölg et al. (2012) |
| extinction coefficient of penetrating SW radiation (snow) | 17.1 $m^{-1}$ | Bintanja & van den Broeke (1995), Mölg et al. (2012) |
| surface albedo scheme | n.a. | Oerlemans & Knap (1998) |
| ice albedo | 0.3 | measurement, Mölg et al. (2012) |
| fresh snow albedo | 0.85 | measurement, Mölg et al. (2012) |
| firn albedo | 0.55 | measurement, Mölg et al. (2012) |
| albedo time scale | 6 days | measurement, Mölg et al. (2012) |
| albedo depth scale | 8 cm | measurement, Mölg et al. (2012) |

## 2.4 Results and Discussion

In this section the calibration process and uncertainty assessment of the AWS and HAR forced MB model is explained (see section 2.4.1) first. After that, model performance is evaluated in detail for point and distributed version (see section 2.4.2). Both model versions are identical except for $SW_{in}$ which comes from a radiation model in case of distributed modelling (see section 2.3.1). In the distributed model we additionally consider the altitude dependency of atmospheric input variables by applying altitudinal gradients (see sections 2.2.1 and 2.2.3).

### 2.4.1 MB model calibration and uncertainty assessment

The applied formulations within the SEB/MB model contain several unknown or poorly constrained parameters. Mean values for these parameters were obtained from observations at the glacier site or taken from literature (see section 2.3.1).

The amount of snowfall, calculated from the SR50 record, leads to the development of an unrealistically high snow pack, when directly serving as model input. Therefore, we corrected the calculated snowfall by setting values <1 mm to zero, which is below the measurement accuracy of the sensor (Table 2.1). As the distributed model runs forced with AWS data start in late April, we assume an initial snow depth on the glacier that increases linearly with altitude. Based on snow depth measurements at the ablation stakes, we choose an initial snow depth gradient of 0.15% $m^{-1}$. In the HAR forced distributed model runs starting at 1 October, glacier wide initial snow depth is set to zero.

MB measurements at the 25 ablation stakes on the glacier between 2009 and 2011 are used to tune the altitudinal precipitation gradient, both for the AWS and the HAR forced distributed model runs. Stake readings are available for 16 intervals with interval lengths between four days and seven months. For calibration, we perform five model runs and randomly leave five stakes out, respectively. This results in mean precipitation gradients of 0.046±0.004% $m^{-1}$ for AWS model runs and 0.040±0.003% $m^{-1}$ for HAR model runs. Calibrating both models over all available ablation stakes leads to precipitation gradients of 0.047% $m^{-1}$ and 0.042% $m^{-1}$ for AWS and HAR driven model, respectively. These negligible differences in the gradients justify the chosen number of only five calibration runs each.

To determine the MB model uncertainty we then run the model with the calibrated precipitation gradient for the five stakes left out in the respective calibration run. For each measurement interval (*j*) and every calibration run, the results for surface height change and MB are averaged over the five stakes. The model uncertainty per day ($U_{day}$) is calculated after:

$$U_{day} = \frac{1}{16}\sum_{j=1}^{16}\frac{\left(X_{j,\max} - X_{j,\min}\right)}{n_j}, \tag{2.22}$$

where $X$ is the mean value over the five ablation stakes of surface height change or MB of the respective calibration run and $n_j$ is the number of days of the measurement interval $j$. The mean daily deviations of surface height change and MB for different precipitation gradients within the MB model ($U_{day}$) define the model uncertainty that needs to be considered for the distributed model (see sections 2.4.2.4, 2.4.3 and 2.4.6). For the application of $U_{day}$ to annual MB values, annual uncertainties are calculated from the daily means. The results are ±0.88 m/yr for surface height change and ±0.65 m w.e./yr for MB for the AWS forced model and ±0.86 m/yr for surface height change and ±0.60 m w.e./yr for MB for the HAR forced model.

### 2.4.2 MB model performance

In this chapter the performance of the MB model is evaluated for several parameters at point scale forced with AWS and HAR data as well as for the distributed model version compared to ablation stakes measurements and time-lapse photography.

#### 2.4.2.1 AWS driven point MB model

Fig. 2.7 compares measured and modelled $LW_{in}$ and $\alpha$ at AWS1, which yields satisfying correlation coefficients (R). The root-mean-square errors (RMSE) of 35.5 W $m^{-2}$ for $LW_{in}$ and 0.096 for $\alpha$ are within the sensors' accuracy (Table 2.1) and confirm the applied parameterizations. At lower values of measured $LW_{in}$ model values are generally too large. Reasons for this effect can be discrepancies in

$T_{air}$, $RH$ and/or $N$ between measurements and model input parameters and uncertainties through the applied parameterization of $\varepsilon$ (eq. 2.7, 2.8). Additionally, measured $LW_{in}$ is not directly measured at AWS1 but calculated from measured $R_{net}$, $T_s$, $SW_{in}$ and $SW_{out}$. The different response times of the sensors cause accuracy problems for $LW_{in}$ (Maussion et al. 2011a).
Furthermore, model performance is evaluated at point scale against observations of surface height, $T_s$ and $T$ at AWS1 (Fig. 2.8). The AWS forced model can reproduce the seasonal pattern of a rather stable or smoothly increasing surface height in winter and surface lowering in varying intensity in summer very well (Fig. 2.8a). With respect to an overall surface lowering of ≈ 6 m a root-mean-square error (RMSE) of 0.049 m is a convincing result. Daily mean measured $T_s$ ranges between -29.7°C in winter and 0°C in summer (Fig. 2.8b). Model results are in high correlation with this variability and an RMSE of 2.12 K is within the measurement uncertainties in the order of 2-2.5 K due to the dependency on emitted radiation as mentioned by Mölg et al. (2008, 2012). Similar good results are evident for $T$ (Fig. 2.8c). To evaluate model performance, we selected measured $T$ at an initial depth of 5.6 m due to the effect of radiative heating of the sensors further up in the snow pack. Simulated $T$ is the mean of the six surrounding layers with an initial depth between 4.4 and 5.0 m. The actual measurement depth of $T$ changes according to the varying surface height and the reinstallation depth of the sensor. These processes are taken into account for the calculation of modelled $T$ from the subsurface temperature profile. An RMSE of only 0.15 K indicates a reasonable parameterization of $Q_{PS}$ and confirms the good performance of the AWS forced SMB and snow layer model at point scale.

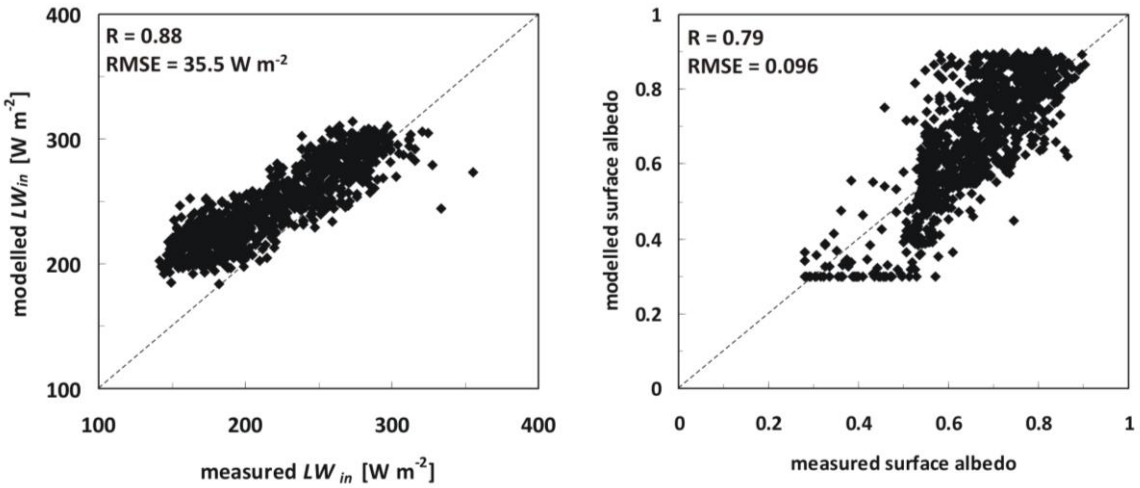


**Fig. 2.7: Measured and modelled daily means of incoming longwave radiation (left) and surface albedo (right) at AWS1 between 24 April 2009 and 10 June 2012.**

### 2.4.2.2 HAR driven point MB model

Evaluation of the HAR forced MB model at point scale was performed in the same way as described for the AWS forced model (see section 2.4.2.1). As expected, the AWS forced model can reproduce the respective parameters to a higher degree than the model forced with HAR data. The main reason for this might be frequency and intensity of precipitation that cannot be exactly reproduced by HAR especially at smaller scales (Fig. 2.9, see section 2.2.3). Deviations are largest for surface height change and seem to be damped with increasing depth. RMSE values are 0.035 m for surface height change, 2.87 K for $T_s$ and 0.16 K for $T$. Nevertheless, with regard to the fact that model input is the output of an atmospheric model with a 10 km-resolution grid, model performance is still satisfying. The results indicate that the HAR forced MB model can be run for whole Zhadang glacier. It is

possible to evaluate the performance of the distributed MB model through individual ablation stakes in the same way as it is done for the AWS forced model (see section 2.4.2.4).

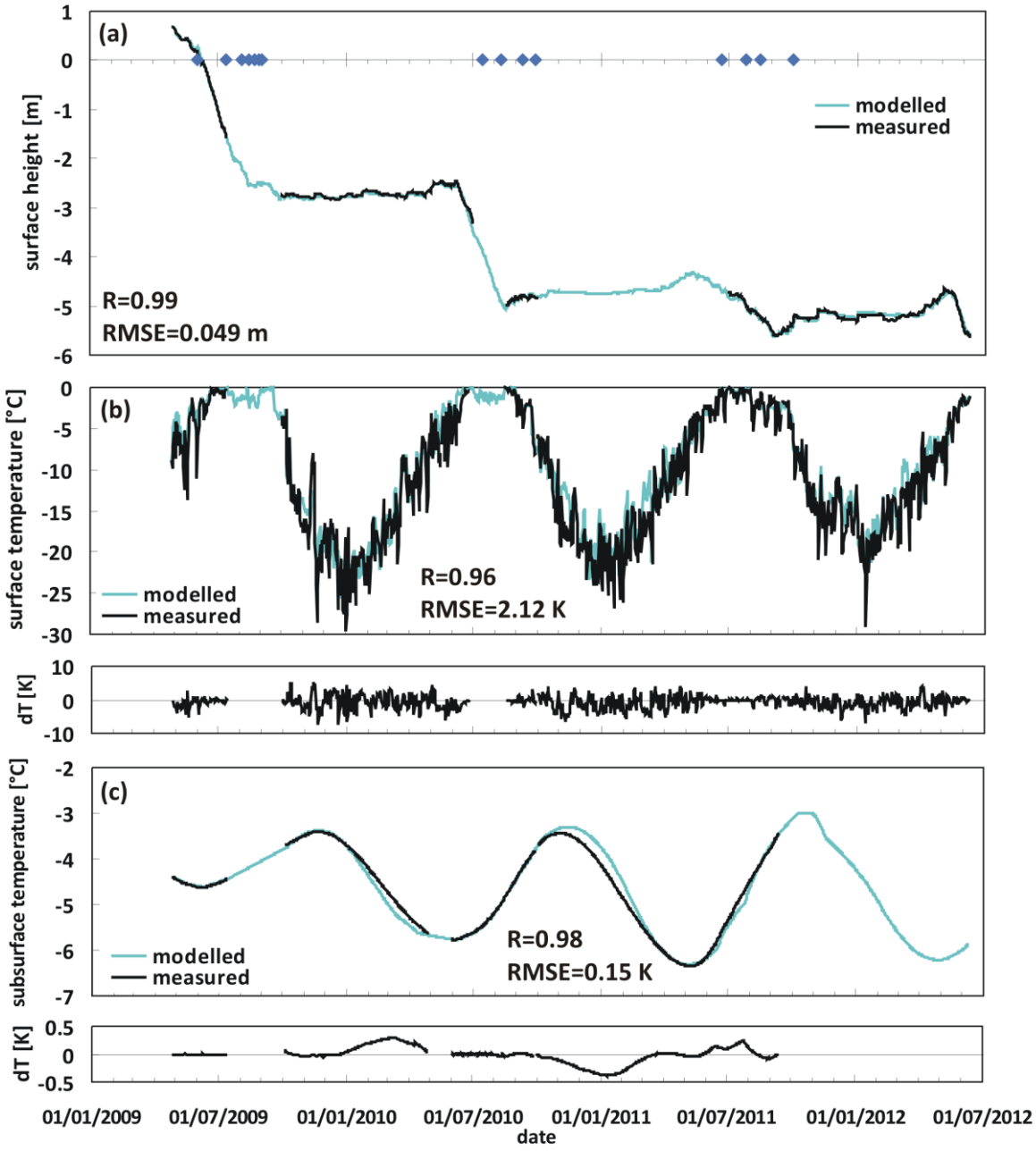


**Fig. 2.8: Measurements and AWS forced MB model results at AWS1. All data are daily mean values. (a) accumulated surface height change, blue dots show available ablation stake measurements; (b) glacier surface temperature and temperature deviations; (c) subsurface temperature and temperature deviations. Sensor depth varies between 4.5 and 2.0 m during the period; note a measurement gap in May 2010; no ice temperatures are available after September 2012.**

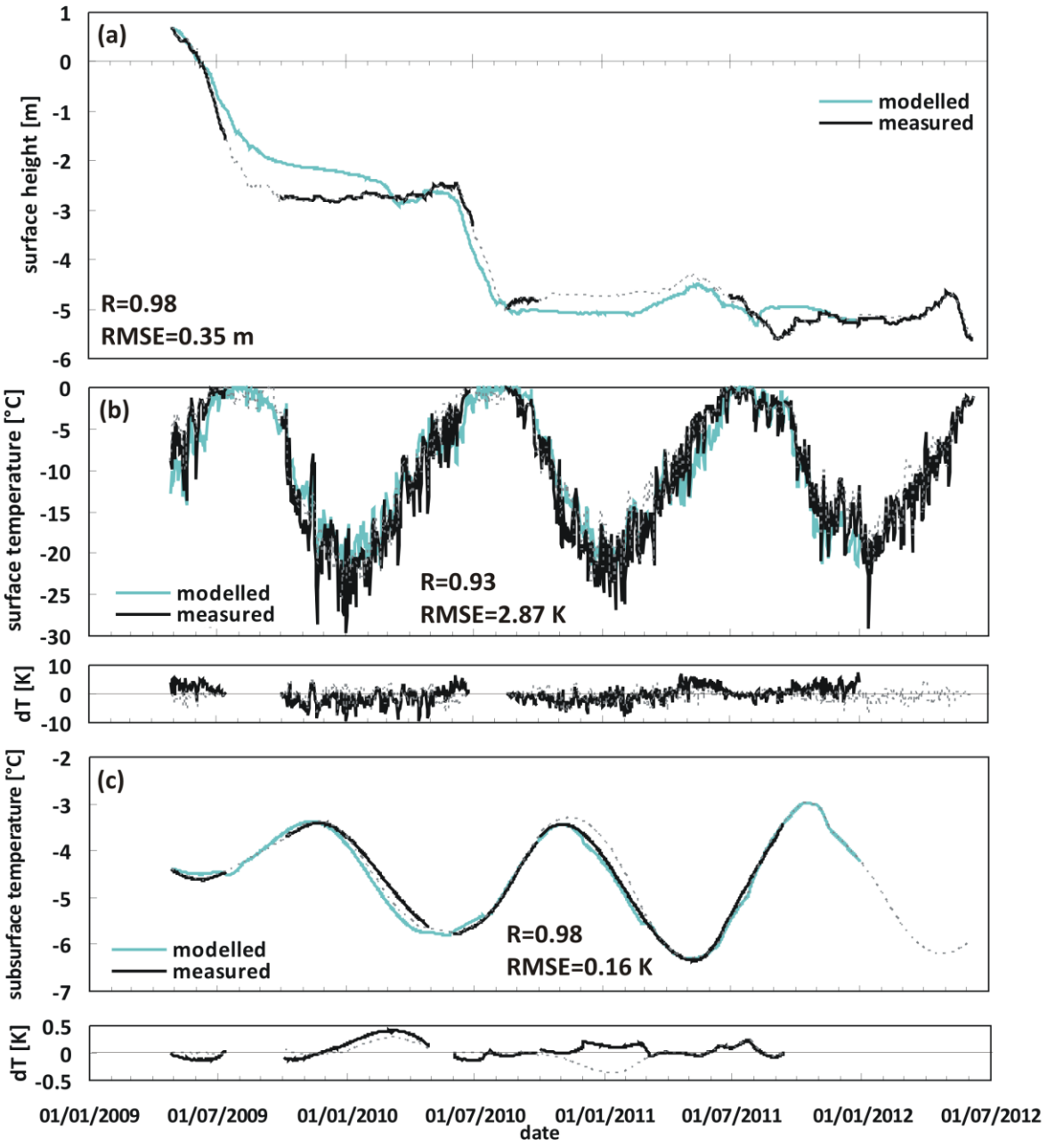


**Fig. 2.9: Measurements and HAR forced MB model results at the location of AWS1. All data are daily mean values. (a) accumulated surface height change; (b) glacier surface temperature and temperature deviations; (c) subsurface temperature and temperature deviations. The dashed grey lines again show the respective results of the AWS forced MB model (Fig. 2.8).**

### 2.4.2.3 Density profiles from the point MB model

Comparing measured and simulated snow density ($\rho$) profiles for selected days reveals the limits within the applied snowpack scheme. In contrast to modelled $\rho$, the observed $\rho$ profiles show a larger variability between the layers (Fig. 2.10). Nevertheless, the result reveals that modelled and observed snow density follows the same overall pattern and is within the same range or order of magnitude. The result indicates that the snow cover scheme used in this study can very well take into account the most relevant processes that are needed for mass balance modelling. Accounting for the small-scale variations would require a detailed approach for snow microstructure and a much higher vertical model resolution including more sophisticated formulations of melt water percolation and

refreezing. After Vionnet et al. (2012) the subsurface module presented in this thesis belongs to the '*snowpack schemes of intermediate complexity*'. It accounts for some internal processes, such as percolation, refreezing and densification for a number of layers (see section 2.3.1). Detailed snowpack models like *Crocus* (Brun et al. 1989, 1992), *SNTHERM* (Jordan 1991) and *SNOWPACK* (Bartelt & Lehning 2002) include an explicit description of the physical snow properties and microstructure, such as grain morphology. However, these models require detailed information on the various snow characteristics and generate high computational costs.

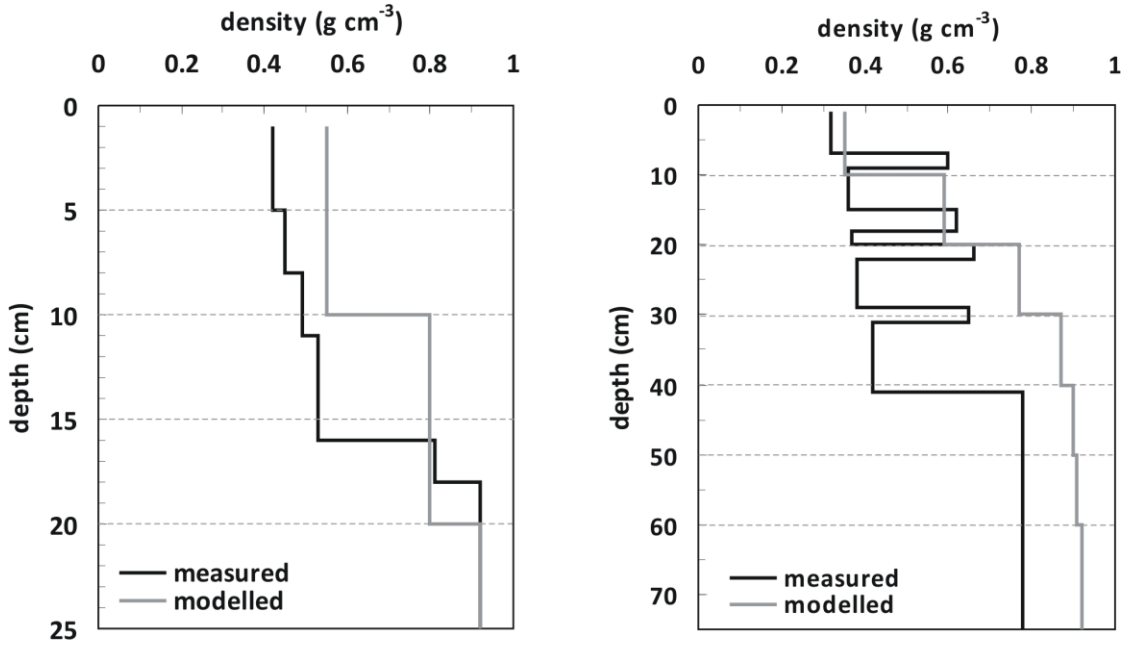


**Fig. 2.10: Observed and modelled snow density profiles for 17 May 2010 (left) and 22 May 2011 (right). Note the different y-axis range of the two plots. The model run is forced with AWS data. Snow model layer depth is 10 cm.**

#### 2.4.2.4 Evaluation of the distributed MB model with ablation stakes

To evaluate the distributed model output for both AWS and HAR forced model, surface height change and MB over the available ablation stakes are calculated (Fig. 2.11, 2.12). Stake readings are available for 16 intervals within the ablation seasons between May 2009 and October 2011 (Fig. 2.8a). Considering all available intervals leads to an RMSE between measurements and results of the AWS forced MB model of 0.22±0.03 m for surface height change and 0.34±0.05 m w.e. for MB (Fig. 2.11). The RMSE per day is ≈0.005 m for surface height change and ≈0.007 m for MB.

The evaluation of HAR forced model results is shown in Fig. 2.12 for surface height change and MB. Determined RMSE for all 16 intervals is 0.33±0.03 m for surface height and 0.36±0.03 m w.e. for MB. The overall scattering in the HAR forced model is much larger mostly due to uncertainties in modelled precipitation (see section 2.4.2.2). Nevertheless, the results of the HAR forced distributed MB model are convincing and indicate that it produces reliable results for the annual specific MB of Zhadang glacier 2001-2011 (see section 2.4.6). The result also shows that the model can be transferred to other glaciers and ice caps where in-situ measurements are sparse or lacking at all.

The uncertainty ranges for the model results given in Fig. 2.11 and 2.12 are calculated from the mean difference between maximum and minimum values of surface height change and MB for every stake measurement interval using minimum and maximum values for surface height change and MB calculated through the different precipitation gradients for the total number of days of the individual

intervals (see section 2.4.1). The uncertainties for the measurements are calculated from the assumption of ±0.05 m uncertainty in stake readings and ±20% uncertainty on measured MB values due to uncertainty involved in the calculation of $\rho$.

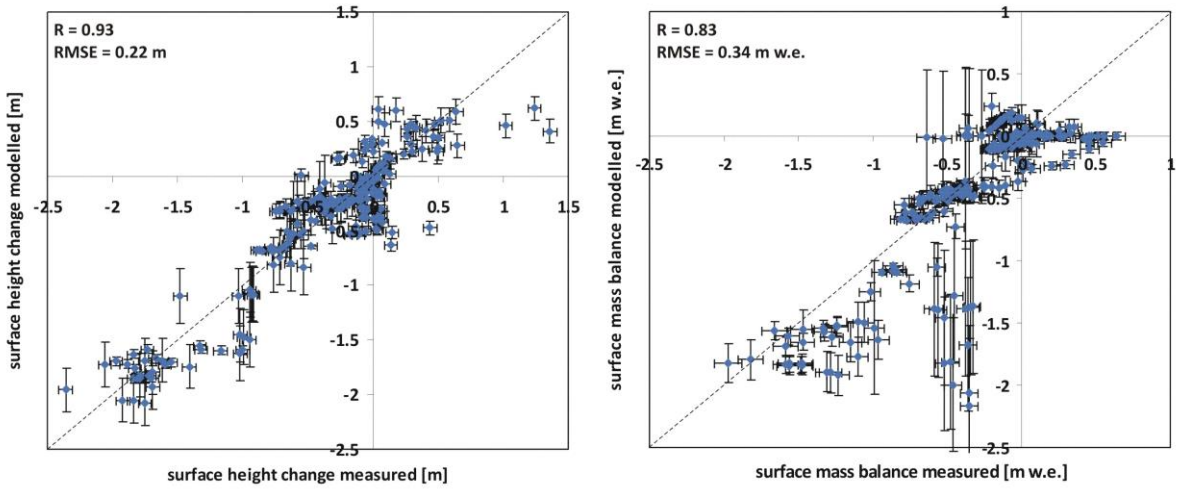


**Fig. 2.11: Observed and modelled surface height change (left) and MB (right) over the available ablation stakes (see Fig. 2.1) and the associated model locations. The MB model is forced with AWS data. The calculation of R, RMSE and the error bars is explained in section 2.4.1 and 2.4.2.4.**

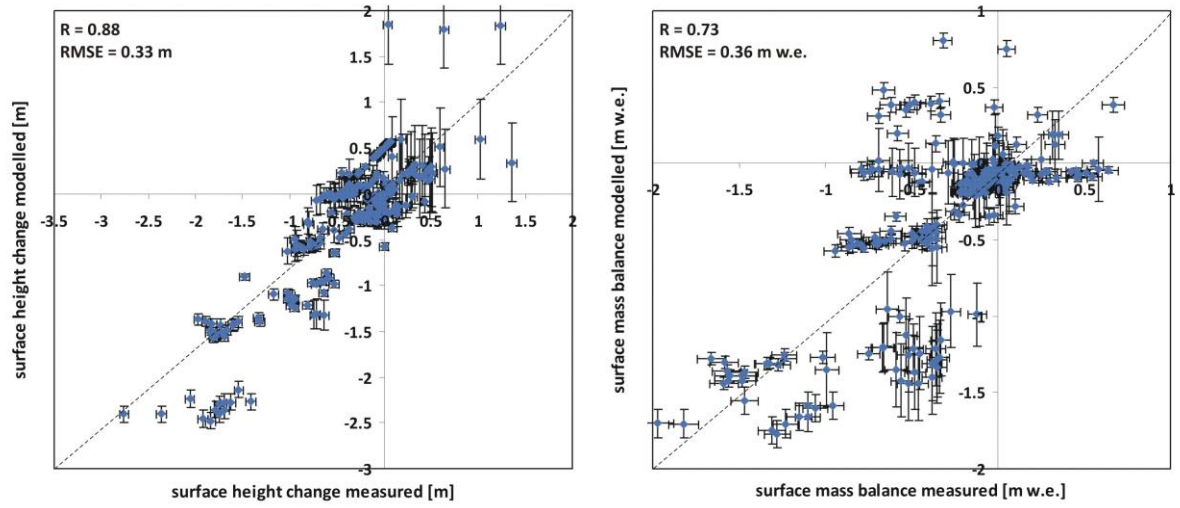


**Fig. 2.12: Observed and modelled surface height change (left) and MB (right) over the available ablation stakes (see Fig. 2.1) and the associated model locations. The MB model is forced with HAR data. The calculation of R, RMSE and the error bars is explained in section 2.4.1 and 2.4.2.4.**

The comparison of measured and modelled MB reveals large discrepancies of more than 1 m w.e. in one interval (Fig. 2.11, 2.12). Both AWS forced and HAR forced model runs overestimate the mass loss in the lower glacier regions compared to the measurements. In the upper glacier regions the differences decrease and the model underestimates the measured mass loss. The respective interval ranges from early September 2009 to mid May 2010. Thus, it includes consecutive periods of melt, sublimation and snowfall events. This might increase both the measurement and the modelling uncertainty. The effect of wind induced snow redistribution is not considered in the MB model but might have a significant contribution to overall winter mass balance (see section 2.4.5). The model uncertainty per day is slightly above (AWS forced model) and slightly below (HAR forced model) the daily mean uncertainty averaged over all available measurements. However, even though the mean

daily uncertainty is moderate, according to the long interval of 256 days the calculated model uncertainty for the total interval is large (AWS driven model: 0.54 m w.e., HAR driven model: 0.24 m w.e.).

### 2.4.2.5 Evaluation of the distributed MB model using time-lapse photography

We used inferred mean transient snow line altitudes from the ortho-pictures for validation of the distributed AWS forced MB model (see section 2.3.2). Camera snow lines are available for the ablation seasons in 2010, 2011 and 2012 (Fig. 2.13). In 2012 available AWS data limit the MB model run to 10 June. For days where a transient snow line exists, we compare mean altitude of the mapped snow line at 16:00 BT to the respective model output. The modelled snow line consists of those pixels, that form the border between snow covered and snow free pixels within the view field of the camera. The respective mean altitude is calculated from the underlying SRTM DEM (Rabus et al. 2003, resampled to 45 m).

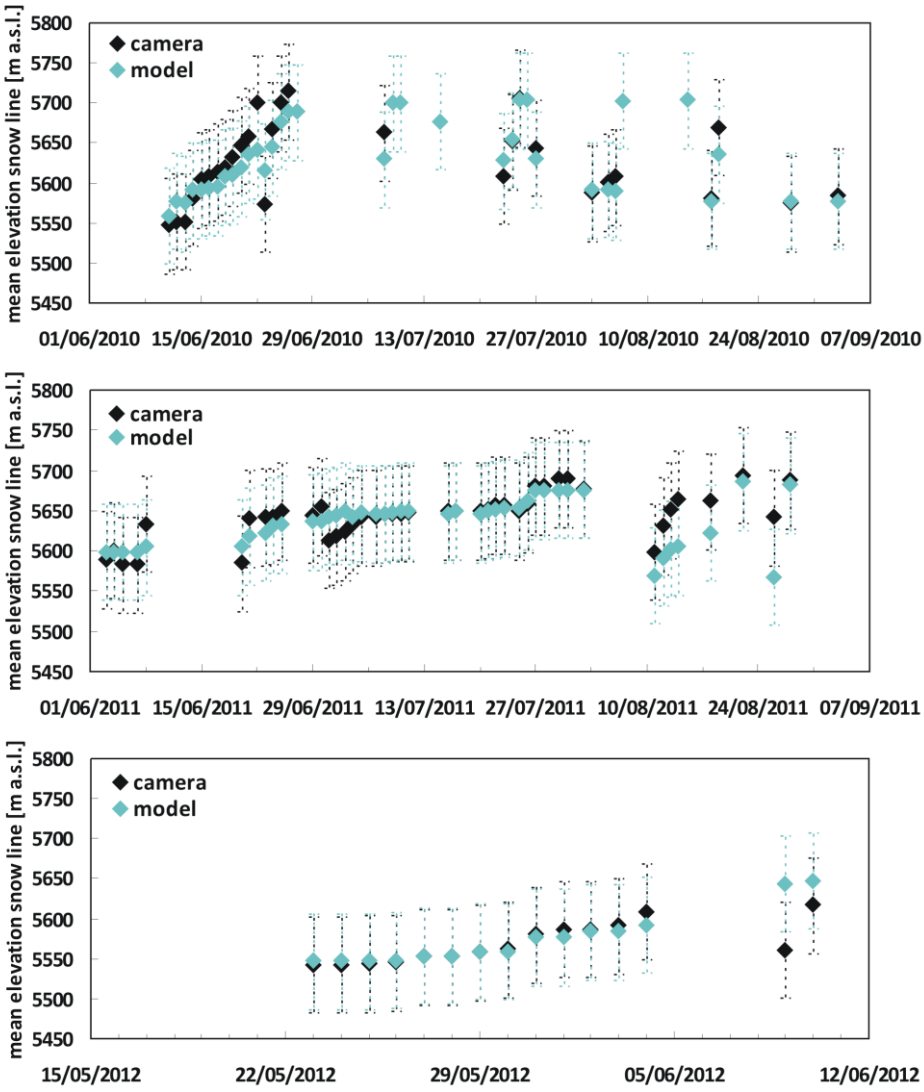


**Fig. 2.13: Mapped and modelled temporal evolution of the mean transient snow line altitude at 16:00 BT for the three ablation seasons, uncertainty is assumed to be ±60 m, respectively (see explanations in section 2.4.2.5).**

For both, mapped and modelled transient snow lines, we assume an uncertainty of ±60 m of altitude. The model uncertainty is calculated from the altitude difference (*ΔH*) between the highest (5780 m a.s.l.) and the lowest (5530 m a.s.l.) SRTM pixel of the glacier area captured by the cameras (Fig. 2.1, 250 m), mean modelled snow depth difference (*Δh*) between highest and lowest SRTM pixel for the AWS driven MB model period 2009-2012 (0.5 m), the number of SRTM pixels along the flow line (*np*=50) and the RMSE of modelled snow depth at the available ablation stakes over all available intervals between May 2009 and October 2011 ($RMSE_h$=0.12 m). *ΔH* and *np* lead to a mean altitude difference (*ΔHp*) of 5 m per pixel along the glacier flowline. From *Δh* and *np* the mean snow depth variation per pixel (*Δhp*) is calculated (0.5/50=0.01). *Δhp* and $RMSE_h$ result in a mean spatial model uncertainty for the calculation of the transient snow line of 12 pixels (0.12/0.01=12). The total uncertainty expressed in metres of altitude is then determined from the spatial uncertainty and *ΔHp* (12*5=60). Uncertainties in the manually mapped snow lines can occur from errors in the image processing (see section 2.3.2) and the subjective assessment of the spatial snow line pattern. The uncertainty is not be quantified exactly. It also depends on the slope angle. It is assumed to be approximately around a few tens of metres. Therefore, we assume the same range of uncertainty of ±60 m as it is calculated for the model uncertainty.

With respect to this uncertainty, an overall RMSE of 20.8 m (Fig. 2.14) between observed and modelled mean altitude of the snowline is a good result. The performance of the distributed MB model in reproducing spatial patterns of the transient snow line can only be evaluated qualitatively. Fig. 2.15 contains two examples for 25 July 2010 and 24 June 2011. On 25 July 2010 the spatial pattern of the transient snow line is clearly detectable on the ortho-picture and very well reproduced by the MB model. Whereas on 24 June 2011 the pattern is characterized by large snow patches that complicate the exact detection of the transient snow line. The respective model output corresponds to this irregular pattern. The results support that the model performance is of good quality.

This finding is in agreement with the result presented in section 2.4.2.4 through the evaluation with the ablation stake network. Additionally, the reliability and transferability of the calibrated precipitation gradient to glacier regions where ablation stakes are missing is supported. A more detailed interpretation of the snow line characteristics of Zhadang glacier between 2010 and 2012 is given in section 2.4.4.

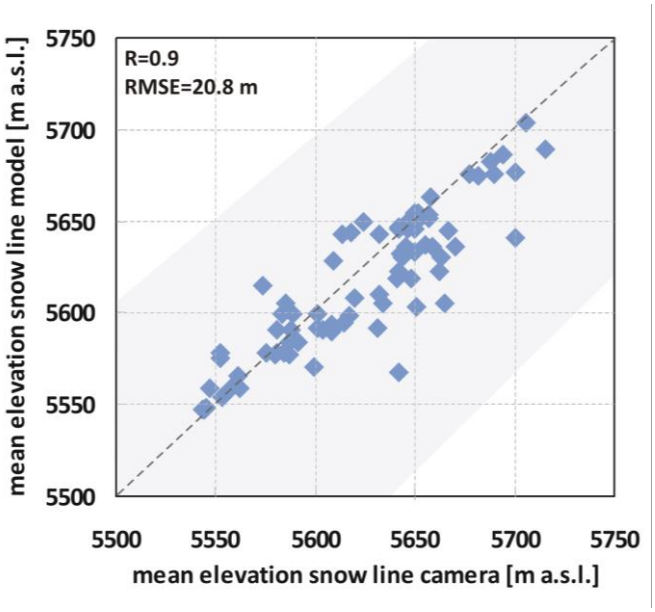


**Fig. 2.14: Mapped and modelled mean transient snow line altitude in the ablation season in 2010, 2011 and 2012 at 16:00 BT, respectively. The range of uncertainty (grey area) is assumed to be ±60 m (see explanations in section 2.4.2.5).**

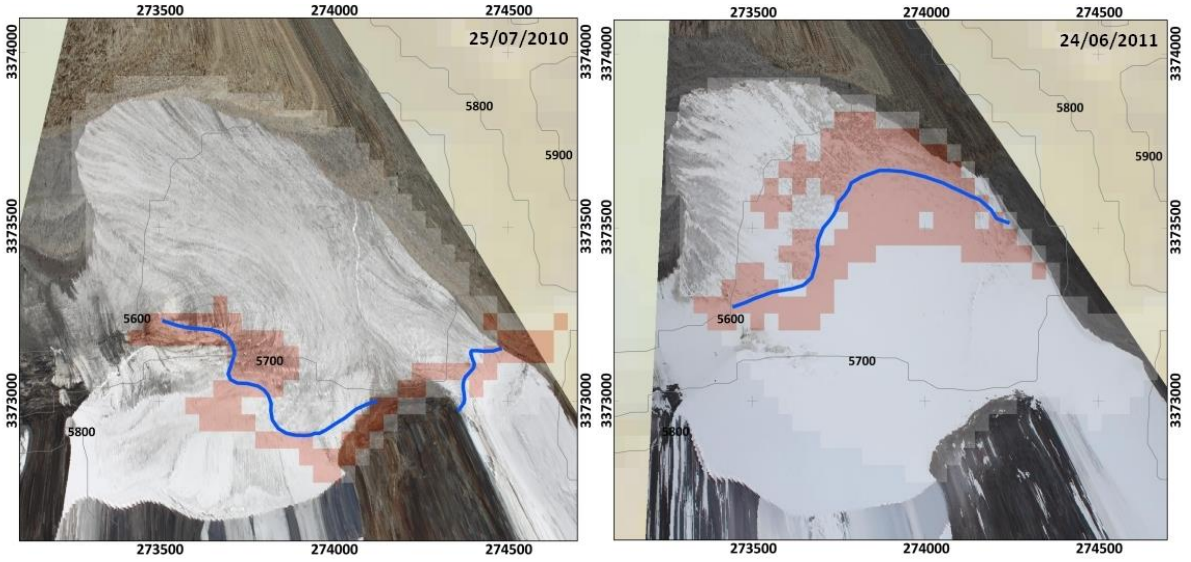


**Fig. 2.15: Examples of the direct spatial evaluation of the transient snow line for two days in 2010 and 2011; orthorectified image of Zhadang glacier in the DEM (SRTM, 45 m) overlayed with mapped snow line (blue) and modelled snow line (red). For camera view fields see Fig. 2.1.**

### 2.4.3 SEB/MB from the AWS driven distributed model 2009-2012

The altitudinal dependence of glacier-wide MB and SEB components for the MB years 2009/10 and 2010/11 as calculated by the MB model is shown in Fig. 2.16. The pattern of annual MB (Fig. 2.16a) is characterized by a distinct steepening of gradients between 5650 and 5800 m a.s.l. that was also found by Mölg et al. (2012) at Zhadang glacier and by Fujita & Ageta (2000) at Xiao Dongkemadi glacier in the Tanggula Shan. The altitude range of this steepening differs within these studies as it does for the two balance years considered in Fig. 2.16. In the year 2009/10 the change in slope occurs between 5700 and 5800 m a.s.l., far below the equilibrium line altitude (ELA, 5950 m a.s.l. in 2009/2010) whereas in 2010/11, when ablation on Zhadang glacier was rather weak (Fig. 2.8 and 2.17), the steepening happens slightly below the ELA between 5650 and 5750 m a.s.l. This is in line with the findings of Mölg et al. (2012) and Fujita & Ageta (2000) and was also observed at Morteratschgletscher by Klok & Oerlemans (2002). A similar pattern can be found in the vertical profiles of $SW_{net}$ (Fig. 2.16d), $Q_{melt}$ (Fig. 2.16e) and therefore surface melt (Fig. 2.16b), and surface albedo ($\alpha$) (Fig. 2.16g). $Q_{melt}$ has the same shape as surface melt because the two parameters are directly connected through $L_M$ (see section 2.3.1). As $\alpha$ influences the other variables (see sections 1.3.4.1, 2.3.1) it is the main driving factor for the shape of the vertical MB profile (Braun & Hock 2004). $SW_{in}$ and $LW_{in}$ are the only ground-independent energy sources for the glacier surface (see section 2.3.1). $SW_{in}$ is nearly constant from around 5600 up to 5800 m a.s.l. due to minimal effects resulting from terrain shading. It shows a first minimum in the uppermost glacier regions mainly because of steep slopes in the eastern and western parts (Braun & Hock 2004) and a second minimum at the glacier tongue, possibly due to the convex shape of the main tongue and the steep slopes west of the second, smaller glacier tongue (Fig. 2.16d). These regions of smallest levels of solar insolation are reflected in the slopes of the vertical profiles of $b$ (Fig. 2.16a) which are slightly steeper in the lowest parts (comparatively less melt) and less steeper in the uppermost parts (sharp transition to positive values). Small $SW_{in}$ at the glacier tongue favours a number of feedback processes that are noticable in the lowest glacier areas, e.g. a comparatively higher $\alpha$ (Fig. 2.16g) and thus smaller $SW_{net}$ (Fig. 2.16d), and minimum $T_s$ (expressed in $LW_{out}$, Fig. 2.16f) in accordance of findings by Braun & Hock (2004) on King

George Island (Antarctica). These effects are damped but not overcompensated by $LW_{in}$, $Q_{sens}$ or $Q_{lat}$ because these values are rather stable or increase only little towards the glacier tongue in the annual mean (Fig. 2.16d,e) (Mölg et al. 2009). Total $Q_G$ approximates zero or is slightly positive at all elevations (Fig. 2.16e). According to negative $Q_{lat}$, sublimation is responsible for a small and rather constant glacier wide mass loss that can be larger than annual mean surface melt in the upper parts (Fig. 2.16b, Fig. 2.17b). The total amount of refreezing depends on both surface melt and the depth of the snowpack. Therefore, maximum refreezing happens where the combination of both is optimal, e.g. where decent amounts of surface melt and a thick snow pack is present. Fig. 2.16c indicates that this is generally the case in the middle part of the glacier. In the MB year 2009/10 the amount of refreezing increased up to 5750 m a.s.l. due to increasing snow cover and then decreased from 5850 m a.s.l to the top due to decreasing melt water availability. Snowfall does not increase linearly with altitude because in the lower regions $T_{air}$ exceeds the threshold for solid precipitation more often than in the upper regions (Klok & Oerlemans 2002). In the MB year 2010/11 a snow cover is evident over longer periods even in the lower regions of the glacier tongue (see section 2.5.4). This leads to larger amounts of refreezing in these areas with a maximum in 5650 m a.s.l. (Fig. 2.16c). Total refreezing in the upper glacier regions in 2010/11 is less than in 2009/10 because of less surface melt (Fig. 2.16b). The snow cover pattern and therefore the amount of refreezing are further modified through terrain effects and snow redistribution (Fig. 2.15, see section 2.4.4). They do not necessarily show a dependency on altitude. Within the considered period, the annual mean proportion of refreezing reaches 37% in the upper glacier regions and ranges between 2% (2009/10) and 13% (2010/11) in the lowermost altitude band. The less negative annual mean glacier wide $b$ in 2010/11 can be explained by a larger amount of solid precipitation (Fig. 2.16c) which leads to higher net accumulation and additionally to lower surface melt (Fig. 2.16b) through increasing $\alpha$ (Fig. 2.16g) through decreasing $SW_{net}$ (Fig. 2.16d) and $T_s$ (expressed through $LW_{out}$, Fig. 2.16f).

The feedback processes stress the importance of the effect of the albedo on glacier SEB and MB. This has been reported in several studies on glaciers in Central Asia (e.g. Aizen & Aizen 1994; Caidong & Sorteberg 2010; Fujita 2007; Yang et al. 2011) and in other regions (e.g. Giesen et al. 2009; Mölg et al. 2008, 2009; Van den Broeke et al. 2011; Van Pelt et al. 2012).

Fig. 2.17 illustrates annual cycles of glacier-wide mean monthly SEB and MB components as calculated by the MB model. In general, $LW_{in}$ (+249.7 W m$^{-2}$) and $SW_{in}$ (+220.0 W m$^{-2}$) dominate energy input over the considered period, followed by $Q_{sens}$ (+20.4 W m$^{-2}$) and $Q_G$ (+1.6 W m$^{-2}$). Energy sinks at the glacier surface are $LW_{out}$ (-284.8 W m$^{-2}$), $SW_{out}$ (-144.1 W m$^{-2}$), $Q_{lat}$ (-29.1 W m$^{-2}$) and $Q_{melt}$ (-22.0 W m$^{-2}$), making $SW_{net}$ (+74.2 W m$^{-2}$, see Table 2.4) the most important energy source, highly depending on $\alpha$. This was also observed by Li et al. (2014b) in the catchment containing Zhadang glacier, by Andreassen et al. (2008) at Storbreen (Norway) and by Mölg & Hardy (2004) at Kilimanjaro. Some of the lowest values of $SW_{net}$ are evident in or around September when larger snowfall amounts in context with storm events increase $\alpha$. In summer 2009, extreme low α causes highest $SW_{net}$ resulting in large amounts of $Q_{melt}$ (Fig. 2.17a) and therefore surface melt (Fig. 2.17b, Fig. 2.8a). $LW_{net}$ shows a rather regular seasonal cycle playing a smaller role as energy sink in summer than in winter (Fig. 2.17a, see also Li et al. 2014b). This can be explained through the seasonal patterns of $LW_{in}$, depending on $T_{air}$, $e$ and $N$ (see section 2.3.1) (higher in summer), and $LW_{out}$, depending on $T_s$ (largest negative values in summer). Averaged over the whole period $Q_C$ is very small and naturally tends to zero (see also Li et al. 2014b, Zhang et al. 201). In winter, when the surface is colder than the underlying layers, $Q_C$ becomes positive. Slightly negative $Q_C$ is evident in spring (Fig. 2.17a) when the surface warms but subsurface layers are still cold from the winter season. $Q_{PS}$ is always negative with larger values when $\alpha$ is low.

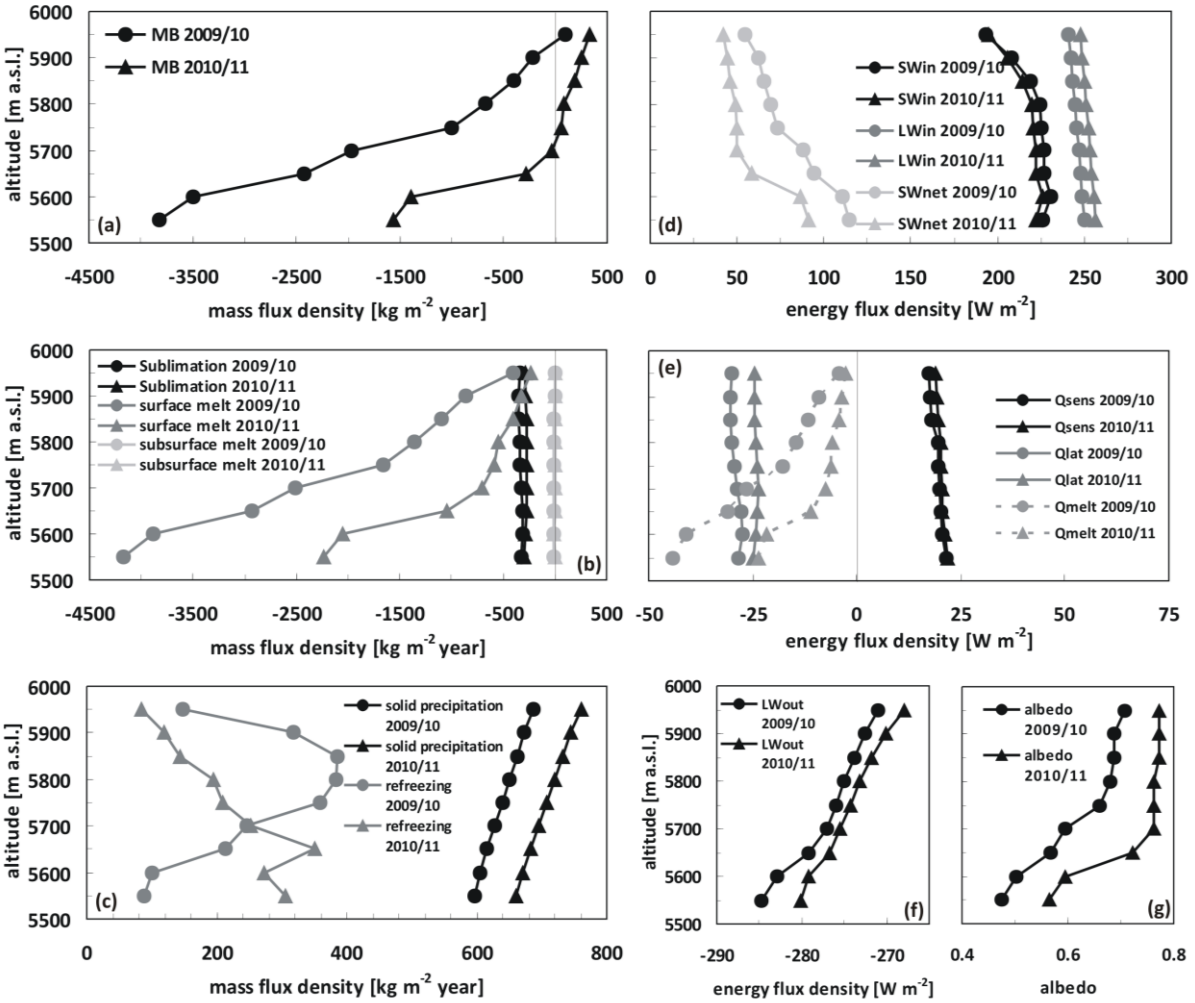


**Fig. 2.16: Modelled vertical profiles of (left) the annual specific mass balance and its components and (right) mean SEB components on Zhadang glacier for the MB years 2009/10 and 2010/11 (1 October – 30 September). Data are averaged for 50-m altitude bands. Note the different x-axis scales of the components (negative means mass or energy loss at the glacier surface, see section 2.3.1 and Tab. 2.2 for abbreviations).**

The generally dry conditions on the TP (Aizen et al. 2002) lead to continuously negative $Q_{lat}$ (Braun & Hock 2004) on monthly scales with largest values in winter when air humidity is smallest (Fig. 2.2c) and higher wind speeds drive turbulence (Fig. 1.11). In absolute values, $Q_{lat}$ is usually larger than $Q_{sens}$ and responsible for significant mass loss through sublimation especially in winter and spring prior to the onset of the monsoon (Fig. 2.17b). The glacier-wide MB estimate for the whole period 2009-2012 is -4900 kg m$^{-2}$ (Table 2.5). In general, sublimation (-1003 kg m$^{-2}$) is the second largest factor of glacier-wide mass loss after surface melt (-6455 kg m$^{-2}$) but clearly dominates ablation in winter, when air temperatures are below 0°C and surface melt is nearly absent (Fig. 2.17b). Subsurface melt (-13 kg m$^{-2}$) plays only a minor role. Solid precipitation (+1874 kg m$^{-2}$) and refreezing (+697 kg m$^{-2}$) contribute to mass gain of the glacier. Maximum snowfall amounts occur in summer (Fig. 2.17b, see section 1.4.1). Refreezing happens in spring, when percolating melt water reaches cold winter snow layers, in summer, when a wet snow layer is present and internal water refreezes at night, and in autumn, when capillary water freezes (see section 2.3.1). When solid precipitation is small, the amount of refreezing is even larger than accumulation by snowfall (Fig. 2.17b). On average, 11% of the surface and subsurface melt refreezes, which is in line with Mölg et al. (2012) and less than the amount obtained for Xiao Dongkemadi glacier (20%, Fujita & Ageta 2000, Fujita et al. 2007). A reason

for the latter can be found in the different glacier types according to their climate setting. After Shi & Liu (2000) Zhadang glacier is a subcontinental (subpolar, polythermal) glacier type whereas Xiao Dongkemadi glacier belongs to the extreme continental (polar, cold) type with lower ice temperatures and therefore larger cold content. Nevertheless, the amount of refreezing confirms previous studies that refreezing is a significant process for many Asian glaciers (Ageta & Fujita 1996, Fujita & Ageta 2000).

**Table 2.4: Mean absolute values of energy flux components as modelled for 27 April 2009 – 10 June 2012 and for the two MB years with proportional contribution to total energy flux.**

| | Sum* [W m$^{-2}$] | $SW_{net}$ | $LW_{net}$ | $Q_{sens}$ | $Q_{lat}$ | $Q_G$ | $Q_{melt}$ |
|---|---|---|---|---|---|---|---|
| total average [W m$^{-2}$] | 170 | 74 | -45 | 20 | -29 | 1.6 | -22 |
| 2009/10 | | 82 | -47 | 19 | -30 | -1.4 | -22 |
| 2010/11 | | 58 | -44 | 21 | -25 | 1.0 | -10 |
| | 100% | 44% | 26% | 12% | 17% | 0.9% | |

*Sum of energy fluxes in absolute values: $|SW_{net}| + |LW_{net}| + |Q_{sens}| + |Q_{lat}| + |Q_G|$

Table 2.4 lists the absolute and relative contributions of energy flux components to total energy flux. For the total considered period, $SW_{net}$ accounted for 44% of the total energy flux, followed by $LW_{net}$ (26%). $Q_{lat}$, $Q_{sens}$ and $Q_G$ contribute with 17%, 12% and 1%, respectively. In the MB year 2009/10 larger $SW_{net}$ was responsible for more $Q_{melt}$ available at the surface, compared to the year 2010/11 (Table 2.4, Fig. 2.17). These results are in agreement with those of Zhang et al. (2013).

**Table 2.5: Calculated glacier-wide mass balance components for the total period 27 April 2009 – 10 June 2012 and for the two MB years.**

| | Solid precipitation | Surface melt | Refrozen water | Subsurface melt | Sublimation | Mass balance* |
|---|---|---|---|---|---|---|
| total [kg m$^{-2}$] | 1873.5 | -6454.7 | 697.0 | -12.5 | -1002.9 | -4899.5±2040 |
| 2009/10 | 632.3 | -2106.5 | 245.1 | -4.5 | -333.7 | -1567.3±653 |
| 2010/11 | 711.1 | -915.7 | 217.8 | -3.5 | -278.6 | -268.8±653 |
| % of mass loss | | | 88 | 0.2 | 12 | |

*Mass balance = solid precipitation - surface melt + Refrozen water - subsurface melt - sublimation

From the AWS forced model period 27 April 2009 – 10 June 2012 two glacier-wide annual MB estimates (1 October to 30 September) for Zhadang glacier can be obtained and compared with previous studies. Due to the gap filling with HAR data (see section 2.2.3) we obtain a continuous time series. Modelled MB is -1567.3±653 kg m$^{-2}$ for 2009/10 and -268.8±653 kg m$^{-2}$ for 2010/11 (Table 2.5). Given uncertainties are obtained through model calibration (see section 2.4.1). MB values are within the range published by Mölg et al. (2014) with a HAR forced MB model of similar structure as the model applied here (Fig. 2.26). The results from this study are also comparable to Zhang et al. (2013) who employed an AWS forced MB model based on daily mean input variables (MB 2009/10: -1969 kg m$^{-2}$, MB2010/11: -431 kg m$^{-2}$). Table 2.5 shows calculated MB components and their relative contribution to total mass loss for the total period and the two MB years. As it can be derived from Fig. 2.17b, specific MB in 2009/10 was more negative than in 2010/11 due to less snowfall and increased surface melt, subsurface melt and sublimation. In total, effective melt (surface melt – refrozen water) accounts for 88% of total mass loss followed by sublimation (12%). Mass loss through subsurface melt is negligible (0.2%). In 2010/11 the total amount of refreezing is less due to decreased surface melt, whereas the proportion of refrozen melt water is much larger than in 2009/10 with 24% compared to 12% in 2009/10.

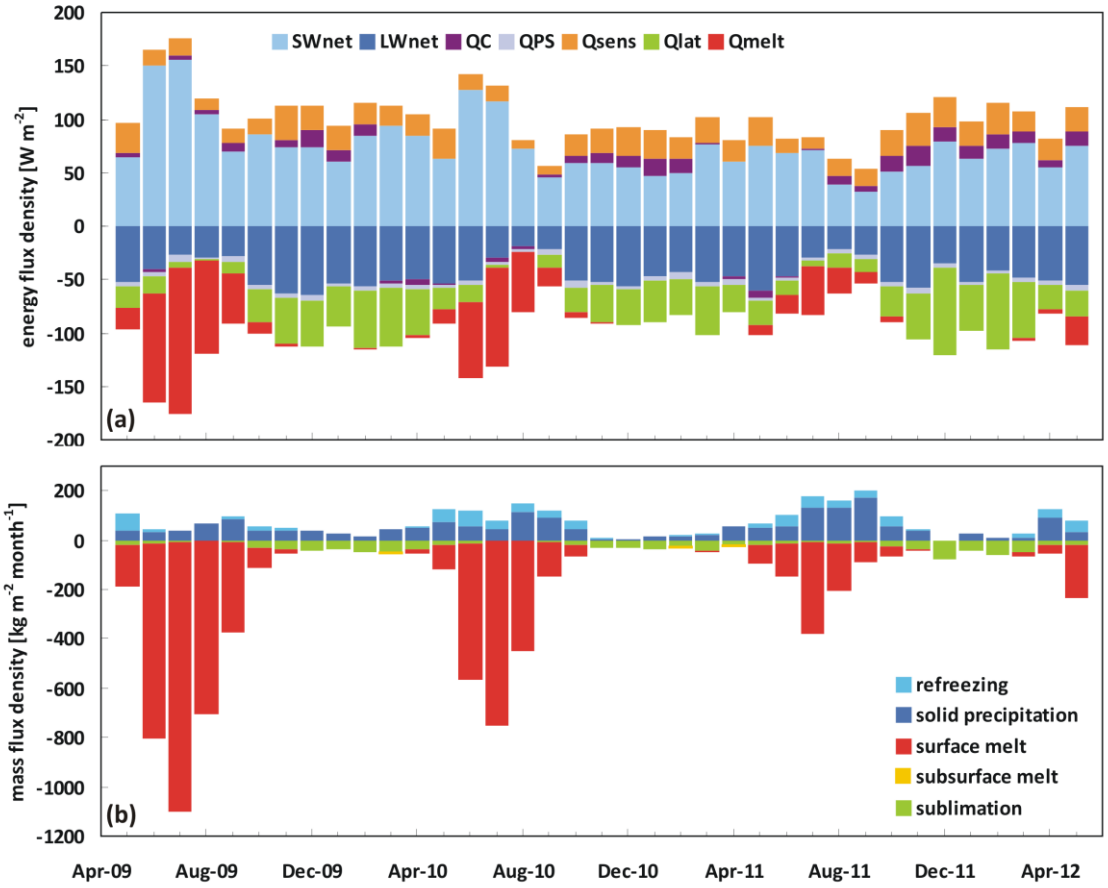


**Fig. 2.17: Glacier-wide monthly (a) SEB components (see section 2.3.1 for abbreviations) and (b) MB components from May 2009 to May 2012 at Zhadang glacier.**

### 2.4.4 Snow line characteristics from the AWS driven distributed model 2010-2012

A comparison of the temporal evolution of the mean altitude of the transient snow line at Zhadang glacier is presented in Fig. 2.13. Due to the installation period of the time-lapse camera system, camera snow lines are available for the ablation seasons in 2010, 2011 and 2012 (see section 2.4.2.5). At days, when mapped snow line is missing but model snow line is visible, the camera view field was hampered by low clouds or fog all day. In case only the picture at 16 BT was unusable, the snow line of a different picture of the same day was selected. At days, when both snow lines are missing, the glacier area within the view field of the cameras (Fig. 2.1) was either totally snow covered or snow free. The latter is the case only in 2010 after the snow line exceeds 5700 m a.s.l. On average, a snow line becomes visible at the lowest parts of the glacier tongue between May and June. In 2010 surface melt starts relatively late in the beginning of June but was very strong until September (Fig. 2.8, 2.19). This is clearly visible in the snow line evolution (Fig. 2.13, 2.19). The spatial and temporal variability of the transient snow line in 2010 is visualized in Fig. 2.19 by a series of ortho-rectified camera images. The animated time series for 2010 to 2012 is available online[1]. In 2010, a snow line develops not until 11 June but then mean altitude rises quickly until the glacier is completely snow free. The following months are characterized by intermediate snow fall events and strong melt resulting in rapid changes in transient snow line altitudes. In September the permanent winter snow cover builds up in the course of storm events in autumn both in 2010 and 2011 (see section 2.4.3). In 2011 the first snow line is visible on 3 June, around one week earlier than in 2010, and rises very

[1] http://www.klimageo.rwth-aachen.de/index.php?id=tibet_snowlines0

slowly, repeatedly interrupted by snowfall events (Fig. 2.13). The uppermost areas of the glacier remain snow covered throughout the whole summer. The rather small ablation in 2011 is also evident in measured and modelled surface height changes (Fig. 2.8) and in modelled SEB and MB components (Fig. 2.17). In 2012 the lowest parts of the glacier tongue become snow free already 23 May but snow line altitude again increases slowly (Fig. 2.13). The observed melt patterns develop in a very inhomogeneous way. They are not clearly to map. This limits the ability of reconstruction through the MB model in 2012 (Fig. 2.18). At first sight, the slow increase in snow line altitude seems to be in conflict with the rapid surface height loss observed at AWS1 (Fig. 2.8) between 19 May and 4 June 2012. However, accumulation through solid precipitation especially in September 2011 and April 2012 (Fig. 2.17) resulted in a snow pack of approx. 1 m at AWS1 (Fig. 2.8). The snow pack was completely removed by melting only by 9 June. This is in agreement with the mean snow line altitude in Fig. 2.13 compared to the measured surface height at AWS1 (5665 m a.s.l., Fig. 2.8). In the lowermost regions of the glacier tongue the winter snow cover was not permanent and therefore rather thin in 2012 (see section 2.4.5). This results in snow lines developing rather early in the melt season of this year.

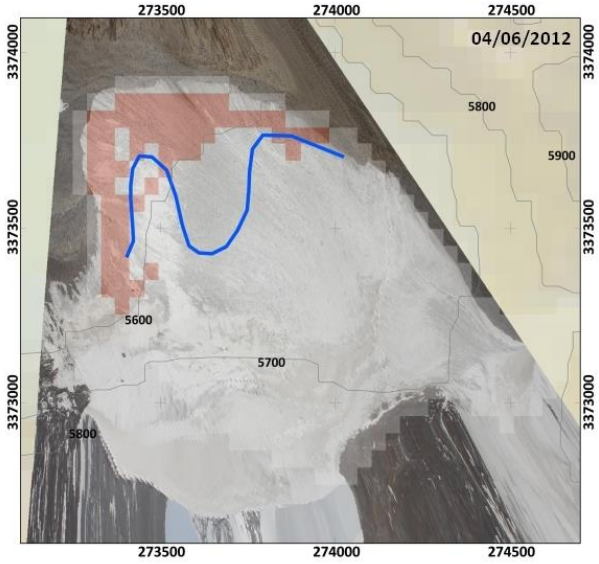


**Fig. 2.18: Transient snow line on 4 June 2012 (for more information see Fig. 2.15).**

Spatial patterns of the transient snow lines in most regions of the glacier tongue within the view field of the cameras are clearly dominated by altitude (Fig. 2.19) and therefore mainly by air temperature. This is reasonable as $SW_{in}$ is distributed homogeneously and in the open valley hardly influenced by topographic shading. The eastern edge of the glacier tongue is an exception with consistently fast increasing snow line altitudes (Fig. 2.15, 2.18, 2.19) probably because of enhanced melt through longwave radiation and sensible heat release from the adjacent rocks. In 2012 large snow patches remained at the western glacier tongue around 5600 m a.s.l. (Fig. 2.18). This could be the effect of topography induced decreased solar insolation described in section 2.4.3. The middle part of the glacier is very flat. The glacier tongue ends in a concave steeper north-facing snout. This shape may support the long duration of the snow cover in this part of the glacier. In the uppermost south eastern glacier regions and in the steep areas in the west topographic shading generally results in long lasting snow cover and slowly retreating snow lines (Fig. 2.15, 2.19).

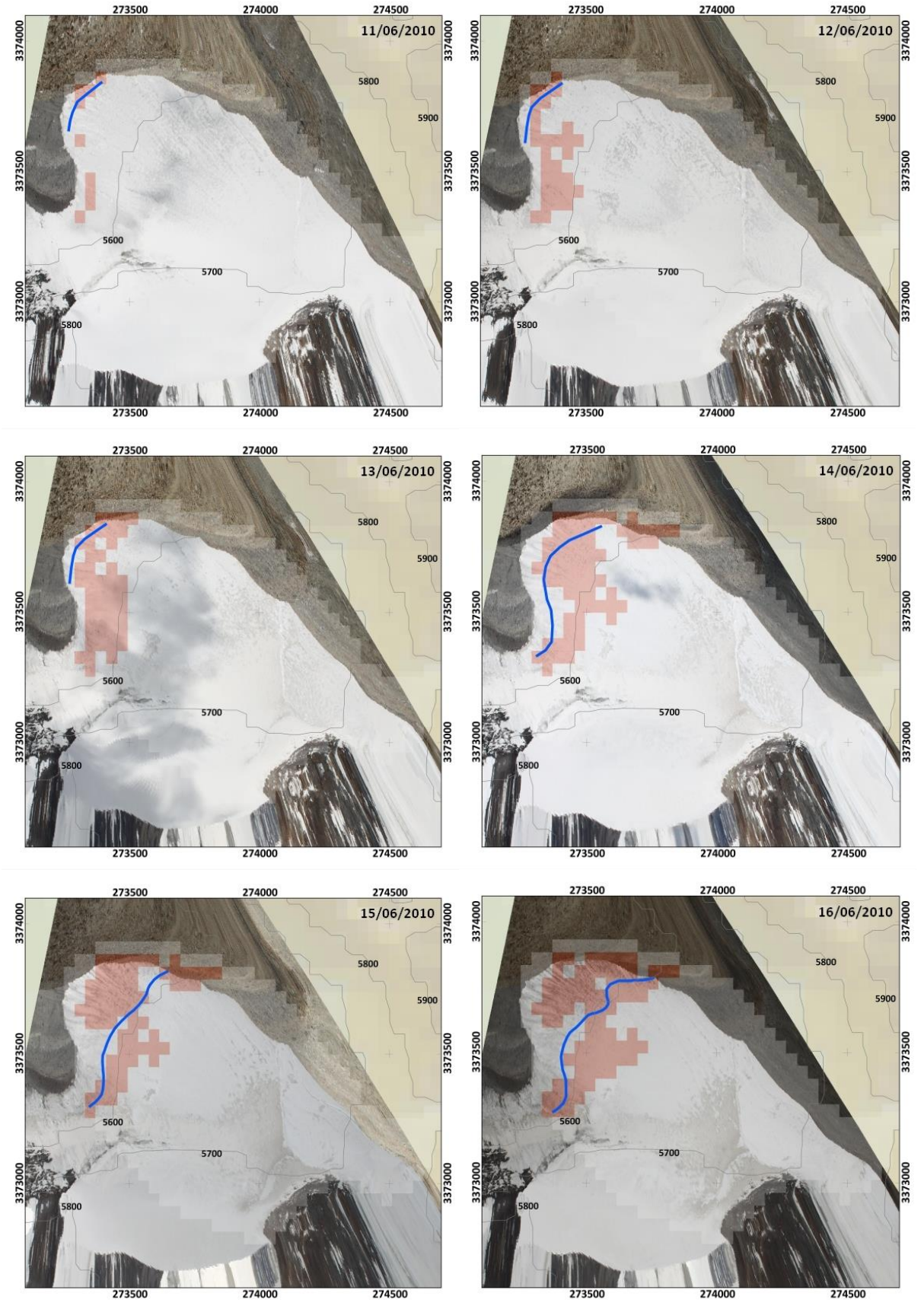


**Fig. 2.19: Spatial and temporal evolution of the transient snow line at Zhadang glacier 2010; the blue line is the mapped transient snow line from the ortho images (see section 2.4.2); the red area indicates the transient snow line generated by the MB model (see section 2.5.2.5). The figure continues on the next pages.**

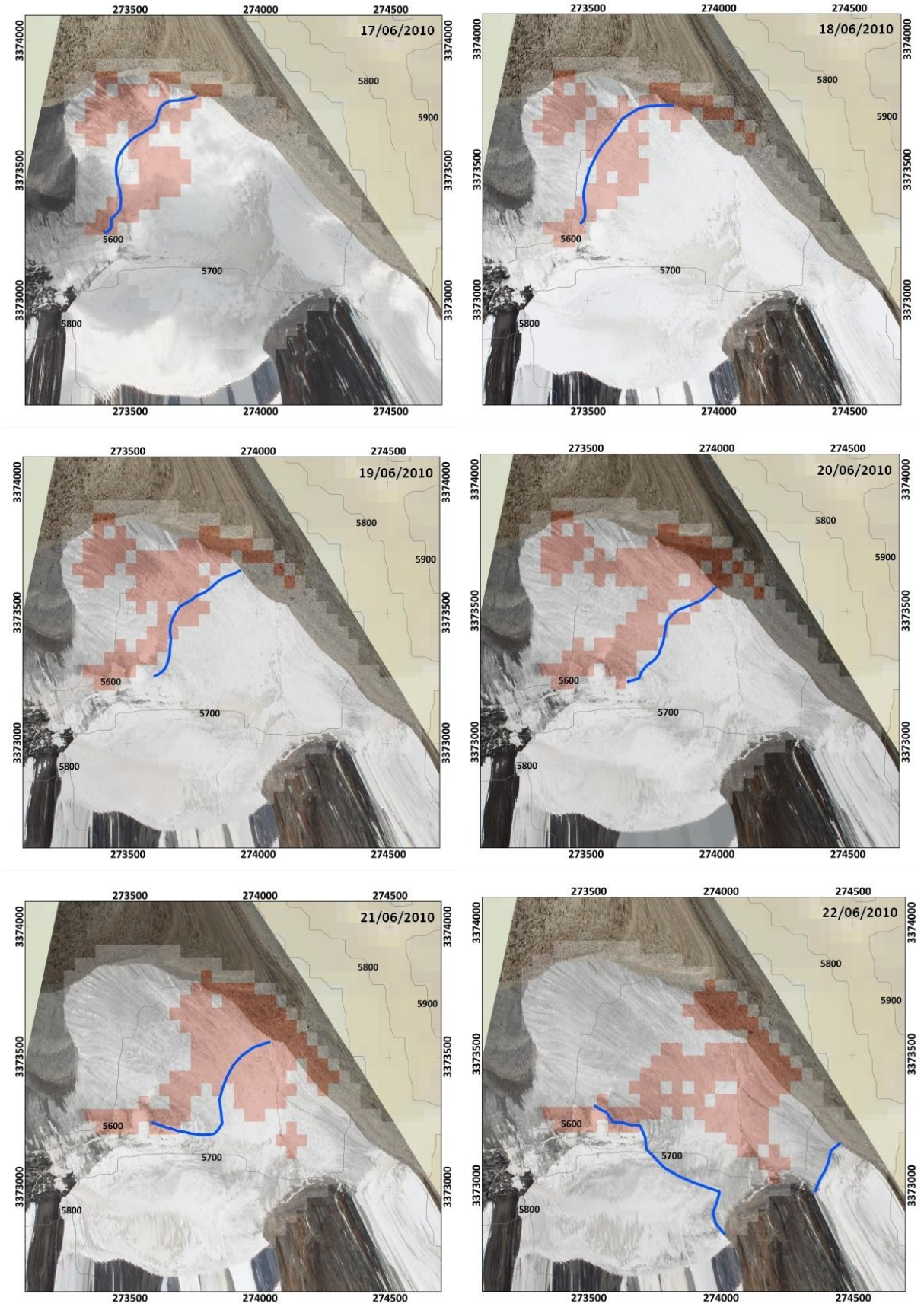


**Fig. 2.19 continued from preceding page**

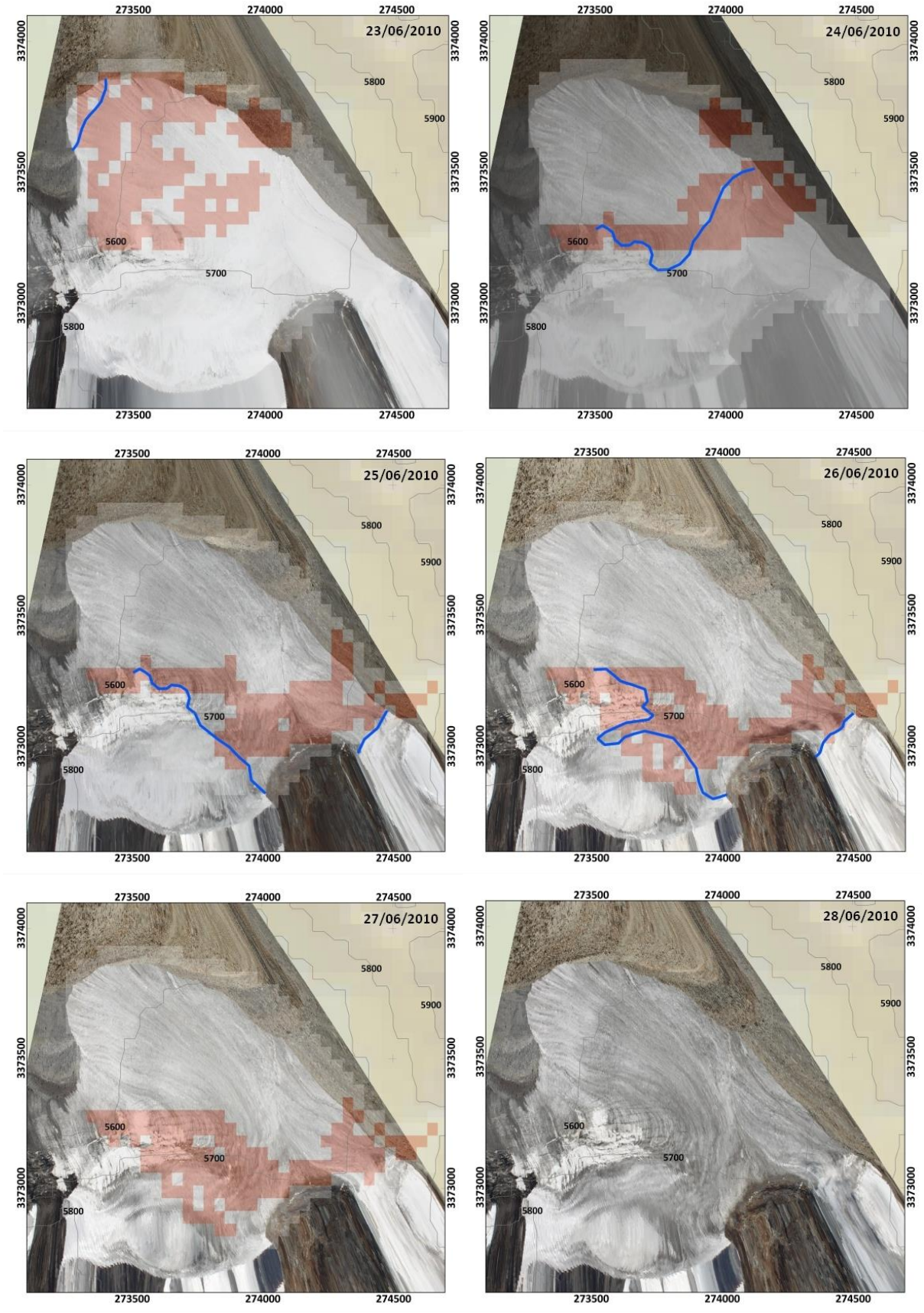


**Fig. 2.19 continued from preceding page**

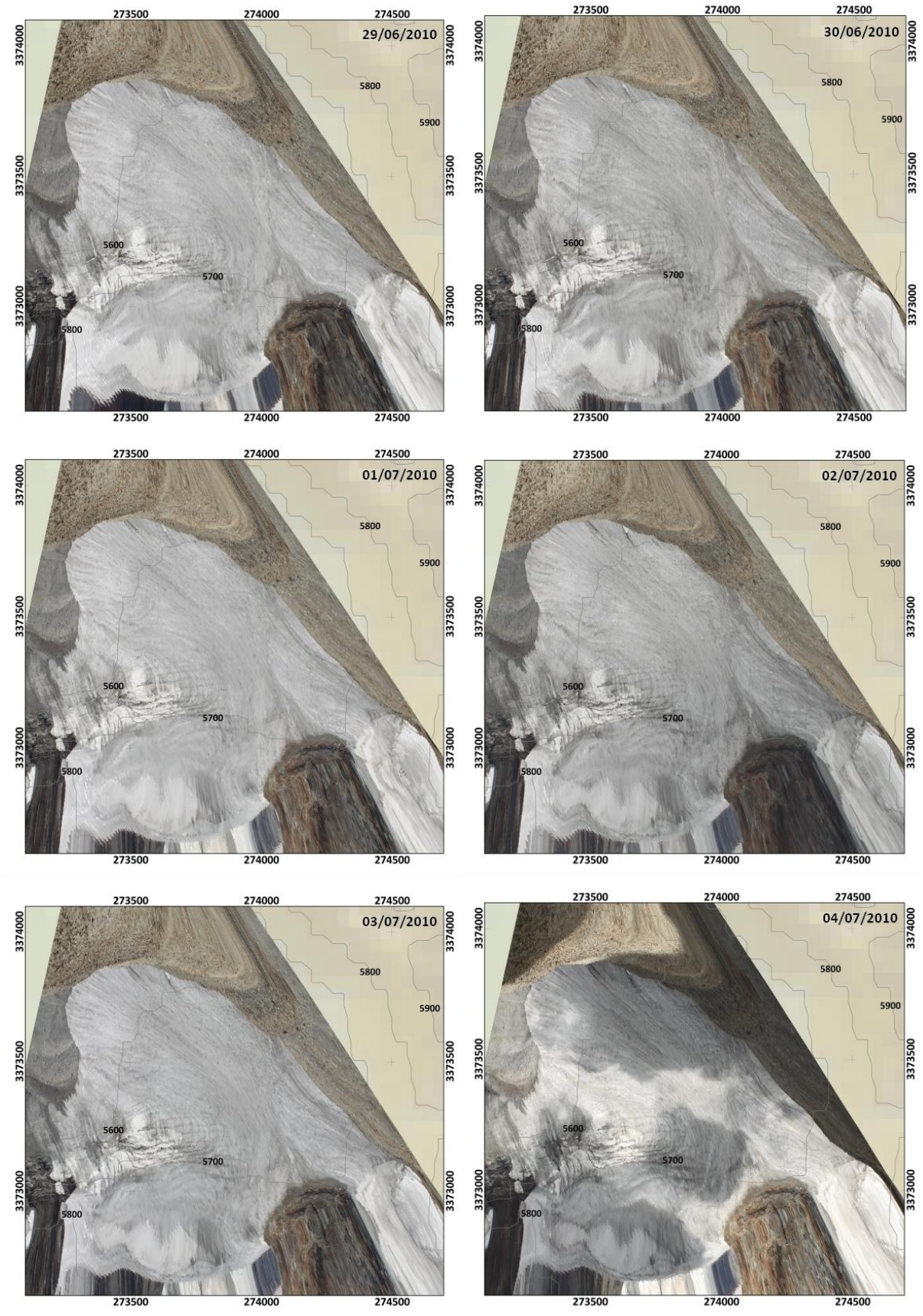


**Fig. 2.19 continued from preceding page**

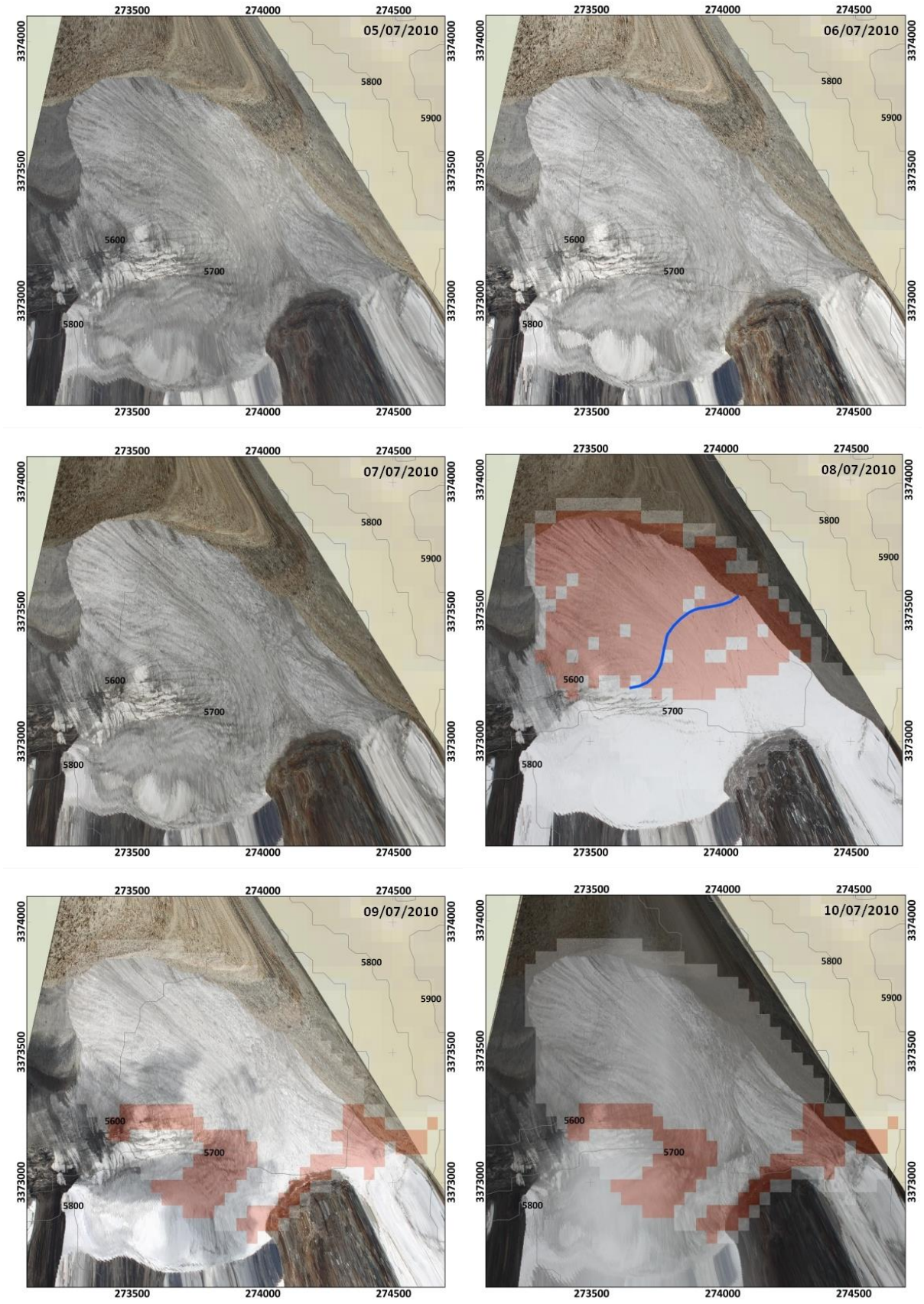


**Fig. 2.19 continued from preceding page**

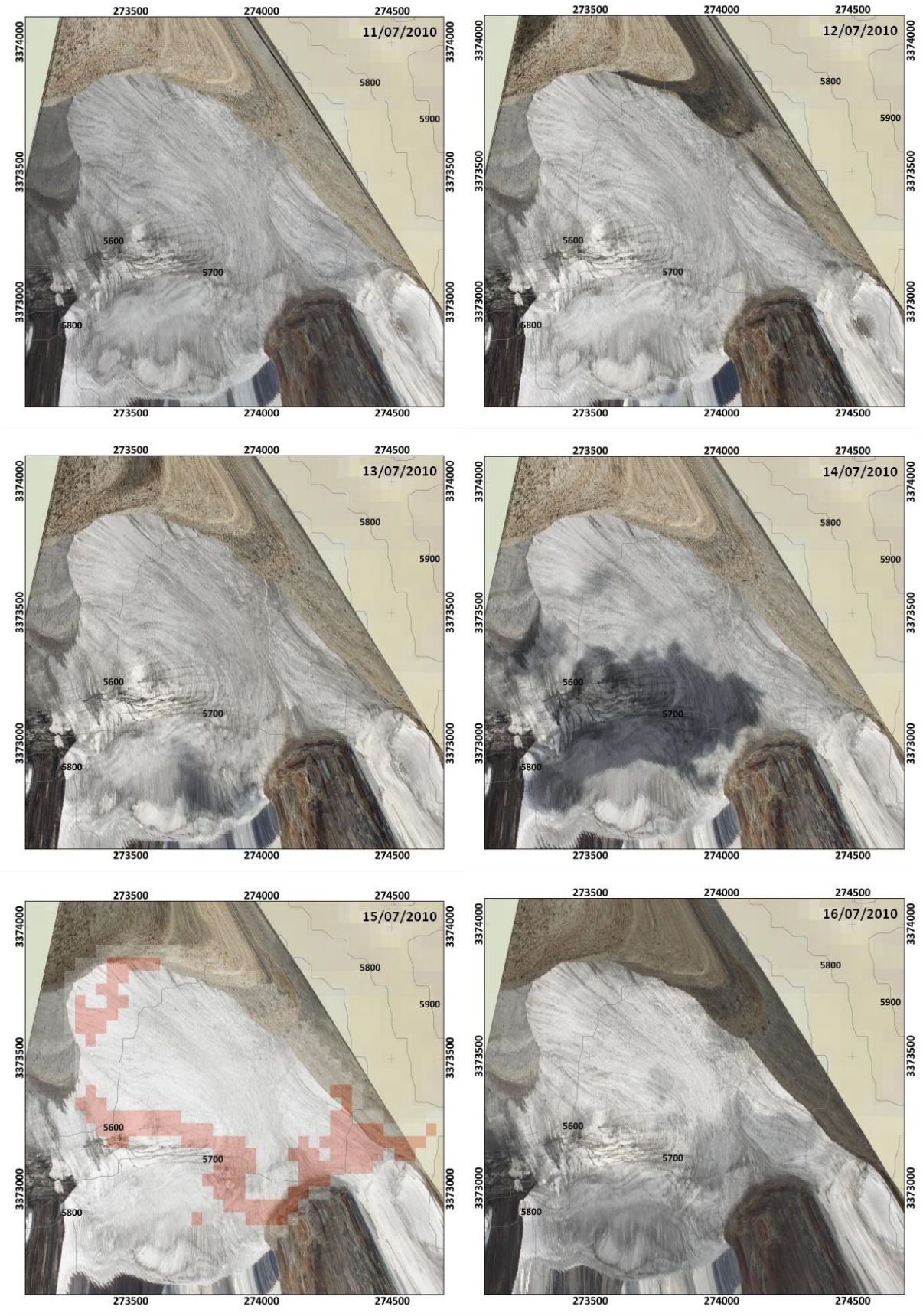


**Fig. 2.19 continued from preceding page**

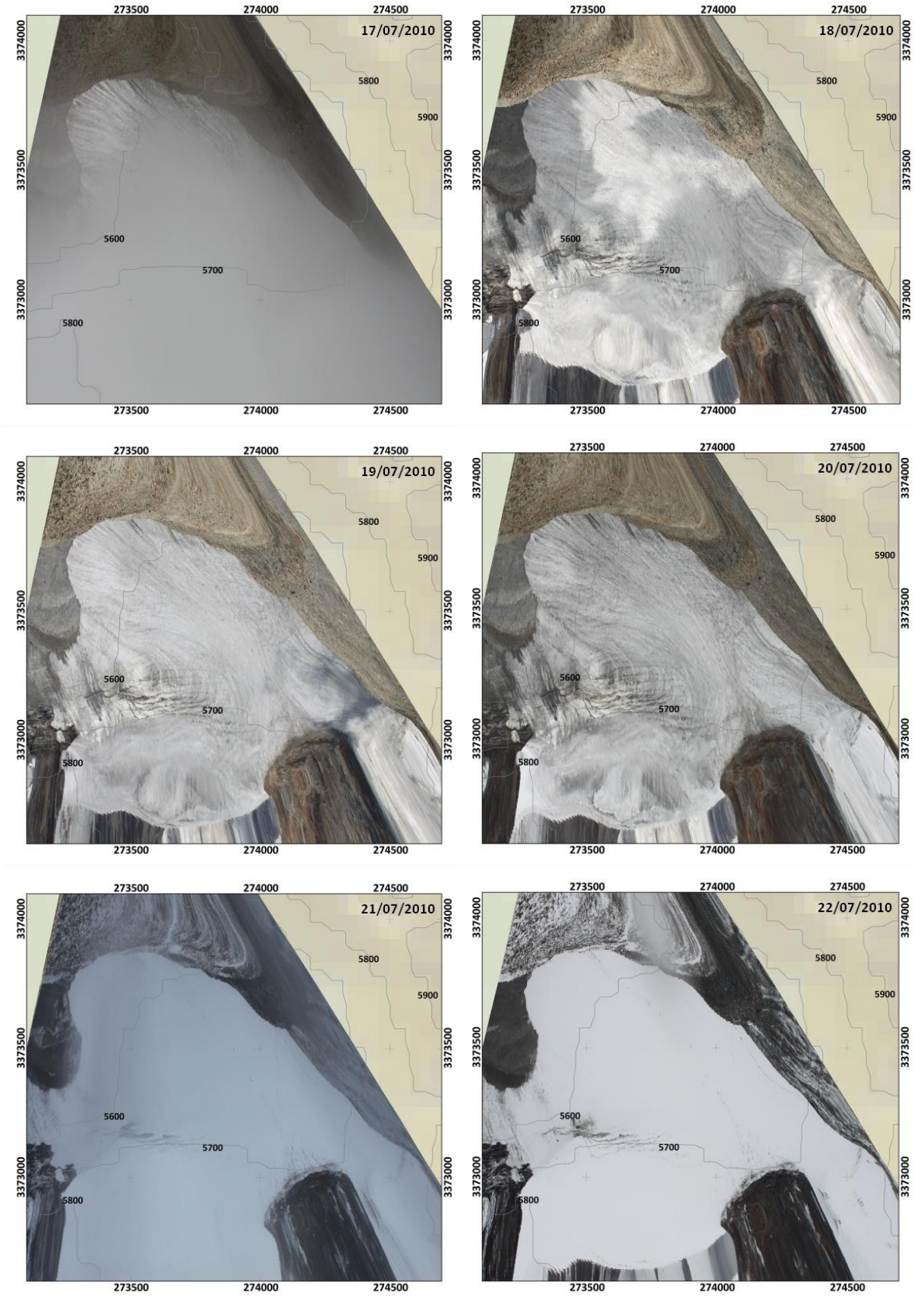


**Fig. 2.19 continued from preceding page**

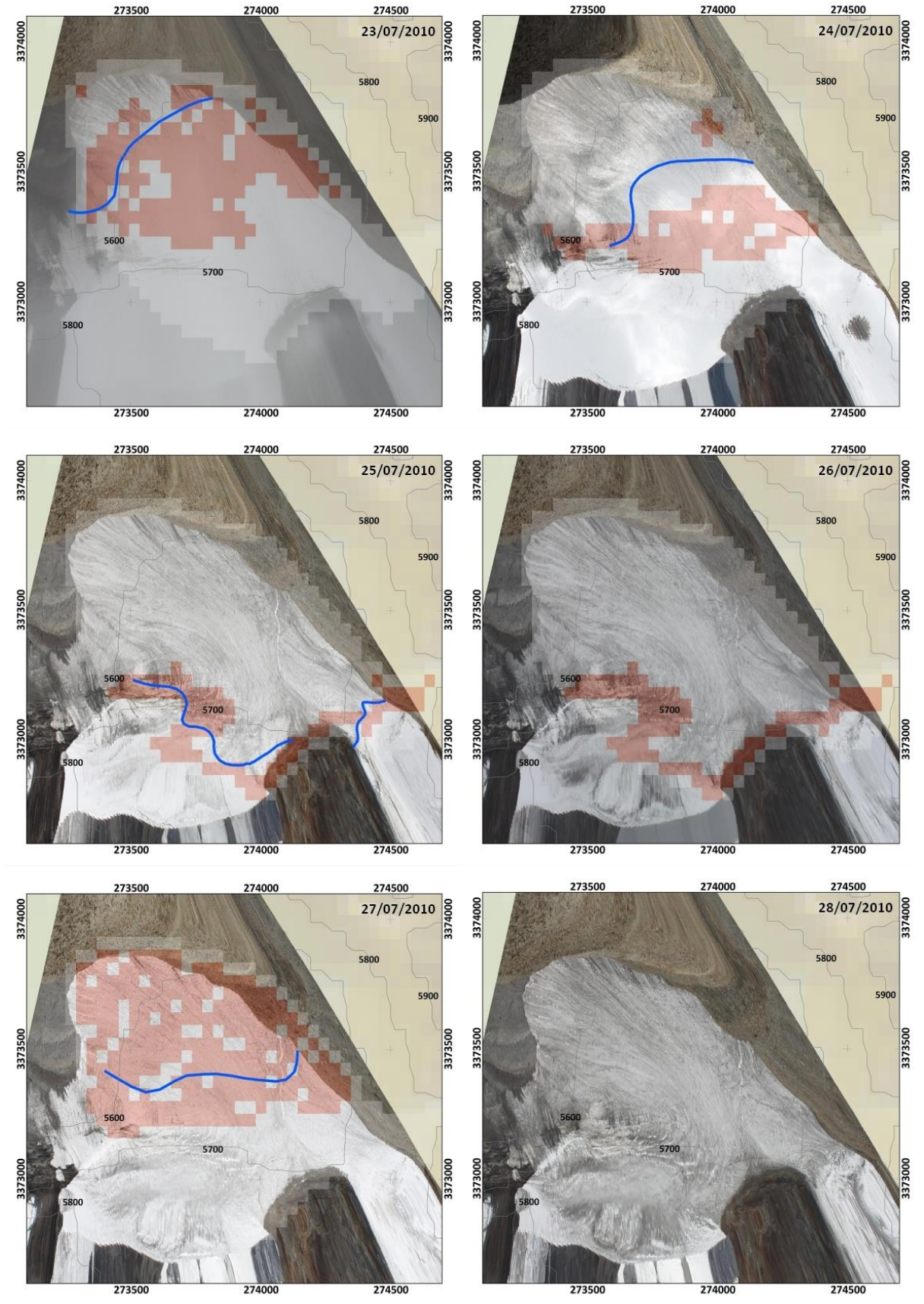


**Fig. 2.19 continued from preceding page**

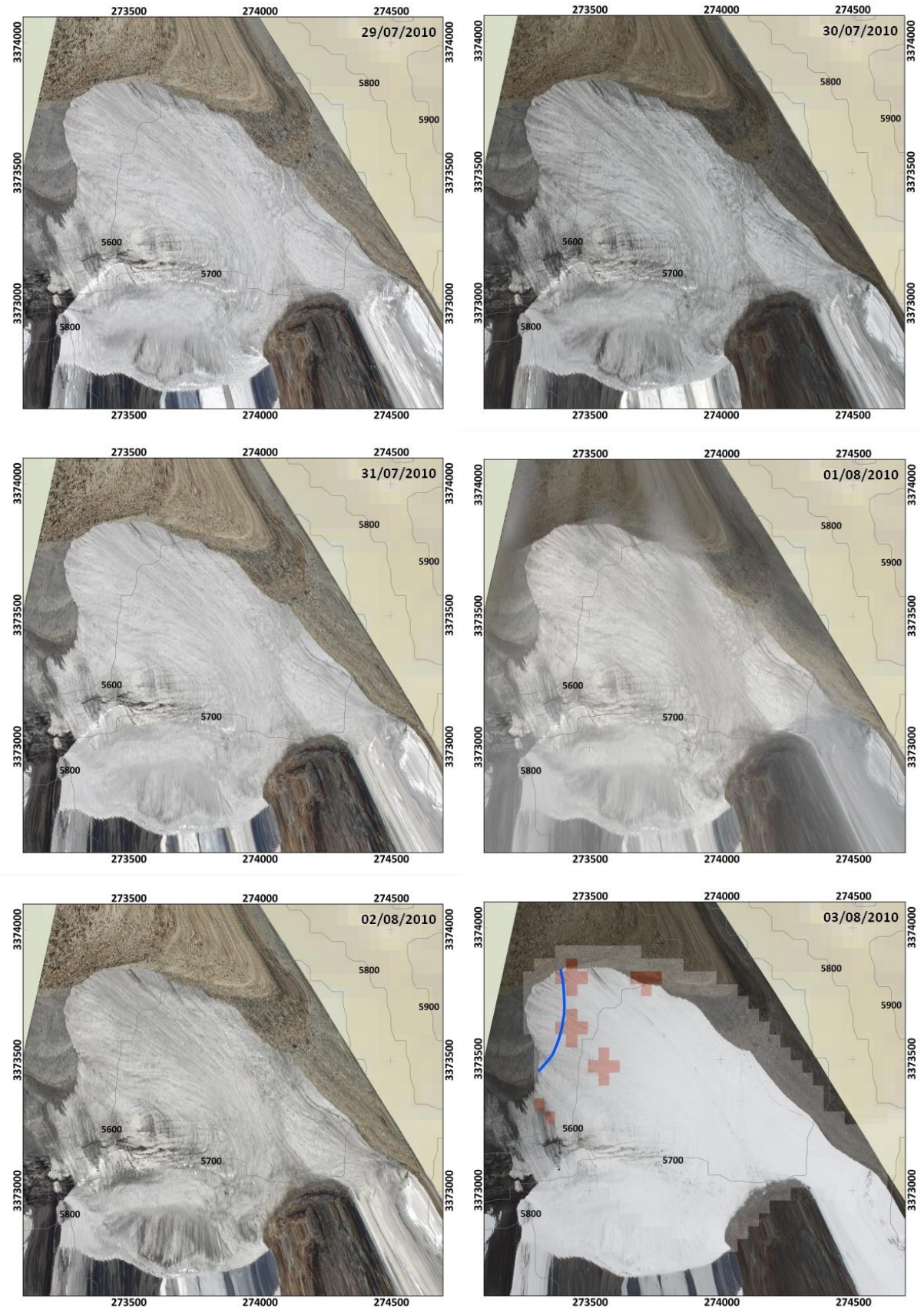


**Fig. 2.19 continued from preceding page**

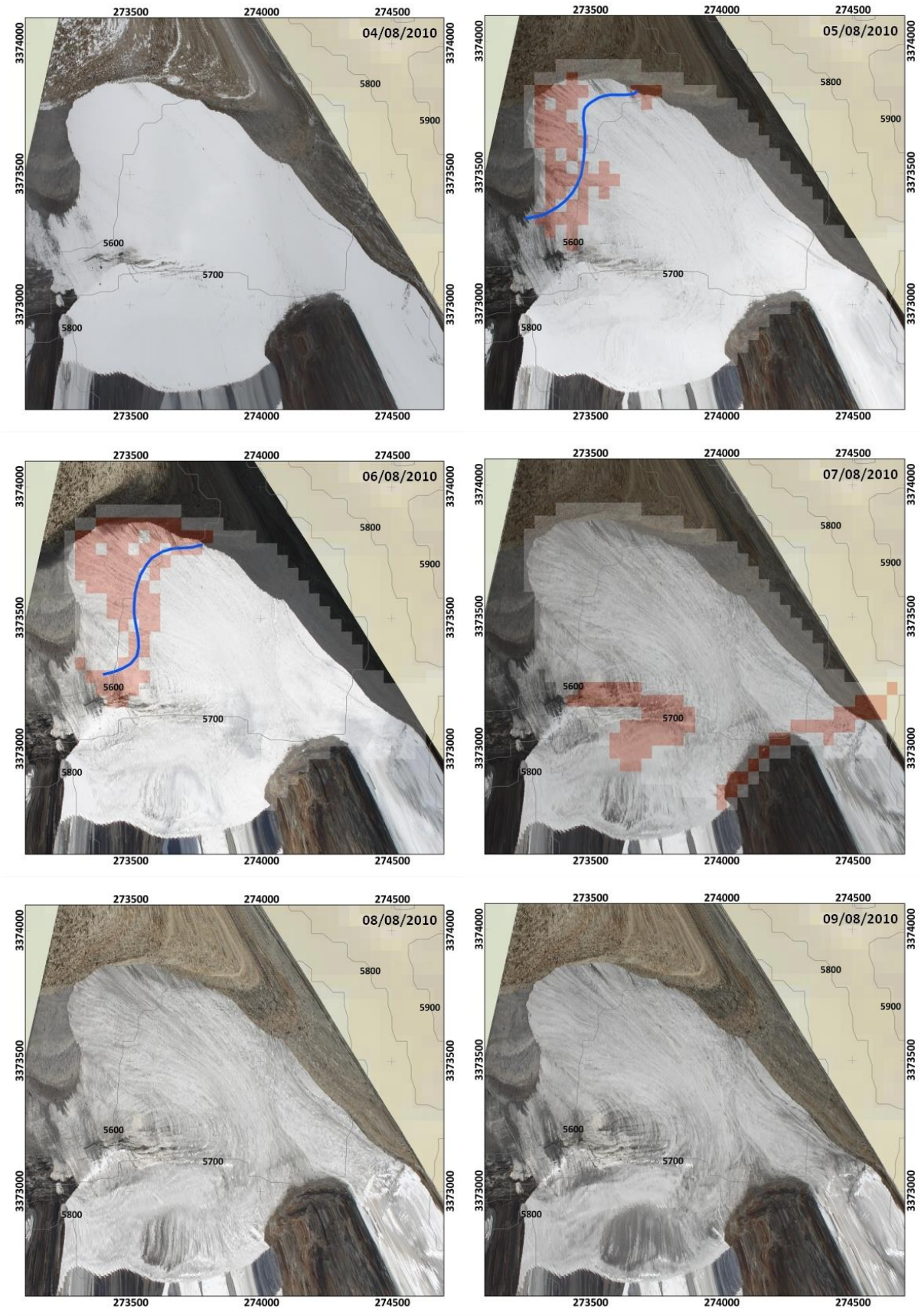


**Fig. 2.19 continued from preceding page**

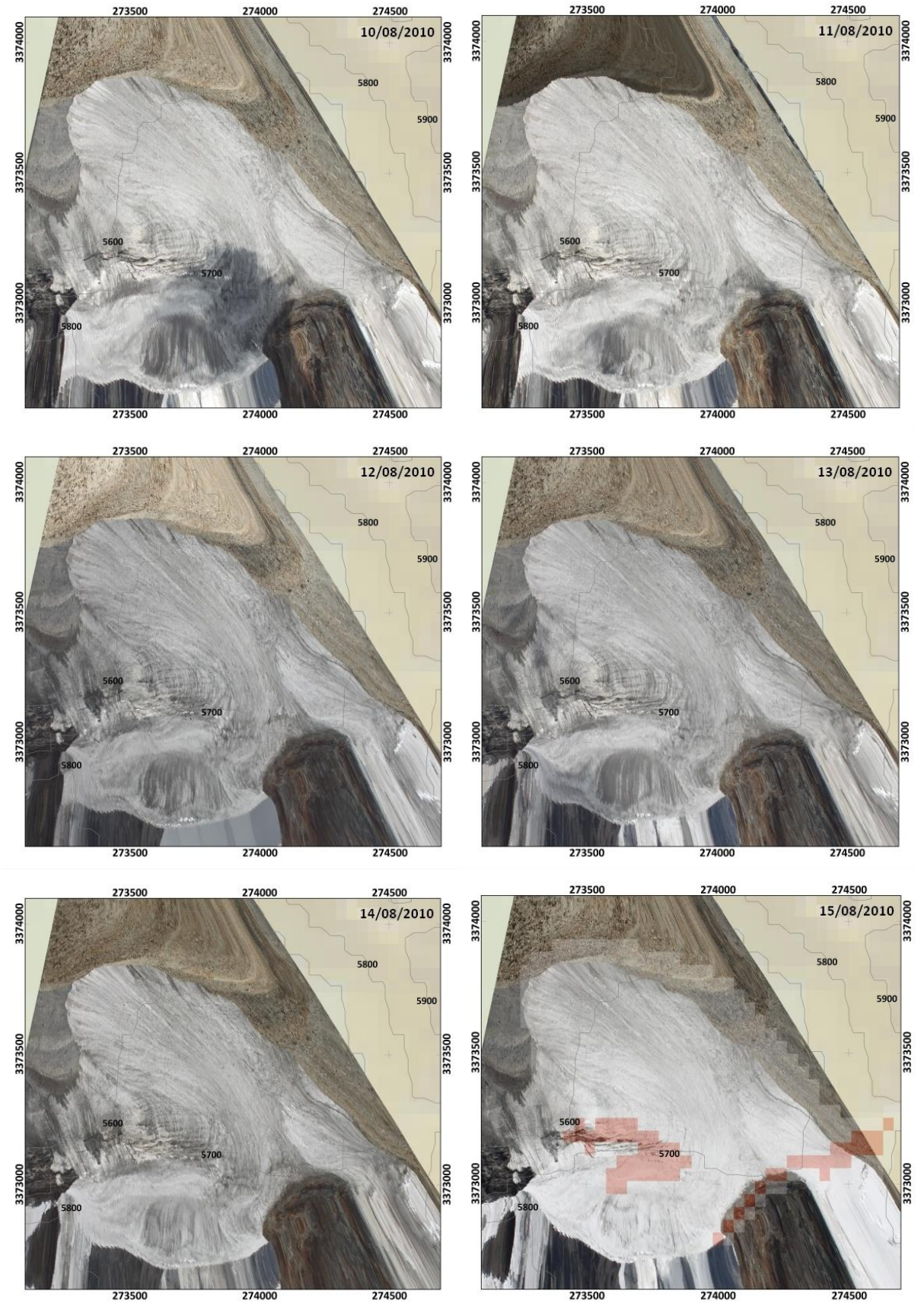


**Fig. 2.19 continued from preceding page**

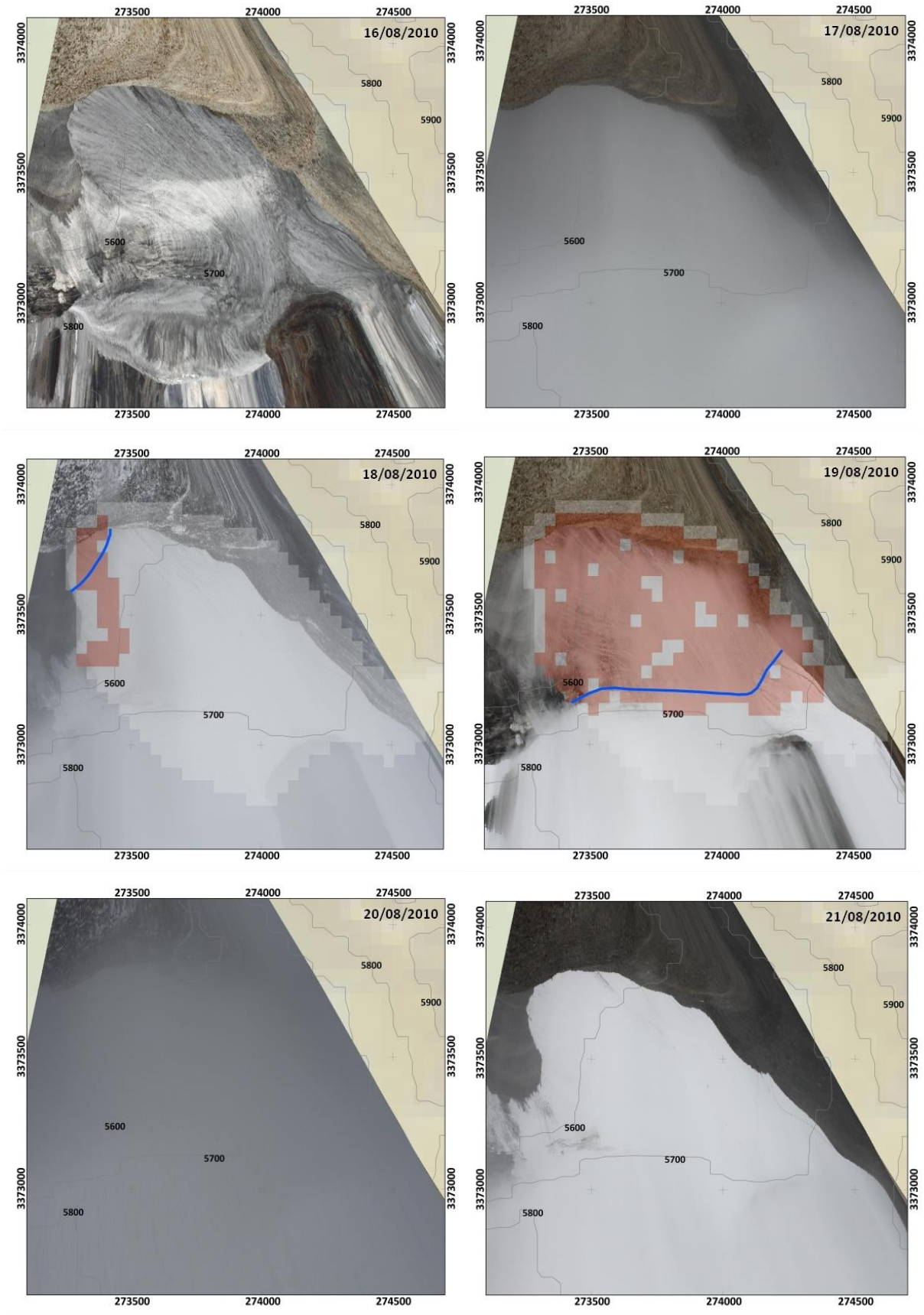


**Fig. 2.19 continued from preceding page**

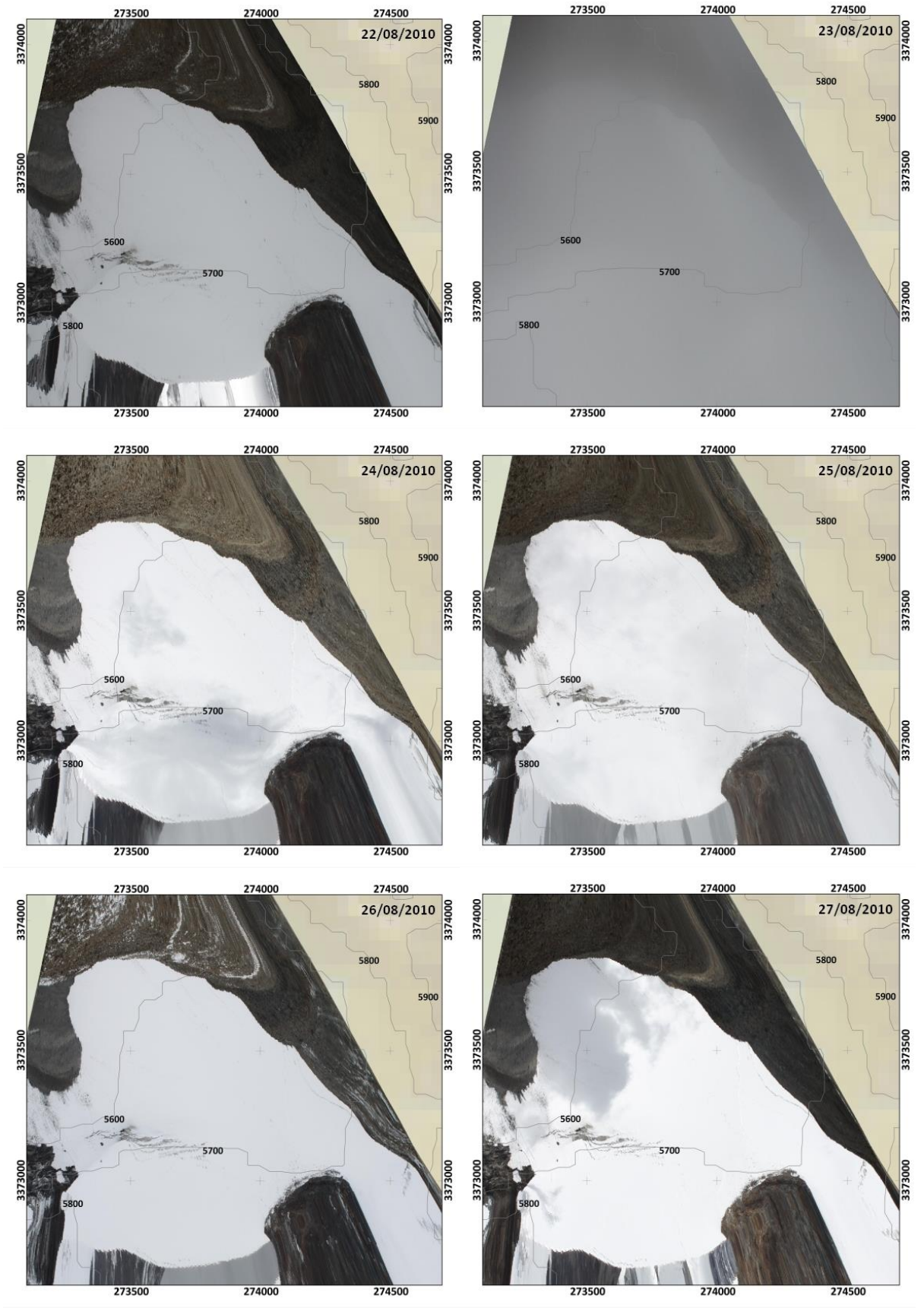


**Fig. 2.19 continued from preceding page**

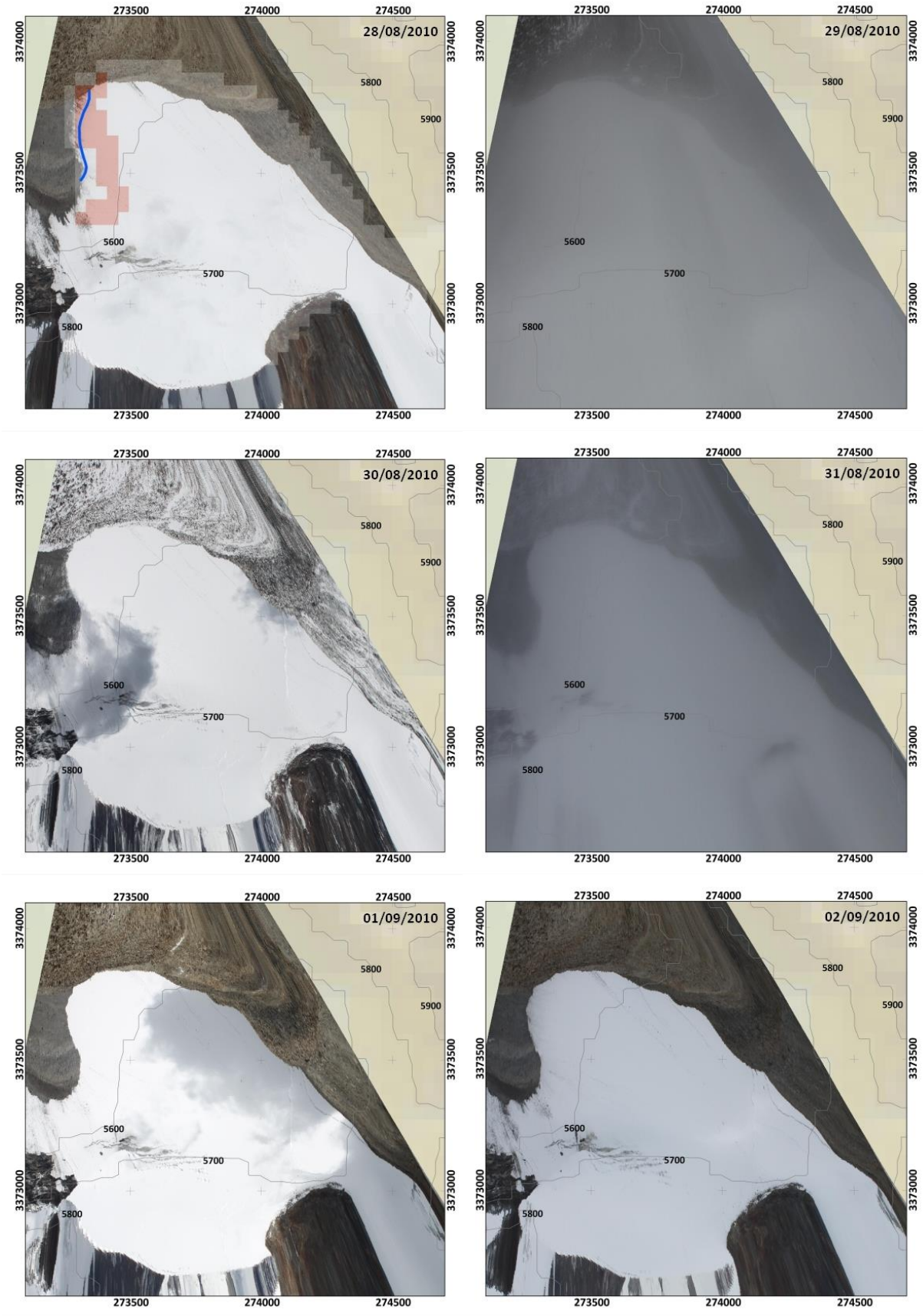


**Fig. 2.19 continued from preceding page**

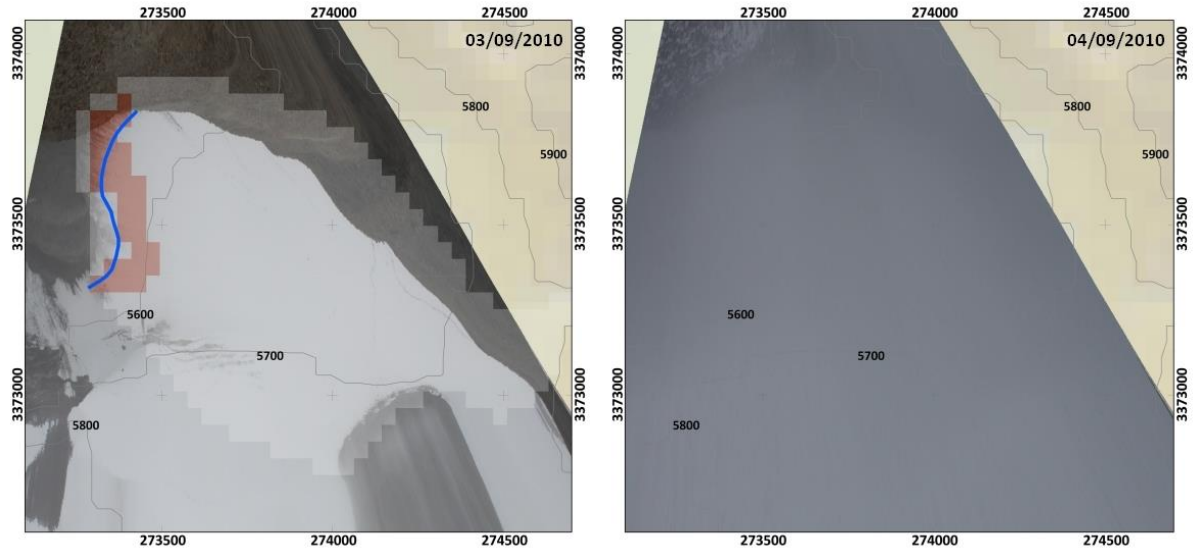


**Fig. 2.19 continued from preceding page**

It could be shown in section 2.4.2.2 and Fig. 2.9 that measured surface height change using HAR data cannot be reproduced as good as with in-situ measurements what is probably caused by uncertainties introduced through HAR precipitation. Therefore, at this point we do not compare observed transient snow lines with modelled snow lines by the HAR forced MB model because mean altitude and temporal evolution at such small scale highly depend on surface melt and therefore intensity and frequency of solid precipitation as $\alpha$ is governing $SW_{net}$ (see section 2.4.3). Nevertheless, comparing monthly mean snow line altitudes or end-of-summer snow lines from the HAR forced MB model with results from remote sensing is a promising option for further evaluation.

## 2.4.5 Strong ablation event in winter

On 9 January 2012 several small snow free areas developed at the western parts of the lowermost glacier tongue and until 29 March 2012 this pattern grew gradually resulting in a larger area of bare ice. Similar snow free areas are evident in steep upper regions of the western and south eastern glacier. The spatial and temporal evolution of the snow free regions is visualized in Fig. 2.20 by a series of ortho-rectified camera images. The animated time series is available online[2]. Records of hourly $T_{air}$ and $T_s$ for the lowermost point of the glacier for that period show that surface melt can not be the driving factor for this process in the beginning of January, because both $T_{air}$ and $T_s$ are well below 0°C (Fig. 2.21a). This is confirmed by Fig. 2.21b illustrating that surface melt is absent until 28 January followed by four days with very small melt rates (max. -0.4 mm w.e. day$^{-1}$). After that no surface melt occurred until 6 March 2012 when again a week with little melting occurs (max. -1.6 mm w.e. day$^{-1}$).

Surface melt happens as hourly values of $T_s$ reach the melting point at the respective days although $T_{air}$ is below 0°C most of the time (Fig. 2.21a). This difference can be explained through $SW_{net}$. Fig. 2.22 shows atmospheric variables, SEB and MB components for the period 5 – 15 March 2012, when highest melt rates occurred, to understand the feedback processes. $SW_{in}$ is high during clear-sky conditions (low *RH* in Fig. 2.22a). Solid precipitation has been minimal since December 2011 (Fig. 2.17b) and therefore $\alpha$ is low causing high $SW_{net}$ (Fig. 2.22a).

[2] http://www.klimageo.rwth-aachen.de/index.php?id=tibet_snowlines0

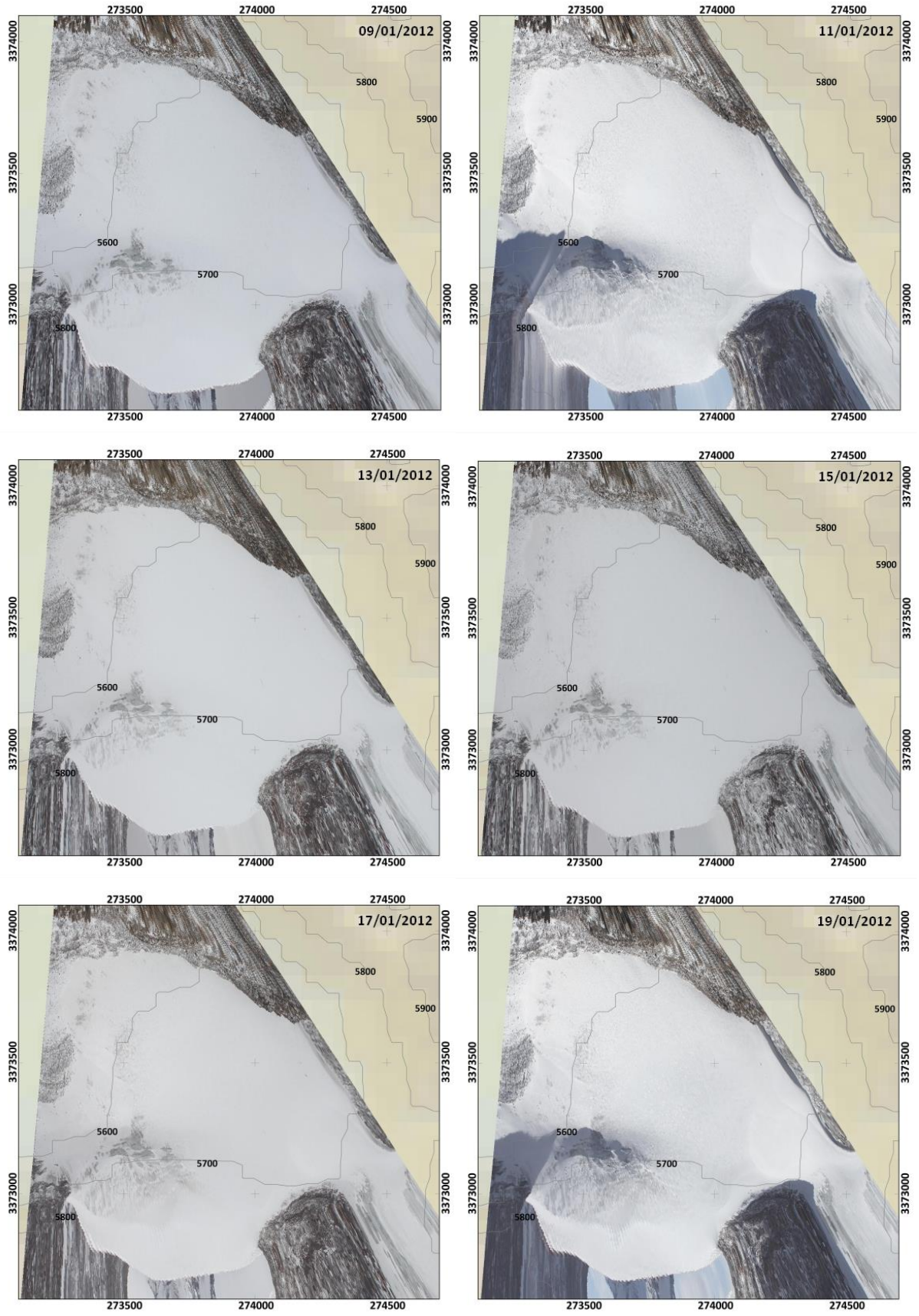


**Fig. 2.20: Time series of ortho-images of the ablation event in winter 2012. The figure continues on the next pages.**

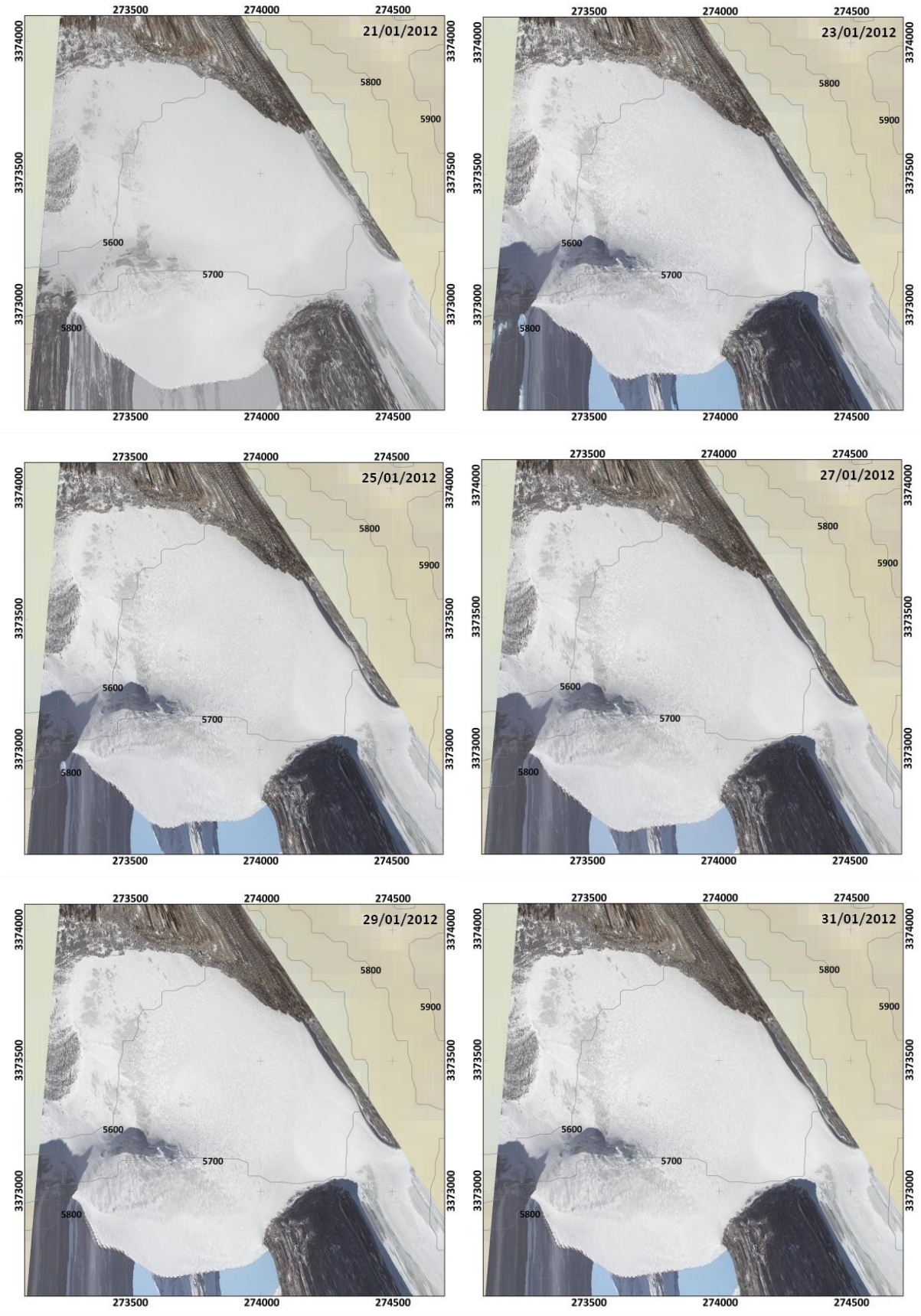


**Fig. 2.20 continued from preceding page**

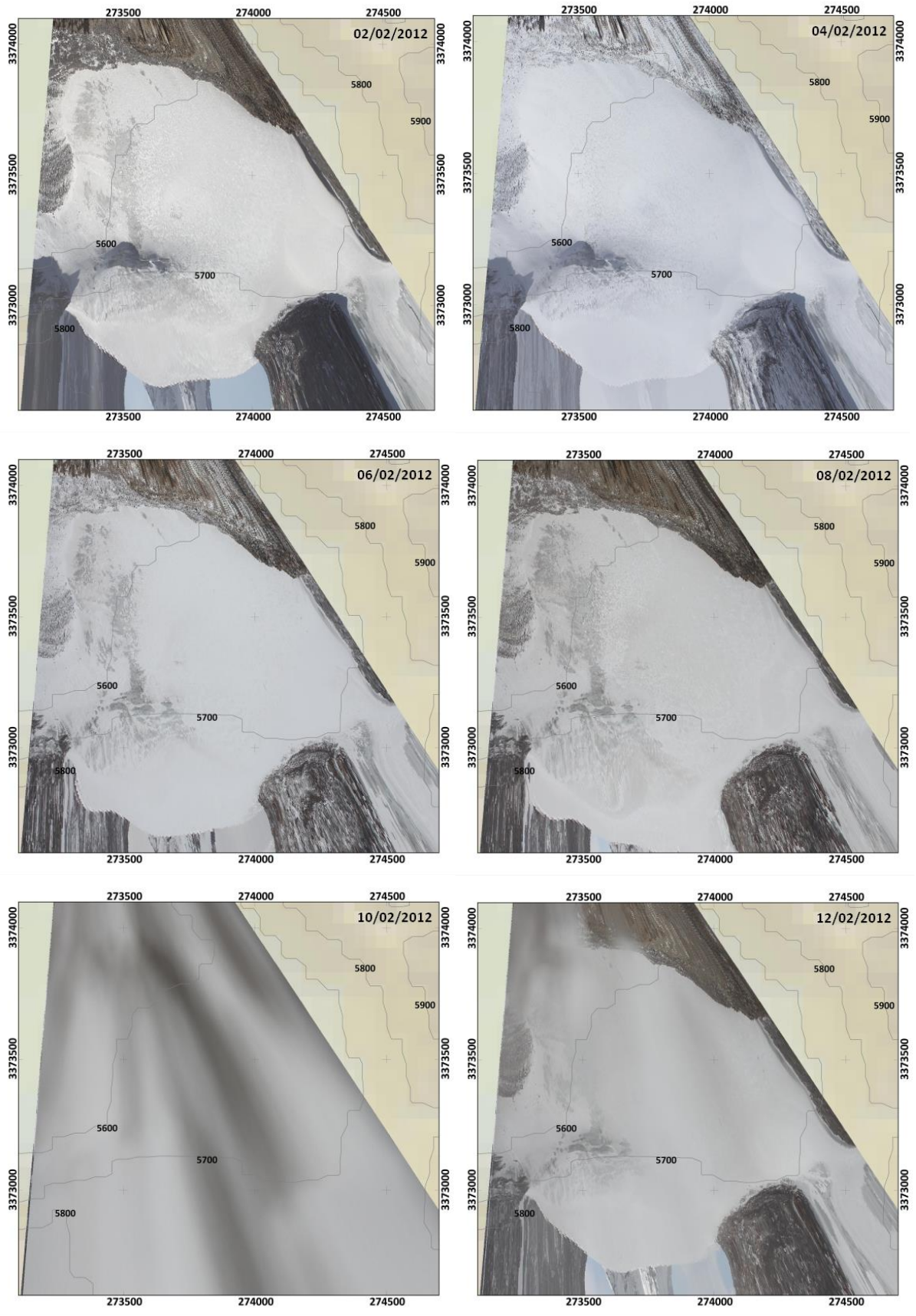


**Fig. 2.20 continued from preceding page**

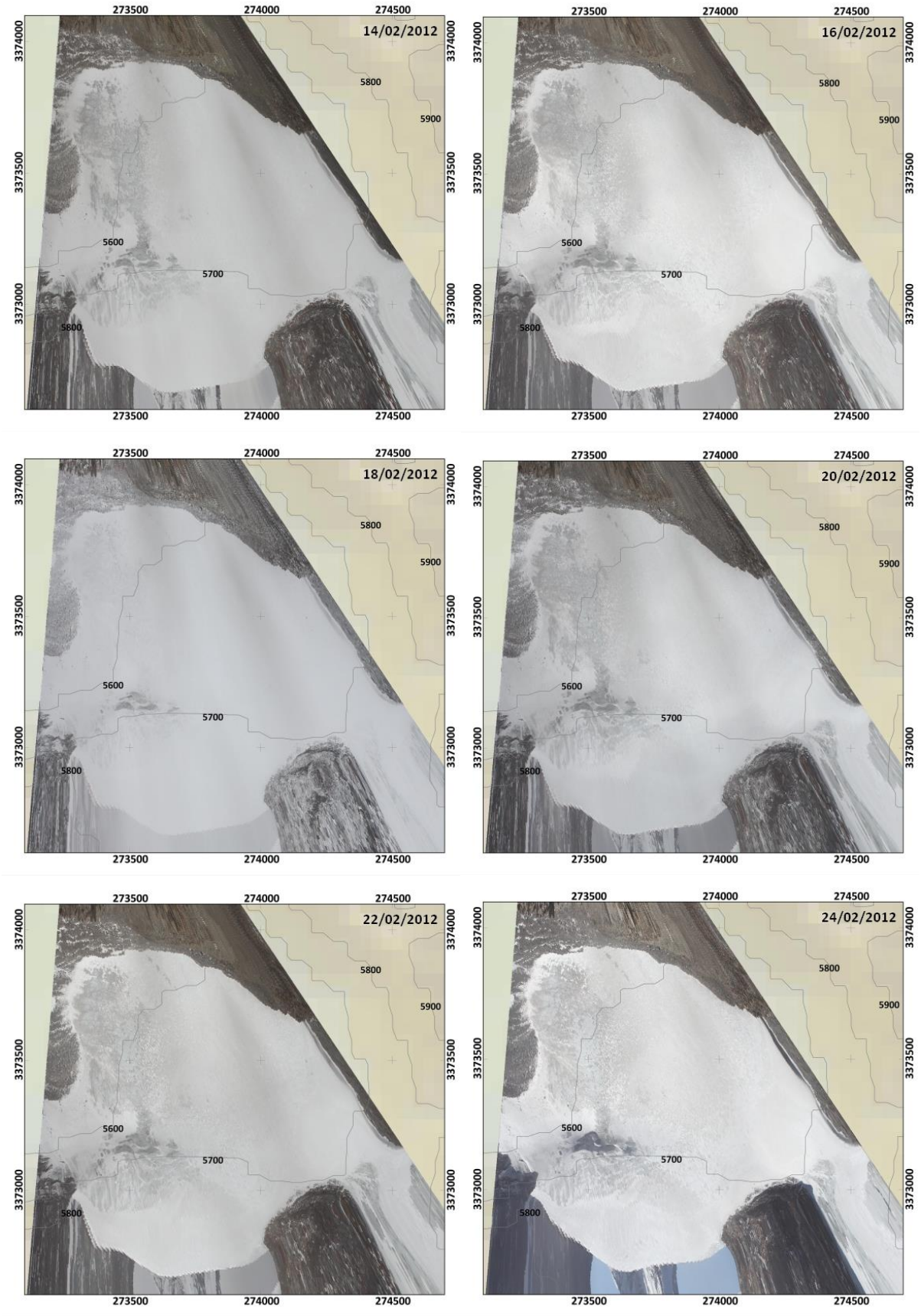


**Fig. 2.20 continued from preceding page**

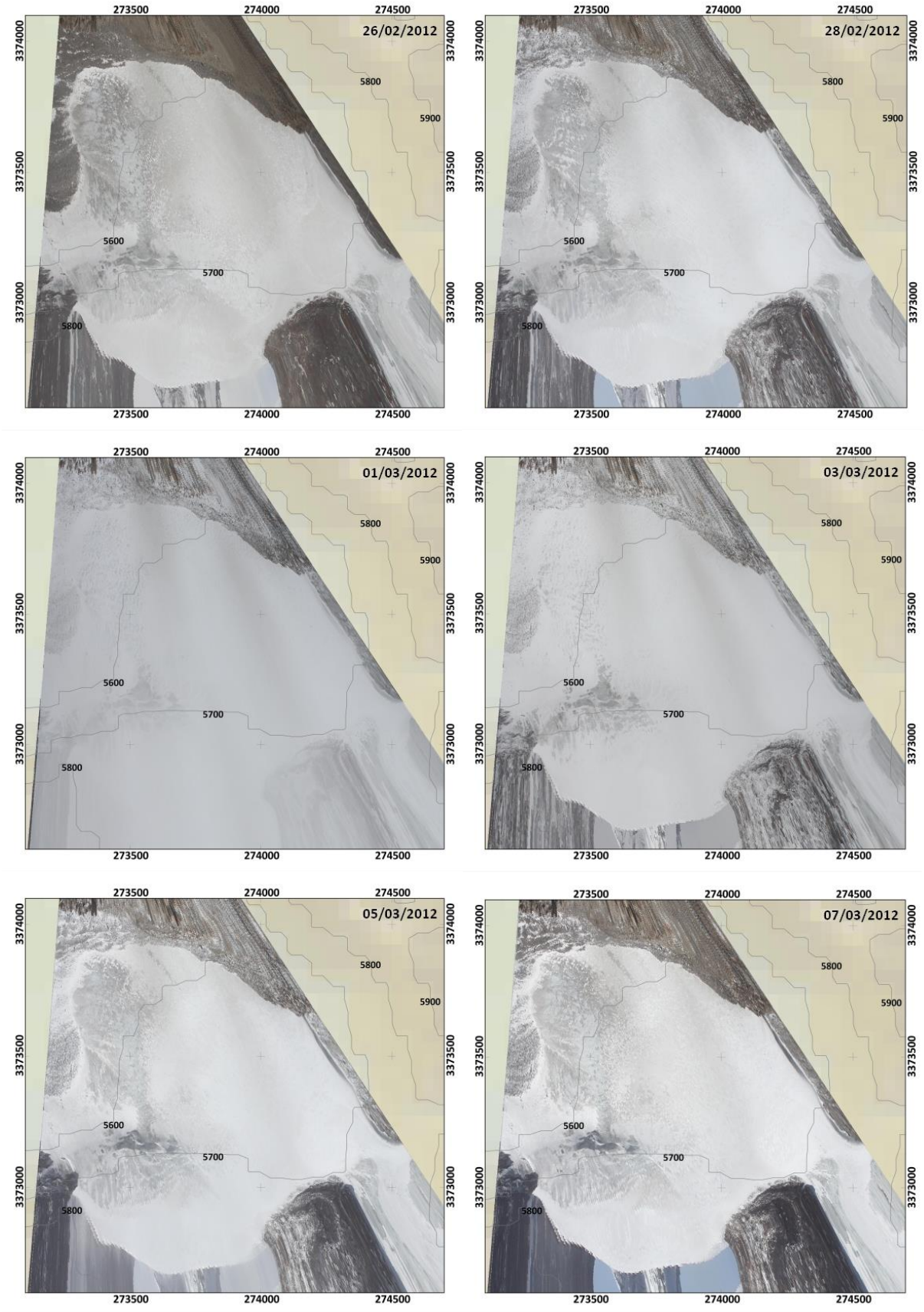


**Fig. 2.20 continued from preceding page**

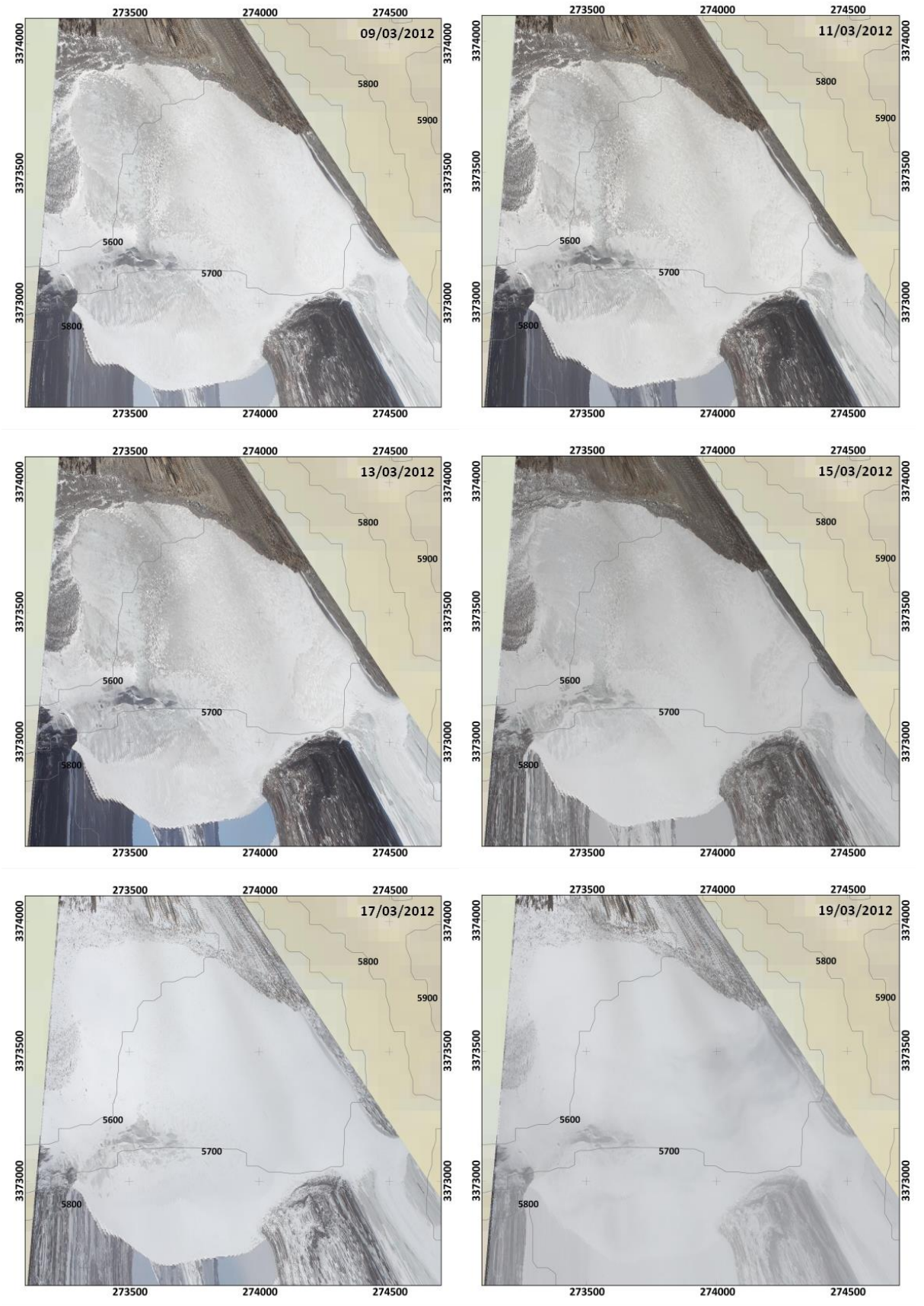


**Fig. 2.20 continued from preceding page**

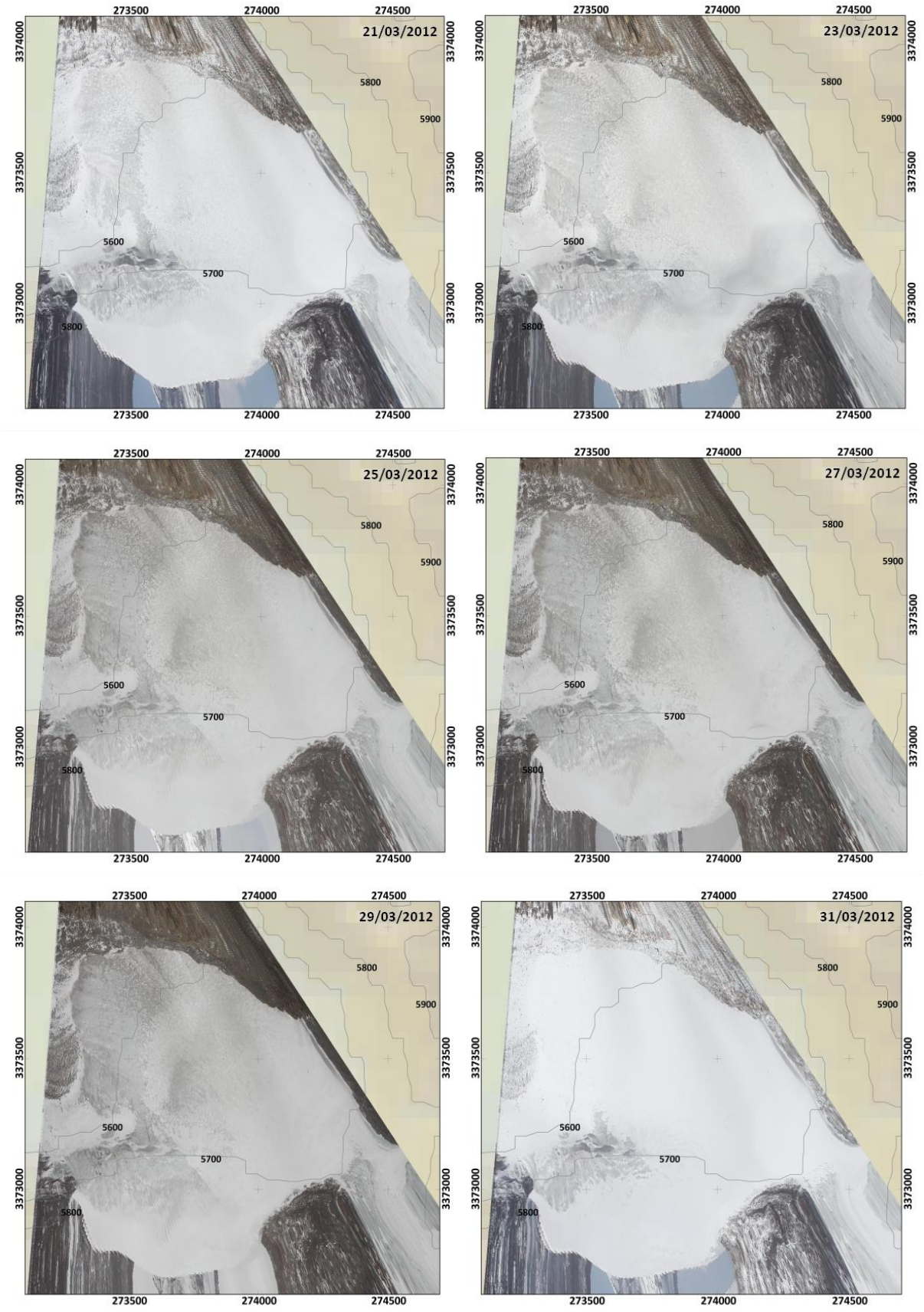


**Fig. 2.20 continued from preceding page**

These large amounts of energy input during daytime can not be compensated completely through negative $LW_{net}$, $Q_G$, $Q_{lat}$ and $Q_{sens}$ thus resulting in $T_s$ to be 0°C, small amounts of $Q_{melt}$ and surface melt (Fig. 2.22). Due to the cold winter snow pack almost all melt water refreezes within the snow layers. Turbulent fluxes are small due to low mean wind speeds ($u$ in Fig. 2.22a) and stability corrections during this period. On 12 March 2012 cool and humid air reached the glacier. Thus, $N$ increased and $SW_{net}$ decreased (see section 1.3.4.1). A snowfall event further decreases $SW_{net}$ (through $\alpha$), increases $RH$ and decreases $Q_{lat}$.

Therefore, the MB model performance is consistent in producing small amounts of surface melt in winter at $T_{air}$ below the melting point and larger mass losses through sublimation at generally dry conditions (Fig. 2.21b). Nevertheless, the model is not able to simulate a snow free glacier surface during that period because total amounts of surface melt (-9.6 mm w.e.), subsurface melt (-3 mm w.e.) and sublimation (-110 mm w.e.) can not remove the entire snow pack. Another process that may lead to significant altitude independent mass loss which is not considered in the MB model scheme is wind drift. To support the assumption of wind induced mass loss at Zhadang glacier hourly wind speeds at AWS2 directly in front of the glacier (see Fig. 2.1) are compared to the ablation patterns visible on the ortho-images (Fig. 2.20). From Fig. 2.21a it becomes obvious that the periods with strongest ablation at the glacier tongue correspond well with phases of highest $u$. Values for hourly mean $u$ frequently exceed 10 m $s^{-1}$ on the indicated days. It can be hypothesized that short term maxima of $u$ are considerably higher and may have caused extensive snow ablation at the wind-exposed regions of the glacier.

Wind induced mass loss was already assumed when scaling HAR precipitation (see section 2.2.3). It can now be hypothesized as a significant contribution to overall winter mass balance through time-lapse imagery.

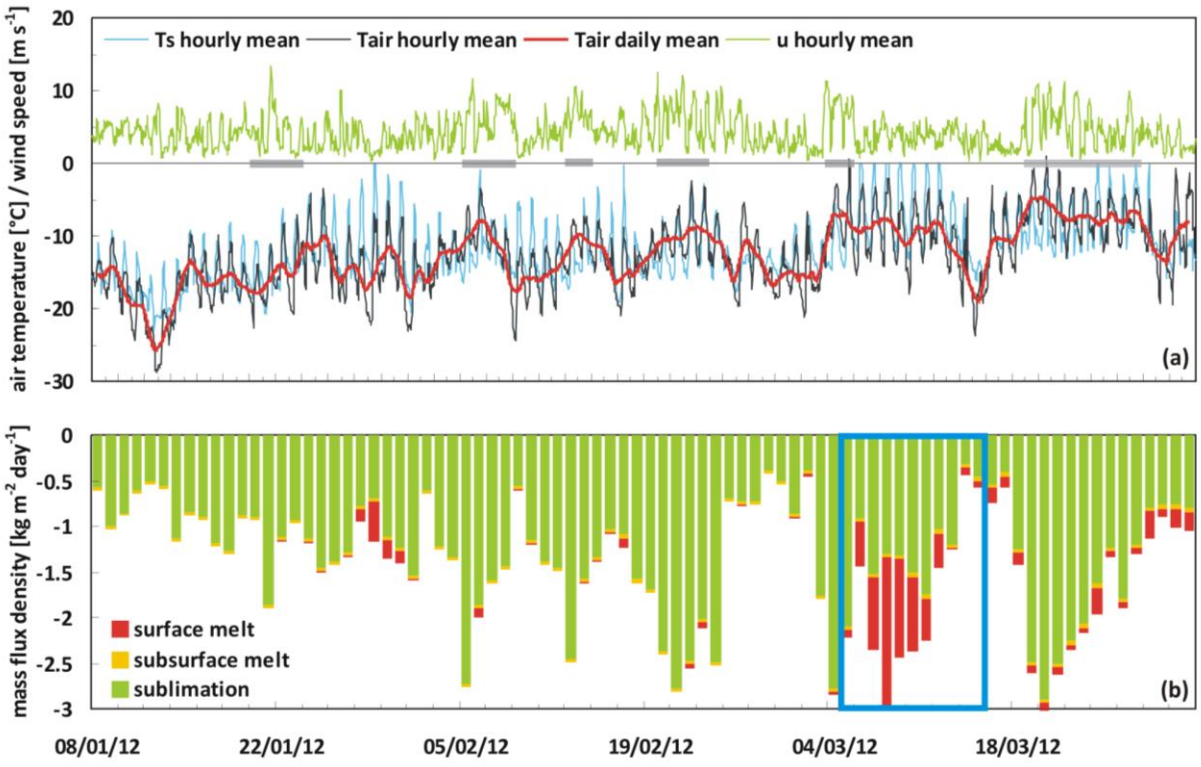


**Fig. 2.21: Period of strong ablation in winter 2012; (a) hourly and daily means of $T_{air}$ and $T_s$, hourly means of $u$ at AWS2. The grey bars indicate periods with strongest ablation (see Fig. 2.20); (b) selected MB components (daily sums) at the lowermost pixel of the glacier tongue (5530 m a.s.l.). The blue frame indicates the period shown in Fig. 2.22.**

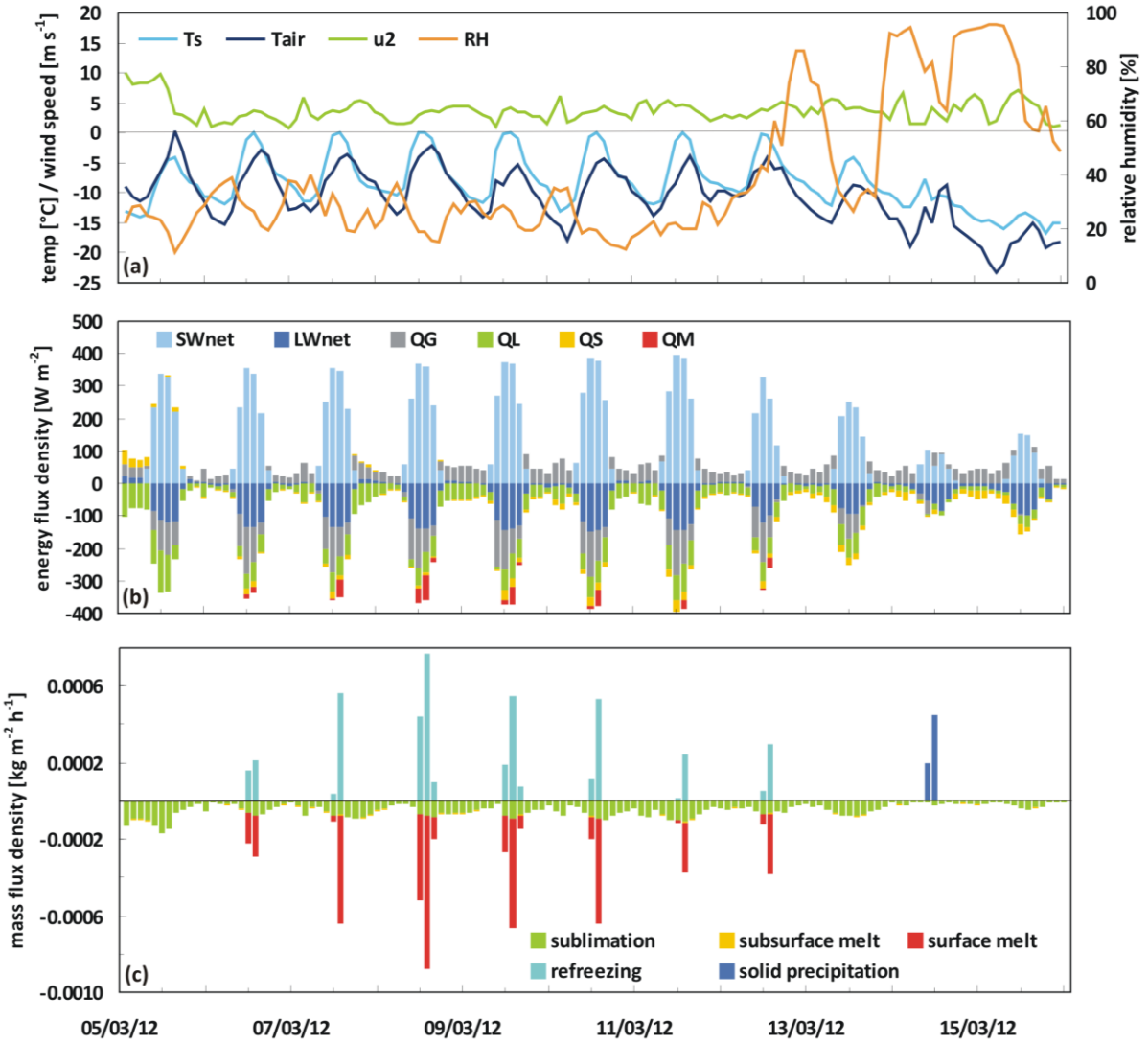


**Fig. 2.22: Two-hourly means for (a) $T_s$, $T_{air}$, $u$ and $RH$, (b) SEB components (see section 2.3.1 for abbreviations) and (c) MB components during 5-15 March 2012 at the lowermost pixel of the glacier tongue (5530 m a.s.l.).**

## 2.4.6 SEB/MB characteristics for the WRF driven model 2001-2011

Glacier-wide elevation profiles of MB and SEB components averaged over the simulation period 2001-2011 are shown in Fig. 2.23. The steepening of the gradient of MB between 5700 and 5800 m a.s.l. that was already evident in Fig. 2.16a (see section 2.4.3) is even more pronounced in the 10-year mean (Fig. 2.23a). Again, similar patterns can be detected in the vertical profiles of $SW_{net}$ (Fig. 2.23c), $Q_{melt}$ (Fig. 2.23d), surface melt (Fig. 2.23a) and $\alpha$ (Fig. 2.23f). The profile of $SW_{in}$ with two minima, one in the uppermost glacier regions and another in the lowest parts, due to terrain shading is much clearer than in section 2.5.3 when it was only referred to a shorter period (Fig. 2.16d). Mean solar insolation at the lowest glacier tongue is significantly less than in the altitude band above. This has an impact on most SEB and MB components by driving a number of feedback processes already explained in section 2.5.3. In contrast to the elevation profiles of $Q_{sens}$ and $Q_{lat}$ for the two MB years 2009/10 and 2010/11, both fluxes show a stronger dependency on altitude through decreasing $T_{air}$ (see also Braun & Hock 2004) and mirror the characteristic pattern with a maximum in the lowest regions (Fig. 2.23d). The 10-year mean amount of refreezing shows a maximum around 5800 m a.s.l.

where conditions of both a sufficient snow pack thickness and melt water availability are fulfilled (Fig. 2.23b, see section 2.4.3). In the lowermost glacier regions, MB is even more negative than surface melt, because mass loss through sublimation can not be compensated through mass gain by solid precipitation and refreezing (Fig. 2.23a,b). The altitudinal gradient of the MB indicates that the modelled mean ELA between 2001 and 2011 is between 5800 and 5850 m a.s.l. (Fig. 2.23a) what is very close to the value given by Bolch et al. (2010) (≈5800 m a.s.l.).
The ELA separates the accumulation area from the rest of the glacier and changes according to the annual MB (Fig. 2.16, Dyurgerov & Meier, 2005). Besides the ELA as an indicator for the state of a glacier the accumulation area ratio (AAR) can be calculated through $AAR = A_c/A$. $A_c$ is the accumulation area and $A$ is the total glacier area (Dyurgerov et al. 2009). The AAR ranges between 0 and 1. On most glaciers it correlates well with the climatic MB, similar to the ELA (Cogley et al. 2011). Both, ELA and AAR are an undelayed response to a change in SEB and MB components, whereas a change in A is a delayed adjustment to climate variations and occurs mainly below the ELA (Dyurgerov et al. 2009). An AAR approaching 1 generally indicates a positive MB. The annual AAR can vary greatly from year to year. This is visualized in Fig. 2.24 for Zhadang glacier. However, the average AAR over a number of years gives a hint on the health of a glacier when compared to the balanced-budget AAR ($AAR_0$, Cogley et al. 2011, Dyurgerov et al. 2009). The $AAR_0$ is the AAR when a glacier is in equilibrium. It can be estimated from the relation between annual AAR and annual MB over a number of years (Fig. 2.24). The $AAR_0$ is the value of AAR at which the regression line of annual AAR and annual MB crosses the axis at MB=0 (Cogley et al. 2011). Its value has been found to vary roughly between 0.5 (50%) and 0.6 (60%) (Cogley et al. 2011, Dyurgerov et al. 2009). At Zhadang glacier a significant linear relationship between AAR and MB is revealed ($R^2$=0.64, Fig. 2.24). For the simulation period 2001-2011 the AAR is 0.07 (7%). The $AAR_0$ is estimated to be 0.6 (60%) (Fig. 2.24). The large discrepancy between AAR and $AAR_0$ indicates that Zhadang glacier is far away from its equilibrium state during the simulated period. Dyugerov et al. (2009) developed a single index $\alpha_d$ to define the difference of AAR and $AAR_0$ for a glacier. $\alpha_d$ is calculated through $\alpha_d = (AAR-AAR_0)/AAR_0$. The index measures the glacier's displacement from the equilibrium. Positive values of $\alpha_d$ suggest that the glacier's accumulation area increased over the respective period. The glacier will have to expand its area by advancing to adjust to the climate conditions. Negative values of $\alpha_d$ indicate that the accumulation area decreased and the glacier is or will be in retreat to reach its equilibrium (Dyurgerov et al. 2009). For Zhadang glacier $\alpha_d$ is determined to be -0.88 (-88%). Thus, the glacier has to decrease its area largely to reach its equilibrium state for the climate conditions of the simulation period. Dyurgerov et al. (2009) determined largest negative $\alpha_d$ values around -65% between 1961 and 2004 for tropical glaciers.

Glacier-wide mean monthly SEB and MB components from the HAR forced model run 2001-2011 are illustrated in Fig. 2.25. An initialisation period of approx. one year is needed for the subsurface module to adapt to the surrounding conditions (see section 2.4.1). Therefore, calculated values for the first MB year (2001/02) should be treated with caution. For Zhadang glacier, the values of the first year are still within the mean ranges and are therefore considered for the following calculations. $SW_{in}$ (+232.1 W m$^{-2}$) and $LW_{in}$ (+208.6 W m$^{-2}$) still dominate energy input but $SW_{in}$ is a little larger than for the period 2009-2012 and dominates over $LW_{in}$ which is smaller compared to the years 2009 – 2012 (see section 2.5.3). $Q_{sens}$ contributes with +24.6 W m$^{-2}$ to the energy input of the glacier surface. Responsible for energy loss are $LW_{out}$ (-260.0 W m$^{-2}$), $SW_{out}$ (-158.5 W m$^{-2}$), $Q_{lat}$ (-35.0 W m$^{-2}$), $Q_{melt}$ (-13.2 W m$^{-2}$) and $Q_G$ (-3.6 W m$^{-2}$). Therefore, $SW_{net}$ (+73.6 W m$^{-2}$) remains the most important energy source for the glacier (Andreassen et al. 2008) as it was for the shorter period 2009-2012 and the pattern of lowest $SW_{net}$ through high $\alpha$ around September, described in section 2.5.3, is obvious in almost every year (Fig. 2.25a). In 2006 this structure is completely missing and the glacier SEB is characterized by highest $SW_{net}$ throughout the year (Fig. 2.25a) caused by low α through very little

snowfall in November and December 2005, January to March and again June to August 2006 (Fig. 2.25b). The result is that the model returns largest amounts of $Q_{melt}$ and therefore surface melt from March to September (Fig. 2.25). This stresses the impact of the monsoon onset as reported by Mölg et al. (2012) and Kang et al. (2009) (see section 2.1) but also the importance of winter snowfall events that keep $\alpha$ high. Generally, $\alpha$ decreases at the end of each year (increasing $SW_{net}$, Fig. 2.25a) because solid precipitation is minimal in that period (see section 1.4.2.1, Fig. 2.25b). Then $\alpha$ gradually increases in late winter and spring (decreasing $SW_{net}$). $LW_{net}$ and $Q_G$ show a rather regular seasonal cycle (Fig. 2.25a) as explained in section 2.4.3. Generally, monthly means of $Q_{sens}$ and $Q_{lat}$ are of opposite sign and sometimes cancel each other out (see also Braun & Hock 2004). $Q_{sens}$ can reach negative values during winter through cold air advection over the glacier or high $SW_{net}$ (through low $\alpha$) and increasing $T_s$ (see section 2.4.5). As described in section 2.4.3 the dry conditions on the TP cause absolute values of $Q_{lat}$ to be usually larger than $Q_{sens}$ and being responsible for significant mass loss through sublimation in every month (Fig. 2.25).

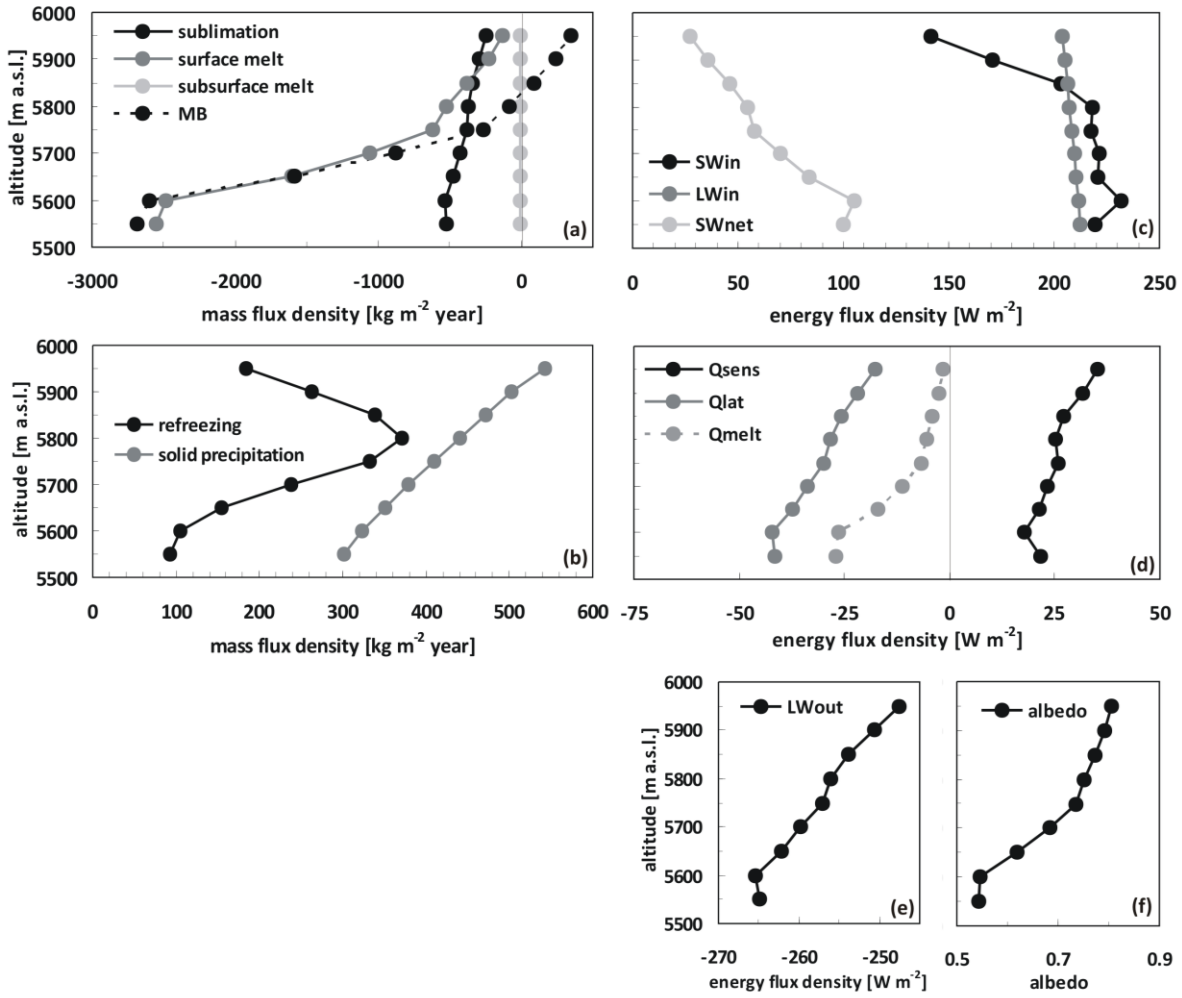


**Fig. 2.23: Modelled vertical profiles of (left) the specific mass balance and its components and (right) mean SEB components on Zhadang glacier averaged over the simulation period October 2001 – September 2011. Data are averaged for 50-m altitude bands. Note the different x-axis scales of the components (negative means mass or energy loss at the glacier surface, see section 2.3.1 and Table 2.2 for abbreviations).**

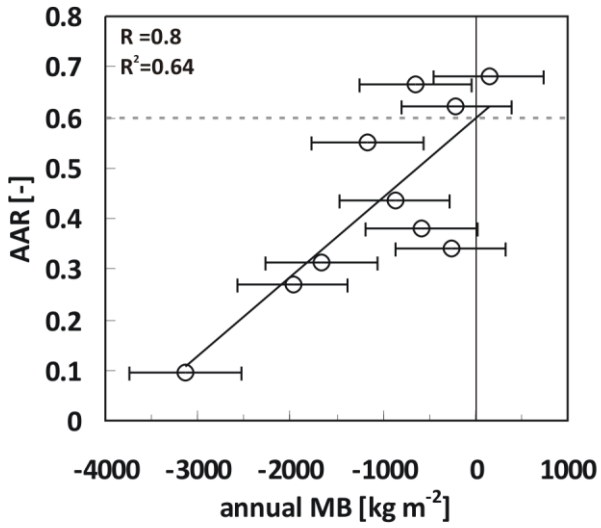


**Fig. 2.24: Relation between annual MB and AAR at Zhadang glacier, 2001-2011. The AAR at MB=0 denotes $AAR_0$.**

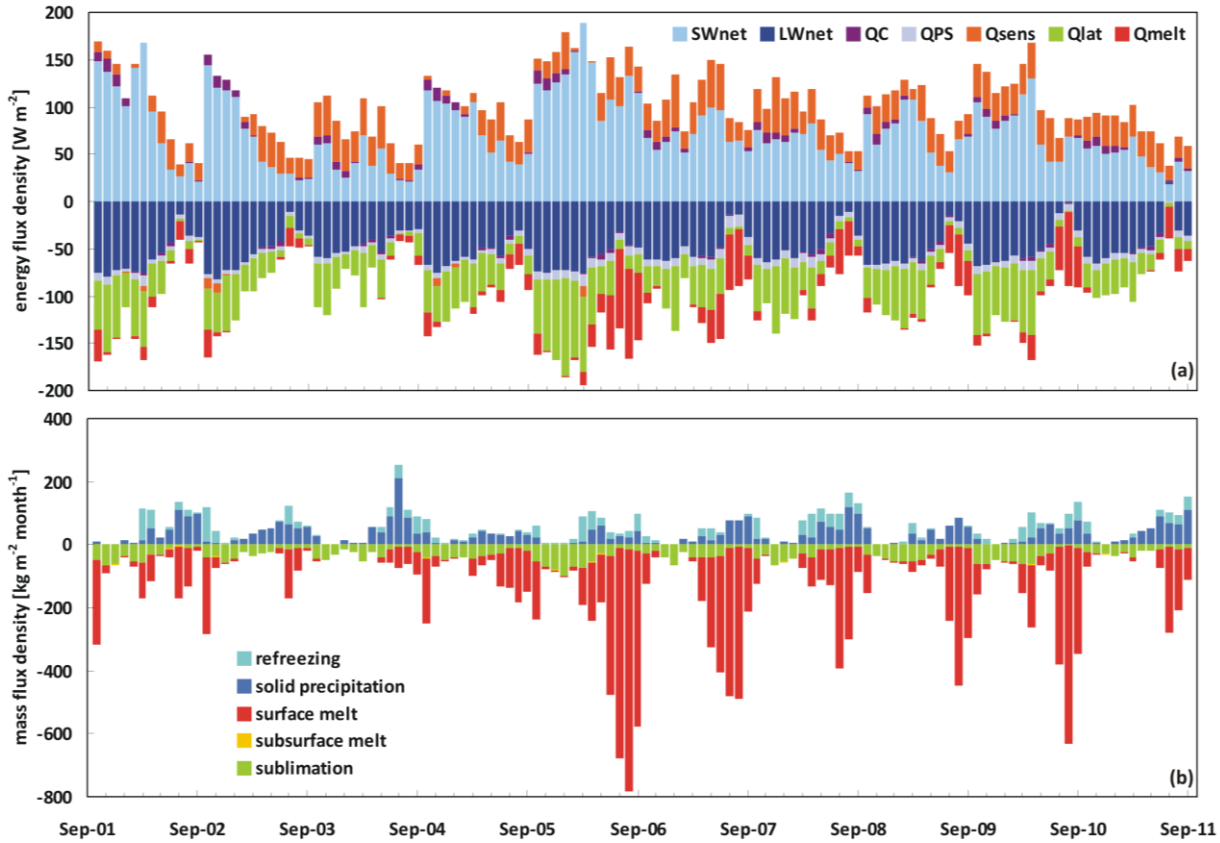


**Fig. 2.25: Glacier-wide monthly (a) SEB components (see section 2.3.1 for abbreviations) and (b) MB components from October 2001 to September 2011 at Zhadang glacier.**

The glacier-wide MB over the considered period (-10363 kg $m^{-2}$/-1036.3 kg $m^{-2}$ $yr^{-1}$) is composed from surface melt (-12623 kg $m^{-2}$/-1262.3 kg $m^{-2}$ $yr^{-1}$), sublimation (-3965 kg $m^{-2}$/-396.5 kg $m^{-2}$ $yr^{-1}$), subsurface melt (-46 kg $m^{-2}$/-4.6 kg $m^{-2}$ $yr^{-1}$), solid precipitation (+4112 kg $m^{-2}$/+411.2 kg $m^{-2}$ $yr^{-1}$) and refreezing (+2159 kg $m^{-2}$/+215.9 kg $m^{-2}$ $yr^{-1}$) (Table 2.7). In total, 17% of surface and subsurface melt refreezes, whereas monthly values range between 100% in winter and 0% in summer (Fig. 2.25b). Seasonal patterns of the components for the period 2001-2011 are similar as described in section 2.4.3. Calcu-

lated solid precipitation is less than the amounts considered in the AWS forced model runs (Table 2.5, 2.7). Explanation for this might be the discrepancy between accumulation at the location of the AWS (input for AWS forced model runs) and precipitation measurements at the rain gauge (reference for the determination of the scaling factor of HAR precipitation).
The extreme large surface melt in 2009, that was observed at AWS1 (see section 2.4.3, Fig. 2.8a) and modelled by the AWS forced MB model (Fig. 2.17) could not be reproduced using HAR data (Fig. 2.25). The reason for this might be the different intensity and frequency of HAR precipitation that suppressed surface melt (Fig. 2.9a) but also discrepancies within the SEB components that cause $Q_{melt}$. This will be discussed in section 2.5. Overall mass loss and surface height change in 2010 and 2011 could be reproduced to a high degree.
Table 2.6 lists the absolute and relative contributions of energy flux components to total energy flux. For the total considered period, $SW_{net}$ accounted for 38%, followed by $LW_{net}$ (27%), $Q_{lat}$ (16%), $Q_{sens}$ (15%) and $Q_G$ (3.3%) of overall energy turnover. These proportions are characteristic for cold and dry climates (Braun & Schneider 2000, Mölg & Hardy 2004). In the MB year 2005/06 $Q_{melt}$ is largest, but low compared to the mean value of $SW_{net}$. The maximum amount of energy input for the glacier surface could be compensated to a certain degree through maximum values of $LW_{net}$ and $Q_{lat}$, serving as energy sinks. In the years 2001/02, 2002/03, 2003/04, 2004/05 and 2010/11 energy input by $SW_{net}$ and $Q_{sens}$ is nearly totally compensated through energy removal by $LW_{out}$ and $Q_{lat}$. Generally, this results in less $Q_{melt}$ and therefore less surface melt and above average annual MB (Fig. 2.23, 2.25). The relation does not hold for the year 2004/05 when MB is below average despite of small $Q_{melt}$ because of little refreezing (Table 2.7).
From the modelled period October 2001 – September 2011 ten glacier-wide annual MB estimates for Zhadang glacier can be obtained and compared to other studies (Table 2.7, Fig. 2.26). Given uncertainties are obtained through model calibration (see section 2.4.1). Table 2.7 shows calculated MB components and their relative contribution to total mass loss for the total period and for each MB year. In the most negative year 2005/06 accumulation through solid precipitation is minimal (Fig. 2.3, 2.25) and cannot compensate together with refreezing for strong surface melt and large amounts of sublimation. The positive MB year 2003/04 can be explained by a combination of above-average solid precipitation and minimal mass loss through surface melt. In general, effective melt (surface melt + subsurface melt – refrozen water) accounts for 72% of total mass loss followed by sublimation (27%). Mass loss through subsurface melt is negligible (0.3%).
Mean modelled MB (-1036±600 kg $m^{-2}$ $yr^{-1}$) is slightly more negative than the value given by Mölg et al. (2014) (-891±105 kg $m^{-2}$ $yr^{-1}$) but within the range of uncertainties. Other MB studies for glaciers in High Asia over a similar time period using satellite data revealed values within this range or less negative. Gardner et al. (2013) obtained a value of -270±160 kg $m^{-2}$ $yr^{-1}$ for the southern and eastern TP and -800±220 kg $m^{-2}$ $yr^{-1}$ for the East Himalayas (2003-2008). Results of Gardelle et al. (2013a,b) range between -220±120 kg $m^{-2}$ $yr^{-1}$ and -450±130 kg $m^{-2}$ $yr^{-1}$ (1999-2011) for the Himalayas that correspond to the findings of Kääb et al. (2012) (2003-2008). Combining satellite and aerial images, Bolch et al. (2011) obtained MB of up to -1960±530 kg $m^{-2}$ $yr^{-1}$ for single glaciers in the Everest region over 2002-2007 (mean value over ten glaciers: -790±520 kg $m^{-2}$ $yr^{-1}$). MB values for single years are generally more negative but mostly within the range published by Mölg et al. (2014) with a HAR forced MB model of similar structure as the model applied here. Kang et al. (2009) and Yu et al. (2013) published annual values for three years based on field data (Fig. 2.26). Calculated mass loss is considerably less than MB model output what is often observed due to the positioning of the ablation stake network (Yao et al. 2012, Zemp et al. 2013). Mölg et al. (2014) revealed that the MB of TP glaciers is driven both by the onset of the Indian Summer Monsoon and the mid-latitude westerly jet through the respective influence on May-June precipitation. The authors associate the jet position in

the monsoon onset period with annual MB of Zhadang glacier. Thus, strongly negative MB occur in case of frequent westerly jets over the TP, that limit the monsoon progression (MB years 2006/07 and 2009/10), or when a curved jet axis extends to the western plateau regions (MB years 2004/05 and 2008/09) (Fig. 2.26). When the main jet activity is concentrated north of the TP, respective MB is above the average (MB years 2001/02-2003/04, 2007/08 and 2010/11) even if the monsoon onset is weak. This is explained through high precipitation in the western Tian Shan and intensified moisture advection to the plateau. The strongly negative MB in 2005/06 coincides with a westerly jet north of the TP, although this pattern generally favours less negative MB. This is explained through low circulation intensities both in the monsoon and the Tian Shan regions which limit the positive effect of the jet position on glacier MB.

**Table 2.6: Mean absolute values of energy flux components as modelled for October 2001 – September 2011 and for the respective MB years with proportional contribution to total energy flux.**

| | Sum* [W m$^{-2}$] | $SW_{net}$ | $LW_{net}$ | $Q_{sens}$ | $Q_{lat}$ | $Q_G$ | $Q_{melt}$ |
|---|---|---|---|---|---|---|---|
| total average [W m$^{-2}$] | 191 | 74 | -51 | 25 | -35 | -3.6 | -13 |
| 2001/02 | | 91 | -58 | 14 | -37 | -2.8 | -9 |
| 2002/03 | | 69 | -54 | 14 | -28 | 0.1 | -6 |
| 2003/04 | | 41 | -45 | 32 | -28 | -1.5 | -3 |
| 2004/05 | | 78 | -56 | 17 | -34 | -1.6 | -9 |
| 2005/06 | | 128 | -61 | 21 | -54 | -6.5 | -33 |
| 2006/07 | | 71 | -49 | 33 | -31 | -6.8 | -22 |
| 2007/08 | | 59 | -46 | 31 | -32 | -4.9 | -12 |
| 2008/09 | | 72 | -52 | 25 | -34 | -3.5 | -13 |
| 2009/10 | | 81 | -48 | 31 | -43 | -5.9 | -19 |
| 2010/11 | | 45 | -45 | 27 | -23 | -2.5 | -7 |
| | 100% | 38% | 27% | 15% | 16% | 3.3% | |

*Sum of energy fluxes in absolute values: $|SW_{net}| + |LW_{net}| + |Q_{sens}| + |Q_{lat}| + |Q_G|$

**Table 2.7: Calculated glacier-wide mass balance components for the total period October 2001 – September 2011 and for the respective MB years.**

| | Solid precipitation | Surface melt | Refrozen water | Subsurface melt | Sublimation | Mass balance* |
|---|---|---|---|---|---|---|
| total [kg m$^{-2}$] | 4112.0 | -12623.1 | 2158.93 | -46.3 | -3964.7 | -10363.2±6000 |
| 2001/02 | 461.0 | -840.6 | 220.7 | -5.8 | -419.4 | -584.1±600 |
| 2002/03 | 426.1 | -541.4 | 247.9 | -5.7 | -333.5 | -206.5±600 |
| 2003/04 | 570.4 | -255.2 | 167.3 | -3.4 | -332.1 | 147.0±600 |
| 2004/05 | 304.0 | -877.2 | 99.1 | -5.0 | -388.5 | -867.6±600 |
| 2005/06 | 252.2 | -3105.8 | 337.4 | -6.1 | -612.0 | -3134.4±600 |
| 2006/07 | 355.3 | -2078.9 | 111.3 | -3.9 | -359.4 | -1975.6±600 |
| 2007/08 | 503.2 | -1186.8 | 410.7 | -3.9 | -371.6 | -648.4±600 |
| 2008/09 | 375.2 | -1212.4 | 69.7 | -4.9 | -391.4 | -1163.8±600 |
| 2009/10 | 346.2 | -1829.1 | 311.6 | -4.3 | -489.4 | -1665.0±600 |
| 2010/11 | 518.4 | -695.7 | 183.3 | -3.3 | -267.5 | -264.8±600 |
| % of mass loss | | | 72 | 0.3 | 27 | |

*Mass balance = solid precipitation + surface melt + refrozen water + subsurface melt + sublimation

For the MB years 2004/05 and 2008/09 estimated MB values including their uncertainties do not correspond to the study of Mölg et al. (2014) (Fig. 2.26). These years are characterized by similar conditions in the Indian Summer Monsoon region and the western Tian Shan with a jet axis far south over the western TP. This causes a weak pressure gradient and less moisture advection from the Tian Shan region (Mölg et al. 2014). In the study of Mölg et al. (2014) this results in below-average MB in

the respective years. In contrast, the MB model presented in section 2.3.1 produces values around or slightly above the 10-year average (Table 2.7, Fig. 2.26).

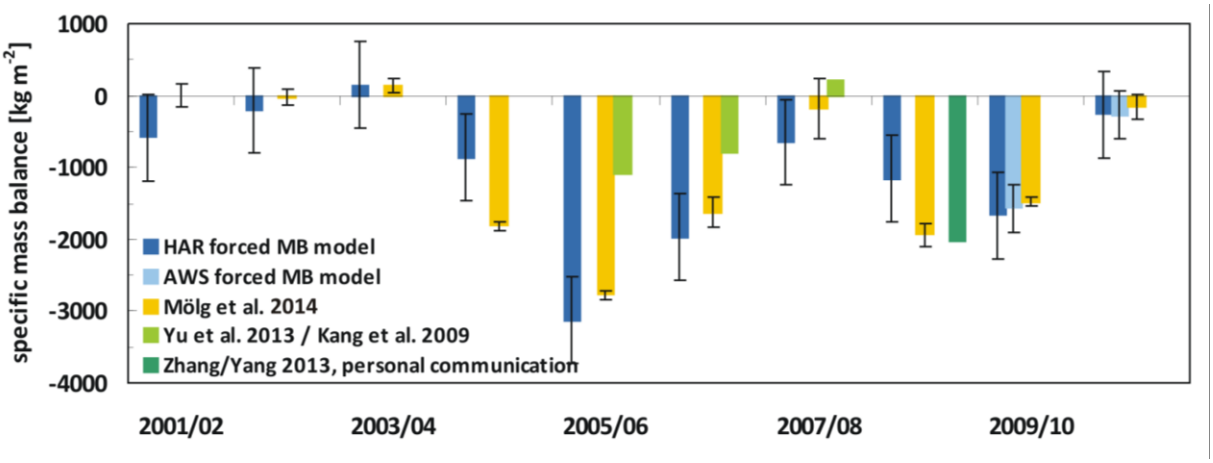


**Fig. 2.26: Glacier-wide annual MB for MB years (October – September) 2001-2011 estimated by the HAR forced MB model and compared to values from other studies.**

## 2.5 Discussion of uncertainties

From the presented results the question arises, which SEB and MB components are responsible for the differences in glacier-wide MB years 2004/05 and 2008/09 between this study and the study of Mölg et al. (2014). Glacier-wide annual SEB and MB components from Mölg et al. (2014) and this study are compared in Fig. 2.27 and 2.28. Generally, deviations may be caused by a 15% larger glacier area, mostly located in the accumulation area, as applied by Mölg et al. (2012, 2014) (see section 1.4.2.1) and by different parameterizations for the various energy fluxes within the two model approaches (Table 2.8). The main parameterizations within the two models and possible impacts on the respective glacier-wide SEB and MB components are compared to each other in Table 2.8. The largest differences are visible in $SW_{out}$. Annual means of $SW_{out}$ are generally larger in the MB model presented in this thesis (Fig. 2.27), probably caused by a different parameterization of $\alpha$ (Table 2.8). Another reason for these discrepancies can be varying surface conditions within the two models throughout the year.

The treatment of the snow pack as a bulk medium in Mölg et al. (2012, 2014) and a differing subsurface temperature scheme might cause larger subsurface melt (Fig. 2.28) despite small differences in $Q_C$ and $Q_{PS}$ (Fig. 2.27). The MB model in this thesis calculates a more negative $Q_{lat}$ (Fig. 2.27) and therefore more sublimation (Fig. 2.28) than the model of Mölg et al. (2012, 2014). This is caused by the assumption of a constant $RH$=100% at the surface (Table 2.8). $Q_{melt}$ is the sum of all SEB components and directly influences surface melt and therefore MB. In most MB years differences in the single SEB components between the two models compensate each other and lead to small differences in $Q_{melt}$ (Fig. 2.27) and surface melt (Fig. 2.28). This is not surprising because both MB models have been calibrated for $Q_{melt}$ to finally reproduce the glacial melt pattern.

In the MB years 2004/05 and 2008/09 mean annual $Q_{melt}$ estimated in this study is around 10 W m$^{-2}$ less than in Mölg et al. (2014) resulting in around 1000 kg m$^{-2}$ less surface melt (Fig. 2.28). Therefore, MB values in the respective years are considerably less negative compared to Mölg et al. (2014). This result does not correspond to the general pattern of more negative MBs in this study due to increased solid precipitation in Mölg et al. (2014). On average, mass gain through snowfall applied in Mölg et al. (2014) is 250 kg m$^{-2}$ yr$^{-1}$ larger than in this study which partly compensates increased subsurface melt together with refreezing (Fig. 2.28) but may also lead to a number of feedback process-

es in both SEB and MB components through changing $\alpha$. Mass gain in Mölg et al. (2014) may also be larger since the larger glacier surface in Mölg et al. (2014) is located in the accumulation area of the glacier (see section 1.4.2.1). The same argument would favour less negative MB in Mölg et al. (2014) compared to this study.

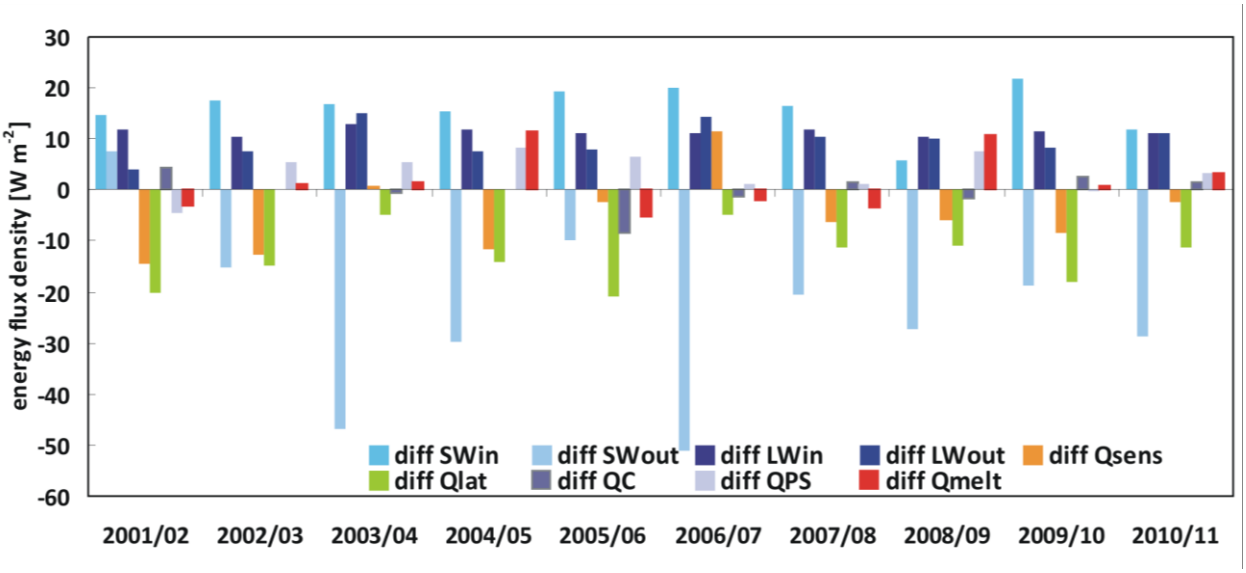


**Fig. 2.27: Glacier-wide annual mean differences in SEB components between the results of Mölg et al. 2014 and this study. Positive values indicate that the energy input for the glacier surface by the respective SEB component is larger (or less energy is removed from the surface) in this study than in Mölg et al. (2014).**

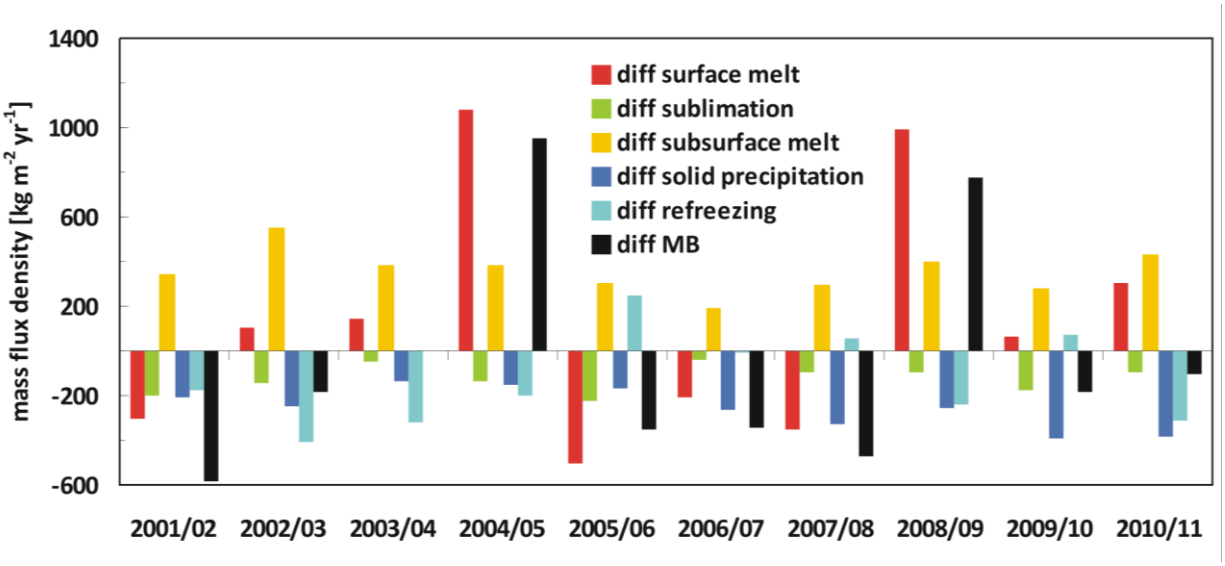


**Fig. 2.28: Glacier-wide annual differences in MB components between the results of Mölg et al. 2014 and this study. Positive values indicate that the respective MB component causes a larger mass gain for the glacier (or less mass loss) in this study than in Mölg et al. (2014).**

## 2.6 Conclusion regarding model results for Zhadang glacier

The presented SEB and MB study at Zhadang glacier aims at introducing the newly developed coupled SEB/MB and multi-layer snow model and furthermore, to verify its performance. Similar model structures and parameterizations are already well established in glaciological research and have now been newly combined and assembled into this model scheme at RWTH Aachen University. Zhadang glacier is subject of intensive atmospheric and glaciological field work within a Sino-German research

project since 2009 and therefore holds a large data basis for the detailed calibration and validation of the MB model. The atmospheric model data (HAR) generated by the TU Berlin provided a second set of input data for the MB model with the opportunity of simulation of up to 10 years. Output data of both, the AWS and the HAR forced model are compared to various atmospheric, glaciological, surface and subsurface data sets for the point location of AWS1 as well as for the ablation stake network distributed over the glacier. The 3-year image time series of a time-lapse camera system next to the glacier provides a valuable contribution to the spatial and temporal validation of the model performance. We used inferred mean transient snow line altitudes and the snow line pattern from the ortho-pictures for validation of the distributed AWS forced MB model. The respective model output corresponds very well to both the mean altitude and the observed spatial patterns. This implies the reliability and transferability of the MB model to glacier regions where measurements are missing. During the process of image processing, a strong ablation event in winter 2012 at the lower glacier tongue could be revealed. A combined analysis of atmospheric measurements and MB model output shows that wind induced mass loss can be hypothesized as a significant contribution to overall winter MB.

Generally, the results of the detailed model evaluation for the intensive observation period 2009-2012 for both the AWS and HAR forced MB model are convincing. Using the 10-year HAR data set, SEB and MB components of Zhadang glacier are calculated for 2001-2011 and interpreted concerning their altitudinal gradients and their inter- and intra-annual patterns. In total, the energy flux at the glacier surface is dominated by $SW_{net}$ (38%). Altogether, 17% of surface and subsurface melt refreezes within the snow pack. This is reasonable for polythermal glaciers. The generally dry atmosphere on the TP causes sublimation to be an important mass loss for Zhadang glacier especially in winter. However, effective melt (72%) is still the dominating mass loss prior to sublimation (27%). This fits to the regional scale pattern of strongly monsoon influenced glaciers.

The detailed comparison for the SEB and MB components with the study of Mölg et al. (2014) reveals that in most years the differences in $Q_{melt}$ are small although other SEB components show large discrepancies between both models. This is not surprising because both MB models have been calibrated for $Q_{melt}$ to finally reproduce the glacial melt pattern. From the modelled period October 2001 - September 2011 ten glacier-wide annual MB estimates for Zhadang glacier for subsequent years are obtained and compared to other studies on the TP and the adjacent mountain regions. Studies over larger areas (e.g. East Himalayas, south eastern TP) generally return less negative MB. However, the results for single glaciers under similar climate forcing, e.g. strong influence of the summer monsoon, are in a very good agreement with the result from this study.

The presented results of the SEB and MB model as forced with downscaled atmospheric reanalysis HAR data promise that it produces reliable results for longer simulations and that it can be transferred to other glaciers and ice caps where in-situ measurements for the model evaluation are sparse or lacking at all.

**Table 2.8: Comparison of the main parameterizations within the coupled snow and SEB model developed and applied in this study and applied in Mölg et al. (2014) and impact on glacier-wide SEB and MB results.**

| Parameter(ization) | this study | Mölg et al. (2014) | Impact on glacier-wide results |
|---|---|---|---|
| altitudinal lapse rates | | | |
| air temperature ($T_{air}$) | -0.007 K $m^{-1}$ | night: -0.0035 K $m^{-1}$<br>day: -0.0095 K $m^{-1}$ | ? |
| precipitation | +0.042% $m^{-1}$ | +0.038% $m^{-1}$ | negligible |
| relative humidity (RH) | +0.022% $m^{-1}$ | - | ? |
| air pressure ($\rho_{air}$) | -0.067 hPa $m^{-1}$ | - | ? |
| threshold for precipiation phase | 1-5°C | 1-6.5°C | >20% difference in solid precipitation / accumulation<br>→ less negative MB in Mölg et al. (2014) |
| precipitation scaling factor | 0.56 | 0.79654 | |
| radiation | | | |
| $SW_{in}$ | radiation model after Kumar et al. (1997) corrected for clouds through HAR $SW_{in}$ | radiation model after Mölg et al. (2009b) optimized after $SW_{in}$ from the AWS | Comparison of $SW_{in}$ sums between HAR and AWS showed slightly more $SW_{in}$ from HAR; but maximum hourly summertime $SW_{in}$ at noon can differ by up to 1000 W $m^{-2}$→ ? |
| α | function of snowfall frequency and depth after Oerlemans & Knap (1998); control parameters (α for fresh snow, firn and ice, effects of ageing and snow depth) are the same as in Mölg et al. (2014) | function of snowfall frequency and depth after Oerlemans & Knap (1998); $\alpha_{ice}$ is variable as a function of dew point temperature | slightly lower $\alpha_{ice}$ causes larger $SW_{net}$ and therefore increasing $Q_{melt}$ and $Q_{PS}$<br>→ temporarily more surface and subsurface melt in Mölg et al. (2014) |
| $LW_{in}$ | after Klok & Oerlemans (2002) | after Mölg et al. (2009b) or Klok & Oerlemans (2002) | less $LW_{in}$ in Mölg et al. |
| $LW_{out}$ | Stefan-Boltzmann law through $T_s$ (ε=0.97) | Stefan-Boltzmann law through $T_s$ | larger $LW_{out}$ in Mölg et al. (2014) (due to differences in $T_s$) |
| turbulent fluxes | | | |
| $Q_{sens}$ | simplified bulk aero-dynamic method after Oerlemans (2001) | analytical expressions of the bulk aerodynamik method following the Monin-Obukhov similarity theory (Mölg & Hardy 2004) | generally larger $Q_{sens}$ in Mölg et al. (2014) |
| $Q_{lat}$ | simplified bulk aerodynamic method after Oerlemans (2001); surface RH is set to 100% | analytical expressions of the bulk aerodynamik method following the Monin-Obukhov similarity theory (Mölg & Hardy 2004) | larger $Q_{lat}$ in this study → increased mass loss through sublimation compared to Mölg et al. (2014) |
| subsurface | | | |
| penetrating SW / subsurface melt | after Bintanja & van den Broeke (1995); depending on $SW_{net}$ | after Bintanja & van den Broeke (1995); depending on $SW_{net}$ | more subsurface melt in Mölg et al. (2014)<br>→ more negative MB |
| refreezing in snow | refreezing process is resolved vertically; layer thickness: 0.2 m | snow pack treated as a bulk medium; refreezing process is not resolved vertically | more refreezing in Mölg et al. (2014)<br>→ less negative MB |
| superimposed ice | not calculated | explicitely calculated | increased internal accumulation in Mölg et al. (2014) → less negative MB |
| densification of dry snow pack | simulated due to T and overburden pressure after Herron & Langway (1980) | simulated from the viscous fluid assumption after Sturm & Holmgren (1998) | ? |
| T | solved from the thermodynamic heat equation; layer thickness: 0.2 m | solved from the thermodynamic heat equation; layer thickness: 0.5 m | ? |
| $Q_C$ | temperature difference between surface and the two uppermost subsurface layers; variable thermal conductivity | temperature difference between surface and first subsurface layer; constant values for thermal conductivity | ? |

# 3 Energy and mass balance for Purogangri ice cap, central Tibetan Plateau, 2000-2011

## 3.1 Introduction and regional climate conditions

Purogangri ice cap (PIC) is the largest ice cap on the Tibetan Plateau (Yi et al. 2002), located in the northern central part of the TiP (Fig. 3.1). Its large area favours the application of various remote sensing techniques to determine the state of the ice cap. In this study, we use the geodetic MB from a TerraSAR-X analysis (Neckel et al. 2013, see section 3.4.1) and the snow line and ELA estimation based on MODIS data (Spieß et al. 2014, see section 3.4.2) to evaluate the MB model performance.
The region is characterized by a cold and relatively dry continental climate (see section 1.4.1). The climate chart based on HAR data (Fig. 1.16) implies that the region is still dominated by Indian monsoon circulation in summer and mid-latitude westerlies in winter. However, precipitation season already starts in March, when the westerly jet starts to shift northward (see sections 1.3.1, 1.4.1). Daily mean air temperature generated by HAR generally rise above zero from June to September in the lower regions of PIC whereas positive daily mean temperatures in the middle parts are limited to July and August. Daily mean air temperatures 2000-2011 range between -29.6°C and 10.8 C (average -8.1°C) in the lowest regions and between -32.7 and 6.4°C (average -11.3°C) at the uppermost HAR grid cell (Fig. 1.16). Lei et al. (2012) give a mean annual air temperature of -6°C around Linggo Co (40 km east of PIC, 5060 m a.s.l.). Monthly means of those HAR variables that serve as input for the applied MB model are shown in Fig. 3.2. $SW_{in}$ reaches its maximum around May and decreases in summer, when monsoonal cloud cover increases. The monsoon season is associated with annual maxima in precipitation and air pressure associated with the Tibetan High (see section 1.3.1) whereas wind speeds are generally low (Fig. 3.2). The mean annual precipitation amount at PIC (380 mm) is lower compared to Zhadang glacier (534 mm). Significant amounts of precipitation already occur in spring (Fig. 1.16, see section 1.4.1). Due to the low air temperatures all spring precipitation falls as snow, positively affecting glacier MB both through increasing accumulation and albedo (see sections 1.3.5, 1.4.1). MB model results reveal that ≈86% of total HAR precipitation fall as snow between 2000 and 2011. This supports the observed below-average mass loss at PIC 2000-2011 (Neckel et al. 2013, Lei et al. 2012) compared to other MB studies for glaciers in High Asia over a similar period (see sections 1.3.2 and 2.4.6).

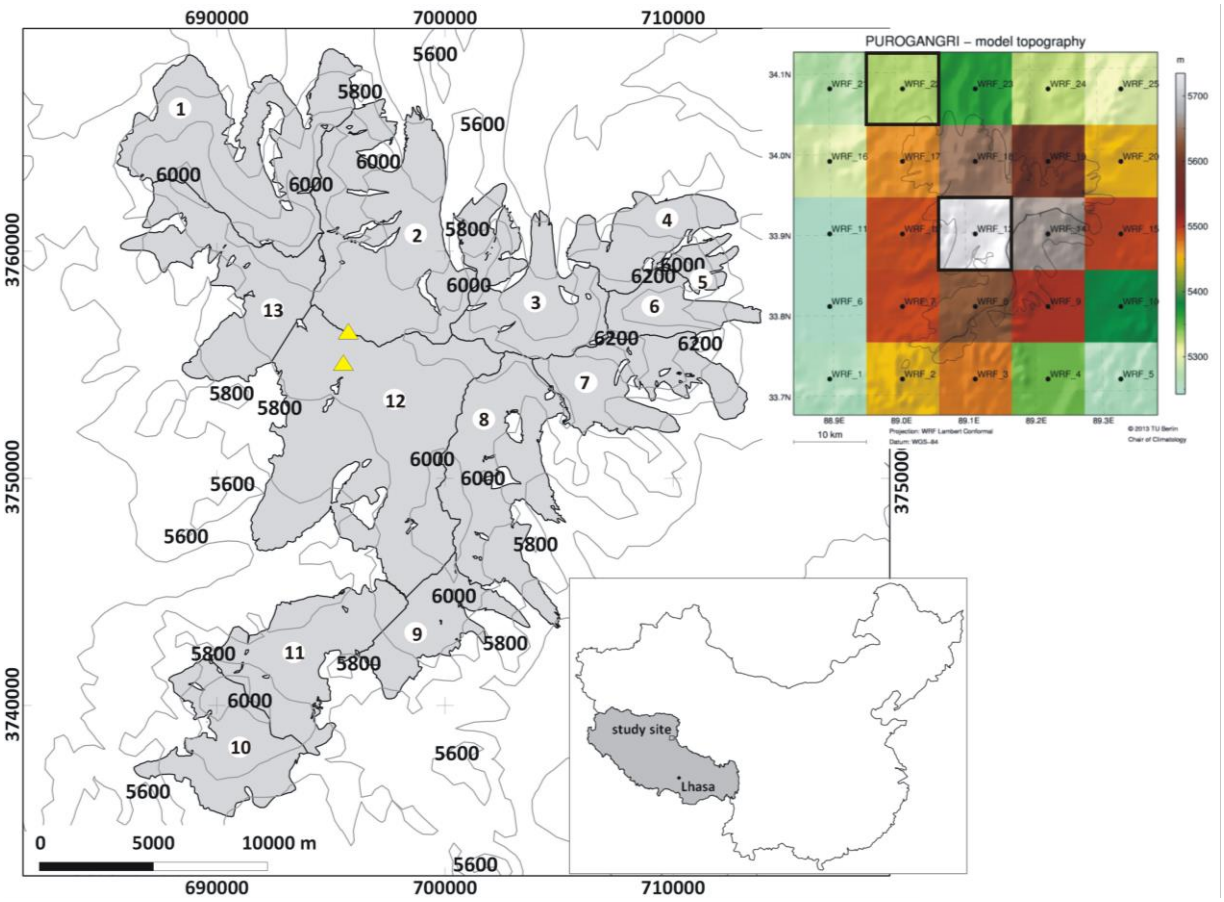


**Fig. 3.1: Purogangri Ice Cap (grey area) with glacier outlines from 2000. Numbers indicate single glaciers. Contours are in meters a.s.l. (200 m spacing); coordinate system is UTM 45N, WGS84. The lower inlay shows the location of the study site within China and Tibet Autonomous Region (grey). The upper inlay shows the HAR model topography of Purogangri Ice Cap and its surroundings. The two HAR grid cells referred to in section 3.1 and Fig. 3.2 are indicated by bold black outlines. The MB model is forced with the uppermost grid cell (WRF_13, 5734 m a.s.l.). Glacier outlines are provided by N. Neckel. Ice core drill sites of the Byrd Polar Research Center (Thompson et al. 2006) are shown as yellow triangles.**

## 3.2 Data basis

For the simulation of SEB and MB for PIC between October 2000 and 2011 we solely use HAR data from the uppermost glacier grid cell to run the distributed MB model. The model is explained in detail in section 2.3.1. It was calibrated and evaluated thoroughly against in-situ measurements at Zhadang glacier (see section 2.4) and is directly transferred and applied to PIC. The MB model structure, the applied parameterizations, constants and assumptions set for Zhadang glacier remain unchanged to ensure the required transferability of the model to other regions without in-situ measurements. Altitudinal gradients of most input parameters are required to run the distributed MB model for the total ice cap (see section 2.2.3). The altitude dependency is calculated from the 15 HAR grid cells contributing to PIC (Fig. 3.1, 3.3). Resulting gradients are -0.0083°K $m^{-1}$ for $T_{air}$, 0.022% $m^{-1}$ for *RH*, -0.067 hPa $m^{-1}$ for $\rho_{air}$ and 0.00004 mm $m^{-1}$ or 0.053% $m^{-1}$ for precipitation. The altitude dependency of *u* and *N* is not significant. Considering the spatial extent of the ice cap, vertical gradients may differ depending on the exposition to e.g. main wind direction. In this study we do not account for this and apply a single mean altitudinal gradient for each parameter for the entire ice cap.

From in-situ measurements at Zhadang glacier Mölg et al. (2012) obtained a scaling factor of 0.56 for the amount of HAR precipitation (see section 2.2.3) that was successfully applied in the HAR forced MB model runs 2001-2011 for Zhadang glacier (see section 2.4). Due to a lack of precipitation mea-

surements around PIC we also apply this scaling factor on HAR precipitation for the ice cap in the reference model run. The calculated mean annual totals are reasonable compared to values determined by Lei et al. (2012) around Linggo Co (see section 1.4.1). The distributed MB model runs on a SRTM DEM (Rabus et al. 2003), resampled to 450 m resolution. The size of the ice cap is kept constant throughout the modelling period and is based on the 2000 glacier extent. As the area change between 2000 and 2012 is small (-1.81±0.04 km$^2$, Neckel et al. 2013) the influence is negligible. $SW_{in,pot}$ is derived from the radiation model after Kumar et al. (1997) as it was done for Zhadang glacier (see section 2.3.1) and corrected for cloud cover through HAR $SW_{in}$. The uppermost HAR grid cell that contributes to the ice cap and that is used as input data covers an area of 10x10 km in the west of PIC (Fig. 3.1). Hourly mean $SW_{in,pot}$ for the respective area in the DEM is determined by the radiation model. Calculation of the correction of $SW_{in,pot}$ for cloud coverage and terrain effects is carried out as outlined in section 2.3.1 for the case of Zhadang glacier.

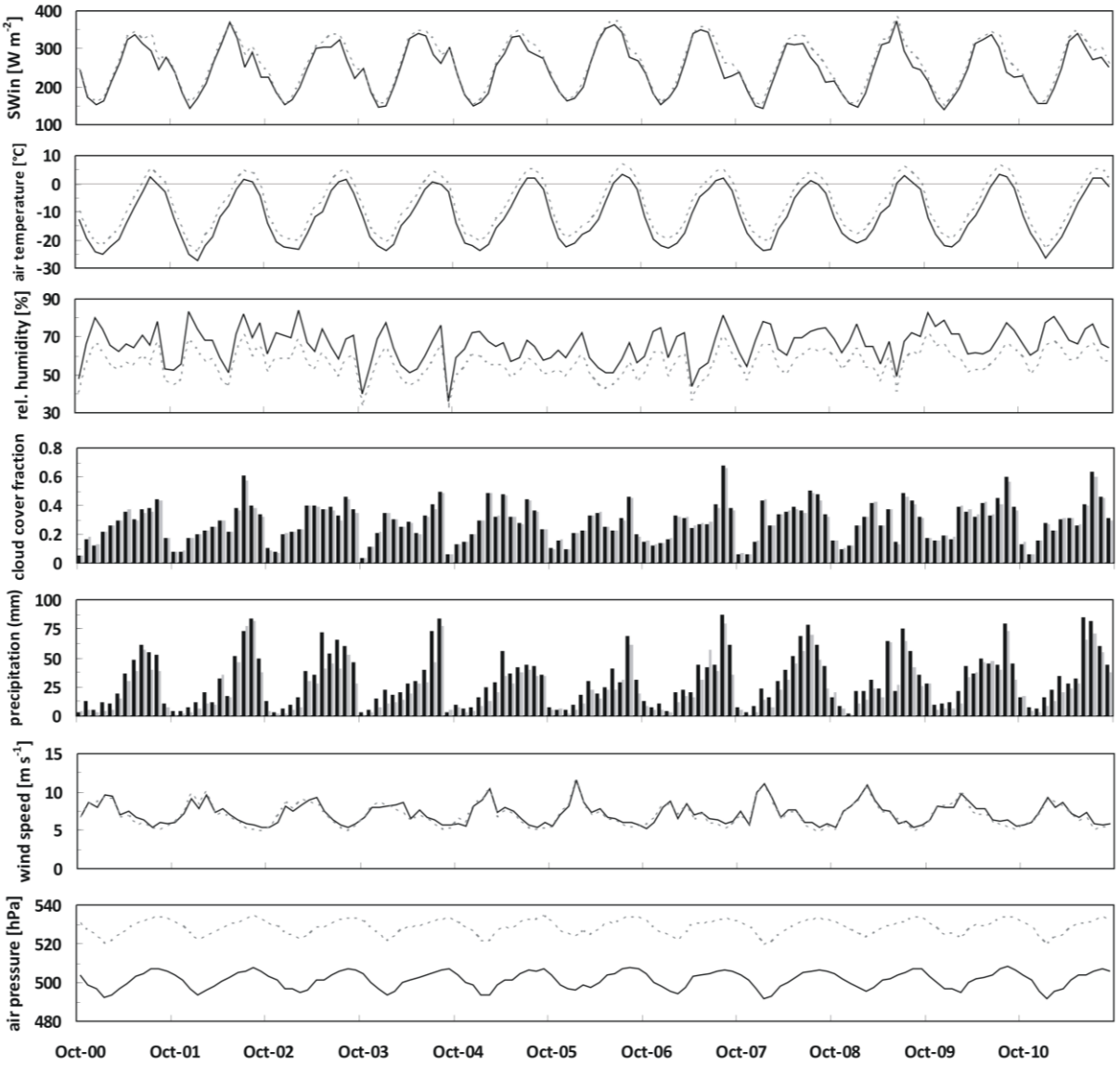


**Fig. 3.2: Monthly means or sums (precipitation) of meteorological variables at the highest (black, 5734 m a.s.l) and lowest (grey/dashed, 5326 m a.s.l) atmospheric grid cell containing Purogangri ice cap, October 2000-September 2011. The MB model is forced with hourly values of the upper grid cell (Fig. 3.1). The scaling factor of 0.56 is already applied on precipitation amounts.**

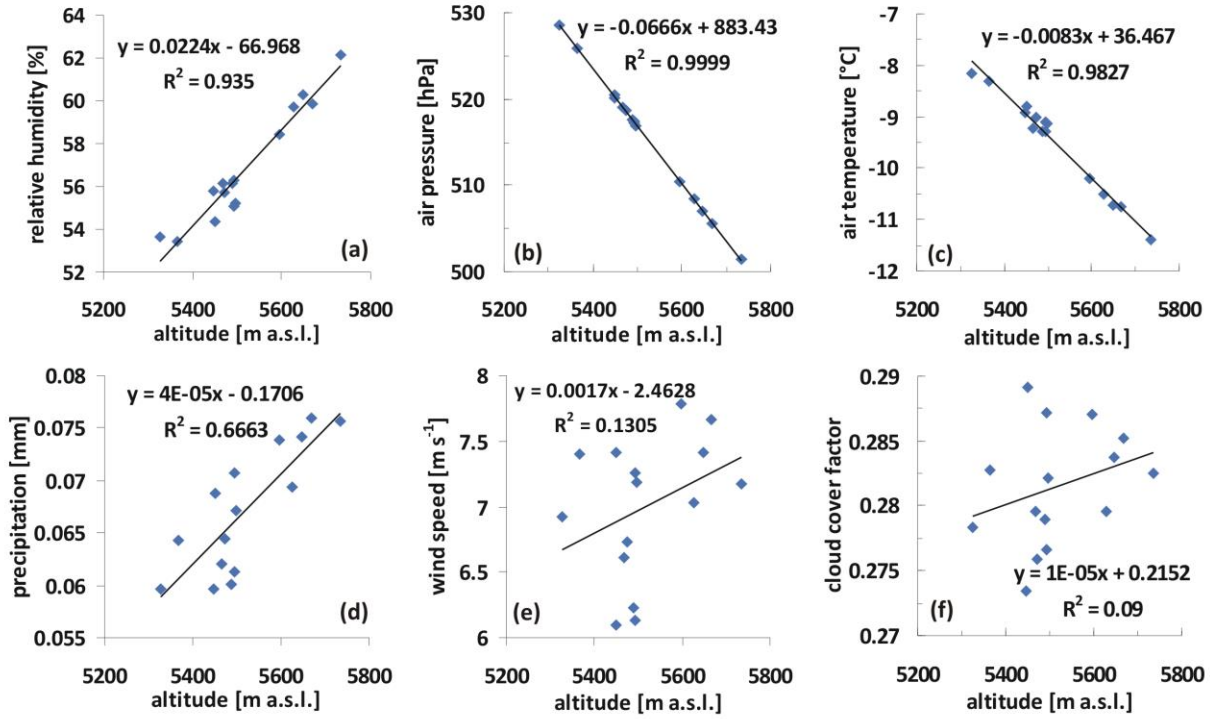


**Fig. 3.3: Altitude dependency of the HAR variables that serve as input for the MB model at PIC (without $SW_{in}$). The slope of the regression line defines the respective altitude gradient per meter. Values are means for each HAR grid cell contributing to the glacier area, 2000-2011 (Fig. 3.1).**

## 3.3 Initialisation of the SEB/MB model for application at Purogangri ice cap

Studies on surface elevation changes of PIC between 1974 and 2012 found a surface lowering in the glacier tongue regions whereas the ice cap thickens in the interior (Lei et al. 2012, Neckel et al. 2013). This thickening implies that the uppermost regions are permanently covered by snow. Therefore, we assume an initial snow depth that slightly increases linearly from 0 cm at the ELA to 20 cm in the uppermost regions. On average, the ELA is estimated between 5700 and 5750 m a.s.l. (Neckel et al. 2013, Yao et al. 2012).

To account for uncertainties in total precipitation amounts (section 3.2) and to obtain a model uncertainty for further MB calculations, we perform three model runs with varying precipitation scaling factors (0.56±0.25). The model run with a scaling factor of 0.56 is called reference run. Furthermore, HAR precipitation amounts are decreased by 25% (scaling factor 0.31) and increased by 25% (scaling factor 0.81) relative to the reference run. The lower factor (0.31) leads to a mean annual precipitation total of 195 mm (lowest HAR grid cell) to 209 mm (highest HAR grid cell). These values are reasonable compared to precipitation values determined by Lei et al. (2012) around Linggo Co (see section 1.4.1). The application of the higher scaling factor (0.81) results in mean annual precipitation sums of 430 to 545 mm, respectively.

## 3.4 Results and discussion

In this section the results of the 11-year simulation period of PIC are interpreted. The SEB/MB model explicitly calculates the different SEB and MB components and allows revealing altitudinal, inter- and intra-annual patterns on the ice cap. The results for the total simulation period are compared to geodetic MB calculations (section 3.4.1, Huintjes et al. 2013a). In a further step, the typical annual cycle

of the modelled transient snow line altitude and the inter-annual pattern of the ELA are presented and compared to the respective results from MODIS data (section 3.4.2, Huintjes et al. 2012).

### 3.4.1 SEB/MB characteristics 2000-2011

The altitudinal dependency of MB and SEB components averaged over the simulation period 2000-2011 is shown in Fig. 3.4. The given uncertainty ranges result from the model runs with varying precipitation scaling factors (see section 3.3). Precipitation amounts are both decreased and increased by 25% compared to the reference run. The reference run is characterized by a precipitation scaling factor of 0.56. The gradient of calculated MB shows a distinct steepening between 5600 and 5700 m a.s.l., slightly below the 11-year ELA (Fig. 3.4a). This pattern is similar with the one modelled for Zhadang glacier (see section 2.4.6) and was also observed at Morteratschgletscher by Klok & Oerlemans (2002). The vertical variation of the MB profile is smaller than at Zhadang glacier and varies largely with decreasing precipitation amounts. The application of a scaling factor of 0.31 on HAR precipitation results in a strong decrease in MB especially in the lower glacier areas and increases the vertical variation (Fig. 3.4a). Studies of Mölg et al. (2009) found a similar effect. A decrease (increase) in precipitation over all altitudes (Fig. 3.4c) causes more (less) surface melt mainly at the lower elevations (Fig. 3.4a). Despite less precipitation at PIC (section 1.4.1), the vertical variation of MB is smaller than at Zhadang glacier (Fig. 2.23). Reasons for this might be lower $T_{air}$, higher $\alpha$ and therefore less $SW_{net}$ and $Q_{melt}$ (and surface melt), especially in the lowermost glacier regions (Fig. 2.23, 3.4). Snowfall does not increase linearly with altitude because in the lower regions $T_{air}$ exceeds the threshold for solid precipitation more often that in the upper regions (see also Klok & Oerlemans 2002).

The shape of the vertical MB profile and its range with varying precipitation is repeated in the gradients of all ground-dependent SEB and MB variables (Fig. 3.4). In the uppermost regions differences in MB are solely forced by varying snowfall amounts. All other parameters are constant and therefore insensitive to precipitation changes. With decreasing precipitation $\alpha$ decreases strongly in the lower glacier regions (Fig. 3.4g). Values for $\alpha$ decrease from 0.65 to 0.32 in the lowest altitude band. This effect also determines the altitude dependent variation of $SW_{net}$, $T_s$ (expressed through $LW_{out}$), $Q_{sens}$, $Q_{lat}$ (sublimation), $Q_{melt}$ (surface melt) and MB. Similar effects have been observed by Braun & Hock (2004) on King George Island (Antarctica), van den Broeke et al. (2011) in Greenland and van Pelt et al. (2012) at Svalbard. Less solid precipitation (Fig. 3.4c) increases surface melt through decreasing $\alpha$ (Klok et al. 2005) especially in the lower regions where $T_{air}$ is higher. This in turn causes $SW_{net}$ (Fig. 3.4d) and $T_S$ to increase (Fig. 3.4f). Increasing $T_s$ yields smaller $Q_{sens}$ directed to the glacier surface and higher $Q_{lat}$ from the glacier surface to the atmosphere (Fig. 3.4e) (see also Klok & Oerlemans 2002). The latter result increases mass loss through sublimation in the lower glacier regions (Fig. 3.4b). These patterns and feedback mechanisms reveal that a precipitation decrease has numerous effects on all SEB and MB components. The combination of decreasing accumulation and increasing mass loss in the lower glacier regions both, from increased surface melt, decreased refreezing and increased sublimation leads to a high sensitivity of glacier MB with respect to varying precipitation at PIC. In the lowermost parts of the ice cap values for $\alpha$, surface melt, refreezing and MB indicate prevailing ablation in the reference run (scaling factor 0.56). Therefore, a precipitation decrease by 25% from the reference run has less or similar impact as in the altitude bands above. This is evident for all components but especially for $\alpha$, $SW_{net}$, $LW_{out}$, $Q_{sens}$ and refreezing (Fig. 3.4). In contrast, the effect of a precipitation increase by 25% is strongest in the lowermost parts.

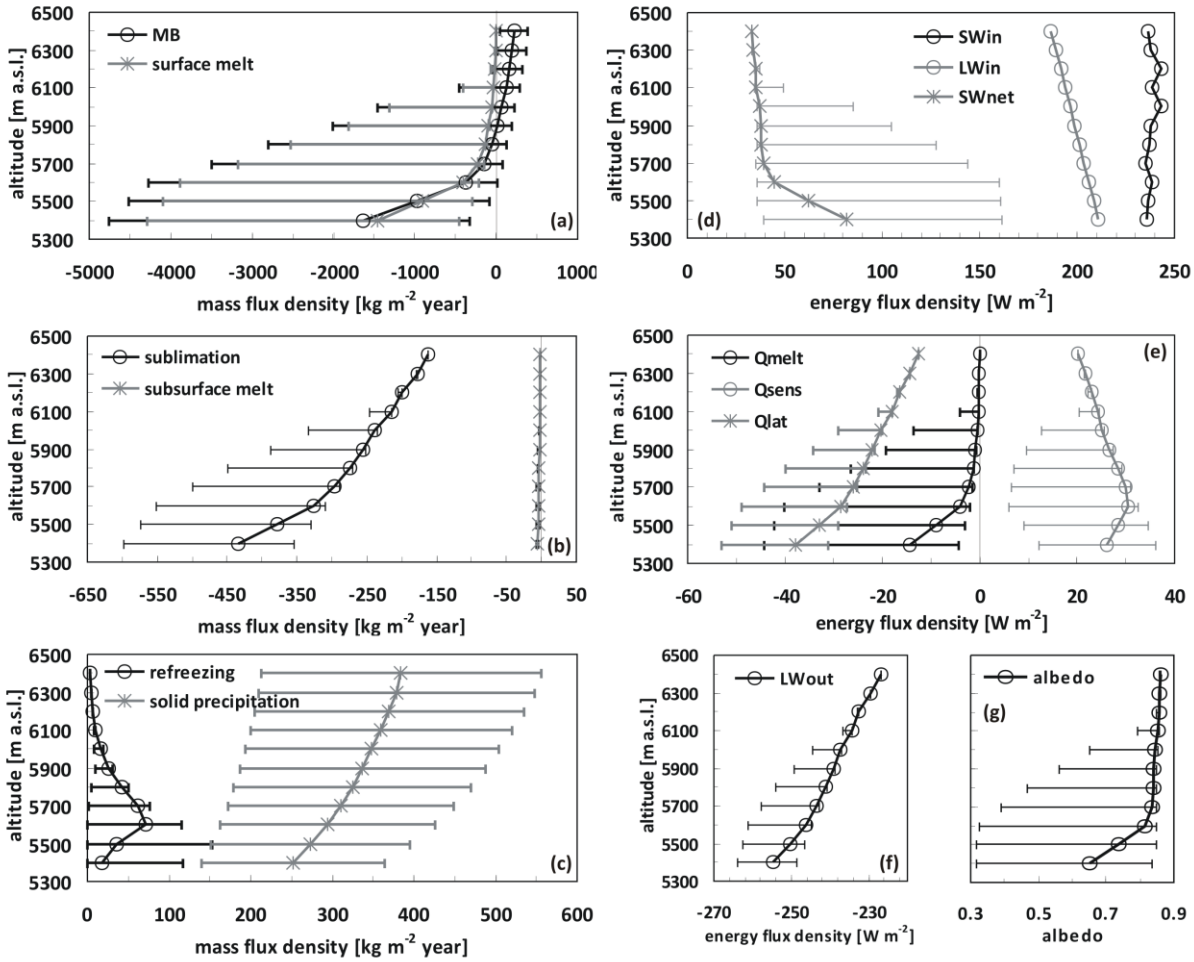


**Fig. 3.4: Modelled vertical profiles of (left) the specific mass balance and its components and (right) mean SEB components at PIC averaged over the simulation period October 2000 – September 2011. Data are averaged for 50-m altitude bands. The uncertainty ranges are calculated assuming different precipitation amounts (see section 3.3). Note the different x-axis scales of the components (negative means mass or energy loss at the glacier surface, see section 2.3.1 and Tab. 2.2 for abbreviations).**

$SW_{in}$ and $LW_{in}$ are the only ground-independent energy sources for the glacier surface (see section 2.3.1) and do not change with varying precipitation amounts (Fig. 3.4d) because energy fluxes from the surrounding terrain are not considered. $SW_{in}$ increases with altitude because the optical air mass decreases (see Klok & Oerlemans 2002) and the glacier surface is hardly affected by terrain obstructions. In the reference run refreezing is largest in ≈5600 m a.s.l. (Fig. 3.4c) where decent amounts of surface melt and a thick snow pack are present. The annual mean proportion of refreezing reached 45% in the upper glacier regions and 1% in the lowermost altitude band. A precipitation decrease by 25% from the reference run raises the altitude of maximum refreezing to 5900 m a.s.l., whereas a precipitation increase by 25% yields to a larger snow pack in the lower glacier regions and therefore significantly larger amounts of refreezing. For all other SEB and MB components, increasing precipitation by 25% compared to the reference run has a much smaller effect than a precipitation decrease by 25%. This is also evident for ELA variations. From the vertical MB profile the ELA of the reference run is estimated between 5800 and 5900 m a.s.l. (Fig. 3.4a). The ELA coincides with the results from Yao et al. (2012) and Neckel et al. (2013) (see section 3.3). A decrease (increase) of the precipitation amount by 25% rises (lowers) the ELA by ≈400 m (≈300 m). Concerning the glacier hypsometry (Fig. 1.16) an ELA increase will have important consequences for the glacier MB because the largest area proportion is located in these altitude bands.

Annual cycles of glacier-wide mean monthly SEB and MB components at PIC as calculated by the MB model for the reference run for the period 2000-2011 are illustrated in Fig. 3.5. It is obvious that the values calculated within the first months (blue box in Fig. 3.5) suffer from the errors that stem from the spin-up time of the MB model (see section 2.3.1). The first MB year is therefore not considered in the following interpretations. In general, $SW_{in}$ (+240.7 W m$^{-2}$) and $LW_{in}$ (+201.1 W m$^{-2}$) dominate the energy input over the considered period, followed by $Q_{sens}$ (+28.3 W m$^{-2}$). Energy sinks at the glacier surface are $LW_{out}$ (-240.2 W m$^{-2}$), $SW_{out}$ (-206.0 W m$^{-2}$), $Q_{lat}$ (-22.2 W m$^{-2}$), $Q_{melt}$ (-1.6 W m$^{-2}$) and $Q_G$ (-1.3 W m$^{-2}$), making $SW_{net}$ (+35.6 W m$^{-2}$, see Table 3.1) the most important energy source followed by $Q_{sens}$. This was also observed by Andreassen et al. (2008) at Storbreen (Norway), by Mölg & Hardy (2004) at Kilimanjaro and by van den Broeke et al. (2011) at glaciers in Greenland. The respective SEB values for the model runs with varying precipitation scaling factors are given in Table 3.1. The lowest values of $SW_{net}$ are evident between December and February when small precipitation amounts but frequent precipitation events coincide with low temperatures and increase $\alpha$ (Fig. 1.16, 3.5a). $LW_{net}$ shows a rather regular seasonal cycle playing a smaller role as energy sink in summer than in winter (Fig. 3.5a). This can be explained through the seasonal patterns of $LW_{in}$, depending on $T_{air}$, $e$ and $N$ (see section 2.3.1) (higher in summer), and $LW_{out}$, depending on $T_s$ (largest negative values in summer). In winter, $LW_{in}$ is significantly smaller whereas $LW_{out}$ varies at smaller scale. During winter the energy loss through $LW_{net}$ is significantly larger than the energy input through $SW_{net}$. This is also evident for the total simulation period (Table 3.1). Averaged over the whole period $Q_C$ is very small and naturally tends to zero. In winter, when the surface is colder than the underlying snow layers, $Q_C$ becomes positive. Negative $Q_C$ is evident in spring (Fig. 3.5a), when the surface warms but subsurface layers are still cold from the winter season. $Q_{PS}$ is always negative with larger values when $\alpha$ is low ($SW_{net}$ is large). The generally dry conditions on the TP lead to negative $Q_{lat}$ and significant sublimation (Fig. 3.5) with largest values in spring and autumn when $RH$ is small (Fig. 3.2), higher wind speeds drive turbulence (Fig. 1.13) and $T_s$ is not too low. Generally, monthly means of $Q_{sens}$ and $Q_{lat}$ are of opposite sign and sometimes cancel each other out. Absolute values of $Q_{sens}$ are slightly larger than $Q_{lat}$ especially in winter when $T_s$ decreases. In summer daily mean $T_{air}$ can rise up to 11°C (see section 3.1) increasing the importance of $Q_{sens}$ for surface melt (see also Braun & Schneider 2000).

Nevertheless, mass loss through sublimation plays an important role for PIC because surface melt is low (Fig. 3.5). Surface melt occurs dominantly in July-September when $LW_{net}$, $Q_{lat}$ and $Q_C$ cannot compensate the energy input through $SW_{net}$ and $Q_{sens}$ (Fig. 3.5a). In the previous months $Q_C$ is a significant energy sink due to the extremely cold subsurface layers resulting from cooling in winter. This prevents the glacier surface from melting although $T_{air}$ increases (Fig. 1.16, 3.5). In September $T_{air}$ decreases but this coincides with a distinct lowering in precipitation (Fig. 1.16). Lower $\alpha$ and positive $Q_C$ due to decreasing $T_S$ transfer energy to the glacier surface which causes melt (Fig. 3.5). The respective SEB values for the model runs with varying precipitation scaling factors are given in Table 3.1. For glacier-wide monthly SEB components of the MB model runs with ±25% of precipitation see Fig. A.1a and Fig. A.2a in the appendix.

The glacier-wide MB estimate of the reference run for the period 2001-2011 (the first year is not considered) is -436 kg m$^{-2}$ (-43.6 kg m$^{-2}$ yr$^{-1}$) (Table 3.2). In general, sublimation is the largest factor of glacier-wide mass loss (-2541 kg m$^{-2}$/ -254.1 kg m$^{-2}$ yr$^{-1}$) followed by surface melt (-1515 kg m$^{-2}$/ -151.5 kg m$^{-2}$ yr$^{-1}$) and clearly dominates ablation in winter, spring and autumn, when air temperatures are below 0°C and surface melt is absent (Fig. 1.16, 3.5b). Subsurface melt (-27 kg m$^{-2}$/ -2.7 kg m$^{-2}$ yr$^{-1}$) plays a minor role. Solid precipitation (+3316 kg m$^{-2}$/+331.6 kg m$^{-2}$ yr$^{-1}$) and refreezing (+332 kg m$^{-2}$/+33.2 kg m$^{-2}$ yr$^{-1}$) contribute to mass gain of the glacier. Maximum snowfall amounts occur in spring and summer (Fig. 1.16, 3.5b, see section 1.4.1). Refreezing at PIC happens mostly in summer, when melt water is produced at the surface and percolates through the cold winter and

spring snow layers. Air temperatures at PIC are considerably below 0°C until June (Fig. 1.16). Therefore, it can be assumed that subsurface temperatures are well below the melting point throughout the summer and allow the refreezing of considerable amounts of melt water. The reference run implies that 22% of the surface and subsurface melt water refreezes within the snow pack between 2001 and 2011. The amount is larger compared to Zhadang glacier (17%) but reasonable taking into account the different thermal regimes (see section 1.4.1). The respective MB values for the model runs with varying precipitation scaling factors are given in Table 3.2. For glacier-wide monthly MB components of the MB model runs with ±25% of precipitation see Fig. A.1b and Fig. A.2b in the appendix.

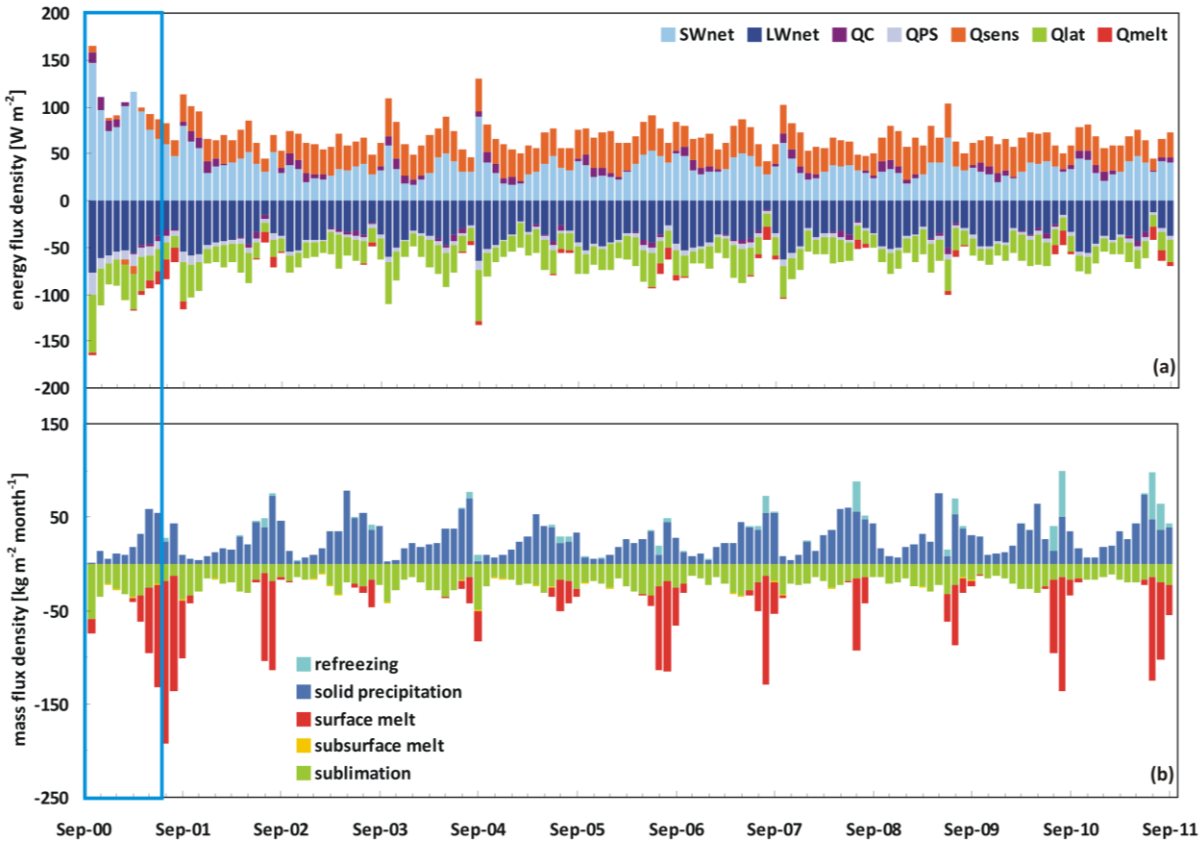


**Fig. 3.5: Glacier-wide monthly (a) SEB components (see section 2.3.1 for abbreviations) and (b) MB components from October 2000 to September 2011 at PIC (reference run). Note that the first months (blue box) should not be considered.**

Table 3.1 lists the absolute and relative contributions of the energy flux components to the overall energy turnover for the three model runs with varying precipitation scaling factors (0.56/0.31/0.81). For the considered period 2001-2011, $LW_{net}$ accounted for 30% (23%/31%), followed by $SW_{net}$ (28%/48%/ 26%), $Q_{sens}$ (21%/7%/23%), $Q_{lat}$ (17%/16%/17%) and $Q_G$ (4%/6%/4%). The relative contribution of $SW_{net}$ and $LW_{net}$, as well as of $Q_{sens}$ and $Q_{lat}$ to the total energy flux is nearly balanced for the reference run. A similar effect was observed by Braun & Hock (2004) on King George Island (Antarctica). The influence of $Q_G$ is only minor. Therefore, simulated $Q_{melt}$ is generally low at PIC over the period 2001-2011 with a minimum in 2002/03 (Table 3.1). Low $Q_{melt}$ results in low surface melt and above average MB (Table 3.2, Fig. 3.6). As simulated surface melt rates at PIC are generally low, variations in mass loss through sublimation and in mass gain through solid precipitation play an important role for the total annual MB (Table 3.2). In 2005/06 surface melt rate is largest and results in the most negative MB because mass gain from precipitation is small and cannot compensate for sub-

limation. However, in 2010/11 surface melt is only slightly lower but MB is positive due to large precipitation amounts, increased refreezing and less sublimation. Over the total simulation period, effective melt (surface melt + subsurface melt - refreezing) accounts only for 32% (84%/21%) and sublimation for 68% (16%/79%) of the total mass loss (Table 3.2).

The importance of the various SEB and MB components to surface melt and MB differs largely within the three model runs. Firstly, with decreasing precipitation compared to the reference run (scaling factor 0.31) the relative contribution of $SW_{net}$ to the total energy flux increases through decreasing $\alpha$. The differences in $SW_{net}$ between the two model runs (0.56/0.31) are largest in 2001/02, 2002/03 and 2005/06. $Q_{sens}$ is significantly smaller in the respective years indicating an increase in $T_s$. This is supported by the large negative increase in $Q_G$ meaning that more energy from the surface is transferred into the snow or ice and warms the subsurface. However, this energy transfer cannot compensate for the large $SW_{net}$ that causes a strong negative increase of $Q_{melt}$, surface melt and an above average decrease of MB in the respective years (Table 3.1, 3.2, Fig. 3.6). In the model run with decreased precipitation relative to the reference run (scaling factor 0.31) MB is closer linked to surface melt, because the contribution of effective melt to total mass loss increased to 84% (Table. 3.2). Annual and total averages of $LW_{net}$ and $Q_{lat}$ do not experience large variations through varying precipitation amounts by ±25%. However, they follow the pattern of $SW_{net}$ with larger variations in the respective years (Table 3.1) because the decrease in $\alpha$ and increasing $T_s$ affect all SEB components (see sections 1.3.4.1 and 2.3.1). The year 2005/06 is characterized by higher $Q_{melt}$ and low annual precipitation even in the reference run (Table 3.1, 3.2). Thus, the tipping point to further increased mass loss is closer than in the other MB years. A precipitation increase relative to the reference run (scaling factor 0.81) causes overall positive MB at PIC (Fig. 3.6) but the differences in the SEB and MB components to the reference run are less distinct (Tab. 3.1, 3.2, Fig. 3.6). It could be revealed in Fig. 3.4 that only the lowest regions of PIC are sensitive to an increase in precipitation by 25% whereas a decrease by 25% affects almost all regions except for the uppermost parts. Therefore, based on the reference run the overall mass balance response for a 25%-increase in precipitation is smaller than for 25% decreasing precipitation.

Model results for PIC can be evaluated against surface height changes and geodetic MB estimations from TerraSAR-X data (Neckel et al. 2013). In this study total modelled MB for the total ice cap between 2001 and 2011 with varying precipitation scaling factors (0.56/0.31/0.81) is -436 kg $m^{-2}$ (-22979 kg $m^{-2}$/+1618 kg $m^{-2}$) with annual means of -44 kg $m^{-2}$ $yr^{-1}$ (-2298 kg $m^{-2}$ $yr^{-1}$/+161 kg $m^{-2}$ $yr^{-1}$). Neckel et al. (2013) employed *Differential Synthetic Aperture Radar Interferometry* (DInSAR) to derive surface elevation changes for PIC between February 2000 and January 2012. An average ice density of 900±17 kg $m^{-3}$ was applied for the conversion into mass changes. Neckel et al. (2013) estimated an annual MB of -44±15 kg $m^{-2}$ $yr^{-1}$ for the period 2000-2012. Respective surface height change over the total ice cap is -0.58 m (-26 m / +2.1 m) within this study and -0.59±2.4 m in Neckel et al. (2013). Both results are totally within the assumed uncertainty ranges and confirm the reasonable performance of the MB model. Additionally, Neckel et al. (2013) give surface height changes and MB for the single glaciers of PIC (see Fig. 3.1). The given values are again compared to the MB model calculations. The results are visualized in Fig. 3.7. For all glaciers the results for surface height change and MB from both studies are within the given uncertainties. The results for glacier 11 can not be compared because large parts of the accumulation area are not covered by the interferometric data set (Fig. 3.8). Possible reasons for the discrepancies in surface height change and MB can be revealed from the spatial comparison of the results of both studies. It is evident in Fig. 3.8 that a glacier thinning occurred in the lower parts of the ice cap while a slightly thickening appears in the upper regions around 6000 m a.s.l. where a large proportion of the glacier area is located (Fig. 1.16). This spatial pattern agrees well within the two data sets. The result of Neckel et al. (2013) indicates a stronger

thickening in some upper parts what might be compensated through stronger thinning in the lowest regions compared to this study. It is explained in section 1.3.4.2 that the applied MB model is expected to produce a steepening of the surface elevation gradient over time compared to remote sensing results because glacier dynamics are neglected. Thus, the results for PIC show an opposite pattern (Fig. 3.8). A possible reason might be a temporal variability in the applied altitude dependent gradients of the HAR variables (Fig. 3.3). Especially changes in the gradients of $T_{air}$ and precipitation would modify the derived spatial patterns. At glacier 7 Neckel et al. (2013) found a thickening at the terminus and a thinning in the upper regions (Fig. 3.8). This was interpreted as a surging event. Obviously, exceptional glacier behaviour like this can not be captured by the applied MB model.

**Table 3.1: Mean absolute values of energy flux components as modelled for October 2000 – September 2011 and for the respective MB years with proportional contribution to total energy flux at PIC. The first value is for a precipitation scaling factor of 0.56, the numbers in brackets are for the model runs for a scaling factor for precipitation of 0.31 and 0.81. Note that values of the MB year 2000/01 are not considered in the calculation of the totals.**

| | Sum* [W m$^{-2}$] | $SW_{net}$ | $LW_{net}$ | $Q_{sens}$ | $Q_{lat}$ | $Q_G$ | $Q_{melt}$ |
|---|---|---|---|---|---|---|---|
| tot. average [W m$^{-2}$] | 136 (222 / 128) | 35 (107 / 32) | -40 (-49 / -39) | 28 (11 / 29) | -22 (-35 / -22) | -1.3 (-14 / -1) | -2 (-22 / -1) |
| 2000/01 | | 86 (156 / 59) | -51 (-59 / -46) | 9 (-2 / 18) | -32 (-43 / -27) | -8 (-22 / -4) | -6 (-31 / -1) |
| 2001/02 | | 43 (151 / 34) | -42 (-56 / -40) | 24 (-1 / 28) | -22 (-41 / -20) | -2 (-21 / -1) | -2 (-33 / -1) |
| 2002/03 | | 31 (136 / 30) | -38 (-54 / -38) | 28 (0.2 / 28) | -20 (-39 / -20) | -1 (-18 / -1) | -0.4 (-27 / -0.5) |
| 2003/04 | | 39 (120 / 39) | -42 (-53 / -42) | 32 (14 / 32) | -28 (-44 / -28) | -2 (-16 / -2) | -1 (-23 / -1) |
| 2004/05 | | 31 (112 / 31) | -37 (-49 / -37) | 29 (9 / 29) | -22 (-37 / -22) | -1 (-14 / -1) | -1 (-23 / -1) |
| 2005/06 | | 37 (121 / 35) | -42 (-53 / -42) | 33 (14 / 33) | -25 (-40 / -25) | -2 (-17 / -1) | -3 (-27 / -1) |
| 2006/07 | | 37 (115 / 32) | -39 (-50 / -39) | 27 (10 / 28) | -22 (-35 / -21) | -2 (-16 / -1) | -2 (-25 / -1) |
| 2007/08 | | 34 (88 / 32) | -38 (-47 / -38) | 26 (11 / 27) | -21 (-31 / -20) | -1 (-10 / -1) | -1 (-13 / -1) |
| 2008/09 | | 31 (76 / 31) | -39 (-45 / -39) | 31 (21 / 31) | -23 (-31 / -23) | -1 (-9 / -1) | -1 (-15 / -1) |
| 2009/10 | | 29 (74 / 28) | -35 (-41 / -35) | 28 (18 / 28) | -20 (-28 / -20) | -1 (-9 / -2) | -2 (-17 / -2) |
| 2010/11 | | 33 (76 / 31) | -39 (-45 / -39) | 25 (15 / 25) | -18 (-24 / -17) | -0.5 (-8 / -2) | -2 (-16 / -2) |
| | 100% | 28 (48 / 26)% | 30 (24 / 31)% | 21 (7 / 23)% | 17 (16 / 17)% | 4 (6 / 4)% | |

*Sum of energy fluxes in absolute values: $|SW_{net}| + |LW_{net}| + |Q_{sens}| + |Q_{lat}| + |Q_G|$

**Table 3.2: Calculated glacier-wide mass balance components for the total period October 2000 – September 2011 and for the respective MB years at PIC. The first value is for a precipitation scaling factor of 0.56, the numbers in brackets are for the model runs with lower (higher) precipitation scaling factors (0.31 / 0.81). Note that values of the MB year 2000/01 are not considered in the calculation of the total values.**

| | Solid precipitation | Surface melt | Refrozen water | Subsurf. melt | Sublimation | Mass balance* |
|---|---|---|---|---|---|---|
| tot. [kg m$^{-2}$] | 3316 (1835 / 4796) | -1515 (-20874 / -1144) | 332 (53 / 490) | -27 (-55 / -26) | -2541 (-3939/-2498) | -436 (-22979/1618) |
| 2000/01 | 280 (155 / 405) | -588 (-2958 / -56) | 5 (0 / 8) | -5 (-7 / -5) | -361 (-481 / -308) | -669 (-3291 / 44) |
| 2001/02 | 314 (174 / 454) | -205 (-3132 / -99) | 15 (0.6 / 31) | -4 (-8 / -4) | -253 (-454 / -232) | -134 (-3419 / 150) |
| 2002/03 | 377 (209 / 545) | -42 (-2532 / -46) | 10 (0.4 / 15) | -3 (-7 / -3) | -236 (-443 / -235) | 107 (-2772 / 277) |
| 2003/04 | 314 (174 / 454) | -72 (-2146 / -72) | 16 (3 / 19) | -2 ( -6/ -2) | -321 (-488 / -321) | -65 (-2464 / 77) |
| 2004/05 | 306 (170 / 443) | -77 (-2224 / -64) | 19 (3 / 23) | -4 (-6 / -4) | -256 (-413 / -256) | -12 (-2471 / 142) |
| 2005/06 | 239 (132 / 345) | -239 (-2592 / -116) | 18 (2 / 29) | -3 (-6 / -3) | -288 (-455 / -285) | -273 (-2919 / -30) |
| 2006/07 | 328 (182 / 474) | -197 (-2389 / -133) | 27 (4 / 55) | -4 (-6 / -4) | -252 (-400 / -242) | -98 (-2610 / 151) |
| 2007/08 | 389 (215 / 562) | -111 (-1271 / -110) | 40 (5 / 55) | -3 (-5 / -3) | -240 (-347 / -234) | -75 (-1403 / 271) |
| 2008/09 | 330 (182 / 477) | -117 (-1445 / -113) | 27 (6 / 40) | -1 (-3 / -1) | -258 (-345 / -258) | -19 (-1605 / 145) |
| 2009/10 | 350 (193 / 506) | -220 (-1654 / -193) | 77 (14 / 110) | -1 ( -3 / -1) | -234 (-316 / -233) | -29 (-1766 / 189) |
| 2010/11 | 370 (205 / 536) | -236 (-1489 / -200) | 84 (16 / 112) | -1 (-3 / -1) | -204 (-277 / -201) | 13 (-1549 / 246) |
| % of mass loss | | 32 (84 / 21) | | 0.7 (0.2 / 0.8) | 68 (16 / 79) | |

*Mass balance = solid precipitation + surface melt + refrozen water + subsurface melt + sublimation

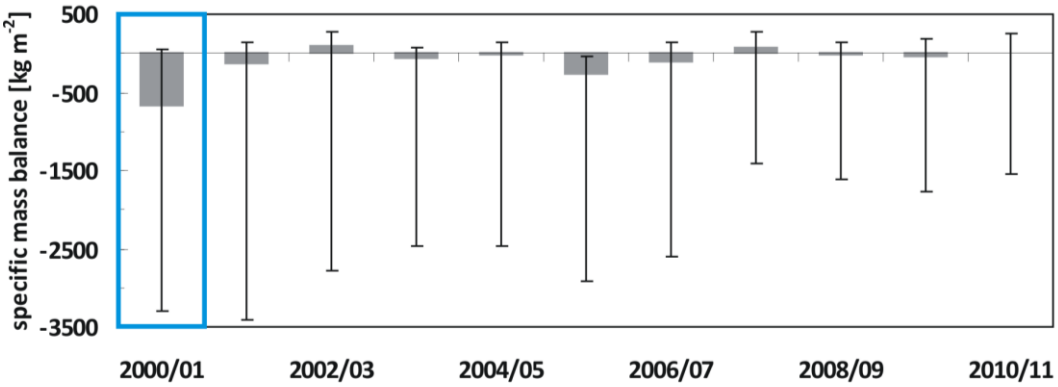


**Fig. 3.6: Glacier-wide annual MB for MB years (October – September) 2000-2011 estimated by the HAR forced MB model for PIC. The model uncertainty is calculated assuming different precipitation amounts (see section 3.3, Table 3.2). Note that the MB in 2000/01 (blue box) should not be considered.**

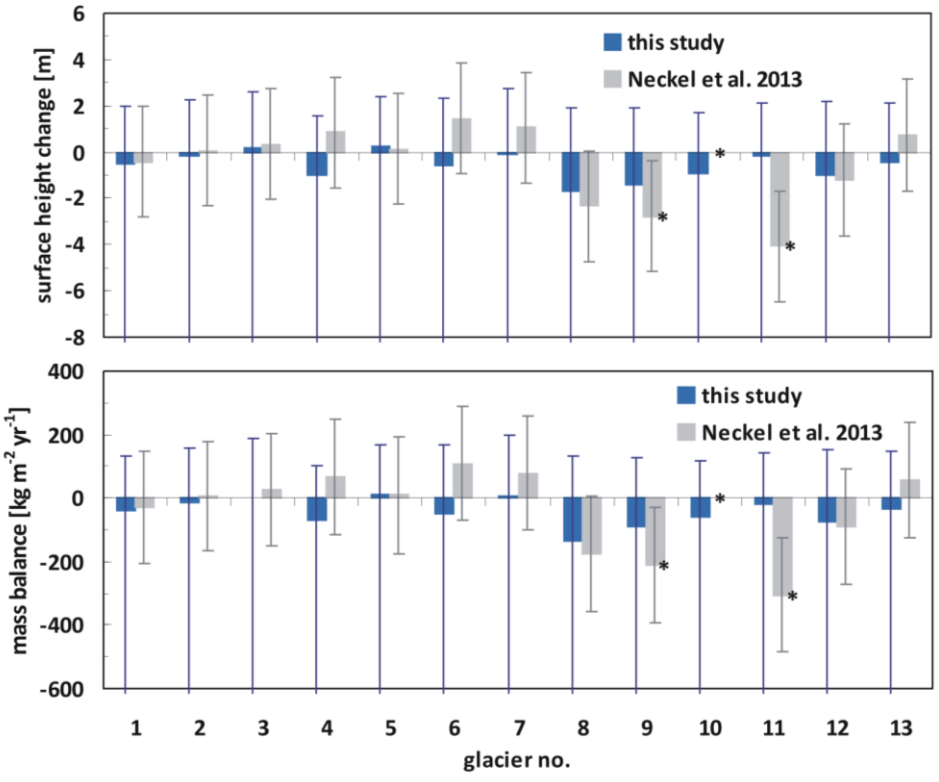


**Fig. 3.7: Mean total surface height change and mean annual MB for the single glaciers of PIC (see Fig. 3.1), 2001-2011. Values within this study are compared to the results of Neckel et al. (2013), 2001-2012. The model uncertainty is calculated assuming different precipitation amounts (see section 3.3). Stars indicate that glaciers are not or only partially covered by the interferometric data set.**

Nevertheless, the presented results for PIC agree well with the findings of Neckel et al. (2013) applying remote sensing techniques. The slightly negative MB is also in agreement with Gardner et al. (2013), Lei et al. (2012), Neckel et al. (2014) and Yao et al. (2012). The authors estimated nearly balanced MB for glaciers and ice caps in the north western TP for a similar period. This behaviour is contrasting to other regions of the TP where glacier MB is predominantly negative (see sections 1.3.1 and 1.4.1).

In 2000 two ice cores were drilled near the main ice divide of PIC (Thompson et al. 2006). The locations of the drill sites are indicated in Fig. 3.1. Thompson et al. (2006) could not reveal a firn layer and

suggest that the surface consists of bare ice caused by increasing $T_{air}$. This finding implies that the drill sites are at or below the ELA where no snow cover from the previous year remains. Modelled surface height changes within this study show that the ice core drill sites are located close to the ELA in a region of stable to slightly positive mass gain (Fig. 3.8). Thus, the observations of Thompson et al. (2006) are in accordance with the model results of this study.

Phan et al. (2014) calculated surface elevation changes for glaciers on the TP between 2003 and 2009 from ICESat and SRTM DEM. The authors especially focused on different glacier behaviour on short distances dependent on orientation and position in a mountain range. The results indicate that the surface elevation of most observed glaciers at north facing slopes increased or decreased slightly. South facing glaciers in the same regions generally showed a stronger decrease of surface height (Phan et al. 2014). For most of the single glaciers of the PIC this relation can be confirmed. Most glaciers that are north or northeast oriented show positive or small negative surface height changes (glaciers 1, 2, 3, 5, 7, 11, see Fig. 3.1, 3.7). The south exposed glaciers (8, 9, 10, 12) generally reveal increased negative surface height changes (Fig. 3.7).

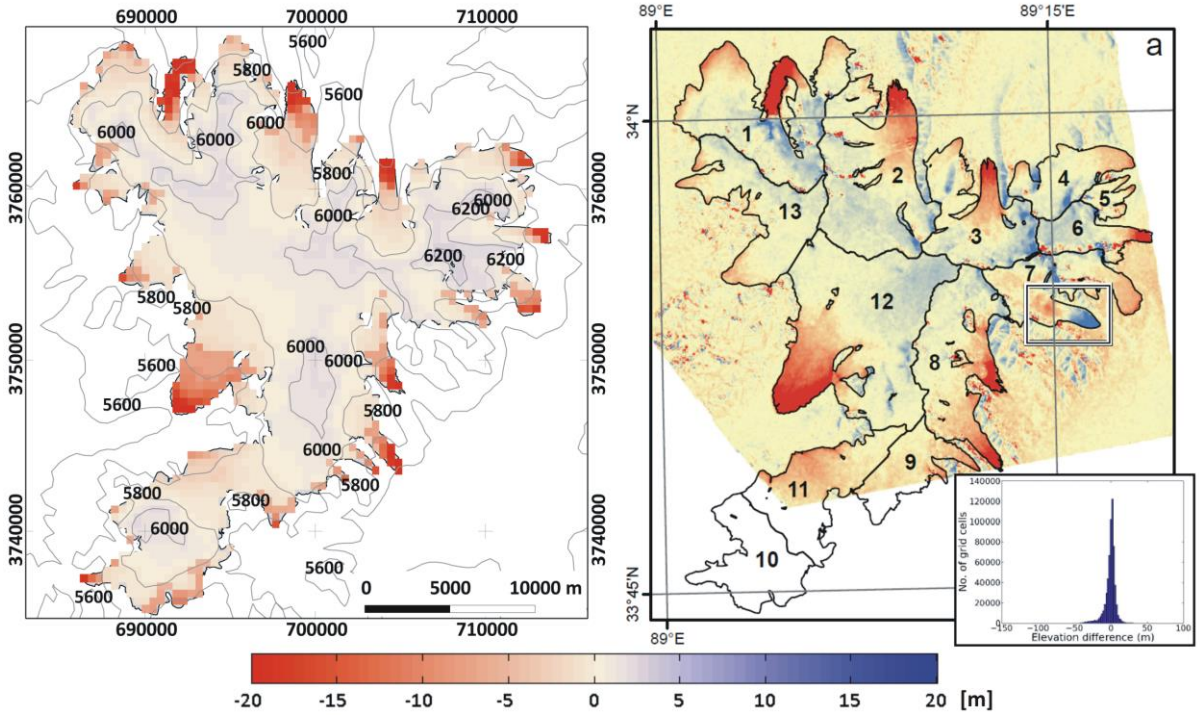


**Fig. 3.8: Spatial comparison of modelled surface height change of PIC for the reference run, 2001-2011 (left), with the results of Neckel et al. (2013) (right).**

## 3.4.2 Snow line and ELA characteristics 2000-2011

To revive the studies on the inter- and intra-annual snow line and ELA characteristics at Zhadang glacier (see section 2.4.4) and to further evaluate the MB model performance, mean intra-annual variations of the glacier-wide mean altitude of the transient snow line are calculated from the MB model results (Fig. 3.9). The mean monthly transient snow line altitude is calculated from the daily MB model output and averaged for every month over the simulation period 2001-2011. The snow line is defined as the area where snow free and snow covered pixels adjoin each other (see section 2.4.2.5). The given values refer to the reference run with a precipitation scaling factor of 0.56. Based upon the reference run precipitation amounts are decreased and increased by 25%, respectively, to obtain the model uncertainty (see section 3.3).

Per definition, isolated patches of exposed ice are not called snow line (Cogley et al. 2011). However, within the MB model this is not considered. In the reference run mean monthly snow lines at PIC between 2001 and 2011 show a rather constant altitude around 5700 m a.s.l. from January to May (Fig. 3.9). In these months the mass gain through solid precipitation increases continually (Fig. 1.16, 3.5) but is mostly compensated through increasing sublimation (Fig. 3.5). In the lower regions of the ice cap, mass loss through sublimation is much stronger than the amount of solid precipitation (Fig. 3.4). Thus, a snow line is visible even in winter. In June $T_{air}$ rises above zero (see section 3.1) and small amounts of surface melt contribute to the mass loss by sublimation. The transient snow line altitude rises slowly (Fig. 3.9). In July $T_{air}$ and surface melt reach their maximum. The generally small precipitation amounts can not compensate for the mass loss and cause the rise of the snow line altitude to its annual maximum around 5800 m a.s.l. (Fig. 3.9). The refreezing process plays an important role for the accumulation at PIC but does not directly influence the snow line. From August to October the mean snow line altitude decreases to 5700 m a.s.l. due to larger precipitation amounts and decreasing $T_{air}$ and surface melt (Fig. 1.16, 3.5). In November and December the transient snow line again rises slightly (Fig. 3.9). This can be explained by minimum precipitation and increasing sublimation (Fig. 3.5). The mean transient snow line altitude between 2001 and 2011 is located in ≈5720 m a.s.l.

With decreasing precipitation amounts by 25% compared to the reference run the snow line altitude rises around 90 m with the largest sensitivities in spring and autumn (Fig. 3.9) when precipitation amounts are average or below average sublimation is large and large $SW_{in}$ causes small amounts of surface melt (Fig. 3.5). A lower $\alpha$ with decreasing precipitation enhances these processes. A precipitation increase by 25% lowers the mean snow line altitude by approx. 10 m with largest sensitivities in July, April, September and December/January (Fig. 3.9). During these months a precipitation increase by 25% has a larger impact because the periods are characterized either by high $T_{air}$ and surface melt (July), large sublimation (April/ September) or very low precipitation (December/January) (Fig. 1.16, 3.5). A precipitation increase by 25% would therefore partly compensate for the mass losses and decrease the snow line altitude (Fig. 3.9).

Results of Spieß et al. (2014) from the evaluation of the MODIS snow product show a similar intra-annual pattern as revealed from the reference run. In her study snow line altitudes are similar in winter and generally lower by approx. 50 m in summer (Fig. 3.9). The discrepancies in the absolute altitudes might be caused by the coarse resolution of both datasets (MB model: 450 m, MODIS: 500 m). From the MB model evaluation in section 3.4.1 we can conclude that the modelled accumulation in the upper regions of the PIC is too small in the reference run. This implies that modelled snow line altitudes may be smaller than they are actually are. Another source of uncertainty is the derivation of the snow lines from MODIS data through uncertainty in albedo (Spieß et al. 2014). However, the overall inter-annual pattern of the transient snow line altitude is similar in both approaches and the evident discrepancies are small concerning the coarse resolution of both datasets.

The snow line at the end of the ablation season (*annual snow line*) usually represents its highest position during a MB year (Cogley et al. 2011). For glaciers on the TP this is not generally the case because many of them belong to the '*summer-accumulation type*' and are characterized by simultaneous accumulation and ablation seasons (see section 1.3.5). It is evident from Fig. 3.9 that at PIC the highest snow line occurs in July when $T_{air}$ reaches its maximum and precipitation is low (Fig. 1.16, 3.5). For glaciers with no or little superimposed ice the annual snow line can be used as a proxy for the annual ELA. The annual ELA is defined as the ELA at the end of the MB year (Cogley et al. 2011) and allows estimations on the glacier MB. At PIC the amount of refreezing plays a significant role in the mass budget especially in summer when surface melt is large (Fig. 3.5). The surface melt lowers the snow pack but certain amounts refreeze within the snow and remain as superimposed ice when

the snow pack is completely removed. This superimposed ice zone still belongs to the accumulation area of the glacier although it is located below the annual snow line. Therefore, the estimation of the annual ELA through the annual snow line might lead to an overestimation of the first (Cogley et al. 2011). In this study, the annual ELA is directly calculated from the annual MB at the end of September. The result is compared to the ELA derived from the annual snow line by Spieß et al. (2014). The modelled annual ELA for 2000 to 2011 at PIC is shown in Fig. 3.10. As expected, the ELA follows the MB pattern (Fig. 3.6) with lower ELA in positive or slightly negative MB years and high ELA in negative MB years.

From the vertical MB profile for the reference run for PIC in section 3.4.1 the ELA between 2000 and 2011 is estimated around 5800 m a.s.l. (Fig. 3.4a). The average over the calculated annual ELA leads to a value of 5790 m a.s.l. for the reference run. This value agrees with the altitude given by Neckel et al. (2013) and Yao et al. (2012). A precipitation decrease by 25% compared to the reference run raises the ELA by 310 m, a precipitation increase by 25% lowers the ELA by 210 m. Results of Spieß et al. (2014) from the evaluation of the MODIS snow product show a similar inter-annual structure but less variability (Fig. 3.10). The altitudes given by Spieß et al. (2014) all range between 5760 and 5830 m a.s.l. whereas the ELA in this study ranges from 5600 to 6000 m a.s.l.. However, the differences are within the given uncertainties. The evident discrepancies are small concerning the coarse resolution of both datasets (MB model: 450 m, MODIS: 500 m) and confirm the reasonable performance of both the MB model in this study and the remote sensing approach of Spieß et al. (2014).

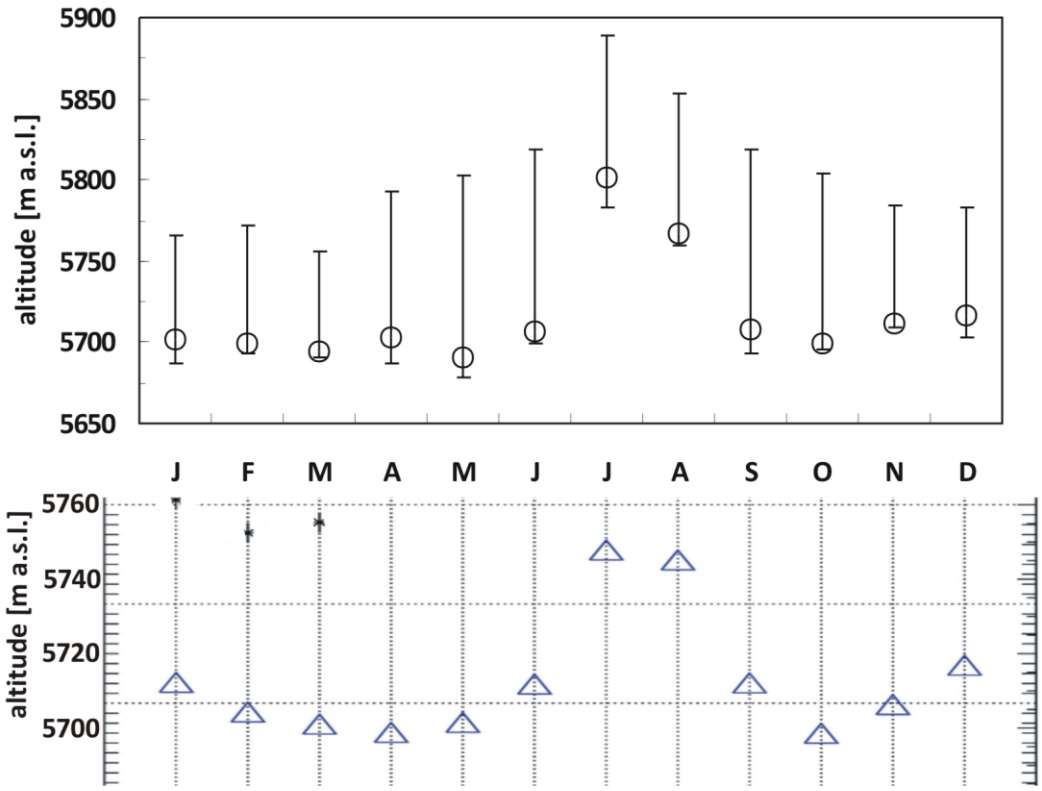


**Fig. 3.9: Comparison of modelled mean intra-annual snow line pattern at PIC, 2001-2011 (top), with the results of Spieß et al. (2014) (bottom). The model uncertainty is calculated assuming different precipitation amounts (see section 3.3).**

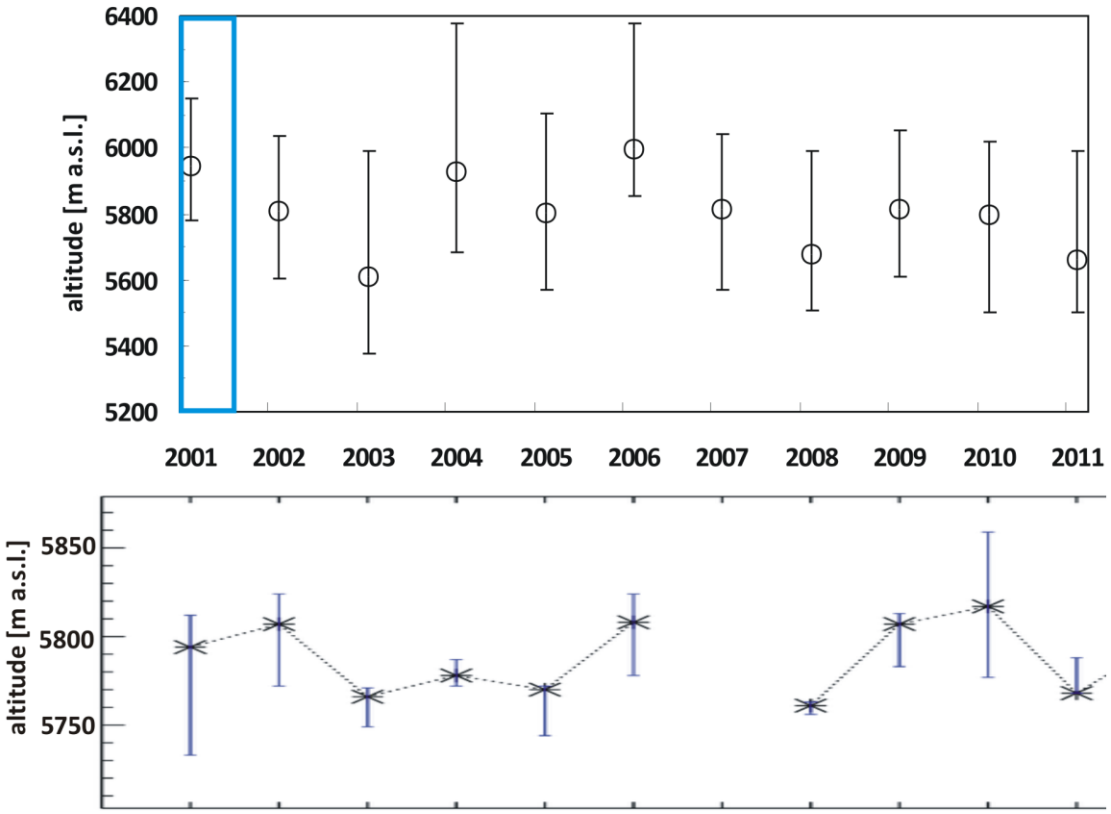


**Fig. 3.10: Comparison of modelled annual ELA at PIC, 2000-2011 (top), with the results of Spieß et al. (2014) (bottom). The uncertainty of the MB model is calculated assuming different precipitation amounts (see section 3.3). Note that the ELA in 2001 (blue box) should not be considered.**

The relation between annual AAR and annual MB at PIC for the period 2001-2011 for the reference run (precipitation scaling factor 0.56) is visualized in Fig. 3.11. The linear relationship between AAR and MB at PIC is significant ($R^2$=0.74, Fig. 3.11). Annual AAR varies between 28% in 2003/04 and 91% in 2002/03. For the total simulation period of the reference run the AAR is 58%. The $AAR_0$ is estimated to be 69%. The index $\alpha_d$ after Dyurgerov et al. (2009) measures the glacier's displacement from the equilibrium (see section 2.4.6). For PIC $\alpha_d$ is determined to be -16%. Thus, the ice cap has to decrease its area only slightly to reach its equilibrium state for the climate conditions of the simulation period with a precipitation scaling factor of 0.56.

A precipitation decrease of 25% compared to the reference run results in an AAR of 1.5% and in a $\alpha_d$ of -98%. This implies that PIC would have to decrease its area largely to reach its equilibrium. Only 8 $km^2$ would remain in steady state with contemporary climate forcing when assuming a precipitation scaling factor of 0.31. A precipitation increase of 25% compared to the reference run leads to an AAR of 94% and in a $\alpha_d$ of +36%. Thus, the ice cap would increase its area and advance in order to reach its equilibrium state when applying a precipitation scaling factor of 0.81. In conclusion, it is obvious that the ice cap's area and volume are highly sensitive to even small long term trends in precipitation.

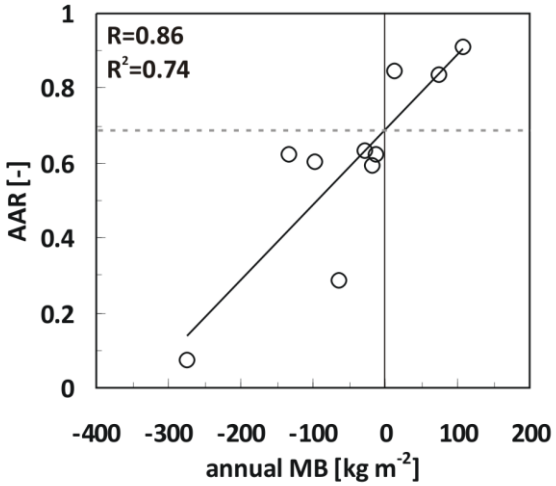


**Fig. 3.11: Relation between annual MB and AAR at PIC, 2001-2011, for the MB model run with a precipitation scaling factor of 0.56. The AAR at MB=0 denotes $AAR_0$.**

## 3.5 Conclusion regarding model results for Purogangri ice cap

Purogangri ice cap (PIC) is the largest ice cap on the Tibetan Plateau with an area of ≈400 km$^2$. Its remote location and the large area hamper in-situ measurements but favour the application of various remote sensing techniques. Using the 11-year HAR data set, SEB and MB components of PIC are calculated for 2000-2011 and interpreted concerning their altitudinal gradients and their inter- and intra-annual patterns. To account for uncertainties in total HAR precipitation amounts and to obtain a model uncertainty for further MB calculations, we perform three model runs with varying precipitation scaling factors (0.56±0.25). In the reference run a factor of 0.56 is applied. This number was obtained by Mölg et al. (2012) for Zhadang glacier. The same factor is successfully applied in this thesis in the HAR forced MB model runs 2001-2011 for Zhadang glacier (see section 2.4). Due to a lack of precipitation measurements directly at the ice cap this scaling factor is also applied on HAR precipitation for PIC. The obtained absolute values are reasonable compared to precipitation values determined by Lei et al. (2012) around Linggo Co (see section 1.4.1). For the reference run, the total energy turnover at the glacier surface is dominated by $LW_{net}$ with 30%. The influence of $LW_{net}$ and $SW_{net}$ (28%) is nearly equal. Increased $\alpha$ decreases the proportion of $SW_{net}$ compared to Zhadang glacier and increases the relative contribution of the turbulent fluxes (38%) especially through $Q_{sens}$. $Q_{sens}$ is large because of high $T_{air}$ in summer and low $T_s$ in winter. A share of 22% of surface and subsurface melt water refreezes within the snow pack. The amount is larger compared to Zhadang glacier (17%) but reasonable taking into account the different thermal regimes (see section 1.4.1). Fujita & Ageta (2000) and Fujita et al. (2007) obtained a value of 20% over a shorter period for Xiao Dongkemadi glacier that is also a cold type glacier. The cold and dry atmosphere on the continental central TP account for the fact, that effective melt accounts only for 32% and sublimation for 68% of the total mass loss in the reference run (Table 3.2). The variation of HAR precipitation as input for the MB model through the application of three different scaling factors creates a range of uncertainty for every SEB and MB component. The overall uncertainty for the annual MB over the simulated period 2000-2011 shows an inter-annual variability depending on the sensitivity of the different parameters on the precipitation amount (Fig. 3.6, Tables 3.1, 3.2). Only the lowest regions of PIC are sensitive to an increase in precipitation by 25% whereas a decrease by 25% affects almost all regions except for the uppermost parts (Fig. 3.4). Therefore, the overall sensitivity for a 25% precipitation increase is smaller than for a 25%-increase relative to the reference run. The ELA is estimated to be located

around 5790 m a.s.l. in the reference run. A precipitation decrease by 25% raises the ELA by ≈300 m, a precipitation increase by 25% lowers the ELA by ≈200 m. These values are within the range given by Neckel et al. (2013) and Yao et al. (2012).

The large area of the PIC favours the application of remote sensing approaches for the analysis of surface elevation changes, MB and snow line altitudes. These data sets are a good opportunity to evaluate the MB model performance because the remote location and the large size of the ice cap hamper in-situ measurements. The comparison of the MB model with glacier-wide surface height changes and geodetic MB estimations from TerraSAR-X data for a similar period (Neckel et al. 2013) show only minor discrepancies for the reference run. Concerning the single glaciers of the ice cap the results for surface height change and MB from both studies are within the given ranges of uncertainties despite the coarse resolution of 450 m of the MB model domain. The spatial evaluation (Fig. 3.7, 3.8) shows no regional errors. This justifies the application of only one mean altitudinal gradient for each HAR input parameter for the entire ice cap (see section 3.2). In general, the MB model simulates less glacier thickening in some higher regions for the reference run what is compensated by less thinning in the lowest parts compared to Neckel et al. (2013). This suggests general discrepancies or a temporal variability in the applied altitude dependent gradients of the HAR variables. Due to a lack of in-situ measurements at the PIC uncertainties in the obtained gradients can not be quantified in more detail.

The model evaluation against MODIS derived snow line altitude and annual ELA (Spieß et al. 2014) confirms the overall satisfying model performance for PIC considering the reference run. The intra- and inter-annual patterns of both studies agree very well whereby modelled snow line altitude is higher in summer and the annual ELA varies stronger between the respective years. The calculated slightly negative overall MB in the reference run is in agreement with Gardner et al. (2013), Lei et al. (2012), Neckel et al. (2014) and Yao et al. (2012). These authors estimated nearly balanced MB for glaciers and ice caps in the north western TP for a similar period. These results support the applicability of the precipitation scaling factor of 0.56 revealed for Zhadang glacier (see section 2.2.3) also for PIC.

It can be concluded from the application of the MB model to PIC that the derived intra- and inter-annual cycles of SEB and MB components are within reasonable limits. The model result largely depends on the respective patterns of the input parameters from HAR. The obtained SEB and MB components are consistent with each other because they interact through physical relationships (see sections 1.3.4 and 2.3.1). The application of a precipitation scaling factor of 0.56 as determined for Zhadang glacier yields satisfying results that could be confirmed based on different remote sensing approaches.

# 4 Energy and mass balance for Naimona'nyi glacier, south western Tibetan Plateau, 2000–2012

## 4.1 Introduction and regional climate conditions

Naimona'nyi glacier is a north to northwest exposed valley glacier (≈7.8 km$^2$), located northeast of Naimona'nyi (chin. Gurla Mandhata) the highest peak of the Nalakankar Himal (≈7700 m a.s.l., Fig. 4.1). The glacier was chosen as a measurement site within the WET project because the staff from ITP conducted climatological and glaciological measurements at the glacier over a shorter period a few years ago (Yao et al. 2012) and the glacier is one of the ice core drilling sites of the ITP (Liu et al. 2006). In September 2011 an AWS was installed on an ice cored moraine west of the glacier tongue (see section 1.4.2.2). The comparison of HAR data with AWS measurements (see section 1.4.2.2) reveals that daily mean $T_{air}$ from HAR is up to 10°K lower than the respective AWS measurement. Hourly $T_{air}$ even differs by up to 12°K. The discrepancies partly might be explained by the influence of terrain effects in the very narrow valley of the glacier tongue (Fig. 4.1). These small scale patterns can not be captured by the atmospheric model (10 km resolution, see section 2.2.3). Thus, the estimates of the MB model forced with HAR data can be expected to differ from in-situ measurements or remote sensing analyses. We use surface height changes and the geodetic MB derived from the analysis of Pleiades data (Holzer et al. 2014) to evaluate the model performance.

The region is clearly dominated by Indian monsoon in summer and mid-latitude westerlies in winter (see section 1.4.1) and most atmospheric variables, generated by HAR show a pronounced seasonal contrast (Fig. 1.14, 1.15, 4.2). Daily mean air temperatures generated by HAR generally rise above zero from mid July to August. Daily means range between -31.8°C and +3.8 C (average -11.6°C) within the period 2000-2012. Monthly means of those HAR variables that serve as input for the applied MB model are shown in Fig. 4.2. $SW_{in}$ reaches its maximum around May and decreases in summer, when monsoonal cloud cover is large. The monsoon season is associated with annual maxima in precipitation, RH and air pressure associated with the Tibetan High (see section 1.3.1) whereas wind speeds are generally low (Fig. 4.2). The glacier is situated in the same mountain chain as Halji glacier but ≈26 km to the north (see sections 1.4.1, 1.4.2.2). The lee-effect of the more northern location is clearly evident in mean annual precipitation amounts (506 mm) that are considerably smaller than at Halji glacier (605 mm) despite the higher altitude of the considered HAR pixel (see section 1.4.1). However, Naimona'nyi glacier has a much larger area and a greater altitudinal extent than Halji glacier (Fig. 1.12, 1.14). Precipitation amounts increase with altitude and $T_{air}$ from HAR is already low

in the lower regions and decreases with altitude. The effect will be low melt rates and significant amounts of solid precipitation. Therefore, it can be assumed that the estimated mass loss from the MB model from 2000-2012 is not large. In contrast, Yao et al. (2012) report a mean ELA around 6300 m a.s.l. and significant mass loss between 2004 and 2010.

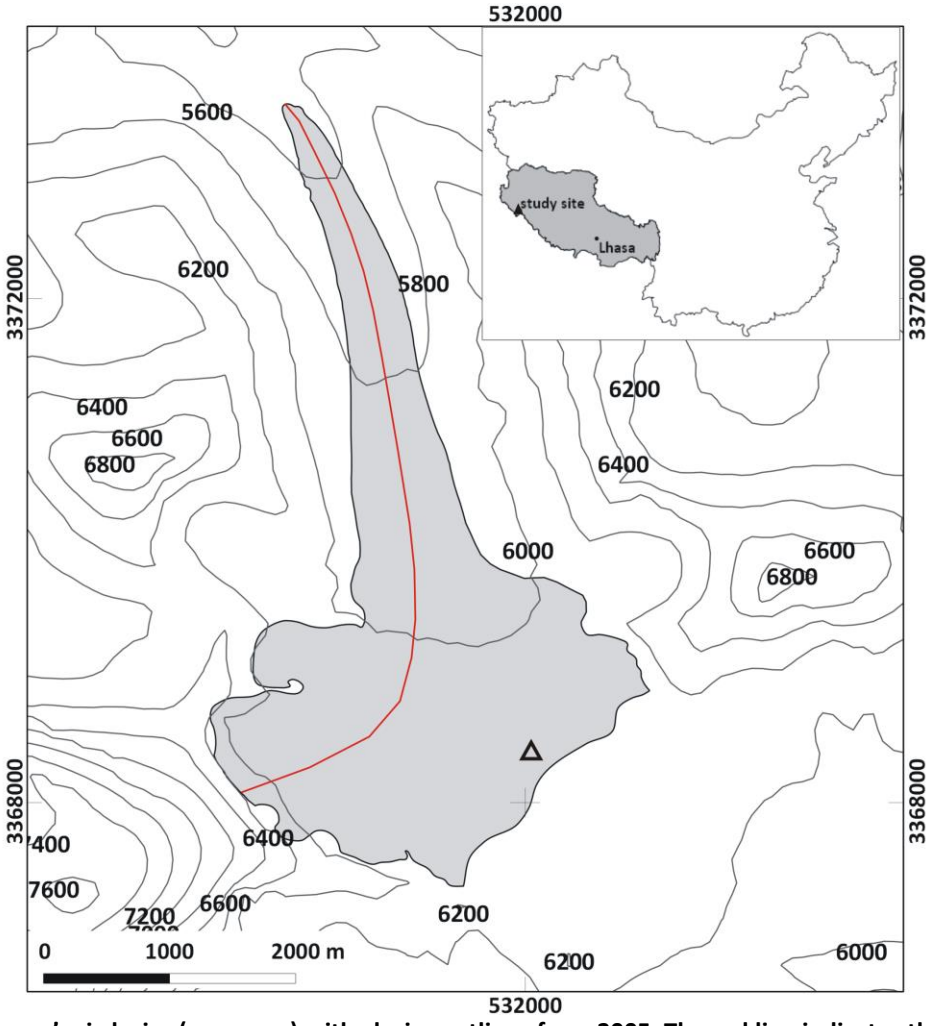


**Fig. 4.1: Naimona'nyi glacier (grey area) with glacier outlines from 2005. The red line indicates the MB profile (see section 4.5); the triangle marks the DEM pixel that is used for the cloud correction of potential $SW_{in}$. Contours are in meters a.s.l. (200 m spacing); coordinate system is UTM 44N, WGS84. The inlay shows the location of the study site within China and Tibet Autonomous Region (grey). Glacier outlines are provided by N. Holzer.**

## 4.2 Data basis

For the simulation of SEB and MB for Naimona'nyi glacier for the period October 2000-2012 we solely use HAR data from the grid cell containing the glacier. The model is explained in detail in section 2.3.1. The model structure, the applied parameterizations, constants and assumptions set for Zhadang glacier remain unchanged and are directly transferred to Naimona'nyi glacier. Altitudinal gradients of most input parameters are required to run the distributed model for the total glacier area (see section 2.2.3). The altitude dependency is calculated from the nine HAR grid cells surrounding Naimona'nyi glacier (Fig. 4.3). Resulting gradients are -0.007°K $m^{-1}$ for $T_{air}$, 0.018% $m^{-1}$ for $RH$, -0.068 hPa $m^{-1}$ for $\rho_{air}$ and 0.00009 mm $m^{-1}$ or 0.089% $m^{-1}$ for precipitation. No explicit altitude dependency is evident for $u$ and $N$.

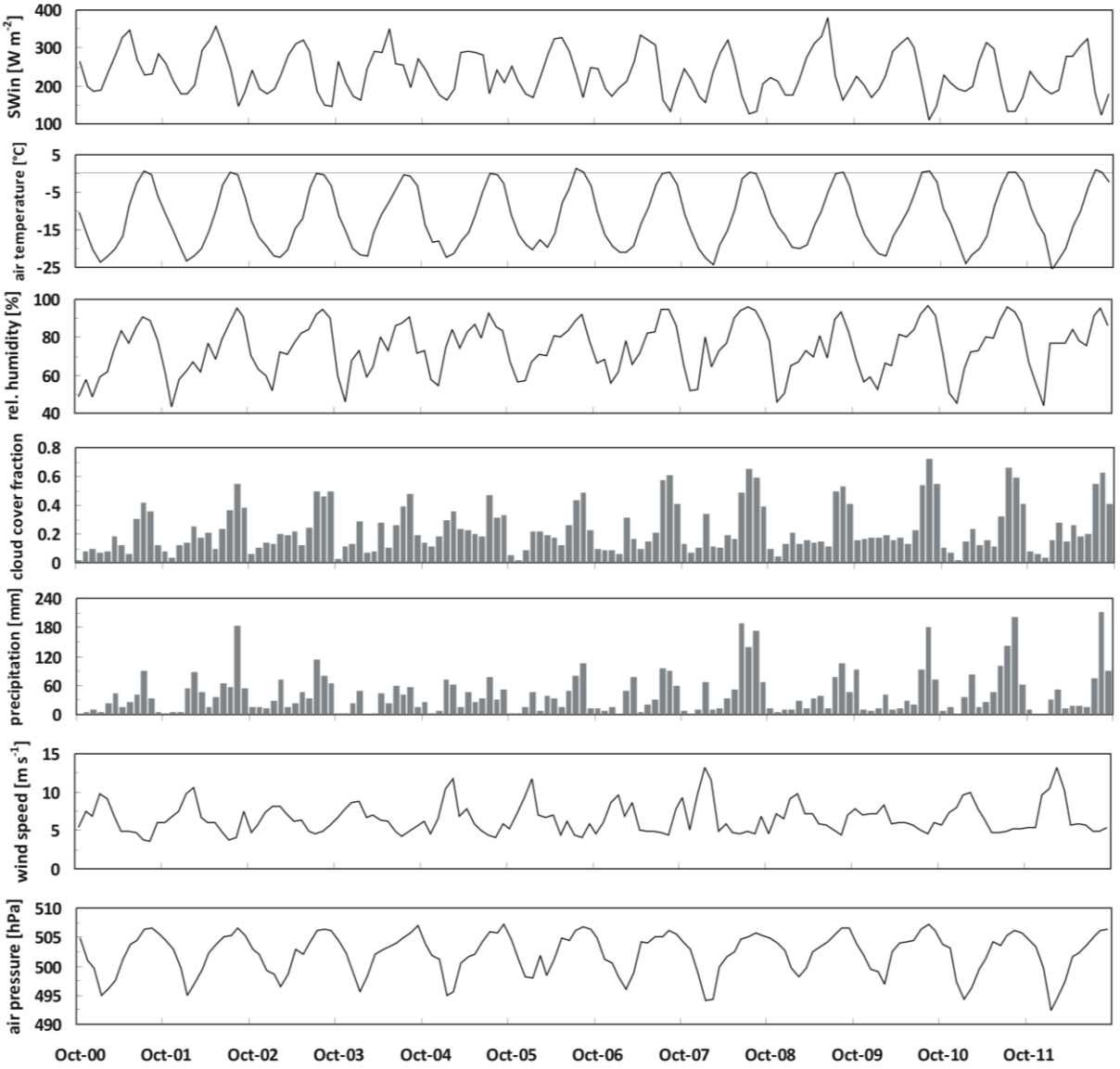


**Fig. 4.2: Monthly means or sums (precipitation) of meteorological variables at the atmospheric grid cell containing Naimona'nyi glacier (5750 m a.s.l.), October 2000-September 2012. The MB model is forced with hourly values of these variables. The scaling factor of 0.56 is already applied on the precipitation amounts.**

The obtained scaling factor of 0.56 for the amount of HAR precipitation at Zhadang glacier (see section 2.2.3) was already applied in the reference MB model runs in the previous studies within this thesis. Since HAR precipitation amounts can not be validated at Naimona'nyi glacier, the same scaling factor is applied in the reference run in this chapter (Fig. 1.14, 4.2) as for PIC and Zhadang glacier. The distributed model runs on a SRTM DEM with a resolution of 90 m (Rabus et al. 2003). The glacier area is kept constant throughout the modelling period and is based on the 2005 glacier extent (Fig. 4.1). As the area change between 2000 and 2010/13 is small (Fig. 4.7) the influence of changing glacier area is negligible. Potential $SW_{in}$ is derived from the radiation model after Kumar et al. (1997) as it was done for Zhadang glacier (see section 2.3.1) and corrected for cloud cover through HAR $SW_{in}$. The altitude of the HAR pixel that contains the glacier area and that is used as input data corresponds to the lower glacier regions (5750 m a.s.l., Fig. 4.1). The effect of shading by the surrounding terrain structure in these regions is apparent. Therefore, we choose a DEM pixel (*j*) in the upper part of the glacier with minimum terrain shading and similar annual cycle as HAR $SW_{in}$ for the cloud

correction (Fig. 4.1). Calculation of the correction of $SW_{in,pot}$ for cloud coverage and terrain effects is carried out as outlined in section 2.3.1 for the case of Zhadang glacier.

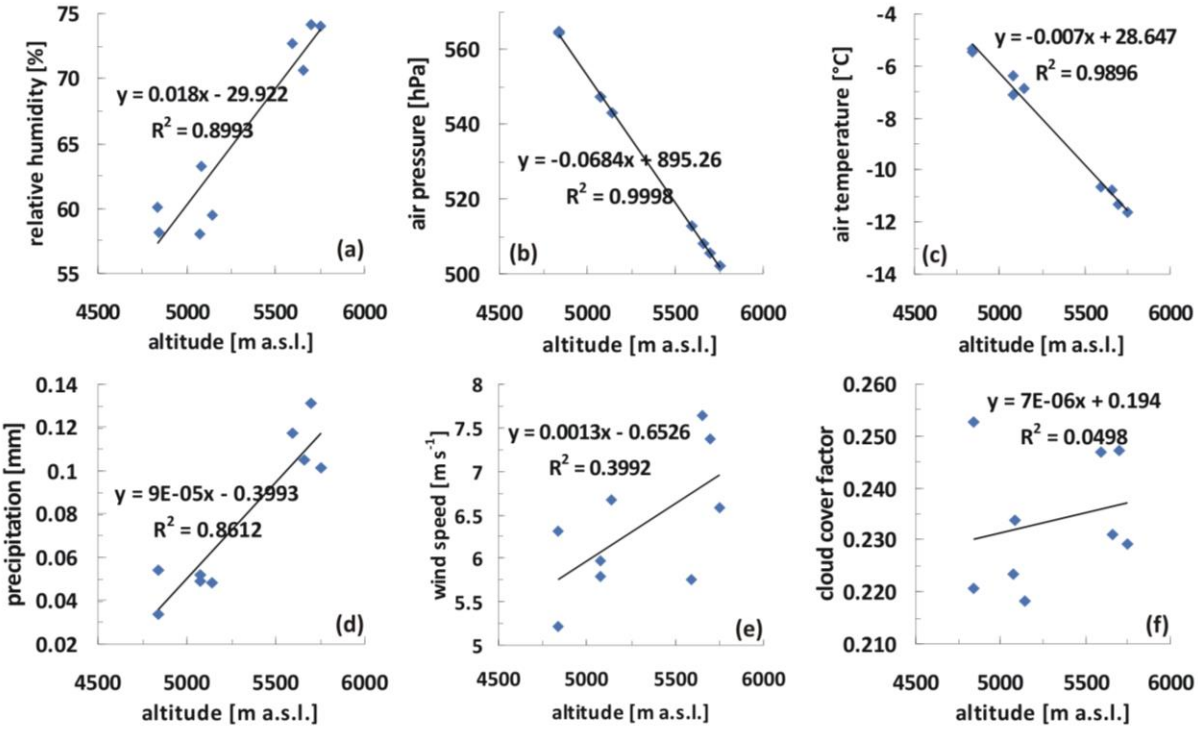


**Fig. 4.3: Altitude dependency of the HAR variables that serve as input for the MB model at Naimona'nyi (without $SW_{in}$). The slope of the regression line defines the respective altitude gradient per meter. Values are means for each HAR grid cell surrounding the glacier, 2000-2012.**

## 4.3 Initialisation of the SEB/MB model for application at Naimona'nyi glacier

So far, only few glaciological observations have been obtained from Naimona'nyi glacier. Thus, information on ELA and snow distribution for initial model assumptions is sparse. Yao et al. (2012) give a mean ELA around 6300 m a.s.l. between 2004 and 2010 based on in–situ measurements (see section 1.4.1). Therefore, we assume no initial snow depth for the total glacier area.

To account for uncertainties in total precipitation amounts from HAR and to obtain a model uncertainty for further MB calculations, we perform three model runs with varying precipitation scaling factors (0.56±0.25). The model run with a scaling factor of 0.56 is called reference run. Furthermore, HAR precipitation amounts are decreased by 25% (scaling factor 0.31) and increased by 25% (scaling factor 0.81) relative to the reference run. The lower factor (0.31) leads to a mean annual total of 280 mm at the HAR grid cell. Applying the higher factor (0.81) results in a mean precipitation sum of 732 mm $yr^{-1}$.

## 4.4 Results and discussion

In this section the results of the 12-year simulation period of Naimona'nyi glacier are interpreted. The SEB/ MB model explicitly calculates the different SEB and MB components and allows revealing altitudinal, inter- and intra-annual patterns on the glacier. The results for the total simulation period are compared to remote sensing surface height changes and geodetic MB calculations (section 4.4.1).

In a further step, the typical annual cycle of the modelled transient snow line altitude and the inter-annual pattern of the ELA are linked to the results of the SEB and MB modelling (section 4.4.2).

### 4.4.1 SEB/MB characteristics 2000-2012

The altitudinal dependence of MB and SEB components averaged over the simulation period 2000-2012 is shown in Fig. 4.4. The given uncertainty ranges result from the model runs with varying precipitation scaling factors (see section 4.3). Precipitation amounts are both decreased and increased by 25% compared to the reference run. The reference run is characterized by a precipitation scaling factor of 0.56. The gradient of the calculated MB in the reference run is almost linear from slightly positive values in the lowermost regions to distinct positive MB in ≈6000 m a.s.l. (Fig. 4.4a). Above 6000 m a.s.l. the gradient steepens slightly. Between 6200 and 6300 m a.s.l. the mean glacier-wide MB reaches its maximum value and then decreases in the uppermost regions. With decreased precipitation by 25% (scaling factor 0.31) the MB becomes negative in the lower parts of the glacier and the change in slope that was evident in all study regions so far, is visible between 5800 and 5900 m a.s.l. slightly above the determined 12-year ELA (5700-5800 m a.s.l., Fig. 4.4a). The vertical variation of the MB gradient is small compared to the previously studied glaciers (see chapters 2-3) and increases with decreasing precipitation amounts. Similar effects could be observed at PIC (section 3.4.1) and Halji glacier (section 5.4.1). However, the variation is less at Naimona'nyi because precipitation amounts are considerable even in the model run with precipitation decreased by 25% compared to the reference run (Table 4.2).

The characteristic shape of the vertical MB profile in the upper parts is also apparent in the gradients of $SW_{in}$, $SW_{net}$ (Fig. 4.4d), $Q_{sens}$, $Q_{lat}$ (Fig. 4.4e), sublimation (Fig. 4.4b) and $LW_{out}$ (Fig. 4.4f) (see also Braun & Hock 2004, van Pelt 2012). $\alpha$ (Fig. 4.4g), $Q_{melt}$ (Fig. 4.4e) and surface melt (Fig. 4.4a) repeat this pattern only slightly because the altitudinal variation of $\alpha$ is minimal due to large precipitation amounts, frequent precipitation events (Fig. 4.5) and a nearly permanent snow cover (see section 4.4.2). With 25% decreasing precipitation from the reference run $\alpha$ decreases only slightly because the seasonal variation of solid precipitation still prevents the glacier from being snow free over longer periods. A 25% precipitation increase slightly increases $\alpha$ in all altitude bands (Fig. 4.4g). Thus, all ground-dependent SEB and MB variables at Naimona'nyi glacier are only little sensitive to precipitation changes by ±25%. The variations in MB are mostly influenced by the variations of solid precipitation itself (Fig. 4.4a, 4.4c). The lower glacier regions and the uppermost altitude band show a higher sensitivity to an increase or decrease in precipitation by 25% from the reference run mainly forced by differences in $Q_{melt}$ and $Q_{lat}$ (Fig. 4.4e). Therefore, surface melt and sublimation are altered in this respect (Fig. 4.5a,b).

$SW_{in}$ and $LW_{in}$ are the only ground-independent energy sources for the glacier surface (see section 2.3.1). They do not change with varying precipitation amounts (Fig. 4.4d) because energy fluxes from the surrounding terrain are not considered. $SW_{in}$ is rather constant until 5800 m a.s.l. (Fig. 4.4d) due to uniform terrain shading at the lower tongue by the neighbouring slopes. Above 5800 m a.s.l., $SW_{in}$ increases with altitude up to 6300 m a.s.l. because the optical air mass decreases (see Klok & Oerlemans 2002) and glacier surface is hardly affected by terrain obstructions. Around 6300 m a.s.l. $SW_{in}$ decreases significantly because these parts of the accumulation area are obstructed to the west and southwest (Fig. 4.1). The uppermost glacier areas are exposed to solar radiation and receive the largest amounts of $SW_{in}$. Thus, increasing $T_s$ (expressed through $LW_{out}$, Fig. 4.4f) yields to smaller $Q_{sens}$ directed to the glacier surface and a higher $Q_{lat}$ from the glacier surface to the atmosphere compared to the altitude bands below (Fig. 4.4e). These feedback processes are also observed by Klok & Oerlemans (2002) at Morteratschgletscher. Higher $Q_{lat}$ results in increased mass loss through sublimation in the uppermost glacier regions compared to the altitude bands below (Fig. 4.4b). A slight increase

of $Q_{melt}$ in these regions causes an increase of surface melt despite minimal $T_{air}$ (Fig. 4.4a, 4.4e). Additionally, largest amounts of $SW_{net}$ are responsible for highest subsurface melt in around 6400 m a.s.l. (Fig. 4.4b, 4.4d). Therefore, mean MB over the total simulation period shows its maximum slightly below the uppermost altitude band. This was also observed by Mölg et al. (2009) for glaciers at the Kilimanjaro. Refreezing is largest in the lowermost glacier regions, decreases in the middle parts and again slightly increases towards the top where some surface and subsurface melt are evident (Fig. 4.4c).

From the vertical MB profile of the reference run no ELA can be estimated (Fig. 4.4a). In the model run with precipitation decreased by 25% compared to the reference run the ELA is located between 5700 and 5800 m a.s.l. (Fig. 4.4a). This altitude is much lower than the value given by Yao et al. (2012) for the period 2005-2011 (Fig. 4.9).

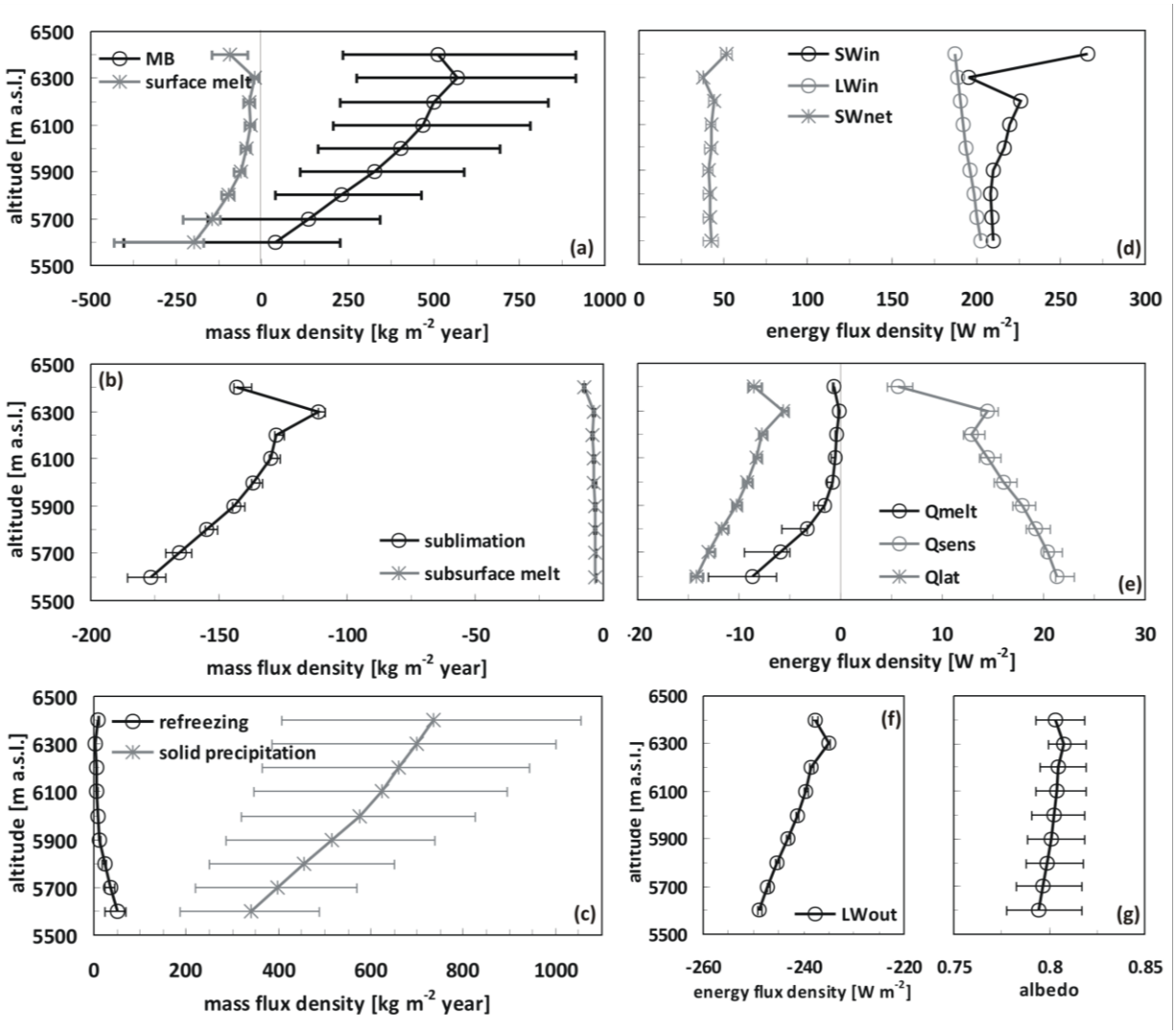


**Fig. 4.4: Modelled vertical profiles of (left) the specific mass balance and its components and (right) mean SEB components at Naimona'nyi glacier averaged over the simulation period October 2000 – September 2012. Data are averaged for 100-m altitude bands. The uncertainty ranges are calculated assuming different precipitation amounts (see section 4.3). Note the different x-axis scales of the components (negative means mass or energy loss at the glacier surface, see section 2.3.1 and Tab. 2.2 for abbreviations).**

Annual cycles of glacier-wide mean monthly SEB and MB components at Naimona'nyi glacier as calculated by the MB model for the reference run for the period 2000-2012 are illustrated in Fig. 4.5. It

is obvious that the values calculated within the first months (blue box in Fig. 4.5) suffer from errors that stem from the spin-up time of the MB model (see section 2.3.1). The first MB year is therefore not considered in the following interpretations. In general, $SW_{in}$ (+216.3 W m$^{-2}$) and $LW_{in}$ (+192.8 W m$^{-2}$) dominate energy input over the considered period, followed by $Q_{sens}$ (+16.6 W m$^{-2}$). Energy sinks at the glacier surface are $LW_{out}$ (-238.7 W m$^{-2}$), $SW_{out}$ (-179.2 W m$^{-2}$), $Q_{lat}$ (-7.4 W m$^{-2}$), $Q_G$ (-2.4 W m$^{-2}$) and $Q_{melt}$ (-0.3 W m$^{-2}$), making $SW_{net}$ (+38.5 W m$^{-2}$, see Table 4.1) the most important energy source highly depending on $\alpha$. This was also observed at Zhadang glacier and PIC and reported by Andreassen et al. (2008) for Storbreen and by Mölg & Hardy (2004) for Kilimanjaro. The lowest values of $SW_{net}$ are evident between July and September when large precipitation amounts increase $\alpha$ (Fig. 1.14, 4.5a). $LW_{net}$ shows a rather regular seasonal cycle playing a smaller role as energy sink in summer than in winter (Fig. 4.5a). This can be explained through the seasonal patterns of $LW_{in}$, depending on $T_{air}$, $e$ and $N$ (see section 2.3.1) (higher in summer), and $LW_{out}$, depending on $T_s$ (largest negative values in summer). In winter, $LW_{in}$ is significantly smaller whereas $LW_{out}$ varies only little. Averaged over the whole period $Q_C$ is very small and naturally tends to zero. In winter, when the surface is colder than the underlying snow layers, $Q_C$ becomes positive. Negative $Q_C$ is evident in spring and summer (Fig. 4.5a), when the surface warms but subsurface layers are still cold from the winter season. $Q_{PS}$ is always negative with larger values when $\alpha$ is low ($SW_{net}$ is large). Generally, $Q_{lat}$ is an energy sink for the glacier surface (Table 4.1). However, on a monthly time scale it is evident that positive values can occur in summer when the region is under influence of maximum precipitation amounts in the course of the year, highest $T_{air}$ and $RH$ (Fig. 1.14, 4.2). A similar pattern of positive $Q_{lat}$ during the summer monsoon period is observed at Chhota Shigri glacier in the western Himalayas based on SEB measurements by Azam et al. (2014). At positive $Q_{lat}$ condensation or deposition of moist air contributes to mass gain at the glacier surface. The contribution of deposition or condensation to the glacier MB or the runoff is not explicitly calculated in the MB model applied in this thesis. During most of the year, the dry conditions on the TP lead to negative $Q_{lat}$ and significant sublimation (Fig. 4.5) with largest values in winter when $RH$ is smallest (Fig. 4.2). Also, higher wind speeds drive turbulence during winter (Fig. 1.15). Generally, monthly means of $Q_{sens}$ and $Q_{lat}$ are of opposite sign and sometimes cancel each other out. Absolute values of $Q_{sens}$ are larger than $Q_{lat}$ implying a higher moisture content of the atmosphere and less sublimation compared to Zhadang glacier (section 2.4.6) or PIC (section 3.4.1). A similar dependency is observed by Nicholson et al. (2013) at Lewis glacier (Mt Kenya). Surface melt rates are small and occur dominantly in July and August, simultaneously with the period of lowest $SW_{net}$ through large $\alpha$. The climate chart for Naimona'nyi glacier confirms that both air temperature and precipitation maxima coincide between July and August (Fig. 1.14). Surface melt can also happen in May, June and September despite low $T_{air}$ (Fig. 4.5). High $SW_{net}$ implies a low $\alpha$ and can raise $T_s$ to zero (see section 2.4.5). During summer, $Q_C$ and $Q_{PS}$ are important energy sinks for the glacier surface (Fig. 4.5a). They transfer energy from the surface into the glacier that would otherwise lead to a significant increase of $Q_{melt}$. The respective SEB values for the model runs with varying precipitation scaling factors are given in Table 4.1. For glacier-wide monthly SEB components of the MB model runs with ±25% of precipitation see Fig. A.3a and Fig. A.4a in the appendix.

The glacier-wide MB estimate of the reference run for the period 2001-2012 (the first year is not considered) is +5667 kg m$^{-2}$ (+515.2 kg m$^{-2}$ yr$^{-1}$) (Table 4.2). In general, sublimation (-1341 kg m$^{-2}$/ -121.9 kg m$^{-2}$ yr$^{-1}$) is the largest factor of glacier-wide mass loss followed by surface melt (-270 kg m$^{-2}$/ -24.5 kg m$^{-2}$ yr$^{-1}$) and clearly dominates ablation in winter, spring and autumn, when air temperatures are below 0°C and surface melt is absent (Fig. 1.14, 4.5b). Subsurface melt (-36 kg m$^{-2}$/-3.3 kg m$^{-2}$ yr$^{-1}$) plays a minor role. Solid precipitation (+7204 kg m$^{-2}$/+654.9 kg m$^{-2}$ yr$^{-1}$) and refreezing (+109 kg m$^{-2}$/ +9.9 kg m$^{-2}$ yr$^{-1}$) contribute to mass gain of the glacier. Maximum snowfall amounts occur in summer

(Fig. 1.14, 4.5b, see section 1.4.1). Refreezing at Naimona'nyi glacier happens mostly in summer, when melt water is produced at the surface and percolates through the cold winter and spring snow layers. Air temperatures according to the HAR dataset at Naimona'nyi glacier are considerably below 0°C until June (Fig. 1.14). Therefore, it can be assumed that subsurface temperatures are well below zero throughout the summer and allow the refreezing of considerable amounts of melt water. The reference run implies that 36% of the surface and subsurface melt water refreezes within the snow pack between 2001 and 2012. These results will be discussed in section 4.5. The respective MB values for the model runs with varying precipitation scaling factors are given in Table 4.2. For glacier-wide monthly MB components of the MB model runs with ±25% of precipitation see Fig. A.3b and Fig. A.4b in the appendix.

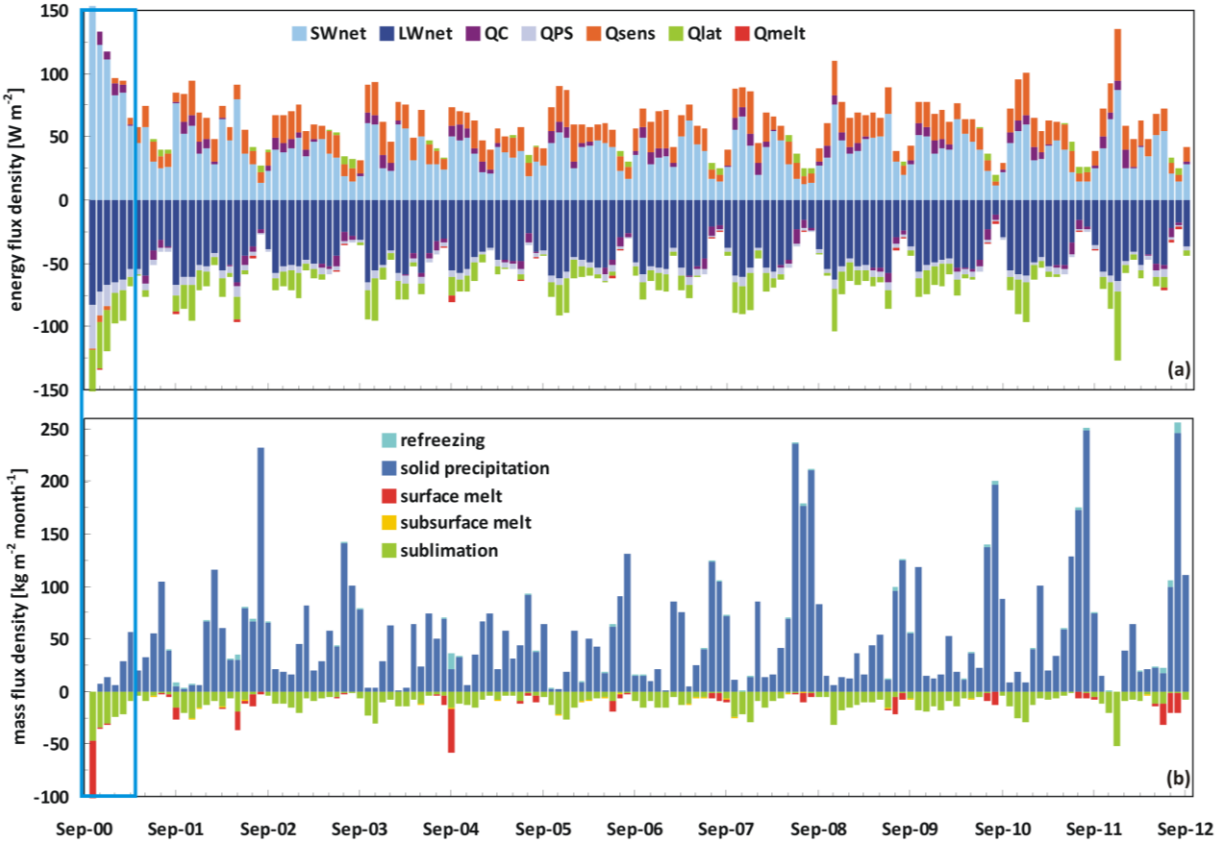


**Fig. 4.5 Glacier-wide monthly (a) SEB components (see section 2.3.1 for abbreviations) and (b) MB components from October 2000 to September 2012 at Naimona'nyi glacier (reference run). Note that the first months (blue box) should not be considered.**

Table 4.1 lists the absolute and relative contributions of the energy flux components to the total energy turnover for the three model runs with varying precipitation scaling factors (0.56/0.31/0.81) when simulated with unchanged $T_{air}$ from the HAR dataset. For the considered period 2001-2012, $LW_{net}$ accounted for 40% (40%/40%), followed by $SW_{net}$ (34%/33%/33%), $Q_{sens}$ (14%/14%/14%), $Q_{lat}$ (7%/7%/ 7%) and $Q_G$ (5%/5%/5%). $Q_{lat}$ is relatively small and its contribution to the total energy flux is nearly the same as the contribution of $Q_G$. $LW_{net}$ dominates over $SW_{net}$. This is not the result of extremely large negative $LW_{net}$ but of the lower proportions of $SW_{net}$ and $Q_{lat}$ compared to the other glaciers (Table 4.1). $SW_{net}$ is relatively low because of overall high $\alpha$ (Fig. 4.4) and $Q_{lat}$ decreased due to higher *RH* associated with larger precipitation amounts compared to e.g. Halji glacier (Fig. 4.2, 5.2). The absolute numbers and the relative contribution of the different SEB components do hardly vary with changing precipitation amounts by ±25% from the reference run (Table 4.1) because the

seasonal distribution of solid precipitation prevents the glacier from being snow free over longer periods what keeps $\alpha$ high (Fig. 4.4). The SEB components without $Q_{melt}$ are nearly balanced. Thus, simulated $Q_{melt}$ and surface melt are generally very low at Naimona'nyi glacier over the period 2001-2012 with a minimum in 2002/03 (Tables 4.1, 4.2) when simulated with unchanged air temperature from the HAR dataset. The inter-annual variations of the glacier-wide MB are dominated by the precipitation amounts. In 2003/04 and 2008/09 solid precipitation is minimal (Table 4.2) resulting in less positive MB (Fig. 4.6). The contribution of surface melt, subsurface melt and refreezing to total MB are negligible. Annual sublimation amounts are rather constant. Therefore, sublimation is not responsible for MB variations (Table 4.2). Over the total simulation period, effective melt (surface melt + subsurface melt – refreezing) accounts for 13% (14%/13%) and sublimation for 87% (86%/87%) of the total mass loss (Table 4.2). As for the SEB components a precipitation change by ±25% hardly affects the MB components despite solid precipitation (Table 4.2). The amount of refreezing melt water varies only slightly because in most years the thickness of the snow pack remains sufficient for the low melt rates even when precipitation is decreased by 25%.

From the modelled period October 2000 – September 2012, 12 glacier-wide MB estimates for Naimona'nyi glacier can be obtained and compared to the measurements of Yao et al. (2012) (Fig. 4.6). The uncertainty ranges of the model values are obtained from the application of different precipitation scaling factors (0.56/0.31/0.81, see section 4.3). Yao et al. (2012) observed a mean mass deficit of ≈-560 kg m$^{-2}$ for Naimona'nyi glacier between 2005/06 and 2009/10 based on an ablation stake network. The corresponding annual MB values are given in Fig. 4.6 in comparison with the MB model results. It is obvious that the two results differ largely and that the estimates within this study indicate significantly lower mass loss which is probably related to too low $T_{air}$ in the HAR dataset. However, while absolute values between both studies are very different, the inter-annual variations in both studies are similar at least for two of the three years (Fig. 4.6). This indicates that relative HAR climatology provides year-to-year variance in such that modelled annual MB variance overall fits to the observations.

**Table 4.1: Mean absolute values of energy flux components as modelled for October 2000 – September 2012 and for the respective MB years with proportional contribution to total energy flux at Naimona'nyi glacier. The first value is for a precipitation scaling factor of 0.56, the numbers in brackets are for the model runs (0.31 / 0.81). Note that values of the MB year 2000/01 are not considered in the calculation of the total average.**

| | Sum* [W m$^{-2}$] | $SW_{net}$ | $LW_{net}$ | $Q_{sens}$ | $Q_{lat}$ | $Q_G$ | $Q_{melt}$ |
|---|---|---|---|---|---|---|---|
| tot. average [W m$^{-2}$] | 115 (115/ 115) | 39 (39 / 38) | -46 (-46 / -46) | 17 (17 / 17) | -7 (-7 / -7) | -2.4 (-2.5/-2.4) | -0.3 (-0.3 / -0.3) |
| 2000/01 | | 75 (88 / 70) | -58 (-61 / -57) | 6 (2 / 8) | -15 (-18 / -14) | -9 (-11 / -8) | -0.8 (-1.5 / -0.8) |
| 2001/02 | | 43 (43 / 43) | -48 (-49 / -49) | 16 (15 / 16) | -9 (-9 / -9) | -3 (-3 / -3) | -0.4 (-0.4 / -0.4) |
| 2002/03 | | 35 (35 / 35) | -45 (-45 / -45) | 15 (15 / 15) | -5 (-5 / -5) | -3 (-3 / -3) | 0 (0 / 0) |
| 2003/04 | | 42 (42 / 42) | -49 (-49 / -49) | 18 (18 / 18) | -10 (-10 / -10) | -3 (-3 / -3) | -0.6 (-0.6 / -0.6) |
| 2004/05 | | 34 (34 / 34) | -44 (-44 / -44) | 15 (15 / 15) | -4 (-4 / -4) | -2 (-2 / -2) | -0.1 (-0.1 / -0.1) |
| 2005/06 | | 39 (39 / 39) | -48 (-48 / -48) | 18 (18 / 18) | -8 (-8 / -8) | -3 (-3 / -3) | -0.2 (-0.2 / -0.2) |
| 2006/07 | | 35 (35 / 35) | -46 (-46 / -46) | 17 (17 / 17) | -6 (-6 / -6) | -3 (-3 / -3) | -0.2 (-0.2 / -0.2) |
| 2007/08 | | 36 (36 / 36) | -43 (-43 / -43) | 15 (15 / 15) | -7 (-7 / -7) | -2 (-2 / -2) | -0.1 (-0.1 / -0.1) |
| 2008/09 | | 44 (44 / 44) | -48 (-48 / -48) | 18 (18 / 18) | -9 (-10 / -9) | -3 (-3 / -3) | -0.3 (-0.3 / -0.3) |
| 2009/10 | | 40 (40 / 40) | -43 (-44 / -43) | 15 (14 / 15) | -7 (-7 / -7) | -2 (-2 / -2) | -0.2 (-0.2 / -0.2) |
| 2010/11 | | 36 (36 / 36) | -44 (-44 / -44) | 18 (18 / 18) | -6 (-6/ -6) | -2 (-2 / -2) | -0.1 (-0.1 / -0.1) |
| 2011/12 | | 41 (41 / 41) | -45 (-45 / -45) | 18 (18 / 18) | -9 (-9 / -9) | -2 (-2 / -2) | -0.6 (-0.6 / -0.6) |
| | 100% | 34 (33 / 33)% | 40 (40 / 40)% | 14 (14 / 14)% | 7 (7 / 7)% | 5 (5 / 5)% | |

*Sum of energy fluxes in absolute values: $|SW_{net}| + |LW_{net}| + |Q_{sens}| + |Q_{lat}| + |Q_G|$

**Table 4.2: Calculated glacier-wide mass balance components for the total period October 2001 – September 2012 and for the respective MB years at Naimona'nyi glacier. The first value is for a precipitation scaling factor of 0.56, the numbers in brackets are for the model runs (0.31/0.81). Note that values of the MB year 2000/01 are not considered in the calculation of the total values.**

| | Solid precipitation | Surface melt | Refrozen water | Subsurf. melt | Sublimation | Mass balance* |
|---|---|---|---|---|---|---|
| tot. [kg m$^{-2}$] | 7204 (3988 / 10420) | -270 (-273 / -270) | 109 (95 / 113) | -36 (-36 / -35) | -1341 (-1344 / -1340) | 5667 (2429 / 9156) |
| 2000/01 | 369 (204 / 534) | -77 (-140 / -77) | 5 (4 / 5) | -2 (-2 / -2) | -202 (-226 / -192) | 94 (-160 / 269) |
| 2001/02 | 764 (423 / 1105) | -36 (-36 / -38) | 13 (12 / 13) | -5 (-5 / -5) | -138 (-140 / -138) | 597 (253 / 936) |
| 2002/03 | 654 (362 / 947) | -3 (-3 / -3) | 2 (2 / 2) | -2 (-2 / -2) | -101 (-101 / -101) | 551 (258 / 843) |
| 2003/04 | 405 (224 / 585) | -53 (-52 / -52) | 19 (16 / 20) | -2 ( -2 / -2) | -145 (-145 / -145) | 224 (41 / 406) |
| 2004/05 | 563 (312 / 814) | -11 (-12 / -10) | 6 (6 / 6) | -3 (-3 / -3) | -85 (-85 / -85) | 469 (217 / 722) |
| 2005/06 | 500 (277 / 724) | -16 (-16/ -17) | 7 (7 / 7) | -4 (-4 / -4) | -128 (-128 / -128) | 360 (137 / 583) |
| 2006/07 | 579 (320 / 837) | -17 (-17 / -17) | 7 (7 / 8) | -3 (-3 / -3) | -105 (-105 / -104) | 462 (202 / 721) |
| 2007/08 | 957 (530 / 1385) | -14 (-14/ -13) | 8 (7 / 8) | -4 (-4 / -4) | -124 (-124 / -124) | 823 (394 / 1251) |
| 2008/09 | 483 (268 / 699) | -26 (-30 / -25) | 9 (9 / 9) | -3 (-3 / -3) | -141 (-141 / -140) | 323 (103 / 540) |
| 2009/10 | 726 (402/ 1051) | -21 (-20 / -22) | 8 (6 / 10) | -4 ( -4 / -4) | -116 (-117 / -116) | 595 (267 / 919) |
| 2010/11 | 916 (507 / 1325) | -14 (-13 / -14) | 6 (4 / 6) | -2 (-2 / -2) | -114 (-114 / -114) | 792 (383 / 1202) |
| 2011/12 | 656 (363 / 949) | -61 (-61 / -60) | 24 (19 / 24) | -4 (-4 / -3) | -144 (-144 / -144) | 472 (174 / 766) |
| % of mass loss | | 10 (11/ 10) | | 2 (2 / 2) | 87 (86 / 87) | |

*Mass balance = solid precipitation + surface melt + refrozen water + subsurface melt + sublimation

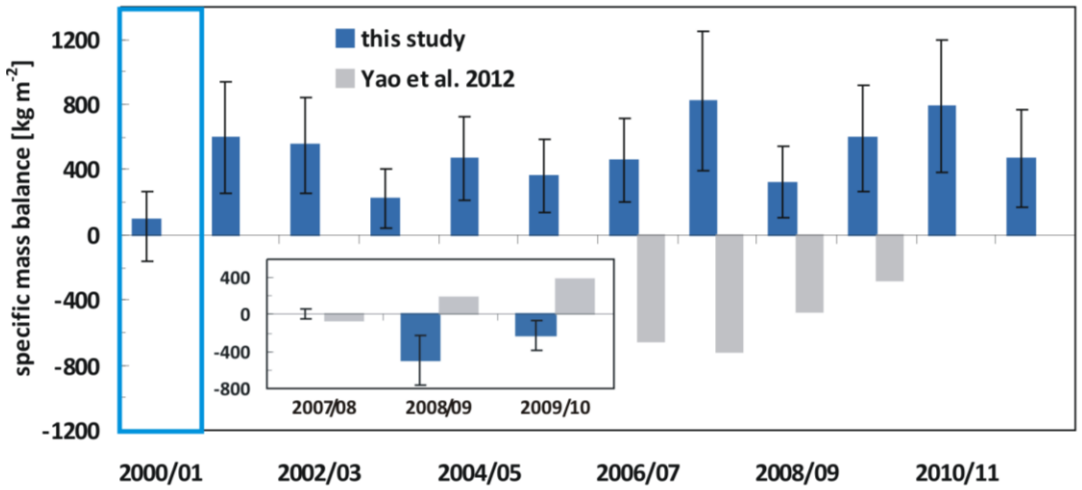


**Fig. 4.6: Glacier-wide annual MB for MB years (October – September) 2000-2012 estimated by the HAR forced MB model for Naimona'nyi glacier and compared to the results published in Yao et al. (2012). The MB value of 2006/07 of Yao et al. (2012) is the total over 2005/06-2006/07. The uncertainty ranges are calculated assuming different precipitation amounts (see section 4.3, Table 4.2). Note that the MB in 2000/01 (blue box) should not be considered. The inlay gives the inter-annual variation of the MB in 2007/08 to 2009/10 relative to the MB total over 2005/06-2006/07 of each study.**

Furthermore, the MB model results for Naimona'nyi glacier can be evaluated against surface height changes and geodetic MB estimations from Pleiades and SRTM data (Holzer et al. 2014). Holzer et al. (2014) calculated surface elevation changes for the Gurla Mandhata region between February 2000 and October 2013 from a DEM generated from optical tri-stereo Pleiades data (2013) relative to a SRTM DEM (2000). An average ice density of 850±60 kg m$^{-3}$ was applied for the conversion into mass changes. Holzer et al. (2014) estimated a MB of -270±330 kg m$^{-2}$ yr$^{-1}$ for the period 2000-2013 with a total surface height change of -4.39±5.23 m (-0.32±0.39 m yr$^{-1}$). In this study, total modelled MB for Naimona'nyi glacier for the period 2001-2012 is +5667 kg m$^{-2}$ (+2429 kg m$^{-2}$ / +8887 kg m$^{-2}$) with annual means of +515 kg m$^{-2}$ yr$^{-1}$ (+221 kg m$^{-2}$ yr$^{-1}$/+808 kg m$^{-2}$ yr$^{-1}$). Respective surface height change for the total glacier area is +7.2 m (+2.8 m/ +11.3 m) with annual means of +0.65 m yr$^{-1}$ (+0.25 m yr$^{-1}$/

+1.03 m $yr^{-1}$) within this study. The lower boundary of the MB model runs comes close to the upper limit of the range of uncertainty of the estimates of Holzer et al. (2014). The spatial comparison of calculated surface height changes from both studies reveals that the overall pattern is captured to a high degree (Fig. 4.7). Note that MB model results of the 0.31-run are shown in Fig. 4.7. A glacier thinning occurs in the lower parts of the glacier tongue while a small thickening appears in the upper regions. The remote sensing results show several small scale features that are independent of altitude in the upper parts of the glacier. These features cannot be captured in the MB model (Fig. 4.7). From the comparisons it can be concluded that the reference run clearly overestimates the MB and the surface height changes estimated from remote sensing analyses of Holzer et al. (2014). With decreased precipitation amounts by 25% the MB model results are more reasonable but still overestimates the MB. The results are less negative than those of previously published less detailed studies based on remote sensing approaches (e.g. Gardelle et al. 2013, Kääb et al. 2012, Neckel et al. 2014). The mean MB for the Pamir/Karakorum/Himalaya region was estimated to be -140±80 kg $m^{-2}$ $yr^{-1}$ between 1999 and 2011 (Gardelle et al. 2013) and -210±50 kg $m^{-2}$ $yr^{-1}$ for the Hindukush/Karakorum/Himalaya region for 2003-2008 (Kääb et al. 2012). For western Nepal the authors give MB values of -320±130 kg $m^{-2}$ $yr^{-1}$ (Gardelle et al. 2013) and -340±50 kg $m^{-2}$ $yr^{-1}$ (Kääb et al. 2012). Neckel et al. (2014) estimate a mass loss of -370±250 kg $m^{-2}$ $yr^{-1}$ between 2003 and 2009 for the Gangdise Shan including the Gurla Mandhata region. However, modelled MB within this study is too positive even when applying a precipitation scaling factor of 0.31. This implies that an overestimation of the total precipitation amounts by HAR in the reference run might not be the main reason for the deviation of the MB model results from other studies (see section 4.5).

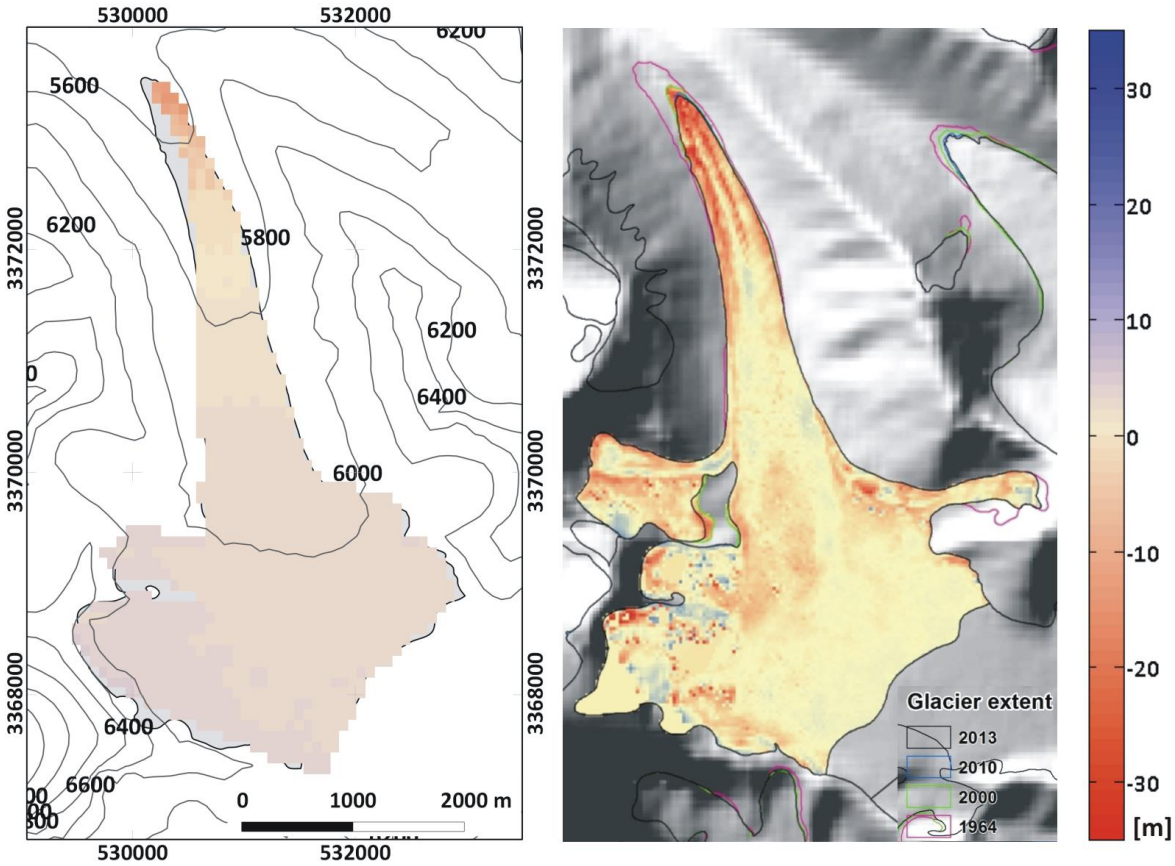


**Fig. 4.7: Spatial comparison of modelled surface height change of Naimona'nyi glacier for the 0.31-model run, 2001-2012 (left), with the results of Holzer et al. (2014) (right) (difference Pleiades DEM 2013 / SRTM DEM 2000). The western parts of the lower glacier tongue are debris covered and therefore not included in the MB model domain.**

### 4.4.2 Snow line and ELA characteristics 2000-2012

Mean monthly variations of the glacier-wide mean altitude of the transient snow line between 2001 and 2012 at Naimona'nyi glacier are calculated from the MB model results (Fig. 4.8). The given values refer to the reference run with a precipitation scaling factor of 0.56. Based upon the reference run precipitation amounts are decreased and increased by 25%, respectively, to obtain the model uncertainty (see section 3.3). Between December and March no snow line is evident on the glacier independent from a precipitation amount of ±25%. During these months the mass gain through solid precipitation is much larger than the mass loss through sublimation. A snow pack is build up that even lasts in those months in which sublimation exceeds accumulation (Fig. 4.5b). In the reference run a snow line develops in the lowermost glacier regions in April and slowly rises up to 5576 m a.s.l. until July. Precipitation amounts are largest in August (Fig. 1.14) and the mean snow line altitude decreases (Fig. 4.8). Between September and November total precipitation amounts decrease considerably (Fig. 1.14). However, $T_{air}$ also decreases so that surface melt is nearly absent and sublimation can only compensate for mass gain in the lowermost glacier regions (Fig. 4.8). Generally, the altitudinal variation of the mean transient snow line is only 16 m in the reference run with the highest position in 5576 m a.s.l. and a mean altitude of 5565 m a.s.l. In total, 36% of surface and subsurface melt refreeze (see section 4.4.1) and form a layer of superimposed ice when the snow pack is removed. Therefore, a snow line can develop and rise up the glacier while MB is still positive. With precipitation decreased by 25% the snow line altitude raises around 15 m with the largest sensitivities in spring and late autumn (Fig. 4.8) when precipitation amounts are generally low (Fig. 1.14). Despite precipitation being reduced by 25% surface melt rates remain rather constant (Table 4.2) because the glacier still receives enough solid precipitation to keep $\alpha$ high (Fig. 4.4). Thus, the SEB components (mainly $SW_{net}$) change only little (Table 4.1). Sublimation still dominates mass loss (Table 4.2). Only in months with little precipitation (April, November, December) sublimation exceeds the amount of accumulation and the transient snow line altitude can rise to 5590 m a.s.l. which is a little higher than the summertime snowline altitude of 5585 m a.s.l. (Fig. 4.8). A precipitation increase by 25% generates so much solid precipitation that a snow line is evident only between May and September. The mean altitude is lowered by ≈3.5 m compared to the reference run. Sensitivities are largest in July (Fig. 4.8).

The modelled annual ELA for 2000 to 2012 at Naimona'nyi glacier is shown in Fig. 4.9. The ELA follows the MB pattern (Fig. 4.6) with very low or no ELA in strongly positive MB years and slightly higher ELA in less positive MB years. From the vertical MB profile for the reference run for Naimona'nyi glacier (section 4.4.1) the ELA between 2000 and 2012 would be located just below the altitude of the lowermost parts of the glacier (Fig. 4.4a). For the 0.31-model run the ELA is estimated around 5700 m a.s.l. (Fig. 4.4a). The average over the calculated annual ELA 2002-2012 (Fig. 4.9) leads to a value of 5770 m a.s.l for the model run with precipitation decreased by 25%. In the reference run the ELA is located on the glacier only in 2004 (Fig. 4.9). In the other years the ELA is lower than the lowermost parts of the glacier. Based on measured MB values at Naimona'nyi glacier from 2005/2006 until 2009/2010 (four MB years, see section 4.4.1) Yao et al. (2012) state a mean ELA around 6300 m a.s.l. (Fig. 4.9). However, Yao et al. (2012) do not provide details on how the ELA was derived. The absolute altitudes do not correspond to the ELA derived from the MB model. However, the inter-annual variation in both studies is similar for two of the three years (Fig. 4.9). In 2007/08 Yao et al. (2012) measured the most negative MB (section 4.4.1) and the highest ELA whereas no ELA develops in the model due to distinct positive MB.

The relation of annual AAR and annual MB at Naimona'nyi glacier for the period 2001-2012 for the MB model run with precipitation decreased by 25% (scaling factor 0.31) is visualized in Fig. 4.10. In the reference run (scaling factor 0.56) annual MB is positive throughout (Fig. 4.6). Thus, $AAR_0$ can not

be obtained. According to the model data using a precipitation scaling factor of 0.31 and unchanged air temperature from the HAR dataset the relationship between AAR and MB is linear ($R^2$=0.79, Fig. 4.10). Linear relationships are also revealed for Zhadang glacier (see section 2.4.6) and PIC (3.4.2). In the reference run the annual AAR varies between 98% in 2008/09 and 100%. For the total simulation period of the reference run the AAR is 100%. In the model run with precipitation decreased by 25% the total AAR is 97%. $AAR_0$ is estimated to be 83% (Fig. 4.10). The index $\alpha_d$ after Dyurgerov et al. (2006) measures the glacier's displacement from the equilibrium (see section 2.4.6). For the reference run at Naimona'nyi glacier $\alpha_d$ is determined to be +21%. Thus, the glacier would have to increase its area and advance to reach its equilibrium state for the climate conditions of the simulation period with a precipitation scaling factor of 0.56 and unchanged HAR air temperature. A precipitation decrease of 25% compared to the reference run results in a $\alpha_d$ of +17%. Thus, the glacier's area and volume are not very sensitive to precipitation trends under the climate conditions created by the HAR data. This result is clearly in contradiction with Yao et al. (2012), Holzer et al. (2014) and own field observations (section 1.4.2.2). The consequences of this mismatch will be discussed in the following section.

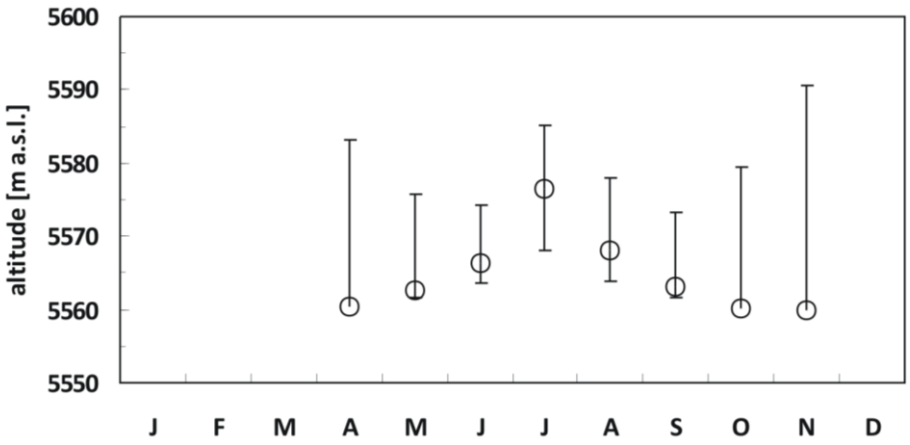


**Fig. 4.8: Modelled mean intra-annual snow line altitude at Naimona'nyi glacier, 2001-2012. The model uncertainty is calculated assuming different precipitation amounts (see section 4.3).**

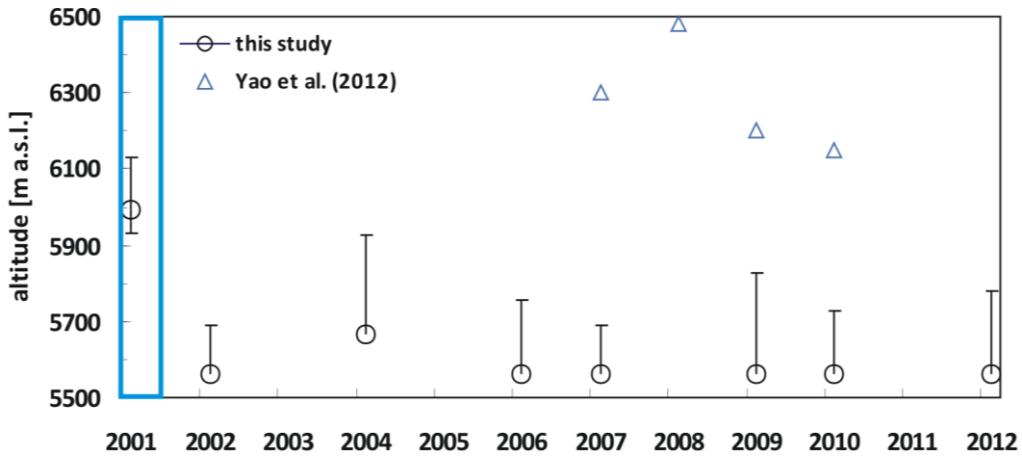


**Fig. 4.9: Glacier-wide annual ELA at Naimona'nyi glacier, 2000-2012, calculated by the HAR forced MB model and compared to the results published in Yao et al. (2012). The ELA of 2007 of Yao et al. (2012) is the resulting ELA at the end of the two mass balance years 2005/06-06/07. The uncertainty ranges are calculated assuming different precipitation amounts (see section 4.3). Note that the ELA in 2001 (blue box) should not be considered.**

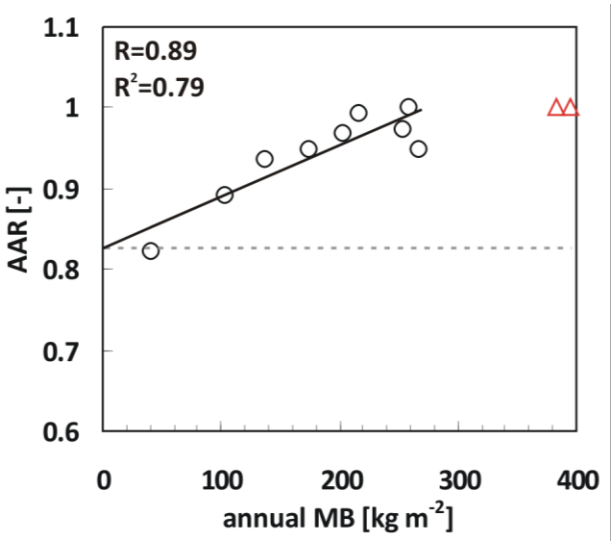


**Fig. 4.10: Relation between annual MB and AAR at Naimona'nyi glacier, 2001-2012, for the MB model run with a precipitation scaling factor of 0.31. The AAR at MB=0 denotes $AAR_0$. The red triangles mark the two MB years where AAR is 1 (100%). They are not considered in the calculation of the regression.**

## 4.5 Discussion of uncertainties

The variation of HAR precipitation as input for the MB model through the application of three different scaling factors (0.56±0.25) creates a range of uncertainty for every SEB and MB component (see section 4.4). At Naimona'nyi glacier the calculated ranges of uncertainty are very small and dominated by the varying precipitation amounts. Even in the 0.31-model run enough solid precipitation is generated to prevent the glacier from being snow free over longer periods when simulated with unchanged $T_{air}$ from the HAR dataset. This keeps $\alpha$ high and reduces the sensitivity of all SEB and MB components (see sections 4.4.1, 4.4.2). The obtained model results are evaluated through the comparison with surface height changes and geodetic MB from remote sensing analysis (Holzer et al. 2014) and in-situ measurements (Yao et al. 2012). Compared to the results of Holzer et al. (2014) the reference run clearly overestimates the MB and the surface height changes. With decreased precipitation amounts (0.31) the MB model results are more reasonable but still seem to overestimate the MB and the surface height changes. The amount of refreezing slightly declines from 36% in the reference run to 31% in the 0.31-run. These values seem to be reasonable when considering that Naimona'nyi glacier might contain cold ice throughout (Benn & Owen 2002, see section 1.4.1). The spatial comparison of calculated surface height changes from this study and Holzer et al. (2014) reveals that the overall pattern is captured to a high degree (Fig. 4.7). The results of both studies are less negative than those of previously published less detailed studies based on remote sensing approaches (e.g. Gardelle et al. 2013, Kääb et al. 2012, Neckel et al. 2014). Also our results do not match the results published by Yao et al. (2012) based on in-situ measurements even when applying a scaling factor of 0.31. This implies that an overestimation of the total precipitation amounts by HAR might not be the single only reason for the deviation of the MB model results from the observations.

The comparison of HAR data with AWS measurements over one year (see section 1.4.2.2) reveals that daily mean $T_{air}$ from HAR is up to 10°K lower than the respective AWS measurement (see section 4.1). Hourly $T_{air}$ even differs by up to 12°K. Differences are largest in winter. However, even in summer hourly HAR $T_{air}$ is lower than AWS $T_{air}$ by up to 8 K (Fig. 1.26). On average over the considered period HAR $T_{air}$ is lower by 3.8 K in winter and 2.0 K in summer compared to the AWS measurements. The sum of positive degree hours (PDH) from HAR at the altitude of the AWS is nearly half of the PDH

measured at the AWS (Fig. 1.26, see section 1.4.2.2). This means that the HAR forced MB model will produce only half of the amount of surface melt at the lower tongue of Naimona'nyi glacier that can be assumed to occur according to the AWS measurements. The period available for the validation of the HAR data is short. Nevertheless, a pronounced cold bias in HAR $T_{air}$ can be revealed. If this underestimation of $T_{air}$ by the HAR output is evident over the whole simulation period, this would have a significant effect on modelled SEB and MB especially in summer. Thus, further MB model runs with varying temperature offset are necessary. To limit the computational effort a north-south profile along the glacier flow-line is generated (Fig. 4.1). The MB model is run for this profile with a positive temperature offset while precipitation amounts are scaled with a factor of 0.31. We chose the scaling factor of 0.31 because the spatial comparison of surface height changes with the results of Holzer et al. (2014) showed that the total precipitation amounts in the upper glacier areas are reasonable (Fig. 4.7). In the higher parts of the glacier, surface height change is dominated by solid precipitation because surface melt is small (Fig. 4.4). Thus, we can assume that HAR precipitation amounts scaled by 0.31 do not significantly underestimate the amounts that occur at Naimona'nyi glacier. Initially, a temperature offset of +3 K is chosen for running the profile because this value corresponds to the average cold bias revealed at Naimona'nyi glacier from the comparison of AWS and HAR temperature data (see section 1.4.2.2). The result is presented in Fig. 4.11 and compared to the respective profiles of the previous model runs with varying precipitation scaling factor and unchanged $T_{air}$. As expected, the differences in MB and surface height through a temperature increase by +3 K are largest in the lower glacier areas. The influence in the uppermost regions is minimal (Fig. 4.11). Total surface height change in the lowermost parts of the profile between 2001 and 2012 is -33.7 m which is close to the values given by Holzer et al. (2014) (Fig. 4.7, 4.11). From the MB profile and the corresponding DEM altitudes a rough estimation of the ELA can be provided. The MB model run for the north-south profile with a precipitation scaling factor of 0.31 and a temperature offset of +3 K results in a mean ELA between 2001 and 2012 of ≈6020 m a.s.l. (Fig. 4.11). This value is still lower than the ELA given by Yao et al. (2012). However, the difference is small. Furthermore, both studies relate to different periods.

To allow the estimation of annual MB values, we calculate glacier-wide monthly values for the SEB and MB components from the respective values of the profile with increased $T_{air}$. Therefore, the same profile is derived for the previous model runs with varying precipitation scaling factors. Then, the relation between the monthly profile-SEB and -MB values and the respective glacier-wide values is determined. Finally, we apply the calculated relations to determine glacier-wide monthly SEB and MB components from the profile with increased $T_{air}$. The result is a best-guess estimate and does not replace the MB model run with similar input data for the total glacier which will be carried out in the near future.

The resulting glacier-wide SEB and MB components are given in Fig. 4.12. The inter- and intra-annual patterns of the different parameters are similar to those explained in section 4.4.1. For the considered period 2001-2012, $SW_{in}$ (+216.3 W m$^{-2}$) and $LW_{in}$ (+192.8 W m$^{-2}$) dominate energy input, followed by $Q_{sens}$ (+14.7 W m$^{-2}$). Energy sinks at the glacier surface are $LW_{out}$ (-251.2 W m$^{-2}$), $SW_{out}$ (-156.1 W m$^{-2}$), $Q_{lat}$ (-10.3 W m$^{-2}$), $Q_G$ (-6.1 W m$^{-2}$) and $Q_{melt}$ (-3.7 W m$^{-2}$). This results in a $SW_{net}$ of +60.2 W m$^{-2}$. In general, the contribution of $LW_{net}$ to the total energy flux slightly decreased compared to the model runs with unchanged $T_{air}$ (Table 4.1) and accounts for 39%, similar to $SW_{net}$ (39%). The contribution of $Q_{sens}$ decreased (10%). $Q_{lat}$ and $Q_G$ change only slightly with an increase in $T_{air}$ of +3 K and account for 8% and 5%, respectively. The given proportions are not totally reliable because they are not calculated using the fully spatially distributed version of the energy and mass balance model. However, the changes in the SEB components through the increase of $T_{air}$ cause a decrease in $\alpha$ and an increase in $SW_{net}$ and $Q_{melt}$ (Fig. 4.12).

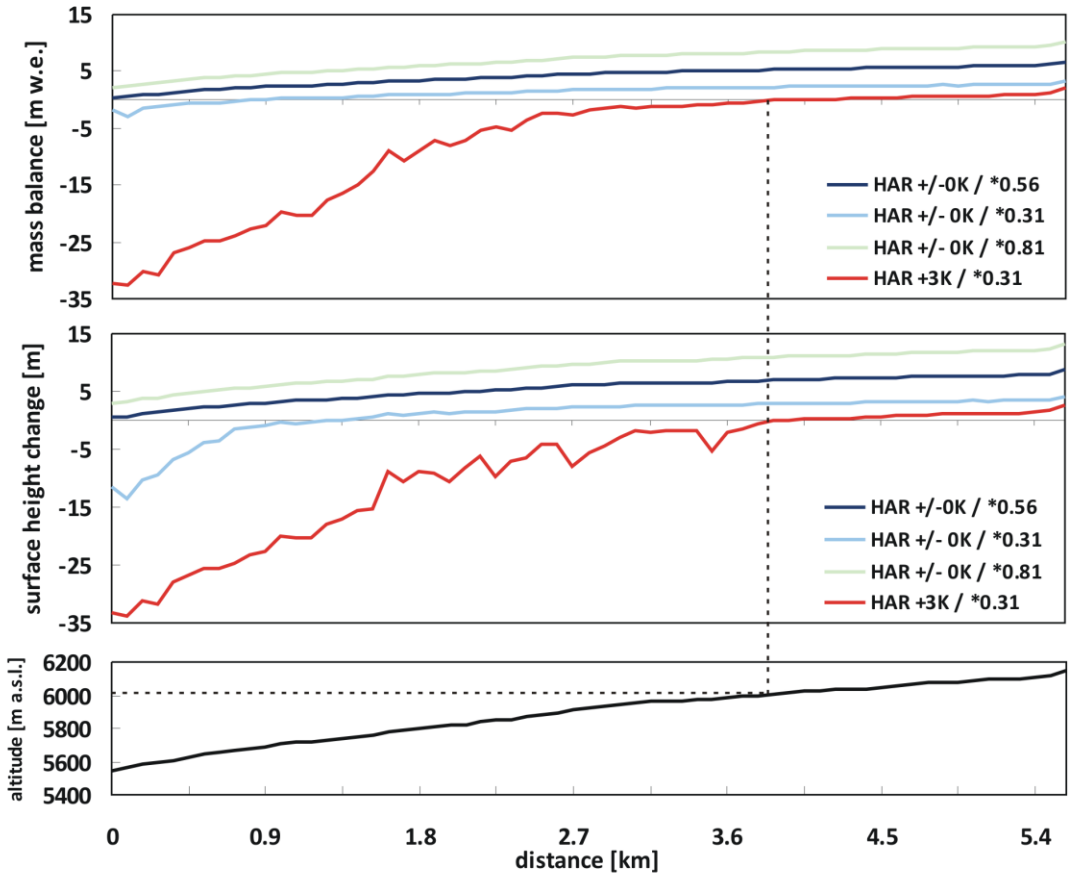


**Fig. 4.11: MB and surface height change for 2001-2012 along a north-south profile at Naimona'nyi glacier for HAR precipitation and temperature offsets. The location of the profile is indicated in Fig. 4.1. The altitude in which the MB is zero (dashed lines) is the ELA.**

The glacier-wide MB estimate in the model run with increased $T_{air}$ for the period 2001-2012 (the first year is not considered) is -2282 kg m$^{-2}$ (-207.5 kg m$^{-2}$ yr$^{-1}$). The annual mean value is fully within the range determined by Holzer et al. (2014). Surface melt (-3923 kg m$^{-2}$/-357 kg m$^{-2}$ yr$^{-1}$) is the largest factor of glacier-wide mass loss followed by sublimation (-1668 kg m$^{-2}$/-151.6 kg m$^{-2}$ yr$^{-1}$) that clearly dominates ablation in winter, when air temperatures are below 0°C and surface melt is absent (Fig. 4.12b). Subsurface melt (-48 kg m$^{-2}$/-4.4 kg m$^{-2}$ yr$^{-1}$) is small. Solid precipitation (+3040 kg m$^{-2}$/ +276 kg m$^{-2}$ yr$^{-1}$) and refreezing (+315 kg m$^{-2}$/+29 kg m$^{-2}$ yr$^{-1}$) contribute to mass gain of the glacier. The amount of solid precipitation is less compared to the MB model run with a similar scaling factor but unchanged $T_{air}$ (Table 4.2). This is because the solid proportion of total precipitation decreases with increasing $T_{air}$. Over the total simulation period, effective melt (surface melt + subsurface melt – refreezing) accounts for 69% and sublimation for 31% of the total mass loss. In total, 8% of the surface and subsurface melt water refreezes.

Annual mean MB from the MB model is in a good agreement to the results of Yao et al. (2012) for three of four years (Fig. 4.13). In 2007/08 solid precipitation from HAR is maximal within the 12-year period and accounts for maximum accumulation and less surface melt through higher α. Thus, the MB model produces only a slightly negative MB. This is in contrast to the most negative MB measured by Yao et al. (2012) in the same MB year.

Overall, results derived from the north-south profile with a precipitation scaling factor of 0.31 and an air temperature offset of +3 K seem to be reasonable compared to the findings of Holzer et al. (2014) and Yao et al. (2012). Similar results can certainly be obtained by different combinations of precipita-

tion scaling factors and air temperature offsets. Thus, further uncertainty analyses with various combinations of both factors need to be carried out in future studies.

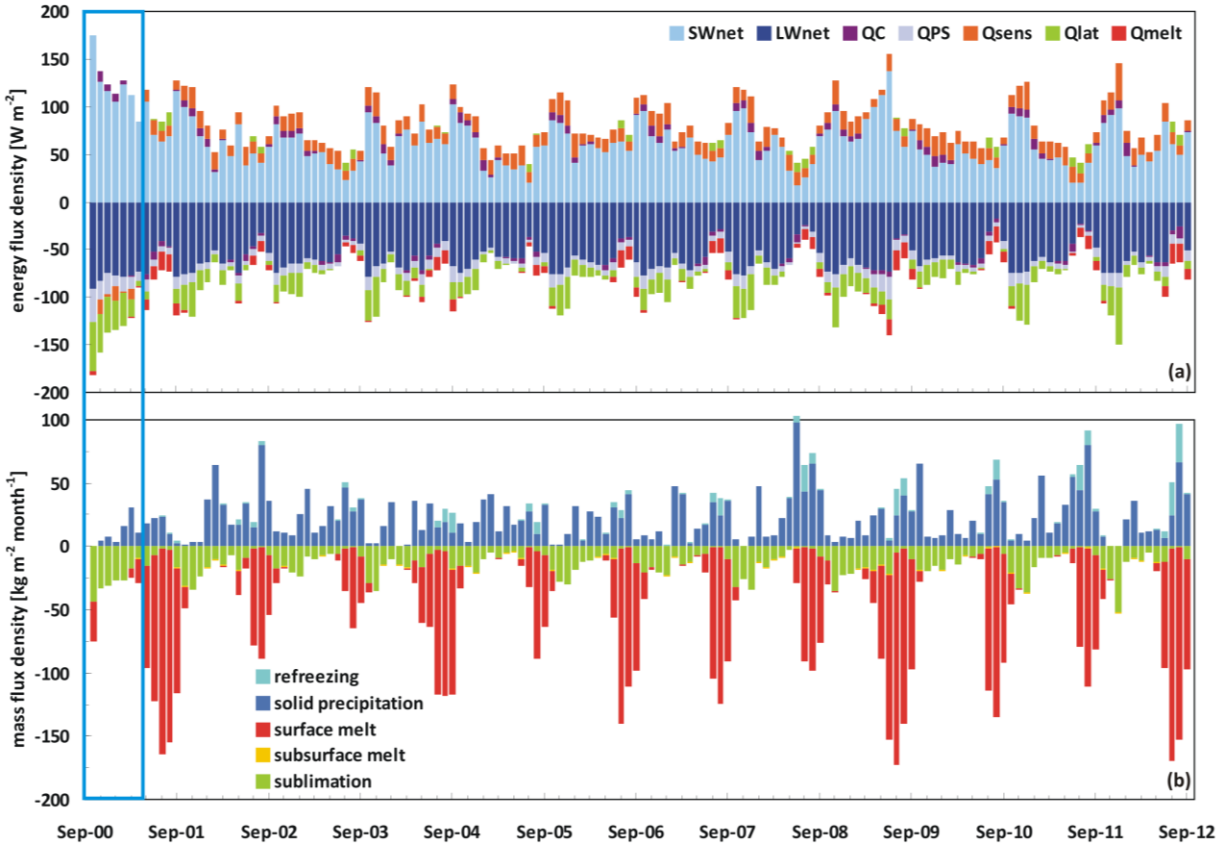


**Fig. 4.12: Glacier-wide monthly (a) SEB components (see section 2.3.1 for abbreviations) and (b) MB components from October 2000 to September 2012 at Naimona'nyi glacier (precipitation scaling factor 0.31 / $T_{air}$ +3 K). Note that the first months (blue box) should not be considered.**

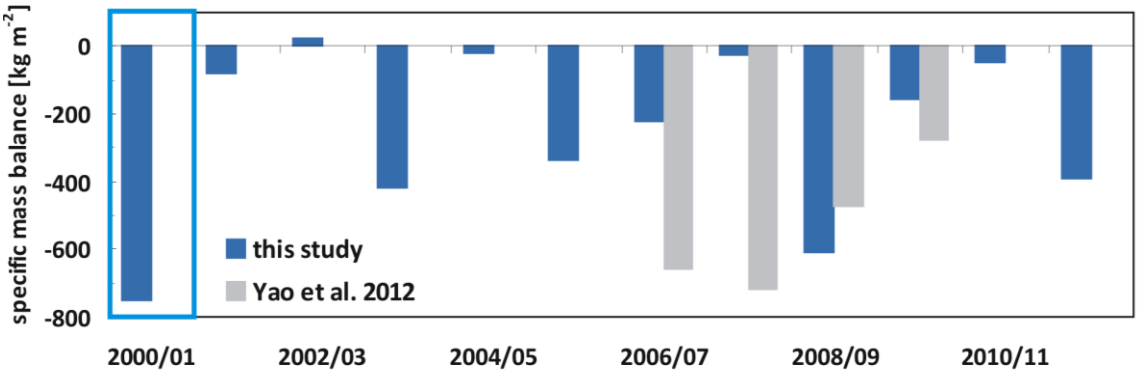


**Fig. 4.13: Glacier-wide annual MB for MB years (October – September) 2000-2012 estimated by the HAR forced MB model for Naimona'nyi glacier glacier (precipitation scaling factor 0.31 / $T_{air}$ +3 K) and compared to the results published in Yao et al. (2012). The MB value of 2006/07 of Yao et al. (2012) is the total over 2005/06-2006/07. Note that the MB in 2000/01 (blue box) should not be considered.**

## 4.6 Conclusion regarding model results for Naimona'nyi glacier

The Naimona'nyi glacier is one of the measurement sites within the WET project. The comparison of atmospheric AWS data at the glacier tongue with HAR data revealed that $T_{air}$ from HAR data exhibits a significant cold bias of 3.8 K in winter and 2.0 K in summer compared to the AWS measurements (see section 1.4.2.2). In this chapter, SEB and MB components of Naimona'nyi glacier are calculated for 2000-2012 and interpreted concerning their altitudinal gradients and their inter- and intra-annual patterns. To account for uncertainties in total HAR precipitation amounts and to obtain a model uncertainty for further MB calculations, we perform three model runs with varying precipitation scaling factors (0.56±0.25) while keeping $T_{air}$ from HAR unchanged. In the reference run a factor of 0.56 is applied. This number was obtained by Mölg et al. (2012) for Zhadang glacier and successfully applied in this thesis in the HAR forced MB model runs 2001-2011 for Zhadang glacier (see section 2.4) and for PIC (see chapter 3). In total, the energy input to the glacier surface of Naimona'nyi is dominated by $LW_{net}$ with 40% both in the reference run and in the model run with 25% decreased precipitation (0.31) when simulated with unchanged $T_{air}$ from the HAR dataset. The increase of $T_{air}$ by +3 K increases surface melt and $\alpha$ because larger glacier areas are snow free. Thus, both the absolute value and the relative importance of $SW_{net}$ increase by 21.7 W m$^{-2}$ or by 6%. When applying $T_{air}$ directly from the HAR output very low air temperatures and frequent amounts of snowfall suppress surface melt and favour refreezing in the reference model run. Thus, effective melt accounts only for 13% and sublimation for 87% of the total mass loss in the reference run (Table 4.2). The increase of $T_{air}$ by +3 K increases the proportion of effective melt to 69%. The variation of HAR precipitation as input for the MB model through the application of three different scaling factors creates only a small range of uncertainty for every SEB and MB component. A pronounced cold bias in HAR $T_{air}$ leads to a high proportion of total precipitation falling as snow even in summer. Thus, glacier-wide $\alpha$ is generally high and reduces the sensitivity of all SEB and MB components (see sections 4.4.1, 4.4.2). Only the lower glacier regions are sensitive to a precipitation decrease by 25% (Fig. 4.4). The ELA at Naimona'nyi for 2002-2012 is estimated around 5770 m a.s.l. (scaling factor 0.31) what is significantly lower than the value given by Yao et al. (2012) (≈6300 m a.s.l.) but within the large scale ELA for the region of the western Himalayas (Fig. 1 in Yao et al. 2002). An ELA of ≈6020 m a.s.l. is estimated from the north-south profile with an air temperature offset of +3 K.

Compared to the results of Holzer et al. (2014) the reference run clearly overestimates the MB and the surface height changes when simulated with unchanged $T_{air}$ from the HAR dataset. With precipitation decreased by 25% (0.31) the MB model results are more reasonable but still seem to overestimate the MB and the surface height changes especially in the lower glacier regions. A pronounced cold bias in HAR $T_{air}$ is evident from the comparison with AWS measurements. To reveal the effects of a positive temperature offset on the glacier behaviour without high computational efforts, the MB model was not run for the total glacier area but for a north-south profile along the glacier flow-line. The profile is calculated with a precipitation scaling factor of 0.31 and a temperature offset of +3 K. The derived surface height changes agree well with the results of Holzer et al. (2014). We imply that the SEB and MB components determined for the profile allow concluding for the whole glacier. Thus, the calculated glacier-wide annual MB need to be treated with caution. However, the results are close to the findings of Holzer et al. (2014) and Yao et al. (2012) and are within the range of several remote sensing studies.

It can be concluded from the application of the MB model to Naimona'nyi glacier that the derived intra- and inter-annual cycles of SEB and MB components are within reasonable limits depending on the respective patterns of the input parameters from HAR. The obtained SEB and MB components are consistent with each other because they interact through physical relationships (see sections 1.3.4 and 2.3.1). The HAR output overestimates the precipitation amounts in the reference run. A

scaling factor of 0.31 is more reasonable (see section 4.4.1). However, at Naimona'nyi glacier the calculated MB and surface height changes still seem to be overestimated. This could be revealed from the comparison with available remote sensing results and few in-situ measurements. In regions with limited availability of in-situ measurements remote sensing data is important for the evaluation of MB models. The overestimation of the calculated MB most probably is caused by a significant underestimation of $T_{air}$ by the HAR output resulting in significantly too small MB estimates especially in the lower regions of the glacier tongue. This effect can be revealed from the comparison with AWS data over one year. The modelled MB and the in-situ and remote sensing based observations indicate that this cold bias of $T_{air}$ by HAR is evident over the whole simulation period. The consequence is a significant effect on modelled SEB and MB. Therefore, a major conclusion from chapter 4 is that glacier SEB and MB modelling based on modelled atmospheric data always requires some kind of meteorological, glaciological or remote sensing based field observation. In consequence, the continuation and extension of at least basic in-situ measurements is a crucial requirement in order to obtain reliable SEB and MB estimates for different benchmark glaciers on the TP.

# 5 Energy and mass balance for Halji glacier, north western Nepal, 2000-2011, as derived from a coupled snow and energy balance model

## 5.1 Introduction and regional climate conditions

Halji glacier is a northeast exposed valley glacier (≈2.3 $km^2$) at the southern slope of the Nalakankar Himal, a northern ridge of the western Himalayas in north western Nepal (Fig. 5.1, see section 1.4.1). Since 2006, a periodic GLOF occurs in Limi valley and threatens the village Halji. The analysis of satellite imagery revealed that the flood is probably released from a supra-glacial lake at ≈5350 m a.s.l. on Halji glacier (≈6 km away) (Kropacek et al. 2013). In the central and eastern Himalayas the growth of glacial lakes, both on (supra-glacial) and in front (pro-glacial) of the glacier, has been observed in recent decades (Ageta et al. 2000, Bayracharya & Mool 2009, Bolch et al. 2012, Fujita et al. 2009, Sakai 2012). Supra-glacial lakes evolve in regions of small surface slopes when the glacier tongue stagnates (Sakai et al. 2000). The release of thermal energy from the water to the glacier ice accelerates the melting process (Sakai et al. 2009). Generally, the risk related to a GLOF in the Himalayas is mainly due to large lake volumes and associated wide reach of the flood (Richardson & Reynolds 2000).

As the GLOF in Limi valley does not happen annually and the reason for the pattern is not yet understood, the developed SEB/MB model (see section 2.3.1) is applied to Halji glacier to estimate glacier MB and melt water runoff. The physically based model is especially valuable in remote areas like Limi valley because it does not directly depend on in-situ measurements. The model allows linking the atmospheric conditions from HAR data to glacier runoff in order to find possible causes for '*GLOF years*' and '*non-GLOF years*'.

The region is clearly dominated by Indian monsoon in summer and mid-latitude westerlies in winter (see section 1.4.1). Most atmospheric variables, generated by HAR show a pronounced seasonal contrast (Fig. 1.13, 5.2). Daily mean air temperatures generated by HAR generally rise above zero from mid June to September and daily means range between -26.9°C and 6.1 C (average -8.5°C) within the period 2000-2011. Monthly means of those HAR variables that serve as input for the applied MB model are shown in Fig. 5.2. $SW_{in}$ reaches its maximum around May and decreases in summer, when monsoonal cloud cover is large. The monsoon season is associated with annual maxima in precipitation, RH and air pressure associated with the Tibetan High (see section 1.3.1) whereas wind speeds are generally low (Fig. 5.2). The mean annual precipitation amount at Halji glacier (605 mm) is larger compared to Zhadang glacier (534 mm) and PIC (380 mm) when applying the same scaling factor of

0.56 (see section 5.2). Significant amounts of precipitation already occur in late winter and spring (Fig. 1.12, see section 1.4.1). These differences in amount and seasonality of precipitation and the lower mean air temperature (-8.5°C) at Halji glacier suggest a lower mass loss during the considered period 2000-2011 compared to Zhadang glacier (-7.5°C).

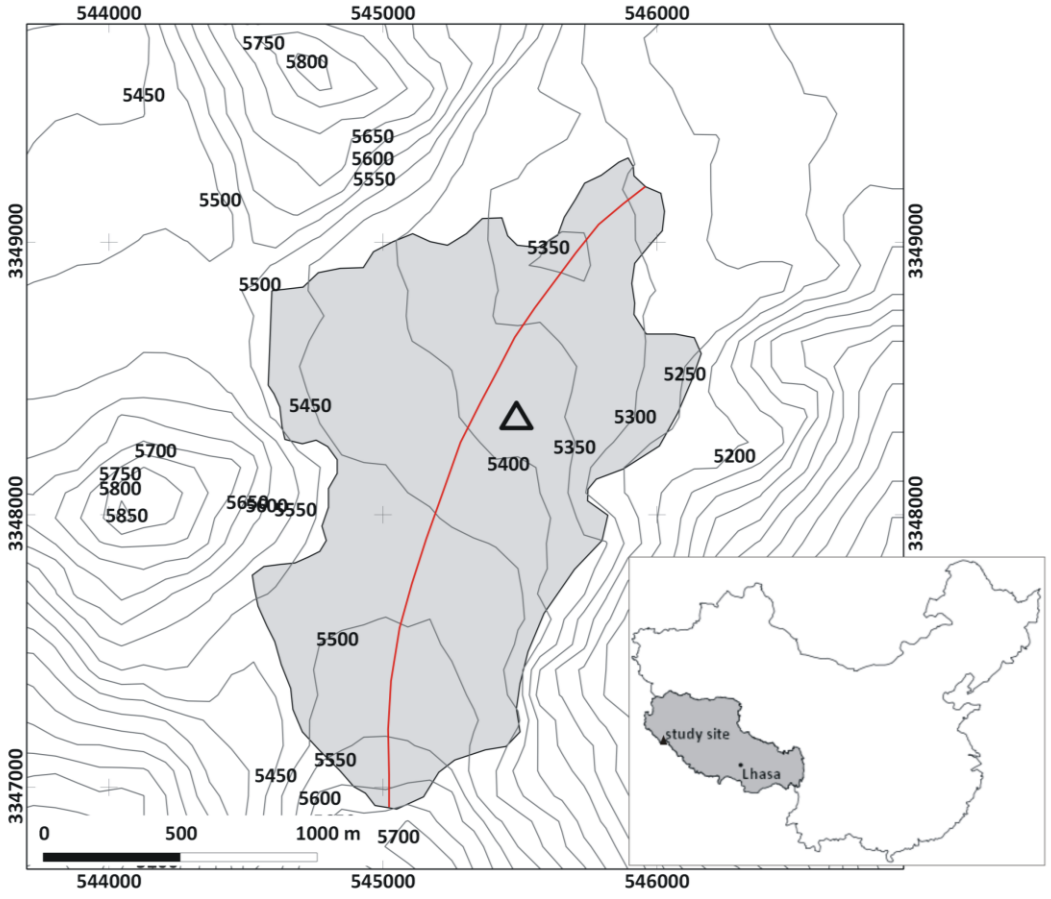


**Fig. 5.1: Halji glacier (grey area) with glacier outlines from 2001. The red line indicates the MB profile (see section 5.5); the triangle marks the DEM pixel that is used for the cloud correction of potential $SW_{in}$. Contours are in meters a.s.l. (50 m spacing); coordinate system is UTM 44N, WGS84. The inlay shows the location of the study site at the border to China and Tibet Autonomous Region (grey).**

## 5.2 Data basis

For the simulation of SEB and MB for Halji glacier for the period October 2000-2011 we solely use HAR data from the grid cell containing the glacier to run the distributed MB model. The model is explained in detail in section 2.3.1. It was calibrated and evaluated thoroughly against in-situ measurements at Zhadang glacier (see section 2.4) and is directly transferred and applied to Halji glacier. The MB model structure, the applied parameterizations, constants and assumptions set for Zhadang glacier remain unchanged to ensure the required transferability of the model to other regions without in-situ measurements. Altitudinal gradients of most input parameters are required to run the distributed model for the total glacier area (see section 2.2.3). The altitude dependency is calculated from the four HAR grid cells surrounding Halji glacier (Fig. 5.3). Resulting gradients are -0.0066°K $m^{-1}$ for $T_{air}$, 0.01% $m^{-1}$ for *RH*, -0.071 hPa $m^{-1}$ for $\rho_{air}$ and 0.00004 mm $m^{-1}$ or 0.033% $m^{-1}$ for precipitation. For *u* and *N* we assume no distinct altitude dependency although values correlate with altitude to a high degree. This is possibly due to the small number of grid cells considered (see sections 2.2.3, 3.2, 5.2). Especially *u* depends more likely on terrain structure than on altitude.

From in-situ measurements at Zhadang glacier Mölg et al. (2012) obtained a scaling factor of 0.56 for the amount of HAR precipitation (see section 2.2.3) that was successfully applied in the HAR forced MB model runs 2001-2011 for Zhadang glacier (see section 2.4). Due to a lack of precipitation measurements we also apply this scaling factor on HAR precipitation for Halji glacier in the reference model run (Fig. 1.12, 5.2). The distributed model runs on a SRTM DEM with a resolution of 90 m (Rabus et al. 2003). The area of the glacier is kept constant throughout the modelling period and is based on the 2001 glacier extent (Fig. 5.1).

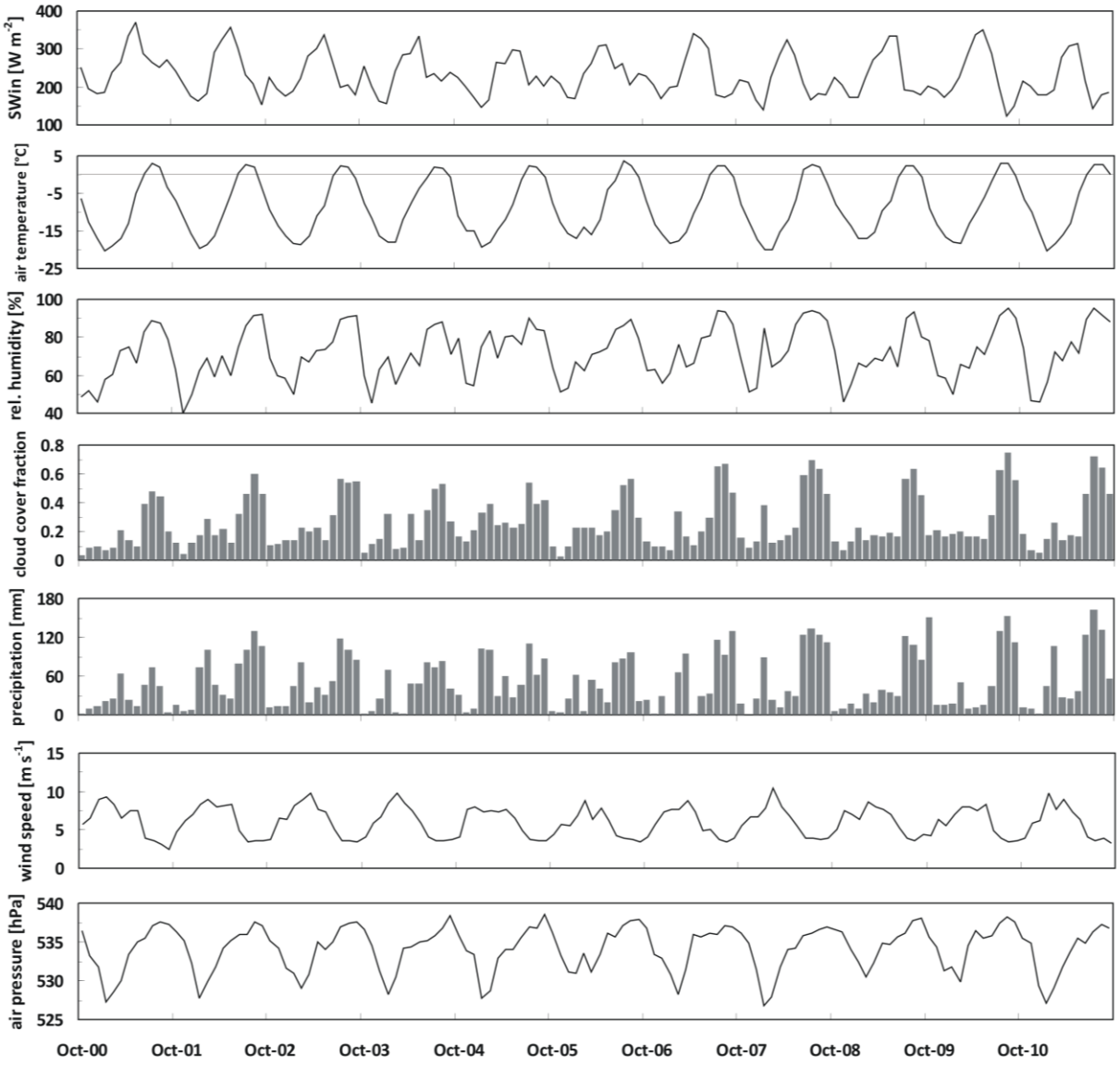


**Fig. 5.2: Monthly means or sums (precipitation) of meteorological variables at the atmospheric grid cell containing Halji glacier (5273 m a.s.l.), October 2000-September 2011. The MB model is forced with hourly values of these variables. The scaling factor of 0.56 is already applied on precipitation amounts.**

Potential $SW_{in}$ is derived from the radiation model after Kumar et al. (1997) as it was done for Zhadang glacier (see section 2.3.1) and corrected for cloud cover through HAR $SW_{in}$. The altitude of the HAR pixel that contains the glacier area and that is used as input data corresponds to the lowermost glacier regions (5273 m a.s.l., Fig. 5.1). The effect of shading by the surrounding terrain structure in these regions is apparent. Therefore, we choose a DEM pixel (*j*) in the middle part of the glacier with minimum terrain shading and similar annual cycle as HAR $SW_{in}$ for the cloud correction (Fig. 5.1). Cal-

culation of the correction of $SW_{in,pot}$ for cloud coverage and terrain effects is carried out as outlined in section 2.3.1 for the case of Zhadang glacier.

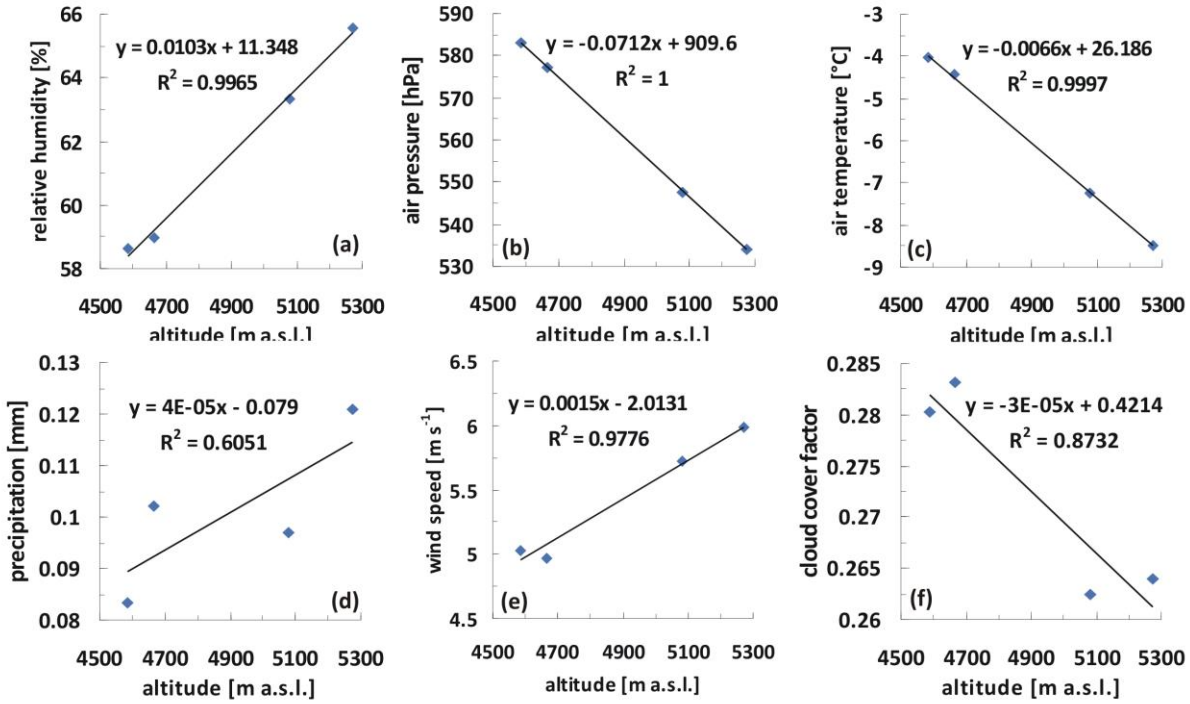


**Fig. 5.3: Altitude dependency of the HAR variables that serve as input for the MB model at Halji glacier (without $SW_{in}$). The slope of the regression line defines the respective altitude gradient per meter. Values are means for each HAR grid cell, 2000-2011.**

## 5.3 Initialisation of the SEB/MB model for application at Halji glacier

So far, Halji glacier has not been subject to any glaciological observations. Therefore, information on ELA or snow distribution for initial model assumptions is lacking. Two snow depth measurements in the north western region of the glacier in December 2013 at an altitude of ≈5300 m a.s.l. reveal a snow pack between 40 and 50 cm and lowermost layers with densities in the range of firn (N. Neckel & B. Schröter, personal communication). Based on this knowledge, we assume an initial snow depth that slightly increases linearly from 0 cm in 5300 m a.s.l. to 12 cm in the uppermost regions.

To account for uncertainties in total precipitation amounts (section 5.2) and to obtain a model uncertainty for further MB calculations, we perform three model runs with varying precipitation scaling factors (0.56±0.25). The model run with a scaling factor of 0.56 is called reference run. Furthermore, HAR precipitation amounts are decreased by 25% (scaling factor 0.31) and increased by 25% (scaling factor 0.81) relative to the reference run. The lower factor (0.31) leads to a mean annual precipitation total of 335 mm, applying the higher factor (0.81) results in precipitation sums of 875 mm $yr^{-1}$.

## 5.4 Results and discussion

In this section the results of the 11-year simulation period of Halji glacier are interpreted. The SEB/MB model explicitly calculates the different SEB and MB components and allows revealing altitudinal, inter- and intra-annual patterns on the glacier (section 5.4.1). In a further step, the typical annual cycle of the modelled transient snow line altitude and the inter-annual pattern of the ELA are linked to the results of the SEB and MB modelling (section 5.4.2).

### 5.4.1 SEB/MB characteristics 2000-2011

The altitudinal dependency of MB and SEB components averaged over the simulation period 2000-2011 is shown in Fig. 5.4. The given uncertainty ranges result from the model runs with varying precipitation scaling factors (see section 5.3). Precipitation amounts are both decreased and increased by 25% compared to the reference run. The reference run is characterized by a precipitation scaling factor of 0.56. The gradient of calculated MB shows a distinct steepening around 5350 m a.s.l., slightly below the 11-year ELA (Fig. 5.4a). This pattern is similar to the one modelled for Zhadang glacier (see section 2.4.6) and was also observed at Morteratschgletscher by Klok & Oerlemans (2002). The vertical variation of the MB profile is smaller than at Zhadang glacier and varies largely with decreasing precipitation amounts. The application of a scaling factor of 0.31 on HAR precipitation results in a strong decrease in MB especially in the lower glacier areas and increases the vertical variation (Fig. 5.4a). Studies of Mölg et al. (2009) at Kilimanjaro found a similar effect. A decrease (increase) in precipitation over all altitudes (Fig. 5.4c) causes more (less) surface melt mainly at the lower elevations (Fig. 5.4a). At Halji glacier, precipitation amounts with the same scaling factor of 0.56 are higher than at Zhadang glacier (see section 1.4.1) resulting in stronger melt in the lower regions and an increased vertical variation of MB at the latter (Fig. 2.23).

The shape of the vertical MB profile is also apparent in the gradients of $SW_{net}$ (Fig. 5.4d), $Q_{melt}$ (Fig. 5.4e), surface melt (Fig. 5.4a) and $\alpha$ (Fig. 5.4g). $Q_{melt}$ has the same shape as surface melt because the two parameters are directly connected through $L_M$ (see section 2.3.1). In the reference run (precipitation scaling factor 0.56) the vertical variation of $\alpha$ is only weak, but increases strongly with decreasing precipitation by 25% (Fig. 5.4g). Values for $\alpha$ decrease from 0.78 to 0.56 in the lower glacier regions. This effect also determines the altitude dependent variation of $SW_{net}$, $T_s$ (expressed through $LW_{out}$), $Q_{sens}$, $Q_{lat}$ (sublimation), $Q_{melt}$ (surface melt) and MB. Similar dependencies are observed by Braun & Hock (2004) on King George Island (Antarctica) and by van Pelt et al. (2012) on Svalbard. Less solid precipitation (Fig. 5.4c) increases surface melt through decreasing $\alpha$ (see also Klok et al. 2005) especially in the lower regions where $T_{air}$ is higher. This in turn causes $SW_{net}$ (Fig. 5.4d) and $T_S$ to increase (Fig. 5.4f). Increasing $T_s$ yields to smaller $Q_{sens}$ directed to the glacier surface and a higher $Q_{lat}$ from the glacier surface to the atmosphere (Fig. 5.4e). These feedback processes are also observed by Klok & Oerlemans (2002) at Morteratschgletscher. Larger negative $Q_{lat}$ results in increased mass loss through sublimation in the lower glacier regions (Fig. 5.4b). These patterns and feedback mechanisms reveal that a precipitation decrease by 25% compared to the reference run has numerous effects on all SEB and MB components. The combination of decreasing accumulation and increasing mass loss in the lower glacier regions both, from increased surface melt, decreased refreezing and increased sublimation lead to a high sensitivity of glacier MB to a 25% decrease in precipitation at Halji glacier.

$SW_{in}$ and $LW_{in}$ are the only ground-independent energy sources for the glacier surface (see section 2.3.1) and do not change with varying precipitation amounts (Fig. 5.4d) because energy fluxes from the surrounding terrain are not considered. $SW_{in}$ is nearly constant with altitude between 5350 and 5550 m a.s.l. and from 5650 m a.s.l. upwards due to minimal terrain shading (Fig. 5.1). It decreases slightly in the lowest regions up to 5350 m a.s.l. The strong decrease in $SW_{in}$ between 5550 and 5650 m a.s.l. can be explained by the steepening of the north facing slope south of the glacier (Fig. 5.1). This sharp decrease in the upper regions is also visible in the vertical patterns of $Q_{sens}$, $Q_{lat}$, sublimation, $LW_{out}$, $Q_{melt}$, surface melt and MB. The direct effect of $SW_{in}$ on MB is not that strong as revealed by Mölg et al. (2009) for glaciers at Kilimanjaro. A reason for this might be the relatively constant high value of $\alpha$ in the upper regions of Halji glacier. Thus, large amounts of $SW_{in}$ are directly reflected.

In the reference run refreezing is largest around 5350 m a.s.l. (Fig. 5.4c) where decent amounts of surface melt and a thick snow pack are present. In the reference run, the annual mean proportion of refreezing reached 50% in the upper glacier regions and 13% in the lowermost altitude band. Respective values for a 25% precipitation decrease (increase) are 46% (51%) in the upper regions and 0.2% (53%) in the lowermost part. A precipitation decrease by 25% from the reference run raises the altitude of maximum refreezing to 5550 m a.s.l., whereas a precipitation increase by 25% yields to a larger snow pack in the lower glacier regions and therefore significantly larger amounts of refreezing. For all other SEB and MB components, increasing precipitation by 25% has a much smaller effect than a precipitation decrease by 25% compared to the reference run. This is also evident for ELA variations. The ELA in the reference run is estimated between 5400 and 5450 m a.s.l. (Fig. 5.4a). The altitude coincides with the large-scale ELA for the region of the western Himalayas given by Yao et al. (2012). A decrease (increase) of the precipitation amount by 25% rises (lowers) the ELA by ≈200 m (≈100 m). Concerning the glacier hypsometry (Fig. 1.12) an ELA increase would have important consequences for the glacier MB because the largest area proportion is located in these altitude bands.

Annual cycles of glacier-wide mean monthly SEB and MB components at Halji glacier as calculated by the MB model for the reference run for the period 2000-2011 are illustrated in Fig. 5.5. It is obvious that the values calculated within the first months (blue box in Fig. 5.5) suffer from the errors that stem from the spin-up time of the MB model (see section 2.3.1). The first MB year is therefore not considered in the following interpretations. In general, $SW_{in}$ (+240.8 W m$^{-2}$) and $LW_{in}$ (+209.3 W m$^{-2}$) dominate energy input over the considered period, followed by $Q_{sens}$ (+19.6 W m$^{-2}$). Energy sinks at the glacier surface are $LW_{out}$ (-254.4 W m$^{-2}$), $SW_{out}$ (-196.8 W m$^{-2}$), $Q_{lat}$ (-16.7 W m$^{-2}$), $Q_{melt}$ (-5.1 W m$^{-2}$) and $Q_G$ (-1.4 W m$^{-2}$), making $SW_{net}$ (+48.7 W m$^{-2}$, see Table 5.1) the most important energy source, highly depending on $\alpha$. This was also observed at Zhadang glacier, PIC and Naimona'nyi glacier. The lowest values of $SW_{net}$ are evident between June and September when large precipitation amounts increase $\alpha$ (Fig. 1.10, 5.5a). $LW_{net}$ shows a rather regular seasonal cycle playing a smaller role as energy sink in summer than in winter (Fig. 5.5a). This can be explained through the seasonal patterns of $LW_{in}$, depending on $T_{air}$, $e$ and $N$ (see section 2.3.1) (higher in summer), and $LW_{out}$, depending on $T_s$ (largest negative values in summer). In winter, $LW_{in}$ is significantly smaller whereas $LW_{out}$ varies only little. Averaged over the whole period $Q_C$ is very small and naturally tends to zero. In winter, when the surface is colder than the underlying snow layers, $Q_C$ becomes positive. Slightly negative $Q_C$ is evident in spring (Fig. 5.5a), when the surface warms but subsurface layers are still cold from the winter season. $Q_{PS}$ is always negative with larger values when $\alpha$ is low ($SW_{net}$ is large). Generally, $Q_{lat}$ is an energy sink for the glacier surface (Table 5.1). However, on a monthly scale it is evident that slightly positive values can occur in July and August when the region is under the influence of maximum precipitation amounts in the course of the year, highest $T_{air}$ and $RH$ (Fig. 1.12, 5.2). A similar pattern of positive $Q_{lat}$ during the summer monsoon period is observed at Chhota Shigri glacier in the western Himalayas based on SEB measurements by Azam et al. (2014) and at Naimona'nyi glacier as reported in chapter 4. During most of the year, the dry conditions on the TP lead to negative $Q_{lat}$ and significant sublimation (Fig. 5.5) with largest values in winter when $RH$ is smallest (Fig. 5.2). Also, higher wind speeds drive turbulence during winter (Fig. 1.13). Generally, monthly means of $Q_{sens}$ and $Q_{lat}$ are of opposite sign and mostly cancel each other out. Absolute values of $Q_{sens}$ are slightly larger than $Q_{lat}$ implying a higher moisture content of the atmosphere and less sublimation compared to Zhadang glacier (section 2.4.6). A similar dependency is observed by Nicholson et al. (2013) at Lewis glacier (Mt Kenya). During the first year of simulation, precipitation amounts are comparatively small and cause highest values of $SW_{net}$, $Q_{melt}$ and surface melt in September to December 2001 (Fig. 5.5a, 5.5b). In the following years surface melt occurs dominantly in June-September, simultaneously with the period of lowest $SW_{net}$ through high $\alpha$. The climate chart for Halji glacier confirms that both air

temperature and precipitation maxima coincide between June and September (Fig. 1.12). The respective SEB values for the model runs with varying precipitation scaling factors are given in Table 5.1. For glacier-wide monthly SEB components of the MB model runs with ±25% of precipitation see Fig. A.5a and Fig. A.6a in the appendix.

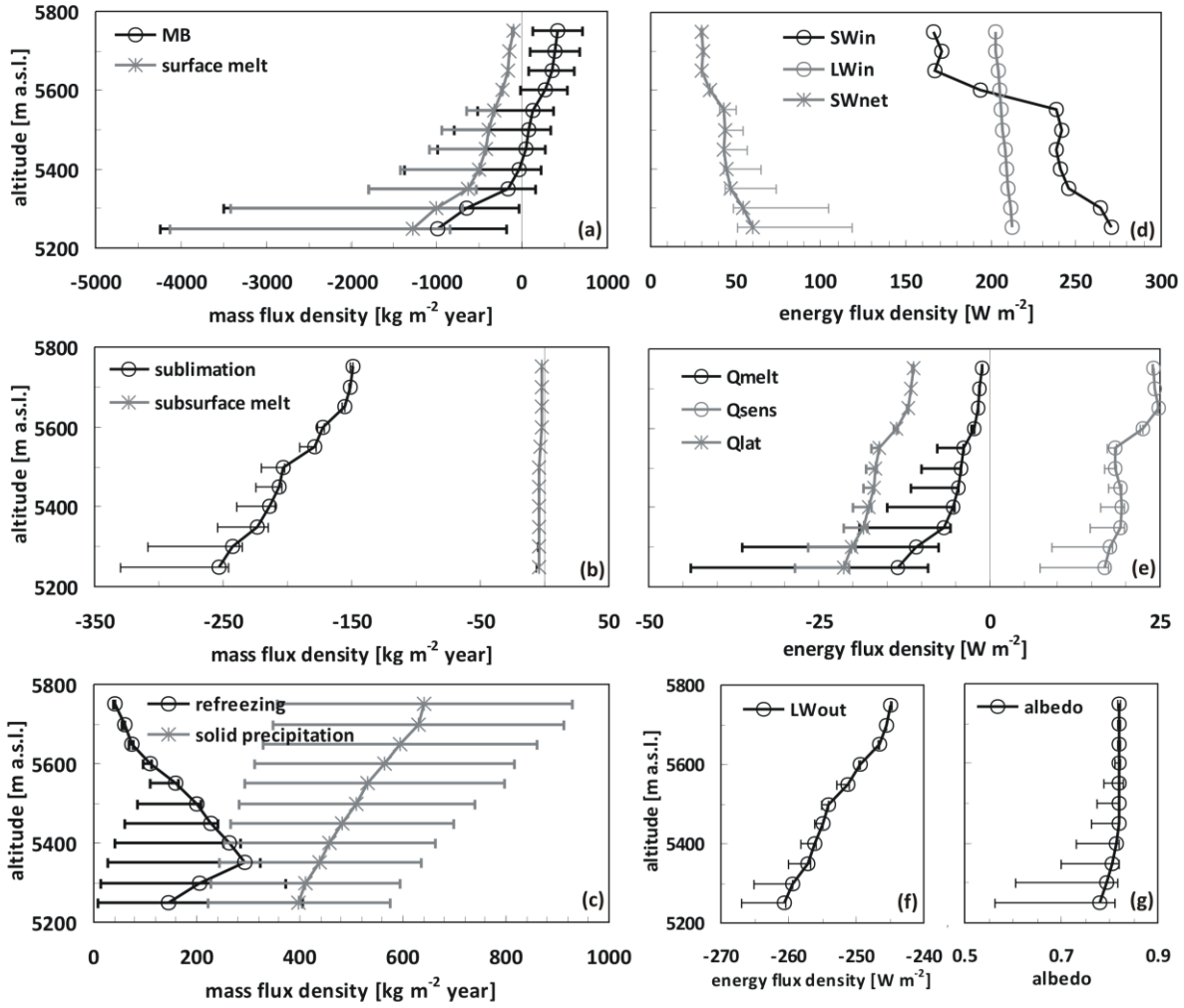


**Fig. 5.4: Modelled vertical profiles of (left) the specific mass balance and its components and (right) mean SEB components on Halji glacier averaged over the simulation period October 2000 – September 2011. Data are averaged for 50-m altitude bands. The uncertainty ranges are calculated assuming different precipitation amounts (see section 5.3). Note the different x-axis scales of the components (negative means mass or energy loss at the glacier surface, see section 2.3.1 and Table. 2.2 for abbreviations).**

The glacier-wide MB estimate of the reference run for the period 2001-2011 (the first year is not considered) is +206 kg m$^{-2}$ (+20.6 kg m$^{-2}$ yr$^{-1}$) (Table 5.2). In general, sublimation (-1998 kg m$^{-2}$/ -199.8 kg m$^{-2}$ yr$^{-1}$) is the second largest factor of glacier-wide mass loss after surface melt (-4831 kg m$^{-2}$/-483.1 kg m$^{-2}$ yr$^{-1}$) but clearly dominates ablation in winter, when air temperatures are below 0°C and surface melt is absent (Fig. 1.12, 5.5b). Subsurface melt (-36 kg m$^{-2}$/-3.6 kg m$^{-2}$ yr$^{-1}$) plays a minor role. Solid precipitation (+4957 kg m$^{-2}$/+495.7 kg m$^{-2}$ yr$^{-1}$) and refreezing (+2714 kg m$^{-2}$/ +271.4 kg m$^{-2}$ yr$^{-1}$) contribute to the mass gain of the glacier. Maximum snowfall amounts occur in summer (Fig. 1.12, 5.5b, see section 1.4.1). Refreezing at Halji glacier happens mostly in summer, when melt water is produced at the surface and percolates through the cold winter and spring snow layers. Air temperatures at Halji glacier are considerably below 0°C until June (Fig. 1.12). Therefore, it can be assumed that subsurface temperatures are well below the melting point throughout the

summer and allow the refreezing of considerable amounts of melt water. The reference run implies that 56% of the surface and subsurface melt water refreezes within the snow pack between 2001 and 2011. These results will be discussed in section 5.5. The respective MB values for the model runs with varying precipitation scaling factors are given in Table 5.2. For glacier-wide monthly MB components of the MB model runs with ±25% of precipitation see Fig. A.5b and Fig. A.6b in the appendix.

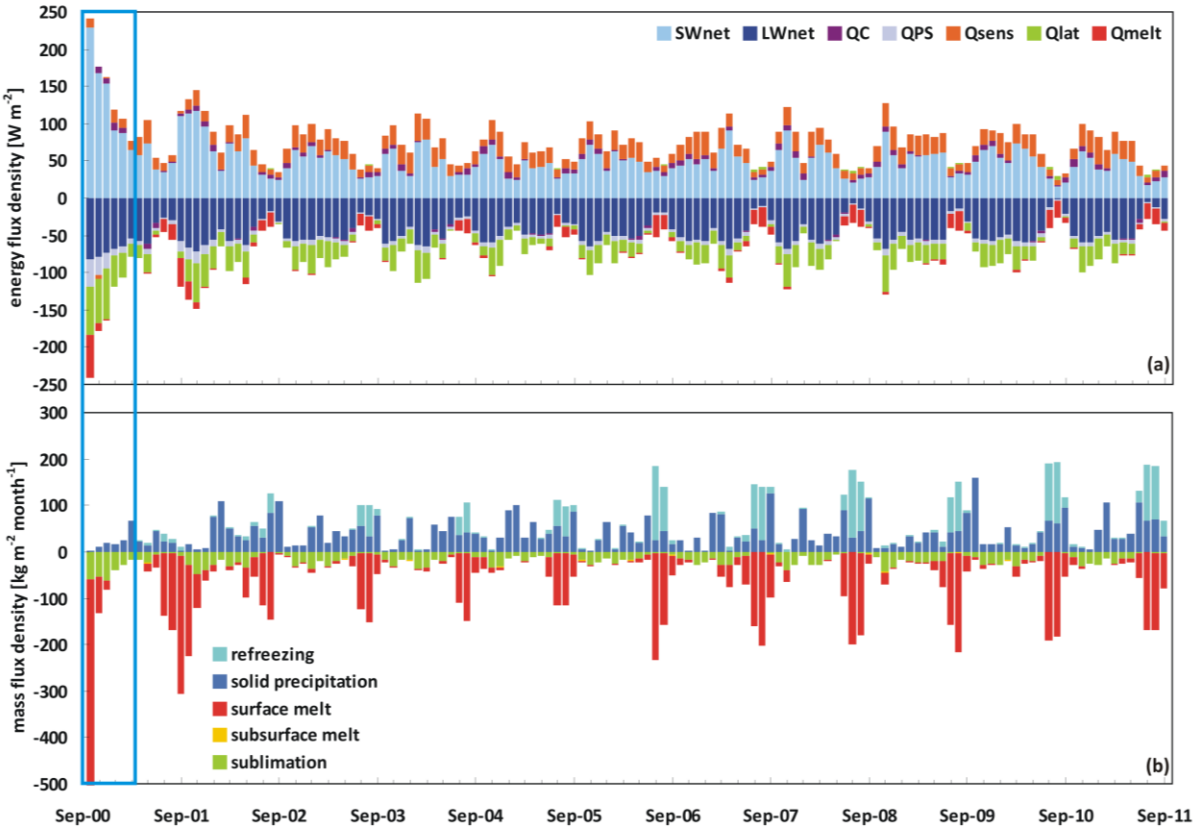


**Fig. 5.5: Glacier-wide monthly (a) SEB components (see section 2.3.1 for abbreviations) and (b) MB components from October 2000 to September 2011 at Halji glacier (reference run). Note that the first months (blue box) should not be considered.**

Table 5.1 lists the absolute and relative contributions of energy flux components to the total energy turnover for the three model runs with varying precipitation scaling factors (0.56/0.31/0.81). For the considered period 2001-2011, $SW_{net}$ accounted for 37% (43%/36%), followed by $LW_{net}$ (34%/30%/34%), $Q_{sens}$ (15%/12%/15%), $Q_{lat}$ (11%) and $Q_G$ (3%/4%/4%). The relative contribution of $SW_{net}$ and $LW_{net}$, as well as of $Q_{sens}$ and $Q_{lat}$ to the total energy flux is nearly balanced for the reference run. A similar effect was observed by Braun & Hock (2004) on King George Island (Antarctica). The influence of $Q_G$ is only minor. Therefore, simulated $Q_{melt}$ is generally low at Halji glacier over the period 2001-2011 with a minimum in 2003/04 (Table 5.1). Low $Q_{melt}$ results in low surface melt compared to Zhadang glacier and PIC with an overall positive MB (Table 5.2). As simulated surface melt rates at Halji glacier are generally low, variations in mass loss through sublimation and in mass gain through solid precipitation and refreezing play an important role for total annual MB (Table 5.2). Over the total simulation period, effective melt (surface melt + subsurface melt – refreezing) accounts for 52% (82%/34%) and sublimation for 48% (18%/66%) of the total mass loss (Table 5.2).

**Table 5.1: Mean absolute values of energy flux components as modelled for October 2000 – September 2011 and for the respective MB years with proportional contribution to total energy flux at Halji glacier. The first value is for a precipitation scaling factor of 0.56, the numbers in brackets are for the model runs for a scaling factor for precipitation of 0.31 and 0.81. Note that values of the MB year 2000/01 are not considered in the calculation of the total average.**

| | Sum* [W m$^{-2}$] | $SW_{net}$ | $LW_{net}$ | $Q_{sens}$ | $Q_{lat}$ | $Q_G$ | $Q_{melt}$ |
|---|---|---|---|---|---|---|---|
| total average [W m$^{-2}$] | 134 (154 / 133) | 49 (65 / 47) | -45 (-47 / -45) | 20 (17 / 20) | -17 (-19 / -16) | -1.4 (-5 / -1) | -5 (-12 / -4) |
| 2000/01 | | 96 (187 / 87) | -57 (-65 / -56) | 12 (1 / 14) | -28 (-36 / -26) | -9.4 (-26 / -7) | -13 (-61 / -10) |
| 2001/02 | | 64 (92 / 53) | -49 (-53 / -47) | 18 (12 / 21) | -23 (-28 / -21) | -4.4 (-10 / -2) | -7 (-14 / -5) |
| 2002/03 | | 48 (50 / 48) | -45 (-46 / -46) | 20 (19 / 20) | -17 (-18 / -18) | -1.5 (-3 / -1) | -4 (-4 / -4) |
| 2003/04 | | 48 (66 / 47) | -47 (-48 / -47) | 22 (20 / 22) | -18 (-20 / -18) | -1.7 (-6 / -1) | -3 (-12 / -3) |
| 2004/05 | | 42 (49 / 42) | -43 (-44 / -43) | 19 (17 / 19) | -13 (-14 / -13) | -0.6 (-3 / -0.1) | -4 (-5 / -3) |
| 2005/06 | | 48 (54 / 47) | -46 (-46 / -46) | 19 (19 / 19) | -15 (-15 / -15) | -1.1 (-3 / -1) | -5 (-9 / -4) |
| 2006/07 | | 48 (79 / 46) | -45 (-48 / -45) | 20 (15 / 19) | -15 (-18 / -15) | -0.8 (-8 / 0) | -7 (-21 / -5) |
| 2007/08 | | 47 (55 / 46) | -44 (-43 / -43) | 17 (16 / 17) | -15 (-16 / -15) | -0.7 (-3 / -0.1) | -6 (-9 / -5) |
| 2008/09 | | 51 (83 / 50) | -47 (-50 / -47) | 22 (17 / 22) | -19 (-23 / -19) | -1.5 (-9 / -1) | -5 (-20 / -4) |
| 2009/10 | | 49 (58 / 49) | -44 (-44 / -44) | 18 (17 / 17) | -16 (-16 / -16) | -1.3 (-4 / -1) | -5 (-10 / -5) |
| 2010/11 | | 41 (62 / 41) | -42 (-45 / -42) | 21 (16 / 21) | -14 (-18 / -14) | -0.1 (-5 / 1) | -5 (-11 / -5) |
| | 100% | 37 (43 / 36)% | 34 (30 / 34)% | 15 (12 / 15)% | 11 (11 / 11)% | 3 (4 / 4)% | |

*Sum of energy fluxes in absolute values: $|SW_{net}| + |LW_{net}| + |Q_{sens}| + |Q_{lat}| + |Q_G|$

**Table 5.2: Calculated glacier-wide mass balance components for the total period October 2000 – September 2011 and for the respective MB years at Halji glacier. The first value is for a precipitation scaling factor of 0.56, the numbers in brackets are for the model runs with lower (higher) precipitation scaling factors (0.31 / 0.81). Note that values of the MB year 2000/01 are not considered in the calculation of the total values.**

| | Solid precipitation | Surface melt | Refrozen water | Subsurf. melt | Sublimation | Mass balance* |
|---|---|---|---|---|---|---|
| tot. [kg m$^{-2}$] | 4957 (2744 / 7170) | -4831 (-10875 / -4175) | 2714 (775 / 3181) | -36 (-41 / -36) | -1998 (-2211/-1970) | 206 (-9830 / 3491) |
| 2000/01 | 268 (149 / 388) | -1200 (-5734 / -981) | 41 (0.1 / 79) | -6 (-7 / -6) | -320 (-403 / -303) | -1216 (-5994/-830) |
| 2001/02 | 602 (334 / 871) | -686 (-1324 / -489) | 84 (25 / 167) | -5 (-6 / -4) | -268 (-321 / -244) | -273 (-1293 / 284) |
| 2002/03 | 484 (268 / 699) | -352 (-391 / -354) | 134 (40 / 204) | -4 (-4 / -3) | -208 (-211 / -208) | 54 (-298 / 318) |
| 2003/04 | 407 (226 / 589) | -316 (-1129 / -267) | 114 (35 / 152) | -3 ( -4 / -3) | -215 (-238 / -215) | -13 (-1110 / 241) |
| 2004/05 | 593 (328 / 857) | -357 (-514 / -319) | 150 (72 / 180) | -4 (-4 / -4) | -165 (-178 / -164) | 217 (-296 / 532) |
| 2005/06 | 389 (215 / 562) | -460 (-832 / -411) | 271 (122 / 321) | -4 (-4 / -4) | -178 (-182 / -178) | 18 (-681 / 258) |
| 2006/07 | 481 (266 / 695) | -623 (-2015 / -478) | 254 (61 / 324) | -3 (-4 / -3) | -182 (-217 / -181) | -73 (-1908 / 326) |
| 2007/08 | 520 (288 / 752) | -532 (-860 / -491) | 303 (60 / 392) | -4 (-4 / -4) | -184 (-190 / -184) | 104 (-707 / 426) |
| 2008/09 | 363 (201 / 525) | -514 (-1877 / -420) | 212 (28 / 289) | -3 (-4 / -4) | -227 (-263 / -227) | -170 (-1915 / 135) |
| 2009/10 | 566 (314 / 819) | -483 (-910 / -468) | 291 (33 / 376) | -4 ( -4 / -4) | -194 (-198 / -194) | 177 (-765 / 493) |
| 2010/11 | 553 (306 / 799) | -509 (-1022 / -478) | 300 (76 / 374) | -3 (-4 / -4) | -176 (-213 / -176) | 165 (-858 / 478) |
| % of mass loss | | 57 (82 / 45) | | 0.8 (0.3 / 1) | 42 (18 / 54) | |

*Mass balance = solid precipitation + surface melt + refrozen water + subsurface melt + sublimation

The importance of the various SEB and MB components to surface melt and MB differs largely within the three model runs with varying precipitation scaling factors. Firstly, with decreasing precipitation compared to the reference run (scaling factor 0.31) the relative contribution of $SW_{net}$ to the total energy flux increases through decreasing $\alpha$. The differences in $SW_{net}$ between the two model runs (0.56/0.31) are largest in 2001/02, 2003/04, 2006/07 and 2008/09-2010/11. Annual and total averages of $LW_{net}$, $Q_{sens}$, $Q_{lat}$ and $Q_G$ do not experience large variations through a 25% precipitation decrease. However, they follow the pattern of $SW_{net}$ with larger variations in the respective years (Table 5.1) because the decrease in $\alpha$ directly affects $T_s$ and therefore all SEB components (see sections 1.3.4.1 and 2.3.1). Especially the negative increase in $Q_G$ is relatively large meaning that more energy

from the surface is transferred into the snow or ice and warms the subsurface. Altogether, this results in a strong negative increase of $Q_{melt}$ and surface melt and an above average decrease of MB in the respective years compared to the 10-year mean (Table 5.1, 5.2, Fig. 5.6). In the model run with decreased precipitation relative to the reference run (scaling factor 0.31) MB is closer linked to surface melt, because the contribution of effective melt to total mass loss increased to 82% (Table. 5.2). The six years in which the MB is most sensitive to a 25% precipitation decrease are characterized by higher $Q_{melt}$ already in the reference run and/or low annual precipitation (Table 5.1, 5.2). Thus, the tipping point to further increased mass loss is closer than in the other MB years. A precipitation increase relative to the reference run (scaling factor 0.81) causes overall positive MB at Halji glacier (Fig. 5.6) but the differences in the SEB and MB components to the reference run are less distinct (Table 5.1, 5.2). A possible reason might be that the reference run already simulates an overall positive MB and relatively high $\alpha$ in the lower glacier regions (Fig. 5.4g) through periodical strong snow fall events. Thus, any further precipitation increase can not have large impacts on these variables.

Simulated annual mean MB at Halji glacier can hardly be evaluated because no in-situ measurements are available so far and the glacier area is too small for intensive remote sensing analyses (see section 5.5). Kropacek et al. (2013) report a periodic GLOF event since 2006 (see section 5.1). The water is released from a supra-glacial lake on Halji glacier. To reveal possible consistencies between glacial runoff generated by the MB model and the occurrence of '*GLOF years*' and '*non-GLOF years*', the annual amount of water supply from the glacier is calculated (Fig. 5.6). Runoff (in kg $m^{-2}$) is determined from surface and subsurface melt, refreezing and liquid precipitation for the total glacier area. The effect of routing, the time delay of the melt water movement vertically through the snowpack and horizontally along the glacier surface (Singh & Singh 2001), is not considered. The actual drainage basin of the supra-glacial lake might be smaller than the total glacier area. This can be neglected because it does not affect the quantitative comparison. Between 2001 and 2011 four '*non-GLOF years*' were observed (Fig. 5.6). In 2002/03 and 2004/05 simulated runoff is small when including the ranges of uncertainties. In these years no GLOF occurred. This might be an indication that the amount of runoff is possibly linked to a GLOF event. However, simulated runoff in the years 2005/06, 2007/08, 2009/10 and 2010/11 is similar but 2009/10 is the only '*non-GLOF year*' of those. In 2001/02 no GLOF event is evident despite high runoff (Fig. 5.6). Thus, the link between simulated runoff and GLOF events at Halji glacier is limited. Kropacek et al. (2013) assume external factors, e.g. sediment damming of the lake, to override the meteorological forcing. Furthermore, the lake geometry and the temporal melt pattern may influence the lake outburst.

Mean modelled MB between 2001 and 2011 for Halji glacier with varying precipitation scaling factors (0.56/0.31/0.81) is +21 kg $m^{-2}$ $yr^{-1}$ (-983 kg $m^{-2}$ $yr^{-1}$/+349 kg $m^{-2}$ $yr^{-1}$). Considering the published results of less detailed studies for glaciers in the Himalayas (e.g. Gardelle et al. 2013a,b, Kääb et al. 2012, Bolch et al. 2011), the obtained MB for the reference run appears to be too positive. The mean MB for the Pamir/Karakorum/Himalaya region was estimated to be -140±80 kg $m^{-2}$ $yr^{-1}$ for 1999-2011 (Gardelle et al. 2013) and -210±50 kg $m^{-2}$ $yr^{-1}$ for the Hindukush/Karakorum/Himalaya region for 2003-2008 (Kääb et al. 2012). For western Nepal the authors give MB values of -320±130 kg $m^{-2}$ $yr^{-1}$ (Gardelle et al. 2013) and -340±50 kg $m^{-2}$ $yr^{-1}$ (Kääb et al. 2012). Neckel et al. (2014) estimate a mass loss of -370±250 kg $m^{-2}$ $yr^{-1}$ between 2003 and 2009 for the Gangdise Shan including the Halji region. The few existing MB measurements over several years reveal the most negative mass balances in the Himalayas, ranging from -1100 kg $m^{-2}$ $yr^{-1}$ to -760 kg $m^{-2}$ $yr^{-1}$ (average -930 kg $m^{-2}$ $yr^{-1}$) between 2002 and 2010 (Yao et al. 2012).

Thus, the MB model result for a precipitation scaling factor of 0.31 (-983 kg $m^{-2}$ $yr^{-1}$) is within the range of the results of Yao et al. (2012). However, the detection of a cold bias in HAR air temperature at Naimona'nyi glacier (see section 4) implies that a similar effect probably has to be considered also

at Halji glacier. Both glaciers are only ≈26 km apart from each other (see section 1.4.1). An increase in $T_{air}$ will in turn demand a precipitation increase to obtain similar MB results. Thus, further uncertainty analyses with various combinations of precipitation scaling factors and air temperature offsets are required (see section 5.5).

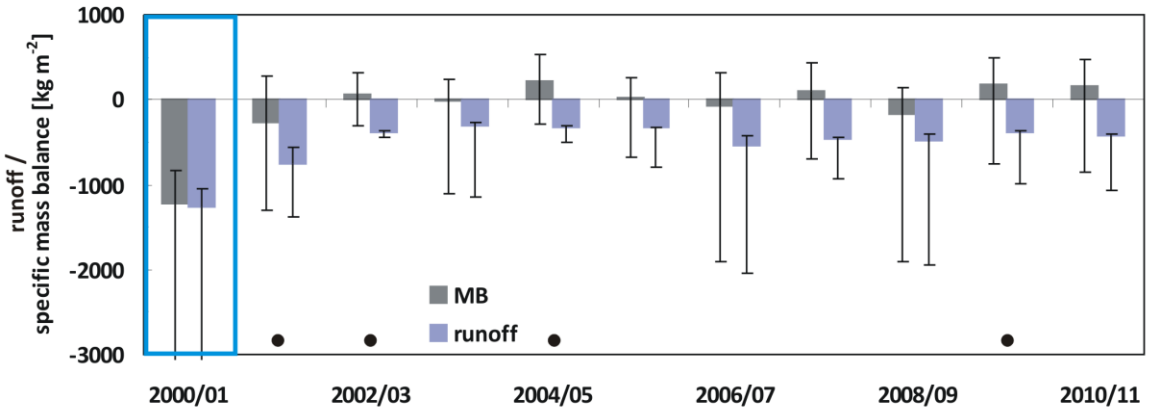


**Fig. 5.6: Glacier-wide annual MB and runoff for MB years (October – September) 2000-2011 estimated by the HAR forced MB model for Halji glacier. The uncertainty ranges are calculated assuming different precipitation amounts (see section 5.3, Table 5.2). The black dots mark the '*non GLOF years*' (Kropacek et al. (2013)). Note that the MB in 2000/01 (blue box) should not be considered.**

## 5.4.2 Snow line and ELA characteristics 2000-2011

To complement the studies on the inter- and intra-annual snow line and ELA characteristics at Zhadang glacier (see section 2.4.4) and PIC (see section 3.4.2), mean monthly variations of the glacier-wide mean altitude of the transient snow line between 2001 and 2011 are calculated from the MB model results (Fig. 5.7). The given values refer to the reference run with a precipitation scaling factor of 0.56. Based upon the reference run precipitation amounts are decreased and increased by 25%, respectively, to obtain the model uncertainty (see section 5.3). Between October and May the snow line fluctuates between 5250 and 5265 m a.s.l. in the reference run. In these months mass gain through solid precipitation is occasionally compensated by sublimation or small amounts of surface melt through large $Q_{sens}$ and $SW_{in}$ that can raise $T_s$ to zero in the lowest regions (Fig. 5.5). Similar processes could be observed at Zhadang glacier (see section 2.4.5). Thus, a snow line can be visible even in winter. In June $T_{air}$ rises above zero (see section 5.1). Increasing amounts of surface melt compensate increasing precipitation amounts (Fig. 1.12) and cause a slow rise of the snowline. In July and August $T_{air}$ and surface melt reach their maximum. The mass loss can not be compensated even by the highest precipitation amounts in the annual cycle. Therefore, snow line altitude rises to its annual maximum around 5320 m a.s.l. (Fig. 5.7). In September and October the snow line altitude lowers due to significantly decreasing $T_{air}$ and surface melt while precipitation amounts are still on average (Fig. 1.12, 5.5, 5.7). In November the transient snow line again rises slightly (Fig. 5.7). This can be explained by minimum precipitation and increasing sublimation (Fig. 5.5). The mean transient snow line altitude between 2001 and 2011 is located in ≈5270 m a.s.l. Especially in summer when amounts of refreezing are large the differences between transient snow line and transient ELA can be large (Cogley et al. 2011). In the reference run at Halji glacier, 56% of surface and subsurface melt refreeze (see section 5.4.1) and form a layer of superimposed ice when the snow pack is removed. Therefore, a snow line can develop and rise up the glacier while MB is still positive. With decreasing precipitation amounts by 25% compared to the reference run the snow line altitude rises around 30 m with the largest sensitivities in spring and autumn (Fig. 5.7). At that time of the year precipitation is slight-

ly below average, sublimation is large and large $SW_{in}$ and $Q_{sens}$ cause surface melt (Fig. 5.5). A lowering of $\alpha$ with decreasing precipitation enhances these processes. A precipitation increase by 25% lowers the mean snow line altitude by approx. 8 m with largest sensitivities in those months with least precipitation (November, December) (Fig. 1.12, 5.7).

The modelled annual ELA for 2000 to 2011 at Halji glacier is shown in Fig. 5.8. The ELA follows the MB pattern (Fig. 5.6) with low ELA in positive or slightly negative MB years and high ELA in negative MB years. From the vertical MB profile for the reference run for Halji glacier in section 5.4.1 the ELA between 2000 and 2011 is estimated around 5400 m a.s.l. (Fig. 3.4a). The average over the calculated annual ELA leads to a value of 5370 m a.s.l. for the reference run. If the first MB year is neglected the mean ELA is 5350 m a.s.l. A precipitation decrease by 25% compared to the reference run raises the ELA by ≈190 m, a precipitation increase by 25% lowers the ELA by ≈80 m.

The relation of annual AAR and annual MB at Halji glacier for the period 2001-2011 for the reference run (precipitation scaling factor 0.56) is visualized in Fig. 5.9. According to the model data using unchanged air temperature form the HAR dataset the relationship between AAR and MB is non-linear. The two most negative MB years (2001/02 and 2008/009) are characterized by very low AAR (44% and 35%) (Fig. 5.9). A possible reason of this strong decrease in AAR at negative MB might be the rather flat glacier surface in the middle part (Fig. 5.1). Large proportions of the total glacier are within the same altitude (Fig. 1.12). Thus, a change in MB can cause larger changes in the AAR. Similar patterns are observed by Dyurgerov et al. (2006) at glaciers in Norway (Nigardsbreen) or the European Alps (Wurtenkees). The authors suggest that some of these non-linear regressions are caused by anomalous increases or decreases of snow accumulation in the upper or lower parts of the glacier. Furthermore, this pattern may be related to the glacier topography and shape that affect the snow cover distribution (Dyurgerov et al. 2006). For glaciers with a non-linear relationship of AAR and MB Dyurgerov et al. (2006) apply a higher-order polynomial regression. At Halji glacier a higher-order polynomial regression (see also Dyurgerov et al. 2009) represents the relationship between AAR and MB very well (Fig. 5.9). In the reference run annual AAR at Halji varies between 35% in 2008/09 and 96% in 2004/05. For the total simulation period of the reference run the AAR is 81%. The $AAR_0$ is estimated to be 80% (Fig. 5.9). The index $\alpha_d$ after Dyurgerov et al. (2009) measures the glacier's displacement from the equilibrium (see section 2.4.6). For Halji glacier $\alpha_d$ is determined to be +2%. Thus, the glacier has to increase slightly to reach its equilibrium state for the climate conditions of the simulation period with a precipitation scaling factor of 0.56. A precipitation decrease of 25% compared to the reference run results in an AAR of 4% and in a $\alpha_d$ of -95%. This implies that Halji glacier would have to decrease its area to a high degree to reach its equilibrium. Over longer timescales only 0.1 $km^2$ of the glacier would remain in steady state when assuming a precipitation scaling factor of 0.31. A precipitation increase of 25% compared to the reference run leads to an AAR of 98% and in a $\alpha_d$ of +22%. Thus, the glacier would increase its area and advance in order to reach its equilibrium state when applying a precipitation scaling factor of 0.81.

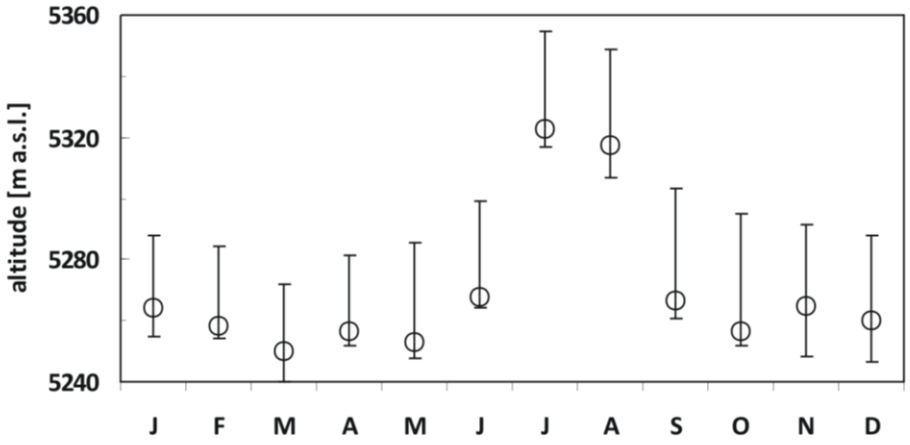


**Fig. 5.7: Modelled mean intra-annual snow line pattern at Halji glacier, 2001-2011. The model uncertainty is calculated assuming different precipitation amounts (see section 5.3).**

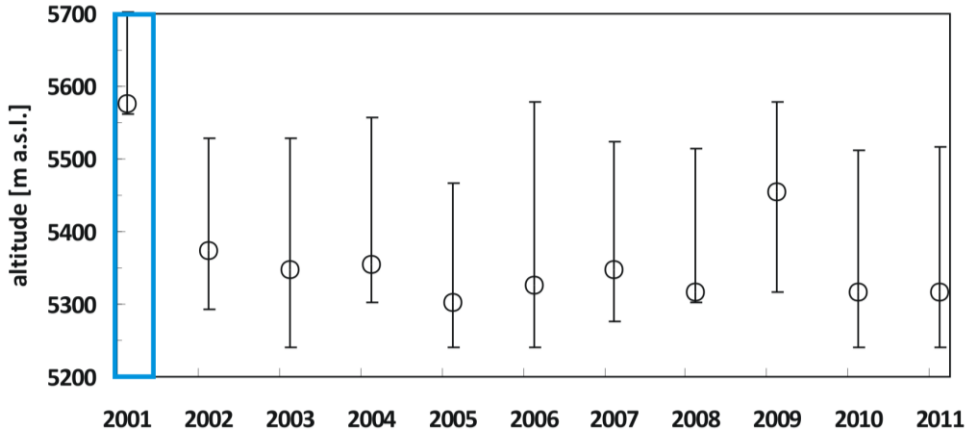


**Fig. 5.8: Glacier-wide annual ELA at Halji glacier, 2000-2011. The uncertainty ranges are calculated assuming different precipitation amounts (see section 5.3). Note that the ELA in 2001 (blue box) should not be considered.**

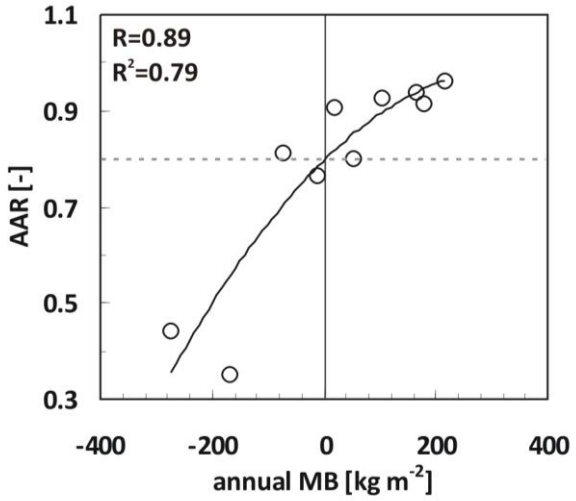


**Fig. 5.9: Relation between annual MB and AAR at Halji glacier, 2001-2011, for the MB model run with a precipitation scaling factor of 0.56. The AAR at MB=0 denotes $AAR_0$.**

## 5.5 Discussion of uncertainties and comparison to measured elevation changes

The variation of HAR precipitation as input for the MB model through the application of three different scaling factors (0.56±0.25) creates a range of uncertainty for every SEB and MB component (see section 5.4). The overall uncertainty for the annual MB over the simulated period 2000-2011 reveals an inter-annual variability depending on the sensitivity of the different parameters on the precipitation amount (Fig. 5.6). The determination of the 'correct' scaling factor is difficult because in-situ measurements or remote sensing analyses for the evaluation are scarce. The comparison of simulated runoff and the occurrence of GLOF events in section 5.4.1 reveal that the inter-annual pattern of the input parameters is not in gross contradiction with observations but cannot solely explain the observed lake outbursts. The overall simulated MB for the reference run is less negative than the average published by various authors for glaciers in the Himalayas, whereas the lower estimate with a precipitation scaling factor of 0.31 seems to be slightly too negative (see section 5.4.1). Furthermore, the MB model calculates a refreezing amount of 56% for the reference run what is far above the observed values for cold glaciers (Fujita & Ageta 2000, Fujita et al. 2007). Due to its location on the TP, the thermal regime of Halji glacier is assumed to be temperate to polythermal (see section 1.4.1). The strong refreezing can be explained by a long-lasting snow cover on the glacier, revealed by the high albedo values (Fig. 5.4g) and the low snow lines (Fig. 5.7). With the lower precipitation estimate only 7% of surface and subsurface melt refreezes (Table 5.2). This value is more reasonable.
Kropacek et al. (2013) calculated surface elevation differences between 2004 and 2009 at Halji glacier from ICESat (Fig. 5.10). The obtained values also cover neighbouring glaciers and are only valid for the indicated profiles. We chose the two ICESat profiles on Halji glacier that nearly overlap spatially (Fig. 5.10a). This was until recently the only data available for validation at Halji glacier. The mean elevation difference for the profiles for the period from November 2003 to October 2007 is ≈-4 m (Fig. 5.10b). The surface height change determined by the MB model for a similar profile over the period 1 October 2003 – 30 September 2007 is +0.8 m for the reference run and -3.1 m for the model run with 25% decreased precipitation (Table 5.3).

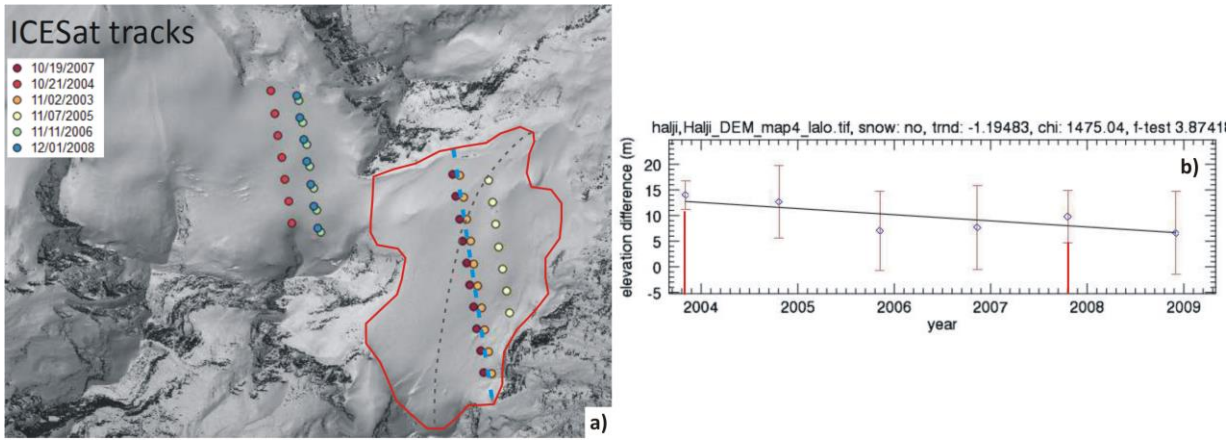


**Fig. 5.10: Surface elevation differences at Halji glacier and its surroundings from ICESat, 2004-2009 (Kropacek et al. 2013); (a) Halji glacier (red outline) with ICESat tracks (coloured dots) and the selected profile for the comparison with the MB model output (blue dashed line); the MB profile along the central flow line is indicated as a grey dashed line as also indicated in Fig. 5.1; (b) average elevation differences determined from the ICESat tracks; the red lines indicate the two similar profiles in 2003 and 2007.**

This finding supports the assumption that a precipitation scaling factor of 0.56 clearly overestimates the total precipitation amounts at Halji glacier when keeping $T_{air}$ unchanged. A scaling factor of 0.31

leads to better results but mass loss seems still too low compared to the ICESat profiles. Considering the observed cold bias in HAR $T_{air}$ at Naimona'nyi glacier (see section 1.4.1 and chapter 4), it is very likely that a similar offset is evident also at Halji glacier. Thus, the variation of HAR precipitation amounts needs to be complemented by variations of $T_{air}$. To limit the computational effort the MB model with varying combinations of precipitation scaling factors and temperature offsets is run for a north-south profile along the western ICESat profiles that cross Halji glacier (blued dashed line in Fig. 5.10a). The results for the modelled surface height change between 1 October 2003 and 30 September 2007 are given in Table 5.3. It is obvious that several combinations of precipitation scaling factors and air temperature offsets lead to reasonable results. This finding confirms the assumption made for Naimona'nyi glacier that the chosen combination is only one of several solutions (see section 4.5). Finally, we chose a precipitation scaling factor of 0.56 and a $T_{air}$ offset of +3 K for further analysis because we assume $T_{air}$ to be distributed rather homogenously over short distances. At Naimona'nyi the comparison of HAR $T_{air}$ with AWS measurements revealed a cold bias of ≈+3 K. Furthermore, the results of the MB model run with the respective temperature offset are in good agreement with other data available for Naimona'nyi glacier (see section 4.5). We assume a similar $T_{air}$ offset to be evident also at Halji glacier.

The results presented in Table 5.3 indicate that the rate of surface height decrease strongly increases with decreasing precipitation and increasing $T_{air}$ (Table 5.3). This physical response is possibly depending on $\alpha$ that strongly impacts surface melt.

**Table 5.3: Surface height change in m for the period 1 October 2003 – 30 September 2007 for the ICESat profile at Halji glacier (Fig. 5.10a) for several precipitation scaling factors and air temperature offsets. The green box indicates the combination that is chosen for further analysis.**

| | ±0K | +1K | +2K | +3K |
|---|---|---|---|---|
| 0.56 | +0.8 | -0.3 | -2.4 | -4.0 |
| 0.43 | -0.1 | -1.6 | -4.3 | -13.9 |
| 0.31 | -3.1 | -5.5 | -15.1 | -24.8 |

Based on the combination of precipitation scaling factor and $T_{air}$ offset determined from the ICESat profile glacier-wide SEB and MB components are calculated by the MB model. The glacier-wide MB estimate in the model run with increased $T_{air}$ by 3 K for the period 2001-2011 is -19765 kg m$^{-2}$ (-1976.5 kg m$^{-2}$ yr$^{-1}$). Recently, Nicolai Holzer from TU Dresden determined surface elevation changes and geodetic MB for Halji glacier between February 2000 and October 2013 from a DEM generated from optical tri-stereo Pleiades data (2013) relative to a SRTM DEM (2000) (personal communication, 2nd July 2014). An average ice density of 850±60 kg m$^{-3}$ was applied for the conversion into mass changes. N. Holzer estimated a MB of -380±300 kg m$^{-2}$ yr$^{-1}$ for the period 2000-2013 with a total surface height change of -5.9±4.43 m (-0.45±0.35 m yr$^{-1}$). These results indicate that mass loss calculated from the MB model with a parameter combination determined from the ICESat profile is too large compared to the remote sensing study of N. Holzer. In order to find a combination of precipitation scaling factor and air temperature offset that leads to a similar MB as determined by N. Holzer we calculated glacier-wide SEB and MB for the combinations 0.56/+2 K and 0.56/+1 K. The resulting annual average MB is -1075 kg m$^{-2}$ yr$^{-1}$ for the combination 0.56/+2 K and -374 kg m$^{-2}$ yr$^{-1}$ for the combination 0.56/+1 K. The latter combination leads to a total surface elevation change of -7.2 m (-0.72 m yr$^{-1}$). The results for MB and surface elevation changes of the MB model within this study are similar to the results determined by N. Holzer when assuming a precipitation scaling factor of 0.56 and a temperature offset of +1 K. The spatial comparison of calculated surface height changes from this study and the remote sensing analyses from N. Holzer reveals that the overall pattern is captured to a high degree (Fig. 5.11). However, several combinations of precipitation scaling factors

and air temperature offsets might lead to reasonable results. Therefore, further calculations with varying parameter combinations will be carried out in the near future.

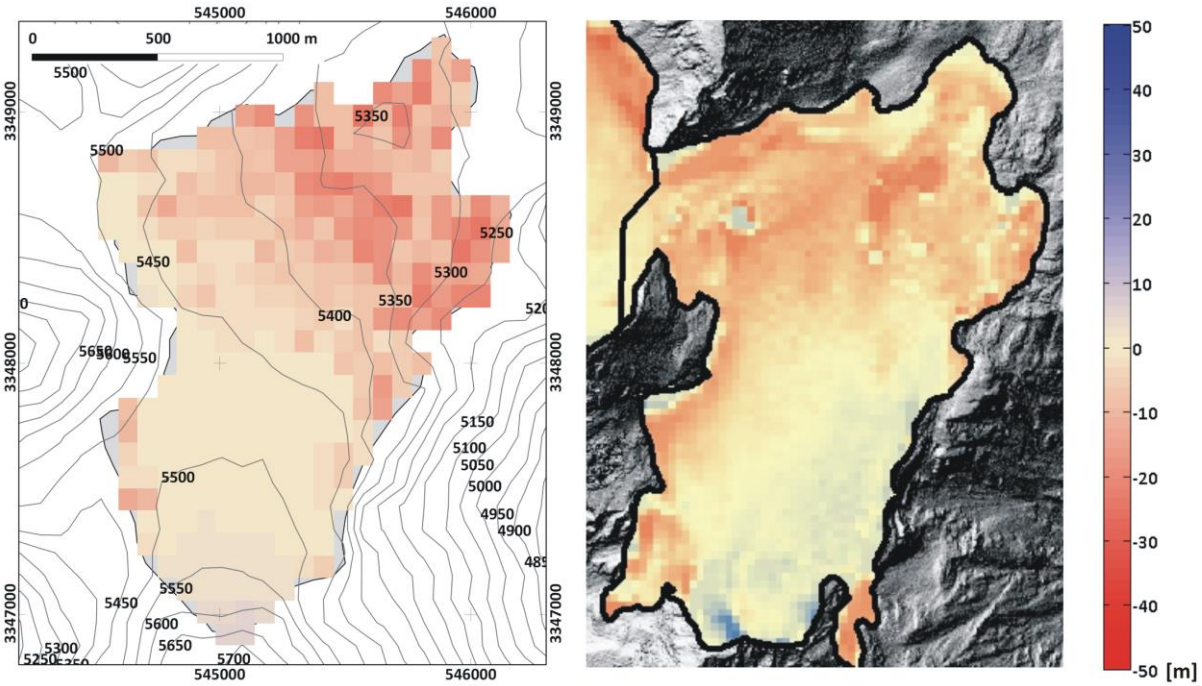


**Fig. 5.11: Spatial comparison of modelled surface height change of Halji glacier (precipitation scaling factor 0.56 / $T_{air}$ +1 K), 2001-2011 (left), with the results provided by N. Holzer, TU Dresden (right) (difference Pleiades DEM 2013 / SRTM DEM 2000).**

To visualize the effects of a temperature offset over all altitudes we calculated a northeast-south profile along the glacier flow-line (see Fig. 5.1 and Fig. 5.10a). MB and surface height change for the previously discussed model runs with three precipitation scaling factors and unchanged $T_{air}$ are compared to the three model runs with varying temperature offsets (Fig. 5.12). The ICESat profile intersects the northeast-south profile in ≈5420 m a.s.l. (Fig. 5.10a and dotted line in Fig. 5.12). Similar to the findings at Naimona'nyi MB differences are largest in the lower glacier areas (Fig. 5.12). From the MB profiles and the corresponding DEM altitudes a rough estimation of the ELA can be provided. The MB model run for the northeast-south profile with a precipitation scaling factor of 0.56 and a temperature offset of +1 K results in a mean ELA between 2001 and 2011 of ≈5460 m a.s.l. (Fig. 5.12). This value coincides with the ELA determined directly from the glacier-wide MB (5467 m a.s.l.).

The resulting glacier-wide SEB and MB components from the MB model run with a precipitation scaling factor of 0.56 and a $T_{air}$ offset of +1 K are given in Fig. 5.13. The inter- and intra-annual patterns of the different parameters are similar to those explained in section 5.4.1. For the considered period 2001-2011, $SW_{in}$ (+240.8 W m$^{-2}$) and $LW_{in}$ (+209.3 W m$^{-2}$) dominate energy input followed by $Q_{sens}$ (+21.9 W m$^{-2}$). Energy sinks at the glacier surface are $LW_{out}$ (-257.6 W m$^{-2}$), $SW_{out}$ (-192.9 W m$^{-2}$), $Q_{lat}$ (-15.3 W m$^{-2}$), $Q_{melt}$ (-8.8 W m$^{-2}$) and $Q_G$ (-1.9 W m$^{-2}$). This results in a $SW_{net}$ of +47.9 W m$^{-2}$. In general, the contributions of the single SEB components to the total energy flux change only slightly compared to the model run with unchanged $T_{air}$ (Table 5.1). $SW_{net}$ accounts for 36%, followed by $LW_{net}$ (35%), $Q_{sens}$ (15%), $Q_{lat}$ (11%) and $Q_G$ (3%).

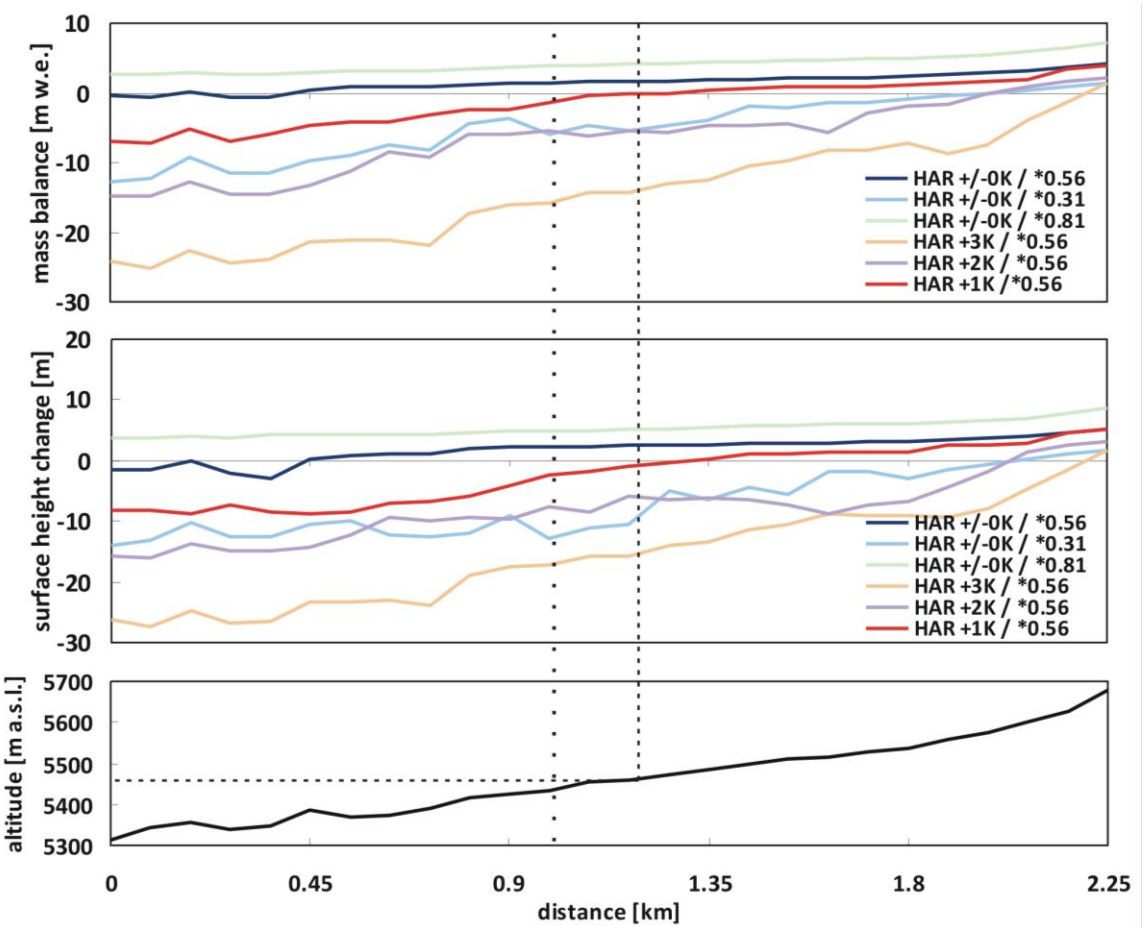


**Fig. 5.12: MB and surface height change for 2001-2011 along a northeast-south profile at Halji glacier for HAR precipitation and temperature offsets. The location of the profile is indicated in Fig. 5.1. The altitude in which the MB is zero (dashed lines) is the ELA. The profile of the chosen ICESat tracks (Fig. 5.10a) intersects the northeast-south profile in ≈5420 m a.s.l. (dotted line).**

The glacier-wide MB estimate in the model run with increased $T_{air}$ by 1 K for the period 2001-2011 is -3741 kg m$^{-2}$ (-374.1 kg m$^{-2}$ yr$^{-1}$). Surface melt (-8302 kg m$^{-2}$/-830.2 kg m$^{-2}$ yr$^{-1}$) is the largest factor of glacier-wide mass loss followed by sublimation (-2093 kg m-$^{2}$/-209.3 kg m$^{-2}$ yr$^{-1}$) that dominates ablation in winter, when air temperatures are below 0°C and surface melt is absent (Fig. 1.12, 5.13b). Subsurface melt (-37 kg m$^{-2}$/-3.7 kg m$^{-2}$ yr$^{-1}$) plays a minor role. Solid precipitation (+4462 kg m$^{-2}$/ +446.2 kg m$^{-2}$ yr$^{-1}$) and refreezing (+2229 kg m$^{-2}$/ +222.9 kg m$^{-2}$ yr$^{-1}$) contribute to the mass gain of the glacier. The amount of solid precipitation is less compared to the MB model run with the same scaling factor but unchanged $T_{air}$ (Table 5.2). This is because the solid proportion of total precipitation decreases with increasing $T_{air}$. Over the total simulation period, effective melt (surface melt + subsurface melt – refreezing) accounts for 74% and sublimation for 26% of the total mass loss. In total, 27% of the surface and subsurface melt refreeze.

Glacier-wide annual MB and runoff as calculated from the MB model (0.56/+1 K) are shown in Fig. 5.14 and compared to the occurrence of GLOF. The results are similar to the respective pattern with unchanged $T_{air}$ (Fig. 5.6).

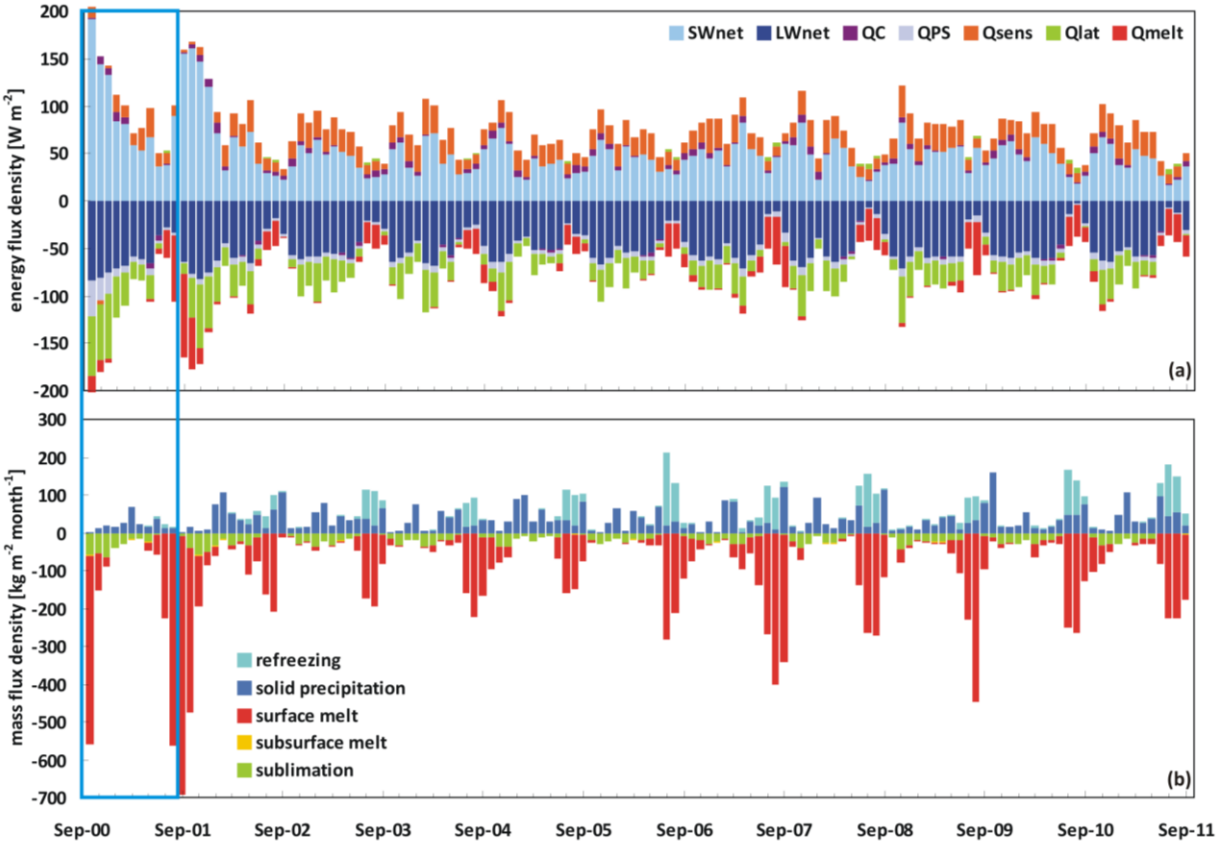


**Fig. 5.13: Glacier-wide monthly (a) SEB components (see section 2.3.1 for abbreviations) and (b) MB components from October 2000 to September 2011 at Halji glacier (precipitation scaling factor 0.56 / $T_{air}$ +1 K). Note that the first months (blue box) should not be considered.**

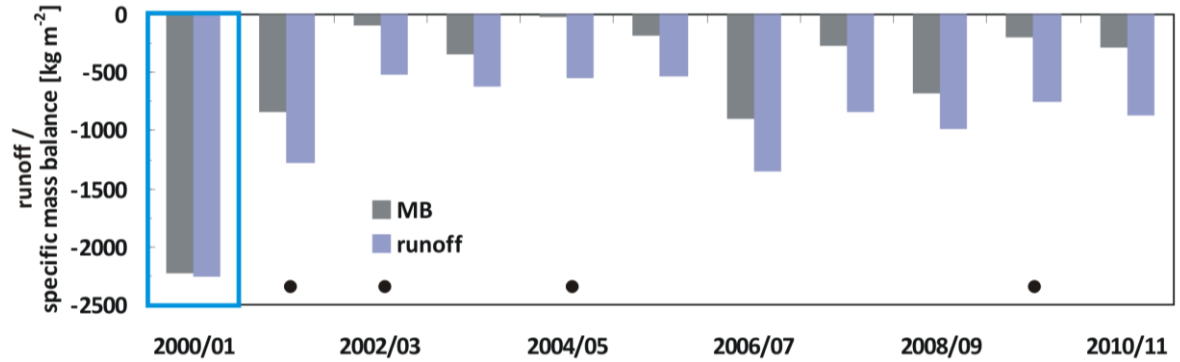


**Fig. 5.14: Glacier-wide annual MB and runoff for MB years (October – September) 2000-2011 estimated by the HAR forced MB model for Halji glacier (precipitation scaling factor 0.56 / $T_{air}$ +1 K). The black dots mark the '*non GLOF years*' (Kropacek et al. (2013)). Note that the MB in 2000/01 (blue box) should not be considered.**

## 5.6 Conclusion regarding model results at Halji glacier

The Limi valley in north western Nepal is a remote area but of special interest for both observations and modelling approaches. A periodic GLOF that originates from a supra-glacial lake on the glacier studied in this chapter threatens the village Halji (Kropacek et al. 2013). Using the 11-year HAR data set, SEB and MB components of Halji glacier are calculated for 2000-2011 and interpreted concerning their altitudinal gradients and their inter- and intra-annual patterns.

To account for uncertainties in total HAR precipitation amounts and to obtain a model uncertainty for further MB calculations, we perform three model runs with varying precipitation scaling factors (0.56±0.25). In the reference run a factor of 0.56 is applied. This number was obtained by Mölg et al. (2012) for Zhadang glacier and successfully applied in this thesis in the HAR forced MB model runs 2001-2011 for Zhadang glacier (see section 2.4). Due to a lack of precipitation measurements this scaling factor is also applied on HAR precipitation for Halji glacier. In total, the energy input to the glacier surface is dominated by $SW_{net}$ with 37% in the reference run and 43% in the model run with decreased precipitation (0.31). In the reference run with unchanged $T_{air}$, 56% of surface and subsurface melt water refreezes within the snow pack. This amount is considered to be too large for temperate to polythermal glaciers. The proportion of 7% (0.31) seems to be more reasonable. In the reference run with unchanged $T_{air}$, effective melt accounts only for 52% of the total mass loss. The increase of $T_{air}$ by +1 K increases the proportion of effective melt to 74% and decreases refreezing to 27%. Generally, the variation of HAR precipitation as input for the MB model through the application of three different scaling factors provides a range of uncertainty for every SEB and MB component. It could be revealed that a precipitation increase has a much smaller effect on all SEB and MB components than a precipitation decrease because the reference run already simulates an overall positive MB. Surface albedo is high even in the lowermost glacier regions. Thus, a further precipitation increase cannot have large impacts on these variables. The ELA is estimated around 5350 m a.s.l. (0.56) what coincides with the large scale ELA for the region of the western Himalayas given by Yao et al. (2012). A decrease (increase) of the precipitation amount rises (lowers) the ELA by ≈190 m (≈80 m). An ELA of ≈5470 m a.s.l. is estimated from the model run with a $T_{air}$ offset of +1 K.

The model results were evaluated regarding consistencies between glacial runoff generated by the MB model and the occurrence of '*GLOF years*' and '*non-GLOF years*'. Results show that the pattern in modelled runoff is not in contradiction with the observed GLOF events in the last decade. The missing GLOF in 2002/03 and 2004/05 is in line with the lowest simulated runoff when including the lower limits of the range of uncertainty. However, the link between simulated runoff and GLOF events at Halji glacier is limited. Kropacek et al. (2013) assume external factors, e.g. sediment damming of the lake, to override the meteorological forcing. Furthermore, the lake geometry and the temporal melt pattern may influence the lake outburst. Additionally, modelled MB is compared to calculated surface elevation differences between 2003 and 2007 at Halji glacier from ICESat. The reference run clearly underestimates the observed mass loss. Applying a scaling factor of 0.31 improves the results but still seems to slightly underestimate the surface height decrease. Considering the observed cold bias in HAR $T_{air}$ at Naimona'nyi glacier (chapter 4), it is very likely that a similar offset is evident also at Halji glacier. To determine reasonable combinations of precipitation scaling factors and air temperature offsets, the MB model was run several times for the ICESat profile only. The modelled surface height change is then compared to the value determined from ICESat. Assuming a rather homogenous spatial distribution of $T_{air}$ between Halji and Naimona'nyi, we chose the combination of a scaling factor of 0.56 and a $T_{air}$-offset of +3 K from several combinations with similar results.

Recent calculations of surface elevation changes and geodetic MB by N. Holzer provide a crucial opportunity for model evaluation. Compared to the results of N. Holzer the MB model run with the

combination of precipitation scaling factor and temperature offset determined from the ICESat profile clearly overestimates mass loss. With the combination 0.56/+1 K the MB model results are more reasonable.

From the application of the MB model to Halji glacier it can be concluded that the derived intra- and inter-annual cycles of SEB and MB components are within reasonable limits. The results depend on the respective patterns of the input parameters from HAR. The obtained SEB and MB components are consistent with each other because they interact through physical relationships (see sections 1.3.4 and 2.3.1). HAR output overestimates the amount of solid precipitation in the reference run. A scaling factor of 0.31 is more reasonable when no correction to HAR air temperature data is included (see sections 5.4 and 5.5). Recent remote sensing analyses provided by N. Holzer largely improve the opportunities for model evaluation. However, the results from N. Holzer lead to a different 'best-fit' combination of precipitation scaling factor and $T_{air}$-offset than the remote sensing analyses by Kropacek et al. (2013). The lack of meteorological field observations hampers the ability to verify HAR precipitation amounts and possible $T_{air}$ offsets.

A cold bias in HAR $T_{air}$, even though possibly smaller that at Naimona'nyi, seems to be nevertheless plausible since both remote sensing studies provide evidence that the results of the MB model reproduce observed glacier change best when $T_{air}$ is increased by at least 1 K. The result from chapter 5 points to the fact that it is difficult to obtain absolute values for glacier-wide MB or runoff in regions where precipitation and/or temperature measurements are not available or MB model results cannot be validated in detail by other means as for example by glaciological MB observations.

# 6 Energy and mass balance for a glacier in the Muztagh Ata region, north western Tibetan Plateau, 2000-2012

## 6.1 Introduction and regional climate conditions

The selected glacier is part of the glaciation of Muztagh Ata, the third highest peak of the Pamir Mountains (≈7500 m a.s.l.), the western margin of the Tibetan Plateau (Fig. 6.1, see section 1.4.1). The region is highly glaciated and therefore favours the application of remote sensing techniques to determine the state of the glaciers. Annual MB between 2005 and 2010 is available for one small glacier (Yao et al. 2012). Most glaciers in this region are characterized by a large amount of debris cover (Shangguan et al. 2006, see section 1.4.1). Since the debris cover modifies the glacier SEB and MB depending on its thickness (see section 1.4.2.2) a debris free glacier was chosen for the MB model application. It is a west exposed valley glacier with an area of ≈8.0 km$^2$ at the western slope of Muztagh Ata (Fig. 6.1).

The region is strongly influenced by the westerlies that are the most important source of moisture (see section 1.4.1). The impact of the monsoon precipitation is absent. Daily mean air temperatures generated by HAR generally rise above zero only in July and August and daily means range between -36.7°C and +6.1 C (average -11.3°C) within the period 2000-2012. Fig. 6.2 shows monthly means of those HAR variables that serve as input for the applied MB model. The atmospheric variables that are influenced by $SW_{in}$ and/or $T_{air}$ show the typical annual cycle (*RH*, *p*, Fig. 6.2). *N* is relatively high throughout the year and reveals a maximum in winter when the humid air masses of the westerly winds are forced to ascent at the Pamirs. Precipitation amounts are generally small but equally distributed over the year with a maximum in spring (Fig. 6.2, see section 1.4.1). The large altitudinal range of the glacier (≈2000 m) causes a significant impact of both temperature and precipitation gradients. Precipitation amounts increase with altitude and $T_{air}$ from HAR is already low in the lower glacier regions (4817 m a.s.l., Fig. 1.18, 6.1) and decreases with altitude. Therefore, it can be assumed that the estimated mass loss from the MB model from 2000-2012 is not large. This assumption is supported by the observations published by Yao et al. (2012). For a neighbouring glacier in the same region the authors give a regional ELA of 5460 m a.s.l. for the years 2001-2010. They find an overall positive MB between 2005 and 2010 (Yao et al. 2012).

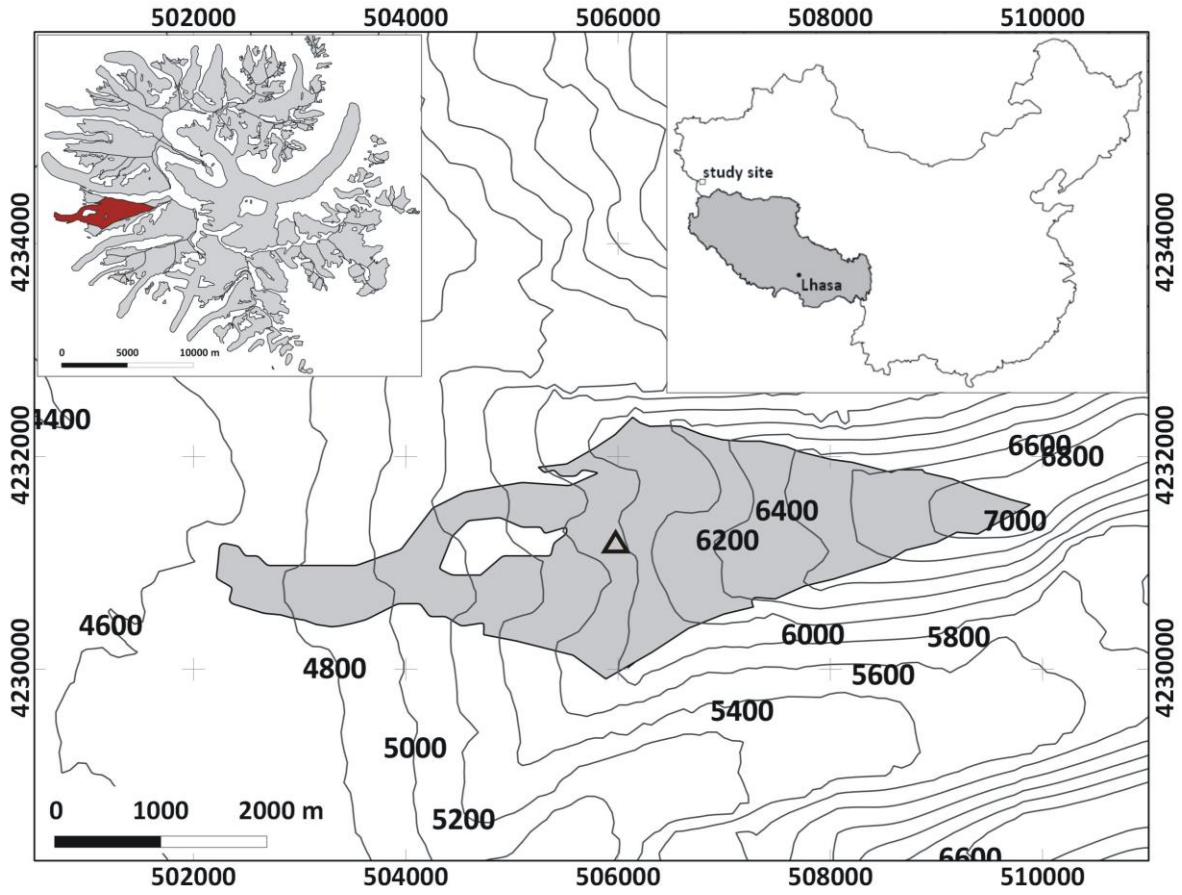


**Fig. 6.1: Selected glacier (grey area) at Muztagh Ata with glacier outlines from 2001. The triangle marks the DEM pixel that is used for the cloud correction of potential $SW_{in}$. Contours are in meters a.s.l. (200 m spacing); coordinate system is UTM 43N, WGS84. The left inlay indicates the selected glacier (red) within the glaciated area of Muztagh Ata (grey). The right inlay shows the location of the study site within China just outside the Tibet Autonomous Region (grey). Glacier outlines are provided by N. Holzer, TU Dresden.**

## 6.2 Data basis

For the simulation of SEB and MB of the selected glacier at Muztagh Ata for the period October 2000-2012 we solely use HAR data from the grid cell containing the glacier to run the distributed MB model. The model is explained in detail in section 2.3.1. The MB model structure, the applied parameterizations, constants and assumptions made for Zhadang glacier remain unchanged and are directly transferred to the Muztagh Ata glacier. Altitudinal gradients of most input parameters are required to run the distributed model for the total glacier area (see section 2.2.3). The altitude dependency is calculated from the nine HAR grid cells surrounding the glacier (Fig. 6.3). Resulting gradients are -0.0063°K $m^{-1}$ for $T_{air}$, 0.019% $m^{-1}$ for $RH$, -0.075 hPa $m^{-1}$ for $\rho_{air}$ and 0.00008 mm $m^{-1}$ or 0.104% $m^{-1}$ for precipitation. The altitude dependency of $u$ and $N$ is not as strong as for the other parameters. It is assumed to be constant for the whole glacier area (see chapters 2-5).

The obtained scaling factor of 0.56 for the amount of HAR precipitation at Zhadang glacier (see section 2.2.3) was already applied in the reference MB model runs in the previous studies within this thesis. Since HAR precipitation amounts can not be validated for the Muztagh Ata region, the same scaling factor is applied in the reference run in this chapter (Fig. 1.18, 6.2). The distributed model runs on a SRTM DEM (Rabus et al. 2003) resampled to 180 m. The size of the glacier is kept constant throughout the modelling period and is based on the 2001 glacier extent (Fig. 6.1). As the glacier area change between 2000 and 2009 is small (Fig. 6.7) the influence of an area change on glacier SEB and

MB is negligible. Potential $SW_{in}$ is derived from the radiation model after Kumar et al. (1997) as it was done for Zhadang glacier (see section 2.3.1) and corrected for cloud cover through HAR $SW_{in}$. The altitude of the HAR pixel that contains the glacier area and that is used as input data corresponds to the lower glacier region (4817 m a.s.l., Fig. 6.1). The effect of shading by the surrounding terrain structure in this region is apparent. Therefore, we choose a DEM pixel (*j*) in the middle part of the glacier with minimum terrain shading and similar annual cycle as HAR $SW_{in}$ for the cloud correction (Fig. 6.1). Calculation of the correction of $SW_{in,pot}$ for cloud coverage and terrain effects is carried out as outlined in section 2.3.1 for the case of Zhadang glacier.

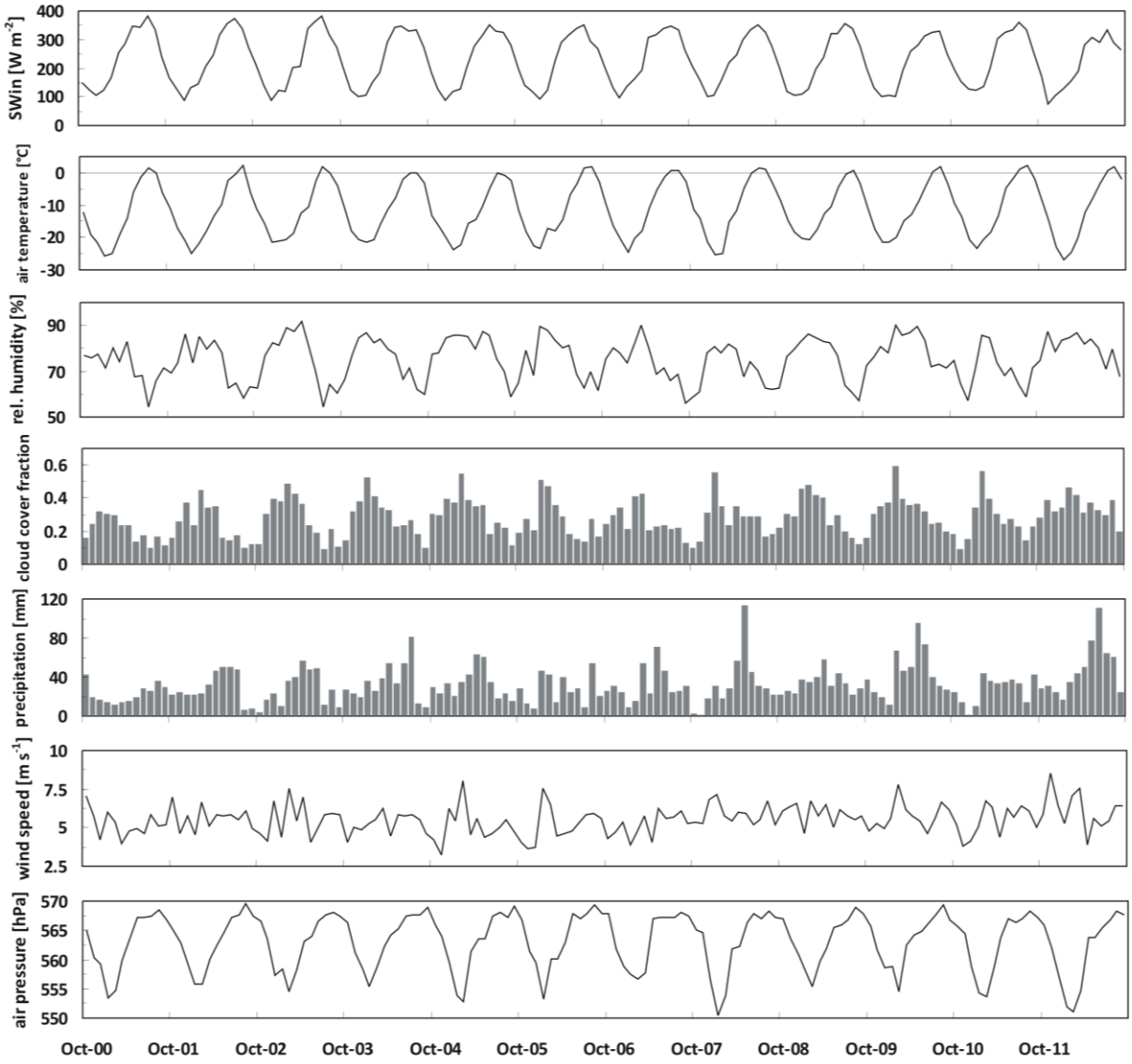


**Fig. 6.2: Monthly means or sums (precipitation) of meteorological variables at the atmospheric grid cell containing the analyzed glacier at Muztagh Ata (4817 m a.s.l.), October 2000-September 2012. The MB model is forced with hourly values of these variables. The scaling factor of 0.56 is already applied on precipitation amounts.**

## 6.3 Initialisation of the SEB/MB model for the application at Muztagh Ata glacier

So far, only few glaciological observations have been carried out in the Muztagh Ata region. Thus, information on ELA and snow distribution for initial model assumptions is sparse. Yao et al. (2012) give

a mean ELA around 5460 m a.s.l. between 2002 and 2010 based on in-situ measurements. Therefore, we assume an initial snow depth distribution slightly increasing linearly from 0 cm in 5500 m a.s.l. to 15 cm in the uppermost regions.

To account for uncertainties in total precipitation amounts from HAR and to obtain a model uncertainty for further MB calculations, we perform three model runs with varying precipitation scaling factors (0.56±0.25). The model run with a scaling factor of 0.56 is called reference run. Furthermore, HAR precipitation amounts are decreased by 25% (scaling factor 0.31) and increased by 25% (scaling factor 0.81) relative to the reference run. The lower factor (0.31) leads to a mean annual precipitation total of 217 mm at the HAR grid cell. Applying the factor of 0.81 results in a mean precipitation sum of 567 mm $yr^{-1}$.

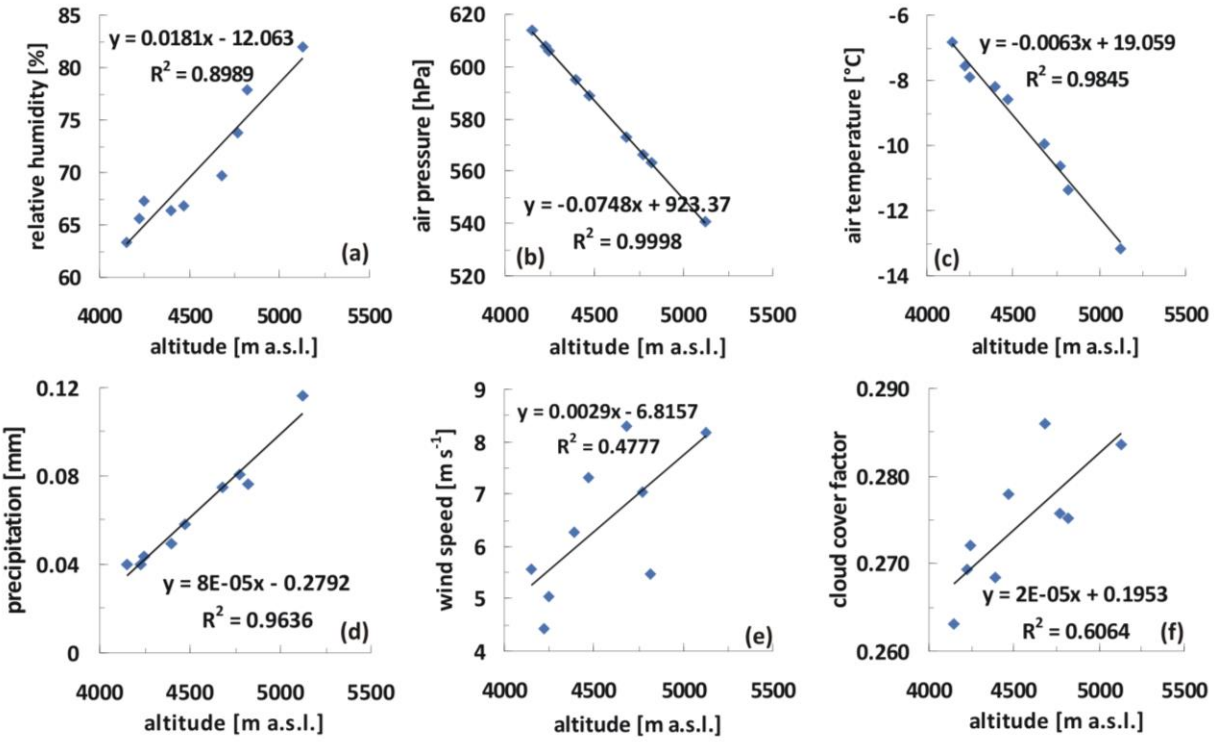


**Fig. 6.3: Altitude dependency of the HAR variables that serve as input for the MB model at Muztagh Ata (without $SW_{in}$). The slope of the regression line defines the respective altitude gradient per meter. Values are means for each HAR grid cell surrounding the glacier, 2000-2012.**

## 6.4 Results and discussion

In this section the results of the 12-year simulation period of the Muztagh Ata glacier are interpreted. The SEB/ MB model explicitly calculates the different SEB and MB components and allows revealing altitudinal, inter- and intra-annual patterns on the glacier. The results for the total simulation period are compared to surface height changes as revealed by remote sensing (section 6.4.1). In a further step, the typical annual cycle of the modelled transient snow line altitude and the inter-annual pattern of the ELA are linked to the results of the SEB and MB modelling (section 6.4.2).

### 6.4.1 SEB/MB characteristics 2000-2012

The altitudinal dependence of MB and SEB components averaged over the simulation period 2000-2012 is shown in Fig. 4.4. The given uncertainty ranges result from the model runs with varying precipitation scaling factors (see section 4.3). Precipitation amounts are both decreased and increased by 25% compared to the reference run. The reference run is characterized by a precipitation scaling fac-

tor of 0.56. The gradient of the calculated MB in the reference run is almost linear from slightly positive values in the lowermost regions to distinct positive MB in the uppermost parts (Fig. 6.4a). With decreased precipitation by 25% (scaling factor 0.31) the MB becomes negative in the lower parts of the glacier and the change in slope that was evident in all study regions so far, is visible between 5200 and 5400 m a.s.l. slightly above the resulting 12-year ELA (≈5000 m a.s.l., Fig. 6.4a). A similar pattern is reported for Naimona'nyi glacier (see section 4.4.1).
Generally, all ground-dependent SEB and MB variables at Muztagh Ata glacier are almost insensitive to precipitation changes by ±25%. The altitudinal variation of $\alpha$ is minimal due to frequent precipitation events (Fig. 6.5), very low $T_{air}$ and a nearly permanent snow cover (see section 6.4.2). With 25% reduced precipitation $\alpha$ decreases only slightly in the lowermost altitude bands because the seasonal variation of solid precipitation still prevents the glacier from being snow free over longer periods. A 25% increase in precipitation has no influence on $\alpha$ (Fig. 6.4g). The variations in MB are mostly influenced by the variations of solid precipitation itself (Fig. 6.4a, 6.4c). Only the lowermost glacier regions show a higher sensitivity to a decrease in precipitation by 25% from the reference run mainly forced by differences in $\alpha$, $Q_{melt}$ and $Q_{lat}$ (Fig. 6.4e,g). Therefore, surface melt and sublimation are altered in this respect (Fig. 6.5a,b). These dependencies are similar to the results at Naimona'nyi glacier (see section 4.4.1).
$SW_{in}$ and $LW_{in}$ are the only ground-independent energy sources for the glacier surface (see section 2.3.1). They do not change with varying precipitation amounts (Fig. 4.4d) because energy fluxes from the surrounding terrain are not considered. $SW_{in}$ is rather continuously decreasing between 5000 and 6400 m a.s.l. and above 6800 m a.s.l. due to slightly increasing terrain shading in the narrow valley (Fig. 6.4d, 6.1). In the lowermost regions and in ≈6600 m a.s.l. $SW_{in}$ decreases significantly. The upper accumulation area is obstructed to the south and southwest (Fig. 6.1). The effect in the lowermost altitude band can not be explained by the low resolution DEM and satellite images. However, it can be assumed that the north exposed and concave shaped lower end of the glacier tongue is shaded by the higher glacier regions in the south (Fig. 6.1). The characteristic shape of the vertical $SW_{in}$ profile is also apparent in the gradients of $SW_{net}$ (Fig. 6.4d), $Q_{sens}$, $Q_{lat}$ (Fig. 6.4e), sublimation, subsurface melt (Fig. 6.4b) and $LW_{out}$ (Fig. 6.4f). Reduced $SW_{in}$ in the lowermost parts slightly decreases $Q_{melt}$ and thus surface melt (Fig. 6.4e,a). With decreased precipitation amounts by 25% this effect on $Q_{melt}$ is overlapped by the effect of reduced α (Fig. 6.4e). Significantly lower $SW_{in}$ around 6600 m a.s.l. slightly decreases $T_s$ (expressed through $LW_{out}$, Fig. 6.4f), yields to higher $Q_{sens}$ directed to the glacier surface and a lower $Q_{lat}$ from the glacier surface to the atmosphere compared to the altitude bands below (Fig. 6.4e). The effects are small because $\alpha$ is constantly high (Fig. 6.4g). These feedback processes are also observed by Klok & Oerlemans (2002) at Morteratschgletscher. Lower $Q_{lat}$ results in decreased mass loss through sublimation in the upper glacier regions compared to the altitude bands above and below (Fig. 6.4b). Additionally, lowest amounts of $SW_{net}$ are responsible for lowest subsurface melt in around 6600 m a.s.l. (Fig. 6.4b, 6.4d).
From the vertical MB profile of the reference run no ELA can be estimated (Fig. 6.4a). In the model run with precipitation decreased by 25% compared to the reference run the ELA is located around 5000 m a.s.l. (Fig. 6.4a). The altitude coincides with the large-scale ELA for the region of the north western TP given by Yao et al. (2012).

Annual cycles of glacier-wide mean monthly SEB and MB components at Muztagh Ata glacier as calculated by the MB model for the reference run for the period 2000-2012 are illustrated in Fig. 6.5. Errors that stem from the spin-up time of the MB model (see section 2.3.1) are not obvious during the first months from Fig. 6.5. However, Table 6.2 reveals that glacier-wide MB in the first year is exceptional low, possibly due to little refreezing. The first MB year is therefore not considered in the following interpretations. In general, $SW_{in}$ (+202.8 W m$^{-2}$) and $LW_{in}$ (+185.5 W m$^{-2}$) dominate energy

input over the considered period in the reference run, followed by $Q_{sens}$ (+13.3 W m$^{-2}$). Energy sinks at the glacier surface are $LW_{out}$ (-227.5 W m$^{-2}$), $SW_{out}$ (-173.0 W m$^{-2}$), $Q_G$ (-1.9 W m$^{-2}$), $Q_{lat}$ (-0.8 W m$^{-2}$) and $Q_{melt}$ (-0.4 W m$^{-2}$), making $SW_{net}$ (+29.8 W m$^{-2}$, see Table 6.1) the most important energy source. This was also observed for the other glaciers studied within this thesis and reported by e.g. Andreassen et al. (2008) for Storbreen and by Mölg & Hardy (2004) for Kilimanjaro.

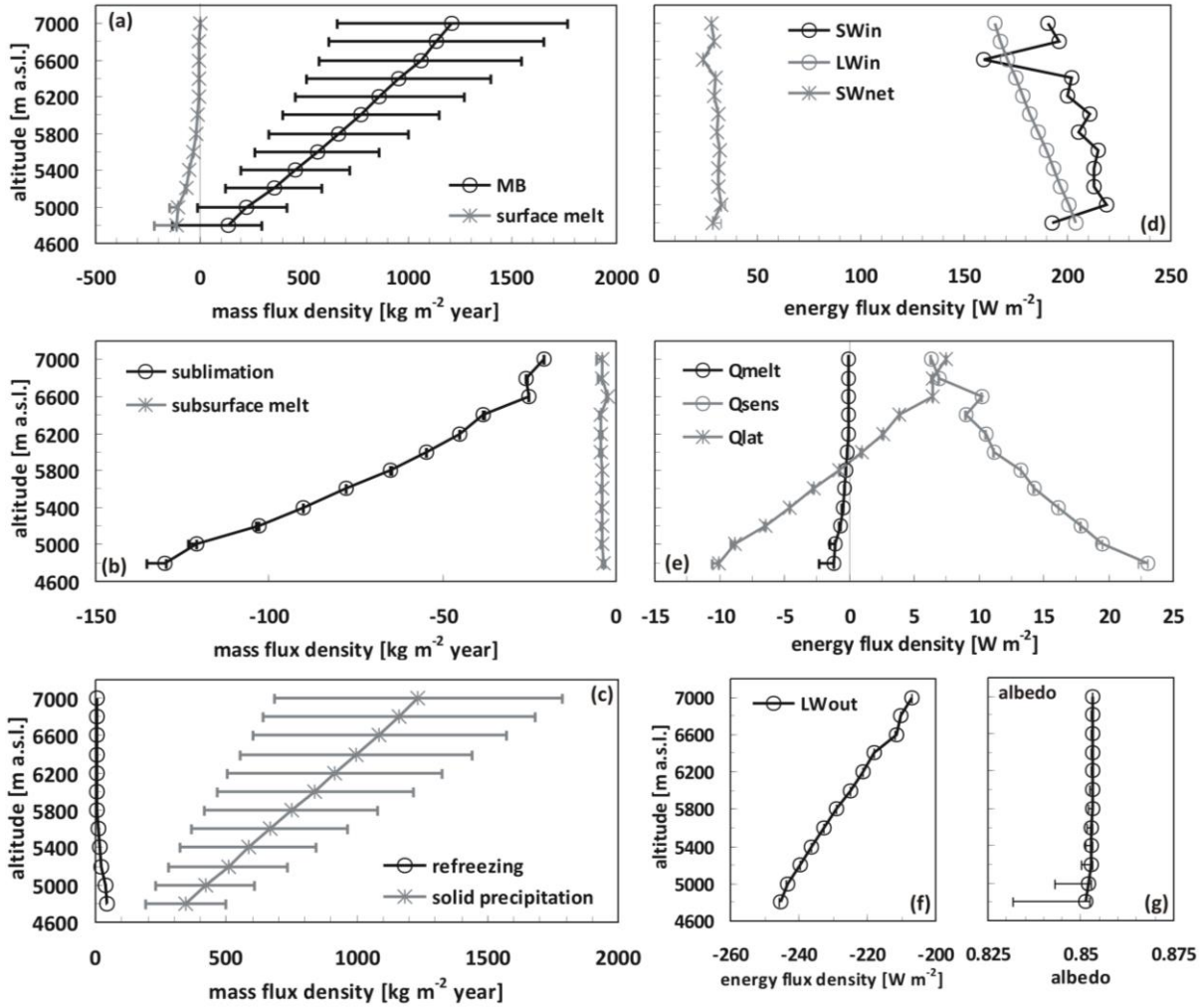


**Fig. 6.4: Modelled vertical profiles of (left) the specific mass balance and its components and (right) mean SEB components at Muztagh Ata glacier averaged over the simulation period October 2000 – September 2012. Data are averaged for 200-m altitude bands. The uncertainty ranges are calculated assuming different precipitation amounts (see section 6.3). Note the different x-axis scales of the components (negative means mass or energy loss at the glacier surface, see section 2.3.1 and Tab. 2.2 for abbreviations).**

The SEB components at Muztagh Ata show distinct and regular seasonal cycles (Fig. 6.5a). The location of the glacier under the influence of the westerlies and very low air temperatures cause highest energy exchanges in summer. The seasonal pattern of most SEB components despite of $Q_{melt}$ and $Q_G$ is reversed compared to the other studied glaciers (chapters 2-5). The lowest values of $SW_{net}$ are evident between November and February when mass loss through both surface melt and sublimation is absent and small but frequent precipitation events keep $\alpha$ high (Fig. 1.18, 6.5a). $LW_{net}$ plays a less important role as energy sink in winter than in summer (Fig. 6.5a). This can be explained through the seasonal patterns of $LW_{in}$, depending on $T_{air}$, $e$ and $N$ (see section 2.3.1). $e$ and $N$ are largest in winter (Fig. 6.2) resulting in higher $LW_{in}$. $LW_{out}$ depends on $T_s$ (largest negative values in

summer). $Q_C$ follows the expected pattern with positive values in winter and negative values in summer (see chapters 2-5). $Q_{PS}$ is always negative with larger values when $\alpha$ is low (and $SW_{net}$ is large) (Fig. 6.5a). Generally, $Q_{lat}$ is a small energy sink for the glacier surface (Table 6.1). However, on a monthly time scale it is evident that positive values regularly occur in winter (Fig. 6.5a) when the region is under the influence of maximum precipitation amounts and highest *RH* in the course of the year (Fig. 1.18, 6.2). At positive $Q_{lat}$ in winter deposition of moist air contributes to mass gain at the glacier surface. The contribution of deposition to the glacier MB is not yet explicitly calculated in the MB model applied in this thesis (see section 4.4.1). In summer, the dry conditions on the western TP lead to negative $Q_{lat}$ and sublimation (Fig. 6.5). $Q_{sens}$ is always positive. Absolute values of $Q_{sens}$ are generally larger than $Q_{lat}$ implying a higher moisture content of the atmosphere and less sublimation compared to the other study sites (chapters 2-5). A similar dependency is observed by Nicholson et al. (2013) at Lewis glacier (Mt Kenya). Furthermore, the very low $T_{air}$ might limit the turbulent energy exchange. Surface melt rates are very small and occur dominantly in July and August when the energy supply by $Q_{sens}$ is largest (Fig. 6.5a). The SEB values for the model runs with varying precipitation scaling factors are given in Table 6.1. For glacier-wide monthly SEB components of the MB model runs with ±25% of precipitation see Fig. A.7a and Fig. A.8a in the appendix.

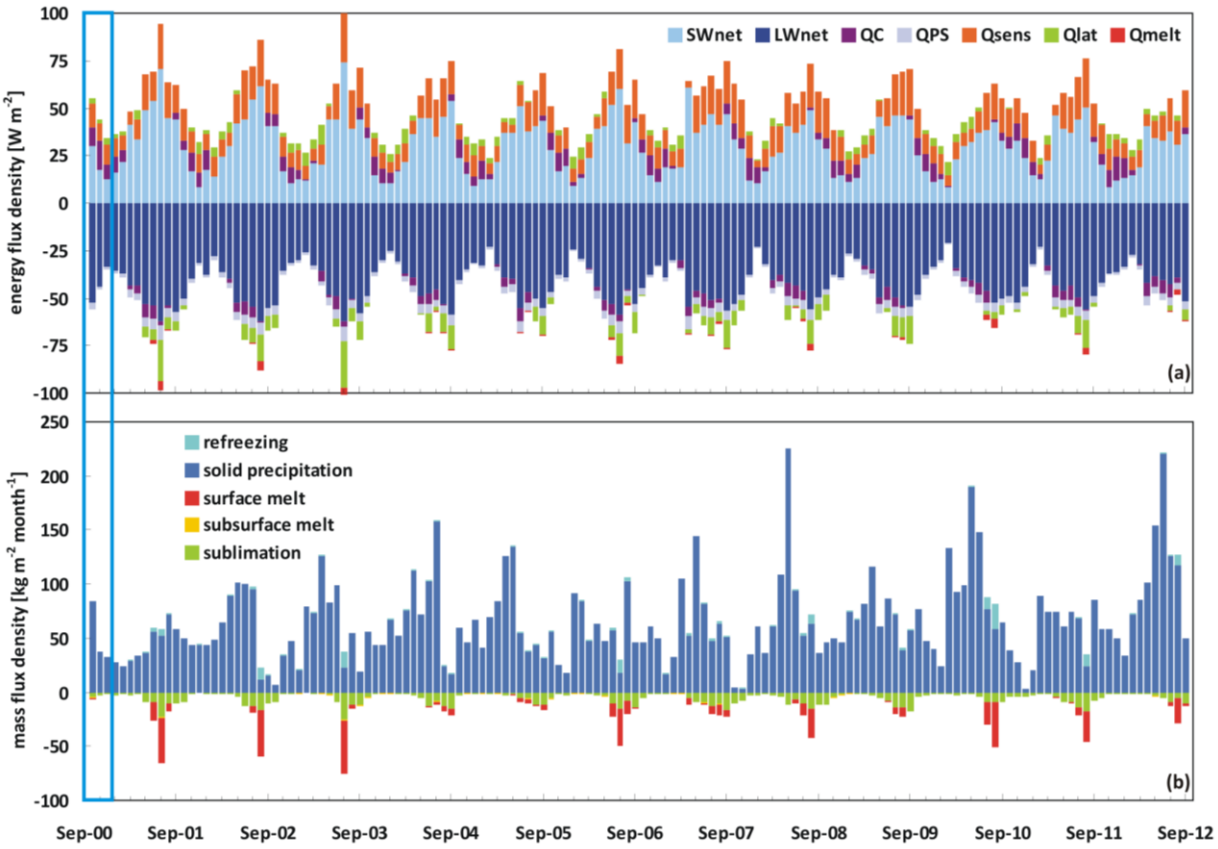


**Fig. 6.5: Glacier-wide monthly (a) SEB components (see section 2.3.1 for abbreviations) and (b) MB components at Muztag Ata glacier from October 2001 to September 2011 (reference run). Note that the first months (blue box) should not be considered.**

The glacier-wide MB estimate of the reference run at Muztagh Ata glacier for the period 2001-2012 (the first year is not considered) is +7765 kg m$^{-2}$ (+705.9 kg m$^{-2}$ yr$^{-1}$) (Table 6.2). In general, sublimation (-753 kg m$^{-2}$/ -68.5 kg m$^{-2}$ yr$^{-1}$) is the largest factor of glacier-wide mass loss followed by surface melt (-405 kg m$^{-2}$/ -36.8 kg m$^{-2}$ yr$^{-1}$) and clearly dominates ablation in spring and autumn (Fig. 6.5b). Subsurface melt (-44 kg m$^{-2}$/-4.0 kg m$^{-2}$ yr$^{-1}$) plays a minor role. Solid precipitation (+8793 kg m$^{-2}$/

+799.4 kg $m^{-2}$ $yr^{-1}$) and refreezing (+174 kg $m^{-2}$/ +15.8 kg $m^{-2}$ $yr^{-1}$) contribute to mass gain of the glacier. Maximum snowfall amounts occur in spring (Fig. 1.18, 6.5b, see section 1.4.1). Refreezing at Muztagh Ata glacier happens mostly in summer, when melt water is generated at the surface and percolates through the cold snow layers. The reference run implies that 39% of the surface and subsurface melt water refreezes within the snow pack between 2001 and 2012. These results will be discussed in section 6.5. The respective MB values for the model runs with varying precipitation scaling factors are given in Table 6.2. For glacier-wide monthly MB components of the MB model runs with ±25% of precipitation see Fig. A.7b and Fig. A.7b in the appendix.

Table 6.1 lists the absolute and relative contributions of the energy flux components to the total energy turnover for the three model runs with varying precipitation scaling factors (0.56/0.31/0.81) when simulated with unchanged $T_{air}$ from the HAR dataset. For the considered period 2001-2012, $LW_{net}$ accounted for 45% (45%/45%), followed by $SW_{net}$ (30%/30%/30%), $Q_{sens}$ (14%/14%/14%), $Q_G$ (7%/6%/7%) and $Q_{lat}$ (5%/5%/ 5%). $Q_{lat}$ is small because the overall moisture content of the air is high (Fig. 6.2). The contribution of $Q_{lat}$ to the total energy flux is even less than the contribution of $Q_G$. $LW_{net}$ dominates over $SW_{net}$ because of high $\alpha$ (Fig. 6.4g). The absolute numbers and the relative contribution of the different SEB components do hardly vary with changing precipitation amounts by ±25% from the reference run (Table 6.1) because the seasonal distribution of solid precipitation prevents the glacier from being snow free over longer periods what keeps $\alpha$ high (Fig. 6.4g). The SEB components without $Q_{melt}$ are nearly balanced. Thus, simulated $Q_{melt}$ and surface melt are very low at Muztagh Ata glacier over the period 2001-2012 with a minimum in 2003/04 (Tables 6.1, 6.2). The inter-annual variations of the glacier-wide MB are dominated by the variability of precipitation. In 2002/03, 2005/06 and 2010/11 solid precipitation is minimal (Table 6.2) resulting in less positive MB (Fig. 6.6). The contributions of surface melt, subsurface melt and refreezing to total MB are negligible. Annual sublimation amounts are rather constant. Therefore, sublimation is not responsible for MB variations (Table 6.2). Over the total simulation period, effective melt (surface melt + subsurface melt – refreezing) accounts for 27% (29%/26%) and sublimation for 73% (71%/ 74%) of the total mass loss (Table 6.2). As for the SEB components a precipitation change by ±25% hardly affects the MB components despite solid precipitation (Table 6.2). The amount of refreezing melt water varies only slightly because in all years the thickness of the snow pack remains sufficient for the low melt rates. When precipitation is decreased by 25% a proportion 34% refreezes.

From the modelled period October 2000 – September 2012, 12 glacier-wide MB estimates for Muztagh Ata glacier can be obtained (Fig. 6.6). The uncertainty ranges of the model values are obtained from the application of different precipitation scaling factors (0.56/0.31/0.81, see section 6.3). Yao et al. (2012) observed an average annual mass gain of ≈+248 kg $m^{-2}$ for a neighbouring west exposed glacier in the Muztagh Ata region between 2005/06 and 2009/10 based on an ablation stake network. The corresponding annual MB values are given in Fig. 6.6 in comparison with the MB model results. The annual variation in the results given by Yao et al. (2012) is much greater than the obtained values within this thesis. However, despite for the year 2006/07 the inter-annual variations in both studies are similar. This indicates that relative HAR climatology provides year-to-year variance in such that modelled annual MB variance overall fits to the observations. The obtained annual average MB by Yao et al. (2012) suggests that the MB model result with a precipitation scaling factor of 0.31 is more reasonable (+345 kg $m^{-2}$ $yr^{-1}$).

**Table 6.1: Mean absolute values of energy flux components as modelled for October 2000 – September 2012 and for the respective MB years with proportional contribution to total energy flux at Muztag Ata glacier. The first value is for a precipitation scaling factor of 0.56, the numbers in brackets are for the model runs (0.31 / 0.81). Note that values of the MB year 2000/01 are not considered in the calculation of the total average.**

| | Sum* [W m$^{-2}$] | $SW_{net}$ | $LW_{net}$ | $Q_{sens}$ | $Q_{lat}$ | $Q_G$ | $Q_{melt}$ |
|---|---|---|---|---|---|---|---|
| tot. average [W m$^{-2}$] | 96 (96 / 96) | 30 (30 / 30) | -42 (-42 / -42) | 13 (13 / 13) | -0.8 (-0.8 / -0.8) | -1.9 (-1.9 / -1.8) | -0.4 (-0.4 / -0.4) |
| 2000/01 | | 36 (43 / 36) | -47 (-49 / -47) | 13 (12 / 13) | -2.2 (-3.0 / -2.1) | -1.6 (-2.5 / -1.6) | -0.7 (-2.3 / -0.7) |
| 2001/02 | | 32 (33 / 32) | -45 (-45 / -45) | 14 (14 / 14) | -1.0 (-1.2 / -1.0) | -1.8 (-1.8 / -1.6) | -0.5 (-0.5 / -0.5) |
| 2002/03 | | 32 (32 / 32) | -43 (-43 / -43) | 13 (13 / 13) | -1.5 (-1.5 / -1.5) | -1.9 (-2.0 / -1.8) | -0.5 (-0.5 / -0.5) |
| 2003/04 | | 31 (31 / 31) | -42 (-42 / -42) | 13 (13 / 13) | -1.0 (-1.0 / -0.9) | -2.3 (-2.3 / -2.3) | -0.1 (-0.2 / -0.1) |
| 2004/05 | | 28 (28 / 28) | -40 (-40 / -40) | 10 (10 / 10) | 1.2 (1.2 / 1.2) | -1.7 (-1.7 / -1.7) | -0.2 (-0.2 / -0.1) |
| 2005/06 | | 31 (31 / 31) | -43 (-43 / -43) | 13 (13 / 13) | -1.0 (-1.0 / -1.0) | -1.9 (-1.9 / -1.9) | -0.6 (-0.6 / -0.6) |
| 2006/07 | | 32 (32 / 32) | -43 (-43 / -43) | 14 (14 / 14) | -2.0 (-2.0 / -2.0) | -2.1 (-2.0 / -2.0) | -0.3 (-0.4 / -0.3) |
| 2007/08 | | 30 (30 / 30) | -42 (-42 / -42) | 16 (16 / 16) | -2.8 (-2.8 / -2.8) | -1.9 (-1.9 / -1.8) | -0.4 (-0.5 / -0.4) |
| 2008/09 | | 29 (29 / 29) | -42 (-42 / -42) | 14 (14 / 14) | -2.1 (-2.1 / -2.1) | -2.0 (-2.0 / -2.0) | -0.2 (-0.2 / -0.1) |
| 2009/10 | | 26 (26 / 26) | -40 (-40 / -40) | 12 (12 / 12) | 2.1 (2.1 / 2.1) | -1.5 (-1.5 / -1.4) | -0.6 (-0.7 / -0.6) |
| 2010/11 | | 32 (32 / 32) | -44 (-44 / -44) | 15 (14 / 15) | -2.5 (-2.5 / -2.5) | -2.3 (-2.3 / -2.2) | -0.4 (-0.5 / -0.4) |
| 2011/12 | | 25 (25 / 25) | -39 (-39 / -39) | 12 (12 / 12) | 2.1 (2.0 / 2.1) | -1.5 (-1.4 / -1.4) | -0.3 (-0.3 / -0.3) |
| | 100% | 30 (30 / 30)% | 45 (45 / 45)% | 14 (14 / 14)% | 5 (5 / 5)% | 7 (6 / 7)% | |

*Sum of energy fluxes in absolute values: $|SW_{net}| + |LW_{net}| + |Q_{sens}| + |Q_{lat}| + |Q_G|$

**Table 6.2: Calculated glacier-wide mass balance components for the total period October 2000 – September 2012 and for the respective MB years at Muztagh Ata glacier. The first value is for a precipitation scaling factor of 0.56, the numbers in brackets are for the model runs (0.31/0.81). Note that values of the MB year 2000/01 are not considered in the calculation of the total values.**

| | Solid precipitation | Surface melt | Refrozen water | Subsurface melt | Sublimation | Mass balance* |
|---|---|---|---|---|---|---|
| total [kg m$^{-2}$] | 8793 (4868 / 7170) | -405 (-431/-401) | 174 (164 / 185) | -44 (-47 / -43) | -753 (-757/-753) | 7765 (3797/11706) |
| 2000/01 | 544 (301 / 388) | -68 (-220 / -68) | 13 (6 / 15) | -3 (-4 / -3) | -79 (-87 / -79) | 407 (-3 / 652) |
| 2001/02 | 709 (393 / 871) | -49 (-46 / -51) | 15 (11 / 19) | -4 (-4 / -4) | -74 (-76 / -74) | 597 (278 / 916) |
| 2002/03 | 664 (368 / 699) | -52 (-48 / -53) | 20 (13 / 23) | -4 (-4 / -4) | -77 (-77 / -77) | 551 (251 / 850) |
| 2003/04 | 824 (456 / 589) | -14 (-15 / -13) | 7 (8 / 7) | -4 ( -5 / -4) | -68 (-68 / -68) | 745 (376 / 1113) |
| 2004/05 | 794 (440 / 857) | -15 (-16 / -14) | 8 (8 / 8) | -5 (-5 / -5) | -48 (-48 / -48) | 735 (379 / 1090) |
| 2005/06 | 656 (363 / 562) | -59 (-61 / -57) | 22 (19 / 22) | -4 (-4 / -4) | -66 (-67 / -66) | 548 (250 / 843) |
| 2006/07 | 752 (416 / 695) | -30 (-38 / -31) | 10 (12 / 10) | -4 (-4 / -4) | -75 (-76 / -76) | 653 (310 / 988) |
| 2007/08 | 781 (432 / 752) | -41 (-45 / -42) | 15 (17 / 17) | -4 (-4 / -4) | -86 (-86 / -86) | 665 (314 / 1015) |
| 2008/09 | 796 (441 / 525) | -15 (-17 / -14) | 7 (8 / 8) | -4 (-4 / -4) | -84 (-84 / -84) | 701 (343 / 1057) |
| 2009/10 | 1050 (581 / 819) | -62 (-66 / -61) | 38 (36 / 39) | -4 ( -4 / -4) | -49 (-49 / -49) | 974 (498 / 1445) |
| 2010/11 | 639 (354 / 799) | -39 (-47 / -37) | 16 (17 / 16) | -3 (-3 / -3) | -78 (-79 / -78) | 536 (241 / 823) |
| 2011/12 | 1127 (624 /) | -29 (-31 / -28) | 15 (14 / 15) | -3 (-4 / -3) | -48 (-48 / -48) | 1061 (556 / 1566) |
| % of mass loss | | 23 (25 / 21) | | 4 (4 / 4) | 73 (71 / 74) | |

*Mass balance = solid precipitation + surface melt + refrozen water + subsurface melt + sublimation

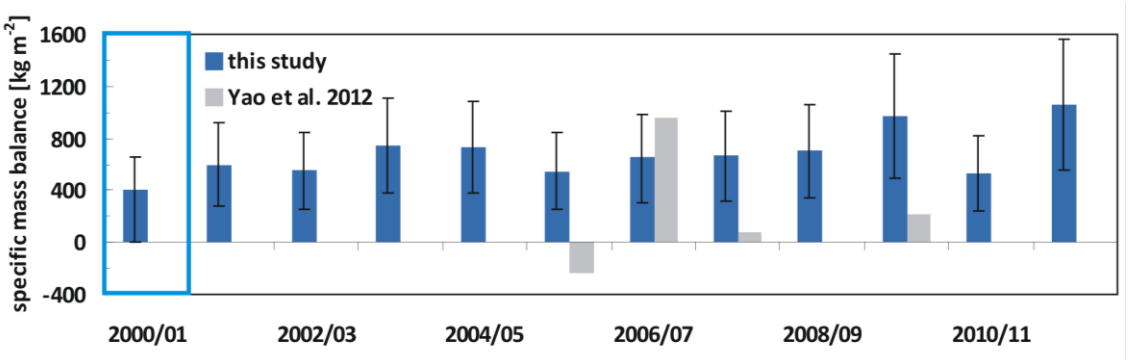


**Fig. 6.6: Glacier-wide annual MB for MB years (October – September) 2000-2012 estimated by the HAR forced MB model for Muztagh Ata glacier and compared to the results published in Yao et al. (2012) for a neighbouring glacier. The MB value of 2009/10 of Yao et al. (2012) is the total over 2008/09-2009/10. The uncertainty ranges are calculated assuming different precipitation amounts (see section 6.3, Table 6.2). Note that the MB in 2000/01 (blue box) should not be considered.**

Furthermore, the MB model results for Muztagh Ata glacier can be compared to surface height changes from Pleiades and SRTM data (unpublished data provided by Nicolai Holzer, TU Dresden). Surface elevation changes for the Muztagh Ata region between 2000 and 2013 are calculated from a DEM generated from Pleiades data (2013) relative to a SRTM DEM (2000). First results for the selected glacier are shown in Fig. 6.7. The spatial comparison of calculated surface height changes from both studies reveals that the overall pattern is captured to a high degree (Fig. 6.7). Note that MB model results of the 0.31-run are shown in Fig. 6.7. The surface elevation changes provided by N. Holzer are small for a period of 13 years. This is in agreement with the 11-year period covered by this study. The remote sensing results show several small scale features that are independent of altitude. These features cannot be captured by the MB model (Fig. 6.7). In this study, annual mean MB with a precipitation scaling factor of 0.31 is +345 kg $m^{-2}$ $yr^{-1}$. Respective surface height change for the total glacier area is +4.5 m with annual means of +0.4 m $yr^{-1}$. N. Holzer applied an average ice density of 850±60 kg $m^{-3}$ for the conversion from elevation changes into mass changes. N. Holzer estimated an average annual MB of +200±270 kg $m^{-2}$ $yr^{-1}$ for the period 2000-2013 with a total surface height change of +3.23±4.43 m (+0.25±0.34 m $yr^{-1}$). The DEM generated from Pleiades data contains several data gaps in the accumulation area of the glacier. A value of zero is assigned to these data gaps (N. Holzer, personal communication). Thus, the mass gain determined from remote sensing might be underestimated. This problem is also stated by Neckel et al. (2014) for the western Kunlun Shan. Nevertheless, the comparison with remote sensing data supports the assumption that the reference run overestimates the MB and the surface height changes at Muztagh Ata glacier. With decreased precipitation amounts by 25% the MB model results are more reasonable.

The results are less negative than those of previously published less detailed studies based on remote sensing approaches (e.g. Gardelle et al. 2013, Gardner et al. 2013, Neckel et al. 2014). Neckel et al. (2014) estimate a slight mass gain of +30±250 kg $m^{-2}$ $yr^{-1}$ between 2003 and 2009 for the western Kunlun Shan (≈200 km southeast of Muztagh Ata, see Fig. 1.1). A similar result of an average MB of +140±130 kg $m^{-2}$ $yr^{-1}$ in the Pamirs (1999-2011) is reported by Gardelle et al. (2013). Gardner et al. (2013) give MB values of +170±150 kg $m^{-2}$ $yr^{-1}$ for the western Kunlun Shan and -130±220 kg $m^{-2}$ $yr^{-1}$ for the Pamir Mountains between 2003 and 2009. It should be noted that several authors report heterogeneous glacier changes with several advancing glaciers on the north western TP (Shangguan et al. 2007, 2006, Yao et al. 2012). The classification of glacier accumulation regimes on the TP by Maussion et al. (2014) suggests a high spatial variation in the Muztagh Ata region (Fig. 1.9). Thus, the patterns of both spatial and temporal glacier MB might be also highly variable.

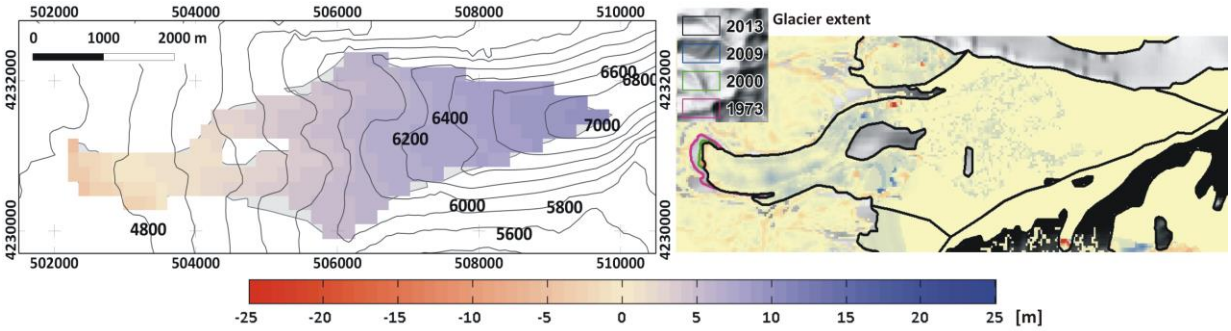


**Fig. 6.7: Spatial comparison of modelled surface height change of Muztagh Ata glacier for the 0.31-model run, 2001-2012 (left), with the results provided by N. Holzer, TU Dresden (right) (difference Pleiades DEM 2013 / SRTM DEM 2000).**

### 6.4.2 Snow line and ELA characteristics 2000-2012

Mean monthly variations of the glacier-wide mean altitude of the transient snow line between 2001 and 2012 at Muztagh Ata glacier are calculated from the MB model results (Fig. 6.8). The given values refer to the reference run with a precipitation scaling factor of 0.56. Based upon the reference run precipitation amounts are decreased and increased by 25%, respectively, to obtain the model uncertainty (see section 6.3). Between October and March no snow line is evident on the glacier independently from the precipitation scaling factor. During these months the mass gain through solid precipitation is much larger than the mass loss through sublimation. A snow line develops in the lowermost glacier regions in April (Fig. 6.8). Precipitation amounts are largest in May (Fig. 1.18). The mean snow line altitude decreases again before it rises up to 4740 m a.s.l. until August. Between May and August precipitation amounts decrease and $T_{air}$ increases to its maximum in July and August (Fig. 1.18). Surface melt and sublimation reach their highest values in the annual cycle in this season (Fig. 6.5). In September $T_{air}$ and surface melt decrease rapidly and allow the increase of a snow pack. Thus, the snow line altitude decreases. Generally, the altitudinal variation of the mean transient snow line is only 77 m in the reference run with a mean altitude of 4690 m a.s.l. In total, 39% of surface and subsurface melt refreeze in the reference run (see section 6.4.1) and form a layer of superimposed ice when the snow pack is removed. Therefore, a snow line can develop and rise up the glacier while MB is still positive. With precipitation decreased by 25% the snow line altitude rises around 7 m with the largest sensitivities in summer (Fig. 6.8) when precipitation amounts decrease within the annual cycle and surface melt and sublimation are largest (Fig. 1.18, 6.5). A precipitation increase by 25% lowers the snow line altitude by ≈3.4 m compared to the reference run. Sensitivities are largest in July and August (Fig. 6.8).

The modelled annual ELA for 2000 to 2012 at Muztagh Ata glacier is shown in Fig. 6.9. The ELA follows the MB pattern (Fig. 6.6) with very low lying or no ELA in strongly positive MB years and slightly higher ELA in less positive MB years. From the vertical MB profile for the reference run for Muztagh Ata glacier (section 6.4.1) the ELA between 2000 and 2012 would be located just below the altitude of the lowermost parts of the glacier (Fig. 6.4a). For the 0.31-model run the ELA is estimated around 5000 m a.s.l. (Fig. 6.4a). The average over the calculated annual ELA 2002-2012 (Fig. 6.9) leads to a value of 4905 m a.s.l for the model run with precipitation decreased by 25%. In the reference run the ELA is lower than the lowermost parts of the glacier in every year (Fig. 6.9). Based on measured MB values at a different glacier in the Muztagh Ata region from 2001/2002 until 2009/2010 Yao et al. (2012) state a mean ELA around 5460 m a.s.l. (Fig. 6.9). The authors do not provide details on how the ELA was derived. The absolute altitudes do not correspond to the ELA derived from the MB mo-

del with 25% decreased precipitation. However, the inter-annual variation in both studies is similar despite for the years 2009/10 (Fig. 6.9).

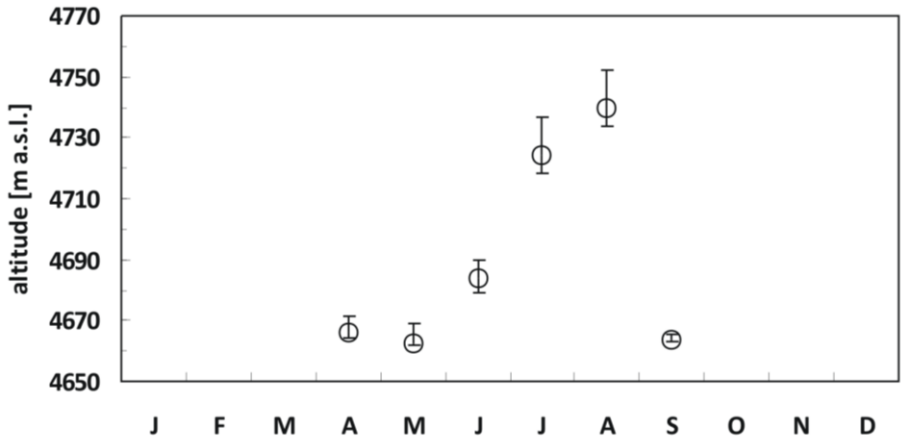


**Fig. 6.8: Modelled mean intra-annual cycle of the snow line at Muztagh Ata glacier, 2001-2012. The model uncertainty is calculated assuming different precipitation amounts (see section 6.3).**

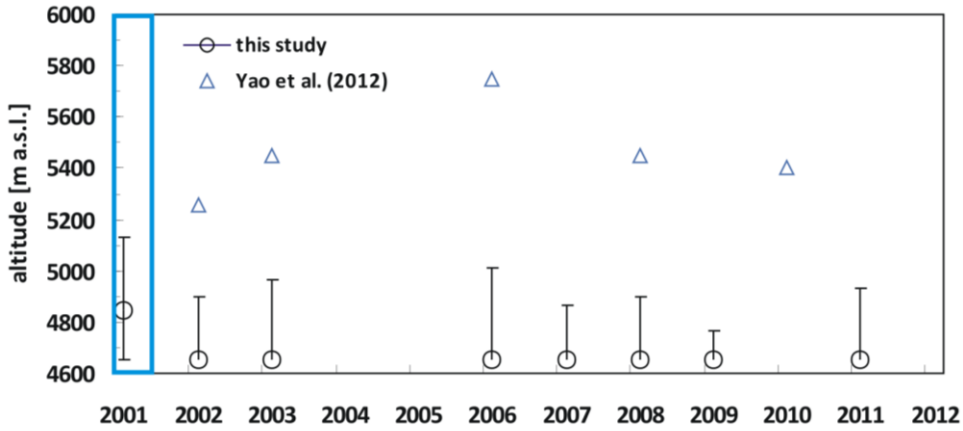


**Fig. 6.9: Glacier-wide annual ELA at Muztagh Ata glacier, 2000-2012, calculated by the HAR forced MB model and compared to the results published in Yao et al. (2012) for a neighbouring glacier. The ELA of 2010 of Yao et al. (2012) is the resulting ELA at the end of the two mass balance years 2008/09-09/10. The uncertainty ranges are calculated assuming different precipitation amounts (see section 6.3). Note that the ELA in 2001 (grey box) should not be considered.**

The relation of annual AAR and annual MB at Muztagh Ata glacier for the period 2001-2012 for the MB model run with precipitation decreased by 25% (scaling factor 0.31) is visualized in Fig. 6.10. In the reference run (scaling factor 0.56) annual MB is positive throughout (Fig. 6.6). Thus, $AAR_0$ can not be obtained. For the determination of $AAR_0$ at Muztagh Ata glacier the first MB year has to be considered although it contains small errors related to the spin-up time of the MB model. However, it is the only year with negative MB. It can be assumed that the relation between MB and AAR still holds although absolute MB may be erroneous. According to the model data using unchanged $T_{air}$ form the HAR dataset the relationship between AAR and MB is linear ($R^2$=0.69, Fig. 6.10). Linear relationships are also revealed for Zhadang glacier (see section 2.4.6), PIC (3.4.2) and Naimona'nyi glacier (see section 4.4.2). In the model run with precipitation decreased by 25% the total AAR is 94% with the smallest value of 87% in 2005/06. $AAR_0$ is estimated to be 82% (Fig. 6.10). The index $\alpha_d$ after Dyurgerov et al. (2006) measures the glacier's displacement from the equilibrium (see section 2.4.6). For the reference run at Muztagh Ata glacier $\alpha_d$ is determined to be +22%. Thus, the glacier would have to increase its area and advance to reach its equilibrium state for the climate conditions of the

simulation period with a precipitation scaling factor of 0.56 and unchanged HAR $T_{air}$. A precipitation decrease of 25% compared to the reference run results in a $\alpha_d$ of +14%. Thus, the glacier's area and volume reveal a weak sensitivity to precipitation trends under the climate conditions created by the HAR data. This result is in accordance with the overall pattern of cold-based, '*spring- and winter-accumulation type*' glaciers on the northern and western TP (see sections 1.3.2 and 1.4.1).

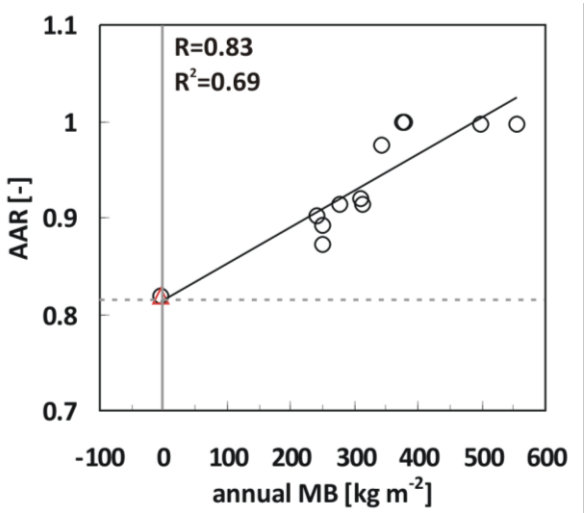


**Fig. 6.10: Relation between annual MB and AAR at Muztagh Ata glacier, 2001-2012, for the MB model run with a precipitation scaling factor of 0.31. The AAR at MB=0 denotes $AAR_0$. The red triangle marks the value of the first MB year (2000/01) that is not considered in the interpretations. It is only considered to allow the calculation of $AAR_0$.**

## 6.5 Discussion of uncertainties

The variation of HAR precipitation as input for the MB model through the application of three different scaling factors (0.56±0.25) creates a range of uncertainty for every SEB and MB component (see section 6.4). At Muztagh Ata glacier the calculated ranges of uncertainty are very small. They are dominated by the varying precipitation amounts. Even in the 0.31-model run enough solid precipitation is generated to prevent the glacier from being snow free over longer periods when simulated with unchanged $T_{air}$ from the HAR dataset. This keeps $\alpha$ high and reduces the sensitivity of all SEB and MB components (see sections 6.4.1, 6.4.2). The comparison with surface height changes from remote sensing analysis for the same glacier between 2000 and 2013 (provided by N. Holzer, TU Dresden) and in-situ measurements at a neighbouring glacier in the Muztagh Ata region (Yao et al. 2012) reveals that the reference run clearly overestimates the MB and the surface height changes. With decreased precipitation amounts (0.31) the MB model results are more reasonable. The amount of refreezing slightly declines from 39% in the reference run to 34% in the 0.31-run. These values seem to be reasonable when considering that Muztagh Ata glacier contains cold ice throughout (Shangguan et al. 2006, see section 1.4.1). The spatial comparison of calculated surface height changes from this study and from N. Holzer (unpublished data) reveals that the overall pattern is captured to a high degree (Fig. 6.7). The calculated annual average MB with a precipitation factor of 0.31 is only slightly higher than the results determined by N. Holzer through the geodetic MB method and the results published by Yao et al. (2012) based on in-situ measurements at a neighbouring glacier.

It is possible that a cold bias in HAR $T_{air}$ that is revealed at Naimona'nyi glacier (chapter 4) and possibly also evident at Halji glacier (chapter 5) might also occur in the Muztagh Ata region. However, no suitable in-situ measurements for the evaluation are available so far.

## 6.6 Conclusion regarding model results for Muztagh Ata region

Muztagh Ata is the northern- and westernmost region of the selected study sites (Fig. 1.1). The region is strongly influenced by the westerlies that are the most important moisture source (see section 1.4.1). The impact of the monsoon precipitation is absent. In this chapter, SEB and MB components of Muztagh Ata glacier are calculated for 2000-2012 and interpreted concerning their altitudinal gradients and their inter- and intra-annual patterns. To account for uncertainties in total HAR precipitation amounts and to obtain a model uncertainty for further MB calculations, we perform three model runs with varying precipitation scaling factors (0.56±0.25) while keeping $T_{air}$ from HAR unchanged. In the reference run a factor of 0.56 is applied. In total, the energy input to the surface of Muztagh Ata glacier is dominated by $LW_{net}$ with 45% both in the reference run and in the model runs with ±25% precipitation. Very low $T_{air}$ and frequent amounts of snowfall suppress surface melt and favour refreezing in all model runs. In the reference run 39% of the surface and subsurface melt refreezes. Effective melt accounts only for 27% and sublimation for 73% of the total mass loss in the reference run (Table 6.2). The variation of HAR precipitation as input for the MB model through the application of three different scaling factors creates only a small range of uncertainty for every SEB and MB component. Generally low $T_{air}$ leads to a very high proportion of total precipitation falling as snow even in summer. Thus, glacier-wide $\alpha$ is generally high and reduces the sensitivity of all SEB and MB components (see section 6.4). Only the lower glacier regions are little sensitive to a precipitation decrease by 25% (Fig. 6.4). The ELA at Muztagh Ata glacier for 2002-2012 is estimated around 4900 m a.s.l. (scaling factor 0.31) which is considerable lower than the value given by Yao et al. (2012) for a neighbouring glacier (≈5460 m a.s.l.) but within the range of large scale ELA variability for the region of the north western TP (Fig. 1 in Yao et al. 2002).

The comparison with surface height changes and MB from remote sensing analysis for the same glacier between 2000 and 2013 (provided by N. Holzer, TU Dresden) and in-situ measurements at a neighbouring glacier (Yao et al. 2012) reveal that the reference run clearly overestimates observed the mass gain. With decreased precipitation amounts (0.31) the MB model results are more reasonable. Generally, the results at Muztagh Ata glacier coincide with the overall picture of the cold-based glaciers on the northern and western TP (see sections 1.3.2 and 1.4.1).

It can be concluded from the application of the MB model to Muztagh Ata glacier that the derived intra- and inter-annual cycles of SEB and MB components are within reasonable limits depending on the respective patterns of the input parameters from HAR. The characteristic annual cycles of a region dominated by the westerlies are captured to a high degree. The obtained SEB and MB components are consistent with each other because they interact through physical relationships (see sections 1.3.4 and 2.3.1). The HAR output overestimates the precipitation amounts in the reference run. A scaling factor of 0.31 is more reasonable when no correction of HAR air temperature data is included. The lack of meteorological and glaciological in-situ observations hampers the model evaluation. It is already stated in chapters 4 and 5 that it is difficult to obtain the correct combination of precipitation scaling factor and air temperature offset in regions where neither precipitation nor temperature measurements are available.

# 7 Comparison and interpretation of the glacier characteristics at the five study sites on the Tibetan Plateau, 2001-2012

Within this chapter the different SEB and MB components of all five glaciers and ice caps presented in this thesis are compared and interpreted concerning their inter- and intra-annual patterns (section 7.1). Furthermore, seven atmospheric circulation and teleconnection patterns that influence the TP are chosen to explain the variability in air temperature, precipitation and MB at the five study sites (section 7.2).

## 7.1 Comparison and interpretation of the SEB and MB components at the five study sites, 2001-2012

The inter-annual patterns of the different SEB and MB components for the individual glaciers and ice caps as derived from the MB model are discussed in the respective chapters 2-6. The comparison of the inter- and intra-annual patterns reveals commonalities and differences between the studied glaciers and their driving mechanisms. For the comparison within this section we chose the results of the model run with the precipitation scaling factor and air temperature offset that fits best to the available observations at each glacier (see chapters 3-6). The obtained best fit combinations are 0.56/±0 K for Zhadang glacier and PIC, 0.31/+3 K for Naimona'nyi glacier, 0.56/+1 K for Halji and 0.31/±0 K for Muztagh Ata glacier. Note that the glacier-wide results for Naimona'nyi are calculated from the respective profile (see chapter 4). The closure of the SEB is not necessarily fulfilled. Thus, absolute values and relative proportions are a best guess. Additional glacier-wide model runs for Naimona'nyi glacier will be carried out in subsequent studies that are not part of this thesis in the near future.

Mean annual cycles of all SEB and MB components for each glacier are summarized in Fig. 7.1 and 7.2. The glacier-wide monthly SEB components as a time series for the five study sites are shown in Fig. B.1 in appendix B. The respective MB components including $T_{air}$ are given in Fig. B.2. Mean monthly glacier-wide $T_{air}$ show a regular cycle in all study regions with distinct negative values in winter and less negative to positive values in summer (Fig. 7.2, B.2f).

All study regions besides Muztagh Ata experience highest $T_{air}$ in summer 2006 (B.2f). At Zhadang glacier this coincides with below-average precipitation amounts resulting in below-average MB (Fig. B.2d, B.2e). This is evident also in Fig. 7.5 that visualizes monthly anomalies for $T_{air}$, precipitation and MB for all five glaciers. Over the total simulation period $T_{air}$ is highest at Zhadang glacier (-8.1°C) and

Halji glacier (-8.4°C) and lowest at Muztagh Ata glacier (-17.3°C). Naimona'nyi (-10.7°C) and PIC (-12.0°C) range in between.

At Zhadang glacier the maximum of solid precipitation generally falls in summer. In July and August, when total precipitation amounts are largest, only 55% of the total precipitation falls as snow because $T_{air}$ is above zero over longer periods (Fig. 7.2). At Halji glacier the liquid proportion of total precipitation even exceeds the solid proportion in July and August (Fig. 7.2). Only 26% of total precipitation falls as snow in those two summer months. At PIC solid precipitation accounts for 73% of the total in July and August. At Naimona'nyi the proportion is a little higher with 78%. $T_{air}$ at Muztagh Ata glacier is below zero most of the time and the amount of snowfall accounts for 98% of total precipitation even in July and August (Fig. 7.2). Note that $T_{air}$ at Naimona'nyi and Halji have been modified by +3 K and +1 K during the validation process (see chapters 4 and 5). Thus, especially mean $T_{air}$, precipitation amounts and the proportions of liquid and solid precipitation might vary. At PIC the mean annual amplitude of $T_{air}$ is largest (25.6 K) confirming the continental character of the region (see section 1.4.1 and chapter 3).

The inter- and intra-annual variability of glacier-wide solid precipitation between the five regions is less regular than the variability of $T_{air}$ (Fig. 7.2, 7.4b,c, B.2d,f). Anomalies in $T_{air}$ only play a role in summer, when $T_{air}$ exceeds zero. The amount and seasonality of solid precipitation strongly influences all SEB and MB components through its influence on $\alpha$ (see sections 1.3.4.1, 1.3.5 and chapters 2-6). Thus, it is reasonable to start the comparison and interpretation of SEB and MB components from the patterns and anomalies of solid precipitation. The mean inter-annual cycles over the total simulation period reveal that all of the five glaciers receive significant amounts of solid precipitation in summer (Fig. 7.2). The frequent snowfall events result in high $\alpha$ and thus low $SW_{net}$ (Fig. 7.1). This effect prevents all five glaciers from increased surface melt. At Zhadang, Naimona'nyi and Halji glaciers $\alpha$ decreases in August when large parts of the glaciers are snow free (Fig. 7.1). Despite lowest $SW_{net}$ in the annual cycle, the energy input to the glacier surface through $SW_{net}$ and $Q_{sens}$ is not compensated by the energy loss through $LW_{net}$, $Q_{lat}$ and $Q_G$ during spring and early summer (Fig. 7.1). Thus, $Q_{melt}$ increases and the resulting surface melt gradually decreases the snow pack. At Naimona'niy and Halji positive $Q_{lat}$ even contributes to the energy input in summer (Fig. 7.1). Decreasing $\alpha$ in August causes largest $Q_{melt}$ and highest surface melt at Zhadang, Naimona'nyi and Halji. However, at PIC and Muztagh Ata the annual mean maximum of $Q_{melt}$ as well appears in August, although $\alpha$ is not exceptional low (Fig. 7.1). Nevertheless, the surface energy removal at PIC and Muztagh Ata in August by $LW_{net}$, $Q_{lat}$ and $Q_G$ is smaller than the energy input by $SW_{net}$ and $Q_{lat}$. The remaining energy is used for surface melt ($Q_{melt}$). On average over the total simulation period, $\alpha$ reaches its minimum values around October-November-December (OND) at all glaciers because solid precipitation is at its annual minimum (Fig. 7.1). At Muztagh Ata precipitation amounts do not show a clear minimum (Fig. 7.2). Thus, $\alpha$ is rather high throughout the year (Fig. 7.1). The average seasonal cycles of the SEB components are similar at Zhadang, PIC, Naimona'nyi and Halji. The patterns are characterized by the domination of the Indian summer monsoon. The region of Muztagh Ata is strongly influenced by the westerlies. Thus, all SEB components despite of $Q_C$ and $Q_{melt}$ show a seasonally reversed pattern compared to the other study sites (Fig. 7.1). This is also valid for sublimation and subsurface melt because both parameters directly depend on $Q_{lat}$ and $Q_{PS}$, respectively. The inter-annual cycles of the other MB components are similar for the five glaciers (Fig. 7.2). The detailed description and interpretation of the SEB and MB components for the single glaciers are given in chapters 2-6.

Generally, the inter-annual cycle of glacier runoff is similar to that of surface melt for the studied glaciers (Fig. 7.2). At PIC, Naimona'nyi and Halji the annual cycles of surface melt and runoff nearly fit perfectly because the amount of refreezing almost equals liquid precipitation (Table 7.1). At Muztagh Ata glacier runoff is significantly less than surface melt especially in August, because 33% of surface

and subsurface melt refreezes in this month. The proportion of liquid precipitation is negligible at Muztagh Ata (Fig. 7.2). At Zhadang glacier large amounts of surface melt refreeze within the snowpack in spring and autumn. Thus, runoff is reduced largely during these seasons (Fig. 7.2). In July and August, refreezing decreases and nearly half of the monsoon precipitation reaches the glacier as rain. This leads to increased glacier runoff compared to surface melt in these months.

An overview on the glacier-wide SEB and MB components over the simulation period and their relative contribution to the total energy turnover and the total mass loss are given in Table 7.1 for the five studied glaciers. The three southernmost glaciers, Zhadang, Naimona'nyi and Halji are characterized by lowest overall $\alpha$ and therefore largest $SW_{net}$ (Table 7.1). At PIC and Muztagh Ata the overall energy loss by $LW_{net}$ is larger than the energy gain by $SW_{net}$. Thus, net radiation is an energy sink for both glaciers. The turbulent fluxes act as a net energy source in these cases. This pattern is more distinct at Muztagh Ata than at PIC probably because very low $T_{air}$ cause a constantly high $\alpha$. Energy loss by $Q_{lat}$ is largest at Zhadang because $RH$ is low and the glacier surface temperatures favour turbulent exchange. At PIC the moisture content of the air is less than at Zhadang but generally low surface temperatures limit $Q_{lat}$ and therefore sublimation (Table 7.1). Low air and surface temperatures might also be a reason for low $Q_{lat}$ at Muztagh Ata. Furthermore, the overall moisture content at Muztagh Ata is high and exhibits no clear annual minimum. At Halji and Naimona'nyi overall $Q_{lat}$ is not a relevant energy sink because it regularly becomes positive in summer (see chapters 4 and 5). The total energy turnover at Zhadang is dominated by $SW_{net}$. At Naimona'nyi and Halji $SW_{net}$ and $LW_{net}$ are of equal importance. At PIC and Muztagh Ata continuously high $\alpha$ results in a higher contribution of $LW_{net}$ to the total energy turnover.

Halji, Muztagh Ata and Zhadang glacier receive the highest annual amounts of solid precipitation, followed by PIC and Naimona'nyi (Table 7.1). The comparison of solid precipitation and total precipitation stresses the importance of $T_{air}$. Total precipitation is largest at Halji and Zhadang and less at Naimona'nyi and PIC. The large discrepancy in total precipitation between Naimona'nyi and Halji is a consequence of the application of different precipitation scaling factors (see chapters 4 and 5). However, the amounts appear to be reasonable when considering the luv and lee situation, local terrain effects (see section 1.4.1) and the heterogeneity of accumulation regimes in this region (Fig. 1.9). The components of the SEB lead to highest overall surface melt at and Zhadang and Halji glacier driven by $T_{air}$, $\alpha$ and $SW_{net}$ (Table 7.1). The amount of refreezing is largest at Halji because more solid precipitation allows a thicker snow pack compared to Zhadang. However, the proportion of surface and subsurface melt that refreezes within the snow pack is largest at Muztagh Ata (Table 7.1). The refreezing process in this region is favoured by small melt rates and very low air and subsurface temperatures. Generally, refreezing plays a significant role in glacier MB at Muztagh Ata, PIC, Halji and Zhadang. Total mass loss through sublimation is largest at Zhadang glacier. However, the amount is small compared to total effective melt (Table 7.1). At PIC and Muztagh Ata the mass loss by sublimation accounts for more than half of the total mass loss. The proportions are 68% at PIC and 71% at Muztagh Ata (Table 7.1).

The calculated runoff consists of effective melt and liquid precipitation. Runoff is largest at Zhadang glacier (Table 7.1). However, the amount by which runoff exceeds surface melt is largest at Halji glacier because the amount of liquid precipitation is high. At Zhadang and Muztagh Ata overall runoff is less than surface melt.

The inter-annual variability of all SEB and MB components including $T_{air}$ for the five studied glaciers as derived from the MB model is summarized in Fig. 7.3 and Fig. 7.4. At PIC and Muztagh Ata inter-annual fluctuations are generally smaller than at Zhadang, Halji and Naimona'nyi. This coincides with the largest overall mass loss and lowest $\alpha$ at the latter three glaciers (Table 7.1).

At Zhadang glacier the inter-annual variability of solid precipitation amounts is the largest of the five glaciers (Fig. 7.4). It is revealed from Fig. 7.5 that these large fluctuations are already evident in total precipitation amounts at Zhadang. Both inter- and intra-annual fluctuations in $T_{air}$ at Zhadang are not larger than at the other study sites (Fig. 7.4, 7.5). Thus, the high variability in solid precipitation at Zhadang is mainly caused by total precipitation amounts. However, it is mentioned in the beginning of this section, that below-average precipitation amounts in summer 2006 coincide with above-average $T_{air}$ (Fig. 7.5). The result is a below-average MB at Zhadang glacier in summer 2006. Precipitation amounts in summer 2005 are nearly the same as in 2006 but $T_{air}$ is lower in 2005. The effect of precipitation on MB in 2005 is less distinct than in 2006 (Fig. 7.5). This finding leads to the assumption that both $T_{air}$ and precipitation are important for MB at Zhadang glacier especially in summer. The correlation of both parameters with glacier MB confirms this assumption (Table 7.2). At Zhadang $T_{air}$ and precipitation have a similar impact on MB in summer (JJAS). As expected, the importance of $T_{air}$ for MB is smaller for annual anomalies. This can be concluded from a lower correlation coefficient between $T_{air}$ and MB compared to the correlation of MB anomalies with summer air temperature variations. The same is revealed for the other glaciers (Table 7.2).

**Table 7.1: SEB and MB components at the five studied glaciers for the total simulation periods 2001-2011/12. Applied scaling factors for precipitation and $T_{air}$ offsets are: Zhadang/PIC: 0.56/±0 K, Naimona'nyi: 0.31/+3 K, Halji: 0.56/+1 K, Muztagh Ata: 0.31/±0 K.**

| | Zhadang | PIC | Naimona'nyi | Halji | Muztagh Ata |
|---|---|---|---|---|---|
| SEB components | | | | | |
| total average [W m$^{-2}$] | | | | | |
| $SW_{net}$ | +74 | +35 | +60 | +48 | +30 |
| $LW_{net}$ | -51 | -40 | -58 | -48 | -42 |
| $Q_{sens}$ | +25 | +28 | +15 | +22 | +13 |
| $Q_{lat}$ | -35 | -22 | -10 | -15 | -0.8 |
| $Q_G$ | -3.6 | -1.3 | -4.1 | -1.9 | -1.9 |
| $Q_{melt}$ | -13 | -1.6 | -3.7 | -9 | -0.4 |
| % of total energy flux | | | | | |
| $SW_{net}$ | 38 | 28 | 39 | 36 | 30 |
| $LW_{net}$ | 27 | 30 | 39 | 35 | 45 |
| $Q_{sens}$ | 15 | 21 | 10 | 15 | 14 |
| $Q_{lat}$ | 16 | 17 | 8 | 11 | 5 |
| $Q_G$ | 3 | 4 | 5 | 3 | 6 |
| MB components | | | | | |
| absolute value per year [kg m$^{-2}$] | | | | | |
| MB | -1036 | -44 | -208 | -374 | +354 |
| total precipitation | +558 | +368 | +300 | +659 | +444 |
| solid precipitation | +411 | +332 | +276 | +446 | +443 |
| surface melt | -1262 | -152 | -357 | -830 | -39 |
| subsurface melt | -4.6 | -2.7 | -4.3 | -3.6 | -4.3 |
| refreezing | +216 | +33 | +29 | +223 | +15 |
| sublimation | -397 | -254 | -152 | -209 | -69 |
| effective melt | -1051 | -122 | -332 | -611 | -28 |
| runoff | -1198 | -158 | -356 | -824 | -30 |
| % of total mass loss | | | | | |
| effective melt | 73 | 32 | 69 | 74 | 29 |
| sublimation | 27 | 68 | 31 | 26 | 71 |
| % of refreezing | 17 | 22 | 8 | 27 | 34 |

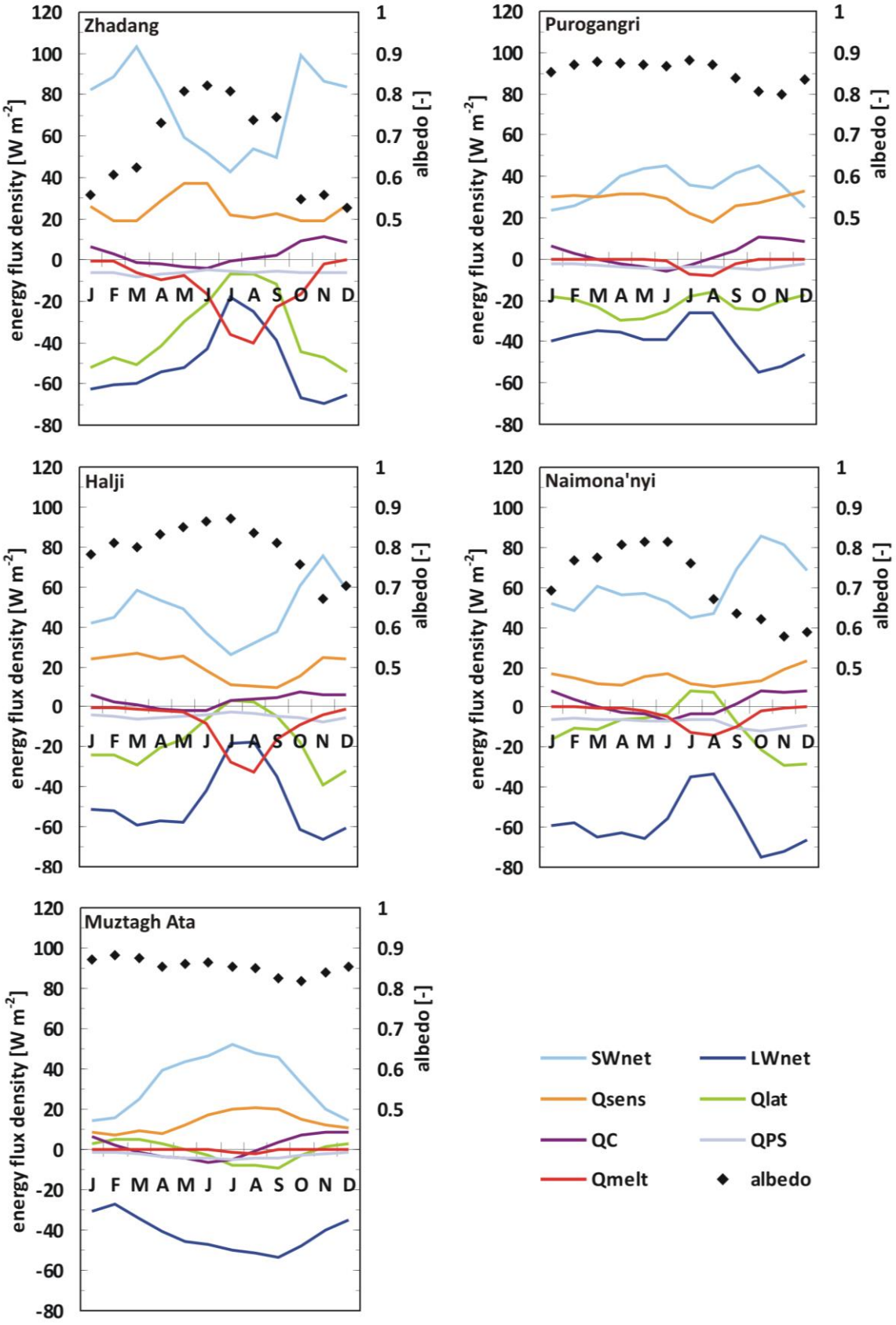


**Fig. 7.1: Glacier-wide mean annual cycles of the SEB components for the studied glaciers on the TP as derived from the HAR driven MB model, 2001-2011/12. Applied scaling factors for precipitation and $T_{air}$ offsets are: Zhadang/PIC: 0.56/±0 K, Naimona'nyi: 0.31/+3 K, Halji: 0.56/+1 K, Muztagh Ata: 0.31/±0 K.**

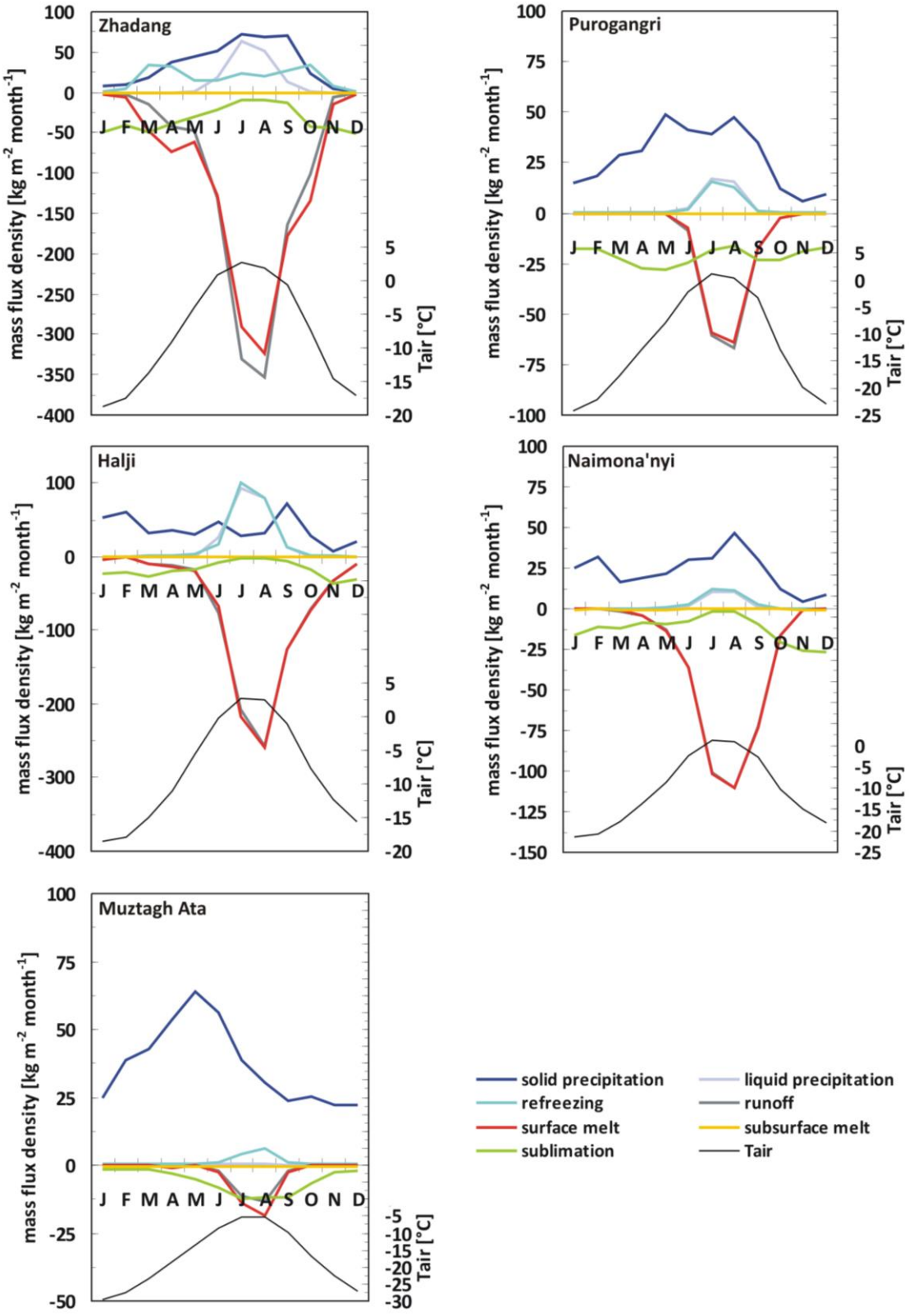


**Fig. 7.2: Glacier-wide mean annual cycles of the MB components including liquid precipitation, runoff and $T_{air}$ for the studied glaciers on the TP as derived from the HAR driven MB model, 2001-2011/12. Applied scaling factors for precipitation and $T_{air}$ offsets are: Zhadang/PIC: 0.56/±0 K, Naimona'nyi: 0.31/+3 K, Halji: 0.56/+1 K, Muztagh Ata: 0.31/±0 K.**

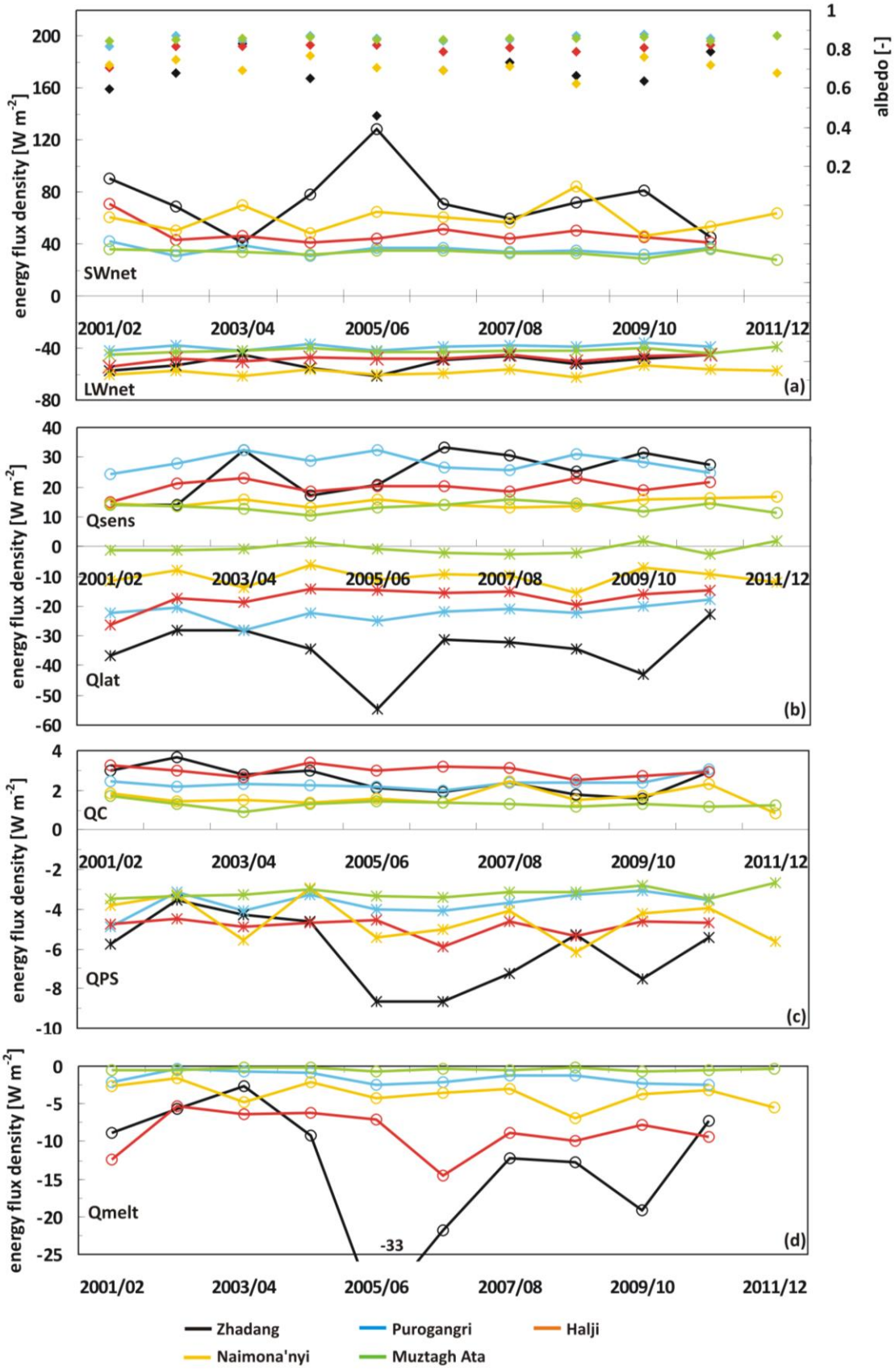


**Fig. 7.3: Glacier-wide inter-annual variation of the SEB components for the five studied glaciers and ice caps, 2001-2012. Applied scaling factors for HAR precipitation and $T_{air}$ offsets are: Zhadang/PIC: 0.56/±0 K, Naimona'nyi: 0.31/+3 K, Halji: 0.56/+1 K, Muztagh Ata: 0.31/±0 K.**

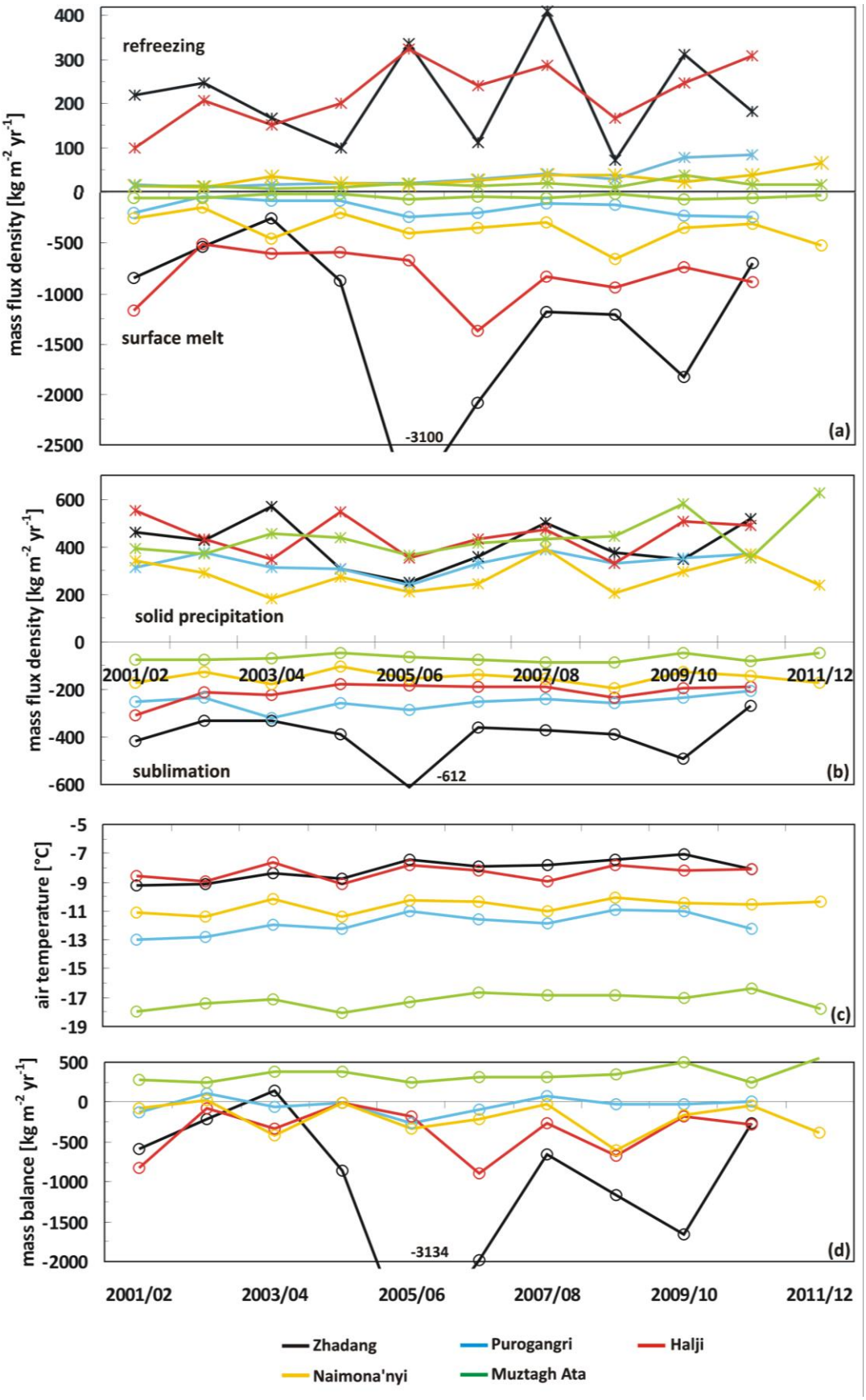


**Fig. 7.4: Glacier-wide inter-annual variation of the MB components and $T_{air}$ for the five studied glaciers and ice caps, 2001-2012. Applied scaling factors for HAR precipitation and $T_{air}$ offsets are: Zhadang/ PIC: 0.56/±0 K, Naimona'nyi: 0.31/+3 K, Halji: 0.56/+1 K, Muztagh Ata: 0.31/±0 K.**

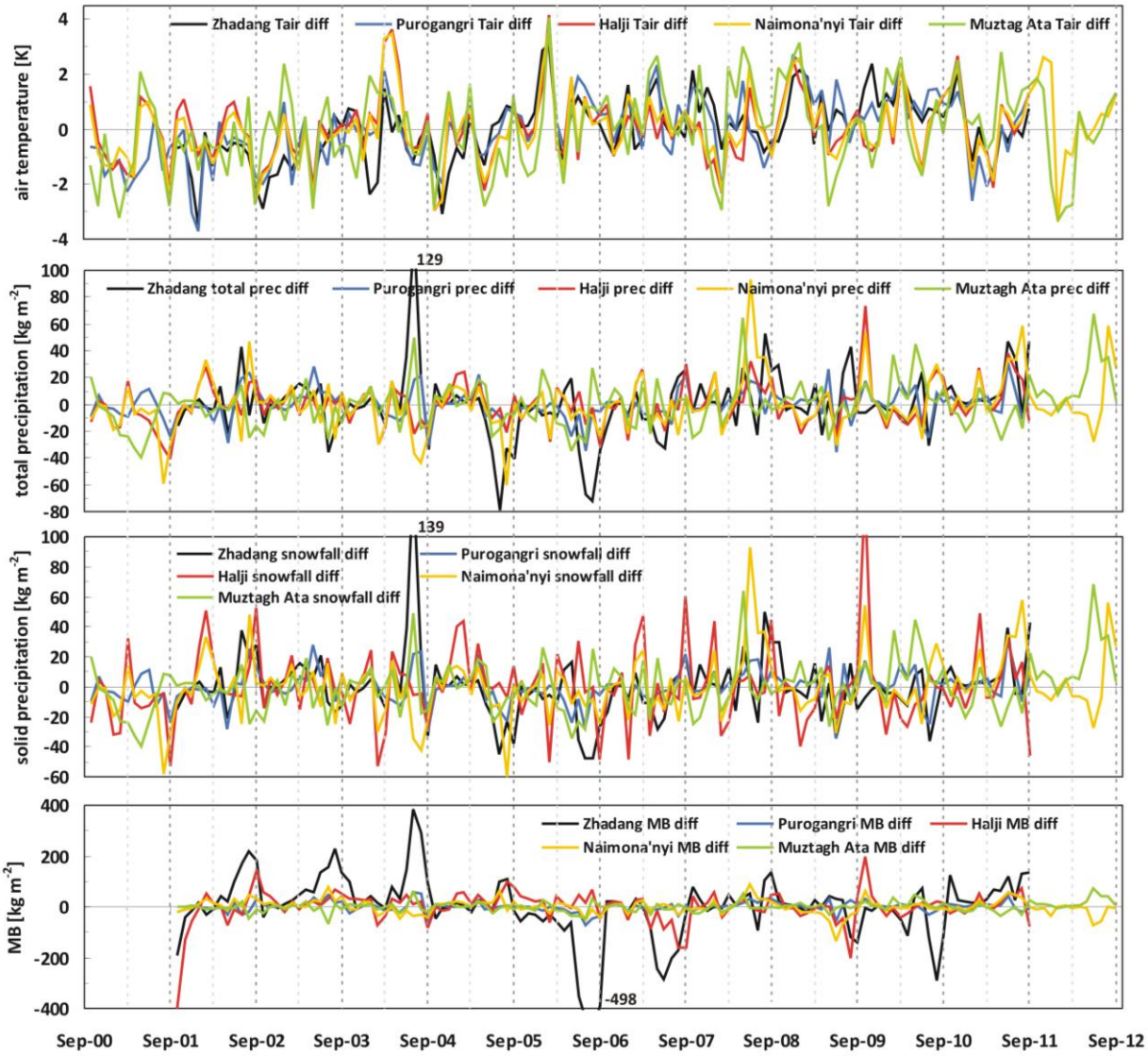


**Fig. 7.5: Monthly glacier-wide anomalies of $T_{air}$, precipitation, snowfall and MB at Zhadang glacier, PIC, Halji glacier, Naimona'nyi glacier and Muztagh Ata glacier, 2000-2012, as derived from the HAR driven MB model. Anomalies are calculated from the difference between the monthly mean over the total simulation period and the monthly mean of the respective year. Applied scaling factors for HAR precipitation and $T_{air}$ offsets are: Zhadang/PIC: 0.56/±0 K, Naimona'nyi: 0.31/+3 K, Halji: 0.56/+1 K, Muztagh Ata: 0.31/±0 K.**

**Table 7.2: Pearson's R and $R^2$ for monthly anomalies of $T_{air}$, precipitation and MB at the five study sites within the simulation period 2001-2011/12. Anomalies are calculated from the difference between the monthly mean over the total simulation period and the monthly mean of the respective year. Applied scaling factors for HAR precipitation and $T_{air}$ offsets are: Zhadang/PIC: 0.56/±0 K, Naimona'nyi: 0.31/+3 K, Halji: 0.56/+1 K, Muztagh Ata: 0.31/±0 K. Green colours indicate positive, yellow colours indicate negative correlations for R larger than ±0.2; the colour intensity increases at R > ±0.4.**

| | MB | | | | | | | | | |
|---|---|---|---|---|---|---|---|---|---|---|
| | Zhadang | | PIC | | Naimona'nyi | | Halji | | Muztagh Ata | |
| | R | $R^2$ | R | $R^2$ | R | $R^2$ | R | $R^2$ | R | $R^2$ |
| Tair | -0.21 | 0.05 | -0.36 | 0.13 | -0.21 | 0.28 | -0.47 | 0.22 | -0.13 | 0.02 |
| Tair JJAS | -0.53 | 0.28 | -0.59 | 0.35 | -0.45 | 0.31 | -0.55 | 0.30 | -0.33 | 0.04 |
| precipitation | 0.51 | 0.26 | 0.67 | 0.45 | 0.63 | 0.39 | 0.41 | 0.16 | 0.96 | 0.92 |
| precipitation JJAS | 0.51 | 0.26 | 0.58 | 0.34 | 0.57 | 0.33 | 0.21 | 0.05 | 0.94 | 0.89 |

MB at Muztagh Ata is clearly dominated by precipitation also in summer (Table 7.2). The correlation of $T_{air}$ and MB is weak possibly because $T_{air}$ is generally low. MB at Halji glacier reveals generally low dependencies for precipitation. The importance of precipitation for MB decreases in summer possibly because large amounts fall as rain and do not contribute to the MB.

The below-average MB at Zhadang in summer 2006 impacts the MB of the total year 2005/06 supported by a high annual mean $T_{air}$ (Fig. 7.4). The below-average precipitation amounts are mirrored in the low annual $\alpha$ and highest $SW_{net}$ over the simulation period at Zhadang glacier (Fig. 7.3). Both values are exceptional compared to the other glaciers. The same is evident for $Q_{lat}$ (sublimation) and $Q_{melt}$ (surface melt). In summer 2004 above-average precipitation amounts cause above-average MB and an overall positive MB in the year 2003/04 at Zhadang (Fig. 7.4, 7.5).

All glaciers are heavily influenced by anomalies in $T_{air}$ and precipitation (Fig. 7.5). As expected, fluctuations in $T_{air}$ are spatially and temporally more homogenous than the precipitation anomalies. In order to obtain insight into the driving mechanisms for these fluctuations, the influence of various teleconnection patterns on $T_{air}$, precipitation and MB at the five study sites is investigated in the following section 7.2.

## 7.2 Air temperature, precipitation and MB at the five study sites and their link to atmospheric teleconnection patterns, 2001-2012

The circulation on the TP is mainly controlled by the mid-latitude westerlies and the Indian and southeast Asian monsoon systems (Bothe et al. 2010, see section 1.3.1). The strength and intensity of the three circulation patterns and therefore the characteristics of the atmospheric variables on inter- and intra-annual scale are related either to local climate anomalies or to large-scale dynamical processes (Bothe et al. 2012). Several authors revealed the interaction of the monsoon systems with the North Atlantic, the tropical Pacific (Feliks et al. 2013, Wu et al. 2009) and the western North Pacific (Takaya & Nakamura 2013) by analyzing the monsoon activity over India and eastern Asia, the North Atlantic Oscillation (NAO) index, the Southern Oscillation (SO) index and the West Pacific (WP) index. Bothe et al. (2010, 2011) focused on the response of standardized precipitation on the TP to changes in the North Atlantic Oscillation (NAO) index, Pacific/North America (PNA) index, East Atlantic/ Western Russia (EAWR) index, Polar/Eurasia (POL) index and indices for the Southern Oscillation. Yi & Sun (2014) carried out a correlation analysis for distinct regions in High Asia. They found that precipitation in the Pamir and Karakorum Mountains between January and March is strongly influenced by the SO index (Yi & Sun 2014).
It is outlined in chapter 1 that the five glaciers and ice caps studied in this thesis are located in different climate regions on the TP. The detailed analyses in chapters 2-6 and section 7.1 reveal similar as well as contrasting intra- and inter-annual patterns of the SEB and MB components for the single glaciers. Thus, the question arises, which teleconnection patterns impact the study regions and whether their influence varies seasonally.

### 7.2.1 Description of the chosen teleconnection patterns

In total, we chose six northern Hemisphere teleconnection patterns that very likely influence the TP: NAO, EAWR, POL, WP, PNA and the Pacific Transition (PT) index (Fig. 7.6). Additionally, we use the SO index because it has strong impacts on both hemispheres (e.g. Dai & Wigley 2000). All climate pattern indices are obtained from the Climate Prediction Center (NOAA)[3] as monthly values.

[3] http://www.cpc.ncep.noaa.gov/

The NAO consists of two centres of air pressure anomaly in the North Atlantic, with one centre located over Greenland (polar low) and the other centre in the North Atlantic between 35°N and 40°N (subtropical high) (e.g. Barnston & Livezey 1987, Wallace & Gutzler 1981, Wu et al. 2009, Climate Prediction Center 2012) (Fig. 7.6). The NAO+ phase is characterized by below-average air pressure over Greenland and above-average air pressure over the subtropical Atlantic. Thus, the pressure gradient between the two centres increases, which in turn results in intensified mid-latitude westerlies (Lauer & Bendix 2004). Additionally, the jet stream is shifted northward. The NAO- phase is associated with an opposite pattern of air pressure anomalies and a decreased pressure gradient between the two regions. The mid-latitude westerlies are weaker. Both phases of the NAO and the associated changes in the intensity of the westerly jet stream cause large-scale variations of the temperature and precipitation patterns (e.g. Hurrell 1995). The effects are largest across Europe and the eastern United States (Climate Prediction Center 2012). However, several studies revealed that the NAO also affects the Asian climate associated with the North Atlantic storm track (e.g. Feliks et al. 2013, Watanabe 2004, Wu et al. 2009). Chang et al. (2001) suggest that the NAO+ phase relates to a weakening of the relationship between the Indian summer monsoon and the SO.

The EAWR pattern consists of four main centres of air pressure anomalies: one centre over Europe, one over northern China, one over the central North Atlantic and one north of the Caspian Sea (Barnston & Livezey 1987, Climate Prediction Center 2012) (Fig. 7.6). It affects Europe and Asia throughout the year. The EAWR+ phase is characterized by above-average air pressure over Europe and northern China and below-average air pressure over the North Atlantic and north of the Caspian Sea. Generally, mean surface temperatures and precipitation departures over eastern China are correlated positively to the EAWR index in winter and spring and negatively in summer and autumn (Climate Prediction Center 2012).

The POL pattern appears in all seasons and consists of air pressure anomalies over the northern polar region and over northern China and Mongolia (Climate Prediction Center 2012) (Fig. 7.6). The POL+ phase is characterized by below-average air pressure over the polar region and above-average air pressure over northern China associated with an enhanced circumpolar vortex (Climate Prediction Center 2012). Between spring and autumn long-term surface temperatures correlate negatively over eastern China and positively over eastern Siberia to the POL index (Climate Prediction Center 2012).

The WP pattern consists of a north-south dipole of air pressure anomalies in the North Pacific. In winter and spring one centre is located over the Kamchatka Peninsula and the other centre over Southeast Asia and the western subtropical Pacific (Barnston & Livezey 1987, Wallace & Gutzler 1981) (Fig. 7.6). In summer the pattern is shifted northward. Thus, the influence of the WP pattern on the TP is strongest in winter and spring. The WP+ phase is characterized by an increased pressure gradient between the two centres and an intensified Pacific (East Asian) jet stream (Climate Prediction Center 2012). Surface temperatures over China and the TP correlate strongly positive to the WP index in winter and also positively in spring but with overall weaker correlation. Precipitation departures correlate negatively over southern China and positively over eastern China in spring (Climate Prediction Center 2012).

The PNA pattern consists of four air pressure anomaly centres: one over Hawaii, one over northern North America, one south of the Aleutian Islands and one over the south eastern United States (Climate Prediction Center 2012) (Fig. 7.6). The PNA+ phase is associated with above-average air pressure over Hawaii and over North America and below-average air pressure south of the Aleutians and the south eastern United States. The result is an enhanced East Asian jet stream with an eastward shift of the jet entrance and exit region. The PNA- phase is characterized by a westward shift of the jet stream towards eastern Asia (Climate Prediction Center 2012). Surface temperatures in southern

China correlate negatively with the PNA index in winter and spring, and positively in summer (Climate Prediction Center 2012).
The PT pattern is reported only for August and September. It consists of four centres of air pressure anomaly: west of Hawaii, over western North America, at the Gulf of Alaska and over the south eastern United States (Climate Prediction Center 2012) (Fig. 7.6). The PT+ phase is characterized by above-average air pressure west of Hawaii and over North America and below-average pressure in the Gulf of Alaska and over the south eastern United States. This is associated with increased wave-train activity in the 500 hPa level between the central subtropical North Pacific and the eastern United States (Climate Prediction Center 2012). Generally, surface temperature departures in southern China correlate positively with the PT index. Precipitation departures on the TP correlate positively in the eastern, middle and western part and negatively in the north and southwest (Climate Prediction Center 2012).
The SO index is calculated based on air pressure anomalies over the eastern tropical Pacific and Indonesia and the western tropical Pacific (Fig. 7.6). The SO- phase is characterized by below-average air pressure over the eastern tropical Pacific and above-average air pressure over Indonesia. Thus, the pressure gradient between the two centres decreases. This in turn results in a reduced strength of the equatorial Walker circulation with e.g. reduced easterly winds across the eastern tropical Pacific in the lower atmosphere (Climate Prediction Center 2005, Lauer & Bendix 2004). Long and intensive periods of SO- are related to above-average sea surface temperatures and above-average rainfall across the eastern tropical Pacific, the so called El Niño episodes (Climate Prediction Center 2005). During intensive SO+ phases, the strength of the Walker circulation increases (La Niña). Thus, easterly winds in the lower atmosphere over the eastern tropical Pacific increase and result in below-average sea surface temperatures in this region (Climate Prediction Center 2005). Long and intensive SO+ and SO- phases have strong impacts on both hemispheres. Generally, the southern TP and India experience above-average air temperatures during SO- episodes in winter. During summer precipitation over India is below-average (Climate Prediction Center 2005). SO+ phases generally result in below-average air temperatures and above-average precipitation over the southern and central TP and India (Bothe et al. 2010, Climate Prediction Center 2005).

### 7.2.2 Seasonal influences of the teleconnection patterns at the study sites

Glacier MB as calculated by the model applied in this thesis is the result of the balance of all different energy and mass flux components (see section 2.3.1). The use of $T_{air}$ as index for empirical glacier melt models is reasonable because it strongly influences almost all energy sources for melt on most glaciers (see sections 1.3.4, 2.3.1). The second obvious variable that significantly alters glacier melt is precipitation through its influence on $\alpha$ (see chapters 2-6). Thus, the three parameters $T_{air}$, precipitation and MB are chosen to reveal the seasonal influence of the teleconnection patterns on each glacier. The Pearson product-moment correlation coefficient (Pearson's R) is calculated for the glacier-wide values of $T_{air}$, precipitation and MB for three consecutive months and the respective index of each climate pattern. We chose the periods DJF, MAM and JJA according to the classification of Maussion et al. (2014) (see section 1.3.5). Additionally, we chose three months periods starting from January (JFM, AMJ, JAS, OND). In OND precipitation and surface albedo reach their minimum in the annual cycle at the five glaciers (see section 7.1). No standardization or time delay to the climate indices is applied to the three variables. The revealed correlation coefficients are generally low (see Tables 7.3-7.7). At this stage neither a detailed analysis of the significance of correlations has been carried out nor has the reduction of significance due to autocorrelation within the time series been considered. This study only aims at providing an overview on possible mechanisms and not their detailed analysis. The latter may be subject of subsequent studies.

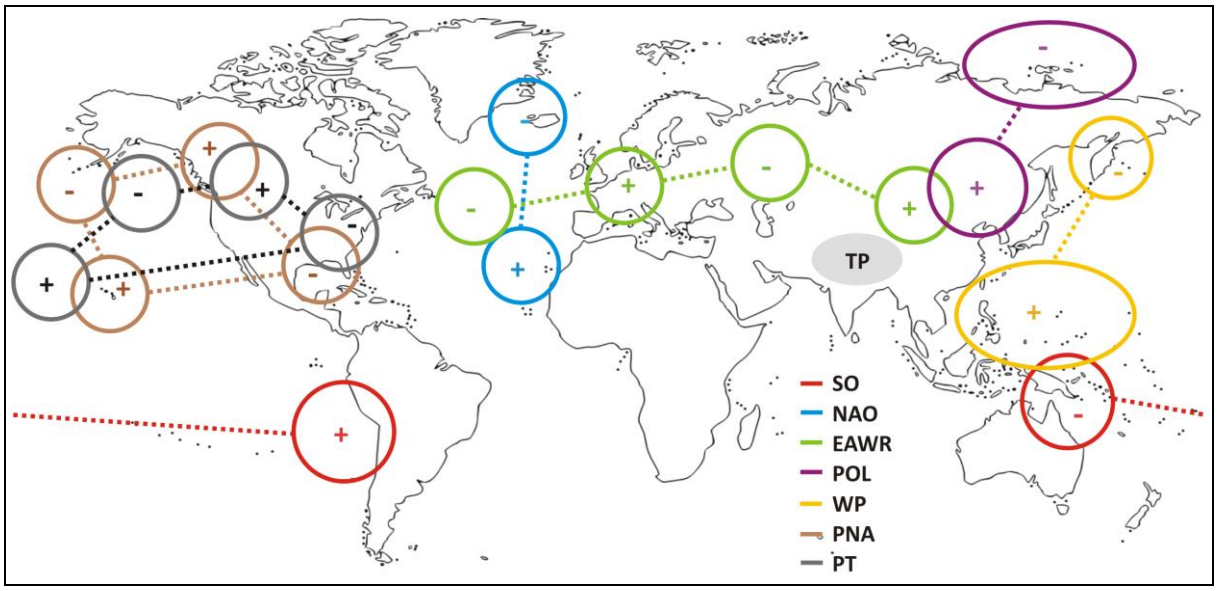


**Fig. 7.6: Location of the air pressure anomaly centres of the chosen teleconnection patterns. The grey area marks the location of the TP; the signs indicate the air pressure anomaly over the region during the positive phase of the respective pattern; after: Climate Prediction Center (2005, 2012).**

During the simulation period, summer MB at Zhadang glacier (JAS) reveals a distinct positive correlation with the NAO index (Table 7.3). One reason for this might be the negative correlation of NAO and $T_{air}$ in this period. The signal of the NAO in precipitation at Zhadang is very weak, possibly because the glacier is situated in the southeast of the TP and air masses from the west are generally dry even if the westerlies are strengthened during NAO+. A similar effect might be evident at PIC (Table 7.4). MB correlates negatively with the NAO index in JFM at PIC and in MAM at Naimona'nyi and Muztagh Ata (Tables 7.4, 7.5, 7.7). However, this cannot be solely explained by the respective patterns in $T_{air}$ and precipitation. The strongest negative correlation of MB with NAO is evident at Muztagh Ata in AMJ through the strong correlation with precipitation in these months (Table 7.7). The negative correlation of NAO and precipitation amounts might be the effect of the northward shift of the jet stream during NAO+. Thus, the TP is less influenced by the moisture transport from the west. This might be an important factor at Muztagh Ata where maximum precipitation amounts occur in spring (see section 1.4.1). At Naimona'nyi, Halji and Muztagh Ata glaciers, precipitation generally correlates negatively with the NAO index in summer and positively in winter (Tables 7.5-7.7). In winter, stronger westerlies might transfer more moisture to the TP. During summer, a stronger jet stream limits the northward progression of monsoonal air masses. The latter effect was also revealed by Mölg et al. (2014) at Zhadang glacier.

The EAWR index generally indicates positive correlations with MB in winter and late summer and negative correlations in spring to summer at PIC, Naimona'nyi, Halji and Muztagh Ata (Tables 7.4-7.7). This structure is mainly governed by the influence of the EAWR pattern on $T_{air}$ in spring and summer and on precipitation in winter. At Zhadang glacier, both $T_{air}$ and precipitation correlate negatively with the EAWR index to a high degree in MAM (Table 7.3). Thus, both effects nearly balance each other such that the EAWR signal in MB is weak.

Over the considered simulation period, the POL pattern and glacier MB at Zhadang glacier and PIC are correlated positively in winter and spring and correlate negatively in summer and autumn (Tables 7.3, 7.4). At Naimona'nyi, Halji and Muztagh Ata, the study sites that are located further to the west, negative correlations are also evident in winter (Tables 7.5-7.7). The structure in the MB correlations is characterized by both $T_{air}$ and precipitation with varying intensities. At Naimona'nyi and Halji gla-

ciers, POL index and precipitation show a distinct negative correlation in OND and similar but weak correlations with $T_{air}$ (Tables 7.5, 7.6). The MB at both glaciers reflects this signal.
Correlations of the WP index with $T_{air}$ are positive in winter and negative in summer at all studied glaciers (Tables 7.3-7.7). A possible reason for this effect might be that the intensified East Asian jet stream during WP+ (see section 7.2.1) limits the southward progression of cold air masses in winter and the influence of warmer air masses from the south in summer. For $T_{air}$ at Zhadang glacier and PIC the signal of the WP pattern is strongest in DJF and shows a second stronger correlation in JJA (Tables 7.3, 7.5). This structure seems to be impacted by temporal delay and a weakening in winter when moving further to the west. At Naimona'nyi and Halji the strongest influences of the WP pattern on $T_{air}$ are occurring in JFM, JJA and JAS (Tables 7.5, 7.6). Muztagh Ata glacier reveals the highest correlations in MAM and JAS (Table 7.7). Correlations of the WP pattern with total precipitation amounts are strongest at Zhadang glacier in JFM (Table 7.3). The reasons for this feedback are not clear. Probably an intensified jet stream leads to very strong winds in winter which might have an effect on the generation of precipitation and/or blowing snow. The correlation pattern with opposite signs for $T_{air}$ and precipitation at Zhadang glacier in winter and spring is probably responsible for the strong signal of the WP index in the MB of Zhadang glacier in JFM (Table 7.3). At Naimona'nyi glacier the WP index correlates strongest with MB in JAS despite similar negative correlations for both, $T_{air}$ and precipitation (Table 7.5). However, the correlation of MB with $T_{air}$ and precipitation for the five glaciers in Table 7.2 reveals that the influence of precipitation on MB at Naimona'nyi is stronger than the influence by of $T_{air}$ also in summer. At the two southernmost glaciers the WP index correlates negatively with precipitation in summer. Probably the increased jet stream limits the northward shift of the summer monsoon.
The signal of the PNA pattern in MB is strongest at Muztagh Ata and Halji with distinct negative correlations in JFM, JJA and JAS (Tables 7.6, 7.7). Except for Zhadang glacier, correlations of the PNA index with MB are strongest in JJA and generally negative in summer and in winter at all glaciers (Tables 7.3-7.7). At all study sites, $T_{air}$ shows the strongest positive correlation with the PNA index in JJA. Only at Zhadang and PIC the negative correlation in DJF is of the same magnitude. At Zhadang glacier, the influence of the PNA pattern on $T_{air}$ and precipitation in JJA is nearly balanced (Table 7.3). Thus, no signal is evident in MB. At Muztagh Ata glacier a distinct negative correlation with precipitation in JJA and JAS is revealed (Table 7.7). Correlations in MAM and AMJ are positive. Both signals dominate the MB pattern at Muztagh Ata in the respective months. The signals of the PNA pattern might be caused by the eastward shift of the main jet entrance and exit region towards the North Atlantic during PNA+ (see section 7.2.1). The shift of the centres of action during PNA+ apparently reduces the influence of the PNA pattern on the TP and additionally may alter the dominating wind directions.
The PT pattern is evident in the JJA air temperature at the two easternmost glaciers, Zhadang and PIC (Tables 7.3, 7.4). However, very weak correlations are revealed for the other glaciers further to the west (Tables 7.5-7.7). Thus, it can be assumed that the influence of the PT pattern on $T_{air}$ is stronger on the eastern TP. The influence of the PT pattern on precipitation is of similar magnitude at all sites. Positive correlations with precipitation are apparent at Zhadang, Naimona'nyi and Muztagh Ata (Tables 7.3, 7.5, 7.7), whereas precipitation correlates negatively at PIC and Halji (Tables 7.4, 7.6). The negative $T_{air}$ and positive precipitation correlations cause the overall positive correlation of the PT index with MB at all five glaciers in summer (Tables 7.3-7.7). The reasons for these feedbacks are not clear.
The SO index indicates strong negative correlations with $T_{air}$ in MAM and AMJ at all five study sites with strongest signals at the two southernmost glaciers (Tables 7.1-7.5). Correlations in JJA are overall positive with the strongest correlation at Zhadang glacier. The SO pattern also influences $T_{air}$ at Zhadang in DJF (Table 7.1). The positive correlation of the SO index with precipitation in OND at Zha-

dang directly influences the MB. MB at Naimona'nyi glacier shows the strongest negative correlation with the SO index in OND, governed by the respective signal in precipitation (Table 7.5). The same is evident at Muztagh Ata in OND and MAM (Table 7.7). At both glaciers MB is stronger influenced by precipitation than by $T_{air}$ during the considered period (Table 7.2). The SO signal in precipitation at Halji glacier is similar to that at Naimona'nyi (Table 7.6). However, the structure is not repeated in the MB because the correlation of precipitation and MB is weaker (Table 7.2). The SO index has strong impacts on both hemispheres (e.g. Dai & Wigley 2000). The tropical Walker circulations are directly connected to the Hadley and Ferrel cells and therefore to the mid-latitude and East Asian jet streams and also the monsoon circulation (Lauer & Bendix 2004). Thus, the influence of the SO index on the TP is complex. Bothe et al. (2010) reveal a connection between El Niño years (SO-) and dryness on the TP in summer as well as between SO+ years and wet conditions on the TP in summer. The correlation analyses within this study agree with these findings at the three southernmost glaciers, Naimona'nyi, Halji and Zhadang.

The exceptional negative MB at Zhadang glacier in summer 2006 is mentioned in section 7.1. The related negative anomaly in precipitation is similar in summer 2006 and summer 2005 (Fig. 7.5). Both fluctuations coincide with a distinct negative PNA index. In summer 2005 a negative WP index supports the signal. The positive $T_{air}$ anomaly in summer 2006 that leads to the below-average MB might be caused by the negative NAO signal in the respective months. The same signal seems to trigger negative MB anomalies in summer 2007 and 2010 at Zhadang and Halji. The strongest positive precipitation anomaly at Zhadang is evident in summer 2004 (see section 7.1, Fig. 7.5). The peak coincides with a distinct positive WP index and a positive PNA index.
In October 2009 MB at Halji glacier is above-average (Fig. 7.5). The anomaly is caused by above-average precipitation amounts and below-average $T_{air}$. These fluctuations relate to distinct negative SO, WP and POL indices. A similar pattern occurs in September 2002 at Halji (Fig. 7.5).
MB at PIC is below-average e.g. in September 2004, July 2006 and June 2009 (Fig. 7.5). These fluctuations coincide with a negative WP index and a positive PNA index. The above-average MB in August 2004 is in line with a positive WP index. Monthly indices of the selected teleconnection patterns are summarized in Fig. C.1 in appendix C.

**Table 7.3: Seasonal Pearson's R for selected northern Hemisphere teleconnection patterns and SO for glacier-wide $T_{air}$, total precipitation and MB at Zhadang glacier, 2001-2011. Applied scaling factors for HAR precipitation and $T_{air}$ offsets are 0.56/±0 K. Green colours indicate positive, yellow colours indicate negative correlations for R larger than ±0.2; the colour intensity increases at R > ±0.4.**

| Tair | DJF | JFM | MAM | AMJ | JJA | JAS | OND |
|---|---|---|---|---|---|---|---|
| SO | 0.23 | 0.09 | -0.30 | -0.17 | 0.27 | 0.04 | 0.08 |
| NAO | -0.09 | -0.08 | -0.07 | -0.28 | -0.11 | -0.34 | -0.13 |
| EAWR | -0.38 | 0.21 | -0.43 | -0.11 | -0.25 | -0.05 | -0.15 |
| POL | -0.11 | -0.10 | -0.11 | 0.04 | 0.14 | -0.25 | -0.30 |
| WP | 0.43 | 0.26 | -0.14 | -0.05 | -0.34 | -0.21 | 0.04 |
| PNA | -0.24 | -0.06 | 0.07 | 0.02 | 0.26 | -0.11 | 0.14 |
| PT | | | | | -0.41 | -0.19 | |

| tot. precip. | DJF | JFM | MAM | AMJ | JJA | JAS | OND |
|---|---|---|---|---|---|---|---|
| SO | -0.07 | -0.02 | -0.21 | -0.21 | 0.05 | 0.09 | 0.22 |
| NAO | 0.09 | 0.06 | 0.09 | -0.17 | -0.02 | -0.03 | 0.04 |
| EAWR | 0.18 | 0.28 | -0.41 | -0.13 | -0.18 | -0.22 | -0.15 |
| POL | 0.01 | 0.27 | -0.05 | 0.05 | -0.07 | 0.09 | -0.07 |
| WP | -0.24 | -0.50 | -0.11 | 0.32 | 0.19 | 0.16 | 0.14 |
| PNA | -0.10 | -0.20 | -0.15 | -0.05 | 0.27 | 0.26 | 0.27 |
| PT | | | | | 0.27 | 0.11 | |

| MB | DJF | JFM | MAM | AMJ | JJA | JAS | OND |
|---|---|---|---|---|---|---|---|
| SOI | -0.02 | -0.05 | -0.05 | -0.13 | 0.03 | -0.04 | 0.29 |
| NAO | -0.08 | 0.17 | 0.13 | -0.06 | 0.25 | 0.43 | 0.08 |
| EAWR | 0.11 | -0.09 | -0.10 | 0.11 | 0.13 | -0.07 | -0.19 |
| POL | 0.09 | 0.30 | 0.08 | 0.05 | -0.24 | -0.26 | -0.11 |
| WP | -0.28 | -0.63 | -0.13 | 0.21 | 0.09 | -0.06 | 0.09 |
| PNA | -0.13 | -0.16 | -0.29 | -0.06 | -0.10 | -0.04 | 0.11 |
| PT | | | | | 0.32 | 0.23 | |

**Table 7.4: Seasonal Pearson's R for selected northern Hemisphere teleconnection patterns and SO for glacier-wide $T_{air}$, total precipitation and MB at PIC, 2001-2011. Applied scaling factors for HAR precipitation and $T_{air}$ offsets are 0.56/±0 K. Green colours indicate positive, yellow colours indicate negative correlations for R larger than ±0.2; the colour intensity increases at R > ±0.4.**

| Tair | DJF | JFM | MAM | AMJ | JJA | JAS | OND |
|---|---|---|---|---|---|---|---|
| SO | -0.04 | -0.09 | -0.37 | -0.17 | 0.16 | 0.04 | 0.07 |
| NAO | -0.11 | -0.16 | 0.01 | -0.23 | -0.16 | -0.35 | 0.01 |
| EAWR | -0.27 | 0.28 | -0.27 | -0.04 | -0.26 | 0.02 | -0.14 |
| POL | -0.09 | -0.09 | -0.10 | -0.07 | 0.29 | -0.13 | -0.22 |
| WP | 0.46 | 0.11 | -0.12 | -0.09 | -0.35 | -0.24 | 0.13 |
| PNA | -0.26 | -0.07 | 0.05 | 0.02 | 0.35 | -0.07 | 0.11 |
| PT | | | | | -0.50 | -0.27 | |

| tot. precip. | DJF | JFM | MAM | AMJ | JJA | JAS | OND |
|---|---|---|---|---|---|---|---|
| SO | -0.04 | -0.02 | -0.19 | -0.09 | -0.03 | -0.08 | -0.10 |
| NAO | -0.03 | -0.19 | -0.07 | -0.13 | -0.12 | -0.23 | -0.20 |
| EAWR | -0.08 | 0.25 | -0.26 | -0.15 | -0.19 | -0.08 | 0.25 |
| POL | -0.04 | 0.09 | -0.03 | -0.24 | -0.15 | 0.04 | -0.21 |
| WP | 0.08 | -0.16 | -0.16 | -0.01 | 0.16 | -0.15 | -0.13 |
| PNA | -0.23 | -0.03 | 0.04 | -0.09 | 0.01 | 0.13 | 0.13 |
| PT | | | | | -0.36 | -0.35 | |

| MB | DJF | JFM | MAM | AMJ | JJA | JAS | OND |
|---|---|---|---|---|---|---|---|
| SO | -0.02 | 0.10 | -0.03 | -0.01 | -0.02 | 0.13 | -0.08 |
| NAO | -0.11 | -0.23 | -0.09 | -0.08 | 0.08 | 0.18 | -0.13 |
| EAWR | 0.01 | 0.11 | -0.33 | -0.22 | 0.04 | -0.13 | 0.14 |
| POL | 0.09 | 0.29 | 0.01 | -0.16 | -0.36 | -0.10 | -0.10 |
| WP | -0.14 | -0.34 | -0.18 | 0.09 | 0.36 | 0.11 | -0.19 |
| PNA | -0.11 | 0.01 | 0.03 | -0.10 | -0.28 | 0.10 | 0.06 |
| PT | | | | | 0.37 | 0.29 | |

**Table 7.5: Seasonal Pearson's R for selected northern Hemisphere teleconnection patterns and SO for glacier-wide $T_{air}$, total precipitation and MB at Naimona'nyi glacier, 2001-2012. Applied scaling factors for HAR precipitation and $T_{air}$ offsets are 0.31/+3 K. Green colours indicate positive, yellow colours indicate negative correlations for R larger than ±0.2; the colour intensity increases at R > ±0.4.**

| Tair | DJF | JFM | MAM | AMJ | JJA | JAS | OND |
|---|---|---|---|---|---|---|---|
| SO | -0.05 | -0.16 | -0.40 | -0.19 | 0.13 | -0.01 | 0.09 |
| NAO | 0.01 | -0.17 | -0.02 | -0.29 | -0.16 | -0.33 | 0.06 |
| EAWR | -0.13 | 0.30 | -0.29 | 0.08 | -0.13 | 0.08 | -0.07 |
| POL | 0.30 | 0.07 | -0.10 | -0.18 | 0.22 | -0.08 | -0.12 |
| WP | 0.17 | 0.26 | -0.16 | -0.02 | -0.15 | -0.33 | 0.17 |
| PNA | -0.18 | -0.07 | 0.04 | -0.04 | 0.28 | -0.07 | 0.10 |
| PT | | | | | -0.10 | -0.16 | |

| tot. precip. | DJF | JFM | MAM | AMJ | JJA | JAS | OND |
|---|---|---|---|---|---|---|---|
| SO | -0.08 | -0.06 | -0.14 | 0.02 | 0.32 | 0.22 | -0.37 |
| NAO | 0.19 | 0.21 | 0.05 | -0.08 | -0.38 | -0.49 | -0.16 |
| EAWR | 0.18 | -0.02 | -0.07 | 0.02 | 0.09 | 0.28 | 0.19 |
| POL | -0.05 | 0.02 | -0.12 | -0.03 | 0.21 | 0.13 | -0.36 |
| WP | -0.01 | -0.16 | -0.05 | 0.14 | -0.14 | -0.33 | -0.27 |
| PNA | -0.31 | -0.37 | -0.03 | -0.18 | 0.10 | 0.06 | 0.05 |
| PT | | | | | 0.26 | 0.01 | |

| MB | DJF | JFM | MAM | AMJ | JJA | JAS | OND |
|---|---|---|---|---|---|---|---|
| SO | -0.18 | -0.05 | -0.05 | 0.10 | 0.15 | 0.16 | -0.52 |
| NAO | 0.07 | 0.20 | -0.20 | 0.05 | 0.12 | 0.05 | -0.16 |
| EAWR | 0.17 | -0.02 | -0.23 | -0.24 | 0.08 | 0.06 | 0.24 |
| POL | -0.20 | 0.00 | 0.05 | 0.06 | -0.16 | -0.07 | -0.35 |
| WP | 0.06 | -0.16 | 0.01 | 0.27 | -0.03 | -0.49 | -0.23 |
| PNA | -0.19 | -0.32 | 0.12 | -0.05 | -0.35 | -0.04 | 0.04 |
| PT | | | | | 0.45 | 0.20 | |

**Table 7.6: Seasonal Pearson's R for selected northern Hemisphere teleconnection patterns and SO for glacier-wide $T_{air}$, total precipitation and MB at Halji glacier, 2001-2011. Applied scaling factors for HAR precipitation and $T_{air}$ offsets are 0.56/+1 K. Green colours indicate positive, yellow colours indicate negative correlations for R larger than ±0.2; the colour intensity increases at R > ±0.4.**

| Tair | DJF | JFM | MAM | AMJ | JJA | JAS | OND |
|---|---|---|---|---|---|---|---|
| SO | -0.14 | -0.15 | -0.40 | -0.21 | 0.11 | -0.01 | 0.10 |
| NAO | -0.14 | -0.12 | 0.06 | -0.21 | -0.19 | -0.29 | 0.00 |
| EAWR | -0.18 | 0.30 | -0.25 | 0.03 | -0.08 | 0.08 | -0.07 |
| POL | 0.16 | -0.01 | -0.16 | -0.17 | 0.11 | -0.15 | -0.12 |
| WP | 0.10 | 0.13 | -0.07 | 0.01 | -0.27 | -0.37 | 0.11 |
| PNA | -0.16 | -0.02 | 0.02 | -0.04 | 0.34 | -0.05 | 0.10 |
| PT | | | | | -0.13 | -0.17 | |

| tot. precip. | DJF | JFM | MAM | AMJ | JJA | JAS | OND |
|---|---|---|---|---|---|---|---|
| SO | -0.07 | -0.08 | -0.01 | -0.09 | 0.38 | 0.39 | -0.32 |
| NAO | 0.34 | 0.25 | 0.09 | -0.02 | -0.39 | -0.28 | -0.05 |
| EAWR | 0.18 | 0.02 | -0.04 | -0.05 | -0.16 | -0.01 | 0.25 |
| POL | -0.07 | -0.04 | -0.06 | -0.07 | 0.04 | 0.08 | -0.40 |
| WP | -0.12 | -0.26 | 0.11 | 0.27 | -0.17 | -0.34 | -0.24 |
| PNA | -0.31 | -0.36 | -0.08 | -0.13 | -0.16 | 0.15 | 0.07 |
| PT | | | | | -0.05 | -0.26 | |

| MB | DJF | JFM | MAM | AMJ | JJA | JAS | OND |
|---|---|---|---|---|---|---|---|
| SO | -0.03 | -0.03 | 0.10 | -0.10 | -0.11 | 0.03 | -0.09 |
| NAO | 0.31 | 0.23 | -0.04 | 0.10 | 0.17 | 0.16 | -0.12 |
| EAWR | 0.10 | -0.10 | -0.21 | -0.32 | 0.14 | 0.11 | -0.02 |
| POL | -0.23 | 0.00 | -0.01 | -0.05 | -0.22 | 0.07 | -0.37 |
| WP | 0.22 | 0.23 | 0.23 | 0.01 | 0.16 | 0.09 | -0.13 |
| PNA | -0.23 | -0.39 | -0.11 | -0.06 | -0.52 | -0.18 | 0.05 |
| PT | | | | | 0.17 | 0.19 | |

**Table 7.7: Seasonal Pearson's R for selected northern Hemisphere teleconnection patterns and SO for glacier-wide $T_{air}$, total precipitation and MB at Muztagh Ata glacier, 2001-2012. Applied scaling factors for HAR precipitation and $T_{air}$ offsets are 0.31/±0 K. Green colours indicate positive, yellow colours indicate negative correlations for R larger than ±0.2; the colour intensity increases at R > ±0.4.**

| Tair | DJF | JFM | MAM | AMJ | JJA | JAS | OND |
|---|---|---|---|---|---|---|---|
| SO | -0.22 | -0.14 | -0.34 | -0.16 | 0.11 | -0.06 | -0.05 |
| NAO | -0.36 | -0.32 | -0.07 | -0.31 | -0.24 | -0.37 | -0.05 |
| EAWR | -0.05 | 0.32 | -0.28 | 0.10 | -0.05 | 0.16 | -0.01 |
| POL | 0.28 | 0.15 | 0.00 | -0.13 | 0.19 | -0.10 | -0.14 |
| WP | 0.17 | -0.01 | -0.22 | -0.04 | -0.13 | -0.35 | 0.12 |
| PNA | -0.10 | -0.03 | 0.05 | -0.02 | 0.23 | -0.07 | 0.15 |
| PT | | | | | -0.01 | -0.17 | |

| tot. precip. | DJF | JFM | MAM | AMJ | JJA | JAS | OND |
|---|---|---|---|---|---|---|---|
| SO | -0.21 | -0.18 | -0.20 | -0.11 | -0.12 | 0.05 | -0.22 |
| NAO | 0.01 | 0.00 | -0.21 | -0.51 | -0.24 | -0.18 | 0.35 |
| EAWR | 0.07 | 0.11 | -0.18 | -0.14 | -0.06 | -0.12 | 0.22 |
| POL | -0.11 | -0.05 | -0.02 | -0.02 | -0.09 | -0.15 | -0.09 |
| WP | 0.28 | 0.09 | -0.20 | -0.28 | 0.12 | 0.19 | 0.34 |
| PNA | -0.15 | -0.18 | 0.25 | 0.23 | -0.46 | -0.20 | 0.09 |
| PT | | | | | 0.27 | 0.36 | |

| MB | DJF | JFM | MAM | AMJ | JJA | JAS | OND |
|---|---|---|---|---|---|---|---|
| SO | -0.19 | -0.14 | -0.22 | -0.12 | -0.12 | 0.07 | -0.30 |
| NAO | 0.02 | -0.04 | -0.33 | -0.52 | -0.19 | -0.10 | 0.26 |
| EAWR | 0.07 | 0.06 | -0.21 | -0.13 | -0.08 | -0.26 | 0.34 |
| POL | -0.19 | -0.11 | 0.05 | 0.02 | -0.10 | -0.08 | -0.08 |
| WP | 0.34 | 0.13 | -0.22 | -0.25 | 0.24 | 0.35 | 0.27 |
| PNA | -0.10 | -0.14 | 0.28 | 0.20 | -0.52 | -0.48 | 0.04 |
| PT | | | | | 0.15 | 0.15 | |

### 7.2.3 Summary regarding the influences of teleconnection patterns on glacier mass balance at the study sites

Generally, the influence of the seven selected teleconnection patterns on $T_{air}$ from HAR at the five study sites within the simulation period 2001-2011/12 is homogeneous. The signs of the respective correlation coefficients usually reveal similar seasonal patterns at the five glaciers (Tables 7.3-7.7). However, the strength of the different signals varies regionally. Concerning the correlations with $T_{air}$, the influences of the selected teleconnection patterns coincide at Zhadang glacier and PIC, as well as at Naimona'nyi and Halji glaciers to a high degree. Partly, $T_{air}$ at Muztagh Ata shows similar dependencies as $T_{air}$ at Naimona'nyi and Halji. The respective signals in HAR precipitation do not reveal regional patterns similar for all teleconnection indices (Tables 7.3-7.7). However, precipitation correlations at Naimona'nyi and Halji glaciers coincide to a higher degree because the two glaciers are only ≈26 km apart. Similar signals in precipitation in two or more regions are rather evident for individual teleconnection patterns. Thus, the correlations of the different indices with MB for the five study regions are even more disperse (Tables 7.3-7.7). The superposition of teleconnection signals in $T_{air}$ and precipitation are further altered by the varying importance of $T_{air}$ and precipitation for glacier MB at the different glaciers (Table 7.2).

Many of the anomalies in MB, $T_{air}$ and precipitation at the five glaciers can be related to teleconnection pattern indices. Some fluctuations seem to follow none of the selected signals. To reveal the atmospheric drivers in detail would require the consideration of further teleconnection indices, the extensive pre-processing of the data series and an extended statistical analysis. Such an approach would require a thorough analysis of the levels of significance of the relations and an investigation of possible non-linear or combined effects between two or more variables. However, this further elaboration cannot be achieved as part of this thesis. It will be worthwhile to address these issues in detail within future research.

# 8 Overall conclusion

***SEB/MB modelling and validation***

The newly developed coupled SEB/MB and multi-layer snow model is calibrated and validated for Zhadang glacier. The glacier is subject of intensive Sino-German atmospheric and glaciological field work since 2009 and therefore holds a large data basis. Output data of both, the AWS and the HAR forced model are compared to various atmospheric, glaciological, surface and subsurface data sets for the point location of AWS1 as well as for the ablation stake network distributed over the glacier. The 3-year image time series of a time-lapse camera system next to the glacier provides an important contribution to the spatial and temporal validation of the model performance. The respective model output corresponds very well to both the mean altitude of the transient snowline and the observed spatial MB patterns. Furthermore, the results of the detailed model evaluation for the intensive observational period 2009-2012 for both the AWS and HAR forced MB model are convincing. The detailed comparison for the SEB and MB components of the HAR model run 2001-2011 with the study of Mölg et al. (2014) with a similar model reveals that in most years the differences in $Q_{melt}$ are small although other SEB components show large discrepancies between both models. The parameterizations for the various energy fluxes are different within both models. However, both models have been calibrated for $Q_{melt}$ to finally reproduce the glacial melt pattern derived from the glaciological MB method. Thus, in most MB years differences in the single SEB components between the two models compensate each other and lead to small differences in $Q_{melt}$ and surface melt.

At all five study sites the derived intra- and inter-annual cycles of SEB and MB components are within reasonable limits. The results of glaciological in-situ MB observations over several years are available at Zhadang and Naimona'nyi glacier for comparison. In the Muztagh Ata region field data is available from a neighbouring glacier. The comparison with the in-situ MB measurements reveals that overall inter-annual variations in this study and the respective observations are similar. Discrepancies are apparent for single years only. The results depend on the respective patterns of the input parameters from HAR. This indicates that relative HAR climatology provides year-to-year variance in such that modelled annual MB variance in general terms fits to the observations at the study sites.

At PIC, Naimona'nyi, Halji and Muztagh Ata glacier surface height changes and geodetic MB estimations from high resolution remote sensing analyses are available for similar periods as covered by this study. These data allow the spatial evaluation of the MB model results. Furthermore, the average annual MB estimations from the remote sensing studies can be compared to the results of this study.

At the four glaciers the spatial comparison of calculated surface height changes from modelling and remote sensing reveals that the overall pattern is captured to a high degree.

The results of the evaluation of absolute values for MB and surface elevation changes through in-situ measurements and remote sensing methods in the five study areas are very heterogeneous. A precipitation scaling factor of 0.56 with respect to HAR precipitation was obtained from the comparison with rain gauge measurements at Zhadang glacier (chapter 2). Applying this factor leads to satisfying results in the HAR forced MB model runs 2001-2011 for Zhadang glacier. HAR $T_{air}$ and $T_{air}$ measurements at the AWS at Zhadang glacier are in good agreement. Due to a lack of precipitation measurements at the glacier sites HAR precipitation amounts can not be validated at the other four study areas. Thus, the same scaling factor of 0.56 is applied in the reference run for each glacier. To account for uncertainties in total HAR precipitation amounts, three model runs with varying precipitation scaling factors (0.56±0.25) are performed.
At PIC (chapter 3) the reference run with unchanged HAR $T_{air}$ leads to reasonable results. The comparison of the MB model with glacier-wide surface height changes and geodetic MB estimations shows only minor discrepancies. The model evaluation against MODIS derived snow line altitude and annual ELA confirms the overall satisfying model performance for PIC considering the reference run.
At Naimona'nyi glacier (chapter 4) the application of a scaling factor of 0.56 with unchanged $T_{air}$ clearly overestimates MB and surface height changes that are available from in-situ MB measurements and remote sensing analysis. With precipitation decreased by 25% (0.31) the MB model results are more reasonable but still seem to overestimate the MB and the surface height changes especially in the lower glacier regions. The comparison of atmospheric AWS data at the glacier tongue with HAR data revealed that $T_{air}$ from HAR data exhibits a significant cold bias of 3.8 K in winter and 2.0 K in summer compared to AWS measurements. Thus, a north-south profile of Naimona'nyi glacier is calculated with a precipitation scaling factor of 0.31 and a temperature offset of +3 K. The derived surface height changes agree well with the results derived by remote sensing. Using these settings modelled glacier-wide annual MB is close to the in-situ MB observations.
At Halji glacier (chapter 5) the application of a scaling factor of 0.56 with unchanged $T_{air}$ overestimates MB and surface height changes that are available from two different remote sensing analyses. A cold bias in HAR $T_{air}$ as revealed at Naimona'nyi glacier is assumed to be evident also at Halji. Therefore, the MB model was run several times for the total glacier area to determine reasonable combinations of precipitation scaling factors and $T_{air}$ offsets. The two different results derived by remote sensing lead to a different 'best-fit' combination of precipitation scaling factor and $T_{air}$-offset at Halji. The lack of meteorological field observations hampers the ability to verify HAR precipitation amounts and possible $T_{air}$ offsets. A cold bias in HAR $T_{air}$, even though possibly smaller that at Naimona'nyi, seems to be nevertheless plausible since both remote sensing studies provide evidence that the results of the MB model reproduce observed glacier change best when $T_{air}$ is increased by at least 1 K. Comparing this study to the more detailed remote sensing study covering the total simulation period suggests a combination of a scaling factor of 0.56 and a $T_{air}$-offset of +1 K to be reasonable.
At Muztagh Ata glacier (chapter 6) the application of a scaling factor of 0.56 with unchanged $T_{air}$ clearly overestimates MB and surface height changes that are available from in-situ MB measurements and remote sensing analysis. With decreased precipitation amounts (0.31) the MB model results are more reasonable.

The different analyses show that the atmospheric data provided by the HAR dataset can not be applied directly for glacier SEB and MB modelling. The ranges of uncertainty that are created through different combinations of precipitation scaling factors and $T_{air}$ offsets are large. Furthermore, the required factors and offsets for the HAR data seem to vary regionally. The applied parameterizations

for the various energy fluxes within the MB model contain several unknown or poorly constrained parameters. Mean values for these parameters were obtained from observations at Zhadang glacier or taken from literature. Through the lack of detailed measurements at the other four remote glacier sites it is impossible to verify the applicability of the chosen parameters to these glaciers in more detail. Furthermore, some physical processes within the glacier SEB and MB are simplified or not considered at all. This makes it difficult to obtain absolute values for glacier-wide MB or surface elevation changes in regions where precipitation and/or temperature measurements are not available and MB model results can not be validated in detail by other means as for example by remote sensing analysis or in situ MB measurements.

A major conclusion from the findings within this thesis is that glacier SEB and MB modelling based on modelled atmospheric data always requires some kind of meteorological, glaciological or remote sensing based field observation. In consequence, the continuation and extension of at least basic in-situ measurements at glaciers on the TP is a crucial requirement in order to obtain reliable and detailed SEB and MB estimates based on complex modelling chains for those glaciers.

***Surface melt, refreezing and runoff***

The obtained SEB and MB components at the single glaciers are consistent with each other because they interact through physical relationships within the MB model (see sections 1.3.4 and 2.3.1).

Generally, the inter-annual cycle of glacier runoff is similar to that of surface melt for the studied glaciers (Fig. 7.2). At Zhadang glacier large amounts of surface melt refreeze within the snowpack in spring and autumn. A maximum proportion of 70% occurs in March. Thus, runoff is reduced largely in these seasons. In July and August, refreezing decreases to ≈7%. Almost half of the monsoon precipitation reaches the glacier as rain. This leads to increased glacier runoff compared to surface melt in these months. In total, 17% of the melt water refreezes at Zhadang glacier. Glacier melt water accounts for 95% of the total runoff with a minimum of 81% in July.

At Naimona'nyi the surface melt and runoff are almost equivalent because the amount of refreezing approximately equals liquid precipitation. In total, only 8% of the generated melt water refreezes. The proportion is largest in mid-winter (30%) and smallest in October (1%). Total amounts of liquid precipitation are not large at Naimona'nyi even in summer. Thus, glacier melt water accounts for 98% of the total runoff with a minimum of 89% in July.

At Halji glacier the surface melt and runoff are almost equivalent because the amount of refreezing approximately equals liquid precipitation. This is the case despite the fact that large amounts of total precipitation in July and August fall as rain. In total, 27% of surface and subsurface melt refreezes at Halji. Proportions are largest in February, July and August with up to 47% and smallest between October and December (4%). Glacier melt water accounts for 90% of the total runoff with minima of 65% in June and 55% in July.

At PIC runoff is slightly exceeding surface melt only in August. In this month the amount of liquid precipitation exceeds the amount of refreezing. In total, 22% of the generated melt water refreezes at PIC. The proportion exceeds 70% from November until April. In September, only 7% refreezes. Glacier melt water accounts for 91% of the total runoff with a minimum of 70% in June.

At Muztagh Ata glacier runoff is significantly smaller than surface melt especially in August. In total, 34% of the generated melt water refreezes. The proportion is highest in winter with nearly 100% and lowest in September (27%). The proportion of liquid precipitation at Muztagh Ata is negligible because of very low $T_{air}$. Glacier melt water accounts for 98% of the total runoff with a minimum of 87% in June.

Generally, the proportion of glacier melt water that actually runs off is largest at Naimona'nyi, one of the two southernmost glaciers. At Muztagh Ata on the north western TP the proportion is smallest. At all studied glaciers surface melt is largest in late summer and significantly contributes to the total runoff.

***SEB and MB components***

The three southernmost glaciers, Zhadang, Naimona'nyi and Halji are characterized by lowest overall $\alpha$ and therefore largest $SW_{net}$. At PIC and Muztagh Ata the overall energy loss by $LW_{net}$ is larger than the energy gain by $SW_{net}$. Thus, net radiation is an energy sink for both glaciers. The turbulent fluxes act as a net energy source. This pattern is more distinct at Muztagh Ata than at PIC probably because very low $T_{air}$ and frequent precipitation events cause persistent high $\alpha$. Overall energy loss by $Q_{lat}$ is largest at Zhadang because *RH* is low and the glacier surface temperatures favour turbulent exchange. Low air and surface temperatures might also be a reason for low $Q_{lat}$ at Muztagh Ata. Furthermore, the overall *RH* Muztagh Ata is high and exhibits no clear annual minimum. At Halji and Naimona'nyi overall $Q_{lat}$ is not a large energy sink because it regularly becomes positive in summer. The high moisture content of the monsoonal air masses favour condensation and deposition. The total energy turnover at Zhadang is dominated by $SW_{net}$. At Naimona'nyi and Halji overall $SW_{net}$ and $LW_{net}$ are of equal importance while $SW_{net}$ dominates in summer and $LW_{net}$ dominates in winter. At PIC and Muztagh Ata the continuously high $\alpha$ results in a high contribution of $LW_{net}$ to total energy turnover. At Muztagh Ata the absolute proportion of $LW_{net}$ is larger than that of $SW_{net}$ year-round.

At PIC and Muztagh Ata the energy gain by $SW_{net}$ is minimal in winter and nearly equal to the energy gain by $Q_{sens}$. At PIC the energy gain through $Q_{sens}$ and thus its contribution to the total energy flux even exceeds that of $SW_{net}$.

Halji, Muztagh Ata and Zhadang glaciers receive the highest annual amounts of solid precipitation, followed by PIC and Naimona'nyi. At Zhadang and Naimona'nyi the maximum of solid precipitation generally falls in summer. Snowfall amounts at PIC reveal two peaks in spring and summer. Muztagh Ata receives maximum solid precipitation amounts in spring. At Halji glacier high proportions of liquid precipitation in summer result in snowfall maxima in late winter and late summer. Overall surface melt is largest at Zhadang and Halji glaciers driven by $T_{air}$, $\alpha$ and $SW_{net}$. The highest amounts of refreezing are generated at Halji glacier because more solid precipitation allows a thicker snow pack compared to Zhadang glacier. At Muztagh Ata the proportion of surface and subsurface melt that refreezes within the snow pack is largest. Total mass loss through sublimation is highest at Zhadang glacier. However, the amount is small compared to total effective melt. At PIC and Muztagh Ata the mass loss by sublimation accounts for more than half of the total mass loss. The proportions are 68% at PIC and 71% at Muztagh Ata.

At all five studied glaciers mass loss through sublimation dominates over surface melt in winter. Sublimation accounts for more than 50% of the total mass loss at least between November and April. At the two northernmost study regions, PIC and Muztagh Ata, effective melt only dominates in July and August.

The overall results for the different regions on the TP coincide with the glacier characteristics outlined in sections 1.3 and 1.4. PIC and Muztagh Ata glacier belong to the extremely continental or cold glacier types with a balanced or slightly positive mass budget. The influence of the Indian summer monsoon is weak or completely absent. Zhadang, Naimona'nyi and Halji are glaciers of the subcontinental or polythermal type and are strongly influenced by the summer monsoon. These glaciers experienced significant mass loss in recent decades. The studies at Naimona'nyi and Halji glaciers con-

firm the high variability in single SEB and MB components between individual glaciers over short distances.

***Influences of teleconnection patterns***

The MB at all five studied glaciers is crucially influenced by anomalies in $T_{air}$ and precipitation. As expected, fluctuations in $T_{air}$ are distributed more homogeneously over the TP at least with respect to the five study sites than the precipitation anomalies. The correlation of seven selected teleconnection patterns with $T_{air}$, precipitation and MB of each glacier reveals that the influences of the respective patterns on $T_{air}$ coincide at Zhadang glacier and PIC, as well as at Naimona'nyi and Halji glaciers to a high degree. The respective signals in HAR precipitation do not reveal regional patterns similar for all teleconnection indices. However, precipitation correlations at Naimona'nyi and Halji glaciers coincide to a higher degree because the two glaciers are only ≈26 km apart. The correlations of the different indices with MB for the five study regions are mostly the result of the overlapping teleconnection signals in $T_{air}$ and precipitation. These influences are altered by the varying importance of $T_{air}$ and precipitation for glacier MB at the selected glaciers.

***Outlook***

The SEB and MB studies on selected glaciers in different regions on the TP allow the comparison and understanding of the various driving mechanisms for the SEB and MB components. However, several HAR output parameters require further adjustment. The ranges of uncertainty that are created through different combinations of precipitation scaling factors and $T_{air}$ offsets are large. Furthermore, the required parameterizations seem to vary regionally. The availability of in-situ observations and remote sensing data for the selected glaciers varies largely. For those glaciers where meteorological or detailed glaciological in-situ observations are lacking further uncertainty analyses with various combinations of precipitation scaling factors and air temperature offsets need to be carried out in future studies. The analysis at Halji glacier revealed that several combinations of precipitation scaling factors and air temperature offsets lead to similar results for MB and surface elevation changes. This also applies to the other glacier sites. Thus, further uncertainty analyses and the detailed evaluation of the SEB and MB components as well as field observations or remote sensing studies are crucial for further process understanding.

# References

Ageta, Y. and Higuchi, K. (1984): Estimation of mass balance components of a summer-accumulation type glacier in the Nepal Himalaya, Geogr. Ann. A., 66, 3, 249-255.

Ageta, Y. and Fujita, K. (1996): Characteristics of mass balance of summer-accumulation type glaciers in the Himalayas and Tibetan Plateau, Z. Gletscherk. Glazialgeol., 32, 61-65.

Ageta, Y., Iwata, S., Yabuki, H., Naito, N., Sakai, A., Narama, C. And Karma, T. (2000): Expansion of glacier lakes in recent decades in the Bhutan Himalayas, IAHS publication, 165-176.

Aizen, V.B. and Aizen, E.M. (1994): Features of regime and mass exchange of some glaciers on central Asia periphery, Bull. Glac. Res., 12, 9-24.

Aizen, V.B., Aizen, E.M. and Nikitin, S.A. (2002): Glacier regime on the northern slope of the Himalaya (Xixibangma glaciers), Quatern. Int., 97-98, 27-39.

An, Z., Kutzbach, J.E., Prell, W.L. and Porter, S.C. (2001): Evolution of Asian monsoons and phased uplift of the Himalaya-Tibetan plateau since Late Miocene times, Nature, 411, 62-66.

Anderson, E.A. (1976): A point energy and mass balance model of a snow cover, Techn. Rep. NWS19, NOAA.

Andreassen, L.M., van den Broeke, M.R., Giesen, R.H. and Oerlemans, J. (2008): A 5 year record of surface energy and mass balance from the ablation zone of Storbreen, Norway, J. Glaciol., 54, 185, 245-258.

Aschwanden, A. and Blatter, H. (2006): Numerical modelling of glacier flow, Excerpt from the Proceedings of the COMSOL users conference, Frankfurt, 3 pp.

Aschwanden, A. (2008): Mechanics and thermodynamics of polythermal glaciers, Dissertation, ETH Zürich, 93 pp.

Azam, M.F., Wagnon, P., Vincent, C., Ramanathan, A.L., Mandal, A. and Pottakkal, J.G. (2014): Processes governing the mass balance of Chhota Shingri Glacier (Western Himalaya, India) assessed by point-scale surface energy balance measurements, TCD, 8, 2867-2922.

Barnard, P.L., Owen, L.A. and Finkel, R.C. (2004a): Style and timing of glacial and paraglacial sedimentation in a monsoonal influenced high Himalayan environment, the upper Bhagirathi Valley, Garhwal Himalaya, Sediment. Geol., 165, 199-221.

Barnard, P.L., Owen, L.A., Sharma, M.C. and Finkel, R.C. (2004b): Late Quaternary landscape evolution of a monsoon-influenced high Himalayan valley, Gori Ganga, Nanda Devi, NE Garhwal, Geomorphology, 61, 91-110.

Barnston, A.G. and Livezey, R.E. (1987): Classification, seasonality and persistence of low-frequency atmospheric circulation patterns, Monthly Weather Review, 115, 1083-1126.

Barrows, T.T., Stone, J.O., Fifield, L.K. and Cresswell, R.G. (2002): The timing of the Last Glacial Maximum in Australia, Quaternary Science Reviews, 21, 159–173.

Bartelt, P. and Lehning, M. (2002): A physical SNOWPACK model for the Swiss avalanche warning: Part I: numerical model, Cold Regions Science and Technology, 35, 123-145.

Baumgartner, A., Liebscher, H.-J. and Benecke, P. (1990): Lehrbuch der Hydrologie, Bd 1: Allgemeine Hydrologie, Gebrüder Borntraeger.

Bajracharya, S.R. and Mool, P. (2009): Glaciers, glacial lakes and glacial lake outburst floods in the Mount Everest region, Nepal, Ann. Glaciol., 50, 53, 81-86.

Benn, D.I. and Owen, L.A. (1998): The role of the Indian summer monsoon and the mid-latitude westerlies in Himalayan glaciation: review and speculative discussion, J. Geol. Soc., 155, 353-363.

Benn, D.I. and Owen,L.A. (2002): Himalayan glacial sedimentary environments: a framework for reconstructing and dating former glacial extents in high mountain regions, Quaternary International, 97/98,3-26.

Bhambri, R., Bolch, T., Kawishwar, P., Dobhal, D.P., Srivastava, D. and Pratap, B. (2013): Heterogeneity in glacier response in the upper Shyok valley, northeast Karakoram, TC, 7, 1385-1398.

Bintanja, R. and van den Broeke, M. (1995): The surface energy balance of Antarctic snow and blue ice, J. Appl. Meteorol., 34, 902-926.

Böhner, J. (2006): General climatic controls and topoclimatic variations in Central and High Asia, Boreas, 35, 279-295.

Bolch, T., Yao, T., Kang, S., Buchroithner, M., Scherer, D., Maussion, F., Huintjes, E. and Schneider, C. (2010): A glacier inventory for the western Nyainqentanglha Range and the Nam Co Basin, Tibet, and glacier changes 1976-2009, TC, 4, 419-433.

Bolch, T., Pieczonka, T. and Benn D.I. (2011): Multi-decadal mass loss of glaciers in the Everest area (Nepal Himalaya) derived from stereo imagery, TC, 5, 349-358.

Bolch, T., Kulkarni, A., Kääb, A., Huggel, C., Paul, F., Cogley, J.G., Frey, H., Kargel, J.S., Fujita, K., Scheel, M., Bajracharya, S. and Stoffel, M. (2012): The state and fate of Himalayan glaciers, Science, 336, 310-314, doi: 10.1126/science.1215828.

Boos, W.R. and Kuang, Z. (2010): Dominant control of the South Asian monsoon by orographic insulation versus plateau heating, Nature, 463, 218-U102.

Boos, W.R. and Kuang, Z. (2013): Sensitivity of the South Asian monsoon to elevated and non-elevated heating, Scientific Reports, 3, 1192, doi: 10.1038/srep01192.

Bothe, O., Fraedrich, K. and Zhu, X. (2011): Large-scale circulations and Tibetan Plateau summer drought and wetness in a high-resolution climate model, Int. J. Climatol., 31, 832-846.

Bothe, O., Fraedrich, K. and Zhu, X. (2012): Tibetan Plateau summer precipitation: covariability with circulation indices, Theor. Appl. Climatol., 108, 293-300.

Bradley, R.S. and Jones, P.D. (1993): 'Little Ice Age' summer temperature variations: their nature and relevance to recent global warming trends, The Holocene, 3, 367-376.

Bräuning, A. (2006): Tree-ring evidence of 'Little Ice Age' glacier advances in southern Tibet, The Holocene, 16, 3, 369-380.

Braithwaite, R.J. (1995): Aerodynamic stability and turbulent sensible heat flux over a melting ice surface, the Greenland ice sheet, J. Glaciol., 41, 562-571.

Braun, M. and Schneider, C. (2000): Characteristics of summer energy balance on the west coast of the Antarctic Peninsula, Ann. Glaciol., 31, 179-183.

Braun, M. and Hock, R. (2004): Spatially distributed surface energy balance and ablation modelling on the ice cap of King George Island (Antarctica), Global and Planetary Change, 42, 45-58.

Brock, B.W., Willis, I.C. and Martin, M.J. (2006): Measurement and parameterization of aerodynamic roughness length variations at Haut Glacier d'Arolla, Switzerland, J. Glaciol., 52, 281-297.

Brun, E., Martin, E., Simon, V., Gendre, C. and Coleou, C. (1989): An energy and mass model of snow cover suitable for operational avalanche forecasting, J. Glaciol., 35, 333-342.

Brun, E., David, P., Sudul, M. and Brunot, G. (1992): A numerical model to simulate snow-cover stratigraphy for operational avalanche forecasting, J. Glaciol., 38, 13-22.

Caidong, C. and Sorteberg, A. (2010): Modelled mass balance of Xibu glacier, Tibetan Plateau: sensitivity to climate change, J. Glaciol., 56, 235-248.

Chen, J. (1989): Preliminary researches on lichenometric chronology of Holocene glacial fluctuations and on other topics in the headwater of Urumqi River, Tianshan Mountains, Sci. China B 32, 1487-1500.

Chen, X., Cui, P., Li, Y., Yang, Z. and Qi, Y. (2007): Changes in glacial lakes and glaciers of post-1986 in the Poiqu River basin, Nyalam, Xizang (Tibet), Geomorphology, 88, 298-311.

Chen, B., Xu, X., Yang, S. and Zhang, W. (2012): On the origin and destination of atmospheric moisture and air mass over the Tibetan Plateau, Theor. Appl. Climatol., 110, 423-435.

Chen, J. and Bordoni, S. (2014): Orographic effects of the Tibetan Plateau on the East Asian summer monsoon: An energetic perspective, J. Climate, doi:10.1175/JCLI-D-13-00479.1.

Cheng, G. and Wu, T. (2007): Responses of permafrost to climate change and their environmental significance, Qinghai-Tibet Plateau, J. Geophys. Res., 112, F02S03, doi:10.1029/2006JF000631.

Chow, V.T. (Eds.)(1964): Handbook of applied hydrology, McGraw-Hill.

Climate Prediction Center (2012): Northern Hemisphere Teleconnection Patterns. Available at: http://www.cpc.ncep.noaa.gov/data/teledoc/telecontents.shtml (11.06.2014)

Climate Prediction Center (2005): The ENSO cycle. Available at: http://www.cpc.ncep.noaa.gov/products/analysis_monitoring/ensocycle/enso_cycle.shtml (11.06.2014)

Cogley, J.G., Hock, R., Rasmussen, L.A., Arendt, A.A., Bauder, A. Braithwaite, R.J., Jansson, P., Kaser, G., Möller, M., Nicholson, L. and Zemp. M. (2011): Glossary of Glacier Mass Balance and Related Terms, IHP-VII Technical Documents in Hydrology No. 86, IACS Contribution No. 2, UNESCO-IHP, Paris.

Cui, X. and Graf, H.F. (2009): Recent land cover changes on the Tibetan Plateau: a review, Climatic Change, 94, 47-61.

Cullen, N.J., Mölg, T., Kaser, G., Steffen, K. and Hardy, D.R. (2007): Energy-balance model validation on the top of Kilimanjaro, Tanzania, using eddy covariance data, Ann. Glaciol., 46, 227-233.

Dai A. and Wigley, T.M.L. (2000): Global patterns of ENSO–induced precipitation, Geophys. Res. Lett., 27, 1283–1286.

Denton, G.H., Heusser, C.J., Lowell, T.V., Moreno, P.I., Anderson, B.G., Heusser, L.E., Schlüchter, C. and Marchant, D.R. (1999): Interhemispheric linkage of paleoclimate during the last glaciation, Geografiska Annaler, 81A, 107–154.

Derbyshire, E. (1981): Glacier regime and glacial sediment facies: a hypothetical framework for the Qinghai–Xizang Plateau. Proceedings of Symposium on Qinghai–Xizang (Tibet) Plateau, Beijing, China, Geological and Ecological studies of Qinghai–Xizang Plateau, 2, 1649-1656.

Ding, Y. (1992): Effects of the Qinghai-Xizang (Tibetan) Plateau on the circulation features over the plateau and its surrounding areas, Advances in Atmospheric Sciences, 9, 1, 112-130.

Ding, Y., Liu, S., Li, J. and Shangguan, D. (2006): The retreat of glaciers in response to recent climate warming in western China, Ann. Glaciol., 43, 97-105.

Domrös, M. and Peng. G. (1988): The Climate of China, Springer, 361 pp.

Dyurgerov, M. (2002): Glacier mass balance and regime: Data of measurements and analysis, Institute of Arctic and Alpine Research, University of Colorado, INSTAAR Occasional Paper No. 55, 88 pp.

Dyurgerov, M. and Meier, M.F. (2005): Glaciers and the changing earth system: a 2004 snapshot, Institute of Arctic and Alpine Research, University of Colorado, INSTAAR Occasional Paper No. 58.

Dyurgerov, M., Meier, M.F. and Bahr, D.B. (2009): A new index of glacier area change: a tool for glacier monitoring, J. Glaciol., 55, 192, 710-716.

Elsberg, D.H., Harrison, W.D., Echelmeyer, K.A. and Krimmel, R.M. (2001): Quantifying the effects of climate and surface change on glacier mass balance, J. Glaciol., 47, 159, 649-658.

Farinotti, D., Magnusson, J., Huss, M. and Bauder, M. (2010): Snow accumulation distribution inferred from time-lapse photography and simple modelling, Hydrol. Process., 24, 2087-2097.

Favier, V., Wagnon, P., Chazarin, J.-P., Maisincho, L. and Coudrain, A. (2004): One-year measurements of surface heat budget on the ablation zone of Antizana Glacier 15, Ecuadorian Andes, J. of Geophys. Res., 109, D18105.

Feliks, Y., Groth, A., Robertson, A.W. and Ghil, M. (2013): Oscillatory climate models in the Indian monsoon, North Atlantic, and tropical Pacific, J. Climate, 26, 9528-9544.

Flohn H. (1957): Large-scale aspects of “summer monsoon” in South and East Asia, J. Meteor. Soc. Japan, 75, 180-186.

Fujita, K. and Ageta, Y. (2000): Effect of summer accumulation on glacier mass balance on the Tibetan Plateau revealed by mass-balance model. J. Glaciol., 46, 244-252.

Fujita, K. (2007): Effect of dust event timing on glacier runoff: sensitivity analysis for a Tibetan glacier, Hydrol. Process., 21, 2892-2896.

Fujita, K., Ohta, T. and Ageta, Y. (2007): Characteristics and climate sensitivities of runoff from a cold-type glacier on the Tibetan Plateau, Hydrol. Process., 21, 21, 2882-2891.

Fujita, K. (2008a): Effect of precipitation seasonality on climatic sensitivity of glacier mass balance, Earth Planet. Sci. Lett., 276, 1-2, 14-19.

Fujita, K. (2008b): Influence of precipitation seasonality on glacier mass balance and its sensitivity to climate change, Ann. Glaciol., 48, 88-92.

Fujita, K., Sakai, A., Nuimura, T., Yamaguchi, S. and Sharma, R.R. (2009): Recent changes in Imja glacial lake and its damming moraine in the Nepal Himalaya revealed by in situ surveys and multi-temporal ASTER imagery, Environ. Res. Lett., 4, doi:10.1088/1748-9326/4/4/045205.

Fujita, K. and Nuimura, T. (2011): Spatially heterogeneous wastage of Himalayan glaciers, PNAS, 108, 34, 14011-14014.

Gao, Y., Cuo, L. and Zhang, Y. (2013): Changes in moisture flux over the Tibetan Plateau during 1979-2011 and possible mechanisms, J. Climate, 27, 1876-1893.

Gardelle, J., Berthier, E. and Arnaud, Y. (2012): Slight mass gain of Karakoram glaciers in the early twenty-first century, Nature Geoscience, DOI: 10.1038/NGEO1450.

Gardelle, J., Berthier, E., Arnaud, Y. and Kääb, A. (2013a): Region-wide glacier mass balances over the Pamir-Karakoram-Himalaya during 1999-2011, TC, 7, 1263-1286.

Gardelle, J., Berthier, E., Arnaud, Y. and Kääb, A. (2013b): Corrigendum to "Region-wide glacier mass balances over the Pamir-Karakoram-Himalaya during 1999-2011", TC, 7, 1885-1886.

Gardner, A.S., Moholdt, G., Cogley, J.G., Wouters, B., Arendt, A.A., Wahr, J., Berthier, E., Hock, R., Pfeffer, W.T., Kaser, G., Ligtenberg, S.R.M., Bolch, T., Sharp, M.J., Hagen, J.O., van den Broeke, M.R. and Paul, F. (2013): A reconciled estimate of glacier contributions to sea level rise: 2003 to 2009, Science, 340, 6134, 852-857.

Giesen, R.H., Andreassen, L.M., van den Broeke, M.R. and Oerlemans, J. (2009): Comparison of the meteorology and surface energy balance at Storbreen and Midtdalsbreen, two glaciers in southern Norway, TC, 3, 57-74.

Gilbert, A., Vincent, C., Six, D., Wagnon, P., Piard, L. and Ginot, P. (2014): Modeling near-surface firn temperature in a cold accumulation zone (Col du Dome, French Alps): from a physical to a semi-parameterized approach, TC, 8, 689-703.

Gromke, C., Manes, C., Walter, B., Lehning, M. and Guala, M. (2011): Aerodynamic roughness length of fresh snow, Bound. Lay. Meteorol., 141, 21-34.

Grove, J.M. and Switsur, R. (1994): Glacial geological evidence for the Medieval Warm Period, Clim. Change, 30, 143-171.

Haeberli, W. (1995): Glacier fluctuations and climate change detection - operational elements of a worldwide monitoring strategy, World Meteorological Organisation, Bulletin 44, 23-31.

Hahn, D.G. and Manabe, S. (1975): The role of mountains in the South Asian monsoon circulation, Journal of the Atmospheric Sciences, 32, 1515-1541.

Hamilton Messtechnik (undated): Grundlagen der Leitfähigkeitsmessung. Available at: http://www.hamilton-messtechnik.de/joomla/index.php/allgemeines/159-grundlagen-der-leitfaehigkeitsmessung (24.01.2014)

Han, W., Fang, X., Ye, C., Teng, X. and Zhang, T. (2014): Tibet forcing Quaternary stepwise enhancement of westerly jet and central Asian aridification: Carbonate isotope records from deep drilling in the Qaidam salt playa, NE Tibet, Global and Planetary Change, 116, 68-75.

Herron, M.H. and Langway, C.C. (1980): Firn Densification: An Empirical Model. J. Glaciol., 25, 93, 373-385.

Herzschuh, U., Kramer, A., Mischke, S. and Zhang, C. (2009): Quantitative climate and vegetation trends since the late glacial on the northeastern Tibetan Plateau deduced from Koucha Lake pollen spectra, Quaternary Research, 71, 162-171.

Herzschuh, U., Birks, H.J.B., Ni, J., Zhao, Y., Liu, H., Liu, X. and Grosse, G. (2010): Holocene land-cover changes on the Tibetan Plateau, The Holocene, 20, 91-104.

Hewitt, K. (2005): The Karakoram Anomaly? Glacier expansion and the 'elevation effect', Karakoram Himalaya, Mountain Research and Development, 25, 4, 332-340.

Heyman, J., Stroeven, A.P., Caffee, M.W., Hättestrand, C., Harbor, J.M., Li, Y., Alexanderson, H., Zhou, L. and Hubbard, A. (2011): Palaeoglaciology of Bayan Har Shan, NE Tibetan Plateau: exposure ages reveal a missing LGM expansion, Quaternary Science Reviews, 30, 15-16, 1988-2001.

Hock, R. and Holmgren, B. (2005): A distributed surface energy-balance model for complex topography and its application to Storglaciären, Sweden, J. Glaciol., 51, 172, 25-36.

Holzer, N., Neckel, N., Buchroithner, M., Gourmelen, N., Colin, J. and Bolch, T. (2014): Glacier variations at Gurla Mandhata (Naimona'nyi), Tibet: a multi-sensoral approach including TanDem-X, Pleiades and KH-7 Gambit-1, Remote Sensing of Environment, in preparation.

Holzhauser, H., Magny, M. and Zumbühl, H.J. (2005): Glacier and lake-level variations in west-central Europe over the last 3500 years. The Holocene, 15, 789-801.

Hsü, K.J. and Chen, H. (1999): Geologic Atlas of China, Elsevier, 262 pp.

Hu, J., Li, Z., Li, J., Zhang, L., Ding, X., Zhu, J. and Sun, Q. (2014): 3-D movements mapping of the alpine glacier in Qinghai-Tibetan Plateau by integrating D-InSAR, MAI and Offset-Tracking: Case study of the Dongkemadi Glacier, Global and Planetary Change, doi: 10.1016/j.gloplacha.2014.04.002.

Huang, M. (1990): On the temperature distribution of glaciers in China, J. Glaciol., 36, 123, 210-216.

Huang, L., Liu, J., Shao, Q. and Liu, R. (2011): Changing inland lakes responding to climate warming in Northeastern Tibetan Plateau, Climatic Change, 109, 479-502.

Hubbard, B. and Glasser, N. (2005): Field techniques in glaciology and glacial geomorphology, Wiley, 400 pp.

Huintjes, E., Yang, W., Kang, S. and Schneider, C. (2011a): Mass balance modelling of Zhadang Glacier, Tibetan Plateau, 7th Sino-German Workshop on Tibetan Plateau Research, Hamburg.

Huintjes, E., Yang, W., Pieczonka, T., Maussion, F., Sauter, T., Kang, S., Yao, T., Bolch, T., Buchroithner, M., Scherer, D. and Schneider, C. (2011b): Glaciological field studies at Zhadang Glacier, Tibetan Plateau, 7th Sino-German Workshop on Tibetan Plateau Research, Hamburg.

Huintjes, E., Spieß, M., Sauter, T., Scherer, D. and Schneider, C. (2012): Gletscher als „Messinstrumente" großräumiger Klimavariabilität auf dem Tibetischen Plateau – Ansätze basierend auf Massenbilanzmodellierung und Schneefernerkundung. Arbeitskreis Klima, Berlin.

Huintjes, E., Neckel, N., Maussion, F., Spieß, M., Scherer, D., Hochschild, V., Sauter, T. and Schneider, C. (2013a): Evolution of Purogangri Ice Cap, central Tibetan Plateau, 2000-2012 - a comparison of two glaciological methods. Himalayan Karakorum Tibet Workshop & International Symposium on Tibetan Plateau 2013, Tübingen.

Huintjes, E., Sauter, T., Schröter, B., Maussion, F., Kropacek, J., Yang, W., Kang, K., Zhang, G., Scherer, D., Buchroithner, M. and Schneider, C. (2013b): Evaluation of a distributed energy balance model for a high-altitude glacier on the Tibetan Plateau using glaciological measurements and a time-lapse camera system. Himalayan Karakorum Tibet Workshop & International Symposium on Tibetan Plateau 2013, Tübingen.

Huintjes, E., Sauter, T., Krenscher, T., Maussion, F., Kropacek J., Yang, W., Zhang, G., Kang, S., Scherer, D., Buchroithner, M. and Schneider, C. (2013c): Evaluation of a distributed energy balance model for a high-altitude glacier on the Tibetan Plateau using a time lapse camera system. EGU General Assembly 2013, Wien.

Hurrell, J. W. (1995): Decadal trends in the North Atlantic Oscillation: Regional temperatures and precipitation, Science, 269, 676-679.

Huss, M., Sold, L., Hoelzle, M., Stokvis, M., Salzmann, N., Farinotti, D. and Zemp, M. (2013): Towards remote monitoring of sub-seasonal glacier mass balance, Ann. Glaciol., 54, 63, 85-93.

Immerzeel, W.W., van Beek, L.P.H. and Bierkens, M.F.P. (2010): Climate change will affect the Asian water towers, Science, 328, 1382-1385.

Ivy-Ochs, H., Kerschner, H., Maisch, M., Christl, M., Kubik, P. and Schlüchter, C. (2009): Latest Pleistocene and Holocene glacier variations in the European Alps, Quat. Sci. Rev., 28, 2137-2149.

Jones, P.D., Briffa, K.R., Barnett, T.P. and Tett, S.F.B. (1998): High-resolution palaeoclimatic records for the last millennium: interpretation, integration and comparison with General Circulation Model Control run temperatures, The Holocene, 8, 477-483.

Jones, P.D., New, M., Parker, D.E., Martin, S. and Rigor, I.C. (1999): Surface air temperature and its changes over the past 150 years, Rev. Geophys., 37, 173-199.

Jordan, R. (1991): A one-dimensional temperature model for snow cover: Technical documentation for SNTHERM, 89. Technical Report, Cold Regions Research and Engineering Lab, Hanover NH.

Kääb, A., Berthier, E., Nuth, C., Gardelle, J. and Arnaud, Y. (2012): Contrasting patterns of early 21st century glacier mass change in the Himalayas, Nature, 488, 495-498.

Kang, S., Chen, F., Gao, T., Zhang, Y., Yang, W., Yu, W. and Yao, T. (2009): Correspondence: Early onset of rainy season suppresses glacier melt: a case study on Zhadang glacier, Tibetan Plateau, J. Glaciol., 55, 192, 755-758.

Kang, S., Xu, Y., You, Q., Flügel, W.-A., Pepin, N. and Yao, T. (2010): Review of climate and cryospheric change in the Tibetan Plateau, Environ. Res. Let., 5, doi:10.1088/1748-9326/5/1/015101.

Kansakar, S., Hannah, D., Gerrard, J. and Rees, G. (2004): Spatial pattern in the precipitation regime of Nepal, Int. J. Climatol., 24, 13, 1645-1659.

Kargel, J.S., Cogley, J.G., Leonard, G.J., Haritashya, U. and Byers, A. (2011): Himalayan glaciers: The big picture is a montage, PNAS, 108, 36, 14709-14710.

Kaser, G., Fountain, A. and Jansson, P. (2003): A manual for monitoring the mass balance of mountain glaciers, Technical Documents in Hydrology, 59, 137 pp.

Kayastha, R.B., Ohta, T. and Ageta, Y. (1999): Application of a mass balance model to a Himalayan glacier, J. Glaciol., 45, 559-567.

Klok, E.J. and Oerlemans, J. (2002): Model study of the spatial distribution of the energy and mass balance of Morteratschgletscher, Switzerland. J. Glaciol., 48, 505-518.

Klok, E.J., Nolan, M. and van den Broeke, M.R. (2005): Analysis of meteorological data and the surface energy balance of McCall Glacier, Alaska, USA, J. Glaciol., 51, 174, 451-461.

Kropacek, J., Braun, A., Kang, S., Feng, C., Ye, Q. and Hochschild, V. (2012): Analysis of lake level changes in Nam Co in central Tibet utilizing synergistic satellite altimetry and optical imagery, Int. J. Appl. Earth Observ. Geoinf., 17, 3-11.

Kropacek, J., Neckel, N., Tyrna, B., Huintjes, E., Schneider, C., Maussion, F. and Scherer, D. (2013): Exploration of a periodic GLOF in Halji, West Nepal using modeling and remote sensing, Himalayan Karakorum Tibet Workshop & International Symposium on Tibetan Plateau 2013, Tübingen.

Kuhle, M. (1994): Present and Pleistocene glaciation on the north-western margin of Tibet between the Karakorum main ridge and the Tarim Basin, supporting the evidence of a Pleistocene inland glaciation in Tibet, GeoJournal, 33.2/3, 133-272.

Kumar, L., Skidmore, A.K., Knowles, E. (1997): Modelling topographic variation in solar radiation in a GIS environment. Int. J. Geographical Information Science, 11, 5, 475-497.

Lauer, W. and Bendix, J. (2004): Klimatologie, Westermann, 352 pp.

Lehmkuhl, F. (1997): Extent and spatial distribution of Pleistocene glaciations in eastern Tibet, Quaternary International, 45/46, 123-134.

Lehmkuhl, F. and Haselein, F. (2000): Quaternary paleoenvironmental change on the Tibetan Plateau and adjacent areas (Western China and Western Mongolia), Quaternary International, 65/66, 121-145.

Lei, Y., Yao, T., Yi, C., Wang, W., Sheng, Y., Li, J. and Joswiak, D. (2012): Glacier mass loss induced the rapid growth of Linggo Co on the central Tibetan Plateau, J. Glaciol., 58, 207, 177-184.

Li, B., Yang, Y., Zhang, Q. and Wang, F. (1985): On the environmental evolution of Xizang (Tibet) in Holocene. In: Liu, T. (Edt.) (1985): Quaternary geology and environment of China, Springer, 234-240.

Li, Q. (Edt.) (1987): Geotectonic evolution of China, Springer, 203 pp.

Li, Z., He, Y., Pu, T., Jia, W., He, X., Pang, H., Zhang, N., Liu, Q., Wang, S., Zhu, G., Wang, S., Chang, L., Du, J. and Xin, H. (2010): Changes of climate, glaciers and runoff in China's monsoonal temperate glacier region during the last several decades, Quaternary International, 218, 13-28.

Li, Z., He, Y., An, W., Song, L, Zhang, W., Catto, N., Wang, Y., Wang, S., Liu, H., Cao, W., Theakstone, W.H., Wang S. and Du, J. (2011): Climate and glacier change in southwestern China during the past several decades, Environ. Res. Lett., 6, doi:10.1088/1748-9326/6/4/045404.

Li, J., Fang, X., Song, C., Pan, B., Ma, Y. and Yan, M. (2014a): Late Miocene-Quaternary rapid stepwise uplift of the NE Tibetan Plateau and its effects on climatic and environmental changes, Quaternary Research, http://dx.doi.org/10.1016/j.yqres.2014.01.002.

Li, B., Yu, Z., Liang, Z. and Acharya, K. (2014b): Hydrologic response of a high altitude glacierized basin in the central Tibetan Plateau, Global and Planetary Change, doi: 10.1016/j.gloplacha.2014.04.006.

Liu, X. and Chen, B. (2000): Climatic warming in the Tibetan Plateau during recent decades, Int. J. Climatol., 20, 1729-1742.

Liu, Y., Yao, T., Tian, L., Xu, B. and Wu, G. (2006): Glaciochemical records from Naimona'Nyi ice core in the Himalayas, J. Geographical Sciences, 16, 4, 465-471.

Liu, J., Wang, S., Yu, S., Yang, D. and Zhang, L. (2009): Climate warming and growth of high-elevation inland lakes on the Tibetan Plateau, Global and Planetary Change, 67, 209-217.

Liu, J., Kang, S., Gong, T. and Lu, A. (2010): Growth of a high-elevation inland lake, associated with climate change and permafrost degradation in Tibet, Hydrol. Earth Syst. Sci., 14, 3, 481-489.

Loibl, D., Lehmkuhl, F. and Grießinger, J. (2014): Reconstructing glacier retreat since the Little Ice Age in SE Tibet by glacier mapping and equilibrium line altitude calculation, Geomorphology, doi: 10.1016/j.geomorph.2014.03.018

Ma, D., Boos, W. and Kuang, Z. (2014): Effects of orography and surface heat fluxes on the south Asian summer monsoon, J. Climate, doi:10.1175/JCLI-D-14-00138.1, in press.

Manabe, S. and Terpstra, T.B. (1974): The effects of mountains on the general circulation of the atmosphere as identified by numerical experiments, Journal of the Atmospheric Sciences, 31, 1, 3-42.

Mann, M.E., Bradley, R.S. and Hughes, M.K. (1999): Northern Hemisphere temperatures during the past millennium: inferences, uncertainties, and limitations. Geophys. Res. Lett., 26, 759-762.

Maussion, F., Huintjes, E., Schneider, C. and Scherer, D. (2010): Exceptional ablation season 2009 on the Zhadang Glacier, Central Tibet - An approach combining field measurements and numerical modelling, EGU General Assembly 2010, Wien.

Maussion, F., Yang, W., Huintjes, E., Pieczonka, T., Scherer, D., Yao, T., Kang, S., Bolch, T., Buchroithner, M. and Schneider, C. (2011a): Glaciological field studies at Zhadang Glacier (5500 – 6095 m), Tibetan Plateau. Workshop on the use of automatic measuring systems on glaciers, IASC Workshop, Pontresina (Switzerland).

Maussion, F., Scherer, D., Finkelnburg, R., Richters, J., Yang, W. and Yao, T. (2011b): WRF simulation of a precipitation event over the Tibetan Plateau, China – an assessment using remote sensing and ground observations, Hydrol. Earth Syst. Sci., 15, 1795-1817.

Maussion, F., Scherer, D., Mölg, T., Collier, E., Curio, J. and Finkelnburg, R. (2014): Precipitation seasonality and variability over the Tibetan Plateau as resolved by the High Asia Reanalysis. J. Climate,27, 1910-1927.

Meyerhoff, A.A., Kamen-Kaye, M., Chen, C. and Taner, I. (1991): China – Stratigraphy, Palaeogeography and Tectonics, Kluwer Academic Publishers, 188 pp.

Miehe, G., Winiger, M., Böhner, J. and Zhang, Y. (2001): The climatic diagram map of High Asia, Erdkunde, 55, 94-98.

Miehe, G., Miehe, S., Vogel, J., Co, S. and Duo, L. (2007): Highest treeline in the northern hemisphere found in southern Tibet, Mountain Research and Development, 27, 2, 169-173.

Miehe, G., Miehe, S., Kaiser, K., Liu, J. and Zhao, X. (2008): Status and dynamics of the Kobresia pygmaea ecosystem on the Tibetan Plateau, Ambio, 37, 4, 272-279.

Mischke, S. and Zhang, C. (2010): Holocene cold events on the Tibetan Plateau, Global and Planetary Change, 72, 155-163.

Mölg, T. and Hardy, D.R. (2004): Ablation and associated energy balance of a horizontal glacier surface on Kilimanjaro. J. Geophys. Res., 109, D16104.

Mölg, T., Cullen, N.J., Hardy, D.R., Kaser, G. and Klok, E.J. (2008): Mass balance of a slope glacier on Kilimanjaro and its sensitivity to climate, Int. J. Climatol., 28, 881-892.

Mölg, T., Cullen, N.J., Hardy, D.R., Winkler, M. and Kaser, G. (2009a): Quantifying climate change in the tropical midtroposphere over East Africa from glacier shrinkage on Kilimanjaro, J. Climate, 22, 4162-4181.

Mölg, T., Cullen, N.J. and Kaser, G. (2009b): Solar radiation, cloudiness and longwave radiation over low-latitude glaciers: Implications for mass balance modelling. J. Glaciol., 55, 292-302.

Mölg, T., Maussion, F., Yang, W., Scherer, D. (2012): The footprint of Asian monsoon dynamics in the mass and energy balance of a Tibetan glacier. TC, 6, 1445-1461.

Mölg, T. and Scherer, D. (2012): Retrieving important mass-balance model parameters from AWS measurements and high-resolution mesoscale atmospheric modelling. J. Glaciol., 58, 209, 625-628.

Mölg, T., Maussion, F. and Scherer, D. (2014): Mid-latitude westerlies as a driver of glacier variability in monsoonal High Asia. Nature Climate Change, 4, 68-73.

Möller, M., Schneider, C. and Kilian, R. (2007): Glacier change and climate forcing in recent decades at Gran Campo Nevado, southernmost Patagonia, Ann. Glaciol., 46, 136-144.

Möller, M. (2011): Observation and modelling of glacier mass balances in Patagonia and Svalbard – Application and enhancement of temperature-index based modelling approaches, Dissertation, RWTH Aachen University, 145 pp.

Molnar, P. (2005): Mio-Pliocene growth of the Tibetan Plateau and evolution of East Asian climate, Paleontologica Electronica, 8.1.2, 23 pp.

Molnar, P., Boos, W.R. and Battisti, D.S. (2010): Orographic controls on climate and paleoclimate of Asia: Thermal and mechanical roles of the Tibetan Plateau, Annu. Rev. Earth Planet. Sci., 38, 77-102.

Morris, E.M. (1989): Turbulent transfer over snow and ice. J. Hydrol., 105, 205-223.

Mukhopadhyay, B. and Khan, A. (2014): Rising river flows and glacial mass balance in central Karakoram, J. Hydrol., 513, 192-203.

Mulch, A. and Chamberlain, C.P. (2006): The rise and growth of Tibet, Nature, 439, 670-671.

Murphy, M.A., An, Y., Harrison, T.M., Dürr, S.B., Chen, Z., Ryerson, F.J., Kidd, W.S.F., Wang, X. and Zhou, X. (1997): Did the Indo-Asian collision alone create the Tibetan plateau?, Geology, 25, 8, 719-722.

Neckel, N., Braun, A., Kropacek, J. and Hochschild, V. (2013): Recent mass balance of the Purogangri Ice Cap, central Tibetan Plateau, by means of differential X-band SAR interferometry, TC, 7, 1623-1633.

Neckel, N., Kropacek, J., Bolch, T. and Hochschild, V. (2014): Glacier mass changes on the Tibetan Plateau 2003-2009 derived from ICESat laser altimetry measurements, Environ. Res. Let., 9, doi:10.1088/1748-9326/9/1/014009.

Nicholson, L.I. and Benn, D.I. (2006): Calculating ice melt beneath a debris layer using meteorological data, J. Glaciol., 52, 178, 463-470.

Nicholson, L.I., Prinz, R., Mölg, T. and Kaser, G. (2013): Micrometeorological conditions and surface mass and energy fluxes on Lewis Glacier, Mt Kenya, in relation to other tropical glacier, TC, 7, 1205-1225.

Nussbaumer, S.U., Zumbühl, H. and Steiner, D. (2007): Fluctuations of the Mer de Glace (Mont Blanc area, France) AD 1500-2050. An interdisciplinary approach using new historical data and neural network simulations, Z. Gletscherk. Glazialgeol., 40, 1-183.

Oerlemans, J. and Knap, W.H. (1998): A 1 year record of global radiation and albedo in the ablation zone of Morteratschgletscher, Switzerland. J. Glaciol., 44, 147, 231-238.

Oerlemans, J. (2001): Glaciers and Climate Change, Swets & Zeitlinger, 148 pp.

Oerlemans, J. (2007): Estimating response times of Vadret da Morteratsch, Vadret da Palü, Briksdalsbreen and Nigardsbreen from their length record, J. Glaciol., 53, 357-362.

Oerlemans, J. (2010): The microclimate of valley glaciers, Igitur, 138 pp.

Ohmura, A. (2001): Physical basis for the temperature-based melt-index method, J. Appl. Meteorol., 40, 4, 753-761.

Owen, L.A., Finkel, R.C. and Caffee, M.W. (2002): A note on the extent of glaciation throughout the Himalaya during the global Last Glacial Maximum, Quaternary Science Reviews, 21, 147-157.

Owen, L.A., Finkel, R.C., Ma, H., Spencer, J.Q., Derbyshire, E., Barnard, P.L. and Caffee, M.W. (2003): Timing and style of Late Quaternary glaciation in northeastern Tibet, GSA Bulletin, 115, 11, 1356-1364.

Owen, L.A., Finkel, R.C., Barnard, P.L., Haizhou, M., Asahi, K., Caffee, M.W. and Derbyshire, E. (2005): Climatic and topographic controls on the style and timing of Late Quaternary glaciation throughout Tibet and the Himalaya defined by 10Be cosmogenic radionuclide surface exposure dating, Quat. Sci. Rev., 24, 1391-1411.

Owen, L.A., Finkel, R.C., Ma, H. and Barnard, P.L. (2006): Late Quaternary landscape evolution in the Kunlun Mountains and Qaidam Basin, Northern Tibet: A framework for examining the links between glaciation, lake level changes and alluvial fan formation, Quaternary International, 154-155, 73-86.

Owen, L.A., Caffee, M.W., Finkel, R.C. and Seong, Y. (2008): Quaternary glaciation of the Himalayan-Tibetan orogen, J. Quaternary Sci., 23, 6-7, 513-531.

Owen, L.A. (2009): Latest Pleistocene and Holocene glacier fluctuations in the Himalaya and Tibet, Quaternary Science Reviews, 28, 2150-2164.

Owen, L.A., Yi, C., Finkel, R.C. and Davis, N.K. (2010): Quaternary glaciation of Gurla Mandhata (Naimon'anyi), Quaternary Science Reviews, 29, 1817-1830.

Palazzi, E., von Hardenberg, J. and Provenzale, A. (2013): Precipitation in the Hindu-Kush Karakoram Himalaya: Observations and future scenarios, J. Geophys. Res.: Atmospheres, 118, 85-100.

Paterson, W.S.B. (1994): The Physics of Glaciers, Pergamon, 480 pp.

Penna, D., Engel, M., Mao, L., Dell'Agnese, A., Bertoldi, G. and Comiti, F. (2014): Tracer-based analysis of spatial and temporal variation of water sources in a glacierized catchment, Hydrol. Earth Syst. Sci. Discuss., 11, 4879-4924.

Phan, V.H., Lindenbergh, R. and Menenti, M. (2011): ICESat derived elevation changes of Tibetan lakes between 2003 and 2009, Int. J. Appl. Earth Observ. Geoinf., 17, 12-22.

Phan, V.H., Lindenbergh, R. and Menenti, M. (2014): Orientation dependent glacial changes at the Tibetan Plateau derived from 2003-2009 ICESat laser altimetry, TCD, 8, 2425-2463.

Qin, J., Yang, K., Liang, S. and Guo, X. (2009): The altitudinal dependence of recent rapid warming over the Tibetan Plateau, Climatic Change, 97, 321-327.

Qiu, J. (2008): The third pole, Nature News, 454, 393-396.

Rabus, B., Eineder, M., Roth, A. and Bamler, R. (2003): The shuttle radar topography mission – a new class of digital elevation models acquired by spaceborne radar, J. Photogramm. Remote Sens., 57, 241-262.

Raper, S.C.B. and Braithwaite, R.J. (2009): Glacier volume response time and its links to climate and topography based on a conceptual model of glacier hypsometry, TC, 3, 183-194.

Reijmer, C.H. and Hock, R. (2008): Internal accumulation on Storglaciären, Sweden, in a multi-layer snow model coupled to a distributed energy and mass balance model, J. Glaciol., 54, 184, 61-72.

Ren, J., Jing, Z., Pu, J. and Qin, X. (2006): Glacier variations and climate change in the central Himalaya over the past few decades, Ann. Glaciol., 43, 218-222.

Richardson, S.D. and Reynolds, J.M. (2000): An overview of glacial hazards in the Himalayas, Quaternary International, 65/66, 31-47.

Royden, L.H., Burchfiel, B.C. and Van der Hilst, R.D. (2008): The geological evolution of the Tibetan Plateau, Science, 22, 321, 1054-1058.

Sakai, A., Chikita, K. and Yamada, T. (2000): Expansion of a moraine-dammed glacial lake, Tsho Rolpa, in Rolwaling Himal, Nepal Himalaya, Limnol. Oceanogr., 45, 6, 1401-1408.

Sakai, A., Nishmura, K., Kadota, T. and Takeuchi, N. (2009): Onset of calving at supraglacial lakes on debris-covered glaciers of the Nepal Himalaya, J. Glaciol., 55, 193, 909-917.

Sakai, A. (2012): Glacial lakes in the Himalayas: A review on formation and expansion processes, Glob. Environ. Res., 16, 23-30.

Scherler, D., Bookhagen, B. and Strecker, M.R. (2011): Spatially variable response of Himalayan glaciers to climate change affected by debris cover, Nature Geoscience, DOI: 10.1038/NGEO1068.

Schiemann, R., Lüthi, D. and Schär, C. (2009): Seasonality and interannual variability of the westerly jet in the Tibetan Plateau region, J. Climate, 22, 2940-2957.

Schneider, C., Huintjes, E., Bhattacharya, A., Sauter, T., Yang, W., Bolch, T., Pieczonka, T., Maussion, F., Kang, S., Buchroithner, M., Scherer, D. and Yao, T. (2011): Calibration of a distributed ablation model for Zhadang Glacier, Tibetan Plateau, using a time lapse camera system. AGU Fall Meeting 2011, San Francisco.

Schneider, C., Yao, T., Scherer, D., Kang, S., Buchroithner, M., Fink, M., Hochschild, V., Bendix, J., Kropacek, J., Maussion, F., Yang, W., Huintjes, E., Biskop, S., Curio, J., Zhang, G., Ruethrich, F., Thies, B., Spiess, M., Neckel, N, Holzer, N. and Schroeter, B. (2013): Advances in the process-related understanding of atmosphere-cryosphere-hydrosphere couplings on the Tibetan Plateau. Himalayan Karakorum Tibet Workshop & International Symposium on Tibetan Plateau 2013, Tübingen.

Schöner, W. (2003): Massenhaushaltsbestimmung alpiner Gletscher, Arbeitsunterlagen für die Lehrveranstaltung “Gletscherhaushaltsuntersuchungen” am Institut für Meteorologie und Physik der Universität für Bodenkultur Wien und am Institut für Meteorologie und Geophysik der Universität Wien, 36 pp.

Schütt, B., Berking, J., Frechen, M. and Yi, C. (2008): Late pleistocene lake level fluctuations of the Nam Co, Tibetan Plateau, China. Z. Geomorph., Supplementary Issues, 52, 2, 57-75.

Seong, Y.B., Owen, L.A., Bishop, M.P., Bush, A., Clendon, Pl, Copland, P., Finkel, R., Kamp, U. and Shroder, J.F. (2007): Quaternary glacial history of the Central Karakoram, Quat. Sci. Rev., 26, 3384-3405.

Seong, Y.B., Owen, L.A., Yi, C. and Finkel, R.C. (2009a): Quaternary glaciation of Muztag Ata and Kongur Shan: Evidence for glacier response to rapid climate changes throughout the Late Glacial and Holocene in westernmost Tibet, GSA Bulletin, 121, 3/4, 348-365.

Seong, Y.B., Owen, L.A., Yi, C., Finkel, R.C. and Schoenbohm, L. (2009b): Geomorphology of anomalously high glaciated mountains at the northwestern end of Tibet: Muztag Ata and Kongur Shan, Geomorphology, 103, 227-250.

Shangguan, D., Liu, S., Ding, Y., Ding, L, Xiong, L., Cai, D., Li, G., Lu, A., Zhang, S. and Zhang, Y. (2006): Monitoring the glacier changes in the Muztag Ata and Konggur mountains, east Pamirs, based on Chinese Glacier Inventory and recent satellite imagery, Ann. Glaciol., 43, 79-85.

Shangguan, D., Liu, S., Ding, Y., Li, J., Zhang, Y., Ding, L., Wang, X., Xie, C. and Li, G. (2007): Glacier changes in the west Kunlun Shan from 1970 to 2001 derived from Landsat TM/ETM+ and Chinese glacier inventory data, Ann. Glaciol., 46, 204-208.

Sheng, Y. and Yao, T. (2009): Integrated assessments of environmental change on the Tibetan Plateau, Environm. Res. Lett., 4, doi:10.1088/1748-9326/4/4/045201.

Shi, Y., Zheng, B. and Li, S. (1992): Last glaciation and maximum glaciation in the Qinghai-Xizang (Tibet) plateau: a controversy to M. Kuhle’s ice sheet hypothesis, Chinese Geographical Science, 2, 4, 293-311.

Shi, Y. and Liu, S. (2000): Estimation on the response of glaciers in China to the global warming in the 21st century, Chinese Sci. Bull., 45, 7, 668-672.

Shi, Y., Liu, C. and Kang, E. (2009): The glacier inventory of China, Ann. Glaciol., 50, 53, 1-4, doi:10.3189/685172756410790595831.

Shi, Y. (2002): Characteristics of late Quaternary monsoonal glaciation on the Tibetan Plateau and in East Asia, Quaternary International, 97/98, 79-91.

Singer, B.S., Ackert, R.P. and Guillou, H. (2004): 40Ar/39Ar and K-Ar chronology of Pleistocene glaciations in Patagonia, Geological Society of America Bulletin, 116, 434–450.

Singh, P. and Singh, V.P. (2001): Snow and glacier hydrology, Kluwer, 742 pp.

Skamarock, W.C. and Klemp, J.B. (2008): A time-split nonhydrostatic atmospheric model for weather research and forecasting applications, J. Comput. Phys., 227, 3465-3485.

Smith, J.A., Farber, D.L., Seltzer, G.O., Finkel, R.C. and Rodbell, D.T. (2002): Chronology of tropical glaciation from cosmogenic dating, Eos (Transactions, American Geophysical Union), 83, 47, F922.

Song, C., Huang, B., Ke, L. and Richards, K.S. (2014a): Seasonal and abrupt changes in the water level of closed lakes on the Tibetan Plateau and implications for climate impacts, Journal of Hydrology, 514, 131-144.

Song, C., Huang, B., Richards, K., Ke, L. and Phan, V.H. (2014b): Accelerated lake expansion on the Tibetan Plateau in the 2000s: induced by glacial melting or other processes?, Water Resour. Res., doi: 10.1002/2013WR014724.

Spieß, M., Maussion, F., Möller, M., Scherer, D. and Schneider, C. (2014): An approach to analyse snow lines from MODIS data for glaciers on the Tibetan Plateau., 7th EARSeL workshop on Land Ice and Snow, Bern.

Sturm, M., Holmgren, J., König, M. and Morris, K. (1997): The thermal conductivity of seasonal snow, J. Glaciol., 43, 143, 26-41.

Sturm, M. and Holmgren, J. (1998): Differences in compaction behaviour of three climate classes of snow, Ann. Glaciol., 26, 125-130.

Su, Z. and Shi, Y. (2002): Response of monsoonal temperate glaciers to global warming since the Little Ice Age, Quaternary International, 97-98, 123-131.

Sun, D. (2004): Monsoon and westerly circulation changes recorded in the late Cenozoic sequences of Northern China, Global and Planetary Change, 41, 63-80.

Takaya, K. and Nakamura, H. (2013): Interannual variability of the East Asian winter monsoon and related modulations of the planetary waves, J. Climate, 26, 9445-9461.

Takeuchi, N., Miyake, T., Nakazawa, F., Narita, H., Fujita, K., Sakai, A., Nakawo, M., Fujii, Y., Duan, K. and Yao, T. (2009): A shallow ice core re-drilled on the Dunde Ice Cap, western China: recent changes in the Asian high mountains, Environ. Res. Lett., 4, doi:10.1088/1748-9326/4/4/045207.

Tao, S. and Ding, Y. (1981): Observational evidence of the influence of the Qinghai-Xizang (Tibet) Plateau on the occurrence of heavy rain and severe convective storms in China, Bulletin American Meteorological Society, 62, 1, 23-30.

Thompson, L.G., Yao, T., Davis, M.E., Mosley-Thompson, E., Mashiotta, T.A., Lin, P., Mikhalenko, V.N. and Zagorodnov, V.S. (2006): Holocene climate variability archived in the Puruogangri ice cap on the central Tibetan Plateau, Ann. Glaciol., 43, 61-69.

UIT (Umwelt- und Ingenieurleistungen) (undated): Bedienhandbuch CTD-GPRS, Version 3.0, Dresden, 34pp.

Van den Broeke, M.R., Smeets, C.J.P.P. and Van de Wal, R.S.W. (2011): The seasonal cycle and interannual variability of surface energy balance and melt in the alblation zone of the west Greenland ice sheet, TC, 5, 377-390.

Van Pelt, W.J.J., Oerlemans, J., Reijmer, C.H., Pohjola, V.A., Pettersson, R. and van Angelen, J.H. (2012): Simulating melt, runoff and refreezing on Nordenskiöldbreen, Svalbard, using a coupled snow and energy balance model. TC, 6, 641-659.

Vionnet, V., Brun, E., Morin, S., Boone, A., Faroux, S., Le Moigne, P., Martin, E. And Willemet, J.M. (2012): The detailed snowpack scheme Crocus and its implementation in SURFEX v7.2, Geoscientific Model Development, 5, 773-791.

Wallace, J.M. and Gutzler, D.S. (1981): Teleconnections in the geopotential height field during the Northern Hemisphere winter, Monthly Weather Review, 109, 784-812.

Wang, F. and Li, B. (1985): The lower boundary of the Quaternary in the Himalayan region in China. In: Liu, T. (Edt.) (1985): Quaternary geology and environment of China, Springer, 18-22.

Wang, R.L., Scarpitta, S.C., Zhang, S.C. and Zheng, M.P. (2002): Later Pleistocene/Holocene climate conditions of Qinghai-Xizhang Plateau (Tibet) based on carbon and oxygen stable isotopes of Zabuye Lake sediments, Earth and Planetary Science Letters, 203, 461-477.

Wang, G., Li, Y., Wu, Q. and Wang, Y. (2006): Impacts of permafrost changes on alpine ecosystem in Qinghai-Tibet Plateau, Science in China Series D: Earth Sciences, 49, 11, 1156-1169.

Wang, G., Hu, H. and Li, T. (2009): The influence of freeze-thaw cycles of active soil layer on surface runoff in a permafrost watershed, J. Hydrol., 375, 3-4, 438-449.

Wei, Y. and Fang, Y. (2013): Spatio-temporal characteristics of global warming in the Tibetan Plateau during the last 50 years based on a generalised temperature zone – elevation model, PLOS ONE, 8, 4, e60044.

Wei, J., Liu, S., Guo, W., Yao, X., Xu, J., Bao, W. and Jiang, Z. (2014): Surface-area changes of glaciers in the Tibetan Plateau interior area since the 1970s using recent Landsat images and historical maps, Ann. Glaciol., 55, 66, 213-222.

Wischnewski, J., Mischke, S., Wang, Y. and Herzschuh, U. (2011): Reconstructing climate variability on the northeastern Tibetan Plateau since the late Lateglacial – a multi-proxy, dual site approach comparing terrestrial and aquatic signals, Quaternary Science Reviews, 30, 82-97.

Wu, B. (2005): Weakening of Indian summer monsoon in recent decades, Adv. Atmos. Sci., 22, 21-29.

Wu, Y. and Zhu, L. (2008): The response of lake-glacier variations to climate change in the Nam Co Catchment, central Tibetan Plateau, during 1970-2000, J. Geogr. Sci., 18, 177-189.

Wu, Z., Wang, B., Li, J. and Jin, F. (2009): An empirical seasonal prediction model of the east Asian summer monsoon using ENSO and NAO, J. Geophys. Res., 114, D18120, doi:10.1029/2009JD011733.

Wu, Q. and Zhang, T. (2010): Changes in active layer thickness over the Qinghai-Tibetan Plateau from 1995 to 2007, J. Geophys. Res., 115, D09107, doi:10.1029/2009JD012974.

Wu, Q., Zhang, T. and Liu, Y. (2010): Permafrost temperatures and thickness on the Qinghai-Tibet Plateau, Global and Planetary Change, 72, 32-38.

Wu, G., Liu, Y., He, B., Bao, Q., Duan, A. and Jin, F. (2012): Thermal controls on the Asian summer monsoon, Scientific Reports, 2, 404, doi: 10.1038/srep00404.

Wu, H., Wang, N., Jiang, X. and Guo, Z. (2014): Variations in water level and glacier mass balance in Nam Co lake, Nyainqentanglha range, Tibetan Plateau, based on ICESat data for 2003-09, Ann. Glaciol., 55, 66, 239-247.

Xie, H., Ye, J., Liu, X. and E, C. (2010): Warming and drying trends on the Tibetan Plateau (1971-2005), Theor. Appl. Climatol., 101, 241-253.

Xu, X. and Yi, C. (2014): Little Ice Age on the Tibetan Plateau and its bordering mountains: Evidence from moraine chronologies, Global and Planetary Change, 116, 41-53.

Xue, X., Guo, J., Han, B., Sun, Q. and Liu, L. (2009): The effect of climate warming and permafrost thaw on desertification in the Qinghai-Tibetan Plateau, Geomorphology, 108, 182-190.

Yang, B., Bräuning, A., Dong, Z., Zhang, Z. and Keqing, J. (2008): Late Holocene monsoonal temperate glacier fluctuations on the Tibetan Plateau, Global and Planetary Change, 60, 126-140.

Yang, B., Bräuning, A., Liu, J., Davis, M.E. and Yajun, S. (2009): Temperature changes on the Tibetan Plateau during the past 600 years inferred from ice cores and tree rings, Global and Planetary Change, 69, 71-78.

Yang, K., Guo, X., He, J., Qin, J. and Koike, T. (2010a): On the climatology and trend of the atmospheric heat source over the Tibetan Plateau: An experiments-supported revisit, J. Climate, 24, 5, 1525-1541.

Yang, M., Nelson, F.E., Shiklomanov, N.I., Guo, D. and Wan, G. (2010b): Permafrost degradation and its environmental effects on the Tibetan Plateau: A review of recent research, Earth-Science Reviews, 103, 31-44.

Yang, W., Guo, X., Yao, T., Yang, K., Zhao, L., Li, S. and Zhu, M. (2011): Summertime surface energy budget and ablation modelling in the ablation zone of a maritime Tibetan glacier, J. Geophys. Res., 116, D14116.

Yang, W., Yao, T., Guo, X., Zhu, M., Li, S. and Kattel, D.B. (2013): Mass balance of a maritime glacier on the southeast Tibetan plateau and its climatic sensitivity, J. Geophys. Res.: Atmospheres, 118, 17, 9579-9594.

Yao, T., Duan, K., Thompson, L.G., Wang, N., Tian, L., Xu, B., Wang, Y. and Yu, W. (2007): Temperature variations over the past millennium on the Tibetan Plateau revealed by four ice cores, Ann. Glaciol., 46, 362-366.

Yao, T., Duan, K., Wang, N., Guo, X. and Yang, X. (2008): Precipitation record since AD 1600 from ice cores on the central Tibetan Plateau, Clim. Past, 4, 175-180.

Yao, T., Thompson, L., Yang, W., Yu, W., Gao, Y., Guo, X., Yang, X., Duan, K., Zhao, H., Xu, B., Pu, J., Lu, A., Xiang, Y., Kattel, D. and Joswiak, D. (2012): Different glacier status with atmospheric circulations in Tibetan Plateau and surroundings, Nature Clim. Change, 2, 663-667.

Ye, D. (1981): Some characteristics of the summer circulation over the Qinghai-Xizang (Tibet) Plateau and its neighborhood, Bulletin American Meteorological Society, 62, 1, 14-19.

Ye, Q., Tandong, Y., Kang, S., Chen, F. and Wang, J. (2006): Glacier variations in the Naimona'nyi region, western Himalaya, in the last three decades, Ann. Glaciol., 43, 385-389.

Ye, Q., Zhu, L., Zheng, H., Naruse, R., Zhang, X. and Kang, S. (2007): Glacier and lake variations in the Yamzhog Yumco basin, southern Tibetan Plateau, from 1980 to 2000 using remote-sensing and GIS technologies, J. Glaciol., 53, 183, 673-676.

Yi, C., Li, X. and Qu, J. (2002): Quaternary glaciation of Puruogangri – the last modern ice field in Tibet, Quaternary International, 97-98, 111-121.

Yi, S. and Sun, W. (2014): Evaluation of glacier changes in High Mountain Asia based on 10-year GRACE-RL05 models, J. Geophys. Res. Solid Earth, 119, 2504-2517.

You, Q., Kang, S., Li, C., Li, M. and Liu, J. (2007): Variation features of meteorological parameters at Nam Co Station, Tibetan Plateau, Meteorol. Mon., 33, 3, 54-60. [In Chinese with English summary.]

You, Q., Kang, S., Pepin, N., Flügel, W.A., Sanchez-Lorenzo, A., Yan, Y. and Zhang, Y. (2010): Climate warming and associated changes in atmospheric circulation in the eastern and central Tibetan Plateau from a homogenized dataset, Global and Planetary change, 72, 11-24.

Yu, W., Yao, T., Kang, S., Pu, J., Yang, W., Gao, T., Zhao, H., Zhou, H., Li, S., Wang, W. and Ma, L. (2013): Different region climate regimes and topography affect the changes in area and mass balance of glaciers on the north and south slopes of the same glacierized massif (the West Nyainqentanglha Range, Tibetan Plateau), J. Hydrol., 495, 64-73.

Zemp, M., Thibert, E., Huss, M., Stumm, D., Rolstad Denby, C., Nuth, C., Nussbaumer, S.U., Moholdt, G., Mercer, A., Mayer, C., Joerg, P.C., Jansson, P., Hynek, B., Fischer, A., Escher-Vetter, H., Elvhoy, H. and Andreassen, L.M. (2013): Reanalysing glacier mass balance measurement series, TC, 7, 1227-1245.

Zhang, Y., Ohata, T. and Kadata, T. (2003): Land surface hydrological processes in the permafrost region of the eastern Tibetan Plateau, J. Hydrol., 283, 41-56.

Zhang, C. and Mischke, S. (2009): A Lateglacial and Holocene lake record from the Nianbaoyeze Mountains and inferences of lake, glacier and climate evolution on the eastern Tibetan Plateau, Quaternary Science Reviews, 28, 1970-1983.

Zhang, G., Xie, H., Kang, S., Yi, D. and Ackley, S.F. (2011a): Monitoring lake level changes on the Tibetan Plateau using ICESat altimetry data (2003-2009), Remote Sensing of Environment, 115, 1733-1742.

Zhang, Y., Fujita, K., Liu, S., Liu, Q. and Nuimura, T. (2011b): Distribution of debris thickness and its effect on ice melt at Hailuogou glacier, southeastern Tibetan Plateau, using in situ surveys and ASTER imagery, J. Glaciol., 57, 206, 1147-1157.

Zhang, G., Kang, S., Fujita, K., Huintjes, E., Xu, J., Yamazaki, T., Haginoya, S., Wei, Y., Scherer, D., Schneider, C. and Yao, T. (2013): Energy and mass balance of Zhadang glacier surface, central Tibetan Plateau, J. Glaciol., 59, 213, 137-148.

Zhang, G., Yao, T., Xie, H., Kang, S. and Lei, Y. (2013): Increased mass over the Tibetan Plateau: From lakes or glaciers?, Geophys. Res. Let., 40, 2125-2130.

Zhao, S. (1986): Physical Geography of China, Science Press, 209 pp.

Zhao, H., Xu, B., Yao, T., Wu, G., Lin, S., Gao, J. and Wang, M. (2012): Deuterium excess record in a southern Tibetan ice core and its potential climatic implications. Clim. Dynam., 38, 1791-1803.

Zheng, B. and Rutter, N. (1998): On the problem of Quaternary glaciations, and the extent and patterns of Pleistocene ice cover in the Qinghai-Xizang (Tibet) plateau, Quaternary International, 45/46, 109-122.

Zhou, S., Kang, S., Gao, T., Zhang, G. (2010): Response of Zhadang Glacier runoff in Nam co Basin, Tibet, to changes in air temperature and precipitation form. Chinese Sci. Bull., 55, 2103-2110.

Zhou, S., Wang, J., Xu, L, Wang, X., Colgan, P.M. and Mickelson, D.M. (2010): Glacial advances in southeastern Tibet during late Quaternary and their implications for climatic changes, Quaternary International, 218, 58-66.

Zhu, L., Xie, M. and Wu, Y. (2010): Quantitative analysis of lake area variations and the influence factors from 1971 to 2004 in the Nam Co basin of the Tibetan Plateau, Chinese Science Bulletin, 55, 13, 1294-1303.

Zomer, R. and Oli, K.P. (eds) (2011): Kailash sacred landscape conservation initiative – Feasibility assessment report, Kathmandu: ICIMOD, 108 pp.

# Appendix

# A Monthly glacier-wide SEB/MB components for the model runs with precipitation scaling factors 0.31 and 0.81 for the four glaciers and ice caps, 2000-2012

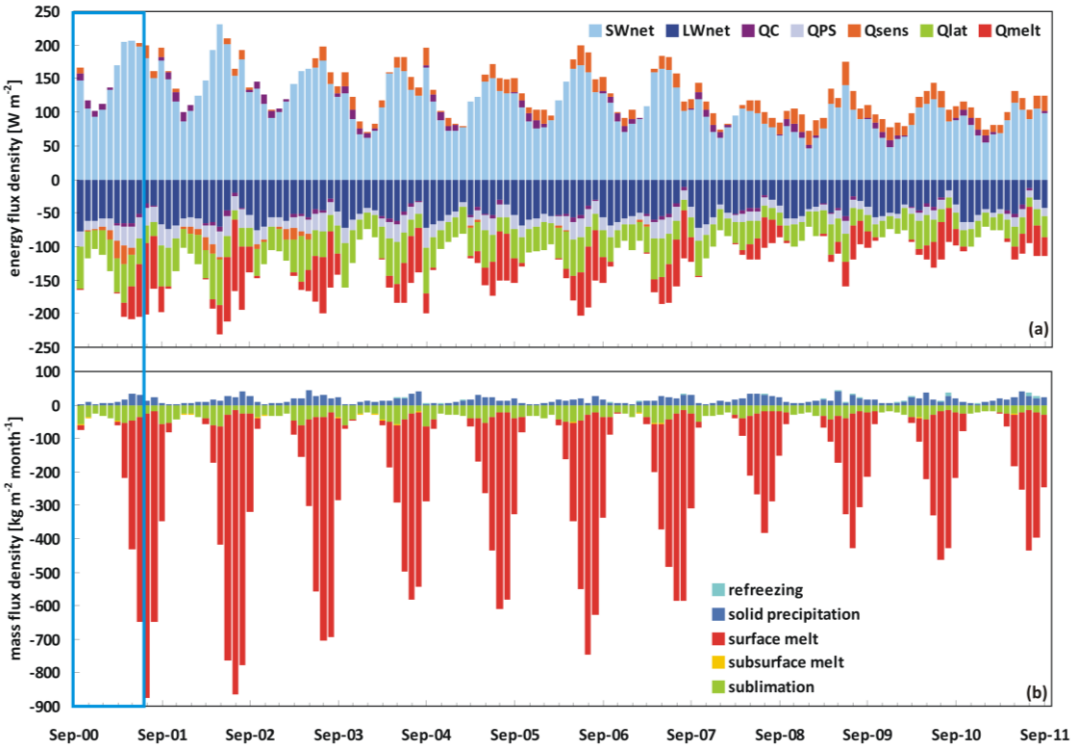


**Fig. A.1: Glacier-wide monthly (a) SEB components (see section 2.3.1 for abbreviations) and (b) MB components from October 2000 to September 2011 at PIC (precipitation scaling factor 0.31). Note that the first months (blue box) should not be considered.**

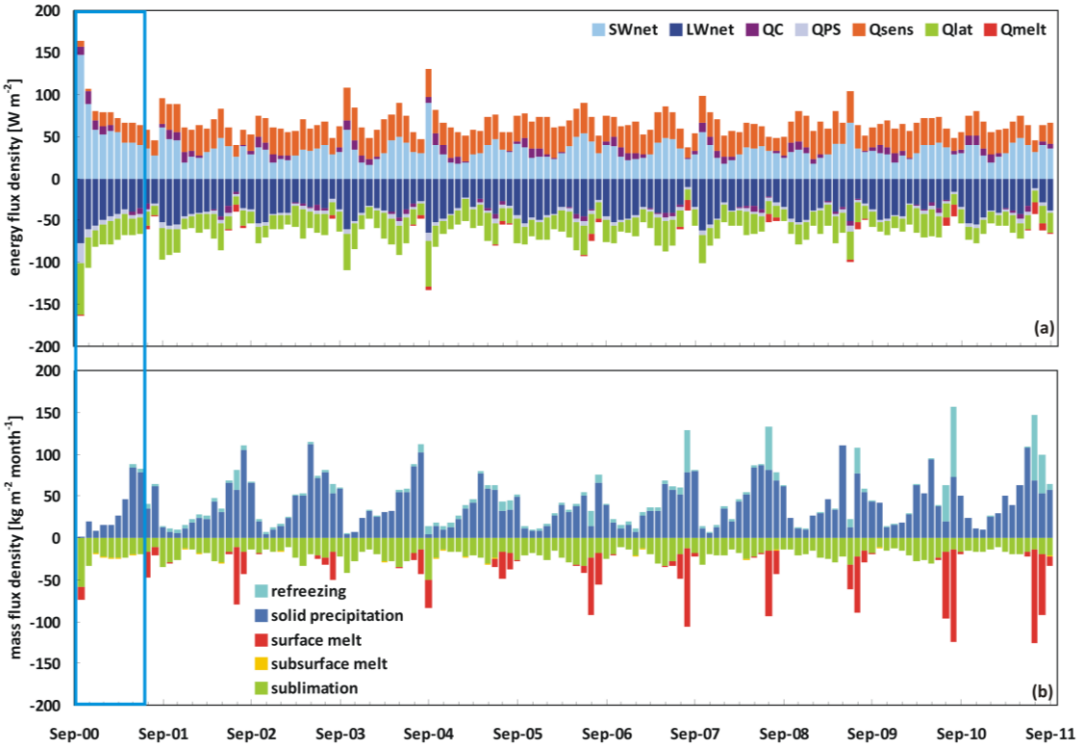


**Fig. A.2: Glacier-wide monthly (a) SEB components (see section 2.3.1 for abbreviations) and (b) MB components from October 2000 to September 2011 at PIC (precipitation scaling factor 0.81). Note that the first months (blue box) should not be considered.**

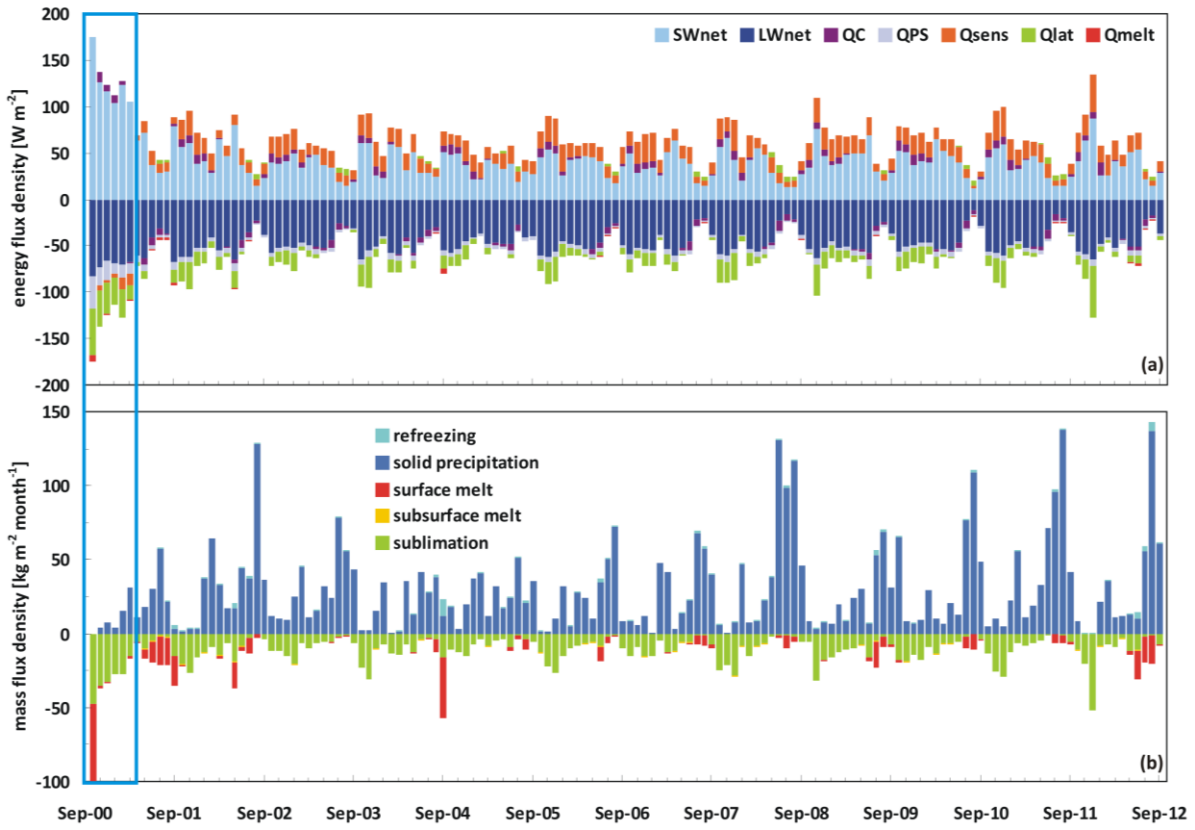


**Fig. A.3: Glacier-wide monthly (a) SEB components (see section 2.3.1 for abbreviations) and (b) MB components from October 2000 to September 2011 at Naimona'nyi glacier (precipitation scaling factor 0.31). Note that the first months (blue box) should not be considered.**

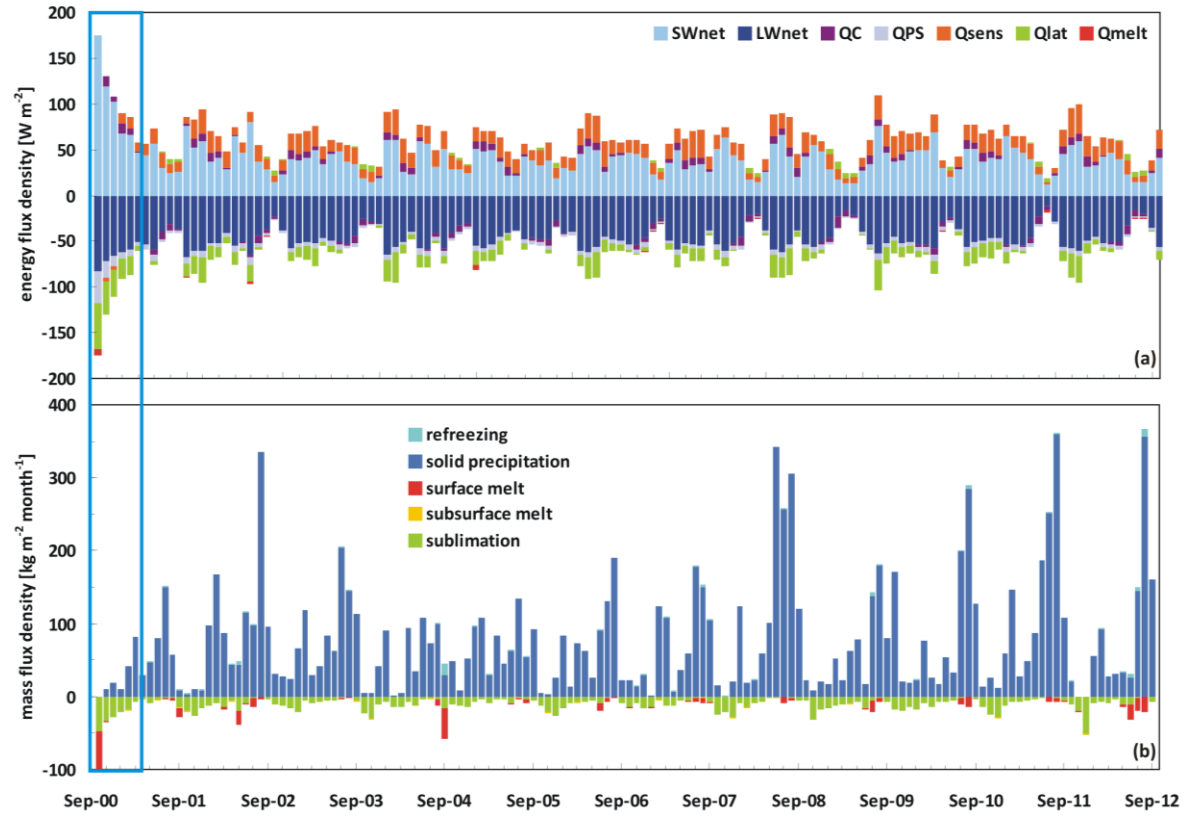


**Fig. A.4: Glacier-wide monthly (a) SEB components (see section 2.3.1 for abbreviations) and (b) MB components from October 2000 to September 2011 at Naimona'nyi glacier (precipitation scaling factor 0.81). Note that the first months (blue box) should not be considered.**

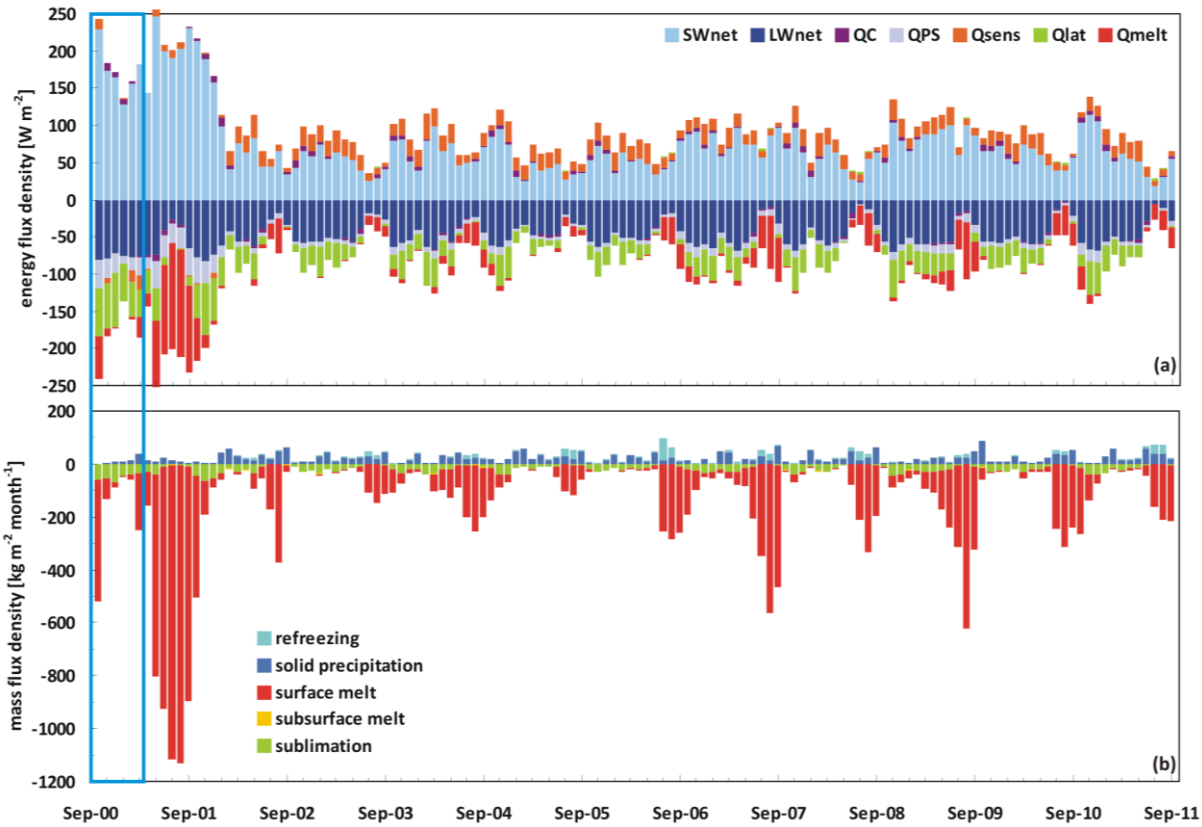


**Fig. A.5: Glacier-wide monthly (a) SEB components (see section 2.3.1 for abbreviations) and (b) MB components from October 2000 to September 2012 at Halji glacier (precipitation scaling factor 0.31). Note that the first months (blue box) should not be considered.**

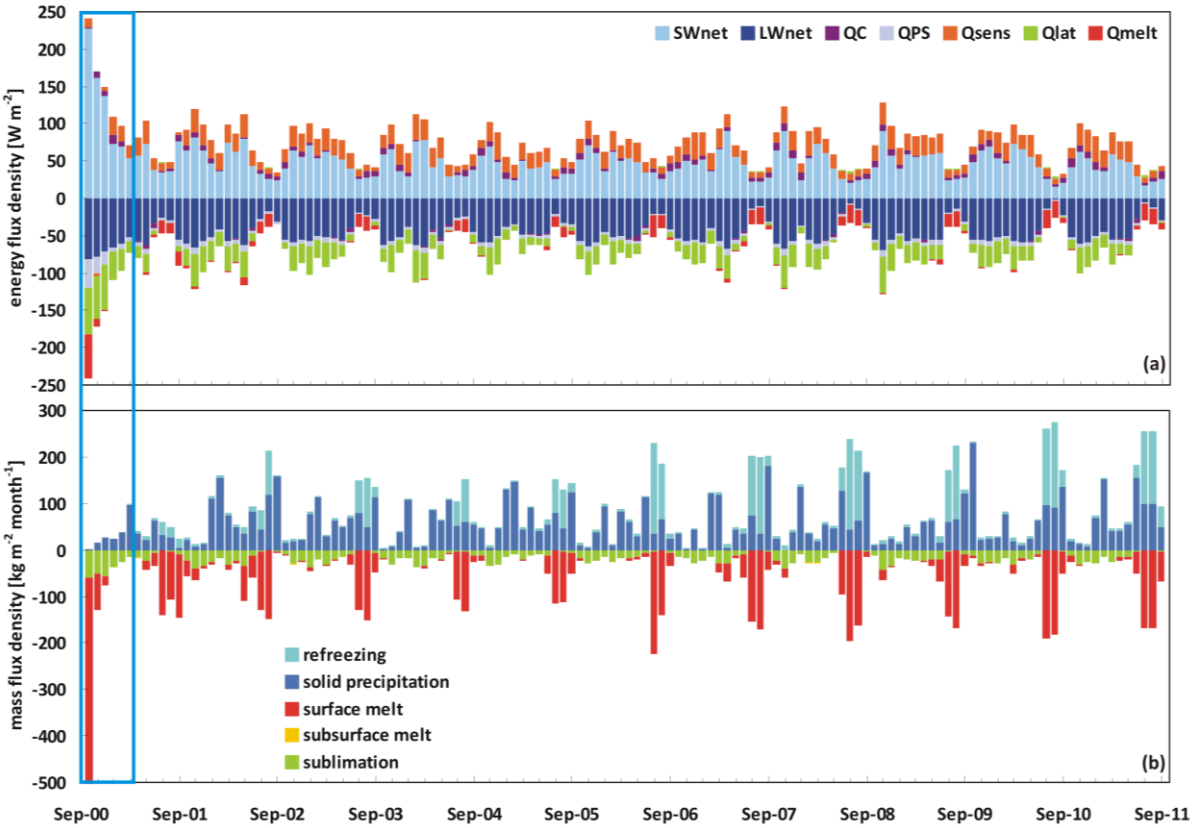


**Fig. A.6: Glacier-wide monthly (a) SEB components (see section 2.3.1 for abbreviations) and (b) MB components from October 2000 to September 2012 at Halji glacier (precipitation scaling factor 0.81). Note that the first months (blue box) should not be considered.**

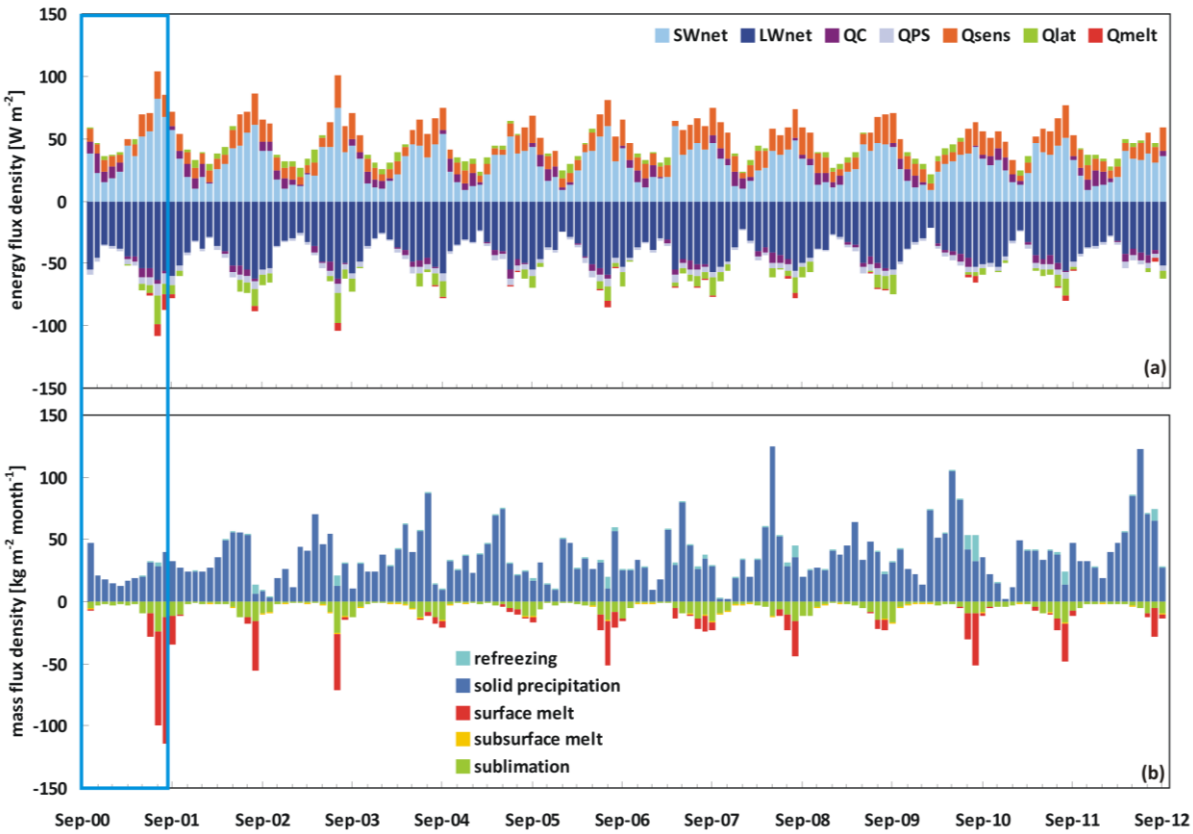


**Fig. A.7: Glacier-wide monthly (a) SEB components (see section 2.3.1 for abbreviations) and (b) MB components from October 2000 to September 2012 at Muztagh Ata glacier (precipitation scaling factor 0.31). Note that the first months (blue box) should not be considered.**

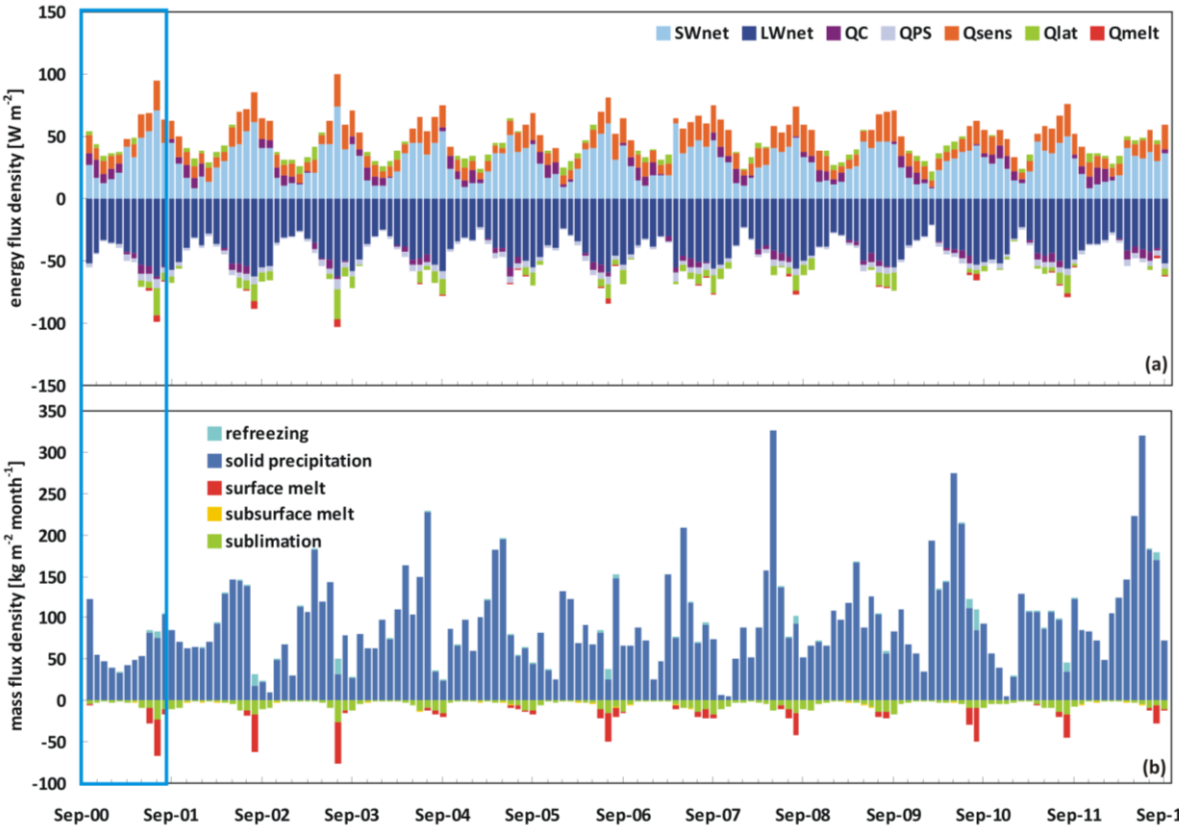


**Fig. A.8: Glacier-wide monthly (a) SEB components (see section 2.3.1 for abbreviations) and (b) MB components from October 2000 to September 2012 at Muztagh Ata glacier (precipitation scaling factor 0.81). Note that the first months (blue box) should not be considered.**

# B Comparison of monthly glacier-wide SEB and MB components for the five glaciers and ice caps, 2000-2012

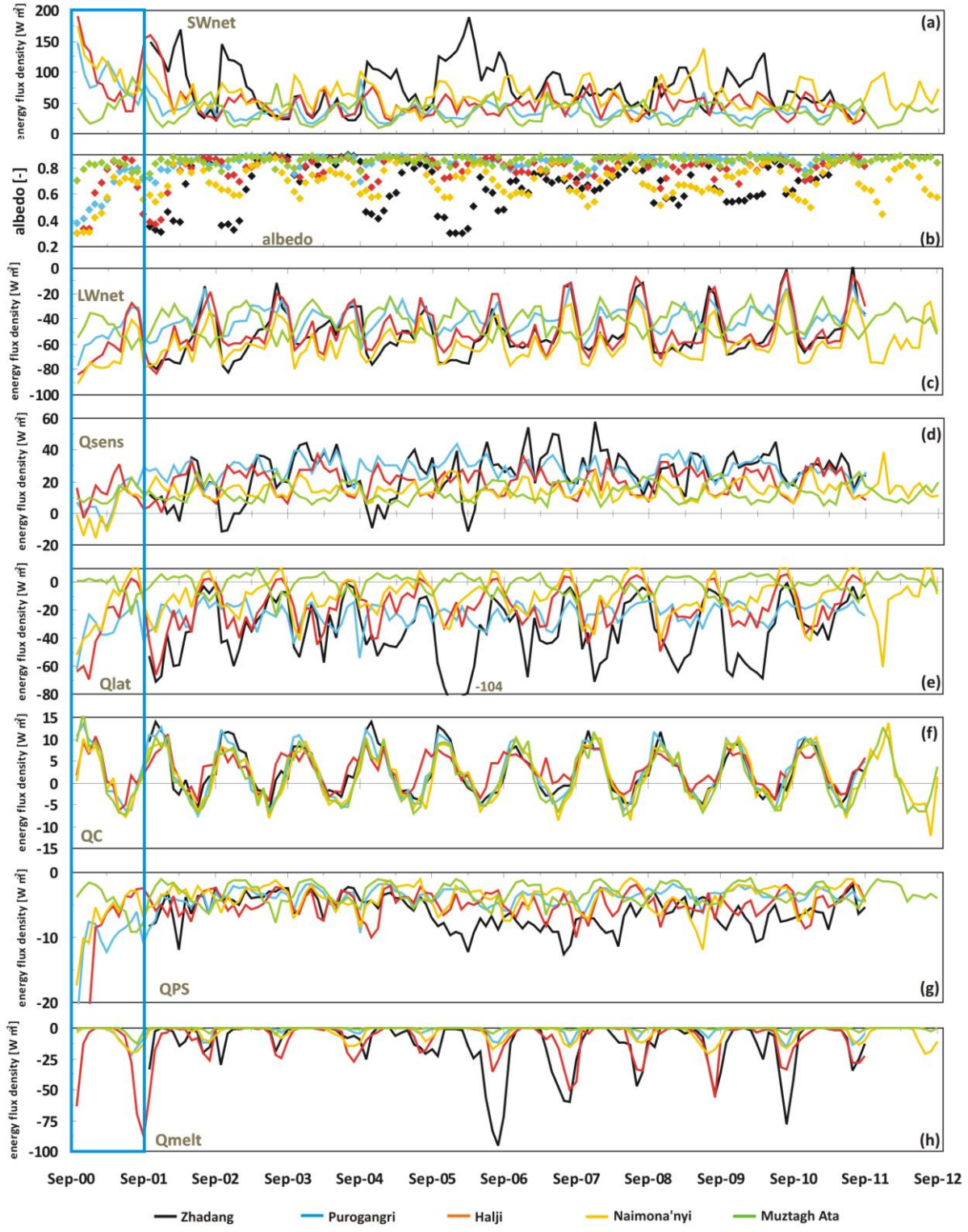


**Fig. B.1: Glacier-wide monthly SEB components for the five study sites, 2000-2012, derived from the HAR driven MB model. Note that the first year (blue box) should not be considered. Applied scaling factors for HAR precipitation and $T_{air}$ offsets are: Zhadang/PIC: 0.56/±0 K, Naimona'nyi: 0.31/+3 K, Halji: 0.56/+1 K, Muztagh Ata: 0.31/±0 K.**

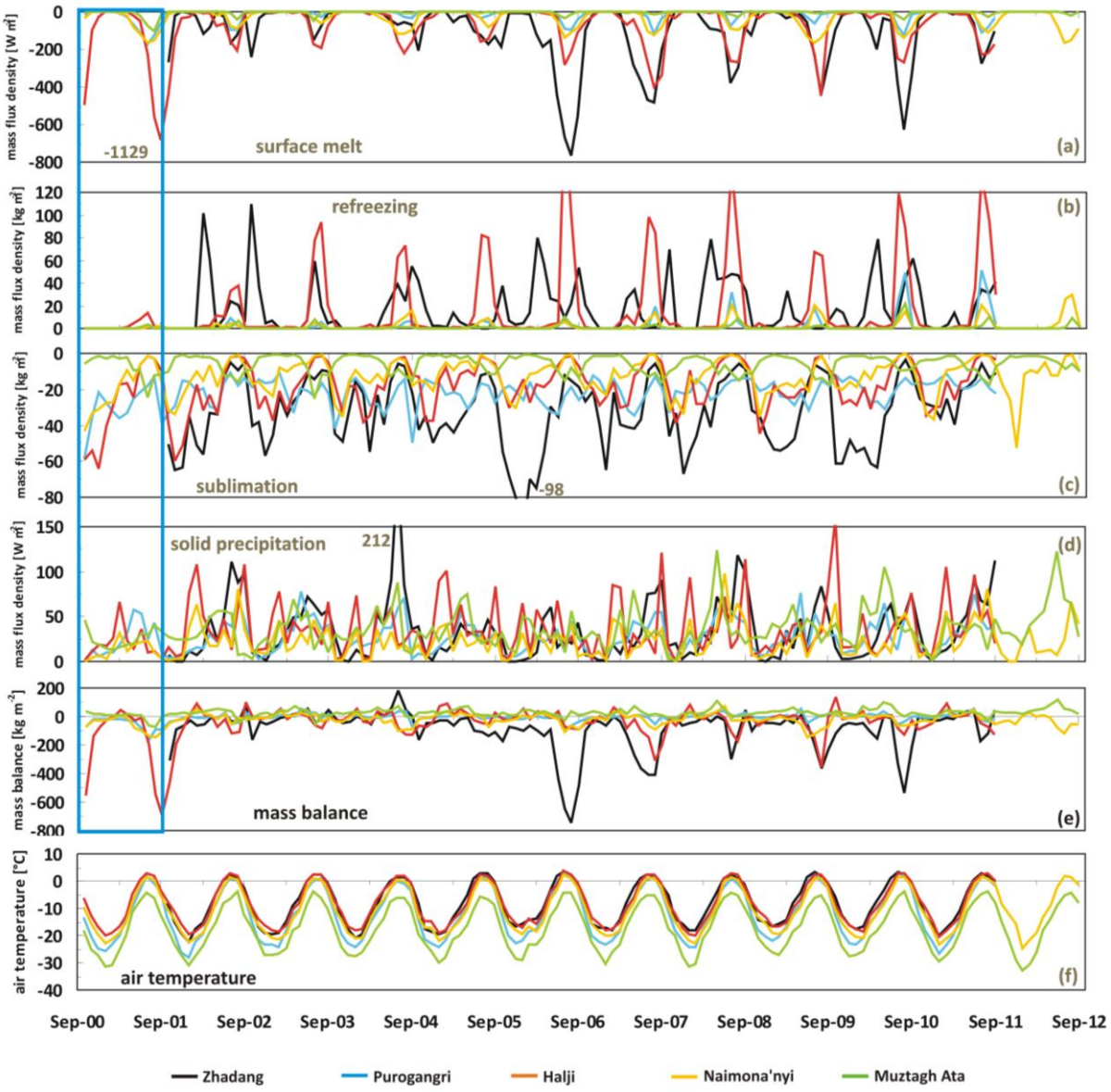


**Fig. B.2: Glacier-wide monthly MB components and $T_{air}$ for the five study sites, 2000-2012, derived from the HAR driven MB model. Note that the first year (blue box) should not be considered for the ground-dependent MB components. Applied scaling factors for HAR precipitation and $T_{air}$ offsets are: Zhadang/PIC: 0.56/±0 K, Naimona'nyi: 0.31/+3 K, Halji: 0.56/+1 K, Muztagh Ata: 0.31/±0 K.**

# C Monthly indices for selected teleconnection patterns, 2000-2012

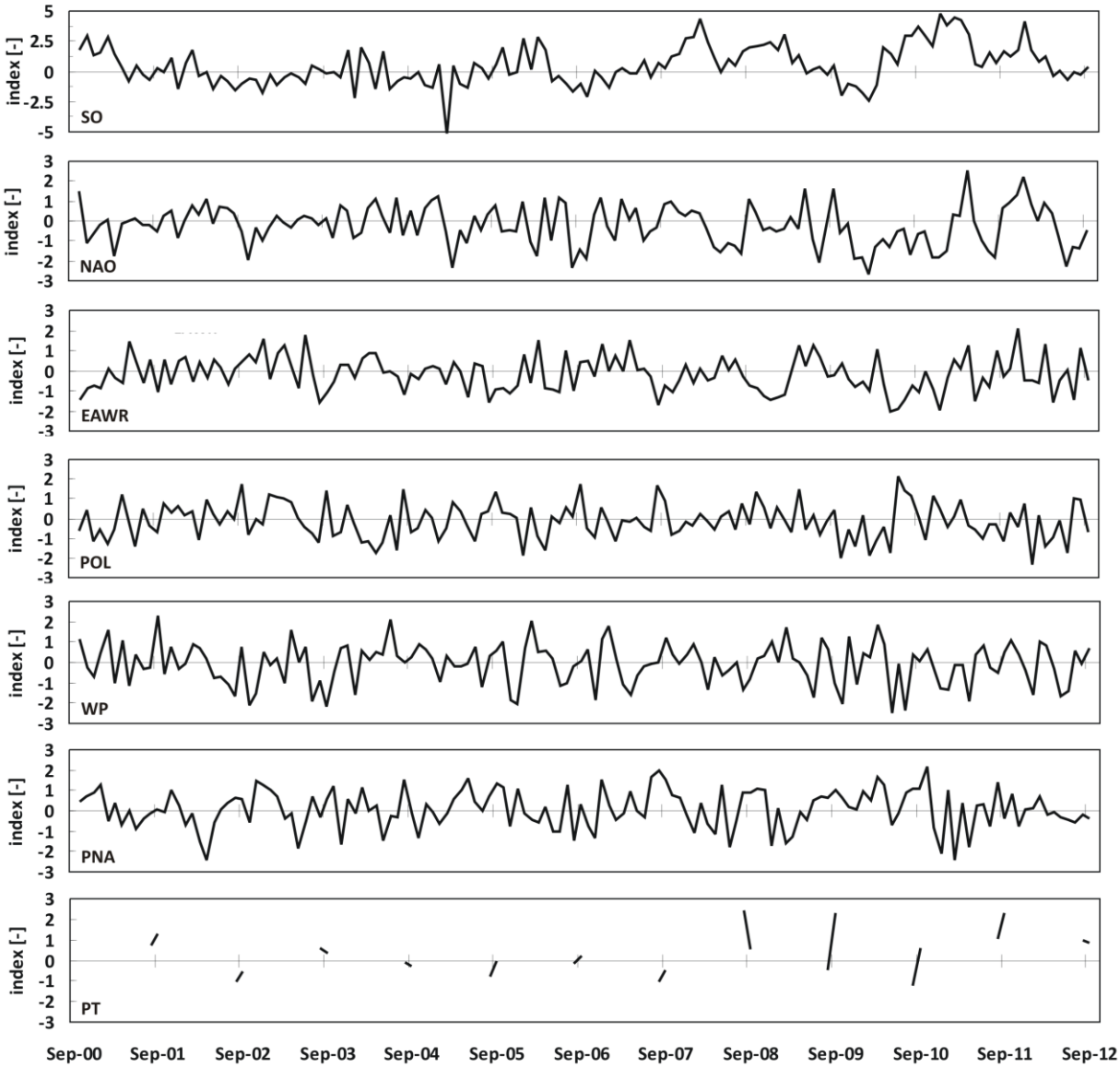


**Fig. C.1: Monthly indices for selected teleconnection patterns that influence the TP, 2000-2012. All indices are obtained from the Climate Prediction Center (NOAA)[4].**

[4] http://www.cpc.ncep.noaa.gov/